NCHRP

Project No. NCHRP 9-44 A

Validating an Endurance Limit for HMA Pavements: Laboratory Experiment and Algorithm Development

Appendix 2

Endurance Limit for HMA Based on Healing Phenomena Using Viscoelastic Continuum Damage Analysis

Prepared for

NATIONAL COOPERATIVE HIGHWAY RESEARCH PROGRAM
TRANSPORTATION RESEARCH BOARD
Of
The National Academies
Submitted by:

Matthew Witczak, Project P.I.
Michael Mamlouk, Project Co-P.I.
Mena Souliman, Research Assistant
Waleed Zeiada, Research Assistant

July 2013

TABLE OF CONTENTS

iv

LIST OF TABLES

LIST OF FIGURES

FIGURE   Page

xviii

CHAPTER 1

INTRODUCTION AND RESEARCH APPROACH

INTRODUCTION

Fatigue damage is one of the primary distresses in asphalt pavements besides thermal cracking and rutting. Fatigue cracks are a series of longitudinal cracks (which may become interconnected) caused by fatigue failure of the HMA surface (or stabilized base) under repeated traffic loading. Better understanding of fatigue damage mechanisms would enable researchers to develop accurate models to enhance the prediction of fatigue life and damage and make significant advances in the design and construction of flexible pavements.

The action of repeated loading caused by traffic induces tensile and shear stresses in the bound layers, eventually leading to loss in the structural integrity of a stabilized layer material. Fatigue typically initiates cracks at points where critical tensile strains and stresses occur. Once the damage initiates at the critical location, the action of traffic ultimately causes these cracks to propagate through the entire bound layer. Two mechanisms of fatigue cracking typically take place depending on the pavement structure. In thin pavements, cracks initiate at the bottom of the HMA layer, where the tensile stress is the highest, and then propagate to the surface. This is usually referred to as "bottom-up" or "classical" fatigue cracking. In thick pavements, cracks most likely initiate at the top in areas of high localized tensile stresses resulting from tire-pavement interaction and asphalt binder aging (usually referred to as top-down cracking).

Different test protocols have been developed over the past few decades for measuring the fatigue behavior of asphalt concrete mixtures. The quality of the fatigue life prediction using any of these test methods depends on how accurate the method is able to simulate the condition of loading, support, stress state, and environment. The most popular fatigue tests used all over the world are the beam fatigue test, trapezoidal cantilever beam test, direct tension test, tension-compression test, indirect diametral test, triaxial test, and wheel-track test. Even with the existence of current advanced technology, it is still difficult to accurately simulate the actual field conditions using these fatigue tests. Therefore, a shift factor is always used to account for the difference between fatigue life obtained in the field and in the laboratory. The magnitude of the shift factor varies depending upon many factors; (Harvey et al., 1997) reported shift factors between 10 and 100.

Fatigue behavior of asphalt concrete mixtures can be characterized using two main approaches. The first is the phenomenological approach where the stress or strain in the HMA layer is related to the number of loading repetitions that causes failure (SHRP A-404, 1994). The phenomenological approach is simple to use; however, it does not account for damage evolution through the fatigue process. The second approach is the mechanistic approach which is inherently more complex than the phenomenological one but is more widely accepted because it uses material properties based on stress-strain relationships (Kim et al., 2003). The mechanistic approach can be implemented through three different methods: dissipated energy, fracture mechanics, and continuum damage mechanics.

Dissipated energy is defined as the area under the stress-strain curve due to the viscoelastic nature of asphalt concrete mixtures at ambient temperature. The earliest work using

1

the dissipated energy with asphaltic materials was reported by Chomton and Valayer (1972) and van Dijk et al. (1972). The use of dissipated energy for fatigue life prediction has been investigated. Current applications of dissipated energy to describe fatigue behavior assume that all of the dissipated energy goes into damaging the material (Ghuzlan, 2001). In reality, this is not the case. For asphalt concrete, a hysteresis loop is created due to the viscoelasticity of the material, even if no damage is induced. Only part of the total dissipated energy goes to damaging the material, and the remainder (or recovered energy) is due to the viscoelasticity of the material and other factors (Little, 1995).

The basic concept of fracture mechanics to define the fatigue properties of asphalt mixtures was initially introduced by Griffith (1921); it considers fatigue as a process of cumulative damage. In this approach, fatigue cracking is characterized by three stages: crack initiation, stable crack propagation, and unstable crack fracture. It is usually assumed that the stable crack propagation consumes most of the fatigue life. The prediction of crack propagation life using fracture mechanics can be described by the well-known Paris' law (Paris and Erdogan, 1963).

A Continuum Damage Mechanics (CDM) approach was developed at North Carolina State University and Texas A&M University. This approach utilizes the viscoelastic correspondence principle and Work Potential Theory (WPT) described by Schapery (1984) to remove viscous effects in monitoring pseudo-stiffness changes in repeated uniaxial tensile tests. Kim (1988) developed a nonlinear elastic-viscoelastic uniaxial constitutive model by employing the extended elastic-viscoelastic correspondence principle in the concept of CDM. This approach successfully accounted for damage growth through crack initiation and propagation and healing for any load history or mode of loading. The main difference between CDM and fracture mechanics is that in CDM, cracks occur at a level and number such that they are modeled as smeared out continuously. In fracture mechanics some small numbers of cracks are considered which are of size of the scale of interest. To generalize, CDM is useful to model the degradation of a mechanical body leading up to macro-cracks and fracture mechanics is useful for modeling the mechanical body after cracks on the scale of the structure have formed.

Current flexible pavement design methods assume that cumulative damage occurs where each load cycle uses up a portion of the finite fatigue life of the HMA. However, recent studies show that HMA may exhibit an endurance limit, where properly constructed thick HMA pavements can be exposed to a very large number of loading cycles without exhibiting fatigue damage.

In 1870, the concept of the Endurance Limit (EL) was originally introduced for metals by August Wöhler (Walter Schlitz, 1996) and was defined as the stress level below which failure never occurs. The same concept was implemented for concrete roads, which was expressed by the stress ratio level. It was recognized that the endurance limit of concrete is attained when the stress level does not exceed 45 percent of the modulus of rupture value (Huang, 1993). For the HMA pavement, it has been shown that when the controlled strain/damage level is very low, distinctively different fatigue behavior can be found even for the same mixture where any small decrease in the strain level will result in a large fatigue life extension (Thomson and Carpenter, 2006). The endurance limit is an important parameter in the design of an optimal thickness of long lasting or perpetual pavements where any additional thickness will not provide any extra service life.

2

Monismith first showed that there appears to be a strain below which there is no fatigue damage to the HMA. Monismith and McLean proposed 70 microstrain as a likely value for the endurance limit (Monismith and McLean, 1972). As perpetual pavements gained more attention in the United States, a substantial amount of laboratory fatigue testing has recently been performed to demonstrate that HMA does exhibit an endurance limit. Most of this work has been performed at the University of Illinois by Carpenter and his colleagues and at the National Center for Asphalt Technology (NCAT) (Prowell et al., 2010).

In the National Cooperative Highway Research Program (NCHRP) Project 9-38, beam fatigue and uniaxial tension testing were conducted to determine fatigue life (Prowell et al., 2010). By conducting a small strain control beam fatigue test, a fatigue life in excess of 50 million cycles was achieved. Structural sections were also constructed at the NCAT Test Track as a part of the study to evaluate the effect of increased asphalt binder content and polymer modification on fatigue life (Priest and Timm, 2006). Data from the Long Term Pavement Performance (LTPP) studies were also analyzed to determine if they support the endurance limit concept. The results obtained from that study support the existence of an endurance limit in HMA mixes (Prowell et al., 2010).

NCHRP Project 9-44 developed a detailed plan to validate an endurance limit for HMA pavements and to incorporate the concept of an endurance limit into a mechanistic-empirical algorithm for bottom initiated fatigue cracking in flexible pavements (NCHRP Project 9-44). Therefore, a concentrated research effort is needed to validate the endurance limit concept, and to devise effective methods for incorporating it in the Pavement ME Design software.

It has been proposed that the healing of microcrack damage is the main reason for the HMA endurance limit (HMA-EL) where the endurance limit represents the balance point between damage and healing. For strain levels above the endurance limit, the damage done is considerably greater than the healing potential of the HMA. When strains are below the HMA-EL value, the damage is small enough that it is completely healed during the rest period between load applications (Shen and Carpenter, 2005). Over the last four decades, numerous researchers have studied the significance of rest periods and healing of asphalt binders as well as asphalt concrete mixture (Monismith et al., 1961; Bazin and Saunier, 1967; Raithby and Sterling, 1970, McElvaney and Pell, 1973; Verstraeten, 1976; Van Dijk and Visser, 1977; Francken, 1979, Bonnaure et al., 1982; Kim et al., 1990; Hsu and Tseng, 1996; Jacobs, 1995; Lytton et al., 1998; Bahia et al., 1999; Little et al, 2001; Daniel and Kim, 2001; Si et al., 2002; Breysse, et al. 2003; Castro et al., 2006; Carpenter and Shen, 2006; Shen, 2006; Seo and Kim, 2008; Shen et al., 2009; Pronk, 2005 and 2009; Mamlouk et al., 2012). The outcomes of this research and others provide a clear and comprehensive understanding of the effect of rest period on fatigue damage and healing mechanisms.

PROBLEM DEFINITION

The endurance limit of HMA is defined as the allowable tensile strain below which fatigue cracking does not occur. NCHRP Project 9-44 stated that the endurance limit does not reflect an absence of load induced damage in the HMA. It is the result of a balance of damage caused by loading and healing or damage recovery that occurs during rest periods. This supports the theory that healing is considered as the main reason for the HMA endurance limit. However,

previous research studied the two aspects separately and did not provide any certain methodology to correlate the fatigue endurance limit to the healing of HMA. On the other hand, the implementation of the HMA endurance limit into the AASHTOWare Pavement ME Design is still incomplete. The current AASHTOWare Pavement ME Design procedure allows for the use of only one value of endurance limit for the entire analysis. However, the endurance limit is believed to vary depending on the mixture properties, pavement temperature, and traffic conditions.

RESEARCH OBJECTIVES

This research is part of the NCHRP Project 9-44A. The main objective of that project is to validate the concept of endurance limit for HMA pavement through laboratory experiments and algorithm development for the determination and implementation into the AASHTOWare Pavement ME Design. The experimental plan of the NCHRP 9-44A project consists of two fatigue tests. The first is the beam fatigue test, while the second is the uniaxial fatigue test. The beam fatigue laboratory experiment includes three binders; PG 58-28, PG 64-22, PG 76-16. The uniaxial fatigue experiment was duplicated for the PG 64-22 binder for the evaluation of the uniaxial fatigue test as well as for comparison purposes. The current study covers the uniaxial fatigue test on a PG 64-22 mixture and a comparison with the corresponding beam fatigue test results. The main objectives of this research are as stated below:
1. Carry out a laboratory experimental program using the uniaxial fatigue test to evaluate the main factors affecting fatigue and healing of HMA.
2. Validate and determine HMA fatigue endurance limit models that mainly consider the healing in HMA.
3. Compare the endurance limit from the uniaxial fatigue experiment and the beam fatigue experiment using the PG 64-22 binder.
4. Develop a methodology to incorporate the endurance limit into the Pavement ME Design software.

RESEARCH OUTLINE

This report is composed of nine chapters and three appendices. Chapter 2 presents the literature review on fatigue damage, laboratory tests, models and characterization methods, rest periods and healing, and fatigue endurance limit of HMA. Chapter 3 includes the theory of viscoelasticity and the uniaxial constitutive model based on the continuum damage mechanics. Chapter 4 describes the design of experiment, materials, specimen preparation and testing plan. Chapter 5 contains a description of the complex modulus experiment conducted to capture the viscoelastic properties represented by the relaxation modulus of the tested asphalt concrete mixtures. This chapter also contains a methodology developed to shift the entire dynamic modulus master curve based on air voids and asphalt content levels. Chapter 6 illustrates the development of proposed uniaxial tension-compression test protocol including test setup, test method, test condition, test software to run both tests, with and without rest period. Chapter 7 presents the uniaxial test results and the methodology developed to determine the fatigue endurance limit based on the healing of the fatigue damage. The development of the Pseudo

Stiffness Ratio (SPR) regression models to determine the endurance limit is presented in Chapter 8. In addition, the endurance limit determined from the uniaxial fatigue test and beam fatigue test are compared in Chapter 8. Chapter 9 includes summary, findings, and recommendations for future research.

Appendix A includes the dynamic modulus test results for the different mixtures; Appendix B contains a proposed test protocol for the uniaxial fatigue test; and Appendix C shows the test results from the uniaxial fatigue test experiments.

CHAPTER 2

LITERATURE REVIEW

FATIGUE CRACKING OF HOT MIX ASPHALT

Load-associated fatigue cracking is one of the most significant distress modes in flexible pavements besides thermal cracking and rutting. The action of repeated loading, caused by traffic induced tensile and shear stresses in the bound layers, eventually leads to a loss in the structural integrity of a stabilized layer material. Fatigue cracking is a progressive distress and can be classified into three different stages. The early stage of fatigue cracking consists of intermittent longitudinal wheel path cracks. The intermediate stage of fatigue cracking is called alligator cracking because the cracking pattern resembles an alligator's skin. In some extreme cases, the final stage of fatigue cracking is disintegration when potholes form.

Over the last several decades of pavement technology, it has been common to assume that fatigue cracking normally initiates at the bottom of the asphalt layer and propagates to the surface (bottom-up cracking). However, recent worldwide studies have also clearly demonstrated that fatigue cracking may be also initiated from the top and propagate down (top-down cracking). This type of fatigue is not as well defined from a mechanistic viewpoint as the more classical "bottom-up" fatigue. In general, it is hypothesized that critical tensile and/or shear stresses that develop at the surface and cause extremely large contact pressures at the tire edge-pavement interface, coupled with an highly aged (stiff) thin surface layer that have become oxidized, is felt to be responsible for the surface cracking that developed (Abojaradeh, 2003).

The mechanism of fatigue failure (bottom-up cracking) can be described as a three-stage process involving the crack initiation, propagation, and final fracture failure. During the crack initiation, micro-cracks grow from microscopic size until they reach a critical size of about 7.5-mm (Little et al., 2001). Fatigue initiated cracks develop at points where critical tensile strains and stresses occur. Additionally, the critical strain is also a function of the stiffness of the mix. The location of the initiation may be extremely small and difficult to distinguish from the succeeding stage of propagation, or crack growth. In crack propagation, a single crack or a few cracks grow, followed by more and larger cracks propagating and coalescing to complete the disintegration process. As the propagation of the fatigue crack continues, gradually reducing the cross-sectional area and eventually weakens the martial greatly that final complete fracture occurs.

MODE OF LOADING

Fatigue tests are carried out in two different modes of loading: controlled strain (displacement) or controlled stress (force) mode. The type of loading is characterized by the ratio R of the minimum force (or displacement) over the maximum force. Thus, a pure sinusoidal signal is characterized by R = -1. A haversine signal is characterized by R = 0. A variety of loading patterns, such as sinusoidal, haversine, square, and triangular-shaped waveforms with or without rest periods have been used to simulate field traffic load pulses. The most commonly

used wave forms in the characterization of the mix and development of fatigue life prediction models are sinusoidal and haversine (Huang, 2004).

In the controlled strain test, the strain amplitude is maintained constant and the force required maintaining the initial strain level decreases gradually after crack initiation, as the flexural stiffness of the mix is effectively decreased. The failure, or termination point, is commonly selected as a certain reduction in the initial stiffness from that at the commencement of the test, generally 50-percent, as discussed in Section 2.4.

The controlled strain mode of loading simulates conditions in thin asphalt pavement layers usually less than 2-inches. In this case, the pavement layer is not the main load-carrying component. The strain in the asphalt layer is governed by the underlying layers and is not greatly affected by the change in the asphalt layer stiffness. This situation is conceptually more related to the category of constant strain.

In the controlled stress mode of loading, the stress amplitude is maintained constant. Because of the repetitive application of the stress, the strain amplitude increases until it reaches twice the initial amplitude, when the flexural stiffness is reduced to half the initial flexural stiffness, which constitutes failure. According to Button et al. (1987), the constant stress type of loading is generally considered applicable to thick asphalt pavement layers usually more than 8 inches. In this type of structure, the thick asphalt layer is the main load-carrying component and the strain increases as the material gets weaker under repeated loading. However, with the reduction in the stiffness, because of the thickness, changes in the stress are not significant and this fact leads to a constant stress situation.

The strain mode of loading accounts for both crack initiation and propagation while the stress mode of loading does not account for both crack initiation and propagation, because the number of cycles to crack propagation is small compared to the number of cycles to failure which is defined by the fracture of the sample (Pell, 1973). Therefore, fatigue life is usually greater in control strain than control stress (in general approximately 2.4 times greater) (Tayebali et al., 1994)

The fatigue performance of asphalt mixes with lower flexural stiffness is superior under controlled strain loading than under controlled stress testing at similar initial strain amplitudes. While in the controlled stress mode, mixes with higher flexural stiffness have been shown to have longer fatigue lives, and flatter slopes in the stress-fatigue relationship irrespective of whether the repeated flexure testing was conducted using two- or four-point bending (Epps and Monismith, 1969; Pell and Cooper, 1975).

Controlled stress tests are more severe than controlled strain tests and the energy is absorbed more rapidly. The initial dissipated energy per cycle is high, and the rate of energy dissipation is faster, in the controlled stress mode of loading. It is well known that there will be variability and scatter in the results of fatigue testing. However, when the stress in a controlled stress test is converted to strain, and strain is plotted against the number of cycles to failure, then the scatter is considerably reduced (Monismith, 1966b). This suggests that controlled strain tests reduce the scatter and variability associated with fatigue testing. Variability is also associated with sample (test specimen) dimensions, with the larger the sample size, the smaller the scatter and variability in the fatigue test results.

FATIGUE TEST METHODS

Different test methodologies have been developed over the past several decades for measuring the fatigue behavior of asphalt concrete mixtures. The prediction quality of the fatigue life using any of these test methods depends on how accurately the method simulates the condition of loading, support, stress state, and environment. Moreover, selecting any of these test methods can be influenced by the availability and cost of equipment, in addition to ease of use. FIGURE 1 represents a schematic diagram showing most of the available fatigue tests.
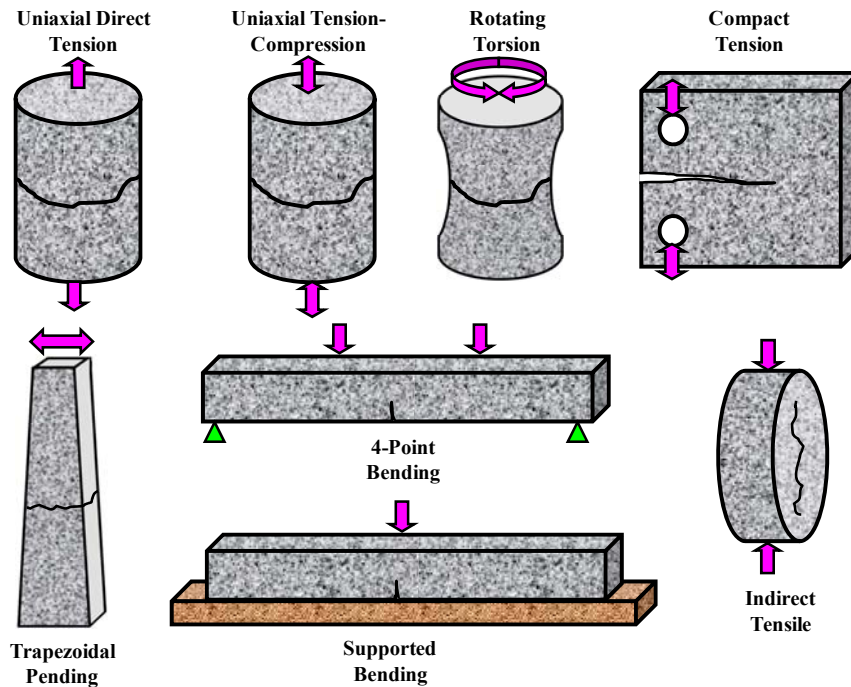
FIGURE 1 Commonly used fatigue test arrangements.

It is almost impossible for laboratory fatigue tests to completely simulate the field conditions as there are too many field variables that are not considered, such as specimen fabrication, compound loading, random rest periods, and multi-stress state. Therefore, there is difference in fatigue life obtained based on field and laboratory conditions. To account for this difference in fatigue life, a shifting factor is usually used to relate laboratory to field performance. The magnitude of the shift factor varies and depends upon many factors such as the thickness of the asphalt layer, the mix properties, traffic volume and composition, environmental conditions, fatigue failure criterion, and type of fatigue test.

Brief descriptions along with the advantages and disadvantages and limitations of selected test methodologies can be found in SHRP's "Summary Report on Fatigue Response of Asphalt Mixes" (Tangella, 1990). The following is a summary of most popular fatigue tests in the SHRP summary report.

Simple Flexure Tests

Simple flexure tests are widely used for measuring the stiffness modulus and assessing the fatigue resistance of asphaltic paving materials. This method is well known, widespread in use, and readily understood. A number of' different types of flexural equipment have been developed to study the fatigue characteristics of asphalt concrete mixtures including:

Three- and Four-Point Bending Tests

The flexural fatigue test has been used by various researchers to evaluate the fatigue performance of pavements (Witczak et al., 2001). The Shell Laboratory at Amsterdam has used the center-point loading equipment to test specimens with dimensions 1.2-inch (30-mm) x 1.6-inch (40-mm) x 9-inch (230-mm). In this test, specimens are tested in the controlled-deflection (strain) mode.

In four-point test, the dimension of the beams can vary from one laboratory to another. The AASHTO T 321 flexural fatigue testing protocol requires preparation of oversize beams that later have to be sawed to the required dimensions. The final required dimensions are 15±1/4-inch (380±6-mm) in length, 2±1/4 inch (50±6-mm) in height, and 2.5±1/4-inch (63±6-mm) in width. The procedure does not specify a specific method for preparation. Several methods have been used to prepare beam in the laboratory including full-scale rolling wheel compaction, miniature rolling wheel compaction, and vibratory loading.

Rotating Cantilever Beam Test

At the University of Nottingham, U. K., Pell and Hanson (1973) used a rotating cantilever machine where the specimen is mounted vertically on a rotating cantilever shaft. A load is applied at the top of the specimen to induce a bending stress of constant amplitude through the specimen. The tests were usually conducted at a temperature of 50°F (10°C) and a speed of 1,000 rpm. Dynamic stiffness was measured by applying constant sinusoidal amplitude deformations.

Another way to carry out this test was done by Pell using a controlled-strain torsional fatigue machine where the sample is clamped vertically on a shaft. The bottom of the sample is clamped to the bottom of the machine and the loading arrangement gives a sinusoidal varying shear strain of constant amplitude to the specimen.

Trapezoidal Cantilever Beam Test

The trapezoidal cantilever beam test has been popular in Europe. Tests on trapezoidal specimens have been conducted by Shell researchers (Van Dijk, 1975) and LCPC (Bonnot, 1986). The larger dimension of the trapezoidal specimen is fixed and the smaller end is subjected to either a sinusoidal applied strain or stress. The trapezoid shape of the specimens is designed to cause failure at about mid height where the bending stress is largest rather than at the base where boundary conditions might adversely affect interpretation of test results. As an example, specimens tested by Van Dijk had a base cross section of 2.2-inch by 0.8-inch (55-mm by 20-

mm), a top cross section of 0.8-inch by 0.8-inch (20-mm by 20-mm), and a height of 10-inch (250-mm).

Supported Flexure Test

The supported flexure test was used to better simulate stress state and mode of loading in field conditions. Several researchers have used this test with two different specimen shapes: circular slab and beam. Majidzadeh (Majidzadeh et al., 1971) and others used circular samples supported on a rubber mat and subjected to a circular shaped, repeated load applied to the center of the slab, resulting in a stress state in the slab which is very similar to that occurring in the pavement structure. Barksdale (1977) used asphalt concrete beams placed on a 4 inch thickness of rubber mat supporting the beam and subjected to a haversine load pulse of 0.06 second duration and 45 rpm frequency.

This test method can reduce the scatter of test results by better duplication of field conditions.

Direct Tension Test

The Transport and Road Research Laboratory (TRRL) (now the Transport Research Laboratory) of the United Kingdom has performed uniaxial tensile tests without stress reversal using a loading frequency of 25 Hz; duration of 40 milliseconds; and rest periods varying from 0 to 1 sec. Starting from very short rest periods, fatigue life increases rapidly with an increase in rest period before reaching a limiting value at about 0.4 seconds, beyond which increasing the duration of the rest period had very little further effect (Raithby and Ramshaw, 1972). These tests were conducted in the controlled-stress mode. Later on, direct tension tests were performed in the Netherlands (Kunst, 1989) at frequencies of 1 and 0.1 Hz using haversine loading in the controlled-strain mode. More recently, this test has been used in the United States by Texas A &M University and North Carolina State University to characterize microdamage healing in asphalt and asphalt concrete using viscoelastic continuum damage, fracture mechanics and dissipated energy approaches.

One advantage of the direct tension test is that the test specimen may be circular as well as rectangular in cross section. In addition, it is less costly as testing time is shorter because fewer loading cycles are sustained before failure. The primary disadvantage of this test is that loading condition does not necessarily represent field conditions.

Tension/Compression Test

The tension/compression fatigue test was developed at the Transport and Road Research Laboratory (TRRL) (Raithby and Ramshaw, 1972). Axial tensile and compressive loadings were applied using a servo-controlled electro-hydraulic machine. Prism specimens were 3-inch (75-mm) square cross sections and 9-inch (225-mm) lengths. Loading frequencies were 16.7 and 25 Hz, and the effects of rest periods, shape of wave form, and the sequence of load application (compression/tension, tension/compression, compression only, and tension only) were evaluated.

It was concluded that short rest periods, such as occur in practice between successive axle load applications, have an important effect on the fatigue life. The effect of load form is not very great; a sinusoidal load pulse would appear to be a reasonable representation, and pure compressive cyclic loading gives the largest fatigue life followed by tensile/compressive cyclic loading, tensile cyclic loading, and compressive/tensile cyclic loading.

Except for the ability to simulate the loading pulse observed in the field, this test does not well represent field conditions, required more time, is more costly, and required more specialized equipment.

Diametral Test

The diametral fatigue test is an indirect tensile (IDT) test conducted by repetitively loading a cylindrical specimen with a compressive load which acts parallel to and along the vertical diametral plane. This loading configuration develops a reasonably uniform tensile stress in the specimen perpendicular to the direction of the applied load and along the vertical diametral plane. Test specimens are usually 4- or 6-inch diameter and 2.5- to 3.0-inch high. Load is transmitted to the sides of the right circular cylinder through a 0.5-inch wide loading strip. Usually a haversine or sine load pulse is applied. The load frequency most commonly used is 20 to 120 cycles per minute.

The unique thing about this test is that it can be used to characterize a variety of asphalt concrete mixture properties, especially properties related to resilient elasticity, thermal cracking, fatigue cracking and permanent deformation (Kennedy, 1977). Repeated load indirect tensile tests have been conducted at the Center for Highway Research at the University of Texas at Austin (Moore and Kennedy, 1971; Navarro and Kennedy, 1975; Cowher, 1975; Kennedy, 1977). The diametral test offers a biaxial state of stress, which is possibly of a type that better represents field conditions. A key problem with this method is that it will significantly underestimate fatigue life if the principal tensile stress is used as the damage determinant.

One of previous studies of fatigue characterization using the IDT was carried out in Sweden by Said (1975). Said in his work tested 300 cores from different pavement sections using repeated controlled stress loading at two temperatures, 39°F and 59°F (4°C and 15°C). Said concluded the IDT is sufficiently accurate for routine investigation of asphalt concrete fatigue characterization with a shift factor of 10 to correlate to field.

In summary, the diametral test is simple in nature, more representative of field condition due to biaxial state of stress, and can be performed not only on laboratory specimens but on field cores as well. A key problem with this method is that it will significantly underestimate fatigue life if the principal tensile stress is used as the damage determinant. Also, there is a possible concern about the absence of stress reversal and the accumulation of permanent deformation.

Triaxial Test

Several agencies such as the University of Nottingham (Pell and Cooper, 1975) and the University of California, Berkeley (Sousa, 1986) developed this type of device to best represent the in situ state of stress. Pell and Cooper tested cylindrical specimens with a diameter of 4 inches (100 mm) and a height of 8 inches (200 mm). Specimens were bonded to end caps with epoxy resin and mounted on the rig. Specimens enclosed in a triaxial cell were subjected to a

11

sinusoidal varying axial stress. One concern about this kind of test is that the shear strains must be well controlled, otherwise the predicted fatigue lives could be considerably different than the field results.

Sousa (1986) developed equipment capable of applying shear strains by torsion (repeated or constant) together with radial tensile stress using specimens fabricated as hollow cylinders. To date, only shear fatigue (torsion) tests have been conducted. This equipment could be further developed to apply repeated radial tensile stresses through the pulsating fluid within the hollow cylinder, thus simulating the necessary conditions including shear stresses (through torsion) and vertical stresses.

Triaxial tests simulate the field loading condition in which compression is followed by tension and the results can be used for mixture design and, with field correlation factors, for structural design. This type of test is costly, requires specialized equipment, and is time consuming.

Wheel-Track Test

In order to better simulate the effects of a rolling wheel on the pavement and to better understand the pattern of crack initiation and propagation, wheel-track tests have been developed to study fatigue characteristics of asphalt pavements. The wheel-track test can be conducted in the laboratory and on full-scale pavement sections.

Van Dijk (1975) developed a laboratory loaded wheel with a pneumatic tire that rolled back and forth over a slab of asphalt concrete. The wheel has a diameter of 10 inches (0.25 m) and its path is 24 inches (0.60 m) long with a width in the range of 2 to 2.75 inches (0.05 to 0.07 m). The slab is supported by a rubber mat. Strains at the bottom of slab were measured and crack initiation and propagation detected. Results can be expressed in terms of three fatigue stages associated with the development of hairline cracks (N_1), real cracks (N_2), and failure of the slab (N_3). Based on the test results, Van Dijk suggested that controlled-strain data may be more appropriate to define pavement cracking than controlled-stress data.

The main limitations of laboratory wheel-track tests are the small dimensions and the slow speed of the rolling wheel as compared to field conditions. In addition, the test is time consuming and does not measure a fundamental mixture property. Moreover, for mixes of low stiffness, rutting becomes significant and may affect fatigue measurements.

Full-scale testing facilities have been built in several countries around the world. Well-known examples include the circular tracks located at Nantes in France, at Pullman, near the Washington State University campus, the Federal Highway Administration's ALF (Accelerated Loading Facility), CALTRAN's Heavy Vehicle Simulator in California, and in Australia (ARRB), New Zealand (Canterbury), Denmark, and the United Kingdom (TRRL). The tracks are often divided into sections, each with a different pavement structure, and loads are applied by several sets of dual truck tires.

With full-scale testing facilities, it is possible to examine the effect of changes in the pavement structural section on pavement performance, and other forms of pavement distress in addition to fatigue can be studied as well. High initial investment cost and annual operation and maintenance costs are the main disadvantages of full-scale test tracks. Also, a parallel,

supplementary laboratory testing program is still needed, since the field track tests do not directly measure fundamental mixture properties.

FATIGUE FAILURE CRITERIA

A large diversity of opinion regarding the identification of fatigue failure point (N_f) due to fatigue damage is found in the literature. Depending on the specific fatigue test mode of loading (stress or strain), N_f has been specified in different ways. In the constant stress mode of testing, one definition of N_f was complete fracture at the end of the fatigue test when the specimen fails due to tensile strains (Pell and Cooper, 1975; Tayebali et al., 1992). Rowe (1993) defined N_f as the reduction of the initial complex modulus by 90%. Van Dijk (1975) defined N_f as the number of loading cycles at which the corresponding strain is twice the initial strain.

In the constant strain mode of testing, several N_f definitions have been adopted. The most common and widely used definition for N_f in the constant strain mode is the 50% reduction in the initial stiffness defined by Pronk and Hopman (1990) and Tayebali et al. (1992, 1993). A 50% reduction in the initial modulus was also defined as fatigue failure by Van Dijk and Vesser (1977). Afterward, the 50% reduction in stiffness was adopted to define N_f by AASHTO in provisional standard TP8-94 (2002).

Rowe and Bouldin (2000) identified N_f by plotting the load cycle value n_i versus the load cycle multiplied by the stiffness S_i at that cycle ($n_i \times S_i$). The fatigue failure point was defined for both controlled stress and strain test types as the point that produces a peak value. This point was found to represent the formation of cracks.

A rational fatigue failure criterion was developed at Arizona State University based on the Rowe and Bouldin's failure definition *(Abojaradeh, 2003)*. A new stiffness term (called stiffness degradation ratio) was defined by normalizing Rowe and Bouldin's parameter $n_i \times S_i$ by dividing it by the initial stiffness S_o taken at the 50th cycle. N_f was defined for both controlled strain and controlled stress modes as the number of load repetitions at the peak value of the stiffness degradation ratio-cycle number relationship. The results of Abojaradeh's method verified that 50% of the initial stiffness was the best value for the failure fatigue criterion.

Energy-based failure concepts have been proposed by many researches as an alternative means to define N_f. Hopman et al. (1989) proposed the use of an 'Energy Ratio' concept to define N_f. By plotting the energy ratio (Load cycle × initial dissipated energy/ dissipated energy at that load cycle, $n_i \times w_o / w_i$) versus the number of load cycles, N_f was defined as the number of load cycles where the energy ratio deviates from a straight line for the strain-control mode. In the case of stress control, N_f was defined as the peak of the curve (FIGURE 2).
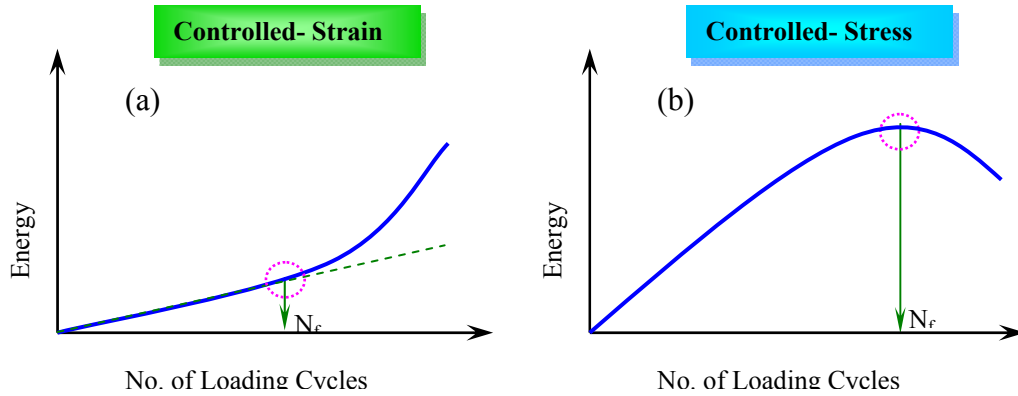
FIGURE 2 Energy ratio versus number of repetitions (a) controlled-strain mode; (b) controlled-stress mode.

In 1997, Pronk proposed a different expression of energy ratio as the ratio of the cumulative dissipated energy up to cycle n to the dissipated energy for cycle n (W_i/w_i). Under constant strain, N_f was defined as the number of load cycles when the energy ratio deviates from a straight line. Under controlled stress, N_f was defined as the peak of the curve. Ghuzlan and Carpenter (2000) used the ratio of the change in dissipated energy between two consecutive cycles (n_i, n_i+1) to the total dissipated energy in the load cycle n_i to define N_f. Failure was selected for both modes of loading as the point where this ratio increased rapidly after a consistent stable trend for this ratio with load cycle.

Kim et al. (1997) introduced the 50% reduction in pseudo stiffness as a failure point in fatigue testing, which was believed to be independent of mode of loading and stress/strain amplitude.

Reese (1997) used phase angle to define the N_f as the cycle at which the phase angle shows a maximum value with time followed by a sharp decrease (FIGURE 3). Using this phase angle failure criterion, Daniel (2001) found that the midpoint of the failure range has occurred at a pseudo stiffness reduction of 29% for a cyclic uniaxial fatigue test and 31% for a monotonic uniaxial test.
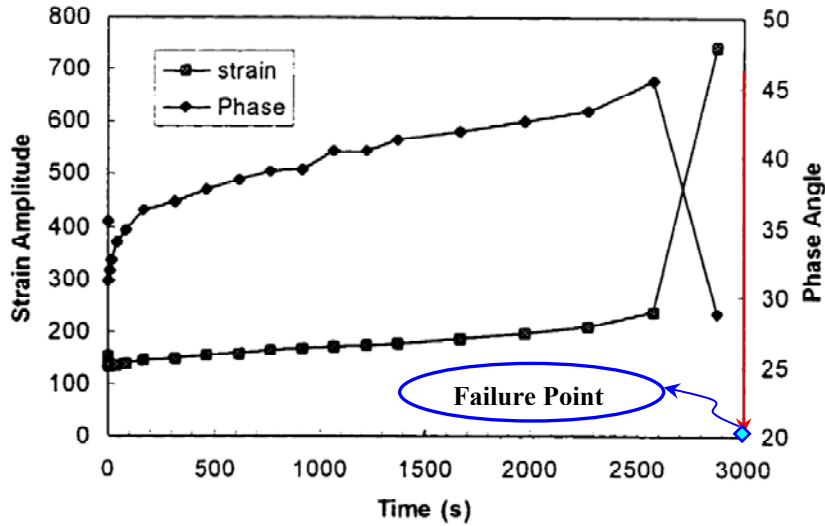
FIGURE 3 Phase angle and on-specimen linear variable differential transducers (LVDT) microstrain amplitude as a function of time for specimen CLO7 (Daniel, 2001).

Al-Khateeb and Shenoy (2004) defined a new qualitative fatigue failure criterion through visual observations of the load-deformation (stress-strain) hysteresis loop. They defined the point of first fatigue failure N_{fff} as that point at which the hysteresis loop or the response waveform started to show the first signs of distortion. The point of complete fatigue failure N_{cff}, on the other hand, was defined as the point at which an extensive (or almost complete) distortion in the hysteresis loop or the response waveform occurred (FIGURE 4).
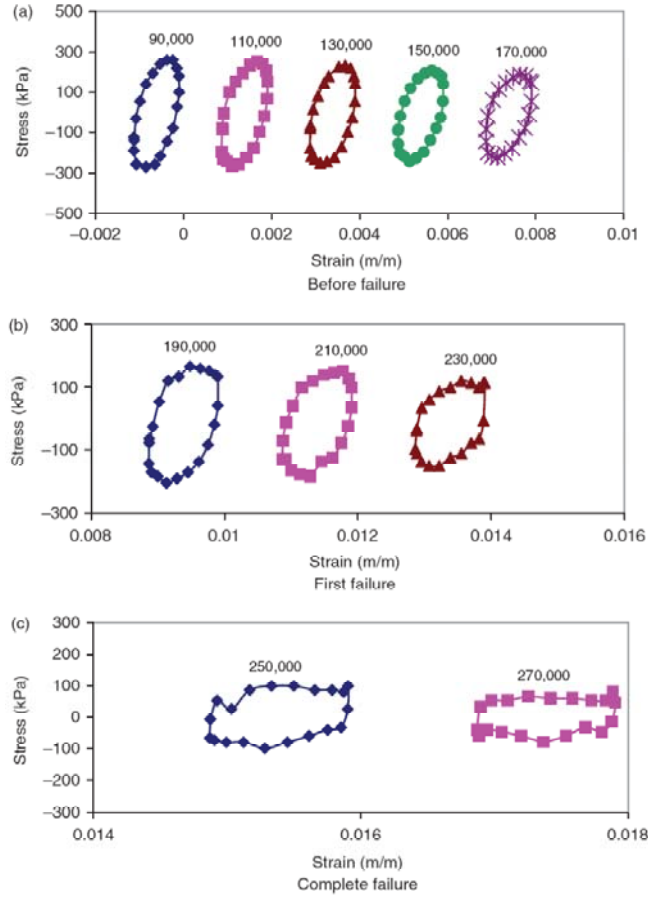
FIGURE 4 Stress-strain hysteresis loop through the progress of fatigue failure (Al-Khateeb and Shenoy, 2004).

Based on the same concept, Al-Khateeb and Shenoy (2011) developed a more quantitative method to identify the fatigue failure for any type of fatigue testing. In this method, the relationship between output signals for consecutive cycles with reference to an initial stable cycle is used for computing 'R^2'. 'R^2' drops sharply from an initial stable value of 1 to less than 0.5 and eventually to almost 0 with increasing loading cycles. The number of cycles determined from the fitted equation at 'R^2' =1 marks the point of first fatigue failure N_{fff} and 'R^2' =0 marks the point of complete fatigue failure N_{cff} (FIGURE 5).
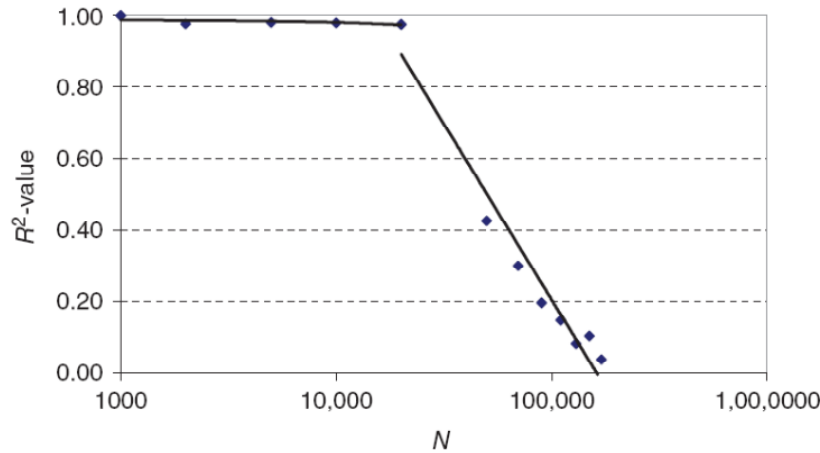
FIGURE 5 R^2 vs N on semi-logarithmic scale (Al-Khateeb and Shenoy, 2011).

Tsai et al. (2005) used a three-stage Weibull model to define the fatigue failure of asphalt mixtures. The three stages defined are initial stage (warm-up), crack initiation, and crack propagation. The three-stage Weibull model consists of three different equations that are based on the stiffness ratio, (SR = S_i/S_o). By plotting ln(-ln(SR)) versus ln(loading cycle, n), three different curves can be distinguished that can be fitted using the three different equations of Weibull model. Once the data are fitted, the failure point is assumed to have a stiffness ratio of 0.5 as shown from FIGURE 6.
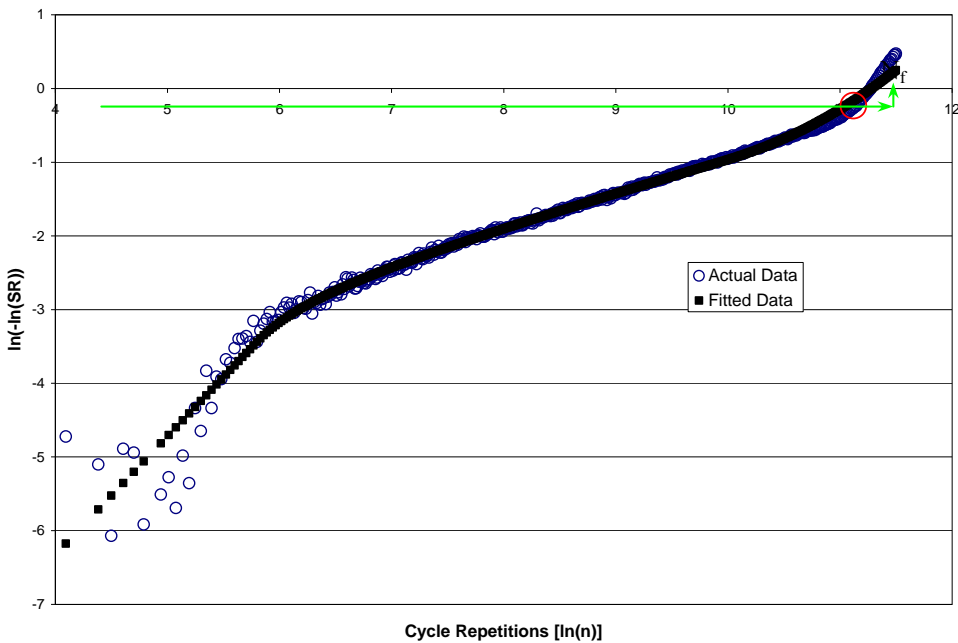
FIGURE 6 Example of three-stage Weibull versus cycle repetitions (Salt River base aggregate, Chevron 76-16 binder, strain control test, 70ºF).

17

EFFECT OF REST PERIOD ON HMA FATIGUE BEHAVIOR

Need for Rest Period

Under real traffic conditions the pavement structure is subjected to a succession of load pulses as the traffic flows past a particular point on the road. The duration and spacing of the load pulses depends on several factors, including vehicle speed, axle configuration, and headway between following vehicles as shown in FIGURE 7. Another important factor that affects the rest period is the fact that loads are not always applied on the same part of the road, but distributed across the cross section.

In most laboratory studies of asphalt concrete mixtures, fatigue testing is usually carried out by means of dynamic tests with loading cycles which are repeated continually, without periods of non-loading (FIGURE 8), which contradicts the actual field traffic loading, which is interrupted by rest periods because of the spaces between axles of the same vehicle or successive vehicles.
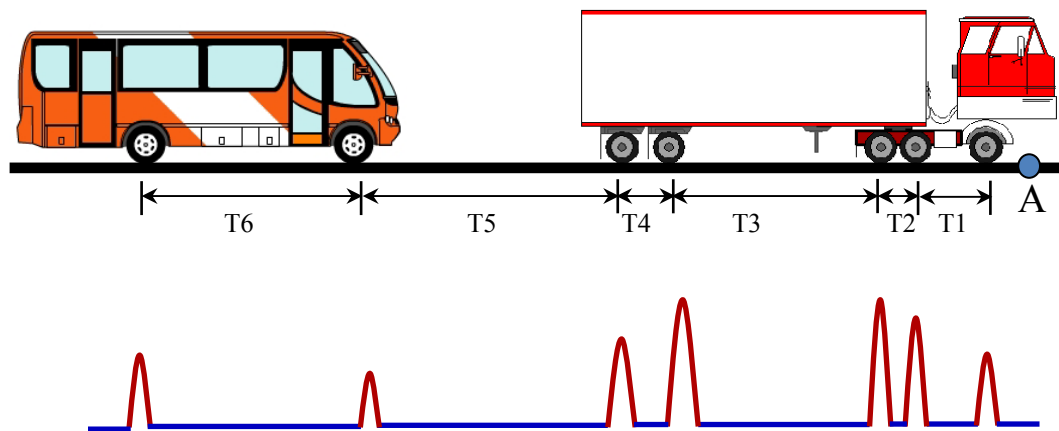
FIGURE 7 Rest times between vehicle's axles passing over the pavement.
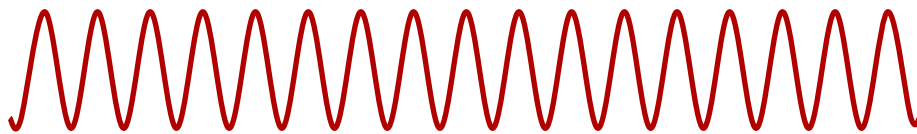
FIGURE 8 Tests without rest.

Effect of Rest Period

Over the last several decades, several researchers have studied the significance of rest periods between load applications during the fatigue testing of HMA. Dissimilar findings have been presented in literature showing diverse opinions on the effect of the rest period. Some researchers think that rest period only leads to a temporary modulus recovery without actually extending the fatigue life, while others found that the modulus recovery did extend fatigue life by

a certain amount. These different conclusions were mainly based on a large variety of tested mixtures, laboratory testing setups, and research approaches.

Depending on the way the material is allowed to rest, there are two different ways of introducing rest periods into fatigue testing:

- With rest intervals: This is a classic fatigue test with continuous loading cycles where rest intervals (storage periods) are introduced after a certain number of continuous loading cycles. At the end of each rest interval, the test is continued until the next rest interval (FIGURE 9a).
- With intermittent loads: Each loading cycle is followed by a rest period of a certain duration (FIGURE 9b).

The second method with intermittent loading appears to more closely resemble the sequence of traffic pulses in the field than the first method, although both testing methods have been used by researchers for studying the effect of rest period and healing on the HMA fatigue behavior.

(a)   (b)
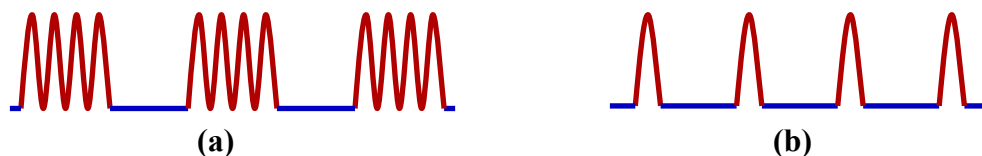
FIGURE 9 Fatigue tests (a) with rest intervals; (b) with intermittent loads.

Monismith et al. (1961) assessed the effect of rest period by conducting repeated flexure tests on beam specimens supported by a spring base. The loading cycles consisted of 1 sec of load and 1 sec, 3 sec, or 19 sec of rest period. The tests were performed at 77ºF (25ºC) and three frequencies, 3, 15, and 30 load applications per minute. The test results suggested that increasing the rest period from 1 to 19 second had no effect on fatigue performance. This conclusion is different from later research results that showed an enhancement of the fatigue life due to rest periods.

Bazin and Saunier (1967) quantified healing by introducing rest periods to asphalt concrete beams which were previously failed under both bending and uniaxial tensile loadings. In the tensile tests, beam specimens were stretched along the longest dimension and the tensile strength and strain at break were measured. In the bending test, the specimens were tested in a dynamic two-point bending apparatus (frequency 50Hz, temperature 50ºF) until rupture occurred (fatigue life N). The broken samples were put in contact and samples were placed vertically resting on smallest base. After different rest periods and temperatures during rest, the samples were tested again to have both the new tensile strength and strain at break in uniaxial tensile and the fatigue life N' in bend test. For the uniaxial tensile test, the amount of healing was evaluated based on healing index while the life ratio (N'/N) was used to evaluate the healing on bend test. The results of the uniaxial tensile test showed that a dense graded asphalt concrete mixture could recover 90% of its original tensile strength after 3 days of recovery at 77°F (25°C) and that the healing seemed to become complete after one month at that temperature. Based on the bending test, a 50% increase in fatigue life for a previously failed sample after a one-day rest under a slight compressive stress 0.22 psi (1.5 kPa) was achieved.

19

Raithby and Sterling (1970) performed uniaxial tensile cyclic tests on beam samples sawed from a rolled mat of asphalt concrete to have dimensions of 3×3×8.6 inches (75-mm×75-mm×225-mm). The tests were conducted in controlled stress mode at two loading frequencies (2.5Hz and 25Hz) and two temperatures (50ºF and 77ºF, 10ºC and 25ºC), with a sinusoidal load pulse, which has equal tensile and compressive stresses in each cycle. Pulsed loading without and with rest periods varying from 40ms to 800μs was applied until failure occurred. In the tests when rest periods were introduced, the specimens were rested at a zero stress. It was observed that the strain recovery during the rest periods resulted in longer fatigue lives by a factor of five or more than the fatigue life under continuous loading.

McElvaney and Pell (1973) performed rotating bending fatigue tests on a typical English base course mix at 50ºF (10ºC) using a 16.7 Hz frequency. The specimens were subjected to multi-level loading with random durations of rest period. It was concluded that rest periods have a beneficial effect on the fatigue life depending on the damage accumulated during loading periods. No evidence was found for a limiting value of the fatigue life extension.

Verstraeten (1976) performed dynamic two-point bending tests in a constant stress mode (frequency 54 Hz, temperatures 23ºF and 59ºF). The loading conditions were maintained either until failure or 80% of stiffness reduction. Then, the specimens were stored for periods varying from 3 to 21 hours at temperatures from 23ºF to 95ºF (-5ºC to 35ºC). The author concluded that the longer the rest periods and the higher the temperatures, the greater the beneficial effect, although their effects on the susceptibility of mixtures to fatigue could not be quantified.

Francken (1979) carried out experiments on a typical Belgian mix using a two-point bending apparatus. The test was run under constant stress mode of loading at 55.6 Hz frequency. The test results showed an increase in-service life when rest periods were incorporated in the fatigue tests. From the test results, a new empirical relation that accounts for the effect of rest period was derived. It is a relation between the cumulative cycle damage ratio in Miner's law (N_i/N_c) and the loading ratio (n_r/n_l):

$$\frac{N_i}{N_c} = 1 + 2.8(\frac{n_r}{n_l})^{0.44} \qquad\qquad (1)$$

where:

n_r = number of rest periods,

n_l = number of loading cycles.

The author pointed out that the use of this formula is restricted to the particular asphalt mix investigated.

Hsu and Tseng (1996) conducted a repeated load fatigue test on beam specimens using a haversine wave with a loading duration of 0.1 sec. To study the effect of the rest period on the fatigue response of asphalt concrete mixtures, 1, 4, and 8 loading ratios, which represent the ratio of the duration of the rest period to that of loading, were applied. During the test, approximately 10% of the applied load was pulled upward on the specimen for each loading to simulate the rebound of the pavement for each passing of the vehicles. The results of the controlled stress test showed that asphalt concrete mixtures with higher loading ratios and asphalt content 0.5% more than optimum exhibited longer fatigue life.

Breysse et al. (2003) performed the two-point bending fatigue test on trapezoidal specimens, clamped at the lower base and submitted to cyclic loading at its free end, to study the balance between damage and recovery in HMA. A controlled-displacement test was done at 68°F

(20°C) and a 40 Hz loading frequency. In this study, specimens were continuously loaded until the overall stiffness reduction reached a given ratio α%. The stiffness recovery during the rest periods was monitored by applying a low magnitude loading (supposed not to create any damage) until the response was stabilized. This process was repeated iteratively as many times as wanted, for the same α% ratio. The tests were driven for various α values (10 – 50%) to study the effect of low and severe damage histories on the stiffness recovery values. The results showed the maximum magnitude of recovery depends on the number of previously applied fatigue cycles. It was noticed that part of the recovery observed due to the interrupted loading sequence is a temporary stiffness recovery rather than true healing. This is why the material will return its original status (damaged status) very quickly after reload.

Castro et al. (2006) had conducted flexural beam fatigue tests with and without rest periods. As a consequence, a constant rest period of 1 second following every 0.1 second loading was applied to the test. The fatigue curves had been evaluated by means of discriminant analysis o rigorously confirm that they were different. It was concluded that the rest period could increase the fatigue life of HMA specimens up to 10 times, compared to tests without rest periods.

Optimum Rest Period

Although an increase in the duration of the rest period produces an increase in fatigue life due to crack healing, exceeding a certain value of rest time may only have a small effect on the mixture fatigue life. At the same time, for the same number of cycles, the longer the rest period duration, the longer the test duration. Consequently, it is essential to find the rest period such that its increase would not cause a significant increase in fatigue life and so avoid excessive test times. This rest period can be referred to as the optimum rest period.

In an attempt to investigate a rational value of the optimum rest period, Raithby and Sterling (1972) applied a range of rest periods between zero and 25 times the loading time on a rolled asphalt base course using a dynamic push-pull test. A constant stress mode applied with different waveforms (sine, triangle, and square). It was found that fatigue life does not increase significantly for rest periods greater than ten times the loading time and the influence of the waveform was less important than the duration of rest periods.

Van Dijk and Visser, (1977) had tested a rolled asphalt base course mixture in a three-point bending apparatus in a constant strain mode (40 Hz frequency and 68ºF (20ºC)) with loading ratios varying from 1 to 25. The results showed that the maximum beneficial effect of rest period on the fatigue life (life ratio of about 10) was determined by extrapolation to be achieved at a loading ratio of about 50.

Bonnaure et al. (1982) performed a three-point bending fatigue test with various rest period ratios (0, 3, 5, 10, and 25 times the length of the loading cycle). The tests were done under both constant stress and constant strain modes of loading at 41ºF, 68ºF, and 77ºF (5ºC, 20ºC, and 25ºC) and 40Hz frequency. The results indicated that the maximum beneficial effect of the rest period on the fatigue life was at a rest period equal to 25 times the loading cycle. It was concluded also that the constant stress mode results in a greater increase in fatigue life than the constant strain mode.

In a rigorous sense, the optimum rest period will differ with mixture properties (gradation, binder content, binder grade, mixture volumetric, etc.), test type (simple flexure,

21

uniaxial, triaxial, etc.), and test conditions (mode of loading, temperature, frequency, stress or strain levels, etc.).

HEALING OF ASPHALT CONCRETE MIXTURES

Much research has been devoted to investigate the healing mechanism in asphalt mixtures and determine if healing happens only during rest periods or also during the loading and unloading periods. The effect of mixture components and volumetric properties, test conditions (such as temperature, rest periods, stress or strain levels, frequency, and laboratory testing setup), material damage level, and the analysis approach on the healing rate have also been studied.

Mechanism of Healing

Healing is generally considered as the capability of a material to self-recover its mechanical properties (stiffness or strength) to some degree upon resting due to the closure of cracks. In fact, various metallic and non-metallic engineering materials are found to have this ability.

For metallic materials such as steel, aluminum, etc., Suresh (1998) categorized the various mechanisms of fatigue crack closure or healing that are induced by a variety of mechanical, microstructural, and environmental factors based on his own work and that of others. These mechanisms of crack closure include the following:
1. Residual plastic stretch at crack wake (plasticity-induced crack closure),
2. Corrosion layers formed within a fatigue crack (oxide-induced crack closure),
3. Microscopic roughness of the fatigue fracture surfaces (roughness-induced crack closure),
4. Viscous fluids penetrating inside the crack (viscous fluid-induced crack closure), and
5. Stress- or strain- induced phase transformations at the crack tip (transformation-induced crack closure).

For non-metallic materials and composites such as glass, polymers, Portland cement concrete, and asphalt concrete mixtures, there are several other mechanisms which slow the growth of fatigue cracks and induce crack healing; these mechanisms can be summarized as follow (Suresh, 1998):
1. Crack deflection,
2. Crack-bridging or trapping, and
3. Crack-shielding due to micro-cracking, phase transformations or dislocations.

For asphalt concrete mixtures, while a significant amount of work has documented the effect of rest periods on the fatigue life of asphalt mastics and mixtures, little research has focused on the mechanism of healing.

Kim et al. (1990) defined two main "healing" mechanisms that occur during the rest period. One is the relaxation of stresses (time-dependent) in the system due to the viscoelastic nature of asphalt concrete, and the other is the chemical healing across microcrack and macro-crack faces. To evaluate chemical healing separately from the time-dependent effects of relaxation, the correspondence principle of nonlinear viscoelastic media was applied to asphalt concrete specimens subjected to intermittent cyclic uniaxial testing. After successfully

accounting for the effects of relaxation, the authors were able to quantify the chemical healing using the concept of the healing index, which represents the healing potential of different binders at different rest times. This index is defined as the ratio of the recovered dissipated pseudo energy density following a rest period to the dissipated pseudo energy density measured prior to the rest period (FIGURE 10):

$$HI = \frac{\phi_{after} - \phi_{before}}{\phi_{before}} \tag{2}$$

where:

ϕ_{after} = dissipated PSE when the damaged sample is loaded, and

ϕ_{before}= dissipated PSE when the healed sample is loaded.
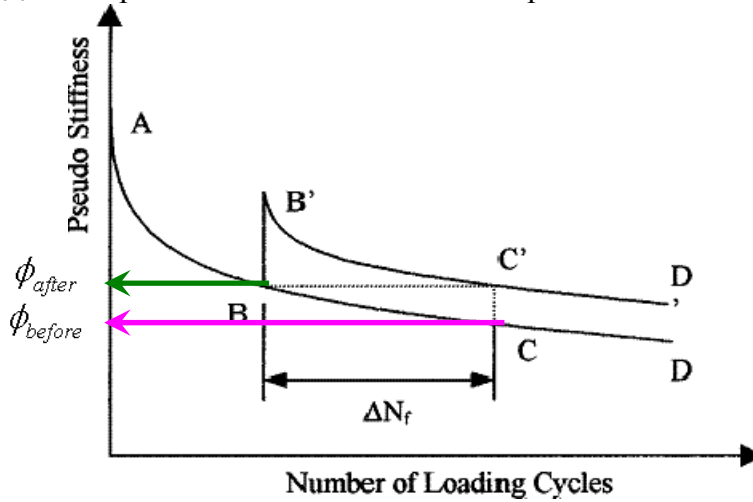
FIGURE 10 Change in pseudo stiffness before and after a rest period (Kim et al., 1990).

Phillips (1998) proposed that the healing of binders is a three-step process consisting of:
1. The closure of micro-cracks due to wetting (adhesion of two crack surfaces together driven by surface energy);
2. The closure of macro-cracks due to consolidating stresses and binder flow; and
3. The complete recovery of mechanical properties due to diffusion of asphaltene structures.

Step 1 is supposed to be the fastest, resulting only in the recovery of stiffness, while steps 2 and 3 are thought to occur more slowly but improve both the stiffness and strength of the material.

Jacobs (1995) studied the fatigue properties of asphalt mixes under sinusoidal loading and found that the introduction of rest periods has a beneficial effect on the fatigue resistance of the mixes. He proposed that this healing effect is caused by diffusion of maltenes (low molecular weight bitumen component) through the micro-cracks, re-establishing the bonds in the cracked area. The maltenes are involved, as they are the most mobile components of the bitumen, although higher molecular weight molecules could also diffuse during longer rest periods, resulting in completely restored material properties.

23

Lytton (2000) used the "dissipated pseudo strain energy concept" to explain the fracture and healing process. The fracture or healing of an asphalt mixture is related to two mechanisms: the surface energy storage and the surface energy release. Which one dominates is related to polar or non-polar characteristic of the binder. The energy stored on or near the newly created crack faces governs the energy available to make the crack grow. This surface energy depends mainly on the chemical composition of the binder. The micro-fracture and healing of the asphalt-aggregate mixture is governed by the energy balance per unit of crack area between the "dissipated pseudo-strain energy" released and the energy that is stored on the surface of the crack.

Freund and Suresh (2003) showed that the actual fatigue behavior can be expressed as dynamic energy equilibrium between surface energy (SE) and dissipated energy (DE) and can be formulated as:

Chemical potential (healing potential) = SE – DE　　　　　　　　　　(3)

This situation can be clarified using the flow chart shown in FIGURE 11 Based on this equilibrium formula, the damage would occur if surface energy is smaller than the dissipated energy, i.e., the healing potential is negative, thus the material has the tendency to increase surface energy through creating more surfaces. On the other hand, the healing would occur if the dissipated energy is at a very low level and the healing potential is positive, so the energy equilibrium leads to a decrease of surface energy, that is, some open crack surfaces will close.
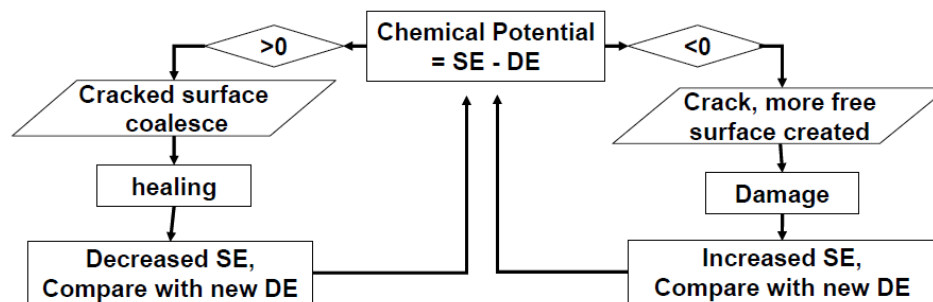
FIGURE 11 Energy equilibrium flow chart (Shen, 2006).

Studies on Healing

Developing an improved methodology that can describe and quantify the healing of asphalt concrete mixtures would represent a step forward toward more mechanistic pavement design as well as more rational characterization of asphalt mixtures. Moreover, other important concepts such as endurance limit can be validated based on the healing phenomenon that is assumed to have a great influence on asphalt mixture's fatigue behavior.

As stated before, Kim et al. (1990) distinguished between mechanical healing and chemical healing. To explore both mechanisms, laboratory experiments to study healing have been done at the mixture level as well as the asphalt and mastic level.

Mechanical Healing of Asphalt Mixtures

At the mixture level, the healing phenomenon has been extensively studied. Balbissi (1983) studied the effect of rest periods on the fatigue life of plasticized sulfur binders used in asphalt-like mixtures. The results indicated an increase in the fatigue life and more dissipation of energy as the number and length of the rest periods was increased. It also indicated that although longer rest period durations tended to increase the amount of recovery, the incremental benefit was diminished as rest period duration increased above 30 minutes.

Kim (1988) used the pseudo strain concept to calculate the magnitude of pseudo strain energy that can be recovered following rest periods of various lengths. Kim found that the pseudo strain energy is substantial and dependent on the length of the rest period, the temperature of the sample during the rest period, and the chemistry and rheological nature of the binder. The fact that pseudo strain energy was used by Kim to evaluate the "healing" effects of rest periods is significant, as the use of pseudo strain allows the time-dependent, viscoelastic effects (mechanical healing) to be separated from healing of micro-cracks (chemical healing) in damage areas.

Kim and Kim (1996) performed a field study on fatigue damage growth and microdamage healing during rest periods. The stress wave test technique and dispersion analysis method based on Short Kernel method (Douglas and Holt, 1993) employed in their study effectively assessed the changes in elastic modulus due to fatigue damage growth and microdamage healing in an asphalt surface layer. It was found that the elastic modulus decreases following a characteristic S-shape curve when plotted against number of loading cycles. The major reduction in the elastic modulus occurred during early stage of fatigue life when there were no visible cracks on the pavement surface. The authors concluded that this reduction was related to microcrack initiation, propagation, and densification. Moreover, it was found that the introduction of rest between loading cycles shifts the curve upward, resulting in a longer fatigue life.

Daniel and Kim (2001) evaluated the effect of rest periods and temperature on fatigue damage and healing potentials of two different asphalt mixtures when subjected to fatigue loading. This was accomplished using a three-point bending beam fatigue machine to induce damage. The impact resonance method was then used to evaluate the stiffness of the specimens through cycles of damage and healing. It was considered that the impact resonance method measures the very short time or low temperature response, which is in the elastic range of a viscoelastic material. Thus, the increase in modulus after rest periods is not affected by time – dependent relaxation and is attributed to microcrack healing in the asphalt concrete. The method used to study healing was based on a type of interrupted testing which introduced a specific length of rest period after a certain number of load cycles. Three groups of tests were performed: (1) testing under repetitive loading to failure at 68ºF (20ºC); (2) testing under repetitive loading at 68ºF (20ºC) with three rest periods at 68ºF (20ºC); and (3) testing under repetitive loading at 68ºF (20ºC) with three rest periods at 140ºF (60ºC). It was noticed that the higher healing temperature appeared to increase the amount of healing that occurred during the rest periods (FIGURE 12). The qualitative study of the two asphalt mixtures showed a different healing potential for each mixture based on two different binder grades (AC-20 and AR-4000).

Zhang et al. (2001) used indirect tension (IDT) test with repeated load (0.1 second haversine load followed by a 0.9 second rest period) at 50ºF (10ºC) to evaluate healing. A full 12-hour rest at 86ºF (30ºC) was introduced after certain amounts of load repetitions. Based on

25

dissipated creep strain energy limit from a strength test, the authors presented a threshold concept indicating that microdamage is healable during rest periods, when temperature increases, or both. Once the threshold of dissipated creep strain energy limit is exceeded, a non-healable macro-crack will propagate.

Si et al. (2002) performed a strain-controlled, repeated cyclic uniaxial fatigue test to evaluate the fatigue damage and healing of different asphalt concrete mixtures with two different types of both binder and aggregate by introducing a series of rest periods at 1,000 cycle intervals after the first 10,000 cycles. The test was terminated at 24,000 load cycles. The pseudo-strain concept was applied to characterize both damage and healing during the damage process. Both the pseudo-stiffness and dissipated pseudo-strain energy were adopted as they provide a clearer picture of damage by separating out the confounding effect of time dependency and viscoelastic effects from healing of micro-cracks. However, dissipated pseudo-strain energy was a strong and consistent quantifier of damage and healing. It was clear that the healing mechanism and process is complex; it was affected by the magnitude of damage prior to the rest period and hence the amount of damage material to be healed. Furthermore, microdamage healing is material property dependent.
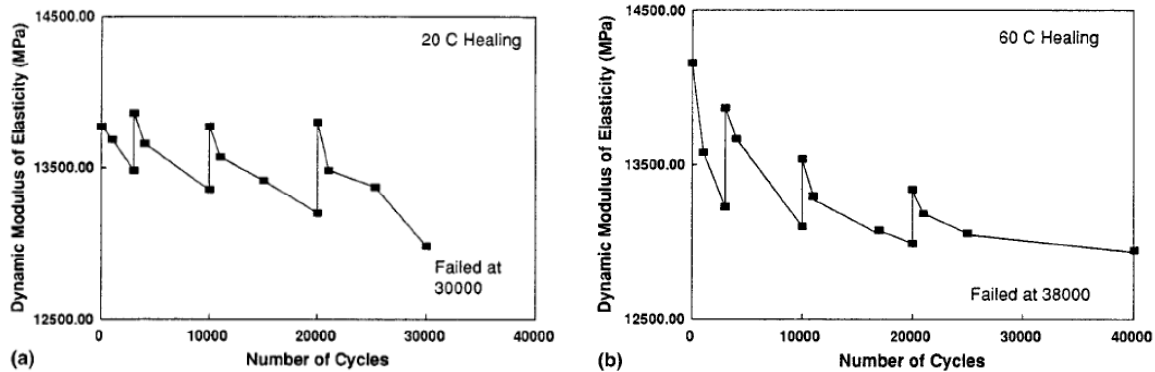
FIGURE 12 Typical dynamic modulus of elasticity through fatigue damage and rest periods: (a) 68°F healing; (b) 140°F healing (Daniel and Kim, 2001).

Seo and Kim (2008) used acoustic emission (AE) technology to characterize the damage accumulation and strength recovery in asphalt concrete mixture. A series of uniaxial tensile cyclic tests with and without rest period had been conducted on a 19-mm nominal maximum aggregate size asphalt concrete at 20ºC. During the fatigue tests, key AE parameters including emission counts were acquired from two piezo-type sensors attached to the middle of a 6-inch (150-mm) high, 3-inch (75-mm) diameter cylindrical specimen. Test results indicated that accumulative AE energy and AE count may be used not only to assess the initiation and propagation of fatigue damage, but also to quantify the beneficial effect of rest period on the performance of asphalt concrete. The frequency-amplitude analysis showed that crack formations coincided with the peaks of maximum AE amplitude (A_{max}) with higher frequencies, while healing is best described by A_{max} with lower frequencies during the rest periods. In addition, it was demonstrated that the Kaiser effect, the stress dependence of AE generation, does not hold for fatigue in asphalt concrete.

Chemical Healing of Asphalt and Mastic

Usually, the term of chemical healing is used to refer to the healing of asphalt and mastic. According to Petersen (1984), the association force (secondary bond) is the main factor controlling the physical properties of asphalt cement. That is, the higher the polarity, the stronger the association force and the more viscous the fraction, even if molecular weights are relatively low.

Kim et al. (1990) investigated the effect of asphalt composition on the healing of asphalt cement. It was proposed that the healing mechanism is related to the flow properties of the asphalt. The longer aliphatic side chains on the various polynuclear aromatics hinder molecular structuring, allowing for greater fluidity and micellar dispersion. Based on that concept, healing potential was found to be directly proportional to the amounts of longer-chained aliphatic molecules in the saturates and long-chained aliphatic side chains in the naphthene aromatic, polar aromatic and asphaltene generic fractions. The authors proposed the methylene (-CH$_2$) to methyl (-CH$_3$) ratio (MMHC) as a quantifier of the nature of the long-chained aliphatic molecules and side chains where MMHC is defined as the ratio of the number of methyl and methylene hydrogen atoms (H$_{-CH2}$ + H$_{-CH3}$) to the number of methyl and methylene carbon atoms (C$_{-CH2}$ + C$_{-CH3}$) in independent aliphatic molecules or aliphatic chains attached to cyc1oalkanes or aromatic centers. Based on the MMHC data, healing models were developed to correlate the healing index, HI, to the MMHC ratio though second order polynomials:

$$HI = -19.70 + 18.50 \ (MMHC) - 4.248(MMHC)^2, \quad (R^2 = 0.996) \tag{4}$$

where strain amplitude = 0.00674 unit, and

$$HI = -11.14 + 0.82 \ (MMHC) - 2.529(MMHC)^2, \quad (R^2 = 0.966) \tag{5}$$

where the strain amplitude is 0.0092 units,

Bahia et al. (1999) studied the effect of rest periods on fatigue damage recovery in dynamic shear rheometer (DSR) tests using various base and modified binders. In this study the asphalt specimens were tested first for 5000 cycles then were allowed to rest for specific rest periods before testing again. The rest periods included in this work were 0.5, 3 and 12 hours. The benefit of different rest periods were evaluated by comparing the initial fatigue curve (G* vs. number of cycles) to the second one after a certain rest period. If the two curves are similar, this no permanent damage was occurring and the binder was fully recovered to its original status. The results confirmed that healing has a significant effect on recovery from fatigue damage and that recovery was a time-dependent phenomenon and a function of composition of the base asphalt and type of modifiers.

Kim et al. (2003) studied the effect of fatigue fracture and fracture healing during controlled-strain, dynamic mechanical analysis (DMA) testing using sand asphalt samples. The sand asphalt samples were fabricated with two SHRP standard binders, AAD-1 and AAM-1. DMA testing was performed at 77°F (25°C) and 10 Hz. The mechanical response during DMA testing was monitored using three different damage indicators: change in dynamic modulus, change in pseudo stiffness, and change in dissipated strain energy. Dynamic mechanical analysis was found to be effective in characterizing the fatigue behavior and healing of asphalt binders and mastics in torsional fatigue. The authors reported that healing during several rest periods introduced at equal levels of damage increased the fatigue life. It was found that asphalt AAM-1

27

is a substantially better healer than asphalt AAD-1. This is consistent with previous studies on the fatigue and healing characteristics of these binders.

Chowdary (2004) investigated the healing of an asphalt sand mix in the laboratory. Cyclic triaxial tests were carried out on sand asphalt samples. The samples were tested at a constant load with rest periods introduced between successive loading cycles to observe the deformation response. A set of loading and rest cycles were applied and the recovery of deformation in the subsequent loading cycles after a rest period of one hour was chosen as a parameter to characterize the healing of sand asphalt mixtures. The experimental investigations and the results obtained have adequately proved the healing or beneficial deformation recovery of sand asphalt mixtures with rest periods. The amount of healing was observed to be dependent on the magnitude of lateral pressure applied on the specimen in the triaxial test.

Shen et al. (2009) studied the fatigue and healing of asphalt binders using laboratory dynamic shear rheometer (DSR) testing and a specifically designed intermittent loading sequence. The Ratio of Dissipated Energy Change (RDEC) approach was adopted to analyze the fatigue and healing characteristics of different asphalt binders. The test results showed that with the inclusion of a 6-second rest period, the fatigue life was extended about 7 times for PG 64-28 binder but 17 times for a PG70-28 binder. A strong correlation between healing of asphalt binder and the healing phenomenon observed in the HMA mixtures was demonstrated.

Healing Models

Schapery (1989) developed a model for healing in linear, isotropic viscoelastic materials assuming "interfacial forces of attraction and external" or applied "loading". The inclusion of surface forces in Schapery's model is significant, accounting for the case where complete contact of the fractured surfaces is not initially achieved by dominating loading. After expanding the first principles approach to healing speed, Schapery (1989) derived a relationship between healing speed, $h_2^\bullet$, and several material properties including surface energy:

$$h_2^\bullet = \left[\frac{2\gamma_m E_R^2 D_{1c} \Gamma_h}{(1-\nu^2) C_m^{1/m} H_v} \right]^{1/mc} \beta \tag{6}$$

where:

E_R	=Reference modulus, a constant derived of the stress transformation,
ν	= Poisson's ratio,
D_{1c}	=Compressive creep compliance constant (D_o component of the power law compliance is zero),
H_v	= Healing integral,
Γ_h	= Wetting surface energy,
m_c	=Slope of compressive,
γ_m	=Creep compliance versus time, and
C_m	= Average microcrack length.

The healing rate ($h_2^\bullet$) was directly related to the surface energy density, i.e., a greater surface energy density signifies a greater potential for healing, all other conditions being the same.

Lytton et al. (1998) developed a similar model to explain the healing rate between fracture surfaces. The recovery rate depends essentially on the same properties that appear in Schapery's earlier model, but a key difference is the assumption that the surface energy is an inhibitor of healing. Assuming that the surface energy is an energy density required to close a given area of crack face, the lower this surface energy density is then the greater is the amount of healing. A higher surface energy density reduces the amount of crack surface that can be closed with the same amount of available energy. Lytton derived the following relationship between "healing speed" and surface energy, among other factors:

$$h_1^\bullet = \left[\frac{(K_{th})E_R D_{1c} H_v}{2\Gamma_h}\right]^{1/mc} \beta \qquad (7)$$

where K_{th} is a fitting constant.

Pronk (2005 and 2009) developed a model called Partial Healing (PH) model to describe the evolution of the complex stiffness modulus and phase angle during a bending test for a certain loading condition as well as the healing (in terms of complex stiffness modulus) after a rest period (FIGURES 13 and 14). The model is based on the assumption that the fatigue damage can be related to the dissipated energy per cycle. The PH model consists of two integral equations representing the evolution of the loss and storage modulus (Pronk, 2001).

Loss modulus $= S \sin(\phi) = F\{t\} = F_0\, e^{-Bt}\left[Cosh\{Ct\} + D\, Sinh\{Ct\}\right]$ (8)

Storage modulus $= S \cos(\phi) =$

$$G\{t\} = G_0 - F_0\left[\frac{\alpha_2}{C}e^{-Bt}\, Sinh\{Ct\} + \frac{\gamma_2}{\gamma_1}\left(1 - e^{-Bt}\left[Cosh\{Ct\} + E\, Sinh\{Ct\}\right]\right)\right] \qquad (9)$$

in which: $B = \dfrac{\alpha_1 + \beta + \gamma_1}{2}$, $C = \sqrt{(B^2 - \beta\gamma_1)} \rightarrow \beta\gamma_1 = B^2 - C^2$, $D=(\beta - B)/C$, and $E = (B - \gamma_1)/C$

where:

    S   = Stiffness modulus,
    ϕ = Phase angle, and
    $\alpha_1, \alpha_1, \gamma_1, \gamma_1$ and β = Model parameters.

These integrals represent the reversible (healing) and irreversible damage increase during loading. A mathematical deduction was applied for the solution to represent the case of load periods of N cycles followed by rest periods of M cycles. It was concluded that prediction of the PH model was much better when the model parameters ($\alpha_1, \alpha_1, \gamma_1, \gamma_1$ and β) were determined from a fit on the evolutions in the first and second load periods rather than using the first load period only.
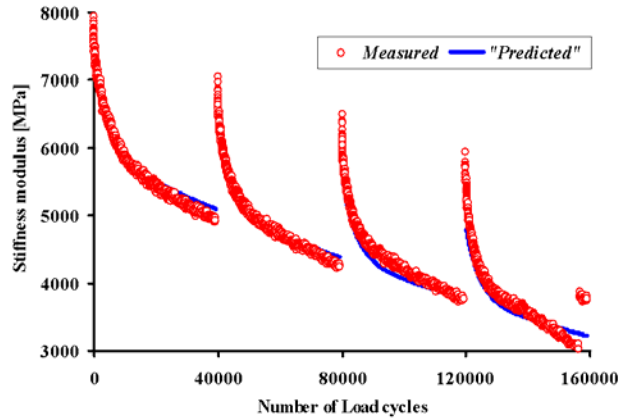
FIGURE 13 Comparison between measured and predicted stiffness moduli (Pronk, 2009).
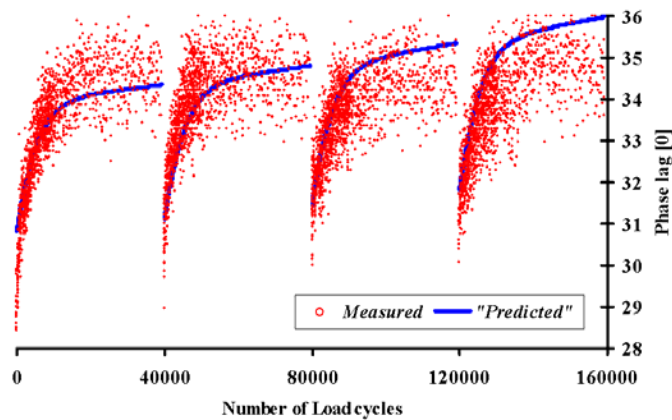
FIGURE 14 Comparison between measured and predicted phase angles (Pronk, 2009).

CHARACTERIZATION OF HMA FATIGUE BEHAVIOR

There are two main approaches that can be utilized to characterize the fatigue behavior of asphalt concrete mixtures: phenomenological and mechanistic. The phenomenological approach is simple to use, however, it does not account for damage evolution through the fatigue process. On the other hand, the mechanistic approach is inherently more complex than the phenomenological one but it is more widely accepted because it uses material properties based on stress-strain relationships (Kim et al., 2003). The mechanistic approach can be implemented through any of the followings:

- Dissipated energy,
- Fracture mechanics, and
- Continuum damage mechanics.

Phenomenological Approach

The phenomenological approach usually relates the stress or strains in the HMA layer to the number of load repetitions that cause failure (SHRP A-404, 1994). It is a combination of the

phenomenological observation and the laboratory- tabulated data derived from designated fatigue tests.

This approach has been widely used with Miner's (1945) linear law of cumulative damage in conventional asphalt pavement design and performance analysis. The damage is calculated as the ratio of the predicted number of traffic repetitions to the allowable number of load repetitions (to some failure level) as shown in Equation 10. Theoretically, fatigue cracking should occur at an accumulated damage value of 1.0. If a normal distribution is assumed for the damage ratio calculated, the percentage of area cracked can be computed and checked with field performance.

$$D = \sum_{i=1}^{T} \frac{n_i}{N_i} \tag{10}$$

where:

    D = damage.
    T = total number of periods.
    n_i = actual traffic for period i.
    N_i = allowable failure repetitions under conditions prevailing in period i.

Results from the fatigue test can be formulated depending on the mode of loading: stress or strain loading mode. Pell (1967) demonstrated that the tensile strain is the more important parameter for fatigue cracking. He introduced an approach to relate the initial strain to load repetition, even in a controlled stress mode of testing, as follows:

$$N_f = K_1 \left(\frac{1}{\varepsilon_o} \right)^{k_2} \tag{11}$$

where:

    N_f = number of load applications to fatigue failure;
    ε_o = tensile strain;
    k_1, k_2 = material regression constants from the laboratory testing.

Because of the phenomenological nature of this relationship, some have proposed applying adjustments to this relation to obtain a "better fit" with observed behavior differences. Bonnaure et al. (1980) and Finn et al. (1977) noted differences in the coefficients of this equation for different temperatures. They proposed a fatigue formula using modulus as follows:

$$N_f = K_1 \left(\frac{1}{\varepsilon_o} \right)^{k_2} \left(\frac{1}{E} \right)^{k_3} \tag{12}$$

where:

    E   = stiffness of the material;

    k_1, k_2, k_3 = material regression constants from the laboratory testing.

A drawback of the phenomenological approach is that it does not provide a mechanism of damage accumulation in the mixture under the repetitive load. Furthermore, the accumulation of

damage is treated as linear in the strain-fatigue life relationship which has been found incorrect at low strain/damage condition (Carpenter et al., 2003). Because it is material and loading mode dependent, this approach cannot be applied directly to the complex loading scenarios that are actually common to in-service pavements; the traditional phenomenological approach also does not account for the complexity of asphalt mixture mechanism such as healing and stress redistributions, which are known to have significant effect on fatigue behavior of asphalt mixtures (Shen, 2006).

Various agencies have calibrated these models to their specific pavements and mixtures. Carpenter (2006) presented the most common fatigue models used by several agencies. The following sections describe some well-known fatigue models used by national and international agencies as well.

Illinois DOT/University of Illinois Model

Elliott and Thompson (1986) used deflection-based performance equations from the AASHO Road Test at two Present Serviceability Index (PSI) to estimate the value of the k_3 coefficient. These two equations are based on the spring normal Benkelman Beam deflection. They developed an algorithm that relates load repetitions to failure with the surface deflection:

$$N_{18} = 5.6 \times 10^{11} / \Delta^{4.6} \tag{13}$$

where:

N_{18} = Number of 18-kip loads to fatigue failure, and

Δ = Surface deflection (mils) for 18-kip axle load (Benkelman Beam).

This relation was substituted in the fatigue equation and the final estimate of the k_2 coefficient was established for each equation. Values of the k_2 and k_3 coefficients were used with the Road Test data and the design algorithm for asphalt strain to calculate an average k_1 value. From this analysis, the following fatigue model was developed by Elliot and Thompson (1986):

$$\text{Log } N = 2.4136 - 3.16 \times \text{Log } \varepsilon - 1.4 \times \text{Log } E_{ac} \tag{14}$$

where:

N = number of load repetitions to cracking,

ε = predicted AC strain (in/in), and

E_{ac} = AC dynamic stiffness modulus (psi).

The typical fatigue relation used by the Illinois Department of Transportation, from Thompson (1987), is:

$$N_f = 5 \times 10^{-6} \left(\frac{1}{\varepsilon} \right)^{3.0} \tag{15}$$

SHRP A-404 Model

An accelerated performance test for defining the fatigue response of asphalt-aggregate mixes and their use in mix analysis and design systems was presented in SHRP A-404 (1994). The effect of the following variables on fatigue performance of asphalt concrete mixtures was investigated in this study: asphalt type (8 types), aggregate type (2 types), asphalt content, air voids content (2 levels), strain levels (2 levels), replicates (2 replicates), frequency (10 Hz), and test temperature (68°F). Based on the experiment, the following model was obtained:

$$N_f = 466.4e^{0.052VFB} (\varepsilon_o)^{-3.948} (S_o)^{-2.270} \tag{16}$$

where:

N_f = fatigue life,

ε_o = initial strain (in/in),

S_o = initial loss stiffness (psi), and

VFB = percentage of voids filled with bitumen.

The Asphalt Institute Model

The fatigue relation for the Asphalt Institute (AI) was developed based on laboratory fatigue data for selected sections of the AASHO Road Test by the Asphalt Institute (1982) and Finn et al. (1977). The following fatigue relation was developed by the Asphalt Institute (1982):

$$N_f = 18.4 \times (C)(4.325 \times 10^{-3})(\varepsilon_t)^{-3.291}|E^*|^{0.854} \tag{17}$$

where:

N_f = number of 18,000 lb equivalent single-axle loads

ε_t = tensile strain in asphalt layer, (in/in)

$|E^*|$ = asphalt mixture dynamic modulus (psi)

C   = function of volume of both voids and asphalt

$$C = 10^M \tag{18}$$

where:

$$M = (\frac{Vb}{Vv + Vb} - 0.69)$$

Vb = volume of asphalt, percent

Vv = volume of air voids, percent

SHELL Pavement Design Manual Model

The SHELL fatigue criterion is based on strain and modulus. The following formula is used to predict fatigue life (Shell (1978)):

$$N = 4.91 \times 10^{-13} (0.86\ V_b + 1.08)^{5.0} (1/\varepsilon)^{5.0} (1/S_{mix})^{1.8} \qquad (19)$$

where:

N = number of load cycles to failure,

V_b = volume of asphalt in the mixture (%),

ε = maximum tensile asphalt concrete strain, (in/in), and

S_{mix} = dynamic modulus of the asphalt mixture, (ksi).

Transport and Road Research Laboratory (TRRL) United Kingdom Model

The TRRL fatigue criterion was developed in TRRL Report 1132, Powell et al. (1984), and is based on the field performance of 34 sections of experimental road with dense base macadam and 29 sections of experimental rolled asphalt base. A multi-layer elastic model was used to calculate the dynamic strains. The accumulation of fatigue damage was calculated based on Miner's hypothesis. Considerable adjustment was needed to correlate between laboratory fatigue relations and field performance.

The design life could be calculated using the following relationships:

For 85% probability of survival and an equivalent temperature of 20°C (68°F):

For dense bitumen macadam (100 pen.):

$$N_f = (4.169 \times 10_{-10})(1/\varepsilon_r)^{4.16} \qquad (20)$$

For hot rolled asphalt (50 pen.):

$$N_f = (1.660 \times 10^{-10})(1/\varepsilon_r)^{4.32} \qquad (21)$$

where:

N_f = the road life in standard axles, and

ε_r = the horizontal tensile strain at the underside of the bound layer under a standard wheel load.

PDMAP – NCHRP Project 1-10B

The PDMAP (Probabilistic Distress Models for Asphalt Pavements) program was developed to enable highway engineers to predict distress conditions of given pavement sections. The PDMAP program employs probabilistic analysis, which computes the expected amount of damage with specified reliability factor at any time during the analysis period (Finn et al. (1977)).

The prediction model for fatigue cracking used in PDMAP is based on the fatigue testing done by Monismith et al. (1970) as follows:

$$\text{Log } N_f = 14.82 - 3.291 \text{ Log } (\varepsilon/10^{-6}) - 0.854 \text{ Log } (|E^*|/10^3) \qquad (22)$$

where:

N_f = load applications of constant stress to cause fatigue failure;

ε = initial strain on the bottom of the asphalt concrete;

$|E^*|$ = complex modulus (psi).

Cracking and rutting observations from the AASHO Road Test were used to calibrate the above equation. A shift factor of 13 was used for the 10 percent cracking and 18.4 for the 45 percent cracking.

NCHRP 1-37A Calibrated Fatigue Model

This model contains significant modifications to the standard form of the fatigue equation, but still relies on the basic strain-modulus form. Because thick and thin pavements exhibit different behavior when analyzed with the standard phenomenological model, changing from constant strain in a thin pavement to constant stress in a thick HMA layer, the NCHRP Project 1-37A research team elected to add a variable to change coefficients as the HMA layer becomes thicker. This model takes its basic form from the Asphalt Institute equation.

An extensive calibration process using LTPP field section data was conducted to establish the coefficients for different mixtures and different parts of the United States. The final form of the model from El-Basyouny and Witzcak (2005) is:

$$N_f = \beta_{f1} \, k_1 (\varepsilon_t)^{-\beta f_2 k_2} (E)^{-\beta f_3 k_3} \qquad (23)$$

where:

N_f = Number of load repetitions to fatigue failure,

ε_t = tensile strain at the critical location,

E = the dynamic modulus of the HMA,

k_1, k_2, k_3 = Laboratory regression coefficients, and

$\beta_{f1}, \beta_{f2}, \beta_{f3}$ = Calibration parameters.

Basically, the exponents k_2 and k_3 are constants, and the coefficient k_1 contains the mixture variables. Other coefficients are included for constant stress to constant strain considerations. The calibration parameters are designed to reduce the bias and scatter in the prediction.

Mechanistic Approach

The mechanistic approach explores the mechanisms of fatigue behavior on a more fundamental basis than the phenomenological approach. The dissipated energy, fracture

mechanics, and continuum damage mechanics methods may be categorized as mechanistic approaches to the study of asphalt concrete behavior.

Dissipated Energy

When applying load to a material, the material will exhibit some strain induced by the acting stress. The area under the stress-strain curve represents the energy being input into the material. When the load is removed from the material, the stress is removed and the strain is recovered as shown in FIGURE 15. If the loading and unloading curves coincide, all the energy put into the material is recovered after the load is removed. If the two curves do not coincide, there is energy lost in the material. This energy can be lost through mechanical work, heat generation, or damage in the material in a manner that cannot be used to return the material to its original shape. This energy difference is the dissipated energy of the material caused by the load cycle (Ghuzlan, 2001). So, dissipated energy can be defined as the damping energy or the energy loss per load cycle in any repeated or dynamic test.

The equation for calculating dissipated energy per cycle in a linear viscoelastic material in the flexural fatigue test is given by the following equation (Tayebali et al., 1994):

$$\omega_i = \pi \sigma_i \in_i \sin \phi_i \tag{24}$$

where:

ω_i = Dissipated Energy at load cycle i,

σ_i = Stress at the load cycle i,

$\in_i$ = Strain at the load cycle i, and

ϕ_i = Phase angle between stress and strain at load cycle i.
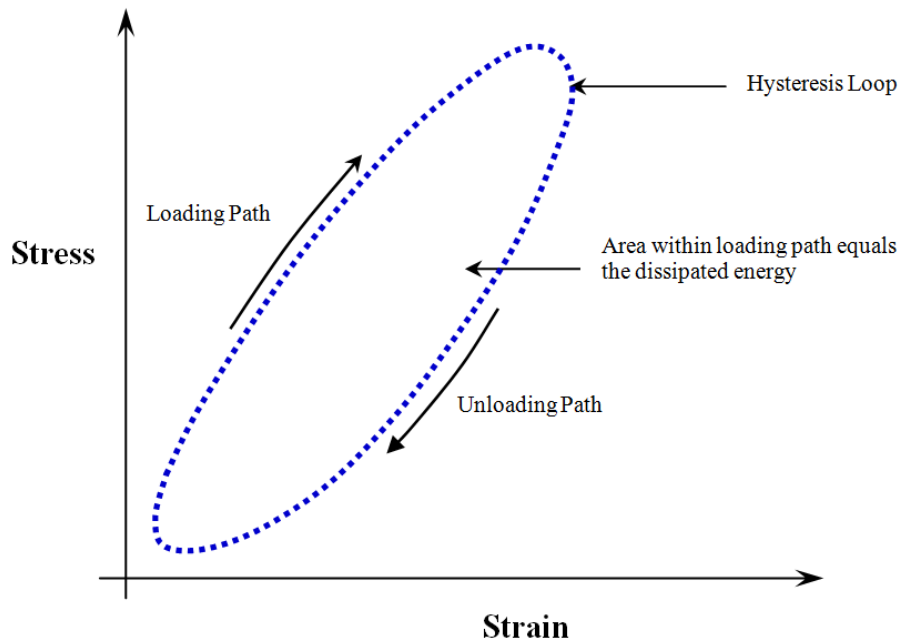
FIGURE 15 Stress-strain curve for viscoelastic solid.

Current applications of dissipated energy to describe fatigue behavior assume that all of the dissipated energy goes into damaging the material (Ghuzlan, 2001). In reality, this is not the case for asphalt concrete as a hysteresis loop is created due to the viscoelasticity of the material, even if no damage is induced. Only part of the total dissipated energy goes to damaging the material, and the remainder is accounted for by viscoelasticity and other factors.

It was experimentally demonstrated by Manfredi (2001) that energy dissipated during plastic cycles at low amplitude, without induced damage, will not contribute to damage and should be excluded from the total energy when damage is considered. It was observed that viscoelastic materials have a capacity to store and dissipate mechanical energy. Subsequently, when sustaining external loading, part of the dissipated mechanical energy can be converted into thermal energy through viscoelastic damping, therefore reducing material fatigue damage (Hilton and Yi, 1992). As a source of released energy, this part of dissipated energy will not create fatigue crack propagation and should be eliminated from the total dissipated energy calculation for predicting fatigue failure.

It was found in a study conducted by Van Dijk and Visser (1977) that the fatigue behavior under different dynamic tests and sets of conditions for different mixes can be described by a single mix specific relationship. This relationship is the number of the cycles to fatigue failure related mainly to the amount of energy dissipated during the fatigue test. All the factors including rest period, mode of loading, temperature, and frequency, did not significantly influence the dissipated energy relationship. The authors reported that the slopes of the lines representing different mixes are nearly the same and similar to the 0.67 slope suggested by Chomton and Valayer (1972). On the other hand, some researchers found that this relationship was mix dependent (Van Dijk et al., 1972; and SHRP A-404, 1994). The University of California at Berkeley study (SHRP A-404, 1994) reported that all lines are not parallel and have different slopes. Based on previous dissipated energy studies on the fatigue life of asphalt concrete mixtures, various representations and applications were proposed as discussed below.

Initial Dissipated Energy Approach

Initial Dissipated Energy (IDE) is the dissipated energy measured at the initial loading cycles and which is usually the dissipated energy at the 50th loading cycle. Initial dissipated energy can be a good indicator of fatigue performance for similar mixture types. It was found by Ghuzlan (2001) that the initial dissipated energy is one of the most important factors that affect HMA's fatigue behavior. SHRP A-404 (1994) used the following surrogate model to relate the initial dissipated energy to fatigue life:

$$N_f = 6.72 \, e^{\,0.049 \, VFB} \, (w_o)^{-2.047} \tag{25}$$

where:

N_f = design life,

VFB   = percentage of voids filled with bitumen, and

w_o = initial dissipated energy.

One disadvantage of the initial dissipated energy approach is that it is not appropriate for the whole loading range, in particular for a low strain fatigue test (Carpenter and Shen, 2005 and 2006). This approach also does not account for the effect of healing.

Cumulative Dissipated Energy Approach

The cumulative dissipated energy is the summation of all dissipated energy per cycle and is defined by the following equation:

$$W_N = \sum_{i=1}^{N_F} \pi \sigma_i \in_i \sin \phi_i \tag{26}$$

A relationship between the cumulative dissipated energy and the number of the loading cycles is characterized as:

$$W_N = A \, (N_f)^Z \tag{27}$$

where:

W_N = cumulative dissipated energy to failure,

A, Z = experimentally derived mix coefficients, and

N_f = number of load cycles to failure.

It was concluded by Van Dijk (1975 and 1977) that there was a strong relationship between the cumulative dissipated energy and the number of loading cycles to failure. This relationship is not affected by the loading mode, frequency (between 10 and 50 Hz), temperature (between 50 and 104 ºF), or the occurrence of rest periods where it is highly material dependent.

Work Ratio Approach

This approach was first introduced by Van Dijk and Visser (1997) and further developed by Rowe (1993). The work ratio, $\psi N1$, is defined as the ratio between the product of the initial dissipated energy in cycle 1, w_0, and N1 divided by the cumulative dissipated energy, as shown in Equation 28:

$$\psi_{N1} = \frac{woN1}{W_{N1}} \tag{28}$$

where:

w_0 = initial dissipated energy;

N1 = number of load cycles to crack initiation;

W_{N1} = cumulative dissipated energy at cycle N1.

Rowe (1993) found that the work ratio can be used effectively to predict the fatigue life to crack initiation through Equation 23. The crack initiation is assumed to occur at 60% reduction of original extensional complex modulus as shown in Equation 29.

$$N1 = 205 \, V_b^{6.44} \, w_0^{-2.01} \, \psi_{N1}^{1.64} = \tag{29}$$

where:

N1 = number of load cycles to crack initiation,

38

V_b = volume of binder (%),

w_0 = initial dissipated energy, and

ψ_{N1} = work ratio.

Dissipated Energy Ratio Approach

Tayebali et al. (1992) introduced two terms: the stiffness ratio which is the ratio of stiffness at load cycle (i) to the initial stiffness; and the dissipated energy ratio which is defined as the ratio of the cumulative dissipated energy up to load cycle (i) to the cumulative dissipated energy. It was suggested by him that there is a unique relationship between the stiffness ratio and the dissipated energy ratio, but not necessarily between cumulative dissipated energy and fatigue life, which is also verified by SHRP A-404 (1994). This relationship was found to be mix and temperature dependent.

Carpenter and Jansen first initiated an improved implementation of the dissipated energy concept for HMA fatigue analysis, in which a dissipated energy ratio was used as a parameter to relate to fatigue life (Carpenter and Jansen, 1997). This approach believes that not all the dissipated energy is responsible for material damage. For each cycle, the loss of energy due to material mechanical work and other environmental influences remains almost unchanged. Therefore, if the dissipated energy starts to change dramatically, it could be explained as the development of damage. Later, this approach was examined and refined by Ghuzlan and Carpenter (Ghuzlan and Carpenter, 2000; Ghuzlan, 2001; and Carpenter et al., 2003). It is found that the relationship between dissipated energy ratio and fatigue life is fundamental as it is independent of loading level, loading mode, and mix type (Carpenter et al., 2003).

Ratio of Dissipated Energy Change Approach

The dissipated energy ratio (DER) approach was further improved by Shen (2006) and was renamed as the ratio of dissipated energy change (RDEC) approach considering the fact that it is using the ratio of the amount of dissipated energy change between different loading cycles to represent the damage propagation. The ratio of dissipated energy change is defined as the average change in dissipated energy between two cycles divided by the dissipated energy from the first of the two cycles (NCHRP 9-44, 2008):

$$\text{RDEC}_a = \frac{(\text{DE}_a - \text{DE}_b)}{(b - a) \times \text{DE}_a} \tag{30}$$

where:

RDEC_a = ratio of dissipated energy change for cycle a,

DE_a = dissipated energy for cycle a, and

DE_b = dissipated energy for cycle b.

The basic premise of this approach is that the change in dissipated energy per cycle of loading is related to the growth of damage that occurs in HMA for a given mixture; a plot of the ratio of dissipated energy change as a function of loading cycle forms a broad "U" shape as shown in FIGURE 16. Lower plateau values (PV) imply lower damage per cycle. The plateau

value for a given mixture depends on the mixture properties, the applied strain level, and the duration of rest periods. Plateau values decrease with decreasing applied strain and increasing rest period duration (Carpenter and Shen, 2006).
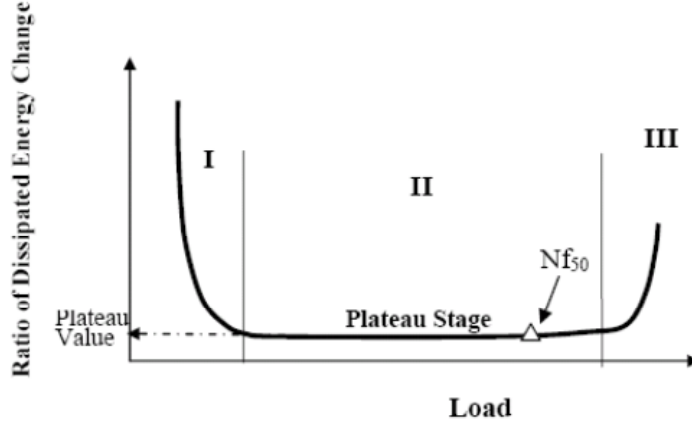
FIGURE 16 Typical ratio of dissipated energy change versus loading cycles plot (Carpenter et al., 2003).

The distinction of the RDEC approach is the relationship between the energy parameter, plateau value (PV), and the fatigue life (N_f). This relation, as presented in Equation 31, is unique for all HMA mixes, all loading modes (controlled stress and controlled strain), all loading levels (normal and low damage levels), and various testing conditions (frequency, rest periods, etc.) (Shen, 2006).

$$N_f = 0.4801(PV)^{-0.9007} \tag{31}$$

Furthermore, a preliminary PV prediction model was developed by Shen and Carpenter (2007) based on material properties and load response. The PV prediction model was constructed with a regression R^2 of 0.9017 and a standard error of estimate of 0.3437, as shown in Equation 32.

$$PV = 2.612 \times 10^{-10} \ IDE^{2.758} \ S^{2.493} \ VP^{3.055} \ GP^{-2.445} \tag{32}$$

where:

IDE = the initial dissipated energy,

S = flexural stiffness of HMA mix from the laboratory fatigue test, MPa,

VP = volumetric parameter $VP = \dfrac{AV}{AV + V_b}$,

AV = air voids %,

V_b = the asphalt content by volume,

40

GP = the aggregate gradation parameter $GP = \dfrac{P_{NMS} - P_{PCS}}{P_{200}}$,

P_{NMS} = percent of aggregate passing the nominal maximum size sieve,

P_{PCS} = percent of aggregate passing the primary control sieve, and

P_{200} = percent of aggregate passing #200 (0.075mm) sieve.

Fracture Mechanics

Considering fatigue as a process of cumulative damage, fracture mechanics principles were utilized by several researchers to investigate cracking of paving mixtures. In this approach, fatigue cracking was characterized into three stages: crack initiation, stable crack propagation, and unstable crack fracture. It is usually assumed that the stable crack propagation consumes most of the fatigue life. The prediction of crack propagation life using fracture mechanics can be described by the well-known Paris' law (Paris and Erdogan, 1963):

$$\frac{dc}{dN} = A(\Delta K)^n \tag{33}$$

where:

    dc/dN = crack propagation rate per load cycle,
    N   = number of loading repetitions,
    C   = crack length,
    ΔK = stress intensity factor range during loading and unloading, and
    A, n   = material parameters.

Integration of the Paris equation between initial crack length, c_o, and critical crack length, c_f, gives the fatigue life (*Liang and Zhou, 1997*).

$$N_f = \int_{c_o}^{c_f} \frac{dc}{A(\Delta K)^n} \tag{34}$$

Schapery (1973) theoretically justified the use of Paris' law for the description of the crack growth process in viscoelastic materials and presented a relationship between crack growth velocity and material properties such as the creep compliance, tensile strength, and fracture energy to determine A and n in Paris's equation. Germann and Laytton (1979) found that the calculated values of A and n agree fairly well with those determined experimentally for high asphalt content samples. However, at lower asphalt content, the theoretical and experimental values differ significantly. It has been stated that although Schapery's analysis may be applicable in some instances, it has not been widely accepted. Even if the constants A and n can be related to some material properties as Schapery suggested they are still used in a power law relationship which at best can only describe a linear region of fatigue crack propagation, i.e. it will not describe fatigue crack propagation over the entire range of the crack driving force (Aglan and Figueroa, 1991). Majidzadah et al. (1972) stated that, at all temperatures for sand asphalt and asphalt concrete beams, A in Paris' law becomes a material constant. However, at higher temperature, A and n can no longer be considered as a material constant.

According to fracture mechanics theory, three possible fracture modes can be identified. These modes are Mode I-opening and closing mode (tension), Mode II-Shear sliding mode (shear), and mode III-Tearing mode (torsion). These different modes are shown in FIGURE 17. For thermal cracking of pavement materials, normally, Mode I is predominant. For fatigue cracking induced by traffic loads, normally, mode I and II could be considered to occur. Knowing that, under mode I, cracks would never propagate to the surface of the pavement and, consequently, Mode II solutions were generated for load-associated fatigue crack propagation analysis.

M ode I   M ode II   M ode III
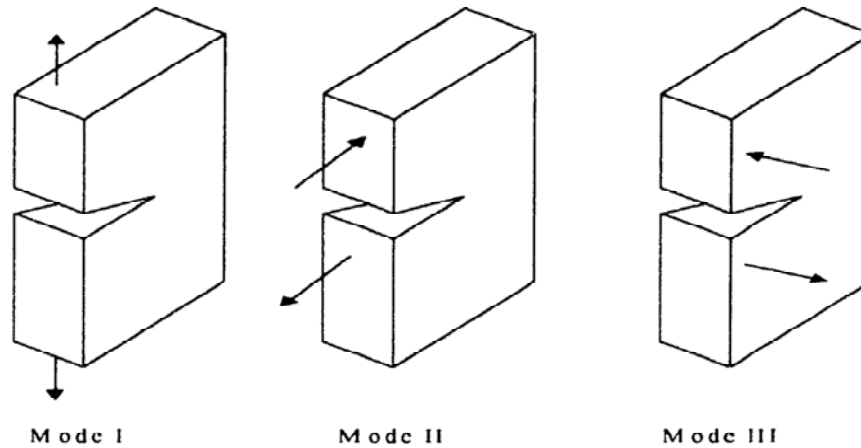
FIGURE 17 The three modes of loading to describe crack growth (Anderson, 1995).

Jacobs et al. (1996) investigated the applicability of fracture mechanics to asphalt concrete and showed that a crack in asphalt concrete grows discontinuously, indicating the limitation of the fracture mechanics approach for asphalt concrete (In linear elastic fracture mechanics, the crack propagates continuously). It was pointed out that the discontinuous crack propagation could be due to the inhomogeneity of asphalt concrete. Still, the measured discontinuous crack growth was treated as a continuous single crack in case the comparison was based on the maximum normal stresses occurring during the fracture process. Thus, the fracture mechanics principle was applied to describing the crack growth process. With finite element analysis, Jacobs found a relationship between the A and n value, as follows:

$$\log A = a + bn \tag{35}$$

where

a, b = regression parameters.

This relationship is important for practical purpose as Schapery (1973 and 1978) demonstrates that n values could be estimated by using simple test instead of time money consuming fatigue and crack growth test.

The constant K represents the proportion in which the stress approaches infinity and completely defines the crack tip stress conditions. The stress intensity factor in Paris' law can be replaced by the energy release rate J-integral. Many researchers have successfully calculated the energy dissipation with finite element methods instead of measuring the stress intensity factor

form laboratory specimens. Therefore, Paris' law fracture parameters A and n could be derived directly from the energy approach (Chen, 1997; and Si, 2001).

Continuum Damage Mechanics

Asphalt concrete is a history-dependent composite material. Therefore, accurate prediction of its behavior under realistic traffic loading conditions requires the application of the theory of viscoelasticity. To develop a realistic mechanistic model for asphalt concrete undergoing damage, the viscoelasticity and damage growth should be considered in the constitutive modeling.

In general, a continuum damage model consists typically of three major components:

- ➢ Selection of damage variables,
- ➢ Definition of strain energy density (as a function of damage variables and other state variables), and
- ➢ A damage evolution law.

If the model considers only fixed damage, the damage evolution law is not needed (Park et al., 1996).

A Continuum Damage Mechanics Approach (CDM) was developed through research efforts at North Carolina State University and Texas A&M University. This approach utilizes the viscoelastic correspondence principle and Work Potential Theory (WPT) described by Schapery (1984) to remove viscous effects in monitoring changes in pseudo-stiffness in repeated uniaxial tensile tests. Therefore, physical variables were replaced by pseudo variables based on the extended elastic-viscoelastic correspondence principle to transform a viscoelastic (linear, nonlinear, or both) problem to an elastic case. Schapery (1990 and 1991) developed a series of damage models for elastic and viscoelastic media based on thermodynamics of irreversible process and work potential theories with internal state variable to describe evolution of microstructural changes. The theories developed have been successfully applied to asphalt concrete mixtures (Park et al., 1996).

Kim (1988) developed a nonlinear elastic-viscoelastic uniaxial constitutive model by employing the extended elastic-viscoelastic correspondence principle in the concept of continuum damage mechanics that successfully accounted for damage growth through crack initiation and propagation and healing for any load history or mode of loading (Kim et al. 1997a, b). The major difference in Kim's approach from the dissipated energy approach stems from the recognition of the fact that the energy dissipation under cyclic loading is not only related to the damage growth, but also due to linear viscoelastic time dependency of asphalt concrete. The damage-independent viscoelastic time dependency was eliminated by the extended elastic-viscoelastic correspondence principle, and additional time dependency due to nonlinear damage was used to develop the damage-induced viscoelastic constitutive relations. All response of asphalt concrete specimens under fatigue loading was assigned to three mechanisms (Kim et al., 1998): fatigue damage growth, time dependence due to the viscoelastic nature of the material, and chemical healing across micro-cracks and micro-cracks interfaces.

A pseudo strain relation for a viscoelastic body with damage and without temperature change can be given by Equation 36.

$$\sigma = C(S_m)\varepsilon^R \qquad (36)$$

where

σ = stress,

ε^R = pseudo strain,

S_m = internal state variable of damage, and

$C(S_m)$ = internal function of damage.

More recently, Lee (1996) extended Kim's work and developed a more generalized uniaxial constitutive fatigue model for asphalt concrete mixtures. Lee's model can predict damage growth and recovery due to compound loading histories, in both controlled-strain and controlled-stress modes, composed of randomly applied multi-level loading with different loading rates and varying rest periods. The general form of the uniaxial pseudo variable constitutive equation for a viscoelastic body during damage can be expressed as follows (Kim, 2003):

$$\sigma = I_P C(S_m)\varepsilon^R \qquad (37)$$

where

I_P = initial pseudo-stiffness.

The constitutive model seems to be an elastic model due to the use of a pseudo variable and accounts for the response of the viscoelastic body and damage by a *C* function. The *C* function is then specially categorized into three selected functions in the following constitutive equation that was developed by Kim et al. (1997a):

$$\sigma = I_P(\varepsilon^R)\left[F + G + H\right] \qquad (38)$$

where:

F = damage function representing the change in the slope of the pseudo stiffness of each σ-ε^R loop,

G = hysteresis function representing the difference between loading and unloading paths, and

H = micro-damage healing function representing the change in secant pseudo-stiffness due to rest periods.

The damage function F is responsible for algebraically reducing the predicted stress evolved in the specimen during uniaxial fatigue loading; its counterpart for the healing regime of the test, H, accounts for the recovery during rest periods and the adjustment of the predicted stress levels thereafter. This constitutive model is capable of accurately predicting fatigue behavior of asphalt concrete under (1) constant-strain-rate monotonic loading; and (2) controlled-strain and controlled-stress cyclic loading.

Christensen and Bonaquist (2005) developed an approximate method to analyze the beam fatigue data using the continuum damage approach where damage estimates were based upon stresses and strains in the middle third of the beam but were applied to the entire beam. In this analysis, the beam was divided into ten equal layers from top to bottom, each 0.2-in. thick. The loading history is divided into ten logarithmically spaced intervals; damage is calculated during each of these intervals for each beam layer, and then a new modulus value is calculated for the following loading interval, as described below in FIGURE 18. It was observed that the relationship between the damage ratio at the beam's lower surface and the overall flexural stiffness damage ratio throughout the progress of a flexural fatigue test remained essentially constant regardless of the assumed material properties. So, this relationship was used to perform a continuum damage analysis using flexural fatigue data as opposed to uniaxial fatigue, by converting overall beam stiffness to pseudo-stiffness for the lower beam surface.
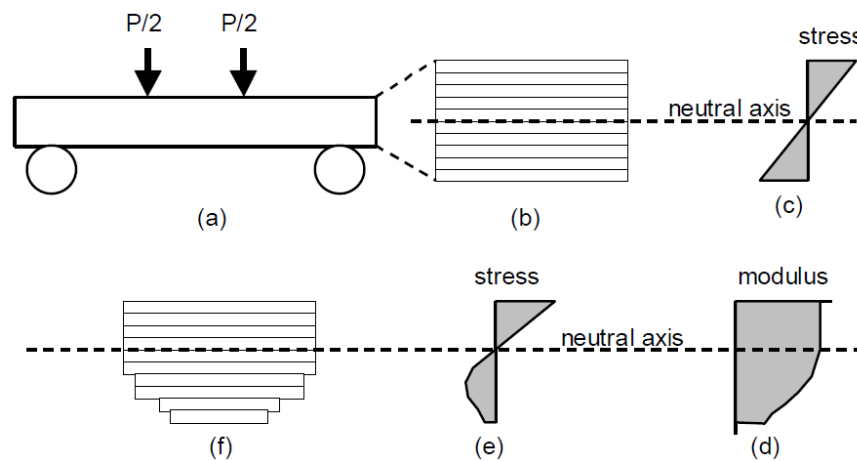
FIGURE 18 Continuum damage analysis of flexural fatigue (Christensen and Bonaquist, 2005).

In a parallel effort, Mello et al. (2009) successfully applied the continuum damage model to the beam fatigue test. The damage parameter expression that was used followed the same expression that Daniel (2001) proposed where the time intervals were corrected to account only for the time period during which the sample is under tension in haversine loading tests. In case of beam tests with harmonic loading, the tension time corresponds to only half of the total cycle time, as illustrated in FIGURE 19. Based on this, the expression to obtain the damage parameter from four-point bending tests was obtained by accounting only for that time.
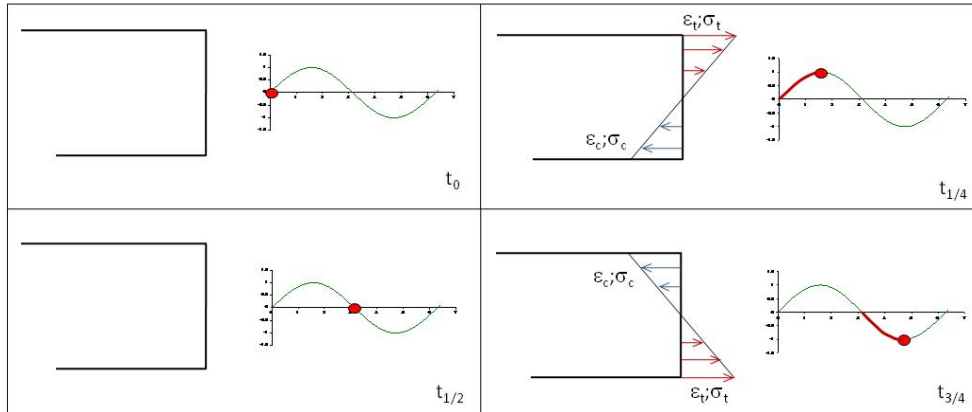
FIGURE 19 Stresses and strains in a transverse section of a beam subjected to a harmonic sine loading (Mello et al., 2009).

FATIGUE ENDURANCE LIMIT OF HMA

The concept of the endurance limit (EL) was originally introduced for metals in 1870 by Wöhler (Walter Schlitz, 1996) and was defined as the stress level below which failure never occurs, even for an indefinitely large number of loading cycles. Ferrous alloys and titanium alloys have a distinct limit, an amplitude below which there appears to be no number of cycles that will cause failure. Other structural metals such as aluminum and copper do not have a distinct limit and will eventually fail even from small stress amplitudes (FIGURE 20). An effective endurance limit for these materials is sometimes defined as the stress that causes failure at 1×10^8 or 5×10^8 loading cycles.
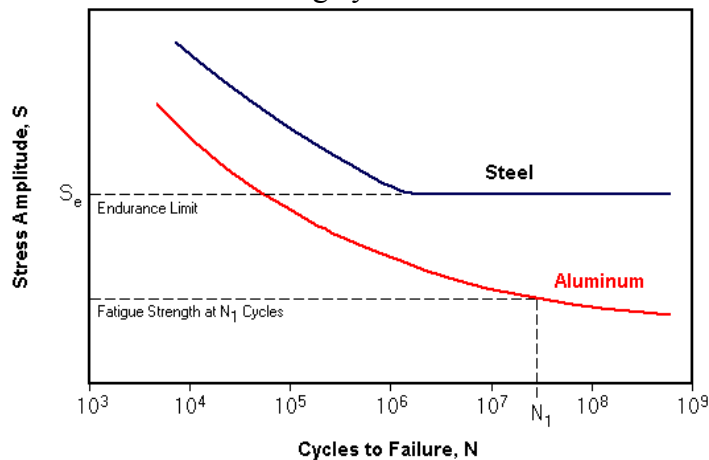
FIGURE 20 Typical S-N curve.

Definition of HMA Endurance Limit

The fatigue EL is a critical concept in the design of pavement structures that must resist large numbers of repeated loads. If the actual stress or strain levels applied to the pavement are kept below the endurance limit, the structure will be able, in theory, to withstand an infinite number of load applications. Based on a review of recent literature concerning the fatigue response of HMA, and recommendations made through NCHRP Project 9-44, a more formal definition of the endurance limit has been proposed as "A level of strain below which there is no cumulative damage over an indefinite number of load cycles". It has been hypothetically assumed that "HMA does exhibit an endurance limit". This endurance limit, however, does not reflect an absence of load induced damage in the HMA. It is the result of a balance between the damage caused by loading and the healing or damage recovery that occurs during rest periods. The endurance limit for HMA is, therefore, not a single value, but will change depending on the HMA material properties, the applied loading, and the environmental conditions.

Importance of Endurance Limit in Perpetual Pavement Design

The Asphalt Pavement Alliance, APA, has defined a perpetual pavement as "*an asphalt pavement designed and built to last longer than 50 years without requiring major structural rehabilitation or reconstruction, and needing only periodic surface renewal in response to distresses confined to the top of the pavement*" (APA, 2002). Ferne (2006) expanded upon this idea and defined the asphalt perpetual pavement through its life as a "*well-designed and constructed pavement that could last indefinitely without deterioration in the structural elements provided it is not overlooked and the appropriate maintenance is carried out*". Therefore, the performance of perpetual pavements is a function not only of the design but also traffic, climate, subgrade and pavement parameters (such as modulus), pavement materials, construction, and maintenance levels. These factors combined will contribute to how a pavement will perform over the course of its life (Walubita et al., 2008). Other expressions such as "long-life", "long-lasting", and "extended life" have also been used to describe the perpetual pavement.

Recently, pavement engineers have begun to introduce methodologies of designing pavements to resist rutting and bottom-up fatigue cracking, which are the two main pavement distresses seen on roadways. For perpetual HMA pavements, subgrade stress/strain levels are generally within acceptable limits and subgrade permanent deformations are not significant. Therefore, HMA thickness requirements for high-volume highway traffic are controlled by HMA fatigue cracking considerations (Brown et al., 2002).

Two different approaches are mainly recommended in the perpetual pavement concept. The first one is to construct a bottom lift for the base layer with a softer binder grade, higher binder content, or both. This type of mix in the bottom lift can stretch without cracking; thus it will have an increased fatigue life. The second approach is to increase the total thickness of asphalt layers as well as the stiffness of all layers such that the tensile strains at the bottom of the asphalt layer will be kept below the endurance limit that avoids bottom-up fatigue cracking (Romanoschi et al., 2006). In this case, the endurance limit concept can provide a mechanistic design tool where increasing the HMA layer thickness beyond that established by the endurance

limit would provide no increased structural resistance to fatigue damage and would represent an unneeded expense as shown in FIGURE 21.
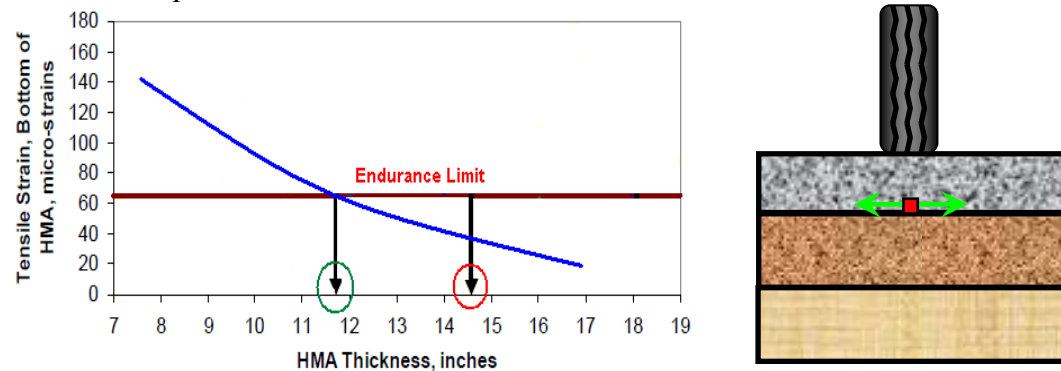
FIGURE 21 Endurance limit concept in perpetual HMA pavement design.

By controlling bottom-up fatigue cracking by keeping the tensile strain at the bottom of the HMA asphalt layer lower than the endurance limit, the pavement structure will probably be subject only to top-down fatigue cracking as a result of tire interaction and binder aging in the wearing course (Mahoney, 2001). Moreover, the pavement structure may show limited rutting belong in the surface layers. At this point, since the distresses in the pavement are kept in the wearing course, deep structural maintenance could be avoided and only surface treatment such as "mill and fill" maintenance would be enough to remedy surface cracks and rutting.

Evidence of HMA Endurance Limit in Laboratory and Field Studies

A number of laboratory and field studies have been conducted over the last five decades to check for the existence of an HMA fatigue endurance limit. Monismith and McLean (1972) first proposed 70 microstrain as a likely value of the endurance limit for asphalt pavements However, there was not sufficient test data to substantiate this observation. These authors observed that the log-log relationship between strain and loading cycles converged below 70 ms at approximately 5 million cycles (FIGURE 22). Based on this finding, Monismith and McLean designed a pavement structure that increased the fatigue life of the pavement from 12 to approximately 19-plus years using low strain design principles. Maupin and Freeman (1976) performed several simple flexure fatigue tests (third point loading) on asphalt concrete beams using controlled stress and controlled strain mode of loadings. The test results also showed that the fatigue curves converged in a similar way to that found by Monismith and McLean.
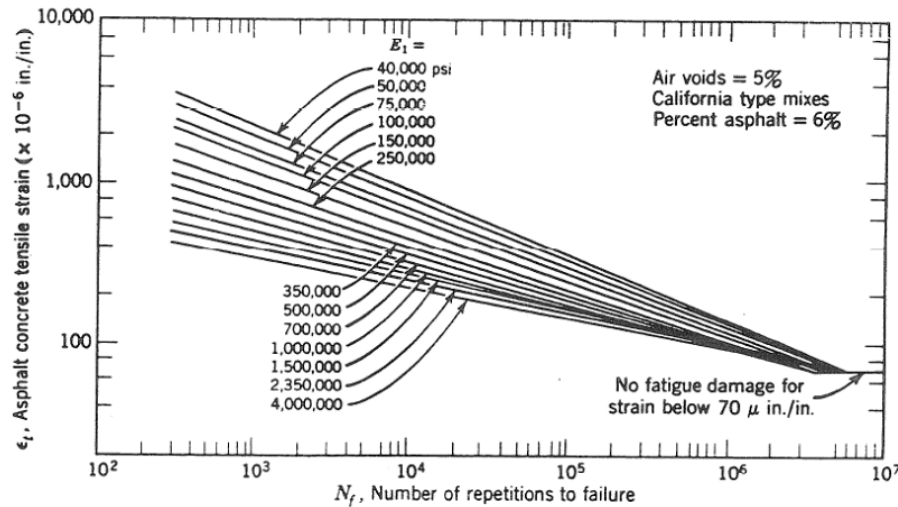
FIGURE 22 Typical failure criteria (fatigue limit) (Monismith et al., 1970).

Nishizawa et al. (1996) concluded that fatigue cracking does not occur when the tensile strain at the bottom of the asphalt pavement is held at less than 200 ms, and they suggested a design value of 150 ms. Research at the NCAT Test Track (Willis et al., 2009) has shown that pavements can withstand bending strains greater than 70 to 100. It was observed that some well-built field test sections were robust enough to withstand trafficking of close to 20 million equivalent single-axle loads (ESALs) even if they designed at higher strain levels.

Recent publications by Carpenter et al. (2003), Shen and Carpenter (2005), and Thomson and Carpenter (2006) investigated the fatigue endurance limit concept in asphalt mixtures. These studies strongly suggested that there is a fatigue endurance limit below which asphalt mixtures tend to have an extraordinarily long fatigue life. It has been showed that when the controlled strain/damage level is very low, distinctively different fatigue behavior can be found even for the same mixture. That is, there is a breakpoint between the normal strain-N_f curve and low strain-N_f curve. For the normal strain range, the strain-N_f curve can be defined by a power law relationship (or a linear relationship under log-log plot). For the lower strain range, the fatigue behavior of the asphalt mixtures changed such that any small decrease in the strain level will result in a large fatigue life extension (FIGURE 23). The strain level below the breakpoint can be considered as an endurance limit for each mixture type where HMA materials can have extremely long fatigue life.
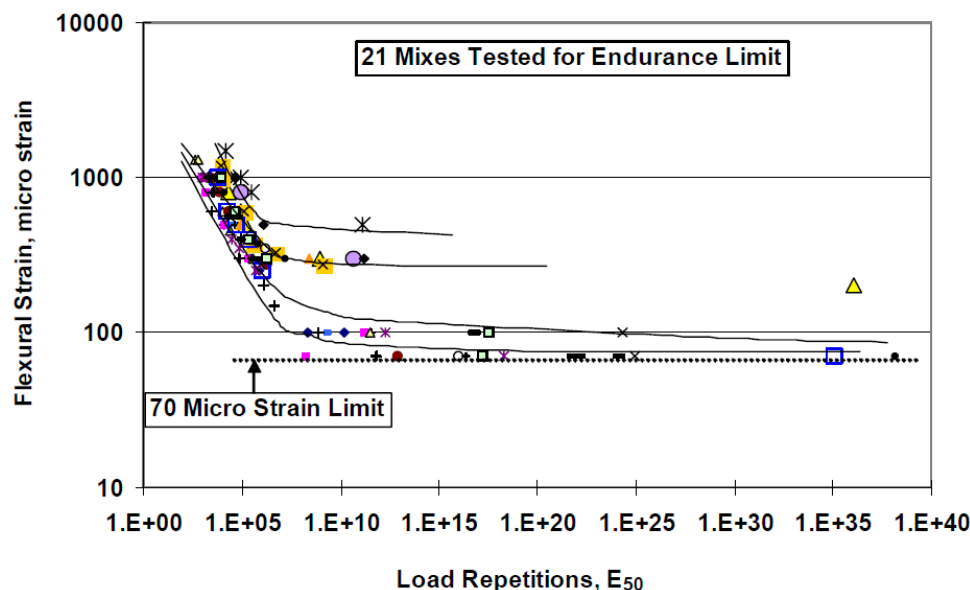
FIGURE 23 Strain – load relationship illustrating the fatigue endurance limit (Thomson and Carpenter, 2006).

Prediction of HMA Endurance Limit through Laboratory Studies

The definition of a long-life pavement varies from place to place. Nunn (1997) defines long-life pavements in the United Kingdom (UK) as those that last at least 40 years without structural strengthening. Similar studies done in the United States have confirmed the European experience on the performance of the perpetual pavement (Wu et al., 2004). Prowell et al. (2010) suggest that the maximum possible number of ESALs that a pavement would be subjected to over a 40-year period is approximately 500 million. Considering a shift factor of 10 between laboratory beam fatigue results and field performance for up to 10% fatigue cracking in the wheel path as recommended by Leahy et al. (1995), the fatigue endurance limit can be considered as the strain level that causes a beam fatigue specimen to fail at exactly 50 million loading cycles. Carrying out one fatigue test to such very high numbers of cycles can last for almost 60 days if the test is conducted continuously and at 10 Hz frequency. Methods based on extrapolating data or other shortcut methods can be used to predict the fatigue endurance limit of HMA from a smaller number of cycles to failure.

There are a number of methods that can be used to extrapolate the fatigue life at lower strain value (close to the endurance limit). These methods vary according to the model used. These models include exponential models (AASHTO T 321), logarithm model (Prowell and Brown, 2006), power models (Shen, unpublished data), Weibull survivor function (Tsai et al., 2002), two-stage Weibull functions (Tsai et al., 2004), and three-stage Weibull functions (Tsai et al., 2005). In addition, Prowell and Brown (2006) utilized the linear portion of the stiffness versus loading cycles curve in the extrapolation analysis at low strain levels. Peterson et al. (2004) stated that extrapolation of fatigue life at failure (50% reduction of initial stiffness) at lower strain values can be done from a test that only tested to 4 million loading cycles. Shen and

Carpenter (2005) extrapolated test results based on tests conducted to greater than 8 million cycles.

In NCHRP Project 9-38, Prowell and Brown (2006) performed beam fatigue tests at the National Center for Asphalt Technology (NCAT). To determine the fatigue endurance limit of various asphalt concrete mixtures, different extrapolation methods were applied to fatigue tests carried out at low strain values up to 10 million loading cycles. In addition, a few tests were carried out up to 50 million cycles to confirm the existence of endurance limit. It was observed that both the logarithmic model and the Weibull function showed better extrapolation of the test data at lower cycles to predict endurance limit. FIGURES 24 and 25 showed extrapolation comparisons of different applied models.
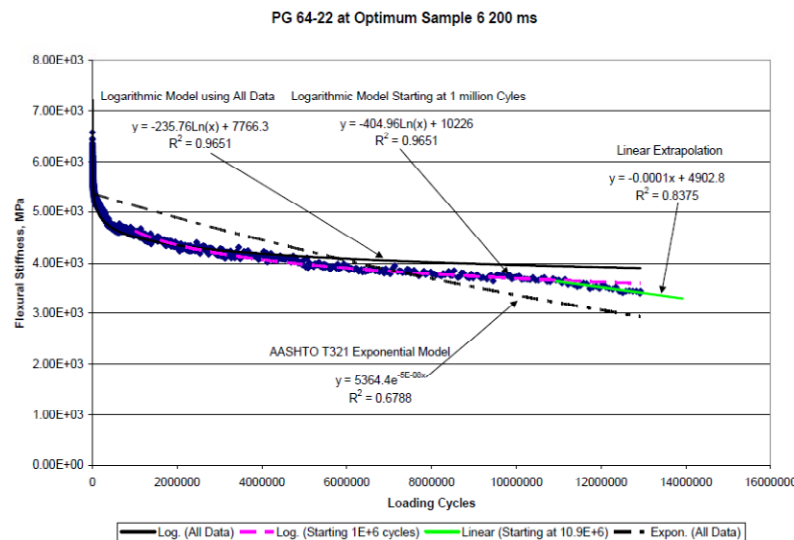
FIGURE 24 Various methods of extrapolation (Prowell and Brown, 2006).
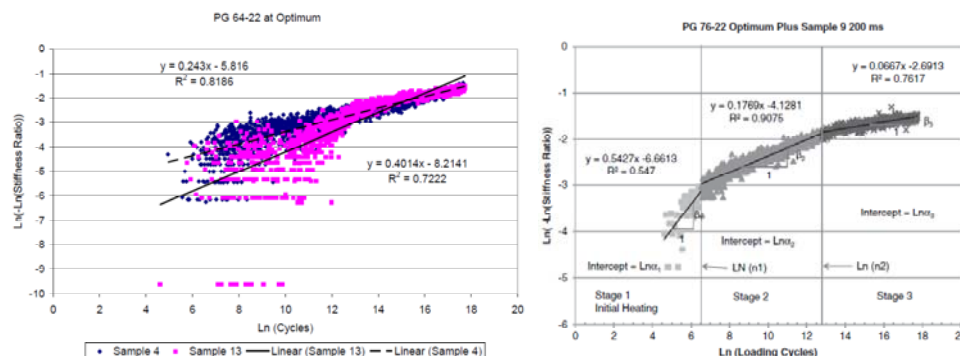
FIGURE 25 One-stage vs. three-stage Weibull extrapolation (Prowell et al., 2010).

Based on research conducted at University of Illinois, Shen and Carpenter (2005) used the Plateau Value (PV) of the Ratio of Dissipated Energy Change (RDEC) to develop a new method for predicting the endurance limit of asphalt concrete mixtures. The PV is the value of RDEC when it becomes almost constant or minimum, which means that there is a minimum

percent of input energy being turned into damage. Shen and Carpenter refined this technique and suggested that the RDEC plateau value should be calculated at the number of cycles that produced 50% of the initial sample stiffness. It has been indicated that there is a linear relationship between the log of the PV and the log of cycles to 50% initial stiffness for both normal and low (below the endurance limit) strain levels. This relationship was found to be unique for all HMA mixes, all loading modes (controlled stress and controlled strain), all loading levels (normal and low damage levels), and various testing conditions (frequency, rest periods, etc.) as indicated from FIGURE 26.

Considering this unique relationship between PV and N_f, the extremely long fatigue life under low strain/damage condition can be extrapolated for tests conducted for only limited amount of cycles. Laboratory tests and statistical analysis suggested that there is no significant difference between the PV predicted from shortened load repetitions as low as 500,000-cycle load repetitions and extended load repetitions as long as 3 millions cycle load. A tentative plateau value of 8.57E-9 was identified as indicating the endurance which is corresponding to the breakpoint in the fatigue life at 1.10E+7. This break point was identified based on a large body of fatigue test results obtained at normal strain ranges and extrapolated results at a low strain range as shown in FIGURE 27.
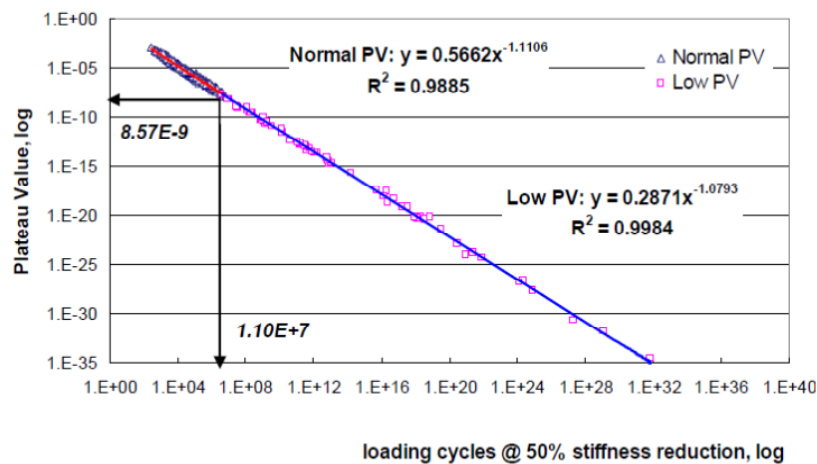
FIGURE 26 PV vs. Nf @ 50% stiffness reduction curve for all data (Shen and Carpenter, 2005).
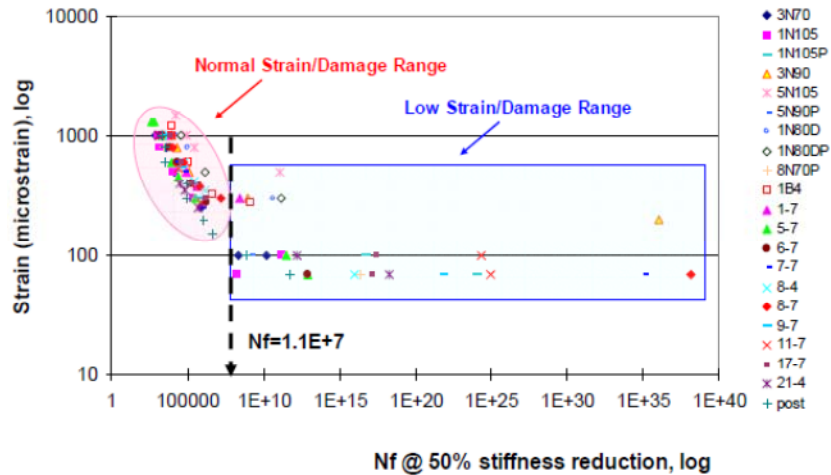
FIGURE 27 Traditional fatigue plots for all the data (Shen and Carpenter, 2005).

Underwood and Kim (2009) tried to validate the concept of PV using data from the uniaxial direct tension fatigue test. The same procedure as for the beam fatigue test was followed (Shen and Carpenter, 2005). However, though only limited experimental data, which represent a small range of materials, were used, the analysis supported the existence of such a curve for direct tension tests as seen in FIGURE 28.
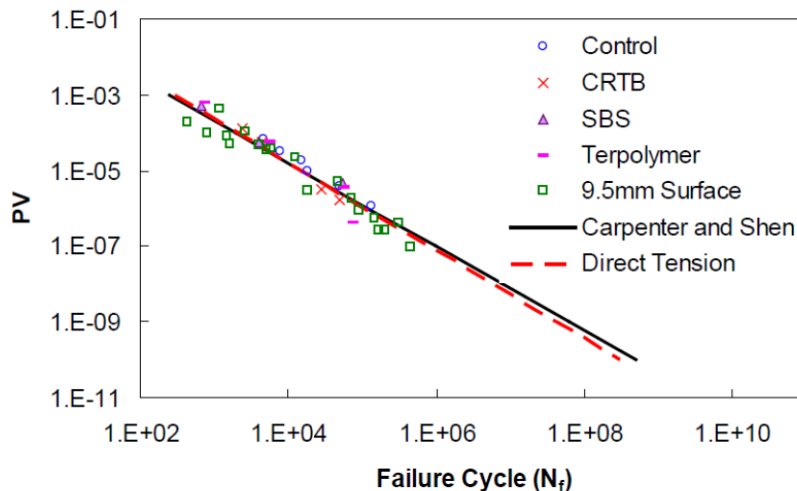
FIGURE 28 Relationship between the PV and N_f for direct tension samples (Underwood and Kim, 2009).

Soltani et al. (2006) developed a method that can be used to investigate the existence of an endurance limit for HMA using a new uniaxial fatigue testing protocol. Cylindrical specimens, 4.7-inch (120-mm) in height and 3.1-inch (80-mm) in diameter, were tested by applying a tension-compression loading at 50°F (10°C) and 10 Hz. The test method consists of applying three stages of continuous loading without any rest period. At Stage I and III, the same strain value is applied at a level lower than the endurance limit so no fatigue damage would

53

occur. During Stage II, a variable strain level is applied starting with a value high enough to produce damage in the first test and gradually decreased in the following tests. The difference between the moduli at the end of Stage I and III was used to indicate the level of fatigue damage imposed during Stage II. If the modulus values in stage III are lower than those in stage I, Damaged occurred at Stage II as the applied strain level is higher than the endurance limit as showed in FIGURE 29a. On the other hand, if the modulus values at stages III and I are equal, the strain level at Stage II is the fatigue endurance limit as showed in FIGURE 29b.
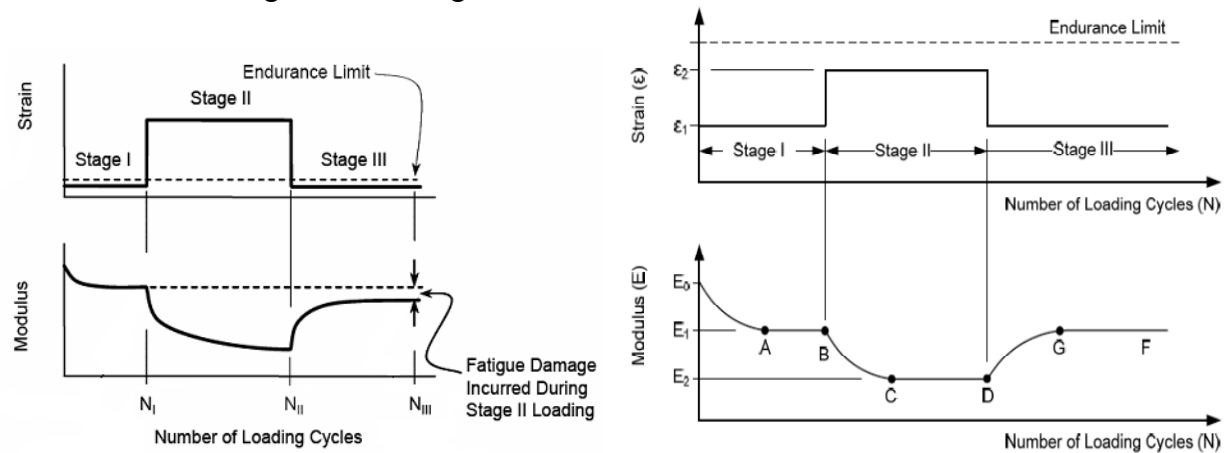
FIGURE 29 Schematic of loading in Stages I, II and III (Soltani et al., 2006).

As a part of NCHRP Project 9-38, Bhattacharjee et al. (2009) at University of New Hampshire developed an alternative approach to determine the endurance limit of asphalt concrete using the elastic-viscoelastic correspondence principle. This was done by separating the effect of viscoelasticity from damage development and without the need for long-term fatigue tests. Uniaxial direct tension fatigue tests under crosshead strain control were conducted by applying blocks of haversine loading to a uniaxial test specimen. Initially, a relatively low strain amplitude that is thought to be below the fatigue endurance limit is applied. Approximately 10,000 cycles are applied at this amplitude to allow the specimen to reach steady-state response. The applied strain amplitude is then increased and 10,000 more cycles are applied. The time lag between the loading blocks was about 5 to 10 seconds. This procedure is continued until the specimen fails as shown in FIGURE 30. The strain data then was converted to pseudo strain using the elastic-viscoelastic correspondence principle. The endurance limit was determined by identifying the strain level at which loop between stress and pseudo strain began to develop, indicating that damage had started to develop (FIGURE 31).

The major disadvantage of this methodology is that the identification of the loop formation in some cases is tricky and it is difficult to visually recognize whether a loop has truly formed or has only apparently formed due to data noise or other experimental difficulties. To overcome this drawback, Underwood and Kim (2009) suggested that using the slope of the stress-pseudo strain graph or the secant pseudo stiffness value (*C*) as a damage indicator is less subjective than identifying a loop. In case of no damage where the applied strain is considered as the endurance limit, the secant pseudo stiffness will equal unity ; in the case of damage, the secant pseudo stiffness will be less than unity. The researchers recommended a more practical

54

threshold value of 0.95 for the secant pseudo stiffness at the end of cycling of a given strain level to account for specimen-to-specimen variability and data noise. This threshold value means that the damage growth is so slow that it can be neglected.
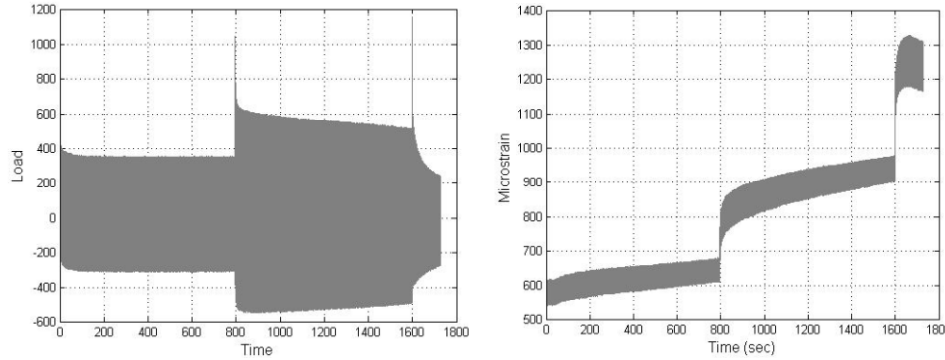
FIGURE 30 Typical loading and strain history for increasing amplitude uniaxial fatigue test (Bhattacharjee et al., 2009).
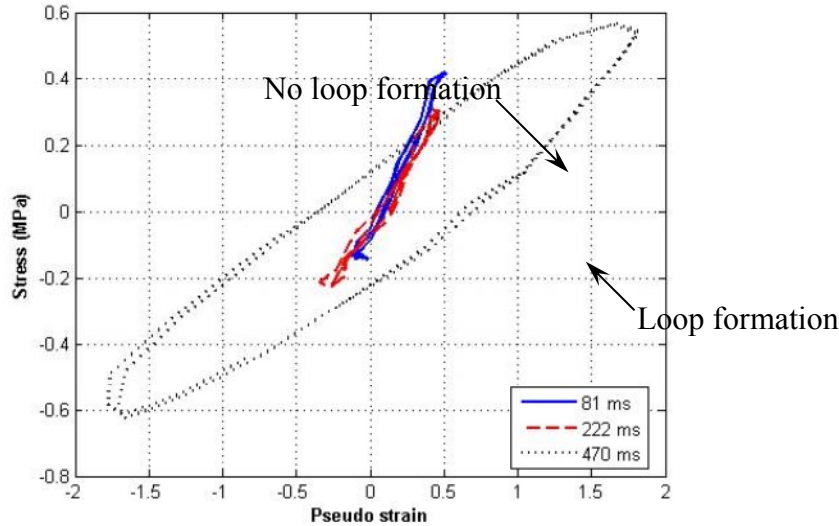
FIGURE 31 Stress-vs-pseudo strain at increasing strain levels (Bhattacharjee et al., 2009).

Underwood and Kim (2009) used the Viscoelastic and Continuum Damage (VECD) approach to predict the fatigue endurance limit with the incorporation of the temperatures effect and rest periods as well. The effect of rest period was considered explicitly in this approach by incorporating the model that was given by Lee and Kim (1998b). The method required at the beginning to define the material damage characteristic curve which is the relationship between the pseudo stiffness, C, (removes the material time effects) and the damage parameter, S, (represents any microstructural change that leads to a reduction in material integrity). A relationship to accurately predict the fatigue life at failure based on the VECD model was mathematically derived by Hou (2009). This relationship (Equation 39) was developed for a controlled-strain direct tension cycle test assuming the power law damage model.

55

$$N_f = \frac{(f_R)(2^{3\alpha})S_f^{\alpha-\alpha C_{12}+1}}{(\alpha-\alpha C_{12}+1)(C_{11}C_{12})^{\alpha}\left[(\beta+1)(\varepsilon_{0,pp})(|E^*|_{LVE})\right]^{2\alpha}K_1} \qquad (39)$$

where:

N_f	= number of loading cycles at failure,
A	= damage evolution rate,
f_R	= reduced Frequency,
S_f	= damage parameter at failure,
C_{11}, C_{12}	= regression coefficients of the power model used to fit the C-S curve,
β	= correction factor based on the mean of strain amplitude,
$\varepsilon_{0,pp}$	= peak-to-peak strain amplitude,
$|E^*|_{LVE}$	= linear viscoelastic dynamic modulus at the particular temperature and frequency, and
K_1	= calculated parameter depend on the time history of loading.

Having this closed form solution, the endurance level can be obtained as the strain level corresponding to a certain defined high number of load repetition (50,000,000) for a certain temperature and rest period. The researchers also suggested another method by using the traditional fatigue approach. In this method, the VECD model was used to predict the N_f for three to five different strain magnitudes. These predicted failure curves were then fit to the traditional fatigue relationship where K_1 and K_2 are regression coefficients that reflect the effect of temperature, frequency of loading, rest period, modulus or other factors.

Using the definition of EL proposed by Prowell et al. (2009), the strain amplitude that yields N_f of 50,000,000 for any given rest period and temperature is considered to be the EL as shown in FIGURE 32.
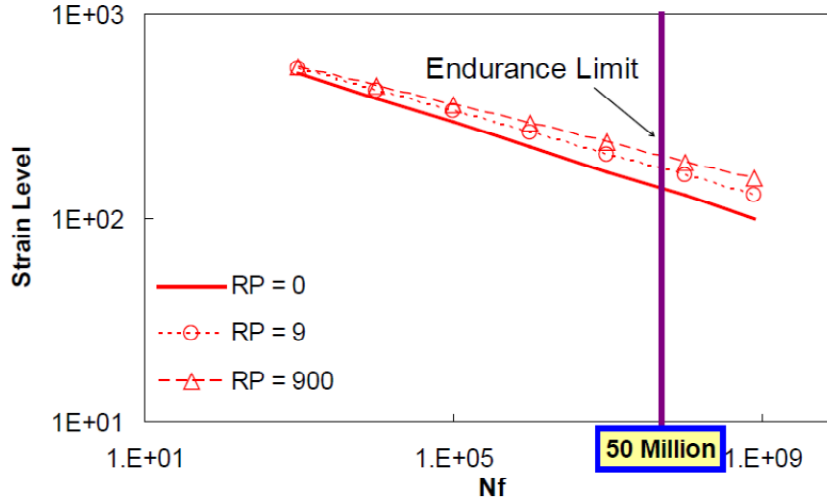
FIGURE 32 Effect of healing on traditional fatigue relationship at 5°C (Underwood and Kim, 2009).

Christensen and Bonaquist (2009) followed the same methodology as Underwood and Kim but used a similar mathematical formula (Equation 40) that predicts the strain level required to sustain any number of design load repetitions with a generalized power law (Christensen and Bonaquist, 2005).

$$\varepsilon_o^{2\alpha} = \frac{fS_f^p}{p(0.125 I C_{11} C_{12})^\alpha N_f (|E*|)^{2\alpha}}$$

(40)

where:

f = Frequency,
I = normalized pseudo stiffness, and
p = $1 + (1 - C_{12})\, \alpha$.

And S_f is the damage parameter value at failure measured from the damage characteristic curve for the mixture at the point where C= 0.3 (Daniel and Kim, 2002).

Another methodology was created by Christensen and Bonaquist, (2009). They developed a simplified continuum damage analysis using the concept of reduced cycles defined by Equation 41 in which the damage parameter, S, is replaced by reduced cycles that also collapse all the data at different strains and different temperatures into a unique relationship as shown in FIGURE 33. This method directly accounts for the endurance limit by applying the concept of effective strain, which is defined as applied strain minus the endurance limit. The analysis allows for the calculation of endurance limits from relatively limited fatigue data. One advantage of this method is that the reduced cycles are easier to calculate and understand compared to the damage parameter, S, that can only be computed using approximate, numerical integration.

$$N_R = N_{R-ini} + N\left(\frac{f_0}{f}\right)\left(\frac{|E*|_{LVE}}{|E*|_{LVE/0}}\right)^{2\alpha}\left(\frac{\varepsilon^E}{\varepsilon_0^E}\right)^{2\alpha}\left[\frac{1}{a(T/T_0)}\right]$$

(41)

where:

N_R = reduced cycles,
N_{R-ini} = initial value of reduced cycles, prior to the selected loading period,
N = actual loading cycles,
f_0 = reference frequency (10 Hz suggested),
f = actual test frequency,
$|E*|_{LVE}$ = undamaged (LVE) dynamic modulus under given conditions, lb/in^2,
$|E*|_{LVE/0}$ = reference initial (LVE) dynamic modulus, lb/in^2 (the LVE
      modulus at 68ºF (20ºC) is suggested),
α = continuum damage material constant with a typical value of
      about 2.0,
ε^E = effective strain level = applied strain minus the endurance limit

      strain,
ε_0^E = reference effective strain level (0.0002 suggested), and

$a(T/T_0)$ = shift factor at test temperature T relative to reference
      temperature T_0.

57
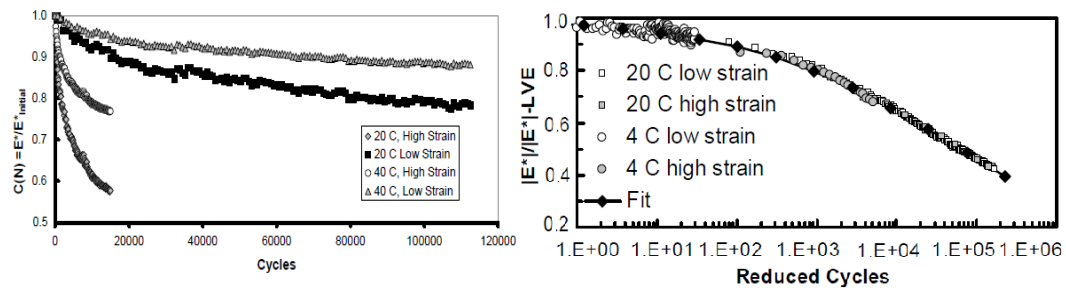
FIGURE 33 Typical damage ratio curves collapsed into a unique damage relationship using continuum damage analysis (Christensen and Bonaquist, 2009).

CHAPTER 3

THEORY OF VISCOELASTICITY AND DAMAGE MECHANICS

In modeling the hysteretic behavior of asphalt concrete mixtures under multi-repetitive loading with random duration of rest, the following constitutive factors are deemed important (Lee, 1996):

  I.   Viscoelasticity of the matrix that cause hysteretic behavior under cyclic loading and relaxation during rest periods,
  II. Fatigue damage growth under cyclic loading,
  III. Healing during the rest periods, and
  IV. Temperature dependence of the asphalt matrix.

Effects of temperature on the constitutive behavior can be included in the viscoelastic material properties, such as creep compliance and relaxation modulus, using the time-temperature superposition principle (Kim and Lee, 1995a). It is difficult to evaluate the effect of the remaining three factors as their mechanisms occur simultaneously under cyclic loading with rest periods. For example, the inelastic response of the material during loading and unloading paths can be due to damage incurred in the material, the viscoelastic nature of the material, or both. Also, relaxation and healing also occur at the same time during rest periods. Consequently, it is essential to separate the viscoelasticity from damage and healing in order to accurately predict the inelastic response of the material.

This chapter presents the basic theories that are applied in this research, starting with the theory of viscoelasticity, followed by the elastic-viscoelastic correspondence principle and time-temperature superposition to eliminate the time dependence of the material of the material from the hysteretic stress-strain behavior by using the pseudo strain concept. Finally the work potential theory (Schapery, 1990), one of the continuum damage mechanics principles based on irreversible thermodynamics, is employed to model damage and microdamage healing. In addition, the constitutive model developed by Lee (Lee, 1996) is also presented.

THEORY OF VISCOELASTICITY

Background

The classical theory of elasticity, in accordance with Hook's law, deals with the mechanical properties of elastic solids where the stress is always directly proportional to the strain by a material constant (Young's modulus) when the deformation is small and independent of the rate of strain, as shown in FIGURE 34. In this case, the strain energy is completely recovered during unloading. On the other hand, the classical theory of hydrodynamics deals with the mechanical properties of viscous liquids, in accordance with Newton's law, where the stress is directly proportional to the rate of strain by a material constant (viscosity) and is independent of the strain itself, as shown in FIGURE 35. In this case, the strain energy is completely dissipated during loading. These two theories are idealizations of characteristics of elastic solids for infinitesimal strain and viscous liquids for infinitesimal strain rates. Some engineering materials, especially those soft enough to be deformed substantially without breaking, such as

asphalt concrete, may exhibit behavior that combine liquid like and solid like characteristics. In this case, some of the energy input is stored and recovered in each cycle, and some is dissipated. The energy dissipated during a full cycle of loading and unloading represents the material damping characteristic and is graphically represented by the area contained with a stress-strain diagram as seen in FIGURE 36 (Zhiming, 2001). Material whose behavior exhibits such characteristics is called viscoelastic.
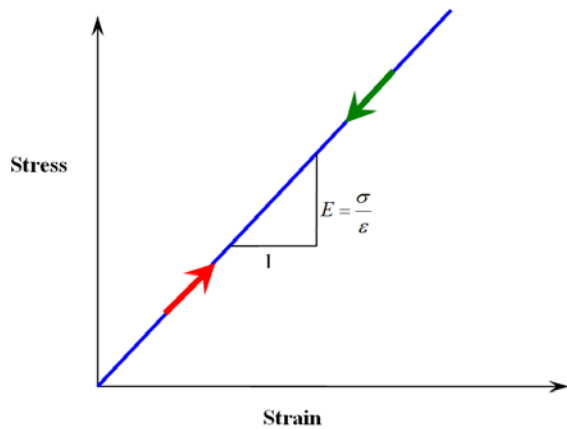
FIGURE 34 Stress-strain curve for linear elastic (Hookean) solid.
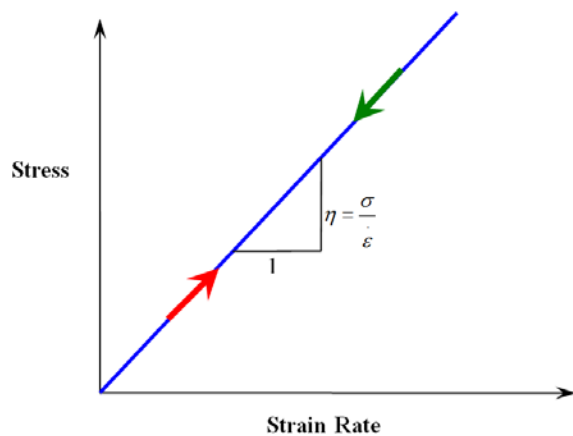
FIGURE 35 Stress-strain curve for linear viscus (Newtonian) fluid.
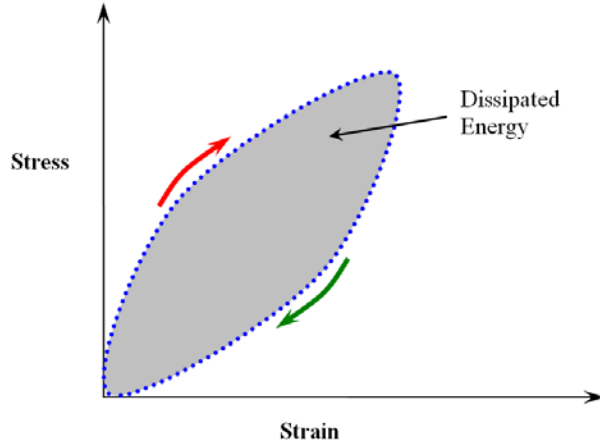
FIGURE 36 Stress-Strain curve for a viscoelastic material.

Viscoelastic Constitutive Equation

Viscoelastic materials such as asphalt concrete mixtures exhibit time or rate dependence. Demonstrating that, the response of such materials depends not only on current state of input (load or deformation), but also on all past history of input, i.e., the materials have a memory for all past history of input. Viscoelastic material behavior is separated into two main categories: linear and nonlinear. Linear viscoelastic materials show dependence of the time history of the loading or deformation and the response due to change in the level of stress or strain may be superimposed. Nonlinear viscoelastic materials have behavior that is dependent on stress or strain history and the response in stress or strain may not be superimposed.

The response of a linear viscoelastic material to any input history is described using the convolution integral. A system is considered to be a linear if the conditions of homogeneity and superposition are fulfilled:

Homogeneity:	$R\{AI\} = A\,R\{I\}$	(42)
Superposition:	$R\{I_1+I_2\} = R\{I_1\} + R\{I_2\}$	(43)

where:

I, I_1, I_2 = input histories,
R   = response, and
A   = arbitrary constant.

The brackets { } indicate that the response is a function of the input history. The homogeneity, or the proportionality, condition means that the output is directly proportional to the input. For example, if the input is doubled, the response doubled as well.   On the other hand, the superposition condition means that response to the sum of two inputs is equivalent to the sum of the responses from the individual inputs.

Considering the linear response of a viscoelastic material, and the homogeneity and superposition concepts, the input-response relationship can be expressed using the following hereditary integral that represent the constitutive behavior of a viscoelastic materials:

$$R = \int_{-\infty}^{t} R_H(t,\tau)\frac{dI(\tau)}{d\tau}\,d\tau \tag{44}$$

61

where:

R_H = response function,
t = time,
τ = time-history integration variable, and
I = input history.

The relationship is called hereditary integral because the conditions at a time t depend on prior history.

With a known unit response function, the response to any input history can be calculated. The lower limit of the integration can be reduced to 0^- (0^-, just before time zero) if the input starts at time t = 0 and both the input and response are equal to zero at t<0. The value of 0^- is used instead of 0 to allow for the possibility of a discontinuous change in the input at time t = 0. For notational simplicity, 0 is used as a lower limit in all successive equations and should be interpreted as 0^- unless specified otherwise. Equation 44 is applicable to an aging system in which the response measurement at any time is a function of both of the time of loading and the time of fabrication. The unit response function, R_H, is then a three dimensional surface.

Usually, the assumption that asphalt concrete mixtures behave as a non-aging system is made. Then the unit response function is simplified to a two-dimensional line and Equation 44 reduces to:

$$R = \int_0^t R_H(t-\tau)\frac{dI(\tau)}{d\tau}d\tau \tag{45}$$

For uniaxial loading, the corresponding hereditary integrals of stress-strain relationship for non-aged & linear viscoelastic material are:

$$\varepsilon = \int_0^t D(t-\tau)\frac{d\sigma}{d\tau}d\tau \tag{46}$$

$$\sigma = \int_0^t E(t-\tau)\frac{d\varepsilon}{d\tau}d\tau \tag{47}$$

where:

ε, σ = physical strains and physical stresses, and
E(t), D(t) = relaxation modulus and creep compliance, respectively.

CORRESPONDENCE PRINCIPLE

The theory of linear viscoelasticity and some nonlinear viscoelasticity models have been established in the past. However, solution of various kinds of viscoelastic boundary value problems remains a complex problem. Fortunately, viscoelasticity theory allows viscoelastic problems to be transformed so that they are mathematically equivalent to those for elastic problems with the substitution of elastic moduli. This correspondence can be made by taking an appropriate transformation of the governing field and boundary equations of viscoelastic problems with respect to time. In general, the principle employs the Laplace transformation for linear viscoelastic materials.

Schapery (1984) proposed the extended elastic-viscoelastic correspondence principle (CP) which can be applicable to both linear and nonlinear viscoelastic materials. Schapery

suggested that constitutive equations for certain viscoelastic media are identical to those for the elastic cases, but stresses and strains are not necessarily physical quantities in the viscoelastic body. Instead, they are *pseudo variables* in the form of convolution integrals.

The following uniaxial versions of constitutive equations for linear elastic and linear viscoelastic bodies without and with damage are presented. They also show how models of different complexity may evolve from simpler ones:

> Elastic Body without Damage: $\sigma = E_R \, \varepsilon$ (48)
> Elastic Body with Damage: $\sigma = C(S_m) \, \varepsilon$ (49)
> Viscoelastic Body without Damage: $\sigma = E_R \, \varepsilon^R$ (50)
> Viscoelastic Body with Damage: $\sigma = C(S_m) \, \varepsilon^R$ (51)

where ε, σ are physical stresses and physical strains, ε^R is the pseudo strain, E_R, is a constant and $C(S_m)$ indicates that C is a function of Internal State Variable (ISV) S_m that represents the changing stiffness of the material due to microstructure changes such as accumulating damage or healing. In Equation 50, E_R is the Young's modulus.

A correspondence is seen between the elastic and viscoelastic constitutive equations: the viscoelastic behavior can be described by the elastic equations with pseudo strain replacing the corresponding physical strain. For example, a correspondence can be found between Equation 50 and a linear elastic stress-strain relationship (Hooke's law). The power of pseudo strain can be seen in FIGURE 37. FIGURE 37a shows the stress-strain behavior of a controlled-stress cyclic loading within the material's linear viscoelastic range (such as a complex modulus test). Because the material is being tested in its linear viscoelastic range, no damage is induced and the hysteretic behavior and accumulation strain are due to the viscoelasticity only. FIGURE 37b shows the same stress data plotted against the calculated pseudo strain. All of the cycles collapse to a single line with a slope of 1.0 ($E_R = 1.0$). The use of pseudo strain essentially accounts for the viscoelasticity of the material and allows for the separate characterization of damage within the specimen.
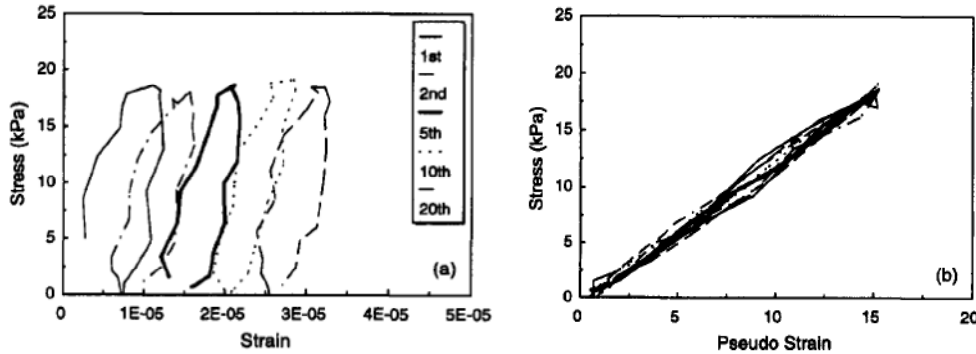
FIGURE 37 Stress application of correspondence principle to cyclic data with negligible damage: (a) stress-strain; (b) stress-pseudo strain (Lee and Kim, 1998b).

In order to introduce pseudo strain and pseudo stress, consider a uniaxial stress-strain relationship for linear, non-aging viscoelastic materials, Equation 47, which can be written as:

$$\varepsilon^R = \frac{\sigma}{E_R} \qquad\qquad (52)$$

By substituting the stress value from Equation 47 to Equation 52, the pseudo strain relationship can be written such as:

$$\varepsilon^R = \frac{1}{E_R} \int_0^t E(t-\tau) \frac{d\varepsilon}{d\tau} d\tau \qquad (53)$$

In the same way, the pseudo stress relationship can be represented by the following equation:

$$\sigma^R = E_R \int_0^t D(t-\tau) \frac{d\sigma}{d\tau} d\tau \qquad (54)$$

where:

ε^R, σ^R = pseudo stresses and pseudo strains,

t   = elapsed time from specimen fabrication and time of interest, and

τ = time when loading began.

Using the concept of pseudo variables, Schapery (1984) introduced three different correspondence principles. The first case uses both pseudo strain and stress (general boundary condition). The physical stress and pseudo strain were used in the second case (as the crack increases, the traction boundary condition grows). The last correspondence principle employs the pseudo stress and physical strain (as the crack heals, the traction boundary condition reduces).

For the case of a growing traction boundary surface, such as crack growth, the viscoelastic problem can be reduced to an elastic case by using physical stresses and pseudo strains. The uniaxial pseudo strain (ε_{ij}^R) is defined as:

$$\varepsilon_{ij}^R = \frac{1}{E_R} \int_0^t E(t-\tau) \frac{d\varepsilon_{ij}}{d\tau} d\tau \qquad (55)$$

Calculation of pseudo strain using Equation 55 requires the expression of the relaxation modulus as a function of time.

UNIAXIAL CONSTITUTIVE MODEL USING WORK POTENTIAL THEORY

Constitutive Theory

Schapery (1990) applied the method of the thermodynamics of irreversible processes and the observed phenomenon of path independence of work in damage-inducing processes to develop the work potential theory that describes the mechanical behavior of elastic composite materials with growing damage. The theory is general enough to allow for strong nonlinearities and to describe a variety of mechanisms including micro- and macro-crack growth in monolithic and composite materials. Three fundamental elements comprise the work potential theory:

1. **Strain energy density function:**
   $$W = W(\varepsilon, S_m) \qquad (56)$$

2. **Stress-strain relationship:**
   $$\sigma_{ij} = \frac{\partial W}{\partial \varepsilon_{ij}} \qquad (57)$$

3. **Damage evolution law:**

64

$$-\frac{\partial W}{\partial S_m} = \frac{\partial W_s}{\partial S_m} \tag{58}$$

where σ_{ij} and ε_{ij} are stress and strain tensors, respectively. S_m are internal state variables, ISVs, (or damage parameters) representing structural changes in the material (e.g., damage, healing, etc.) and $W_s = W_s(S_m)$ is the dissipated energy due to structural changes. Using Schapery's elastic-viscoelastic correspondence principle (CP) and rate type evolution law (Schapery, 1984; Schapery, 1990 and Park et al., 1996), the physical strains, ε_{ij}, are replaced with pseudo strains, ε_{ij}^R, to include the effect of viscoelasticity. However, the damage evolution laws cannot directly be translated into evolution laws for viscoelastic materials through the correspondence principle. Not only is the available force for growth of S_m rate-dependent (through pseudo strains), but the resistance against the growth of S_m is rate-dependent for most viscoelastic materials. Therefore, a form which is similar to the well-known power law crack growth laws for viscoelastic materials (Schapery, 1984) will be adopted as it can reasonably represent the actual damage evolution processes of many viscoelastic materials as shown in Equation 61.

Finally, the work potential theory applied to viscoelastic media with the rate type damage evolution law is presented by the following three components for uniaxial loading condition:

1. ***Pseudo strain energy density function:*** A pseudo strain energy function exists in the following form:
   a. $\quad W^R = W^R(\varepsilon_{ij}^R, S_m)$ (59)

2. ***Stress-strain relationship:*** The pseudo-strain energy function has the following property:
   a. $\quad \sigma_{ij} = \dfrac{\partial W}{\partial \varepsilon_{ij}^R}$ (60)

3. ***Damage evolution law:*** Damage evolution in viscoelastic material is governed by the following:

$$\dot{S}_m = \left(-\frac{\partial W^R}{\partial S_m} \right)^{\alpha_m} \tag{61}$$

where ε^R and σ^R are the pseudo strain and stress tensors respectively. S_m are internal state variables, ISVs, (or damage parameters) representing structural changes in the material (e.g., damage, healing, etc.). S_m overdot is the damage evolution rate, and α_m, are material constants.

Using Schapery's work potential theory (Schapery, 1990) and correspondence principle that eliminate the time dependence of material, Lee and Kim (1998b) developed a mode of loading-independent constitutive model for the fatigue and microdamage healing of asphalt concrete under cyclic loading. They used uniaxial tensile cyclic loading tests with various loading amplitudes under controlled-strain and controlled-stress modes. FIGURE 38 show typical stress-pseudo strain hysteresis loops at different numbers of cycles in the controlled-strain and controlled-stress modes respectively. Relatively high stress and strain amplitudes are used to induce significant damage in the specimen. The following three characteristics can be observed from these figures due to the damage incurred in the specimens:

1. Nonlinear behavior of the loading and unloading paths in each cycle,
2. Change in the slope of each σ-ε^R cycle as cyclic loading continues (i.e., reduction in the pseudo stiffness of the material as damage accumulates), and

3. Accumulation of permanent pseudo-strain in the controlled-stress mode (i.e., shift of the loop from the origin as cyclic loading continues).

The first two characteristics are observed in both modes of loading, while the third characteristic is unique to the controlled-stress mode.

To represent the change in the slope of σ-ε^R loops in both modes of loading using a single parameter, the secant pseudo stiffness, S^R, is defined as:

$$S^R = \frac{\sigma_m}{\varepsilon_m^R} \tag{62}$$

where ε_m^R is the peak pseudo strain in each stress pseudo-strain cycle, and σ_m is a stress corresponding to ε_m^R.
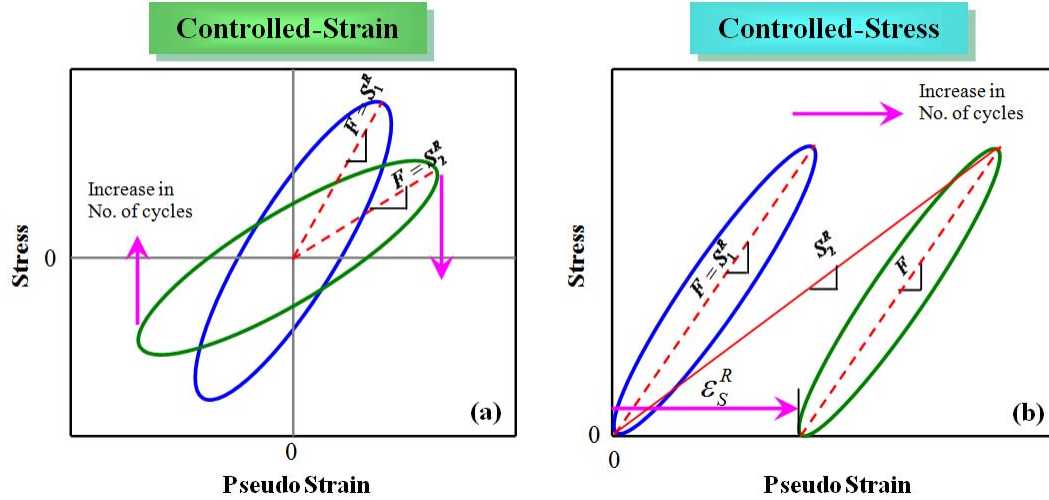
FIGURE 38 Stress-pseudo strain curve behavior and pseudo stiffness changes in: (a) controlled-strain mode; (b) controlled-stress mode (Lee and Kim, 1998b).

Since S^R is determined from stress and pseudo-strain values, instead of physical strain, the advantage of using pseudo strain, that is eliminating the time dependence from the hysteretic behavior, is still gained. Thus, the change in S^R represents damage growth and healing separately from the time dependence, which allows a simple function of SR to describe these mechanisms under complicated loading histories. In modeling, Lee (Lee, 1996) found it necessary to normalize the pseudo stiffness by the initial pseudo stiffness, I, to account for sample-to-sample variation. The normalized pseudo stiffness, C, is then:

$$C = \frac{S^R}{I} \tag{63}$$

Determination of Damage Parameter S

The work potential theory specifies an internal state variable S_m to quantify damage, which is defined as any microstructural changes that result in stiffness reduction. For asphalt concrete in tension, this variable is related primarily to microdamage phenomenon. Therefore, only one internal state variable (i.e., S_1) is used to model the damage growth in tension.

66

Kim et al. (1997a) characterized the growing damage by using the function C in Equation 51 for a controlled-strain testing mode through the following constitutive equations:

$$W_m^R = \frac{1}{2}C_1(S_1)(\varepsilon_m^R)^2$$ (64)

$$\sigma_m = IC_1(S_1)\varepsilon_m^R$$ (65)

where W_m^R is the pseudo strain energy density function when $\varepsilon^R = \varepsilon_m^R$ and C_1 is defined as in Equation 63, and S_1 is an internal state variable. The subscript on the C and S variables indicates that damage is occurring in the virgin material opposed to a material that has undergone healing.

The function C_1 represents S^R, as can be seen from Equations 63 and 65 since I = 1.0. The evolution law becomes:

$$\dot{S}_m = \frac{dS}{dt} = \left(-\frac{\partial W_m^R}{\partial S_m}\right)^{\alpha_m}$$ (66)

To characterize the function C_1 in the Equation 65, the damage evolution law and experimental data are used. With the measured stresses and calculated pseudo strains, C_1 values can be determined through Equation 63. To find the dependence of C_1 and S_1, the value of S_1 must be obtained through Equation 66. The current form of Equation 66 is not suitable for finding S_1 because it requires prior knowledge of the $C_1(S_1)$ function through Equation 64. Substituting Equation 66 into 64, Equation 67 is derived:

$$\frac{dS_1}{dt} = [-\frac{1}{2}\frac{dS_1}{dC_1}(\varepsilon_m^R)^2]^{\alpha_m}$$ (67)

To eliminate S from the *dS/dC* term of the evolution Equation 67, Lee (1996) proposed a solution that utilizes the chain rule:

$$\frac{dC}{dS} = \frac{dC}{dt}\frac{dt}{ds}$$ (68)

From Equations 67 and 68, the damage evolution rate, dS/dt, is represented by Equation 68:

$$\frac{dS_1}{dt} = [-\frac{1}{2}\frac{dC_1}{dt}(\varepsilon_m^R)^2]^{\alpha_m}$$ (69)

As a result, S_1 can be obtained:

$$S_1 = \int_0^t \left[-\frac{I}{2}\frac{dC_1}{dt}(\varepsilon_m^R)^2\right]^{\frac{\alpha}{(1+\alpha)}} dt$$ (70)

Both the function C_1 and ε_m^R are dependent upon time t, thus a numerical approximation can be used with the measured data to obtain S_1 as a function of time (Daniel, 2001; Daniel and Kim, 2002):

$$S_1(t) = \sum_{i=1}^N \left[-\frac{I}{2}(C_i - C_{i-1})(\varepsilon_m^R)^2\right]^{\frac{\alpha}{(1+\alpha)}}(t_i - t_{i-1})^{\frac{1}{(1+\alpha)}}$$ (71)

Daniel and Kim (2002) showed that the damage characteristics of a material are independent of the mode of loading and can be determined using a simpler test, such as the constant crosshead rate monotonic test. Chehab et al. (2002) and Underwood et al. (2006)

67

verified that the time-temperature superposition (t-TS) principle at high levels of damage is equally significant. Based on this validation, Equation 71 can be modified as following:

$$S_1(\xi) = \sum_{i=1}^{N} \left[-\frac{I}{2}(C_i - C_{i-1})(\varepsilon_m^R)^2 \right]^{\frac{\alpha}{(1+\alpha)}} (\xi_i - \xi_{i-1})^{\frac{1}{(1+\alpha)}} \tag{72}$$

where ξ is the reduced time. Equations 71 or 72 can also be written in the following form (Kim, 2009):

$$S_{i+1} = S_i + \left[-\frac{I}{2}(C_i - C_{i-1})(\varepsilon^R)^2 \right]^{\frac{\alpha}{(1+\alpha)}} \Delta\xi_i^{\frac{1}{(1+\alpha)}} \tag{73}$$

Underwood et al. (2010) developed a simplified VECD modeling technique based on the analysis of cyclic data. This method allows the prediction of the fatigue lives of asphalt concrete at various strain–stress amplitudes under different temperatures using the dynamic modulus master curve and the cyclic fatigue data from a single temperature and single stress or strain amplitude. The proposed S function had the following form:

$$S_{N+1} = S_N + \left[-\frac{DMR}{2}(C_N - C_{N-1})(\varepsilon^R)^2 \right]^{\frac{\alpha}{(1+\alpha)}} (\Delta\xi)^{\frac{1}{(1+\alpha)}} (K_1)^{\frac{1}{(1+\alpha)}} \tag{74}$$

where:

DMR = Dynamic Modular Ratio = $|E^*|_{fp} / |E^*|_{LVE}$ and $|E^*|_{fp}$ is fingerprint modulus,

Δt_R = the change in the average reduced time between analysis cycles, and

K_1 = a developed functional parameter to account for the analysis of cyclic data.

The parameter α is supposed to be a material property. A few correlations have been proposed to estimate the value of this constant, relating it to viscoelastic properties of asphalt mixtures. Lee and Kim (1998a, b) attempted to relate α to the slope m in the central part of the Master Curve for the log E(t)-log(t) relationship. It was suggested that it is most appropriate to use $\alpha = 1/m$ for the type of stress-controlled tests $\alpha = 1/m + 1$ for the crosshead strain tests.

This relationship is valid by cross-plotting the measured C_1 values against the S_1 values obtained from Equation 71 to obtain the damage characteristic curve. The relationship between C_1 and S_1 can be found by performing a regression on the data. Lee (1996) found that the function follows the form:

$$C_1(S_1) = C_{10} - C_{11}(S_1)^{C_{12}} \tag{75}$$

where the C_{1x} are the regression coefficients. The regression coefficient C_{10} is close to 1.0, as would be expressed at a negligible damage level (S_1 goes to zero) because the material is in linear viscoelastic range of behavior and there exists a one-to-one relationship between the stress and pseudo strain (i.e., $S^R = 1.0$). Using this model, Lee (Lee, 1996) was able to successfully predict the damage growth of asphalt concrete under monotonic loading at various strain rates and cyclic loading under both controlled stress mode and controlled strain as well.

The S_1- C_1 relationship can be also fitted to the analytical form represented in Equation 76 (Lee, 2007 and Kim, 2009).

$$C = e^{aS^b} \tag{76}$$

CHAPTER 4

DESIGN OF EXPERIMENTS, SPECIMEN PREPARATION, AND TESTING PLAN

BACKGROUND

At the HMA Endurance Limit Workshop conducted early in NCHRP Project 9-44 (Hot Mix Asphalt Endurance Limit Workshop, 2007) it was hypothesized that: "HMA does exhibit an endurance limit. This endurance limit, however, does not reflect an absence of load induced damage in the HMA. It is the result of a balance of damage caused by loading and healing or damage recovery that occurs during rest periods."

Based on this hypothesis, the main objective of this research is to develop an algorithm and test methodology to validate an endurance limit for HMA using an uniaxial tension-compression fatigue test and the Viscoelastic and Continuum Damage Model (VECDM). The experimental program of this research was developed to accomplish this objective. The experimental plan investigates the healing of fatigue damage for HMA prepared with a PG 64-22 asphalt binder by building a statistical model and considering the effect of different experimental factors on healing. Once the healing model is developed, the second step is to develop an algorithm to derive the fatigue endurance limit from the healing model.

SELECTION OF FACTORS AFFECTING THE HEALING EXPERIMENT

There are many variables that could possibly influence the fatigue endurance limit of HMA. Some of these factors are shown in TABLE 1. The selection of the number of factors and design of experiment must be carefully evaluated. For example, if 10 factors are considered and 3 levels of each variable are pursued in a full factorial plan, $3^{10}=59,049$ tests would be required.

TABLE 1 List of factors that can affect the fatigue endurance limit (NCHRP 944, 2008)

Topic	Factors
Mixture Compositional Factors	Binder Type
	Binder Age
	Asphalt Content
	Air Voids
	Design Compaction
	Gradation
	Filler Content
Testing Inputs and Conditions	Strain Level
	Loading Frequency
	Loading Wave Shape
	Rest Period Duration

Environmental Condition	Temperature

Furthermore, this number considers only a single replicate. If 2 or 4 replicates were used; the number of tests would increase to about 118,000 (2 replicates) or 236,000 (4 replicates). If one were to go one step further and recognize that a typical laboratory (with one fatigue apparatus) can conduct about 30 tests per month; the total number of years required to complete the laboratory testing experiment, with one laboratory, would be 164 (1 replicate), 328 (2 replicates), or 656 (4 replicates).It is obvious that some type of reduced statistical plan, other than a full factorial, is needed to address all variables and levels. In addition, a decision was made to eliminate some variables to reduce the number of required tests.

DESIGN OF EXPERIMENT

Independent Variables (Factors)

The experiment using only one asphalt binder (PG 64-22) is designed for the uniaxial tension-compression fatigue test. Five important factors were selected:
1.   Asphalt content, AC% (2 levels: optimum $\pm$ 0.5 %)
2.   Air voids, Va% (2 levels: 4.5, 9.5 %)
3.   Strain Level, ε (2 levels: L, M)
4.   Temperature, T (3 levels: 40, 70, 100°F)
5.   Rest period, RP (2 levels: 0, 5 sec)

It was initially planned to start the experiment using three replicates for each factor combination. As results were obtained and evaluated; a statistical analysis was conducted to re-evaluate the efficiency and accuracy of the use of three replicate specimens as discussed later.

In this design, all five factors stated above would be evaluated. From the uniaxial fatigue test results with and without rest periods, the Pseudo Stiffness Ratio (PSR) values are calculated at a certain number of loading cycle. The PSR is simply the pseudo stiffness at certain loading cycles divided by the initial pseudo stiffness. A regression model would be developed to estimate the PSR as a function of all five factors.

$$PSR = f (AC, Va, \varepsilon_t, T, RP) \tag{77}$$

where:
AC   = Asphalt content,
Va   = Air voids,
ε_t = Tensile strain level,
T   = Temperature, and
RP   =Rest period.

To estimate the healing index (HI) at certain parameters values, the PSR values are calculated using the PSR regression model at two different rest periods. The first PSR is calculated at a rest period equal to zero that represents the test without rest period. The second PSR is obtained at a target or assumed rest period greater than zero. Considering the number of cycles until failure for the test without rest period, HI is then calculated as shown in FIGURE 39 and Equation 78.

70

$$HI = \frac{PSR_{WRP} - PSR_{W/ORP}}{1 - PSR_{W/ORP}} \tag{78}$$
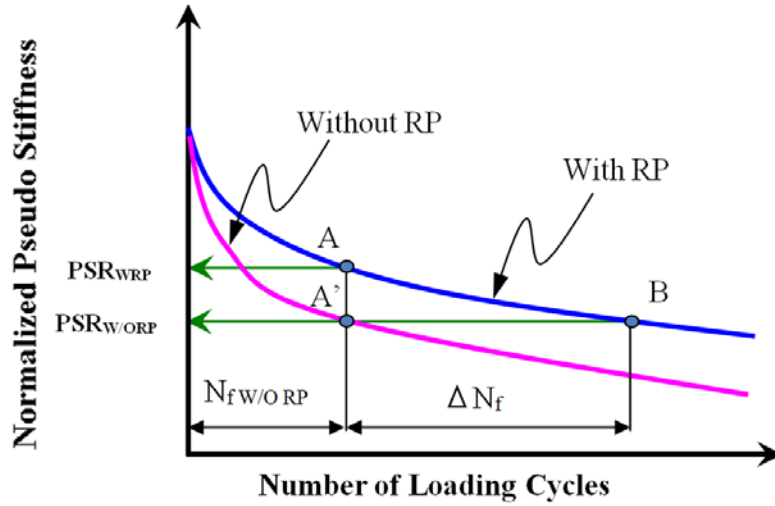
FIGURE 39 Stiffness versus number of loading cycles with and without rest period.

Fractional Factorial Design with Partial Randomization

In order to reduce the number of tests and at the same time determine important effects of all variables, a five-factor fractional factorial statistical design was developed. The statistical fractional factorial design considers the effect of all 5 factors, two-factor interactions, and 3-factor interactions (JMP® Software). Higher factor interactions are ignored in this design since they are unlikely to be significant.

Within the fractional factorial statistical design, there are many design optimality criteria and the most popular criterion is called D-optimality (Montgomery, 2008), which was used in this study. The D-optimality design minimizes the volume of the joint confidence region on the vector of regression coefficient. A computer generated design is used to reduce the number of runs using the JMP software. TABLE 2 shows the factor combinations at which the test would be performed. The table shows that 32 combinations would be tested with 3 replicates for each combination. This design would require a total of 96 tests required for the five-factor full factorial design.

TABLE 2 Factor combinations for the 5-factor fractional factorial completely randomized design

Asphalt Content (%)			4.2		5.2	
Air Voids (%)			4.5	9.5	4.5	9.5
Temp. (°F)	Strain Level	Rest Period (sec)				
40	L	0	green	green	--	green
		5	green	--	green	green
	M	0	green	--	green	green
		5	--	green	green	green
70	L	0	--	green	green	--
		5	green	green	--	green
	M	0	green	green	--	green
		5	green	--	green	green
100	L	0	green	--	--	green
		5	--	green	green	--
	M	0	--	green	green	--
		5	green	green	--	green

green	Test combinations used in the study
--	Empty cells

TABLE 3 lists the main and the two and three-factor interaction terms that can be estimated from this experimental design. Using this fractional factorial design, a model with up to 25 variable parameters can be developed.

TABLE 3 Factors and factor interactions estimated from the experiment

All main effect	Two-factor interactions	Three-factor interactions
Asphalt Content	Asphalt Content*Air Voids	Asphalt Content*Air Voids* Strain Level
Air Voids	Asphalt Content* Strain Level	Asphalt Content*Air Voids*Rest Period
Strain Level	Asphalt Content*Rest Period	Asphalt Content*Air Voids*Temperature
Rest Period	Asphalt Content*Temperature	Asphalt Content* Strain Level*Rest Period
Temperature	Air Voids* Strain Level	Asphalt Content* Strain Level*Temperature
	Air Voids*Rest Period	Asphalt Content* Rest Period*Temperature
	Air Voids*Temperature	Air Voids* Strain Level*Rest Period
	Strain Level*Rest Period	Air Voids* Strain Level*Temperature
	Strain Level*Temperature	Air Voids*Rest Period*Temperature
	Rest Period*Temperature	Strain Level*Rest Period*Temperature
Total of 5	Total of 10	Total of 10

BINDER CHARACTERIZATION

Background

The characterization of the asphalt binder properties can be used as direct input to estimate the complex modulus properties of asphalt mixtures. A full characterization of three binders used in this study was conducted by two laboratories: MACTEC in Phoenix, Arizona, and Arizona State University (Quarterly Progress Report, 2010)

The binder tests performed at MACTEC were mainly to (1) determine the range of compaction and mixing temperatures, (2) characterize asphalt binders using performance graded binder tests including the dynamic shear rheometer (DSR) and the bending beam rheometer (BBR), and (3) asphalt mix design. Arizona State University conducted a comprehensive characterization study of the rheological properties of asphalt binder, using one performance graded binder test (Brookfield viscometer) and two penetration graded binder tests (penetration and softening point) at a wide range of temperatures. All test results from MACTEC and Arizona State University are presented in the following sections.

Binder Source

Three grades of AC binder were provided by Holly Asphalt Company in Phoenix, Arizona, and used by both MACTEC and Arizona State University, in order to conduct the mix design and binder characterization tests. They are all unmodified and classified as PG 58-28, PG 64-22, and PG 76-16.

Aging Levels

For the binder characterization tests (MACTEC and Arizona State University), samples of the three asphalt binder grades were aged with the short-term (RTFO) and long-term (PAV) conditioning protocols in accordance with AASHTO T 240 and AASHTO R 28, respectively.

The basic RTFO procedure (FIGURE 40) includes pouring unaged asphalt binder samples in cylindrical glass bottles and placing these bottles in a rotating carriage within an oven. The carriage rotates within the oven for 85 minutes at 325°F (163°C). Samples are then stored for use in physical properties tests or the PAV.

The basic PAV procedure (FIGURE 41) consists of placing the RTFO aged asphalt binder samples in stainless steel pans and then aging them for 20 hours in a heated vessel pressurized to 305 psi (2.10 MPa) at 212 °F (100°C). Samples are then stored for use in physical property tests.
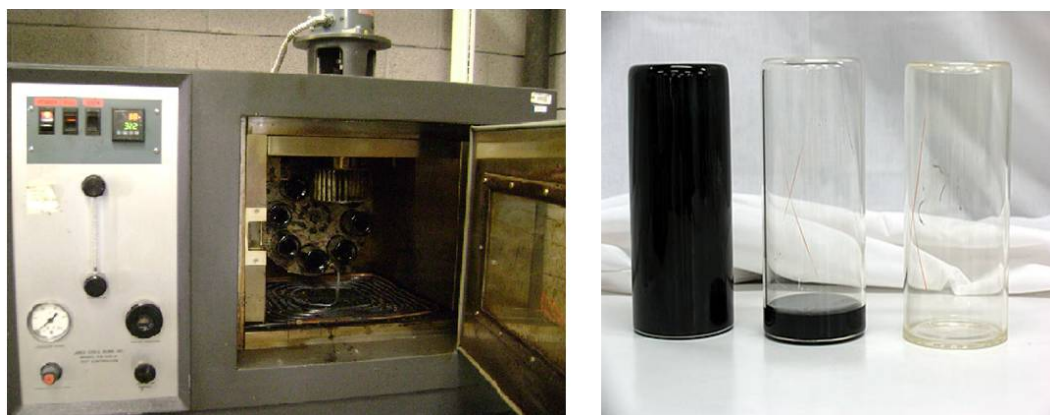
FIGURE 40 RTFO equipment and specimen preparation.

FIGURE 41 PAV equipment and specimen preparation.

MACTEC Test Results

Mixing and Compaction Temperatures

The laboratory mixing and compaction temperatures for the mix design were determined using the viscosity–temperature relationship. The temperatures were selected corresponding with binder viscosity values of 0.17±0.02 Pa·s for mixing and 0.28±0.03 Pa·s for compaction. Viscosity values were determined using a Brookfield Rheometer (ASTM D4402). To develop the viscosity binder temperature curves, three viscosity values were measured at temperatures of 275, 311, and 347°F (135, 155, and 175°C) for the PG 58-28 and PG 64-22 binders, while two viscosity values were measured at temperatures of 275 and 347°F (135 and 175°C) for the PG 76-16 binder. TABLE 4 summarizes the laboratory mixing and compaction temperatures determined.

TABLE 4 Summary of laboratory mixing and compaction temperatures for mix design, °F

(°C)

Temperature, °F (°C)		Binder Type		
		PG 58-28	PG 64-22	PG 76-16
Compaction	Min	275 (135)	287 (142)	310 (154)
	Max	284 (140)	296 (147)	318 (159)
Mixing	Min	295 (146)	308 (153)	329 (165)
	Max	305 (152)	320 (160)	340 (171)

Performance Graded Binder Classification Tests

The DSR and BBR tests were performed to characterize the three asphalt binders used for the mix design and to confirm that the binders met the performance graded binder specification.
For the characterization of binder at intermediate and high temperatures, the DSR test was conducted at 59, 86, 113, 158, 203, and 239°F (15, 30, 45, 70, 95, and 115°C). The complex shear modulus (G*) and phase angle were measured at a constant frequency (10 rad /sec). For the low temperature binder response, the BBR test was conducted and the flexural creep stiffness (S) at 60s at a specified temperature and slope (m-value) were measured. The temperatures used to measure the flexural creep stiffness were -0.4, 10.4, and 21.1°F (-18, -12, and -6°C) for PG 58-28, PG 64-22, and PG 76-16, respectively. TABLE 5 summarizes the test methods and their properties and test conditions. It should be noted that the DSR test was conducted for each aging condition: neat or tank, RTFO, and RTFO+PAV, while the BBR test was conducted only with the PAV conditioned binder.

TABLE 5 Summary of superpave binder characterization tests

Test	Property	Method	Conditions
Dynamic Shear Rheometer	Complex Shear Modulus (G*) and Phase Angle (δ)	AASHTO T 315	10 rad/sec 59, 86, 113, 158, 203, and 239°F (15, 30, 45, 70, 95, and 115°C)
Bending Beam Rheometer	Creep Stiffness (S) and Slope (m-value)	AASHTO T 313	60 sec -0.4, 10.4, and 21.2 °F, (-18, -12, and -6°C)

A viscosity–temperature relationship was developed using the DSR test results (e.g., G* and phase angle) at three aging conditions for the three binders as shown from FIGURES 42 to 44. From the plots it is obvious that the binder becomes more viscous as it is aged. Note that the viscosity values in each plot were obtained from the G* and phase angle values at the specified

test temperatures (Witczak,1998) by converting them into viscosity with the Cox-Merz equation (Cox and Merz, 1958).

$$\eta = \frac{G^*}{10}\left(\frac{1}{\sin\delta}\right)^{4.8628}\times 1000 \qquad (79)$$

where,

η = viscosity, cP
G^* = complex shear modulus, Pa
δ = phase angle, degree

As shown in TABLE 6, the creep stiffness results from the BBR test met the performance graded asphalt binder specification (AASHTO M 320).

TABLE 6 Summary of BBR test results (S and m-value)

Property	Binder Type			Spec
	PG 58-28	PG 64-22	PG 76-16	
Creep Stiffness, S	232	191	138	300 max
Slope, m-value	0.323	0.316	0.337	0.300 min
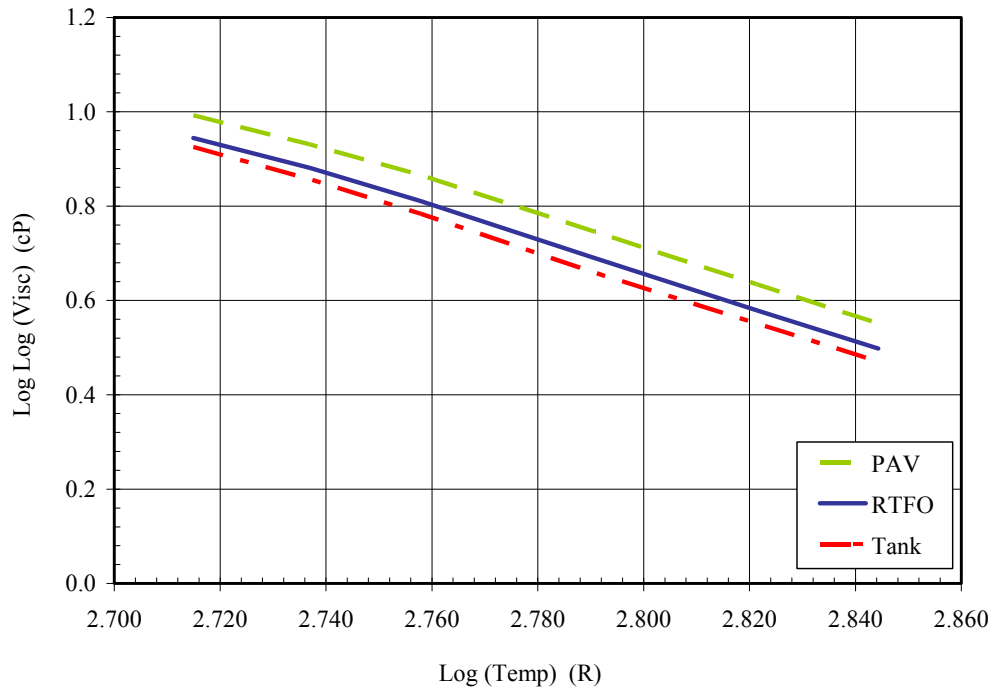
FIGURE 42 Temperature-viscosity relationship from DSR results (PG 58-28).
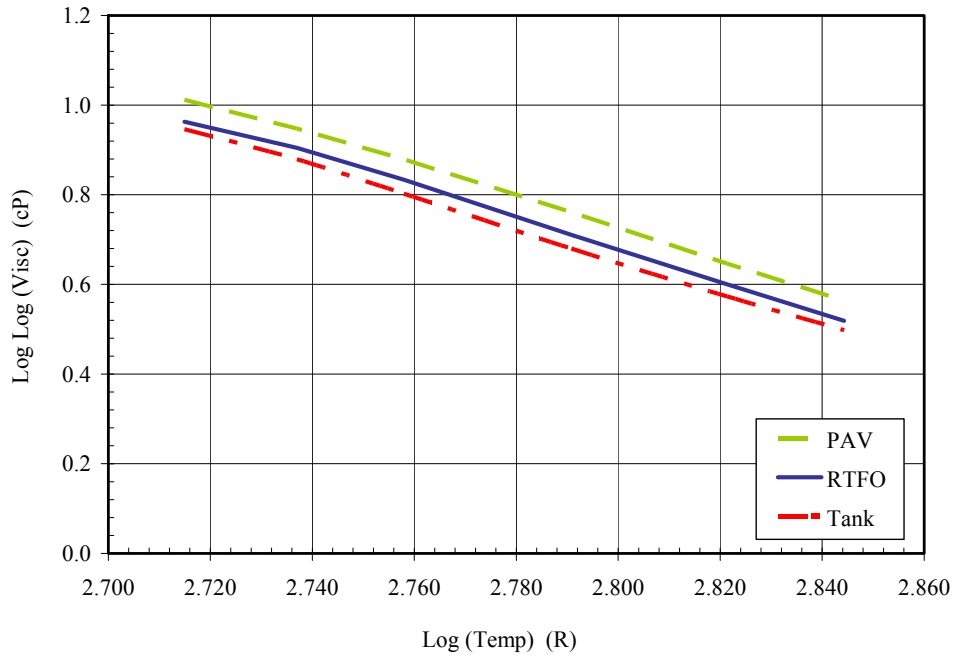
FIGURE 43 Temperature - viscosity relationship from DSR results (PG 64-22).
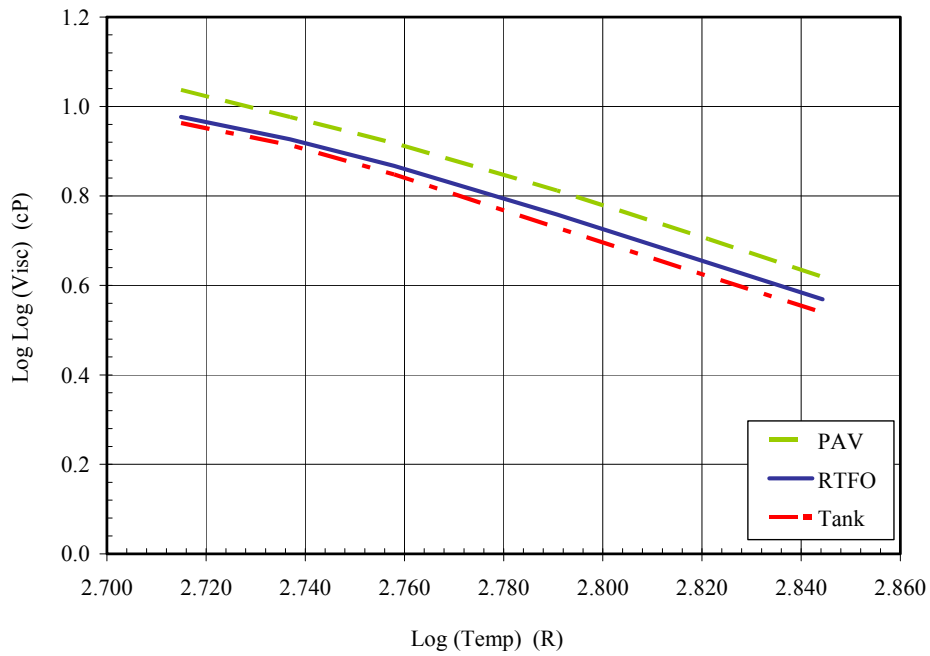
FIGURE 44 Temperature - viscosity relationship from DSR results (PG 76-16).

77

Arizona State University Asphalt Binder Characterization

A comprehensive characterization study of the rheological properties of three binder types (PG 58-28, PG 64-22, and PG 76-16) was conducted by Arizona State University, using one performance graded binder test and two penetration graded binder tests. This testing characterized the asphalt binder used in this project over a wide range of temperatures to enable development of a linear relationship between temperature and viscosity (e.g., Ai-VTSi relationship). All binder tests were performed at three aging conditions: neat (tank) or original, short-term aged (RTFO), and long-term aged (RTFO + PAV). The penetration graded binder tests used in this study were the penetration and softening point (Ring and Ball) tests. The performance graded binder test was the rotational viscosity (Brookfield) test.

It is also worthwhile of mention that each of the three binder types was divided into two sample cans (Sample 1 and 2) and that each can was again duplicated (Replicate A and B). This scheme applies to each aging condition. Thus, for one PG binder at a certain aging condition, four specimens (2 cans * 2 duplicates) were tested for the three binder tests. These four specimens were called a set and a unique set number was assigned to each set. TABLE 7 shows an example of this set numbering scheme.

TABLE 7 Example of binder sample preparation scheme

Binder Type	Aging Condition	Sample Can	Replicate	Set Number
PG 58-28	Neat	1	A	10
			B	12
		2	A	11
			B	13

Test Methods

TABLE 8 summarizes the properties measured, the test standard, and the test condition for each test. Following is a summary of the three binder tests:

TABLE 8 Summary of conventional and Superpave binder characterization tests

Test Type	Property	Method	Conditions
Penetration Graded Test	Penetration	AASHTO T 49	100 g, 5 sec, 40, 55, 77, and 90°F (4, 12.8, 25, and 32°C)
	Softening Point	AASHTO T 53	Measured Temperature
Performance Graded Test	Brookfield Viscosity	AASHTO T 316	200, 250, 300, 350°F (93, 121, 149, 177°C)

Penetration Test. The penetration test was conducted to derive the viscosity at low and intermediate temperatures. The penetration of an asphalt binder is the distance in tenths of a millimeter that a standard needle penetrates vertically into a sample of the material under fixed

conditions of temperature, load, and time. This test is commonly used as a measure of consistency. Higher values of penetration indicate softer consistency. The binder sample was heated and cooled under controlled conditions. The penetration was measured with a penetrometer using a standard needle under a specified condition. Penetration tests were conducted at 40, 55, 77, and 90°F (4, 12.8, 25, and 32°C) using a 100 g load for 5 second. FIGURE 45 shows the penetration test apparatus and specimen preparation. The penetration value can be converted into viscosity by Equation 80:

$$\log \eta = 10.5012 - 2.2601\log(\text{Pen}) + 0.00389\left[\log\left(\text{Pen}\right)\right]^2$$

(80)

where;

η = viscosity, P

Pen   = measured penetration for 100g, 5 sec loading, 0.1 mm
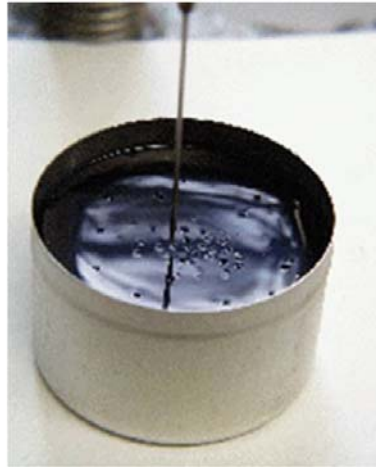
FIGURE 45 Penetration test apparatus and specimen preparation.

Softening Point Test. This test covers the determination of the softening point of asphalt binders using the ring-and-ball apparatus. Two horizontal disks of binder, cast in shouldered brass rings, are heated at controlled rate in a liquid bath while each supports a steel ball. The softening point is reported as the mean of the temperatures at which the two disks softens enough to allow each ball, enveloped in asphalt binder, to fall a vertical distance of 1-inch (25-mm). The softening point is used in the classification of asphalt binders and as one of the elements in establishing the uniformity of shipments or sources of supply. The softening point is indicative of the tendency of the binder to flow at elevated temperatures encountered in service. For most asphalt binders, the Ring and Ball softening point corresponds to a viscosity of 13,000 Poise. FIGURE 46 shows the test apparatus and specimen preparation.
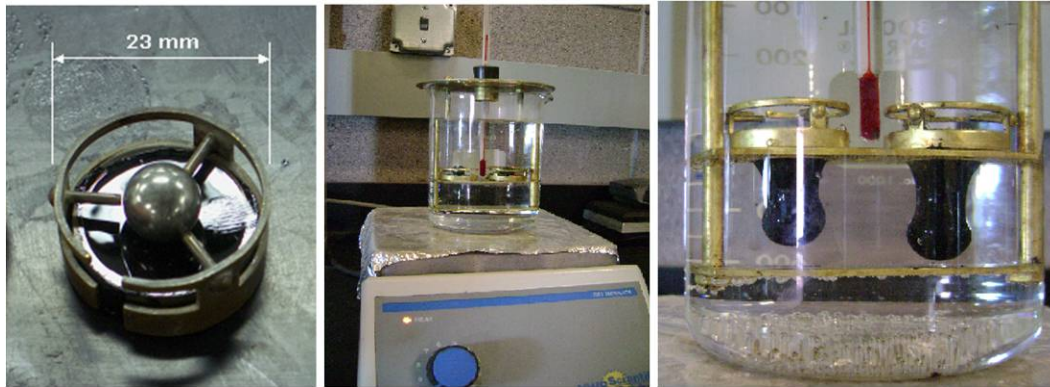
FIGURE 46 Softening point test apparatus and specimen preparation.

Brookfield Viscosity Test. This test determines the viscosity of asphalt binders at higher temperatures. A Brookfield rotational coaxial viscometer was used with a Thermosel^{TM} temperature control system. The rotational viscometer automatically calculates the viscosity at the test temperature. The rotational viscosity is determined by measuring the torque required to maintain a constant rotational speed of a cylindrical spindle while submerged in a binder at a constant temperature. This torque is directly related to the binder viscosity. A rotational viscometer can measure viscosity of asphalt binder under both Newtonian and non-Newtonian binder conditions. Unlike capillary tube viscometers, the rotational viscometers have larger clearances between the components and, therefore, are applicable to modified as well as unmodified asphalt binders. The viscosity at different shear rates at different temperatures can be used to determine the viscosity-temperature susceptibility of asphalt binders. The Brookfield viscometer measures viscosity at four elevated temperatures (200, 250, 300, and 350°F). FIGURE 47 shows the test apparatus and specimen preparation.

FIGURE 47 Brookfield test apparatus and specimen preparation.

Data Analysis

A combination of eight viscosity–temperature data points (four penetration, one softening, and four Brookfield) are plotted together on a viscosity–temperature graph to characterize the binder's viscosity-temperature susceptibility relationship over a wide range of temperature. A linear relationship can be established based upon Equation 81. FIGURES 48 to 50 illustrate the viscosity–temperature relationship for each binder type at all aging levels (tank condition, RTFO, and PAV).

$$\log\log\eta = A + VTS\log T_R \tag{81}$$

where;

η = viscosity, cP
T_R = temperature, Rankine
A = regression intercept
VTS = regression slope of viscosity-temperature susceptibility
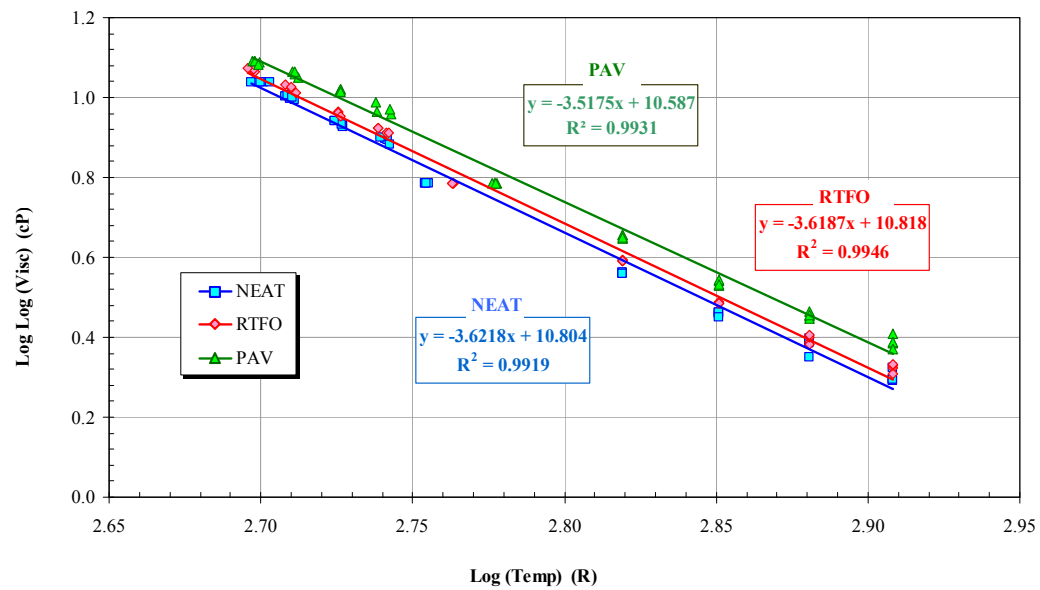
FIGURE 48 Viscosity – temperature relationship of PG 58-28 binder.
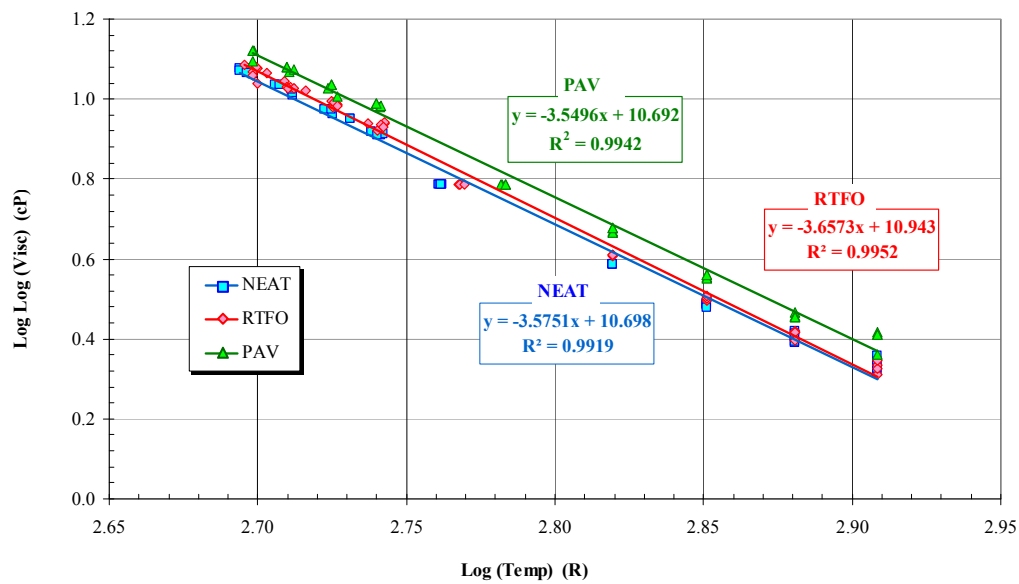
FIGURE 49 Viscosity – temperature relationship of PG 64-22 binder.

82
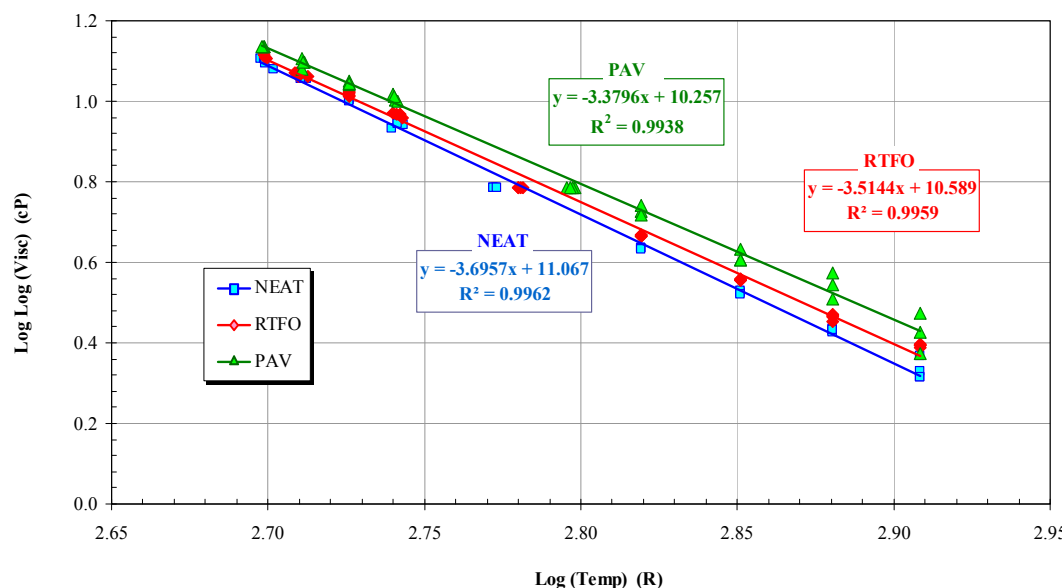
FIGURE 50 Viscosity – temperature relationship of PG 76-16 binder.

Mix Design

The aggregate for this research was a crushed Salt River gravel. The aggregate stockpiles were provided by CEMEX U.S.A. and were delivered from its Plant #111–1386 in Phoenix, Arizona. The aggregate stockpiles delivered included different aggregate sizes, viz., ¾", ½" 3/8", sand, and crushed fines.

A ¾-inch (19-mm) Superpave high traffic asphalt concrete mix design was prepared by MACTEC for this research according to the requirements of Maricopa County, Uniform Standard Specifications for Public Works Construction Section 710. This mix design is intended for use on arterial roads. While three different asphalt concrete mixes were designed, each of which used a particular binder type: PG 58-28, PG 64-22, and PG 76-16, the same aggregate gradation was used for all mix designs. FIGURE 51**Error! Reference source not found.** shows the design aggregate gradation along with the minimum and maximum design specification. FIGURE 51**Error! Reference source not found.** illustrates the design aggregate gradation. TABLE 9 includes composite aggregate properties measured by MACTEC. The summary of the key volumetric properties from the mix design results using the three binders are presented in TABLES 10 and 11**Error! Reference source not found.**.

TABLE 9 Design aggregate gradation

Size	% Passing		
	Design	Minimum	Maximum
1 in.	100.0	100.0	100.0

¾ in.	95.0	90.0	100.0
½ in.	80.0	43.0	89.0
3/8 in.	59.0		
No. 4	39.0		
No. 8	29.0	24.0	36.0
No. 16	23.0		
No. 30	17.0		
No. 50	10.0		
No. 100	5.0		
No. 200	3.3	2.0	6.0
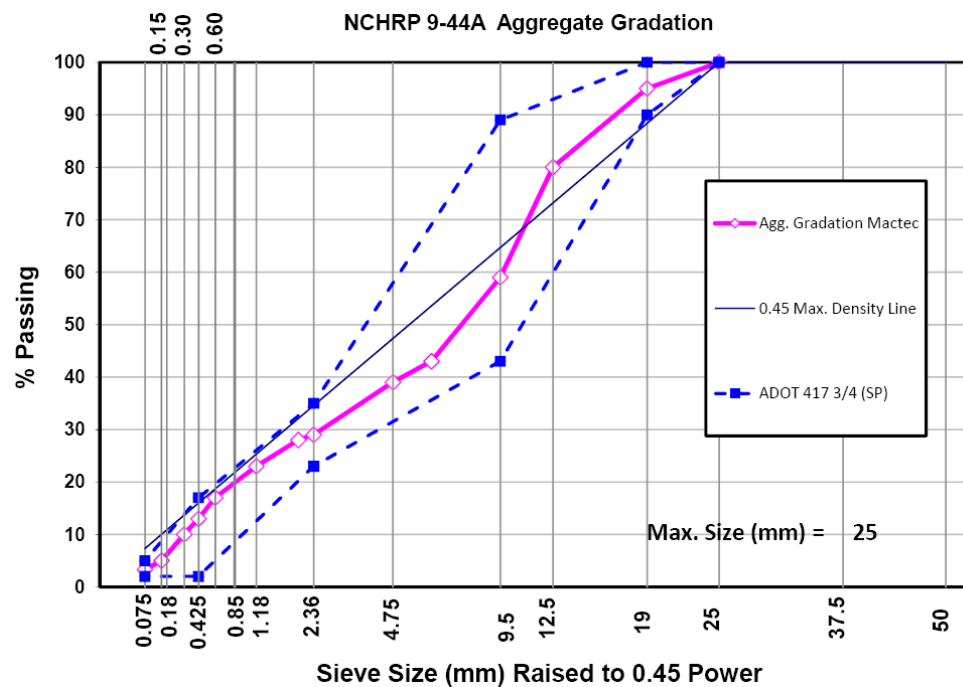
FIGURE 51 Design aggregate gradation.

TABLE 10 Composite aggregate properties

Property	Value	Specifications
Bulk (Dry) Sp. Gravity	2.614	(2.35-2.85)
SSD Sp. Gravity	2.638	
Apparent Sp. Gravity	2.677	
Water absorption (%)	0.90	(0-2.5)

84

Sand Equivalent Value	71	Min 50
Fractured Face One (%)	99	Min 85
Fractured Face Two (%)	96	Min 80
Flat & Elongation (%)	1.0	Max 10
Uncompacted Voids (%)	46.8	Min 45
L.A. Abrasion @ 500 Rev.	16	Max 40

TABLE 11 Summary of the volumetric mix design properties for different binder grades

Volumetric Property	Binder Type			Specs.
	PG 58-28	PG 64-22	PG 76-16	
Asphalt Content (%)	4.8	4.5	4.7	4.5 ~ 5.5
Bulk Specific Gravity (G_{mb})	2.365	2.367	2.351	N/A
Theoretical Maximum Specific Gravity (G_{mm})	2.461	2.467	2.454	N/A
Air Voids (%)	3.9	4.1	4.2	3.8 ~ 4.2
VMA (%)	13.9	13.5	14.3	Min. 13
VFA (%)	71.9	69.9	70.8	N/A
Asphalt Specific Gravity (G_b)	1.024	1.024	1.042	N/A

TESTING PLAN

The testing plan included conducting two primary test methods: the complex modulus test and the uniaxial tension-compression fatigue test, which is a damage-inducing test. The testing plan for each test is shown in FIGURE 52 and described in the following section.
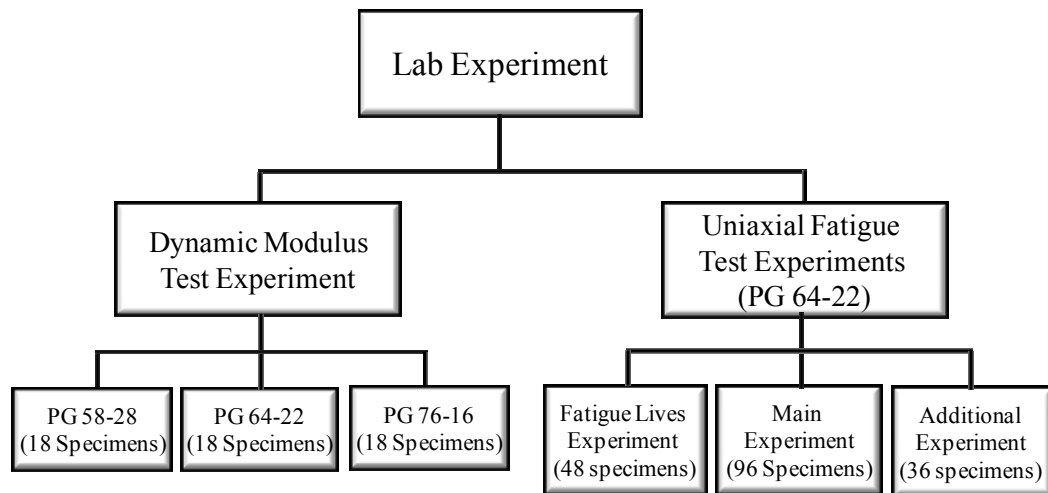
FIGURE 52 Flow chart of research testing plan.

Dynamic Modulus Test (AASHTO TP 62-07)

One important part of the research plan was to develop the dynamic modulus master curves and temperature shifting for different asphalt concrete mixtures. These results were used for two main purposes. The first purpose was to use the dynamic modulus master and phase angle master curves to estimate the viscoelastic properties of the asphalt concrete mixtures by predicting the relaxation modulus required in the analysis of the viscoelastic and continuum damage model. The second purpose was to use the shift factors at different temperatures in the analysis of fatigue damage and healing at different temperatures.

The complex modulus test was conducted according to AASHTO TP 62-07 in a stress-controlled mode of loading within the linear viscoelastic range using a sinusoidal loading wave in compression. The stress magnitudes varied depending on the mixture type, test temperature, and test frequency, to maintain the recoverable strain to 150 microstrain and so insure that no damage occurred during the test. The cylindrical specimens used in this test had a diameter of 100 mm (4 inches) and a height of 150 mm (6 inches).

The complex modulus test plan included testing of the asphalt concrete mixtures prepared with three binders, PG 58-28, PG 64-22, and PG 76-16. Each asphalt concrete mixture was tested at three levels of asphalt content and air voids yielding nine different combinations of the two factors. Two identical replicates were tested for each combination, giving a total of 18 specimens for each mixture or 54 specimens for the three mixtures. Each specimens was tested at five temperatures and six frequencies as explained in Chapter 5.

TABLE 12 shows the number of complex modulus tests at each set of conditions.

TABLE 12 Number of complex modulus tests at each set of conditions

Mixture Type	Asphalt Cement (%)	Air Voids (%)		
		Low	Optimum	High
PG 58-28	Low	2 replicates	2 replicates	2 replicates
	Optimum	2	2	2
	High	2	2	2
PG 64-22	Low	2	2	2
	Optimum	2	2	2
	High	2	2	2
PG 76-16	Low	2	2	2
	Optimum	2	2	2
	High	2	2	2
Total number of specimens		54		

Uniaxial Tension-Compression Fatigue Test Experiments

Uniaxial fatigue test experiments included the testing of PG 64-22 asphalt concrete mixture only. Four asphalt concrete mixtures with different asphalt content and air voids combinations were used in these experiments (4.2% AC& 4.5 %Va, 5.2% AC& 4.5 %Va, 4.2% AC& 9.5 %Va, and 5.2% AC& 9.5 %Va). The research plan for the uniaxial tension-compression fatigue testing consisted of three experiments: fatigue life experiment, main experiment, and additional experiment.

Fatigue Life Experiment

The purpose of this experiment was to determine the strain levels for each mixture type used in the main experiment at different temperatures. The main experiment used two different strain levels at each test temperature (40, 70 and 100°F). The criterion for selecting the two strain levels at each temperature was to reach a fatigue life of 20,000 cycles at the high strain level and 100,000 cycles at the low strain level. To establish each fatigue life, four uniaxial tension-compression fatigue tests were conducted at different strain levels, which required 12 tests for one mixture at three temperatures (40, 70 and 100°F) or 48 tests for the four combinations of asphalt content and air voids (TABLE 13).

TABLE 13 Number of fatigue tests under different conditions

Air Voids (%)	Temp. (^{o}F)	Asphalt Content (%)	
		4.2	5.2
4.5	40	4	4
	70	4	4
	100	4	4
9.5	40	4	4
	70	4	4

	100	4	4
Total		48 Tests	

Main Fatigue Experiment

The objective of the main experiment was to investigate the healing of fatigue damage of the asphalt concrete mixtures and correlate the healing properties to the different factors identified previously in the discussion of the experiment design. In addition, the results from this experiment were used to develop a methodology to predict the HMA endurance limit. The fatigue healing in this research was evaluated by observing the difference between fatigue damage using two different uniaxial fatigue test procedures. The first method is a damage test where the loading is running continuously without any rest between the loading cycles inducing fatigue damage. The second method is the healing or intermittent-load test where a constant rest period is inserted between the loading cycles to allow for healing of fatigue damage. The amount of rest period used on this experiment was 5 seconds inserted between the 0.1-second loading cycles throughout the entire test (rest to loading ratio of 50).
TABLE 14 shows the testing plan for uniaxial tension-compression fatigue test developed from the fractional factorial design of experiment.

TABLE 14 Number of uniaxial tension-compression fatigue tests under different conditions

Rest Period (sec)			0		5	
Air Voids (%)			4.5	9.5	4.5	9.5
Temp. (ºF)	Strain Level	Asphalt Content (%)	Number of Specimens			
40	L	4.2	3	3	3	--
		5.2	--	3	3	3
	M	4.2	3	--	--	3
		5.2	3	3	3	3
70	L	4.2	--	3	3	3
		5.2	3	--	--	3
	M	4.2	3	3	3	--
		5.2	--	3	3	3
100	L	4.2	3	--	--	3
		5.2	3	--	3	--
	M	4.2	--	3	3	3
		5.2	3	--	--	3
Total Number of Specimens			45 Specimens		51 Specimens	

Additional Fatigue Experiment

As only two strain levels were considered in the main experiment, the relationship between the Pseudo Stiffness Ratio (PSR) and the strain levels is, by necessity, linear. However the real relationship may have a different trend. The same situation applies to the rest period as only two levels of the rest periods are applied (0 and 5 seconds). Based on earlier research, the effect of the rest period on the fatigue life and healing might be insignificant beyond a certain value. Therefore, the relationship between the PSR and the rest period is likely not a linear relationship. In this experiment, an additional strain level (high) and two additional rest periods of 1.0 and 10.0 seconds (10 and 100 loading ratio) were added. The selection of the required combinations is justified by using the fractional factorial technique considering only two levels of interaction as shown in TABLE 15 (JMP® Software). Based on this, an additional 20 combinations are required. Because of overlap with the main experiment, the required number of new combinations was 18, with two replicates for each combination.

TABLE 15 Testing plan of additional fatigue test

Asphalt Content (%)			4.2		5.2	
Air Voids (%)			4.5	9.5	4.5	9.5
Temp., °F	Strain Level	Rest Period (sec)				
40	L	0				
		1				
		5		X	XX	
		10				
	M	0				
		1		X		
		5				
		10			X	
	H	0				X
		1			X	
		5	X			
		10				
70	L	0	X			
		1				
		5				
		10			X	
	M	0				
		1			X	
		5		X		
		10				
	H	0				
		1				X
		5				
		10				
100	L	0			X	
		1	X			X
		5				
		10				
	M	0				X

		1				
		5	XX			
		10		X		
		0		X		
	H	1				
		5				X
		10				

X	New combinations of additional experiments
XX	Overlapped combinations with the main experiments

LABORATORY MANUFACTURE OF HMA SPECIMENS

Preparation of Aggregates

Drying of Aggregate Stockpiles

Five different stockpiles were used in this study including ¾", ½" 3/8", sand, and crushed fines. The aggregates were placed in large ovens to dry over night at 110ºF before blending and sieving.

Blending of Aggregate Stockpiles

Dried aggregate stockpiles were blended at percentages provided by CEMEX, U.S.A. The percentages used for each stockpile gradation were as follows:

Sieve Size	Percent Passing
¾"	= 18%
½"	= 12%
3/8"	= 12%
Sand	= 15%
Crushed Fines	= 43%

Sieving of Blended Aggregates

Once the aggregates from each stockpile have been weighed and blended at the determined percentages, three to four heaping shovel fills were placed into a Gilson Test Master TM-4 Floor Sieve Shaker. The sieve shaker was run for a 20 minute period and once completed; the contents of each size sieve were emptied into pre labeled 5 gallon plastic buckets.

Aggregate Batching

Batches were created using the design gradation from MACTEC's mix design (TABLE 16). Batches were made using empty, clean 1-gallon metal paint cans. Paint cans were filled with

the calculated weights from each aggregate size as per the design gradation in order to create one individual specimen.

TABLE 16 Aggregate batching sheet

Sieve Size	Total Passing (%)	Retained (%)	Weight per Core Batch (gm)	Weight per Core Batch (gm)
¾"	95.0	5.0	325	350
½"	80.0	15.0	975	1050
3/8"	59.0	21.0	1365	1470
No. 4	39.0	20.0	1300	1400
No. 8	29.0	10.0	650	700
No. 16	23.0	6.0	390	420
No. 30	17.0	6.0	390	420
No. 50	10.0	7.0	455	490
No. 100	5.0	5.0	325	350
No. 200	3.3	1.7	110.5	119
Pan (<No. 200)		3.3	214.5	231
Total		100	6500	7000

Wet Sieve Analysis

In order to pinpoint the proper amount of fines used in each specimen, Arizona State University performed a wet sieve analysis of aggregates per AASHTO T 11. Two 1,500 gram samples were washed on a weekly basis as a quality control measure. The results were analyzed and any adjustments were made to the batching gradation for that week's worth of batching.

Preparation of Specimens

Mixing of Asphalt Mixture

Prior to the specimen mix manufacturing process, batched aggregate cans were placed in a heated oven at 295ºF (145ºC) overnight to insure that no moisture was present in the aggregate specimens. On the day of sample mixing, an appropriate weight of binder was placed in a heated oven for approximately 60 minutes to gently bring the temperature of the binder up to the desired mixing temperature. The preheated aggregates and the desired amount of binder were then placed into the bucket of a mixing machine and mixed for 120 seconds.

Short-Term Aging

The properly mixed HMA was emptied and evenly spread about into a heated metal tray, approximately 3' x 3' and 3" deep in size, and placed uncovered into a preheated 275ºF (135ºC) convection oven for short-term aging per AASHTO R 30 for conditioning prior to performance testing.

Maximum Theoretical Specific Gravity (G_{mm})

An heated and mixed HMA specimen was poured loose on a table to cool overnight. The next day, the cooled HMA was crumbled and separated by hand and the theoretical maximum specific gravity (G_{mm}) was measured using the AASHTO T 209 Pycnometer Method. This G_{mm} of the specific HMA is used to calculate the air voids (Va %) of all specimens.

HMA Compaction

For the preparation of gyratory specimens used in this study, an IPC (Industrial Processing Services) SERVOPAC gyratory compactor was used. The compactor was set with a vertical stress of 600 kPa at a rate of 38 gyrations per minute and a 1.25º gyration angle. The molds used were 6-inch (150-mm) in diameter. All gyratory plugs were compacted to a standardized height of 6.7-inch (170-mm). The 6-inch (150-mm) diameter plug was then cored with a 4-inch (100-mm) diamond tipped coring bit to produce E* specimens or with a 3-inch (75-mm) diamond tipped coring bit to produce uniaxial fatigue specimens. The 6.7-inch (170-mm) height was trimmed to 6-inch (150-mm) using a 14-inch diamond tipped circular saw blade.

Air Voids Determination

The cored and cut specimens were dried and the air voids (Va%) of the dried specimens were obtained using AASHTO T 166, "Bulk Specific Gravity of Bituminous Mixtures Using Saturated Surface Dry Specimens."

Storing of Prepared Specimens

After measurement of air voids, the specimens were left for 1 day to dry out. The specimen was then placed inside a Zip-Loc bag and stored in a shelving cabinet at room temperature to minimize further aging. The storage time was limited to a month or less before testing.

CHAPTER 5

VISCOELASTIC PROPERTIES OF ASPHALT CONCRETE MIXTURES

BACKGROUND

The viscoelastic response of asphalt concrete mixtures can be captured through mechanical tests conducted in the linear viscoelastic range. Viscoelastic behavior of asphalt concrete mixtures can be described by different mechanical properties. These mechanical properties are complex modulus, relaxation modulus, and creep compliance. In this study, the complex modulus was determined for three mixtures with binder grades of PG 58-28, PG 64-22, and PG 76-16 according to test procedure in AASHTO T 342.

COMPLEX MODULUS

Theoretical Background

For linear viscoelastic materials such as asphalt mixes, the stress-strain relationship under a continuous sinusoidal loading is defined by a complex number called the complex modulus E* (Pellinen, 2001; NCHRP 465, 2002). It is a true complex number that contains both a real and imaginary component of the modulus that defines the elastic and viscous behavior of the linear viscoelastic material. These components are:

$$E^* = E' + iE'' \tag{82}$$

or

$$E^* = \sqrt{(E')^2 + (E'')^2} \tag{83}$$

with

$$E' = (\sigma_o / \varepsilon_o) \cos \phi \quad \text{or} \quad E' = E^* \cos \phi \tag{84}$$
$$E'' = (\sigma_o / \varepsilon_o) \sin \phi \quad \text{or} \quad E'' = E^* \sin \phi \tag{85}$$

where:

σ_o = peak dynamic stress amplitude (psi or kPa),
ε_o = peak recoverable strain (in/in or mm/mm), and
ϕ = phase lag or angle (degrees).

The E' value is generally referred to as the storage (elastic) modulus component of the complex modulus, while E'' is referred to as the loss (viscous) modulus. The loss tangent (tan ϕ) is the ratio of the energy lost to the energy stored in a cyclic deformation and is equal to:

$$\tan \phi = E'' / E' \tag{86}$$

According to the current protocol, complex modulus testing of asphalt materials is conducted using a uniaxial sinusoidal load (AASHTO T 342). Under such conditions, the complex modulus is defined as the ratio of the amplitude of the sinusoidal stress (at any given time, t, and angular load frequency, ω), $\sigma = \sigma_o \sin (\omega t)$, and the amplitude of the sinusoidal strain $\varepsilon = \varepsilon_o \sin (\omega t - \phi)$, at the same time and frequency, that results in a steady-state response (FIGURE 53)

$$E^* = \frac{\sigma}{\varepsilon} = \frac{\sigma_o e^{i\omega t}}{\varepsilon_o e^{i(\omega t - \phi)}} = \frac{\sigma_o \sin \omega t}{\varepsilon_o \sin(\omega t - \phi)} \qquad (87)$$

where,

ω = angular velocity = $2\pi f$,
t   = time, seconds, and
f   = loading frequency (Hz).

$$\phi = (t_i / t_p) \times (360^o) \qquad (88)$$

or

$$\phi = 2\pi f (t_i) \qquad (89)$$

where:

t_i = time lag between a cycle of stress and strain (sec), and
t_p = time for a stress cycle (sec).

The absolute value of the complex modulus $|E^*|$, is defined as the dynamic modulus. Mathematically, the dynamic modulus is defined as the maximum (peak) dynamic stress (σ_o) divided by the recoverable axial strain (ε_o):

$$|E^*| = \frac{\sigma_o}{\varepsilon_o} \qquad (90)$$
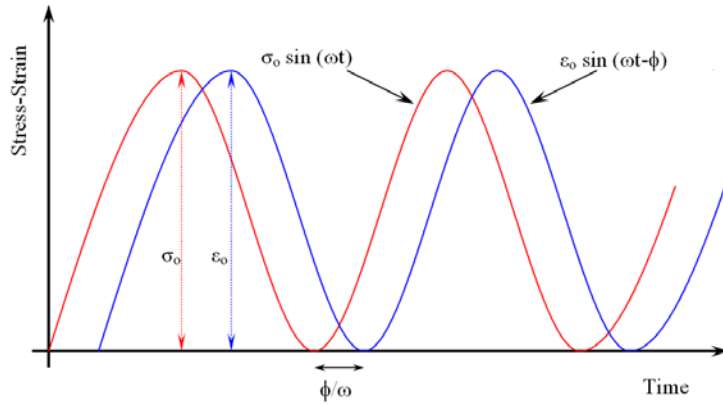
FIGURE 53 Complex modulus test.

Testing System

An Industrial Process Controls (IPC) Universal Testing Machine (UTM-25) was used to conduct the complex modulus test. The UTM-25 machine is a closed-loop servo-hydraulic testing system. The load frame capacity is 5,600 lb (25kN) in static loading and 5,600 lb (25kN) in dynamic loading. The machine is capable of applying load over a wide range of frequencies (from 0.1 to 20 Hz). The servo-hydraulic system is controlled by an IPC controller

The temperature control system of the UTM is refrigeration-based. The temperature control system is able to provide temperatures in the range of 5 to 140ºF (-15 to 60ºC) for extended periods. The excellent temperature homogeneity and gradients are achieved with internal fans and baffles to control air circulation, giving greater confidence in the test results. An asphalt dummy specimen with both skin and core temperature probes is used to monitor and ensure the consistency of the testing temperature.

The measurement system is computer controlled and capable of measuring and recording a minimum of 16 channels simultaneously. The channels are assigned to various sensors. Of the 16 channels, seven channels were used, viz., two channels for on-sample vertical deformation measurements, two channels for the load cell and the actuator linear variable differential transducers (LVDT), two channels for the skin and core temperature probes, and one channel for the confinement pressure measurement.

Loads are measured using electronic load cells capable of measuring loads with an accuracy of $\pm$ 0.1 %. Vertical deformations are measured using two spring-loaded LVDTs. FIGURE 54 illustrates different components of the testing system.
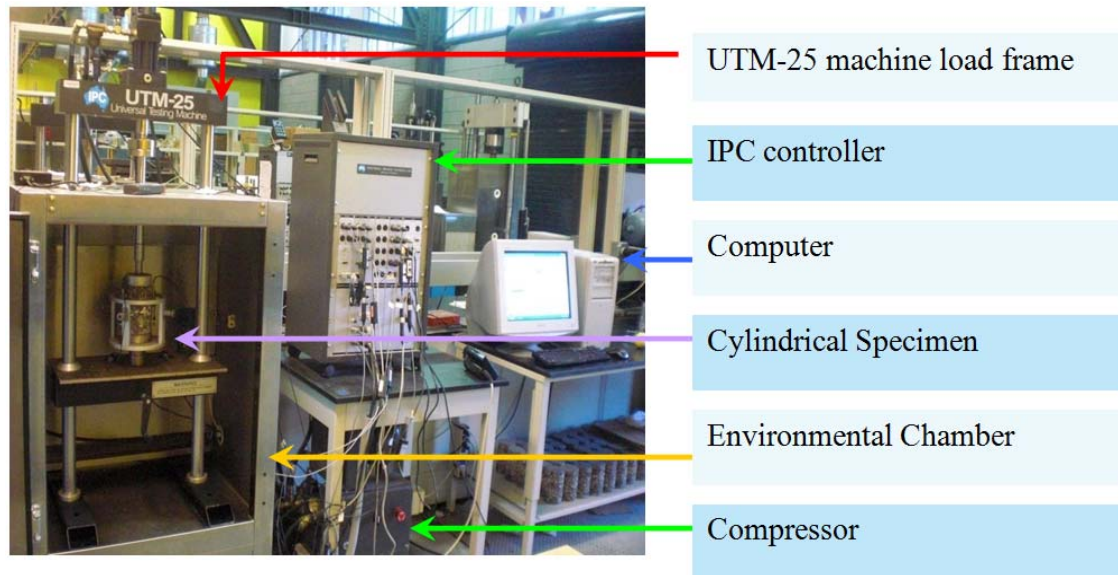
FIGURE 54 Complex modulus test setup.

Mixtures Tested

As discussed in Chapter 4, the dynamic modulus experiment included testing of three different mixtures, each with a different binder type (PG 58-28, PG 64-22, and PG 76-16). For each mixture, 18 different cylindrical specimens, 4-inch (100 mm) in diameter and 6-inch (150 mm) in height, were prepared. These specimens represent 9 different combinations of air voids and asphalt content with two replicates for each combination. For the 64-22 asphalt mixture, the air voids values are the designed Va $\pm$ 3% (4, 7, and 10%). The asphalt content values are the optimum AC $\pm$ 0.5% (4.0, 4.5, and 5%). For PG 58-28 and PG 76-16 mixtures, the air voids values are the designed Va$\pm$ 2.5% (4.5, 7, and 9.5). The asphalt content values were fixed for these two mixtures as 4.2, 4.7, and 5.2%. TABLE 17 shows the different combinations of specimens used for the PG 64-22 asphalt mixture. Table 18 illustrates the combinations of specimens required for the other two mixtures.

TABLE 17 Number of specimens for different combinations of volumetric properties for the PG64-22 asphalt mixture

Binder Type	Asphalt Content (%)	Air Voids (%)		
		4	7	10
	Optimum-0.5 = 4.0	2	2	2
PG64-22	Optimum = 4.5	2	2	2
	Optimum+0.5 = 5.0	2	2	2

TABLE 18 Number of specimens for different combinations of volumetric properties for the PG58-28 and PG76-16 asphalt mixtures

Binder Type	Asphalt Content (%)	Air Voids (%)		
		4.5	7	9.5
	4.2	2	2	2
PG58-28	4.7	2	2	2
	5.2	2	2	2
	4.2	2	2	2
PG76-16	4.7	2	2	2
	5.2	2	2	2

Measured G_{mm} and Air Voids Values of the Tested Specimens

All E* test specimens were prepared according to AASHTO T 342. The measured air voids and bulk specific gravity for the fabricated specimens are listed in TABLES 19 to 21.

TABLE 19 Bulk Sp. Gr., maximum Sp. Gr., and Saturated surface dry air voids of the PG 64-22 specimens

Specimen ID	Bulk S. G. G_{mb}	Measured Max. S. G. G_{mm}	SSD Air Voids (%)
6-105	2.254		9.52
6-106	2.248		9.74
6-703	2.304	2.491	7.51
6-704	2.317		7.00
6-404	2.403		3.53
6-405	2.398		3.73
6O103	2.222		10.07
6O104	2.214		10.42
6O701	2.294	2.471	7.16
6O702	2.293		7.21
6O401	2.366		4.26
6O402	2.366		4.23
6+105	2.218		9.80
6+106	2.207		10.24
6+705	2.271	2.459	7.28
6+706	2.287		6.99
6+405	2.355		4.22
6+406	2.354		4.26

TABLE 20 Bulk Sp. Gr., maximum Sp. Gr., and Saturated surface dry air voids of the PG 58-28 specimens

Specimen ID	Bulk S. G. G_{mb}	Measured Max. S. G. G_{mm}	SSD Air Voids (%)
5-901	2.246		9.53
5-902	2.245		9.56
5-701	2.295	2.482	7.55
5-702	2.296		7.49
5-401	2.364		4.74
5-402	2.365		4.72
5O901	2.222		9.84
5O902	2.224		9.79
5O702	2.281	2.465	7.46
5O703	2.284		7.36
5O402	2.340		5.07
5O403	2.347		4.77
5+901	2.201		9.95
5+902	2.204		9.81
5+703	2.255	2.444	7.74
5+704	2.271		7.06
5+401	2.333		4.53
5+402	2.329		4.72

TABLE 21 Bulk Sp. Gr., maximum Sp. Gr., and Saturated surface dry air voids of the PG 76-16 specimens

Specimen ID	Bulk S. G. G_{mb}	Measured Max. S. G. G_{mm}	SSD Air Voids (%)
7-901	2.251		8.87
7-902	2.239		9.34
7-703	2.299	2.470	6.92
7-704	2.304		6.71
7-403	2.347		4.99
7-404	2.349		4.89
7O903	2.229		9.12
7O904	2.225		9.30
7O701	2.282	2.453	6.97
7O702	2.277		7.13
7O401	2.338		4.69
7O403	2.354		4.56
7+903	2.197		9.85
7+904	2.199		9.77
7+703	2.259	2.437	7.32
7+704	2.274		6.70
7+401	2.329		4.45
7+402	2.319		4.84

Capping of Specimens

During cutting, the tops and the bottoms of the specimens, especially those of high air voids and low asphalt cement combinations, some aggregate particles were lost, leaving voids on the top and bottom surfaces. Special attention was given to treat these surfaces by capping the top and the bottom of the specimen with a suitable capping compound so that the thickness of the cap is about 1/8-inch (3-mm) and not more than 5/16-inch (8-mm) in any location. Before the specimen is tested, the cap was left to cure in order to have strength comparable to that of the specimen material. FIGURE 55 shows the capping device.

FIGURE 55 Capping device.

Summary of Test Procedure

The complex modulus test is conducted in a stress-controlled mode within the linear viscoelastic range. The main purpose of this test is to obtain the viscoelastic properties of the material and to determine the shift factors for the undamaged state by constructing the dynamic modulus master curve. AASHTO T 342 is followed for the E* testing. For each mixture, two replicates were prepared for testing. For each specimen, E* tests are conducted at 14, 40, 70, 100 and 130°F and 25, 10, 5, 1, 0.5 and 0.1 Hz loading frequencies, starting with the highest frequency. A 120 second rest period was used between each frequency to allow some specimen recovery before applying the new loading at a lower frequency. TABLE 22 presents a summary of the E* test conditions.

The stress amplitude was selected by trial and error at the beginning of each temperature run for each replicate so that the recoverable strain at the beginning of the test at 25 Hz frequency was in the range of 30 to 60 microstrain. For moderate and high temperatures (70 to 130°F) the stress levels was decreased as the frequency decreased to insure that the produced strain is smaller than 150 microstrain. This ensures, to the best possible degree, that the response of the material is linear across the temperature range used in the study. The dynamic stress values were 10 to 160 psi for low temperatures (14 to 70°F) and 2 to 20 psi for higher temperatures (100 to 130°F). All E* tests were conducted in a temperature-controlled chamber capable of maintaining temperatures from 3.2 to 140°F (–16 to 60°C).

TABLE 22 Test conditions of the dynamic modulus (E*) test (AASHTO TP 62-07)

Test Temp. (°F)	Freq. (Hz)	Cycles	Cycles to Compute E* & φ
14, 40, 70, 100, 130	25	200	196 to 200
	10	100	196 to 200
	5	50	96 to 100
	1	20	16 to 20
	0.5	15	11 to 15
	0.1	15	11 to 15

Axial deformations of the specimens were measured using two spring-loaded linear variable differential transducers (LVDTs) placed vertically on diametrically opposite sides of the specimen. Parallel brass studs were used to secure the LVDTs in place. Two pairs of studs are glued on the two opposite cylindrical surfaces of a specimen; each stud in a pair, being 4-inch (100-mm) apart and located at approximately the same distance from the top and bottom of the specimen. FIGURE 56 is schematic of the instrumentation of the test samples used in the dynamic modulus testing.

TABLE 23 shows typical tabulated E* test results that include the dynamic modulus and phase angle of each replicate and the averages as well. To show the amount of variability between the replicates at different test temperatures and frequencies, coefficients of variation have been determined. Other E* test results for a total of 27 tested mixtures are presented in Appendix A.
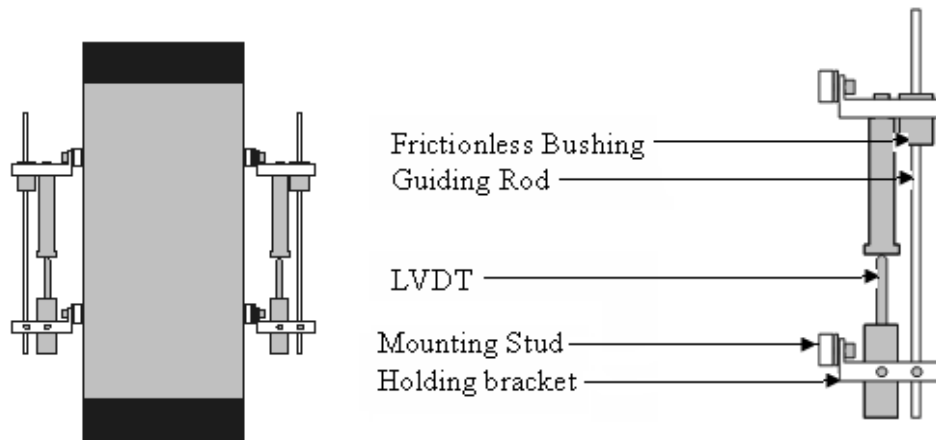
FIGURE 56 Specimen instrumentation of E* testing (AASHTO TP 62-03).

TABLE 23 E* test results of PG 76-16 mixture at 4.2% AC and 7.0% Va

Temp (°F)	Freq (Hz)	Dynamic Modulus, |E*|					Phase Angle, ϕ				
		Repl. 1 7-403 (ksi)	Repl. 2 7-403 (ksi)	Average (ksi)	Std. Dev. (ksi)	Coeff. of Var.	Repl. 1 7-403 (Deg.)	Repl. 2 7-403 (Deg.)	Average (Deg.)	Std. Dev. (Deg.)	Coeff. of Var.
14	25	4015	4089	4052	52	1.3	5.8	5.2	5.5	0.5	8.6
	10	3934	4042	3988	76	1.9	6.9	7.3	7.1	0.3	4.5
	5	3857	3931	3894	52	1.3	7.0	7.6	7.3	0.4	5.6
	1	3633	3682	3658	35	1.0	6.7	7.5	7.1	0.5	7.7
	0.5	3518	3583	3550	46	1.3	7.1	8.1	7.6	0.7	9.6
	0.1	3266	3382	3324	82	2.5	6.9	10.7	8.8	2.6	29.8
40	25	2974	3107	3041	95	3.1	8.3	8.2	8.2	0.1	0.9
	10	2853	2936	2895	59	2.0	10.7	10.1	10.4	0.4	3.6
	5	2735	2717	2726	13	0.5	11.6	11.2	11.4	0.2	2.0
	1	2412	2386	2399	18	0.8	12.7	13.4	13.1	0.5	4.1
	0.5	2282	2245	2264	26	1.2	13.2	14.2	13.7	0.7	5.4
	0.1	1941	1977	1959	26	1.3	14.2	15.6	14.9	1.0	6.7
70	25	1647	2198	1922	390	20.3	12.2	11.9	12.0	0.2	1.6
	10	1476	1953	1715	338	19.7	15.0	15.9	15.4	0.6	4.1
	5	1337	1759	1548	298	19.3	16.7	16.2	16.4	0.3	2.1
	1	1029	1305	1167	195	16.7	21.1	21.7	21.4	0.4	1.9
	0.5	913	1141	1027	161	15.7	23.1	23.9	23.5	0.6	2.6
	0.1	655	801	728	104	14.2	28.0	29.0	28.5	0.7	2.3
100	25	789	945	867	110	12.7	25.9	27.6	26.7	1.2	4.6
	10	690	736	713	33	4.6	28.0	29.4	28.7	1.0	3.6
	5	569	608	588	27	4.6	29.2	30.4	29.8	0.8	2.8
	1	355	369	362	10	2.7	32.7	33.3	33.0	0.4	1.2
	0.5	282	292	287	7	2.5	33.5	34.5	34.0	0.7	2.2
	0.1	171	161	166	7	4.4	34.0	35.3	34.6	0.9	2.6
130	25	252	283	268	22	8.2	34.3	35.2	34.8	0.6	1.8
	10	196	216	206	14	7.0	31.8	33.3	32.6	1.1	3.3
	5	160	175	168	10	6.0	30.5	31.8	31.1	0.9	3.0
	1	100	105	102	4	3.7	26.6	28.0	27.3	1.0	3.8
	0.5	81	84	82	2	2.7	24.5	25.0	24.8	0.4	1.5
	0.1	49	50	50	0	0.3	19.6	20.3	19.9	0.5	2.7

Construction of LVE Material Properties Master Curves

Asphalt concrete mixture is a viscoelastic material that is time and temperature dependent. LVE property master curves of asphalt concrete mixtures enable comparison of viscoelastic materials when tested using different loading times (frequencies) and test temperatures. This process takes advantage of the principle of time-temperature superposition. The data at various temperatures are shifted with regard to a reference temperature (generally taken as 70°F) or a loading time or frequency until the curves merge into single smooth function. In general, the master modulus curve can be mathematically modeled by a sigmoidal function described as:

$$\log|E^*| = \delta + \frac{\alpha}{1 + \dfrac{1}{e^{\beta + \gamma(\log f_r)}}} \tag{91}$$

where:

f_r	= reduced frequency of loading at reference temperature
δ	= minimum value of E*
$\delta + \alpha$	= maximum value of E*
β, γ	= parameters describing the shape of the sigmoidal function

Time-Temperature Superposition Principle and Shift Factors

Time-temperature (or frequency-temperature) superposition or the method of reduced variables is a recognized procedure applied either to determine the temperature dependency of a material or to expand the time or frequency range at a given temperature at which the material behavior is studied. Applicability of the time–temperature superposition principle is restricted to "thermorheologically simple" materials, i.e., materials in which the shift factor is identical for all relaxation times.

Construction of modulus master curve as a function of time or frequency to describe the time dependency of the material is based on the time or frequency-temperature superposition concept. The amount of shifting at each temperature required to form the master curve describes the temperature dependency of the material. The same modulus value can be obtained either at low temperatures and long times or at high temperatures and short times, thus allowing prediction of long-term behavior from short-term tests.

The shift factors a(T) used to shift the dynamic modulus values along frequency values to form a continuous master curve with respect to a reference temperature can be shown in the following form:

$$a(T) = \frac{f_r}{f} \tag{92}$$

where:

a(T)	= shift factor as a function of temperature,
f	= frequency of loading at desired temperature,
f_r	= reduced frequency of loading at reference temperature, and
T	= temperature.

While classical viscoelastic theory suggests a linear relationship between log a(T) and T in degrees Fahrenheit (Anderson et al., 1991), years of testing have shown that for precision, a second order polynomial relationship between the logarithm of the shift factor, i.e., log a(T$_i$), and the temperature in degrees Fahrenheit (T$_i$) should be used (Witczak et al., 1995). The relationship can be expressed as follows:

$$Log\ a(T) = aT_i^2 + bT_i + c \qquad (93)$$

where:

        a(T$_i$)   = shift factor as a function of temperature T$_i$

        T$_i$ = temperature of interest, °F

        a, b and c   = coefficients of the second order polynomial

Many studies have shown that the time-temperature shift factors, which are a function of the material itself, should be the same regardless of which material property they are derived from (Daniel, 2001). Shehab (2002) in his dissertation recommended deriving the shift factors from the storage modulus (E´) master curve rather than dynamic modulus (E*) master curve. The reason for this is that the former method considerers both dynamic modulus and phase angle while the last method ignores the representation of phase angle, which symbolizes an important part of the material's behavior. In this research, the calculation of shift factors is done using Shehab approach as it is considered more rational. Based on that decision, the storage modulus master curve is constructed first to have the shift factors for different temperatures, then the same shift factors are used to develop the dynamic modulus master curve as well as the phase angle master curve.

In order to accomplish the horizontal shifting and sigmoidal function fitting for the storage modulus, initial trial values for the coefficients of the shift factor polynomial relationship (a, b, c) in Equation 93 are assumed, then a least square technique is used to optimize their values by minimizing the amount of error between actual E´ values and the fitted ones using a log-sigmoidal function shown in Equation 94. This procedure can be done using the Solver function in Microsoft Excel® by optimizing both the sigmoidal function parameters (δ´, α´, β´, γ´) in Equation 94 as well as the coefficients (a, b, c) in Equation 93 so that the summation of errors in minimal and shift factor at the reference temperature (70 °F) is unity.

$$\log|E'| = \delta' + \frac{\alpha'}{1 + \dfrac{1}{e^{\beta' + \gamma'(\log f_r)}}} \qquad (94)$$

where:

        δ´   = minimum value of E´,

        δ´+α´   = maximum value of E´, and

        β´, γ´   = parameters describing the shape of E´ sigmoidal function.

FIGURE 57 shows the storage modulus values as a function of reduced frequency at various testing temperatures that are shifted around a reference temperature of 70°F to construct the storage modulus master curve. FIGURE 58 illustrates the log shift factors as a function of the test temperatures. The sigmoidal and shifting parameters for the different mixtures are tabulated in TABLES 24 to 26. In addition, the shift factors at different test temperatures for all mixtures are summarized in TABLES 27 through 29.

The phase angle master curve as well as the dynamic modulus master curve were obtained by shifting the data at different temperatures using the same shift factors. FIGURES 59 and 60 demonstrate the shifting of the phase angle and dynamic modulus values respectively to construct the master curves. The shifted phase angle data then can be fitted using any appropriate function like sigmoidal, normal distribution, or beta distribution functions (Biligiri et. al, 2010).

It can be observed that the phase angle increases with decreasing reduced frequency (increase of temperature or decrease of loading frequency) until a certain point where it starts to decrease. This behavior can be explained by the fact that at low temperature and high loading frequency, the asphalt binder dominates the behavior of asphalt mixtures and the mixture is more elastic so the phase angle is low. By increasing the temperature or decreasing the loading frequency, the asphalt mixture becomes more viscous as the binder becomes softer so the phase angle increases. With the increase of temperature or decrease of frequency, the asphalt binder becomes very soft and the aggregate dominates the behavior of asphalt mixture. As the aggregates and the asphalt mixture exhibit more elastic behavior again, the phase angle will decrease again as the reduced frequency decreases. This is a typical behavior for conventional asphalt mixtures but it may not be the case for modified asphalt mixtures.
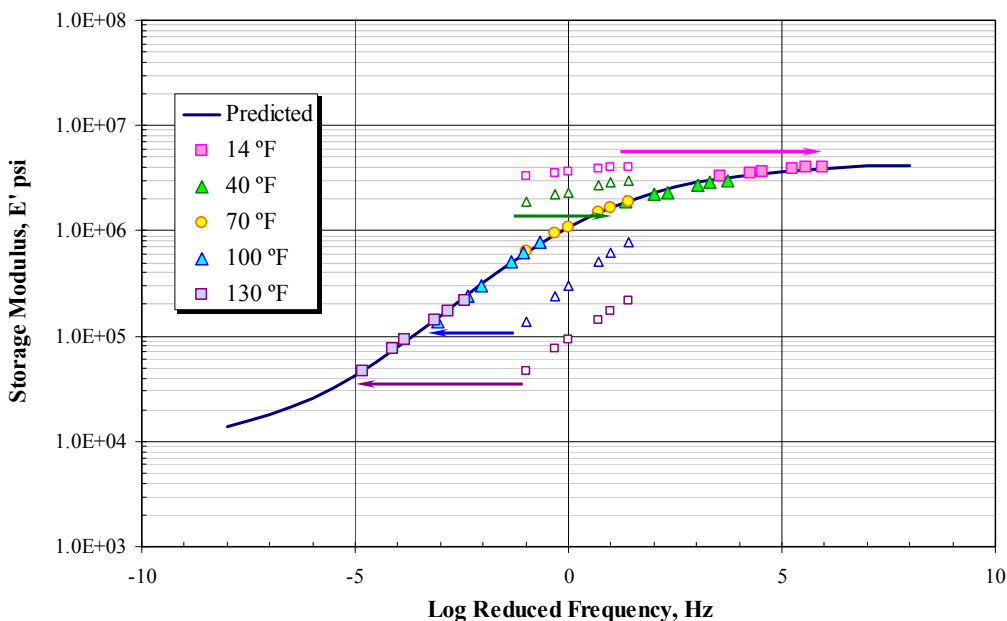
FIGURE 57 Construction of storage modulus master curve.
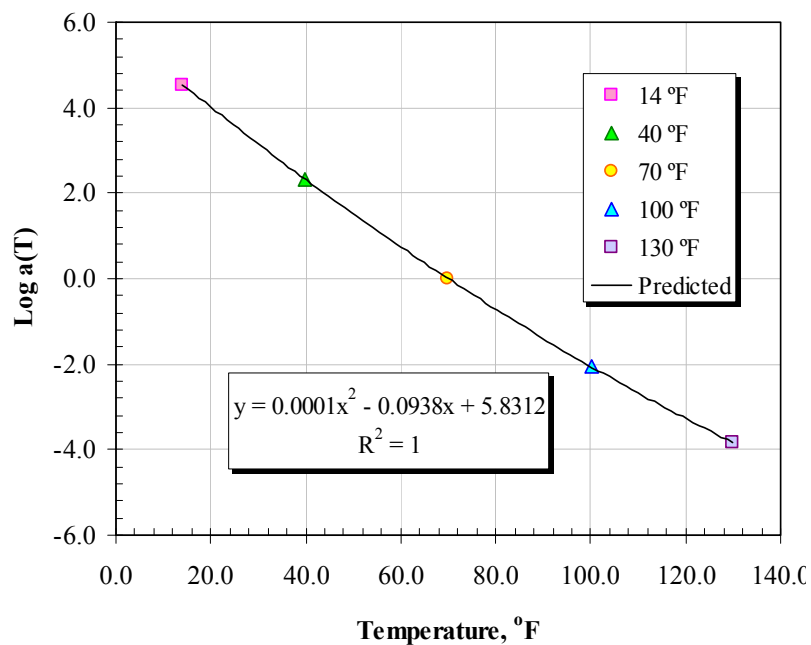
FIGURE 58 Log shift factor as a function of temperature obtained by the construction of storage modulus master curve.
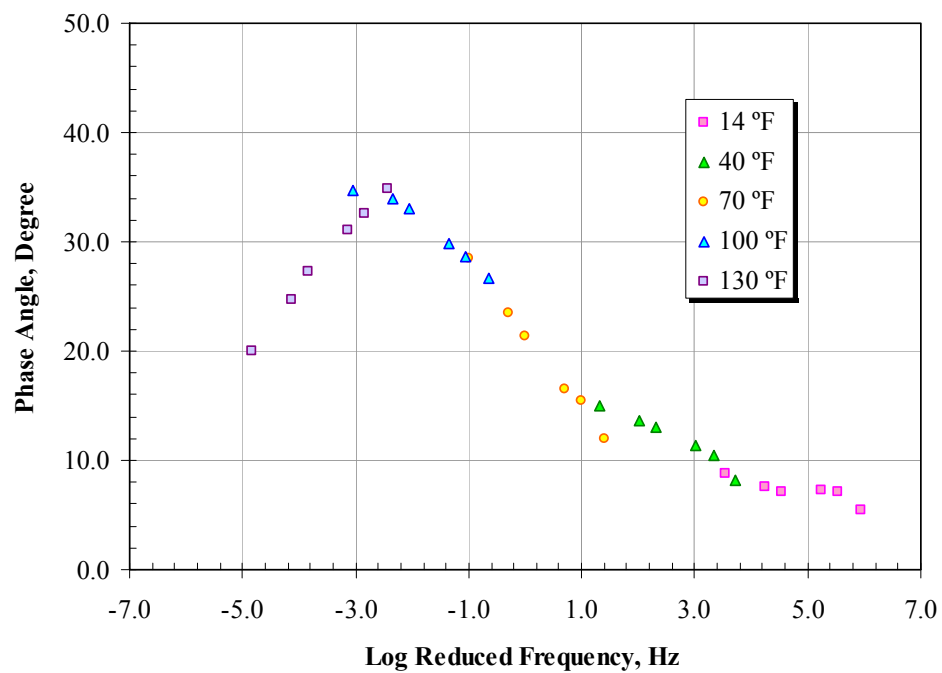
FIGURE 59 Phase angle master curve using the same shift factors obtained from storage modulus master curve.

108
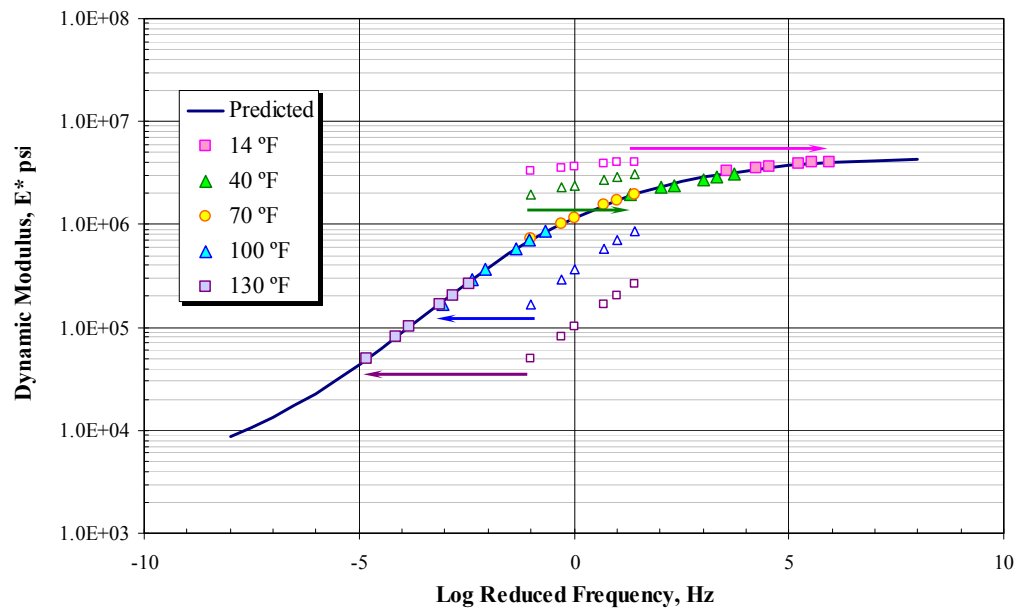
FIGURE 60 Dynamic modulus master curve using the same shift factors obtained from storage modulus master curve.

TABLE 24 E* Sigmoidal and shifting parameters of PG 64-22 mixtures

Binder Content	Parameter	Air Voids		
		4.0 % Va	7.0 % Va	10.0% Va
4.0% AC	δ	3.8670	3.1049	2.9736
	α	2.8194	3.4173	3.5837
	β	1.3622	1.5286	1.0946
	γ	0.4778	0.3758	0.3315
	a	0.000255	0.000435	0.000205
	b	-0.1218	-0.1564	-0.1018
	c	7.2745	8.8141	6.1178
4.5% AC	δ	3.9641	3.4270	2.5035
	α	2.7773	3.1963	4.0883
	β	1.1104	1.1199	1.0443
	γ	0.4531	0.3934	0.2759
	a	0.000033	0.000256	0.000264
	b	-0.0804	-0.1133	-0.1115
	c	5.4608	6.6776	6.5132
5.0% AC	δ	3.5145	3.4975	3.6367
	α	3.1038	3.0937	2.6642
	β	1.3412	1.0357	1.1614
	γ	0.3989	0.3914	0.4650
	a	0.000190	0.000236	0.000238
	b	-0.1064	-0.1078	-0.1112
	c	6.5151	6.3929	6.6135

TABLE 25 E* Sigmoidal and shifting parameters of PG 58-28 mixtures

Binder Content	Parameter	Air Voids		
		4.5 % Va	7.0% Va	9.5% Va
4.2% AC	δ	3.9136	3.9742	3.4565
	α	2.6523	2.4793	3.0600
	β	1.0610	0.9246	0.8641
	γ	0.4705	0.5315	0.3912
	a	0.000268	0.000306	0.000224
	b	-0.1167	-0.1203	-0.1064
	c	6.8500	6.9189	6.3464
4.7% AC	δ	3.6716	3.5602	3.6349
	α	2.9068	3.0335	2.7437
	β	1.0578	0.7921	0.8259
	γ	0.4539	0.4006	0.4496
	a	0.000206	0.000238	0.000205
	b	-0.1012	-0.1046	-0.0975
	c	6.0711	6.1512	5.8209
5.2% AC	δ	3.9508	3.2547	3.5436
	α	2.6120	3.3257	2.8190
	β	0.7883	0.7315	0.6583
	γ	0.5047	0.3336	0.4216
	a	0.000237	0.000293	0.000221
	b	-0.1050	-0.1136	-0.1012
	c	6.1923	6.5092	5.9990

TABLE 26 E* Sigmoidal and shifting parameters of PG 76-16 mixtures

Binder Content	Parameter	Air Voids		
		4.5 % Va	7.0% Va	9.5% Va
4.2% AC	δ	3.8027	3.4867	3.6750
	α	2.9418	3.1785	2.8923
	β	1.2590	1.4572	1.3382
	γ	0.4184	0.4048	0.4404
	a	0.000185	0.000150	0.000285
	b	-0.1002	-0.0938	-0.1213
	c	6.1028	5.8312	7.0942
4.7% AC	δ	3.5381	3.7658	3.6179
	α	3.2352	2.8811	2.9303
	β	1.4347	1.3604	1.3374
	γ	0.3751	0.4282	0.4185
	a	0.000167	0.000142	0.000311
	b	-0.0963	-0.0934	-0.1257
	c	5.9214	5.8447	7.2708
5.2% AC	δ	3.7149	3.9177	3.2502
	α	2.9737	2.6827	3.2307
	β	1.3025	1.1970	1.2411
	γ	0.3911	0.4683	0.3634
	a	0.000311	0.000086	0.000239
	b	-0.1314	-0.0806	-0.1100
	c	7.6733	5.2246	6.5267

TABLE 27 Temperature shift factors of PG 64-22 mixtures

Binder Content	Temperature (°F)	Temperature Shift Factor		
		4.0 % Va	7.0 % Va	10.0% Va
4.0% AC	14	5.619	6.710	4.733
	40	2.819	3.264	2.382
	70	0.000	0.000	0.000
	100	-2.358	-2.479	-2.012
	130	-4.245	-4.164	-3.645
4.5% AC	14	4.342	5.141	5.004
	40	2.306	2.561	2.482
	70	0.000	0.000	0.000
	100	-2.245	-2.099	-2.005
	130	-4.417	-3.727	-3.526
5.0% AC	14	5.063	4.929	5.104
	40	2.571	2.463	2.555
	70	0.000	0.000	0.000
	100	-2.228	-2.037	-2.124
	130	-4.103	-3.641	-3.809

TABLE 28 Temperature shift factors of PG 58-28 mixtures

Binder Content	Temperature (°F)	Temperature Shift Factor		
		4.5 % Va	7.0 % Va	9.5% Va
4.2% AC	14	5.269	5.295	4.901
	40	2.620	2.605	2.457
	70	0.000	0.000	0.000
	100	-2.135	-2.053	-2.051
	130	-3.777	-3.545	-3.688
4.7% AC	14	4.695	4.734	4.496
	40	2.361	2.356	2.255
	70	0.000	0.000	0.000
	100	-1.988	-1.926	-1.885
	130	-3.595	-3.414	-3.392
5.2% AC	14	4.768	4.977	4.626
	40	2.376	2.444	2.312
	70	0.000	0.000	0.000
	100	-1.949	-1.913	-1.913
	130	-3.462	-3.290	-3.418

TABLE 29 Temperature shift factors of PG 76-16 mixtures

Binder Content	Temperature (°F)	Temperature Shift Factor		
		4.5 % Va	7.0 % Va	9.5% Va
4.2% AC	14	4.737	4.547	5.451
	40	2.399	2.325	2.705
	70	0.000	0.000	0.000
	100	-2.065	-2.054	-2.190
	130	-3.787	-3.828	-3.856
4.7% AC	14	4.606	4.564	5.572
	40	2.343	2.341	2.750
	70	0.000	0.000	0.000
	100	-2.041	-2.085	-2.187
	130	-3.770	-3.904	-3.805
5.2% AC	14	5.895	4.112	5.034
	40	2.923	2.141	2.517
	70	0.000	0.000	0.000
	100	-2.362	-1.987	-2.085
	130	-4.153	-3.808	-3.729

Effect of Air Voids and Asphalt Content on E* Master Curve

As mentioned previously, E* tests were conducted on three different asphalt mixtures. Each mixture has nine different combinations of asphalt content and air voids. Two test replicates were prepared for each asphalt mixture. The effects of air voids on the dynamic modulus master curves at various binder contents are presented in FIGURES 61 through 69. It was noticed that the dynamic modulus master curves are shifted from each other in a general pattern, where the higher the air voids, the lower the dynamic modulus master curve. This is rational, as the asphalt mixture becomes weaker at high air voids because of the poor interlock of the aggregate skeleton as well as lower cohesion strength. In general, the Witczak predictive model shows the same trend in |E*| versus air voids. However, this linearity is only prevalent at air voids above 4-5%. Below this value a higher non-linearity trend is observed (Jeong, 2010).

Similarly, the effects of the asphalt content on the dynamic modulus master curves at each air voids level was studied as shown in FIGURES 70 through 78. It was observed that the effect of the asphalt content (within the narrow range of optimum±0.5%) on the dynamic modulus master curves is smaller compared to the effect of the air voids range (± 2.5 or ± 3.0). It was also noticed that there is no general pattern regarding the effect of the asphalt content on the dynamic modulus master curves. However, it can be observed that the effect of the binder on the dynamic modulus master curve follows a certain behavior for each binder type. For the PG 64-22 mixtures, the dynamic modulus master curves, at different binder contents and the same air voids, are overlapped with no specific trend (FIGURES 70 to 72). In case of PG 58-28 mixtures, the master curves with lower asphalt contents exhibit higher dynamic modulus values compared

114

to those at higher asphalt contents as shown in FIGURES 73 to 75. For the PG 76-16 mixtures, the master curves at optimum asphalt content (OAC) show higher dynamic moduli compared to the ones with optimum±0.5% (FIGURES 76 to 78). For both PG 58-28 and PG 76-16 mixtures, the effect of the binder content in shifting the dynamic modulus master curves from each other is high for the higher air voids levels. For the PG 64-22 mixtures, the effect of the air voids values on the dynamic modulus master curves is minimal at higher temperatures and compared to lower and intermediate temperatures. The reason for this is that, at higher temperatures, the aggregate dominates the behavior of the asphalt mixtures; therefore, there role for the asphalt content diminishes. Whereas at lower temperatures, the binder dominates the elastic behavior of the asphalt mixtures, and consequently it has a higher impact on the dynamic modulus of asphalt concrete mixtures.

FIGURES 79 through 81 show the effects of the asphalt content–air voids combinations for the different mixture groups: PG 64-22, PG 58-28, and PG 76-16, respectively. It is clear that the combination with lower asphalt content and air voids showed the highest modulus values whereas increasing the asphalt content and air voids decreases the dynamic modulus.
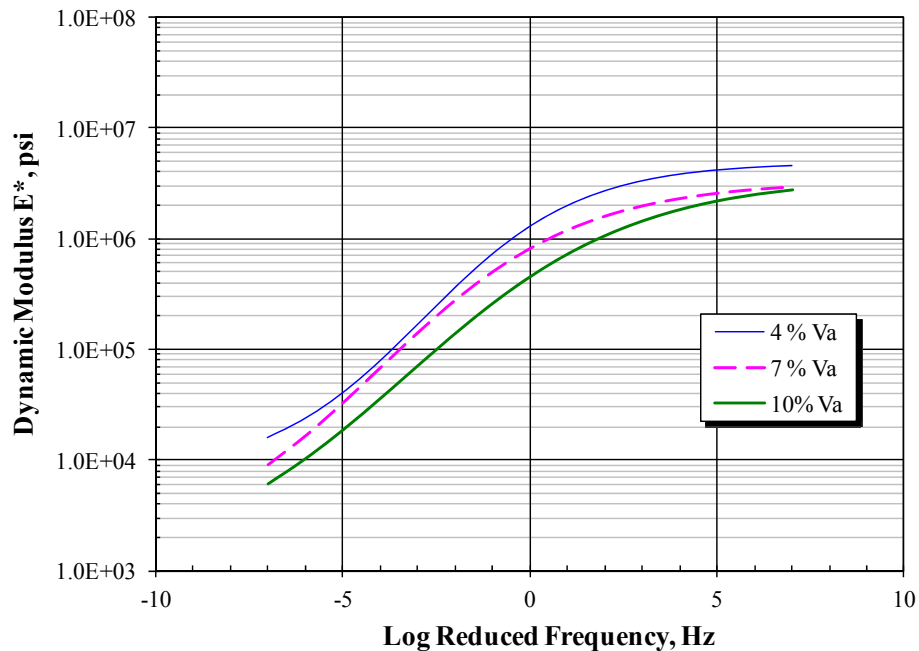
FIGURE 61 Effect of air voids on dynamic modulus master curves of PG 64-22 mixture at 4.0% AC.
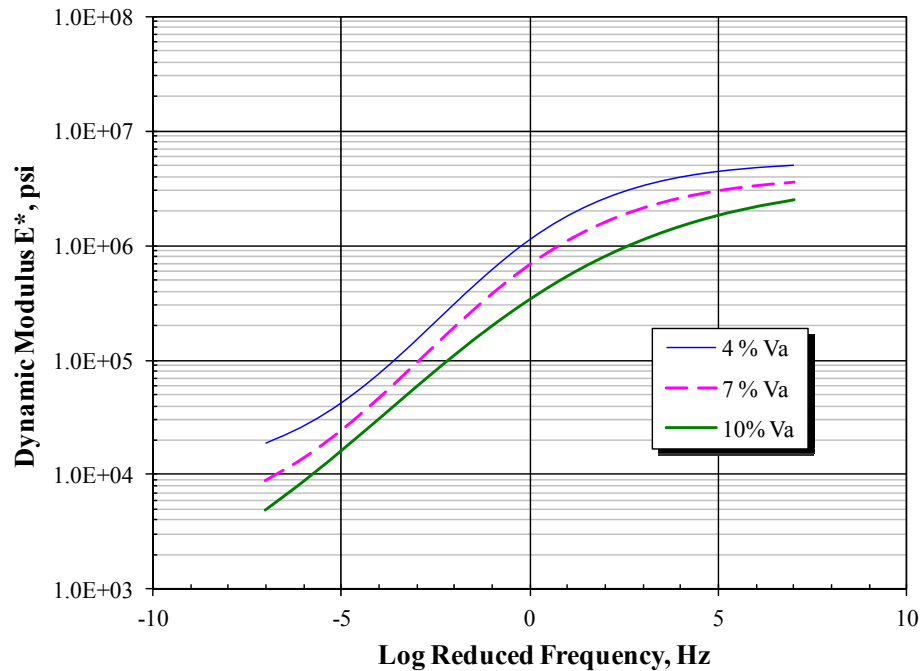
FIGURE 62 Effect of air voids on dynamic modulus master curves of PG 64-22 mixture at 4.5% AC.
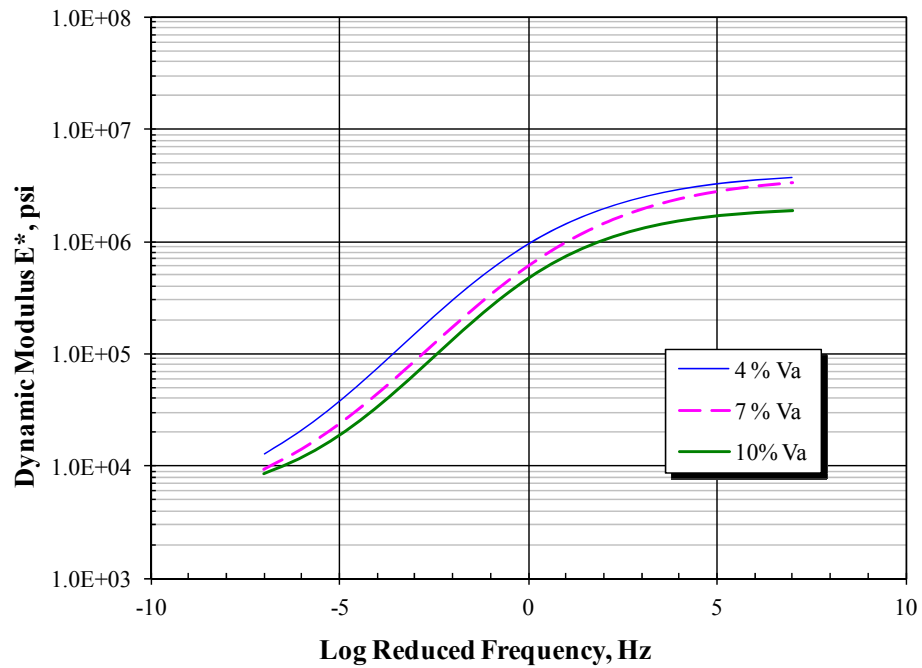
FIGURE 63 Effect of air voids on dynamic modulus master curves of PG 64-22 mixture at 5.0% AC.
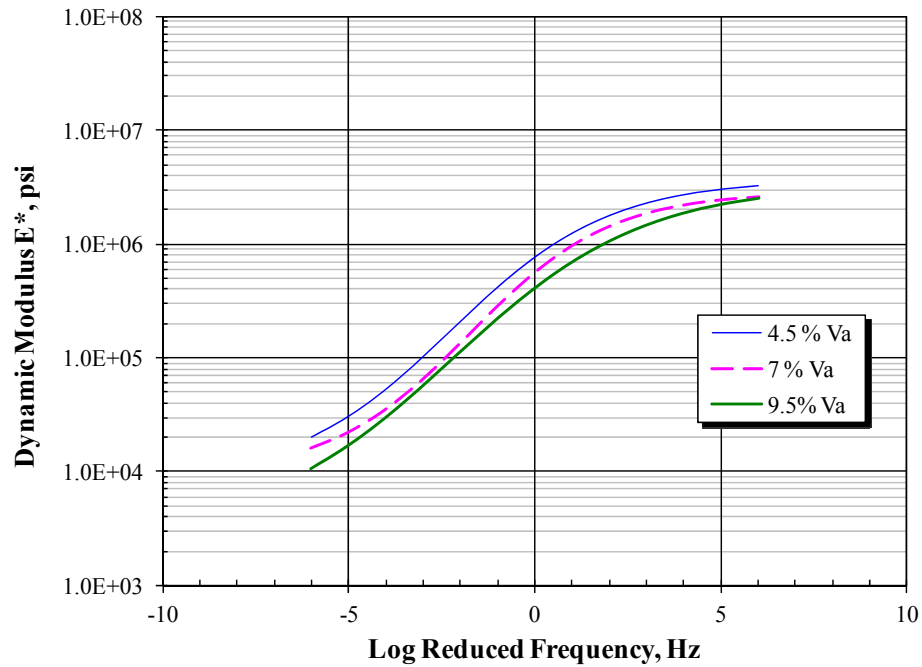
FIGURE 64 Effect of air voids on dynamic modulus master curves of PG 58-28 mixture at 4.2% AC.
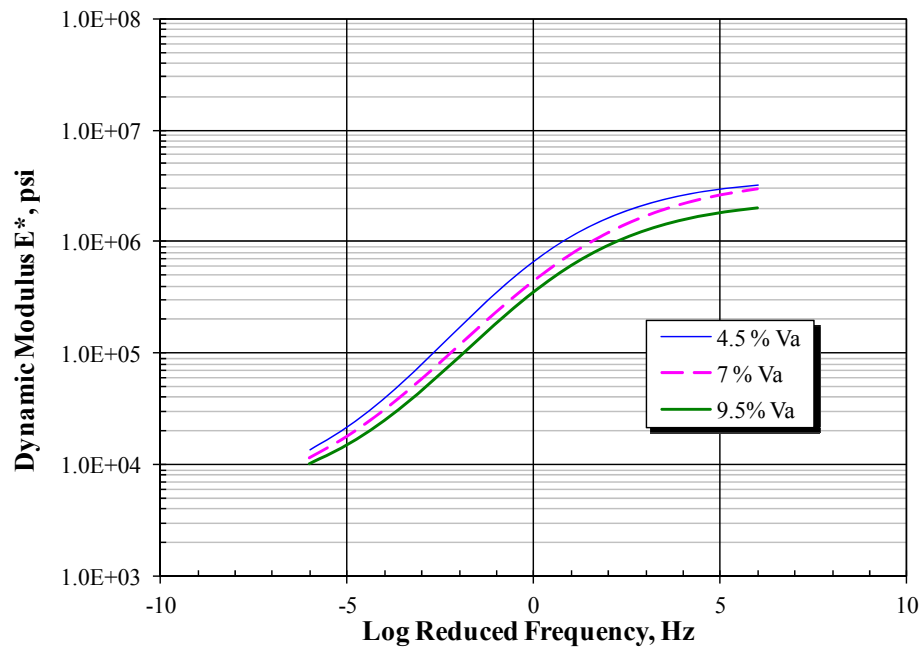
FIGURE 65 Effect of air voids on dynamic modulus master curves of PG 58-28 mixture at 4.7% AC.
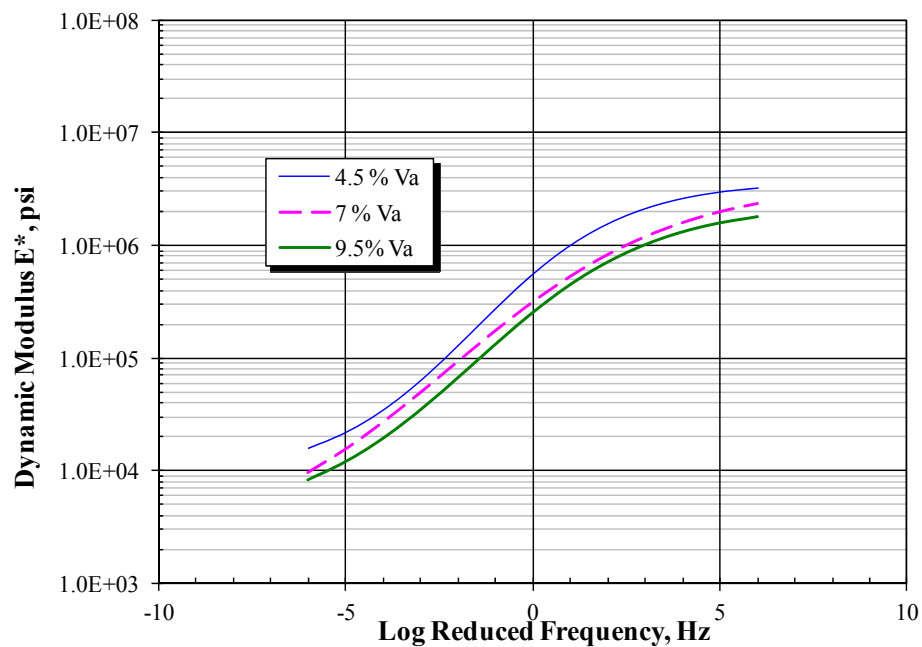
FIGURE 66 Effect of air voids on dynamic modulus master curves of PG 58-28 mixture at 5.2% AC.
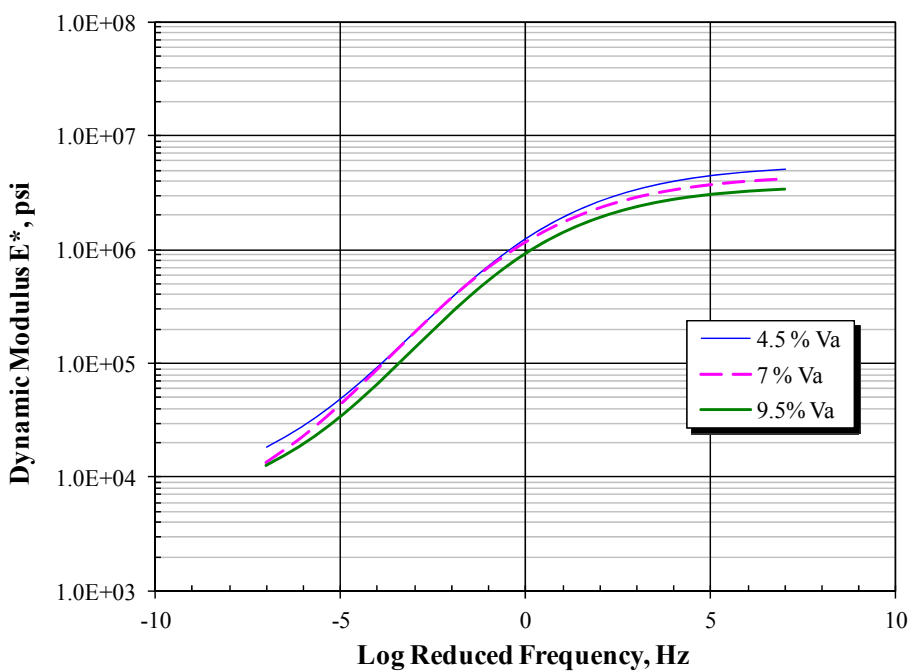
FIGURE 67 Effect of air voids on dynamic modulus master curves of PG 76-16 mixture at 4.2% AC.
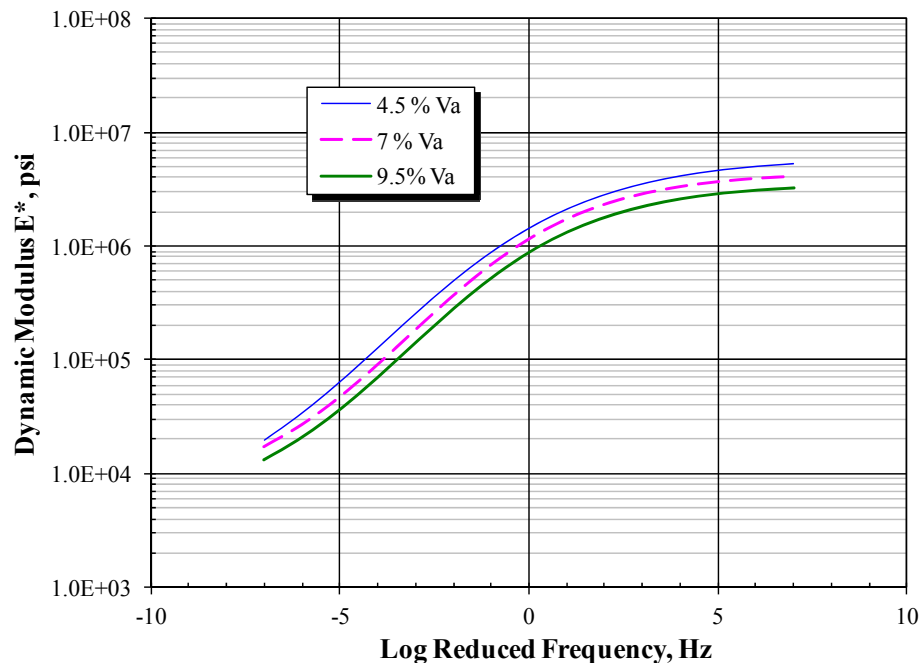
FIGURE 68 Effect of air voids on dynamic modulus master curves of PG 76-16 mixture at 4.7% AC.
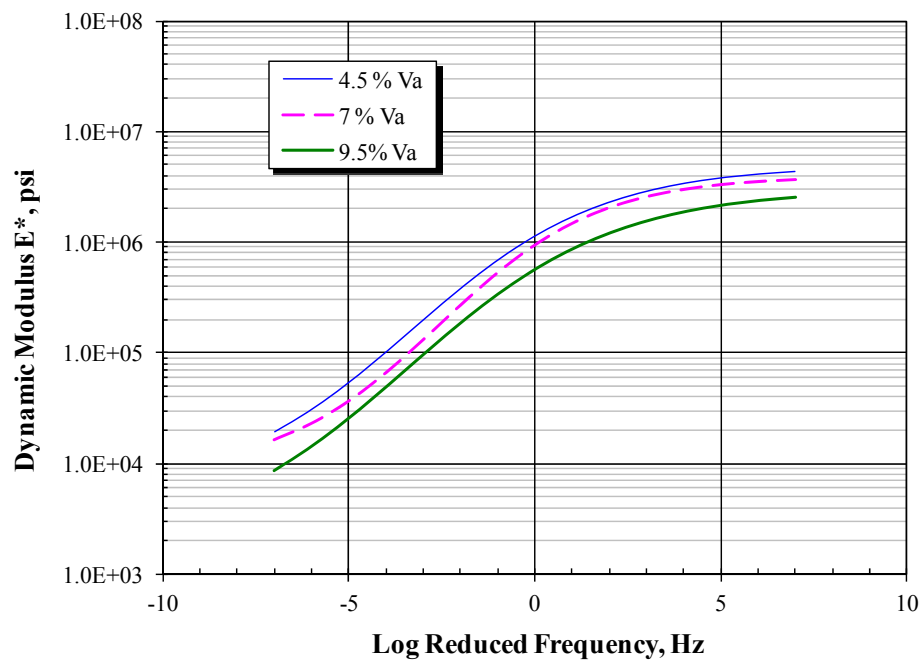
FIGURE 69 Effect of air voids on dynamic modulus master curves of PG 76-16 mixture at 5.2% AC.
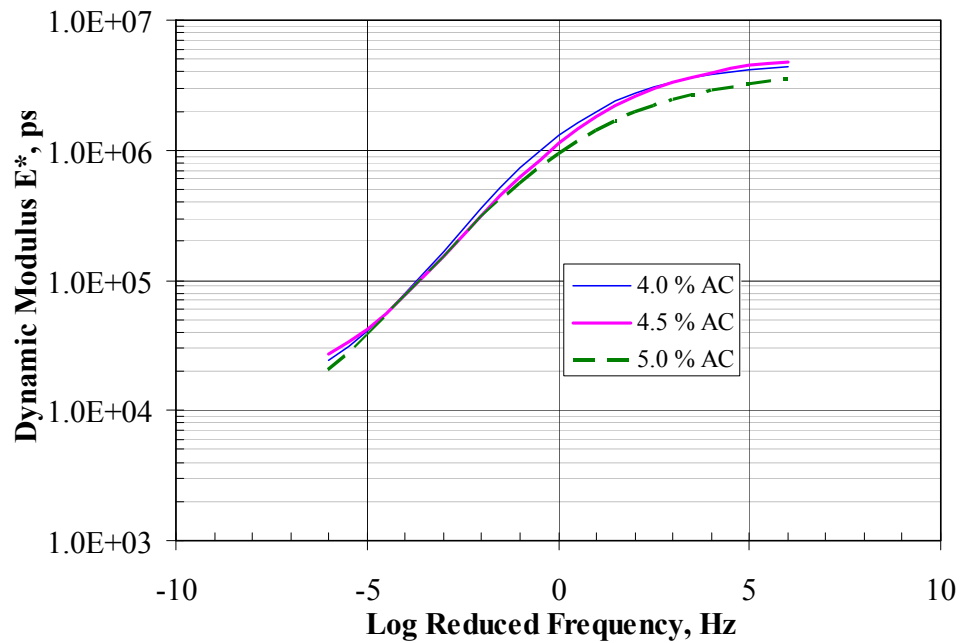
FIGURE 70 Effect of asphalt content on dynamic modulus master curves of PG 64-22 mixture at 4.0 % Va.
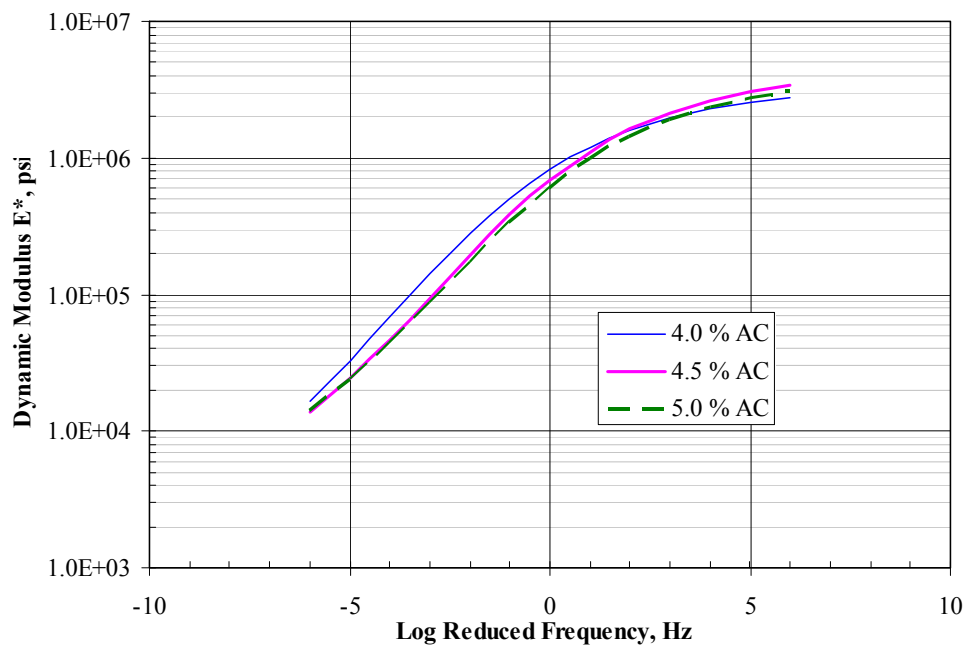
FIGURE 71 Effect of asphalt content on dynamic modulus master curves of PG 64-22 mixture at 7.0 % Va.

120
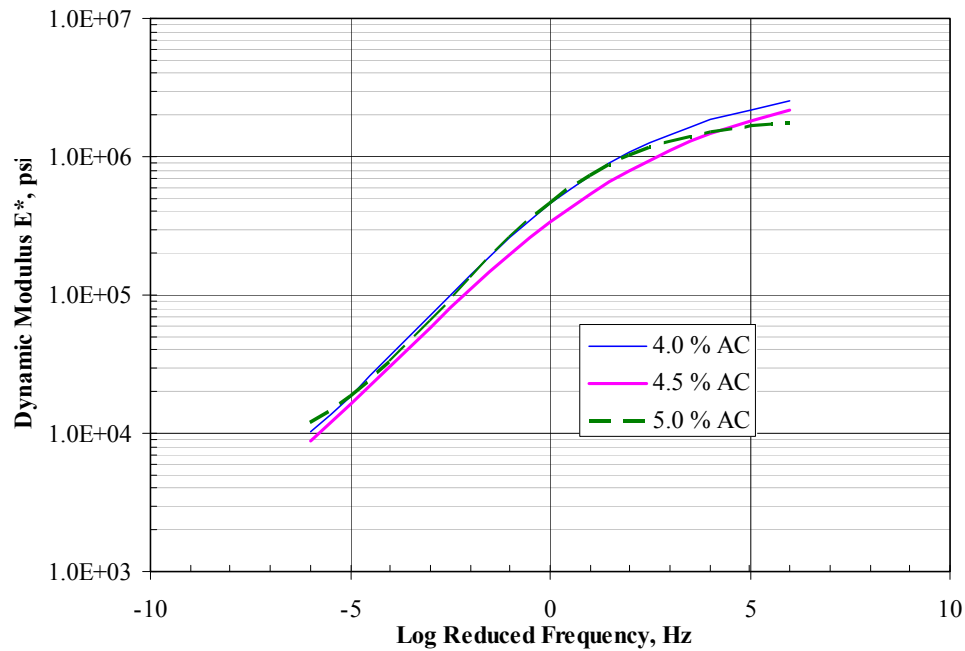
FIGURE 72 Effect of asphalt content on dynamic modulus master curves of PG 64-22 mixture at 10.0 % Va.
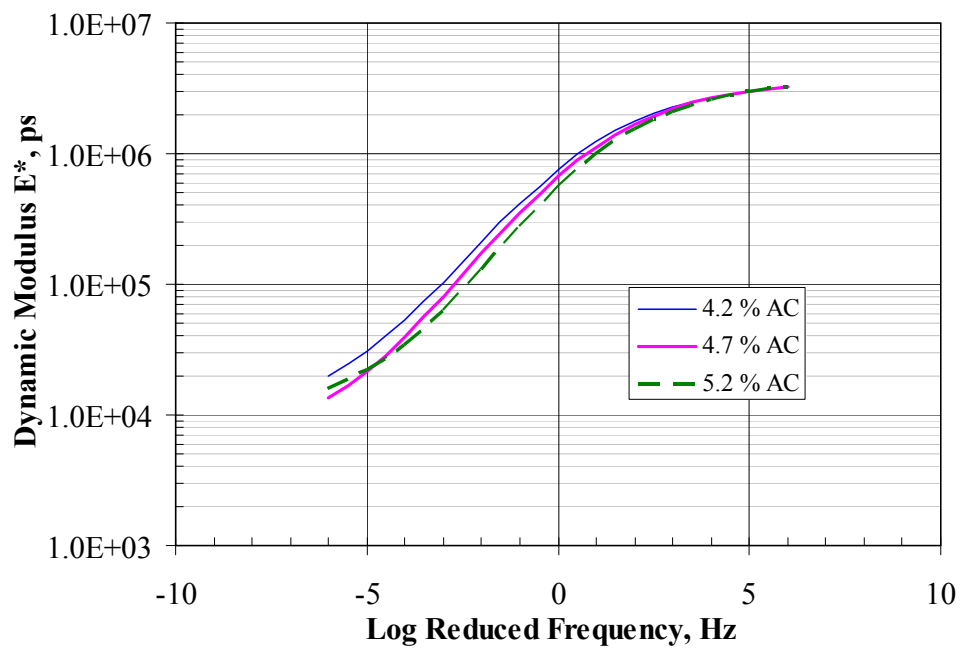
FIGURE 73 Effect of asphalt content on dynamic modulus master curves of PG 58-28 mixture at 4.5 % Va.
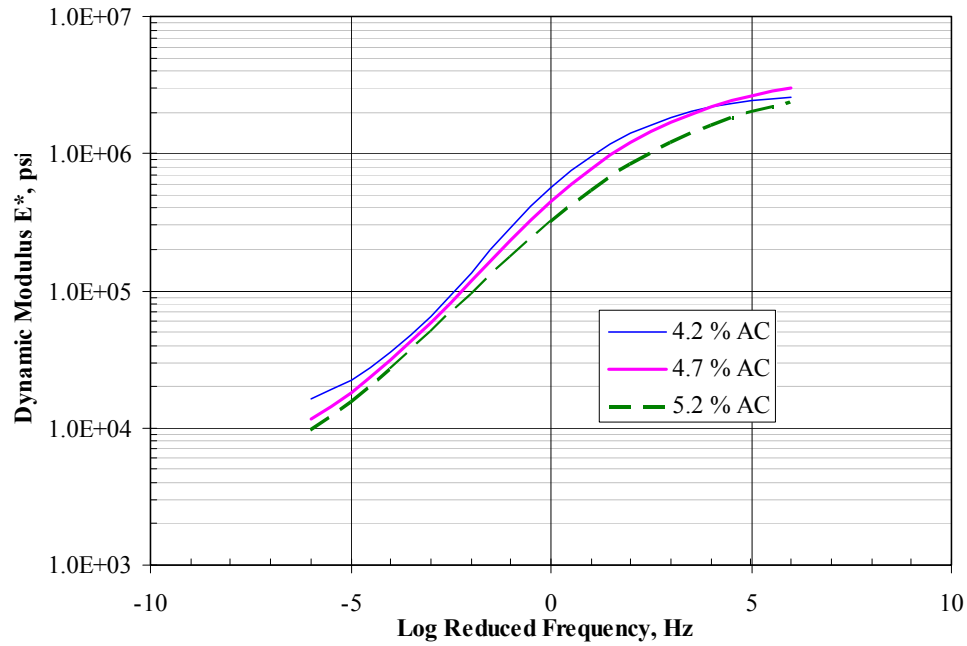
FIGURE 74 Effect of asphalt content on dynamic modulus master curves of PG 58-28 mixture at 7.0 % Va.
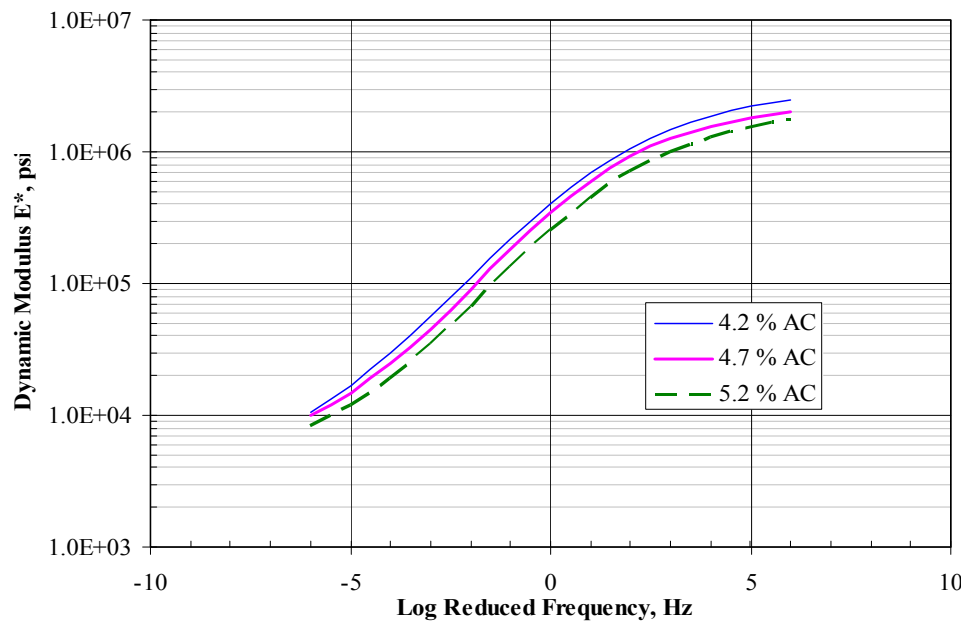
FIGURE 75 Effect of asphalt content on dynamic modulus master curves of PG 58-28 mixture at 9.5 % Va.
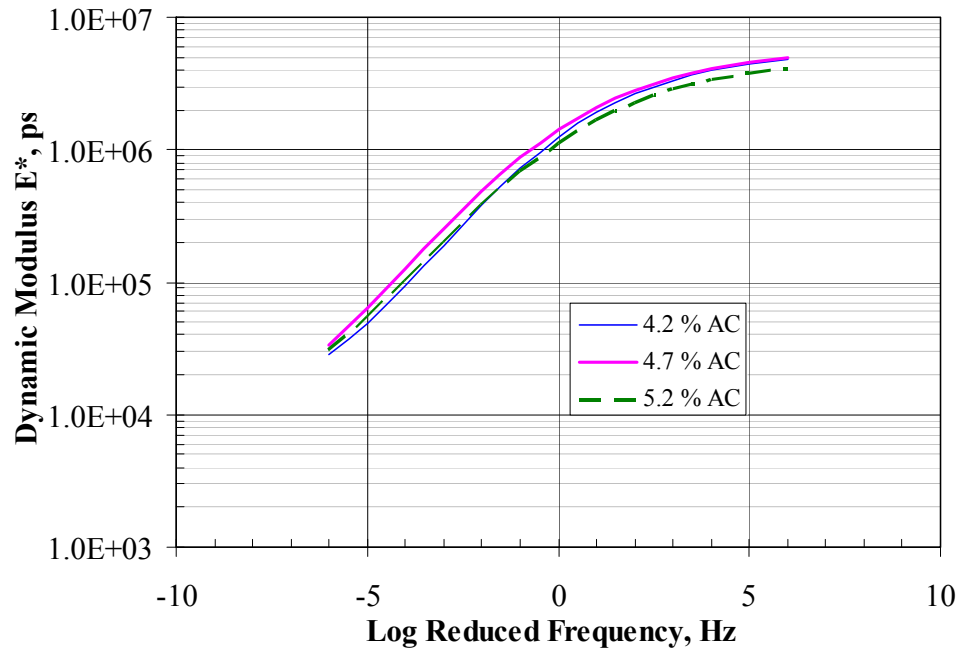
FIGURE 76 Effect of asphalt content on dynamic modulus master curves of PG 76-16 mixture at 4.5 % Va.
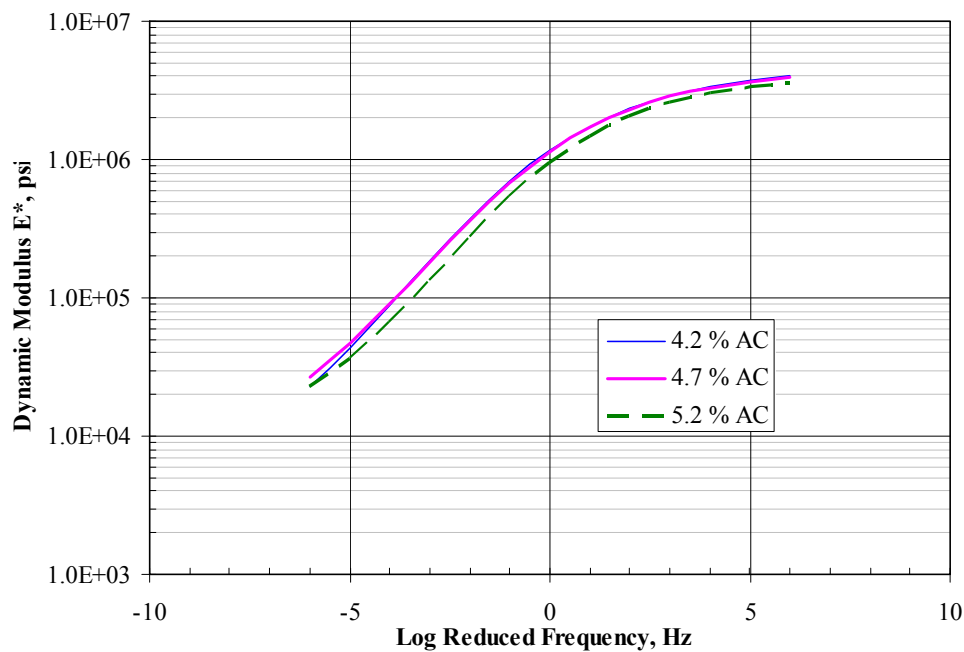
FIGURE 77 Effect of asphalt content on dynamic modulus master curves of PG 76-16 mixture at 7.0 % Va.
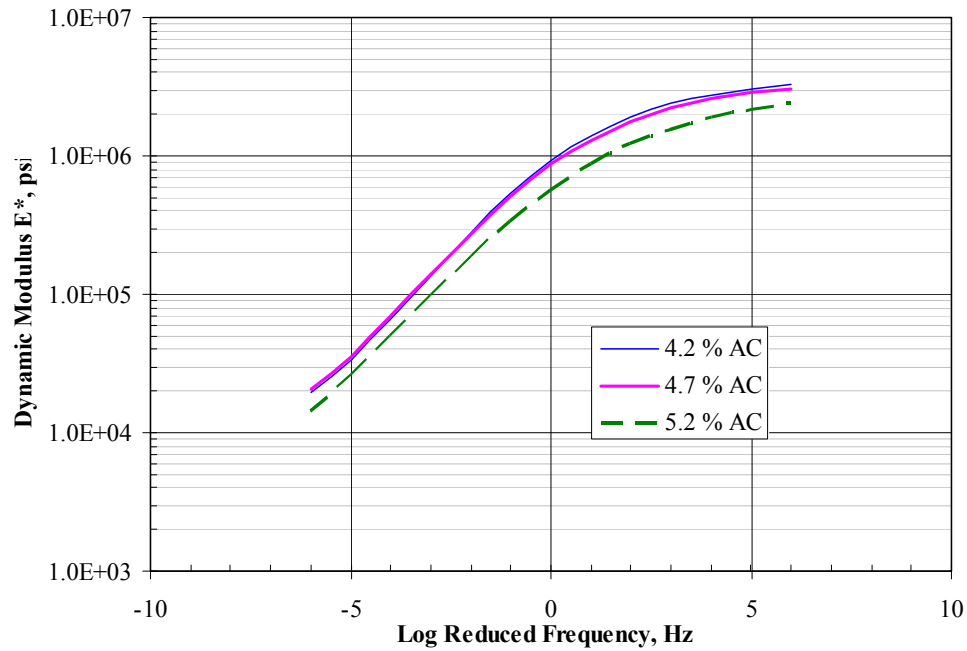
FIGURE 78 Effect of asphalt content on dynamic modulus master curves of PG 76-16 mixture at 9.5 % Va.
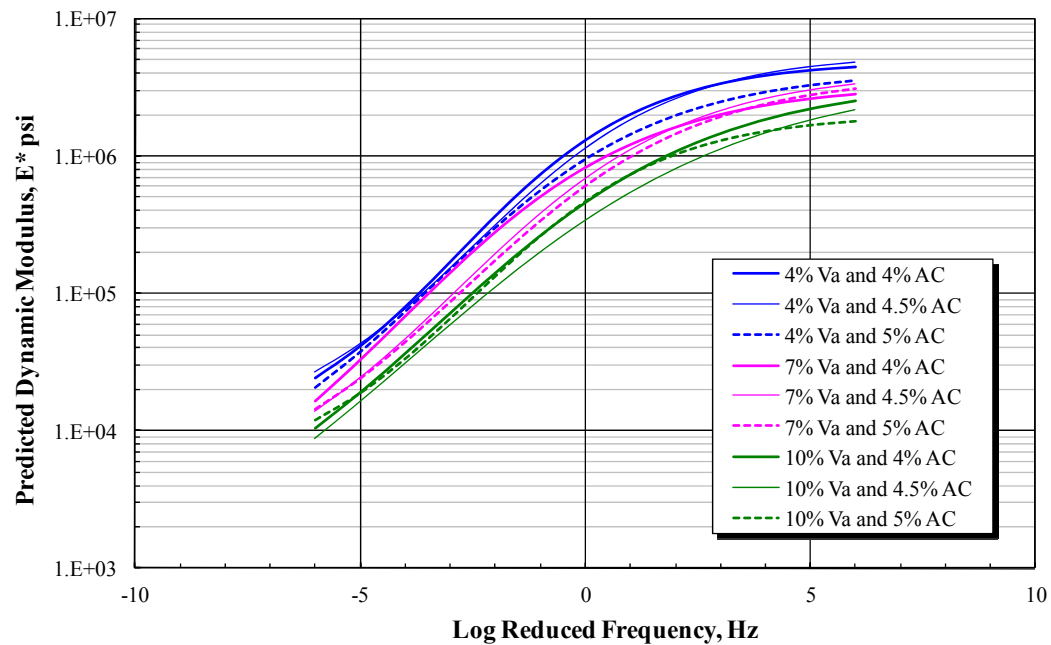
FIGURE 79 Effect of asphalt content and air voids on on dynamic modulus master curves of PG 64-22 mixture.
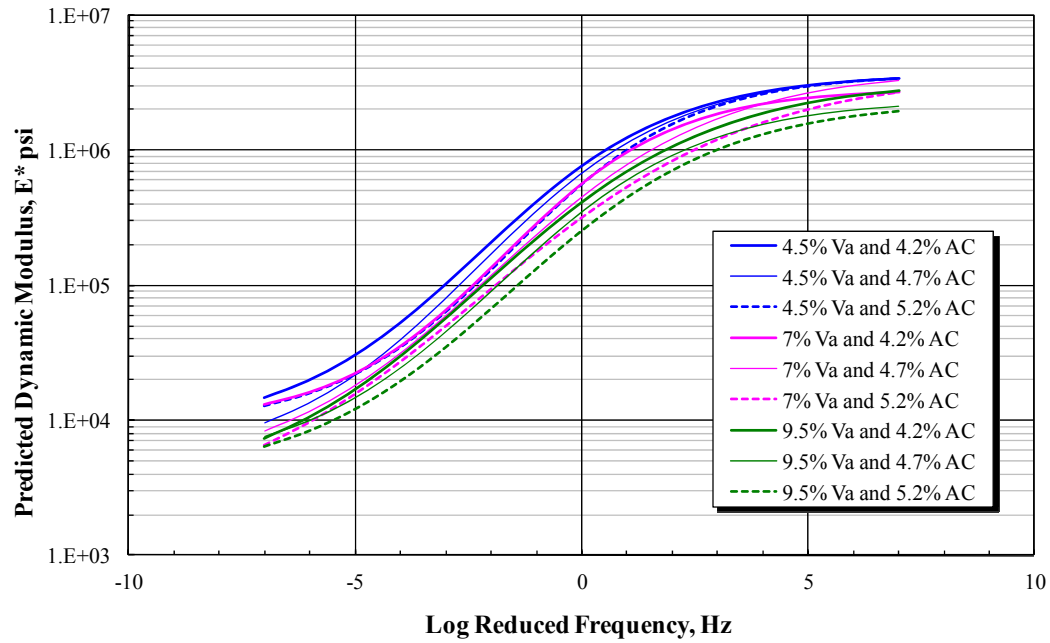
FIGURE 80 Effect of asphalt content and air voids on dynamic modulus master curves of PG 58-28 mixture.
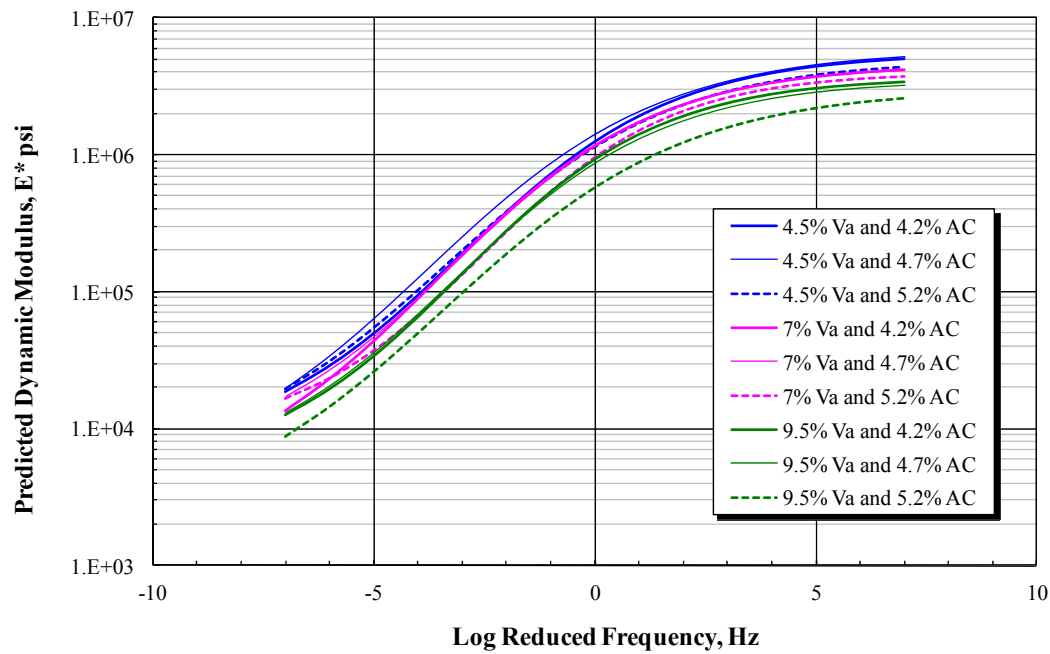
FIGURE 81 Effect of asphalt content and air voids on dynamic modulus master curves of PG 76-16 mixture.

Proposed Approach to Predict the Effect of Air Voids and Asphalt Content on E* Master Curves

As shown earlier, the E* master curves were shifted or moved due the effect of the air voids and the asphalt content. This section includes the proposed approach to predict the shifting of the entire master curve due to changes in air voids, asphalt content, or both. These shifts were mainly dependent on the magnitude of the change of the volumetric parameter (asphalt content or air voids). In addition, the direction of the master curve change or shift depends on the decrease or increase of the volumetric property compared to that at a reference value.

The sigmoidal function used to fit the E* master curve is composed of four main parameters. Two of these parameters are used to determine the maximum and the minimum (δ and α) values of the master curve. The other two parameters (β and γ) are used to describe the shape of the sigmoidal function. The approach developed here applies regression analysis to correlate the sigmoidal parameters obtained from the master curves to the values of air voids and asphalt content. Once the regression models are well established, the sigmoidal parameters can be predicted at any level of air voids and asphalt content, which are then used to generate the |E*| master curve.

For each group of mixtures, the regression models for each sigmoidal parameter were fitted using the Minitab statistical software assuming two levels of interaction. The variables were chosen by best subsets regression. The values of the adjusted R-square, Mallows's Cp, and S-curve model were used in determining the final model. The adequacy of the final model was checked through the normal probability and residual plots.

There was good correlation between the volumetric factors and the maximum log |E*| values ($\mu = \sigma + \delta$) compared to σ or δ alone. Therefore, the regression model for parameter μ was established first. The best regression model of either σ or δ was then considered, while the value of the remaining sigmoidal parameter (σ or δ) was obtained by subtracting the other two parameters. For each group of mixtures, regression models for the four sigmoidal parameters were obtained as summarized in TABLE 30.

TABLE 30 Regression models of the segmoidal paramaeters for the three groups of mixtures

Binder Type	Parameter	Regression Model
PG 64-22	δ	μ - α
	α	-2.32 + (1.08*AC) + (0.994*Va) - (0.201*AC*Va)
	μ =δ+α	-1.56 + (3.79*AC) - (0.00756*AC*Va) - (0.425*AC^2)
	β	15 - (6*AC) + (0.65*AC^2) - (0.00208*Va^2)
	γ	1.51 - (0.224*AC) - (0.174*Va) + (0.0354*AC*Va)
PG 58-28	δ	4.12 – (0.0139*AC*Va)
	α	μ - δ
	μ =δ+α	6.62 - (0.00224*AC*Va) - (0.000008*e^{AV})
	β	2.08 - (0.171*Va) - (0.024*AC^2) + (0.00957*Va^2)
	γ	0.528 - (0.00268*AC*Va)
PG 76-16	δ	μ - α
	α	3.9 - (0.275*AV) + (0.0192*Va^2)
	μ =δ+α	4.18 + (1.18*AC) - (0.00863*AC*Va) - (0.127*AC^2)
	β	-5.03 + (2.84*AC) - (0.313*AC^2) – (0.000407*Va^2)
	γ	0.16 + (0.0756*Va) - (0.00522*Va^2)

Proposed Approach Validation

To validate the proposed approach, regression models for random combinations of factors were used to predict the sigmoidal parameters. The constructed |E*| master curve and the curve predicted based on the regression models were compared. FIGURE 82 shows an example comparing the original and predicted dynamic modulus master curves at the same binder content and air voids levels. It can be observed that both the original and predicted master curves are almost identical.

FIGURE 83 presents an example of the sensitivity analysis using the sigmoidal parameters regression models of the PG 64-22 mixtures. The analysis was conducted by changing the air voids level (4, 6, 8, 10, and 12%) while keeping the asphalt content constant (5.0%). It can be seen that the prediction of the dynamic modulus master curves using the regression models is rational, where the dynamic modulus master curves exhibit higher values at lower air voids levels. It can be also observed that the pattern of these master curves coincide with the pattern obtained from the actual data.

To further examine the prediction accuracy of the models, the regression models of the sigmoidal parameters for the PG 64-22 mixtures were used to predict the master curves at the same nine combinations of binder content and air voids level as shown in FIGURE 84. Again, the dynamic modulus master curves show a trend similar to that obtained from the actual data analysis presented in FIGURE 79. FIGURE 85 shows a comparison of the dynamic modulus

values obtained from the nine original master curves and the shifted master curves for the PG 64-22 mixtures. It is quite noticeable that all the plotted data are almost at the equality line for the three mixture combinations. This is also supported by the excellent statistical measures of accuracy term (S_e/S_y.) shown in the figures. FIGURES 86 to 91 show the same analysis for the other two mixtures groups, which also confirms the same findings explained earlier for the PG 64-22 mixtures.

As the dynamic modulus is a very important input and is required for the analysis in the MEPDG, the previous approach can be applied to many possible scenarios. One possible application of this approach is in quality assurance analysis, where the dynamic modulus master curves can be predicted based on changes in volumetric variables such as asphalt content or air voids. This only requires testing certain mixtures that represent a combination of these volumetric variables to be able to predict the sigmoidal parameters. Then the master curves can be predicted at any volumetric combination, which would consequently save a considerable amount of E* testing.
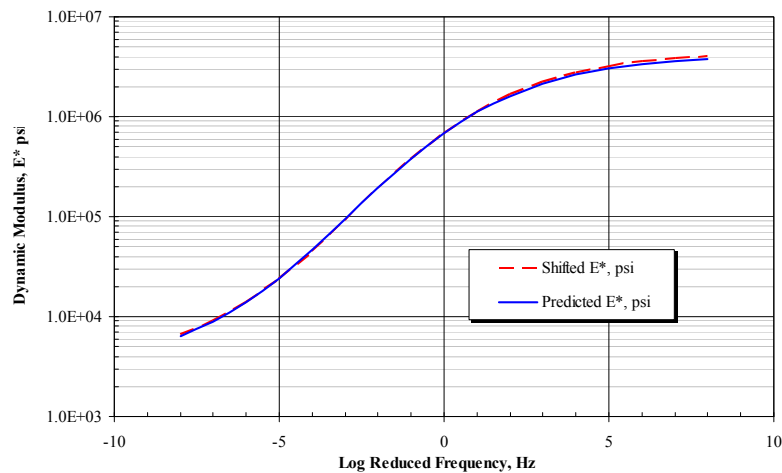
FIGURE 82 An example shows the comparison between the predicted and shifted |E*| master curve (PG 64-22, 7.0% Va and 4.0% AC).
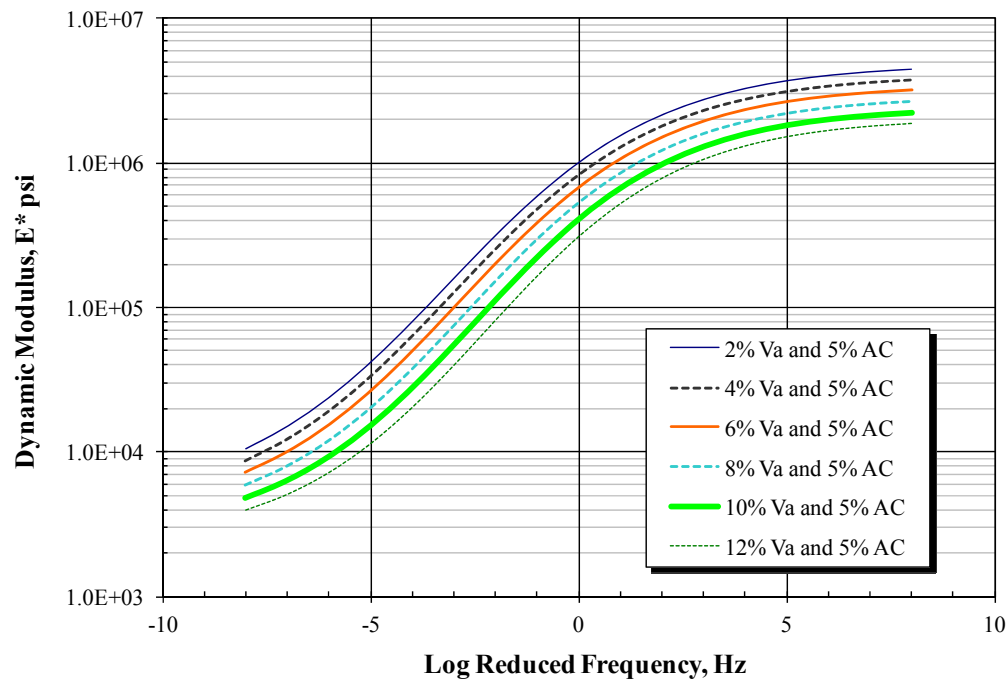
FIGURE 83 Effect of different air voids levels on shifted |E*| master curves of PG 64-22 mixture.
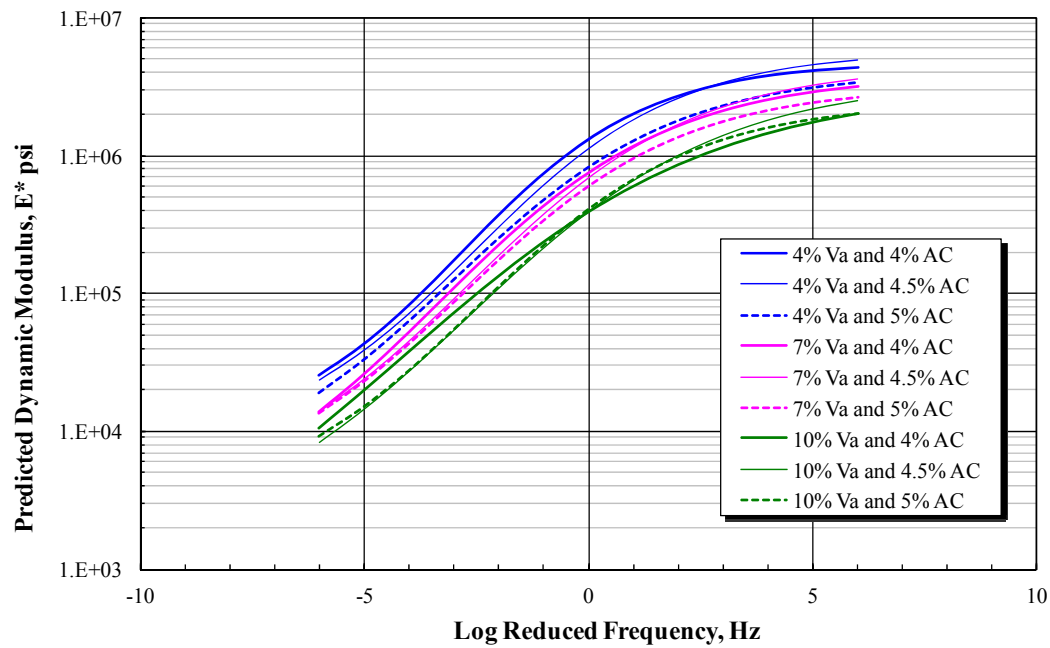
FIGURE 84 Predicted |E*| master curves at different air voids and binder content levels of PG 64-22 mixture.
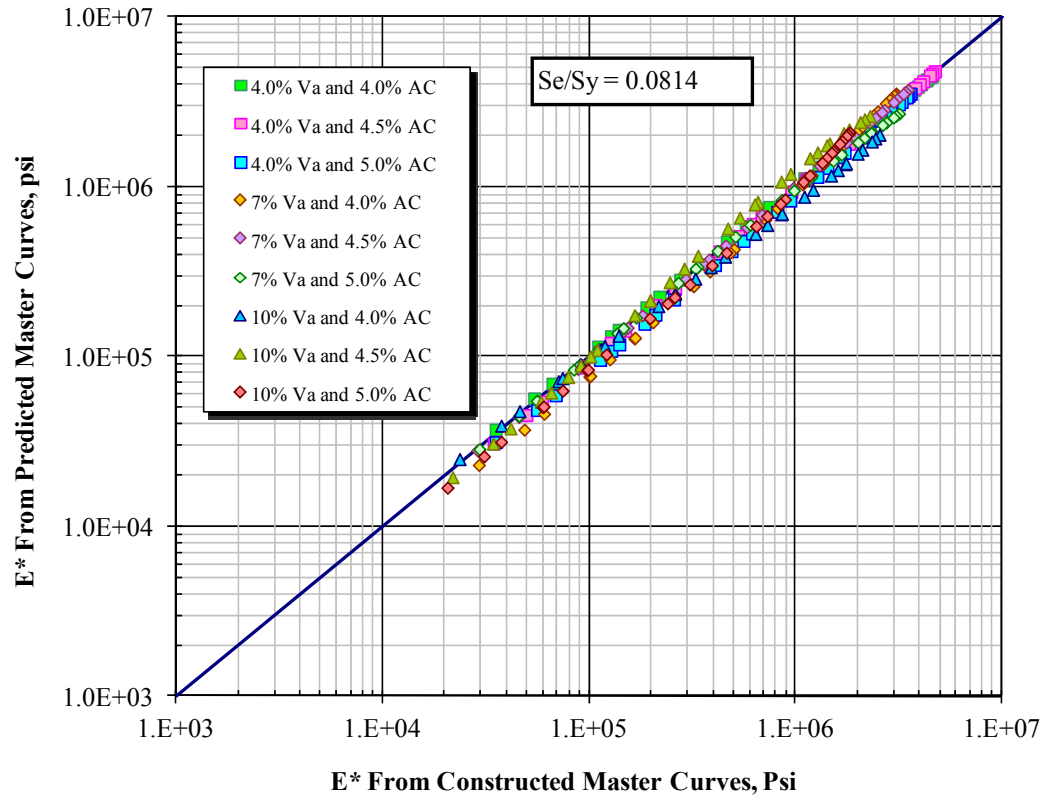
FIGURE 85 Comparison of |E*| values obtained from constructed and predicted master curves of PG 64-22 mixtures.
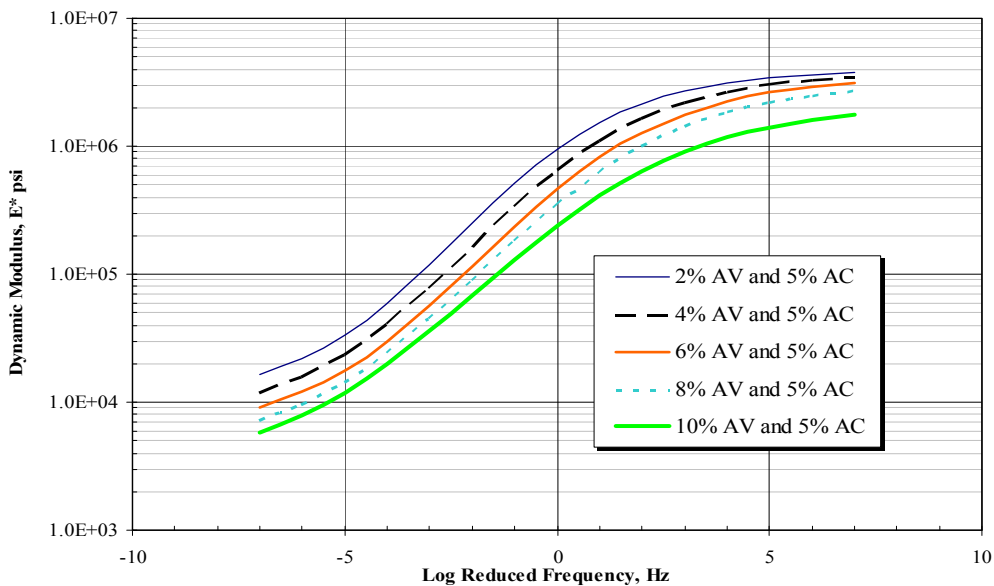
FIGURE 86 Effect of different air voids levels on shifted |E*| master curves of PG 58-28 mixture.
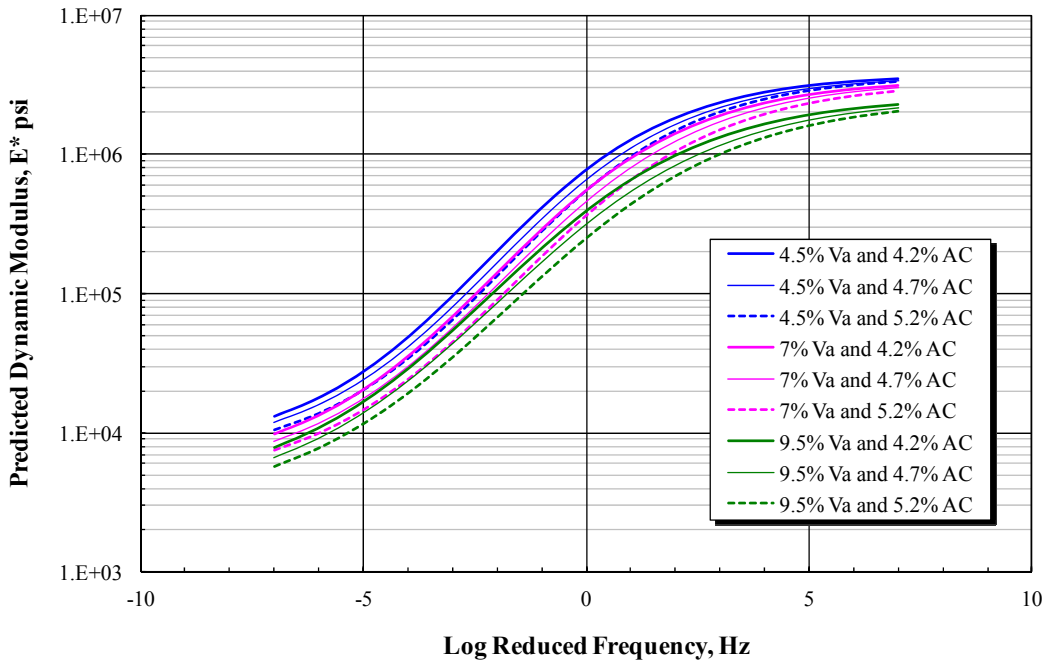
FIGURE 87 Predicted |E*| master curves at different air voids and binder content levels of PG 58-28 mixture.
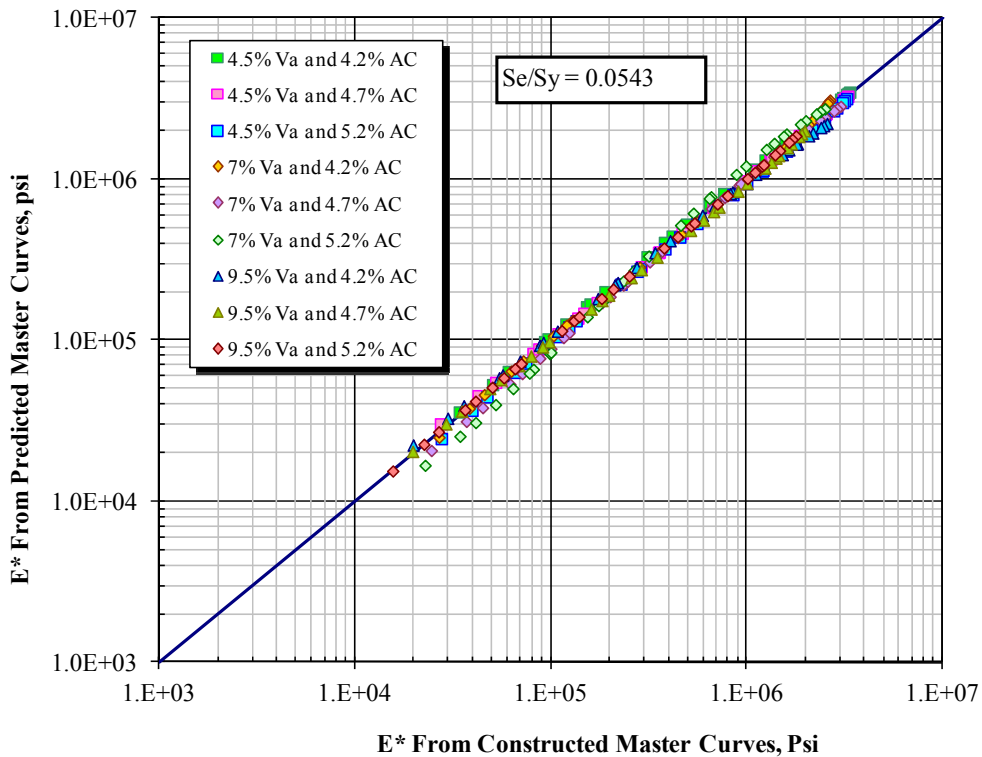
FIGURE 88 Comparison of |E*| values obtained from constructed and predicted master curves of PG 58-28 mixtures.

131
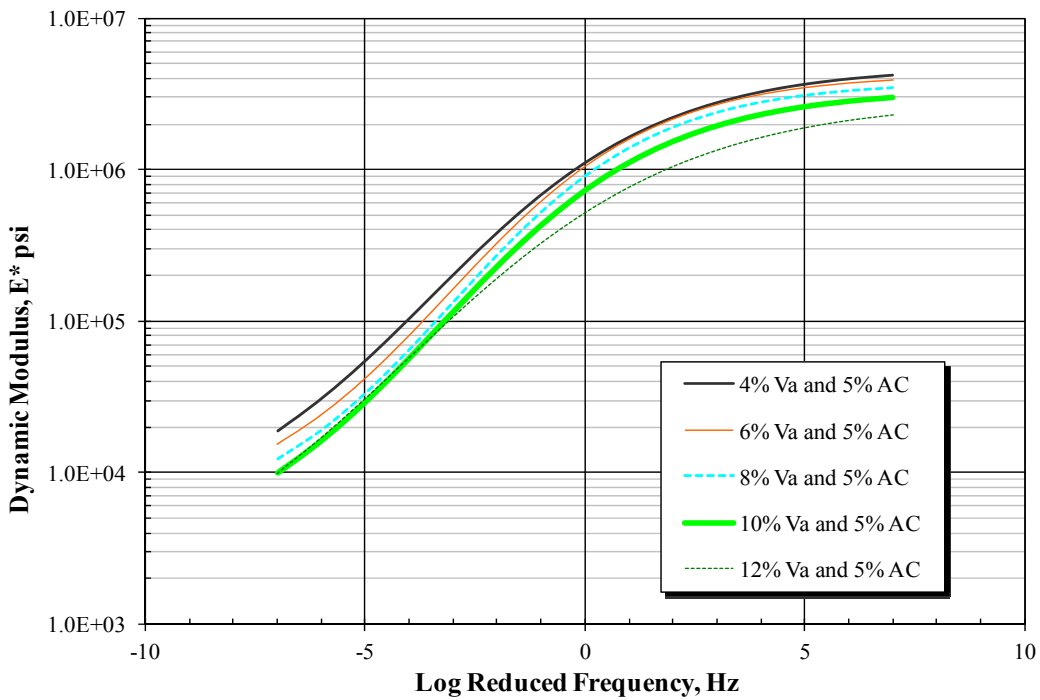
FIGURE 89 Effect of different air voids levels on shifted |E*| master curves of PG 76-16 mixture.
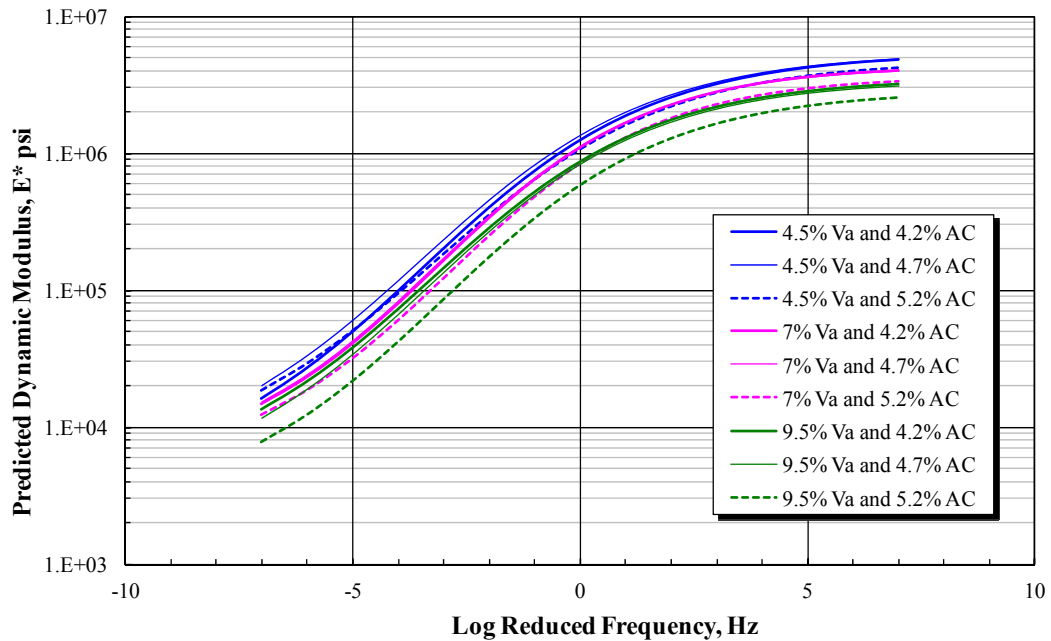
FIGURE 90 Predicted |E*| master curves at different air voids and binder content levels of PG 76-16 mixture.
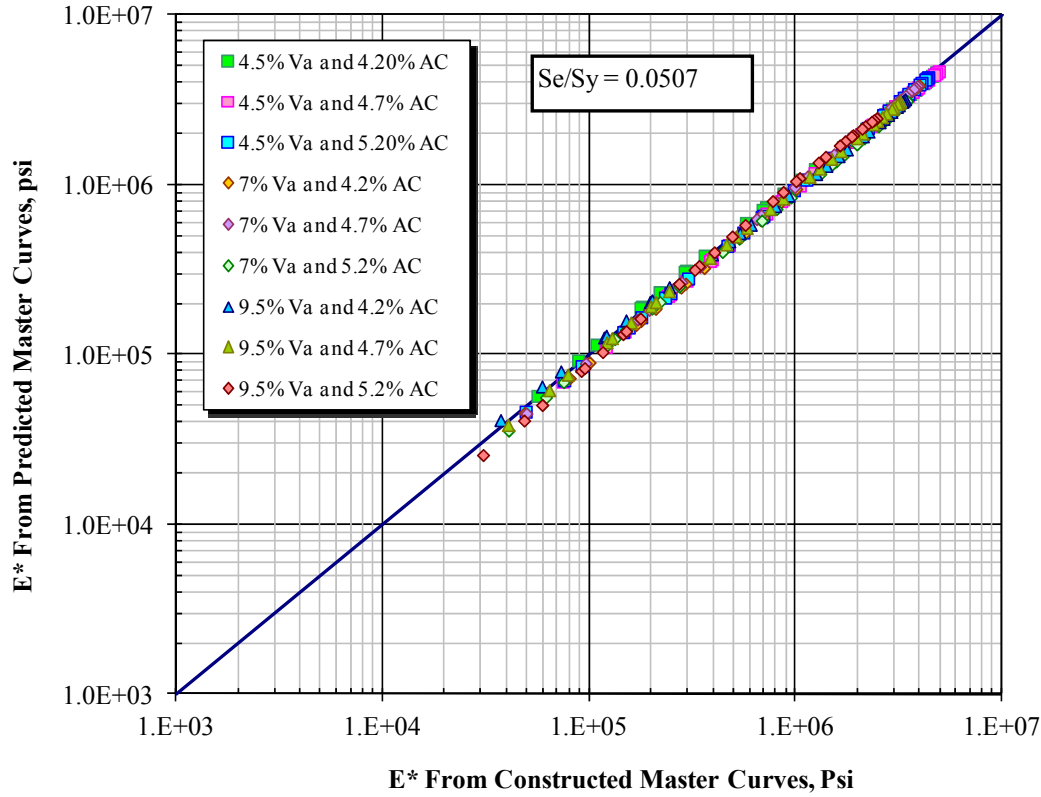
FIGURE 91 Comparison of |E*| values obtained from constructed and predicted master curves of PG 76-16 mixtures.

RELAXATION MODULUS

The relaxation modulus is considered a key viscoelastic property needed not only for the characterization of the viscoelastic behavior but also for the characterization of material damage where nonlinear behavior is exhibited. Obtaining the viscoelastic properties of the investigated asphalt concrete mixtures represents the first step of applying the viscoelastic continuum damage model (VECDM) to validate the endurance limit of these mixtures.

The relaxation modulus, E(t), is defined as the stress response of a viscoelastic material due to a unit step of strain input. The relaxation modulus can be calculated as the time-dependent stress divided by the applied strain level as shown by Equation 95:

$$E(t) = \frac{\sigma(t)}{\varepsilon_o} \tag{95}$$

where:

$E(t)$ = relaxation modulus at time t,
$\sigma(t)$ = stress at time t, and
ε_o = initial applied strain.

133

CONVERSION BETWEEN LINEAR VISCOELASTIC MATERIAL FUNCTIONS

All linear viscoelastic material functions are mathematically equivalent for each mode of loading such as uniaxial or shear. The mathematical interrelationships between linear viscoelastic material functions were established though a detailed derivation of each interrelationship (Ferry, 1980; and Tschoegl, 1989).

There are different reasons why the interconversion may be required. For example, a relaxation modulus for stiff material, which is difficult to obtain from a constant strain relaxation test because it requires a robust testing machine, can be predicted through interconversion between relaxation modulus and creep compliance obtained from a constant stress creep test. Another reason is that a material property often cannot be determined over the complete range of its domain from a single test input; in this case, the range can be extended by combining the responses to different input levels. This normally requires an interconversion between responses in time and frequency domains (Park and Schapery, 1999).

CONVERSION FROM COMPLEX MODULUS TO RELAXATION MODULUS

Schapery et al. (1999) have demonstrated two methods of interconversion between frequency-domain complex modulus and time-domain relaxation modulus. The first method was based on an approximate analysis (Schapery and Park, 1999) while the second method was based on an exact mathematical formulation (Park and Schapery, 1999). The following are illustrations of both methods.

Approximate Interconversion Method

Having dynamic modulus and phase angle values at different test temperatures (14, 40, 70, 100 and 130 °F) and loading frequencies (25, 10, 5, 1, 0.5 and 0.1 Hz), the first step in this method is to obtain the storage modulus E' master curve in a frequency-domain range as explained previously. The relaxation modulus can be determined using the following equation:

$$E(t) \cong \frac{1}{\lambda'} \times E'(\omega)\Big|_{\omega=(1/t)} \tag{96}$$

where:

    t   = reduced time,

    ω = reduced frequency,

    E(t)   = relaxation modulus, and

    λ' = adjustment function corresponding to use of storage modulus conversion which can be defined as following:

$$\lambda' = \Gamma(1-n) \times \cos(n \times \pi / 2) \tag{97}$$

and:

$$n \equiv \frac{d \log E'(\omega)}{d \log(\omega)} \tag{98}$$

Where $\Gamma()$ is the Gamma function and n is the local log-log slope value of the storage modulus used for calculating each relaxation modulus point. The n values at different reduced

frequencies can be obtained by differentiating the sigmoidal function of the storage modulus master curve, which can be written in the following form:

$$n = \frac{d \log E'(f_r)}{d \log(f_r)} = \frac{\alpha' \times \gamma' \times e^{-\beta' - \gamma'(\log f_r)}}{\left(1 + e^{-\beta' - \gamma'(\log f_r)}\right)^2} \tag{99}$$

TABLE 31 shows an example of a relaxation modulus prediction using the approximate method. It can be noticed that the relaxation modulus values are close to the storage modulus values.

Having the predicted relaxation modulus values at different temperatures and frequencies, the relaxation modulus master curves are constructed for all mixtures by using the sigmoidal function and the same shift factors of the storage modulus shown in FIGURE 92. It is observed that at the same asphalt cement content, the relaxation modulus values are higher when air voids are lower.

TABLE 31 Calculation of relaxation modulus values of PG 76-16 binder at 4.2% AC and 7.0% Va

Temp (°F)	Freq (Hz)	Predicted Storage Modulus, E' (psi)	n	Γ(1-n)	λ'	Relaxation Modulus, E(t) (psi)
14	25	3,906,388	0.023	1.014	0.999	3,908,971
	10	3,816,960	0.028	1.017	0.999	3,820,531
	5	3,739,951	0.031	1.019	0.999	3,744,493
	1	3,526,207	0.042	1.026	0.998	3,533,997
	0.5	3,417,735	0.048	1.030	0.997	3,427,467
	0.1	3,124,907	0.064	1.041	0.995	3,140,769
40	25	3,204,008	0.060	1.038	0.996	3,218,094
	10	3,019,649	0.070	1.046	0.994	3,037,999
	5	2,867,927	0.079	1.052	0.992	2,890,088
	1	2,478,933	0.103	1.071	0.987	2,511,801
	0.5	2,298,487	0.115	1.081	0.984	2,336,592
	0.1	1,863,067	0.147	1.109	0.974	1,913,632
70	25	1,908,949	0.143	1.106	0.975	1,958,256
	10	1,659,375	0.163	1.125	0.967	1,715,208
	5	1,474,231	0.179	1.141	0.961	1,534,189
	1	1,073,007	0.216	1.183	0.943	1,138,095
	0.5	918,397	0.233	1.203	0.934	983,264
	0.1	613,762	0.267	1.249	0.913	672,192
100	25	753,547	0.251	1.227	0.923	816,126
	10	593,498	0.270	1.253	0.912	651,121
	5	490,060	0.282	1.271	0.903	542,587
	1	305,272	0.304	1.304	0.888	343,628
	0.5	246,865	0.309	1.312	0.885	279,013
	0.1	149,852	0.309	1.313	0.884	169,435
130	25	234,088	0.309	1.313	0.884	264,747
	10	176,130	0.311	1.315	0.883	199,405
	5	142,104	0.308	1.311	0.885	160,560
	1	87,496	0.292	1.286	0.897	97,590
	0.5	71,720	0.281	1.269	0.904	79,336
	0.1	46,747	0.249	1.225	0.924	50,578
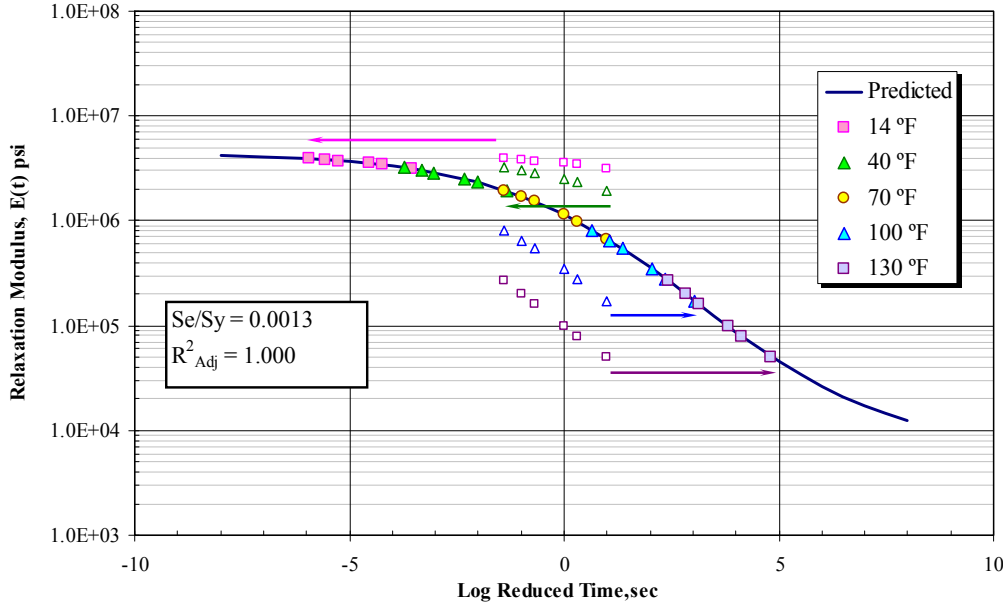
FIGURE 92 Relaxation modulus master curve of PG 76-16 binder at 4.2% AC and 7.0% Va.

Exact Interconversion Method

This method also requires the storage modulus, E', master curve. It is based on the Prony series representation of E' to allow simple interconversion between the frequency and time domains (Park and Schapery, 1999). This representation of E' is based on Wiechert model (or generalized Maxwell model) where the mechanical model consisting of multiple Maxwell elements (a spring and a dashpot in series) placed in parallel as shown in FIGURE 93. E' can be expressed by the following Prony series representations in the frequency domain.

$$E'(\omega) = E_\infty + \sum_{i=1}^{N} \frac{\omega_i^2 \rho_m^2 E_m}{\omega_i^2 \rho_m^2 + 1} \tag{100}$$

where:

$E'(\omega)$ = the storage modulus as a function frequency, ω (kPa or psi),
E_∞ = the long-time equilibrium modulus (kPa or psi),
E_m = the modulus of Prony term number m (kPa or psi),
P_m = the relaxation time of Prony term m (s), and
N = the number of Prony terms used.

The long-time equilibrium (rubbery) E_∞ is basically the modulus corresponding to the lower asymptote of the master curve and is independent of test temperature and loading frequency. The equilibrium modulus can be obtained using Equation 101.

$$E_\infty = 10^{\delta'} \tag{101}$$

Where δ' is minimum value of E'.

138
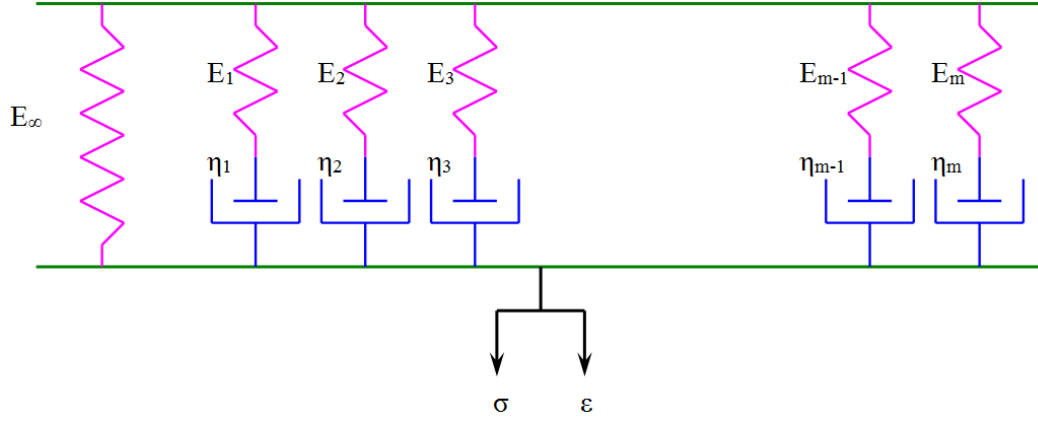
FIGURE 93 Generalized Maxwell (Wiechert) model.

The Prony series coefficients (E_∞, E_m, and ρ_m) can be established by solving the following linear equation:

$$E_m = [B]_{mi}^{-1} \times \{E'\}_{norm} \tag{102}$$

where:

$$B_{mi} = \frac{\omega_i^2 \rho_m^2}{\omega_i^2 \rho_m^2 + 1} \tag{103}$$

and:

$$E'_{norm} = E' - E_\infty \tag{104}$$

B_{mi} = relaxation kernel matrix for determining the Prony coefficients

ω_i = reduced frequency at the temperature and frequency condition, i (rad/s).

Once the Prony series coefficients are calculated, the relaxation modulus values along desired time range are fitted to a Prony series function using the collocation method. This method is more practical for the purpose of analysis of the Pseudo strain (Park and Kim, 2001). The Prony series function can be expressed using the following formula:

$$E(t) = E_\infty + \sum_{i=1}^{N} E_m \exp^{\frac{-t}{\rho_m}} \tag{105}$$

where:

$E(t)$ = the relaxation modulus as a function of time, t, (kPa or psi).

TABLE 32 illustrates an example the Prony series coefficients at different series terms.

TABLE 32 Prony series parameters for different term values of PG 76-16 mixture at 4.2% AC and 7.0% Va

No. of Series Terms	7 Terms		9 Terms		11 Terms		13 Terms		15 Terms		17 Terms	
	ρ_m (s)	E_m (psi)	ρ_m (s)	E_m (psi)	ρ_m (s)	E_m (psi)	ρ_m (s)	E_m (psi)	ρ_m (s)	E_m (psi)	ρ_m (s)	E_m (psi)
1	2.E+03	177172	2.E+04	83827	2.E+05	41278	2.E+06	21536	2.E+07	11878	2.E+08	6849
2	2.E+02	149323	2.E+03	71329	2.E+04	31709	2.E+05	14086	2.E+06	6539	2.E+07	3231
3	2.E+01	325638	2.E+02	176845	2.E+03	84881	2.E+04	38779	2.E+05	17986	2.E+06	8787
4	2.E+00	487250	2.E+01	318754	2.E+02	173456	2.E+03	83113	2.E+04	37804	2.E+05	17423
5	2.E-01	610717	2.E+00	488972	2.E+01	319602	2.E+02	173898	2.E+03	83357	2.E+04	37944
6	2.E-02	630799	2.E-01	610249	2.E+00	488761	2.E+01	319491	2.E+02	173837	2.E+03	83322
7	2.E-03	584921	2.E-02	631846	2.E-01	610303	2.E+00	488788	2.E+01	319507	2.E+02	173845
8	-	-	2.E-03	561460	2.E-02	631806	2.E-01	610296	2.E+00	488784	2.E+01	319504
9	-	-	2.E-04	463998	2.E-03	562154	2.E-02	631808	2.E-01	610297	2.E+00	488785
10	-	-	-	-	2.E-04	446780	2.E-03	562134	2.E-02	631808	2.E-01	610297
11	-	-	-	-	2.E-05	340899	2.E-04	447262	2.E-03	562135	2.E-02	631808
12	-	-	-	-	-	-	2.E-05	328885	2.E-04	447249	2.E-03	562134
13	-	-	-	-	-	-	2.E-06	237863	2.E-05	329210	2.E-04	447249
14	-	-	-	-	-	-	-	-	2.E-06	229761	2.E-05	329202
15	-	-	-	-	-	-	-	-	2.E-07	160432	2.E-06	229975
16	-	-	-	-	-	-	-	-	-	-	2.E-07	155086
17	-	-	-	-	-	-	-	-	-	-	2.E-08	105850

CHAPTER 6

DEVELOPMENT OF UNIAXIAL TENSION-COMPRESSION FATIGUE TEST PROTOCOL AND SOFTWARE

BACKGROUND

Various laboratory testing methods have been developed to characterize the fatigue properties of HMA. The prediction precision of fatigue damage using any of these test methods depends on how closely that method simulates the conditions of loading, support, stress state, and environment that the material is subjected to in the pavement. The beam fatigue test is well-known and the most widely used testing method. The uniaxial fatigue test, either the direct tension (pull) or the tension-compression (push-pull), is a promising fatigue test.

In this research, the uniaxial fatigue test was conducted to evaluate the fatigue damage and healing of asphalt concrete mixtures using the viscoelastic and continuum damage model. The fatigue healing is evaluated by observing the difference between fatigue damage using two different methods of the uniaxial fatigue test. The first method is a test run continuously without any rest between the loading cycles inducing fatigue damage. The second method includes healing, where a constant rest period is inserted between the loading cycles to allow for healing of fatigue damage.

There are many studies conducted to propose a rational test protocol for the uniaxial fatigue test. Currently, there is no standard ASTM or AASHTO test procedure to conduct the uniaxial fatigue test. A main objective of this chapter is to highlight the available proposed uniaxial fatigue test protocols or test methods and to check their suitability for use in this project. The other important objective is to propose an uniaxial fatigue test method and software that is more general and at the same time relevant to the project goals.

CURRENT PROPOSED UNIAXIAL FATIGUE TEST METHODS

Pennsylvania State University (PSU) Test Method

Soltani and Anderson (2005) developed a new test protocol, testing machine, and software for the uniaxial fatigue test. The uniaxial fatigue test protocol includes three stages of continuous loading without rest period. In stages I and III, a strain level, not exceeding the endurance limit of the HMA, is applied. In Stage II, a strain with a magnitude exceeding the endurance limit and consequently causing fatigue damage is applied. The effects of non-fatigue phenomena such as self heating and self cooling are investigated by using 18 thermocouples for the measurement of temperature at various locations in the specimen. FIGURE 94 shows the test setup including test specimen, fixtures, transducers and thermocouples. The following test conditions were used for this test method:
- Test loading: sinusoidal centered at zero (push-pull configuration),
- Test frequency: 10 Hz,
- Test temperature: 50°F (10°C),

- Specimen: cylindrical, 3-inch diameter by 4.7-inch height (75.5-mm diameter by 120-mm height),
- Gauge length: 3 inches (75 mm),
- Number of LVDTs : 3, and
- Test mode: On-specimen controlled strain (controlled by one LVDT only).
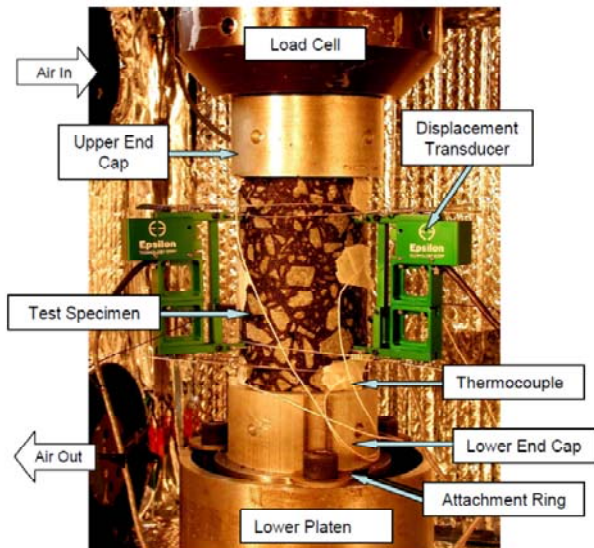
FIGURE 94 Detailed test setup: test specimen, fixtures, transducers, and thermocouples (Soltani et al., 2006).

North Carolina State University (NCSU) Method

As a result of several studies, a uniaxial fatigue test method was developed at NCSU (Daniel and Kim, 2001; Chehab, 2002; and Underwood et al., 2010). This test method was named the Simplified Viscoelastic Continuum Damage Fatigue Test (S-VECD). Recently, test software was developed for the S-VECD fatigue test by the IPC (Industrial Process Control) company. FIGURE 95 shows a specimen test setup for the S-VECD fatigue test method.

FIGURE 95 Specimen test setup (Daniel and Kim, 2001).

The following test conditions were used for the S-VECD fatigue test method:
- Test loading: haversine loading wave shape (direct tension configuration),
- Test frequency: 10 Hz,
- Test temperature: 41 and 77°F (5 and 25°C),
- Specimen: cylindrical, 3-inch diameter by 6-inch height (75-mm diameter by 150-mm height),
- Gauge length: 4 inches (100 mm),
- Number of LVDTs : 4, and
- Test mode: Crosshead strain controlled (controlled by actuator).

Advanced Asphalt Technologies (AAT) Method

Christensen and Bonaquist (2009), at AAT, developed a uniaxial fatigue test method. The IPC Company developed test software called Simplified Continuum Damage Uniaxial (SCDU) fatigue test.

The following test conditions were used for the SCDU fatigue test method:
- Test loading: sinusoidal centered at zero (tension-compression configuration),
- Test frequency: 10 Hz,
- Test temperature: 68°F (20°C),
- Specimen: cylindrical, 4-inch diameter by 6-inch height (100-mm diameter by 150-mm height),
- Gauge length: 3 inches (75 mm),
- Number of LVDTs: 3, and
- Test mode: On-specimen strain controlled (controlled from the 3 LVDTs).

143

ADEQUACY OF THE AVAILABLE TEST METHODS

After a comprehensive investigation of the available test methods and software for the uniaxial fatigue test, it was obvious that none could be used in this research without either certain modifications of test software or further examinations of the test method itself. The following are the main issues regarding these test methods that disallowed their direct use.

Pennsylvania State University (PSU) Test Method

- The test software was developed for a different test machine and controller than the ones available at the Arizona State University laboratory,
- Controlling the on-specimen strain through only one LVDT and ignoring the other sides of the specimen are not reasonable as there are always differences among measurements at different specimen sides,
- The test software can only perform the tension-compression fatigue test and there is no option to run the direct-tension test which disallows investigation of the most appropriate test for this study,
- The test method includes 3 different stages with different strain values, which are not appropriate for this study,
- The software does not allow for rest periods between loading cycles, which is one of the main requirements of the current project, and
- There is a reported issue with the loading synchronization that causes a partial loss of data.

North Carolina State University (NCSU) Method

As the NCSU uniaxial test software was developed by IPC and matches the available test setup at Arizona State University, a few trial runs were conducted and the following issues were found.
- The software was capable of running the uniaxial direct-tension fatigue test only and not the tension-compression test,
- The feedback signal is controlled by the actuator strain and not by the on-specimen strain,
- The number of loading cycles was limited to a maximum of 100,000 cycles,
- The software was not able to apply rest periods between the loading cycles, which is one of the main requirements of the current project,
- There was no option to stop the test after a certain stiffness reduction value (i.e., 50% of the initial stiffness), and
- There was no option to save the dynamic raw data for the loading cycles.

AAT Method

The IPC Company provided Arizona State University with the uniaxial fatigue software developed for AAT. The following was found after running a few trial tests:
- Although the software is capable of running the tension-compression uniaxial fatigue test, it cannot run the direct tension test,

144

- Although the software can conduct the test by controlling the on-specimen LVDT strain, it cannot control the actuator strain,
- The software was not able to apply rest periods between the loading cycles,
- There was no option to stop the test after a certain reduction of the stiffness,
- There is no fingerprint test to evaluate variability between replicates as in the NCSU software, and

Based on the evaluation of the available software, it was clear that none of them can satisfy the requirements of this research. A new uniaxial fatigue software had to be developed that can conduct the uniaxial fatigue test according to the test conditions required in this study.

TESTING SYSTEM SETUP

The description of the different components of the testing system used to develop the Arizona State University uniaxial fatigue test is presented as follows:

Testing Machine

A Universal Testing Machine, UTM-25, was used in this study. The machine can perform the test using a two closed-loop servo-hydraulic testing system manufactured by IPC. The load frame capacity of the UTM-25 machine is 25 kN in static loading and 20 kN in dynamic loading. The machine is capable of applying load over a wide range of frequencies from 0.1 to 20 Hz.

Controller Systems

Two different controller systems were examined to perform the uniaxial fatigue test using the available UTM-25 machine. The first system consisted of two parallel controllers manufactured by the IPC and GCTS companies. The second system consists of a new IPC IMACS controller (FIGURE 96). Although both controller systems are capable of producing the required loading function, it was concluded that the second system was the best to avoid incompatibility issues between the two different controllers of the first system.

UTM-25 machine load frame

IMACS IPC controller

Cylindrical Specimen

Environmental Chamber

Computer
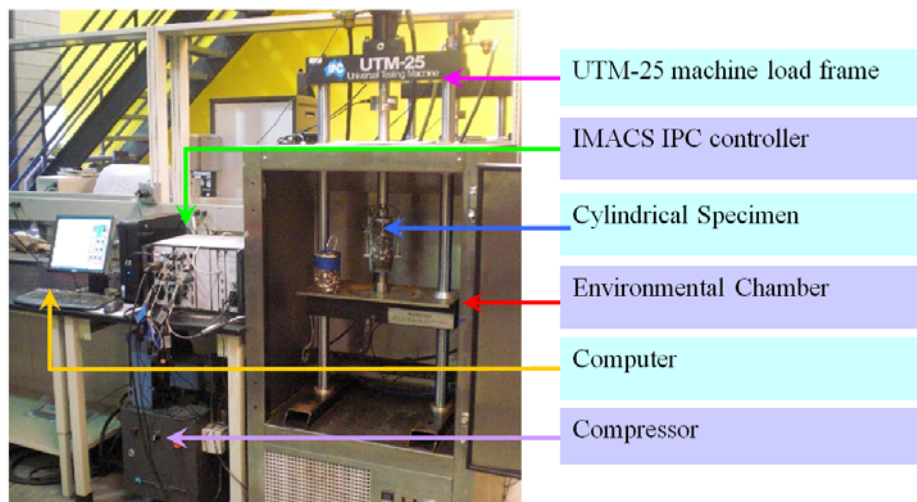
Compressor

FIGURE 96 UTM-25 uniaxial tension-compression test setup

Temperature Control

The temperature control of the UTM system is refrigeration-based. The temperature control system is able to provide a temperature between 5ºF and 140ºF for extended periods. Temperature homogeneity is achieved with internal fans and baffles to ensure competent air circulation. An asphalt dummy specimen with a temperature probe is used to ensure consistency in testing temperature.

Deflection Measurement

The vertical deformation is measured with three spring-loaded LVDTs spaced 120 degrees apart. The LVDTs are attached to the specimen using parallel brass studs to secure the LVDTs in place. Three pairs of studs are glued on the surface of the specimen with 4-inch (100-mm) gauge lengths.

Load Measurement

Loads are measured using electronic load cells. The UTM-25 is equipped with a 5,000 lb. load cell.

SPECIMEN ALIGNMENT

The uniaxial fatigue test requires special attention to the vertical alignment and the centering of the specimen to have accurate test results (SHRP–A –641, 1993; Chehab, 2002; Soltani and Anderson, 2005; and others). The sample alignment technique is of paramount importance in order to ensure that the failure plane occurs far enough from the end platens and perpendicular to the sample axis. For this purpose, a gluing jig was manufactured to ensure proper alignment between the end platens and the specimen axis. At the same time, the device aided in centering the specimen within the end plates and ensured that no eccentricity exists between the specimen and end plates. FIGURE 97 shows the gluing jig that was designed and manufactured at Arizona State University.
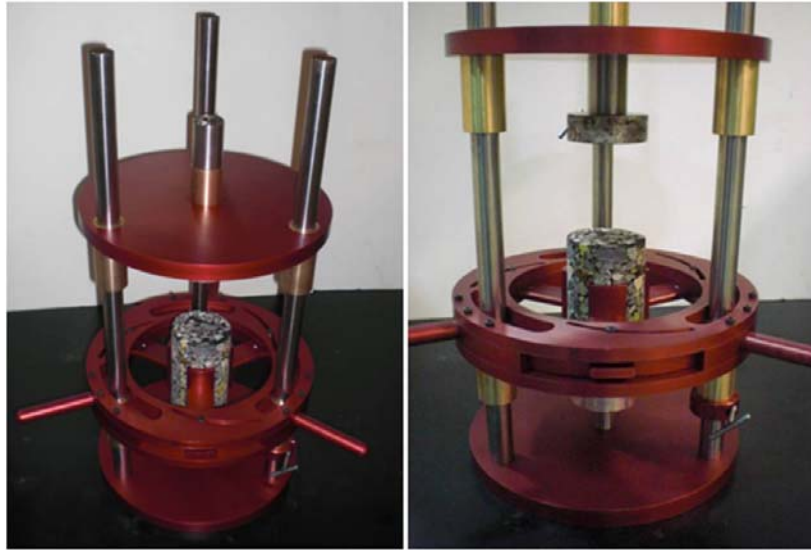
FIGURE 97 Gluing jig for uniaxial tension-compression test specimen

A detailed gluing procedure is presented as stated below:
- Clean the ends of the specimen from any residual dust using a towel.
- Screw the top and bottom end platens to the gluing jig.
- Place the specimen approximately on the center of the bottom end platen.
- Rotate the middle part of the gluing jig till the three vertical rods hold the specimen firmly and exactly on the center of the bottom plate.
- Move the upper part of the jig upward.
- Weigh out an appropriate amount of adhesive for the top side of the specimen only.
    Note 1 –The following epoxy types were found to be satisfactory for gluing the
specimens without having any failure between the platens and the glue:
    - ➢ Davcon Plastic Steel 5 Minutes Putty 10240 (2800 psi strength)
    - ➢ Loctite Epoxy Metal/Concrete (2700 psi strength)
    - ➢ Loctite Fixmaster Superior Metal (5500 psi strength)
    - ➢ ACE Plastic Repair Epoxy (3431 psi strength)
    Note 2 –approximately 40 grams of epoxy were found to be enough for one side of a 75-
mm diameter specimen.
- Mix the two components of the epoxy in the required percentages very well for 30 seconds until an homogeneous putty is obtained.
- Take around 60% of the epoxy and spread it on the top surface of the specimens.
- Move the top part of the jig downward until the upper end platen rests on the upper surface of the specimen.
- Apply enough pressure on the top part of the jig to squeeze out any extra glue between the top end platen and the top surface of the specimen.
- Use the other 40% plus the squeezed-out epoxy to cover around 0.4 inches (10 mm) of the outer surface of both the specimen and the top end platen. This was found to found to decrease the opportunity of having edge failure.

- Allow the adhesive to reach its initial set. Follow the manufacturer's recommendation to determine the time needed to the initial set.
- Rotate the middle part of the specimen to loosen it, then move the upper part upward with the upper end patens and the specimen.
- Prepare the epoxy for the bottom side of the specimen.
- Spread 60% of the epoxy on the top of the lower end platen.
- Lower the upper part of the jig until the specimen rests on the upper end platen.
- Apply pressure to the upper part of the jig to squeeze any extra glue amount outside.
- Use the remaining amount of the glue plus the squeezed amount to cover around 0.4 inches (10 mm) of the outer surface of both the specimen and the lower end platen.
- Leave the specimen undisturbed until the initial set is reached, then remove the specimen from the gluing jig.
- After approximately two hours, attach the mounting studs for the axial LVDTs to the sides of the specimen using epoxy cement.

DEVELOPMENT OF ARIZONA STATE UNIVERSITY UNIAXIAL FATIGUE TEST METHOD

In this research, the uniaxial fatigue test was conducted to evaluate the fatigue damage and healing of asphalt concrete mixtures using the viscoelastic and continuum damage model. The results were used through a developed methodology based on the crack healing to predict the fatigue endurance limit of HMA mixtures. Healing was evaluated by observing the difference between fatigue damage for tests with and without rest periods inserted between load cycles.

New software was developed to meet the test requirements discussed previously. Initially, four available software program (three provided by IPC and one provided by GCTS) were evaluated for their suitability:

1. GCTS Universal software
2. IPC User programmable software (UTS-019, V1.07b)
3. IPC S-VECD software (UTS-032, V1.00)
4. IPC SCDU software (UTS-021)

The outcomes from several preliminarily studies were influential in the development of the new software finally used in this project. The purpose and the main findings of the preliminary studies are discussed next.

Selection of Appropriate Glue Type and Platens

A study was performed to select the appropriate epoxy type and metal platens that would be used in the research. In this study, several monotonic direct tension tests at different strain rates and cyclic uniaxial tension-compression tests were conducted. The GCTS Universal software was used in this study. The selection of the appropriate types of epoxy and platens was based on-specimen failure location, to ensure that failure occurs in the middle portion of the specimen and not close to a specimen end or through the epoxy. Two specimen sizes were used; 3-inch diameter by 6-inch height (75-mm by 150-mm) and 4-inch diameter by 6-inch height (100-mm by 150-mm). Only the actuator LVDT reading was used in order to reduce the

specimen preparation time. TABLES 33 and 34 summarize the different monotonic tests for 4- and 3-inch specimens, respectively. FIGURE 98 shows test results for a successful test.

Based on the outcome and the test results, it was found that:

- Aluminum platens are better than steel platens in providing a better cohesion between specimen and platens.
- Loctite Epoxy Metal/Concrete, Loctite Fixmaster Superior Metal, and Davcon Plastic Steel Liquid (10210) are appropriate for 3-inch diameter specimens. However, ACE Plastic repair epoxy is suitable for 4-inch diameter specimens due to its higher shear strength.
- 3-inch diameter specimens have a greater tendency to fail within the middle of the specimen, while the 4-inch diameter specimens usually fail more frequently near to the end platens as shown in FIGURE 99.

TABLE 33 Summary of monotonic direct tension tests for 4-inch diameter specimens

Specimen ID	Glue Type	Glue Strength (Psi)	Upper Plate	Lower Plate	Strain Rate (mm/min)	Max Load (N)	Test Time (min)	Failure Location
LP702	Devcon 5 min epoxy	1500	Aluminum	Steel	1.0	65	1.76	between glue and lower plate
LP701	Loctite metal /concrete epoxy	2700	Aluminum	Steel	0.25	5805	2.24	between glue and lower plate
LP705	Devcon 2 ton epoxy	2500	Steel	Aluminum	0.1	4493	2.4	between glue and upper plate
MC 94404	Loctite metal /concrete epoxy	2700	Aluminum	Aluminum	0.1	5162	1.34	between glue and upper plate
MC 94403	ACE Plastic repair epoxy	3431	Aluminum	Aluminum	0.1	7417	3.99	Successive failure at top of specimen

TABLE 34 Summary of monotonic direct tension tests for 3-inch diameter specimens

Specimen ID	Glue Type	Glue Strength (Psi)	Upper Plate	Lower Plate	Strain Rate (mm/min)	Max Load (N)	Test Time (min)	Failure Location
MC944-01	Loctite metal /concrete epoxy	2700	Aluminum	Aluminum	0.1	2060	60	Successive failure at top of specimen
MC944-02	Devcon 2 ton epoxy	2500	Aluminum	Aluminum	0.1	2400	17.3	between glue and upper plate
MC944-05	Loctite metal /concrete epoxy	2700	Aluminum	Aluminum	0.1	2800	60	Successive failure at middle of specimen
MC944-06	Loctite Fixmaster Superior Metal	5500	Aluminum	Aluminum	0.15	2750	30	Successive failure at top of specimen
MC944-07	Devcon plastic steel liquid (10210)	2800	Aluminum	Aluminum	.25	2520	18	Successive failure at top of specimen
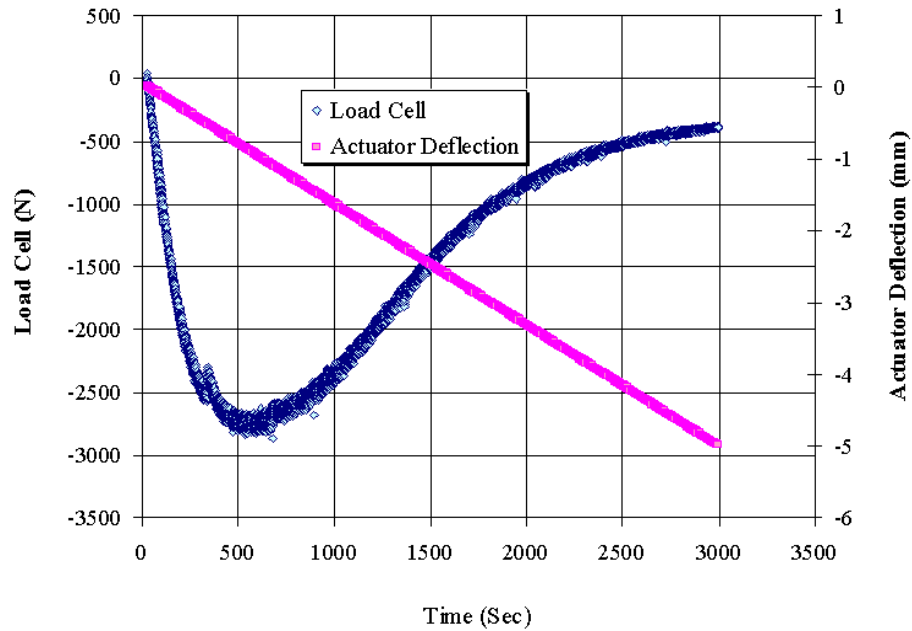
FIGURE 98 Typical monotonic direct tension test results (specimen MC944-05)
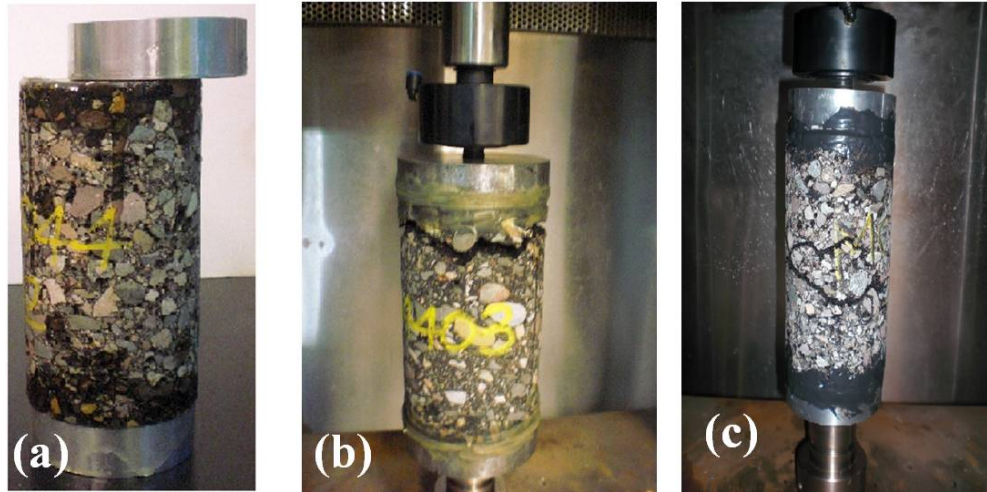
FIGURE 99 Location of failure: (a) Between platen and glue, 4-inch; (b) Close to specimen end, 4-inch; and (c) Middle of specimen, 3-inch.

Machine Compliance

Machine compliance is a very important issue in uniaxial fatigue tests. In this type of testing, not all the actuator movements are transferred to the specimen due to the inadequate machine compliance. Different factors may contribute to the machine compliance. One or more components of the loading system may yield under the applied loads. Machine compliance can be easily investigated by comparing the deformations measured from the actuator LVDT and on-specimen LVDTs or by calculating the machine compliance factor which is the actuator LVDT displacement divided by the on-specimen LVDT displacement. If the machine compliance factor is equal to one, this means that all the actuator movement is transferred to the specimen. In reality, the machine compliance factor is always greater than one, which means that a portion of the actuator displacement fails to get to the test specimen. Knowing the machine compliance factor of the testing machine, the necessary on-specimen displacement can be achieved by applying an actuator displacement equal to the required on-specimen displacement times the machine compliance factor. A machine compliance factor in the range of 5 to 10 is common (Chehab, 2002).

Chehab (2002) stated that the magnitude of the machine compliance depends upon the stiffness of the material. The higher the stiffness of the material being tested the higher the machine compliance factor. Based on that, it can be concluded that the machine compliance will be high at low temperatures where the HMA stiffness is high. Chehab also mentioned that the machine compliance factor increases as the testing frequency increases. The machine compliance can be reduced by regular maintenance of the testing machine. It is important also to clean all the machine's threads and connections and ensure they are very well tightened.

For the purpose of this research, the machine compliance was evaluated for the UTM-25 machine. The GCTS Universal software was used to evaluate two types of locking joints. The first type was an air-vacuum locked joint; the second type was a thread locked joint as shown in FIGURE 100. The evaluation showed that the machine compliance is too high when using the

151

air-vacuum locked joint, while the thread locked joint improved the machine compliance (FIGURES 101 and 102).
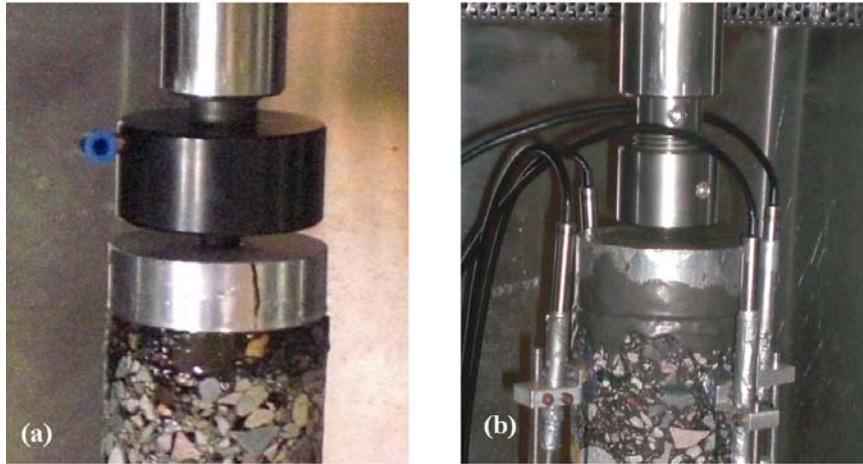
FIGURE 100 Locking joints: a) air-vacuum locked joint; b) thread locked joint.
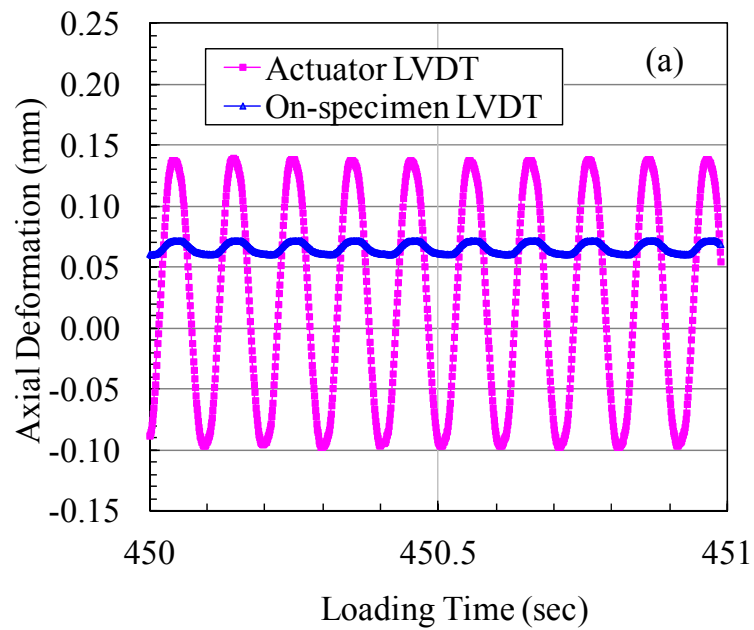
FIGURE 101 Comparison of actuator to on-specimen LVDT deformations using the air-vacuum locked joint.
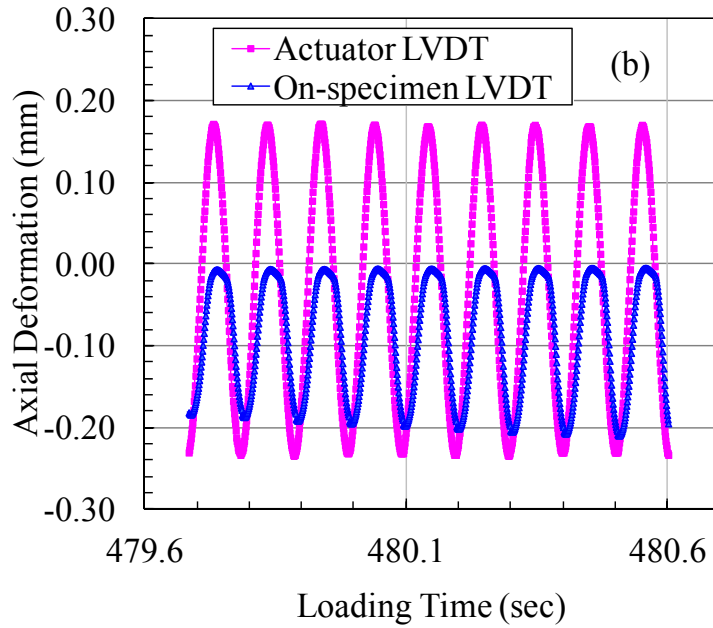
FIGURE 102 Comparison of actuator to on-specimen LVDT deformations using the thread locked joint.

Failure Location and Specimen Height during Compaction

In uniaxial fatigue tests, two types of failure are recognized based on the location of the failure plane. The first failure type is failure in the middle of the specimen and within the gauge length of the LVDTs. The second failure type is failure at one of the specimen ends, either the top or the bottom, and outside of the LVDT gauge length. Furthermore, the middle-failure type can also have three different modes as shown in FIGURE 103, when failure occurs at the top, middle or bottom of the LVDTs gauge length. Middle-failure within the LVDT gauge length is essential, as the LVDTs are then able to capture the response of the specimen during the entire loading cycle. Conversely, an end-failure test is of dubious value as acceptable LVDT measurements are only available for the test range before failure starts to take place.

Hou et al. (2010) concluded that both middle-failure and end-failure results do not affect the damage characterization. However, the end-failure test results cannot be considered in the fatigue failure (fatigue life) analysis. As the analysis in this research requires having the fatigue life at failure data, it is crucial to have the failure occurs within the LVDT gauge length.
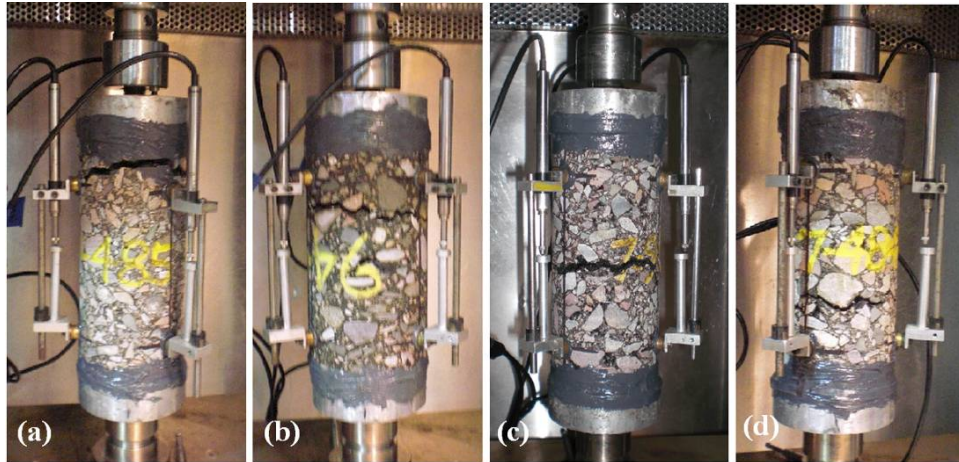
FIGURE 103 Different failure types of uniaxial fatigue test: (a) end-failure, (b) middle-failure at top, (c) middle-failure, and (d) middle-failure at bottom.

Assuming proper alignment, special care has also to be taken regarding the air voids distribution along the specimen height in order to achieve middle failure.

Specimens compacted using gyratory compactors tend to have non-uniform air voids distribution both along the diameter and height, with the air voids distribution usually higher for the outside shell compared to the inside core (Chehab, 2002). To obtain a uniform air voids distribution within a specimen for testing, it has to be cored from a larger compacted specimen with the top and bottom sections removed. The gyratory plug is usually compacted to 6.7-inch (170-mm) height and 6-inch (150-mm) diameter. The gyratory plug is then cored to produce a cylindrical specimen of a given lower diameter based on the test type and specification (usually 3- or 4-inch diameter). The upper and lower specimen ends are then trimmed to a specific specimen height according to the test protocol (usually 6-inch height).

It was hypothesized that higher heights of compaction would allow for trimming more from the two ends with high air voids. This would leave a more homogeneous air voids distribution along the remaining specimen height (6-inch), which promises to yield more frequent failure in the middle of the specimen in the uniaxial tension-compression fatigue test.

To investigate this hypothesis, a pilot study was performed in which gyratory plugs were compacted at three compaction heights, (6.7-, 7.1-, and 7.9-inch (170-, 180- and 200-mm)) (FIGURE 104). Three-inch (75-mm) diameter, 150-mm high specimens were cored and cut from the plugs. Some of these specimens were used to investigate the air voids distribution at different compaction heights, while the other specimens were tested to failure using the uniaxial tension-compression fatigue test up to determine the failure location. All specimens for this study were prepared using the PG 76-16 binder at 4.2% asphalt content. TABLE 35 summarizes the testing program of the pilot study. Since the volume of the material needed for the 200 mm height plugs was too large to put in the mold, it was only possible to compact two plugs at 9.5% air voids.

154
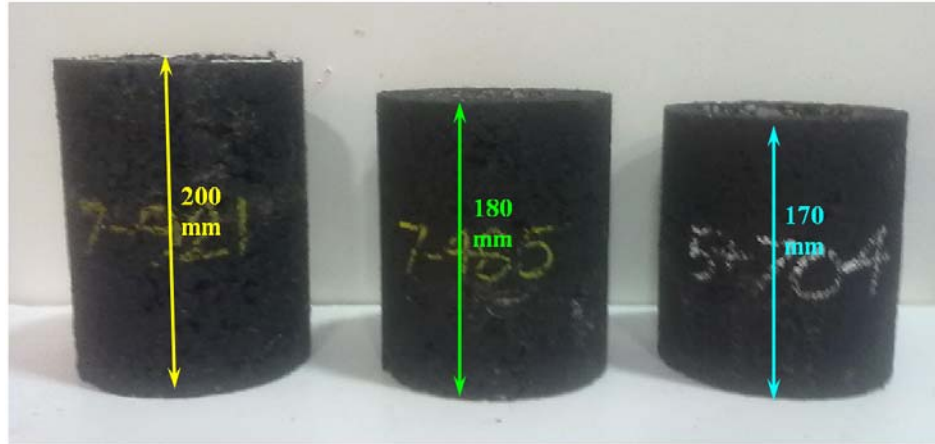
FIGURE 104 Compaction of plugs with different height.

TABLE 35 Testing plan of the compaction study

Compaction Height (inch)	Target Air Voids (%)	No. of Specimens for Air Voids Distribution	No. of Specimens for Fatigue Test
6.7	8.0	3	5
7.1	9.5	3	3
	7.0	3	0
	4.5	3	3
7.9	9.5	1	1

In a gyratory compacted specimen, the air voids at the top is usually higher than the air voids at the bottom. Therefore, a greater thickness is usually trimmed from the top compared to the bottom of the specimen (Chehab et al., 2000). In this study, for 6.7-inch (170-mm) high compacted specimens, 0.3-inch (8-mm) were trimmed from the bottom and 0.5-inch (12-mm) were trimmed from the top. For the 7.1-inch (180-mm) high specimens, 0.4-inch (10-mm) was trimmed from bottom and 0.8-inch (20-mm) was trimmed from top. Finally, in the case of the 7.9-inch (200-mm) high plugs, 0.6-inch (15-mm) was trimmed from bottom and 1.4-inch (35-mm) was trimmed from top.

To examine the air voids distribution with specimen height, the air voids for both cored and cut specimens were determined initially. The second step was to cut the specimen into two halves, 3-inch (75-mm) in height each, designated as the top half (T) and the bottom half (B). The two halves were then completely dried for 24 hours and the air voids were determined for both halves. The last step was to divide the specimen into four quarters by cutting each half into two quarters of approximately 1.5-inch (37-mm) height each. The two quarters from the top half were designated as top-top quarter (TT) and top-bottom quarter (TB), where the two quarters from the bottom half were designated as bottom-top quarter (BT) and bottom-bottom quarter

(BB). The air voids were then determined for the four quarters after drying for 24 hours. FIGURE 105 shows the steps of specimen cutting, while FIGURE 106 illustrates an example of air voids calculation for each part.

FIGURE 105 Steps of specimen cutting for different air voids calculations.
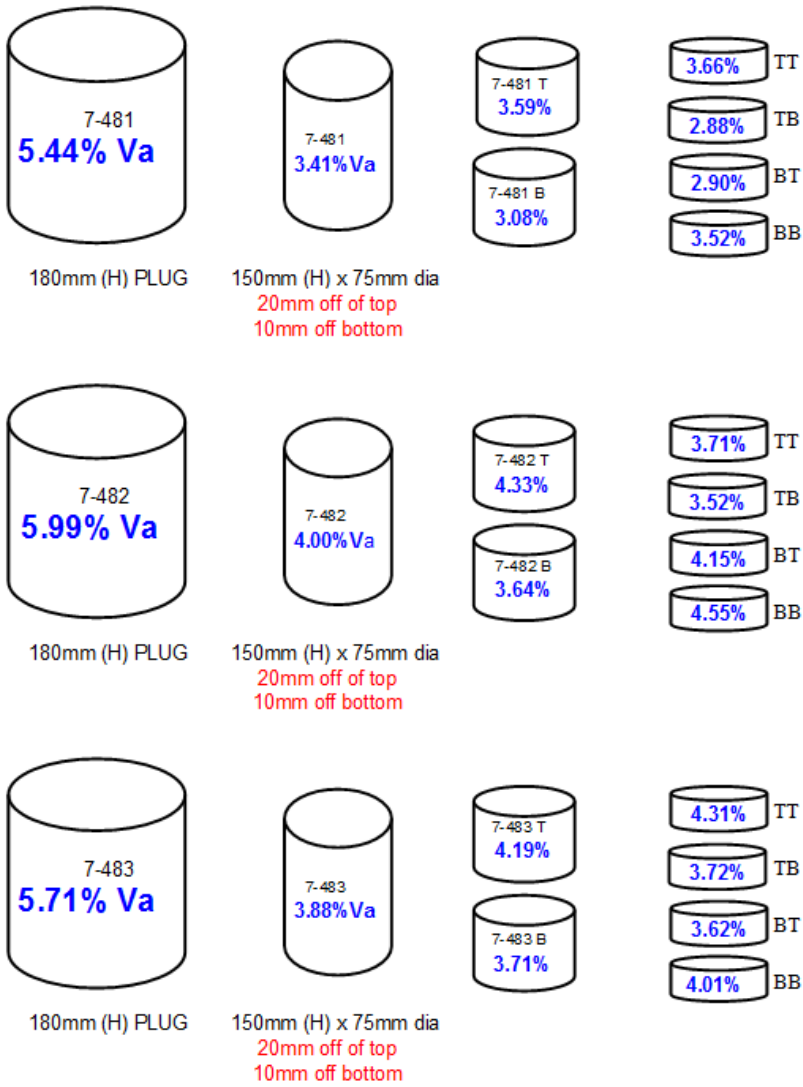
FIGURE 106 An example of air voids calculations for each part.

The air voids calculations and analysis are summarized for each group of replicates based on the compaction height and the air voids levels in TABLES 36 through 40. Each table contains the air voids calculations based on the whole specimen, two halves, and 4 quarters. The percent air voids difference between the top and bottom halves as well as the top and bottom quarters within the same group were determined. To have a better chance in specimen failure in the middle or at least within the LVDT gauge length, the average percent difference of the air voids between the top and the bottom quarters of the same half should be minimal. It can be observed from the different tables that the average top and bottom air voids percent difference is lower for the 7.1-inch (180-mm) high samples (for the three groups at 4.5, 7.0, and 9.5%) compared to the 6.7-inch (170-mm) high samples. This means that specimens cored and cut out of the 7.1-inch (180-mm) compacted plugs will have a better chance of failing in the middle compared to those compacted to a height of 6.7 inches (170mm). The specimen compacted to a 7.9-inch (200-mm) height showed a higher air voids percent difference compared to both 6.7- and 7.1-inch (170- and 180-mm) plugs. However, this observation was only based on one replicate.

TABLE 36 Average of air voids calculations for 6.7-inch height at 8.0% Va

Sample ID	1 Part	2 Parts			4 Parts			
	Air Voids	Air Voids	Difference	Average Difference	Air Voids	Difference	Ave. Top Difference	Ave Bottom Difference
944-18	8.29	8.45	0.71	0.85	8.56 / 7.62	0.94	1.42	1.21
		7.74			7.49 / 9.27	1.78		
944-19	8.19	8.59	1.23		9.50 / 7.65	1.85		
		7.36			7.99 / 8.77	0.78		
944-20	8.40	8.82	0.61		9.56 / 8.08	1.48		
		8.21			7.66 / 8.73	1.07		

TABLE 37 Average of air voids calculations for 7.1-inch height at 9.5% Va

Sample ID	1 Part Air Voids	2 Parts Air Voids	Difference	Average Difference	4 Parts Air Voids	Difference	Ave. Top Difference	Ave Bottom Difference
7-981	8.67	9.27	0.34		9.66 / 8.84	0.82		
		8.93			8.69 / 9.63	0.94		
7-982	9.66	9.87	1.52	0.88	10.02 / 8.82	1.2	1.21	1.55
		8.35			7.74 / 9.44	1.7		
7-983	9.82	10.28	0.78		10.49 / 8.89	1.6		
		9.50			8.38 / 10.39	2.01		

TABLE 38 Average of air voids calculations for 7.1-inch height at 7.0% Va

Sample ID	1 Part Air Voids	2 Parts Air Voids	Difference	Average Difference	4 Parts Air Voids	Difference	Ave. Top Difference	Ave Bottom Difference
7-781	6.27	6.55	0.56		7.17 / 6.05	1.12		
		5.99			5.75 / 6.70	0.95		
7-782	6.71	7.26	0.94	0.77	7.39 / 7.10	0.29	0.84	0.68
		6.32			6.12 / 6.56	0.44		
7-783	7.22	7.41	0.77		7.86 / 6.76	1.1		
		8.18			6.44 / 7.08	0.64		

TABLE 39 Average of air voids calculations for 7.1-inch height at 4.5% Va

Sample ID	1 Part Air Voids	2 Parts Air Voids	Difference	Average Difference	4 Parts Air Voids	Difference	Ave. Top Difference	Ave. Bottom Difference
7-481	3.41	3.59	0.51		3.66	0.78		
					2.88			
		3.08			2.90	0.62		
					3.52			
7-482	4.00	4.33	0.69	0.58	3.71	0.19	0.52	0.47
					3.52			
		3.64			4.15	0.4		
					4.55			
7-483	3.88	4.19	0.54		4.31	0.59		
					3.72			
		4.73			3.62	0.39		
					4.01			

TABLE 40 Average of air voids calculations for 7.9-inch height at 9.5% Va

200 mm Plugs, 9.0%AV					
Sample ID	1 Part Air Voids	2 Parts Air Voids	Difference	4 Parts Air Voids	Difference
7-922	8.67	9.55	0.46	10.52	1.79
				8.73	
		11.01		9.28	1.63
				11.91	

The air voids distributions for each group based on the compaction height and the air voids level are plotted in FIGURES 107 to 111. The following general trends can be observed:

- The air voids values at the specimen ends are relatively higher compared to the values at the middle of the specimen.
- The upper half of the specimen has higher air voids than the lower half.
- Despite greater thicknesses being trimmed from the top compared to the bottom of specimens, the top of the specimens in most cases had higher air voids than the bottom; which confirmed the approach followed in trimming the top and bottom ends.

Regarding the uniaxial fatigue test, the results concerning the failure location were very encouraging and agreed with the conclusion from the air voids distribution analysis. For the 6.7-inch (170-mm) compaction height group, only one specimen out of five failed in the LVDT gauge length (20 % success). On the other hand, the 7.1-inch (180-mm) compaction height groups at 4.5 and 9.5% had five out of six specimens failing in the LVDT gauge length (83% success). For the 7.9-inch (200-mm) compaction height, the specimen failed in the LVDT gauge length, but this was only for one specimen.

TABLE 41 summaries the failure location at different compaction heights.
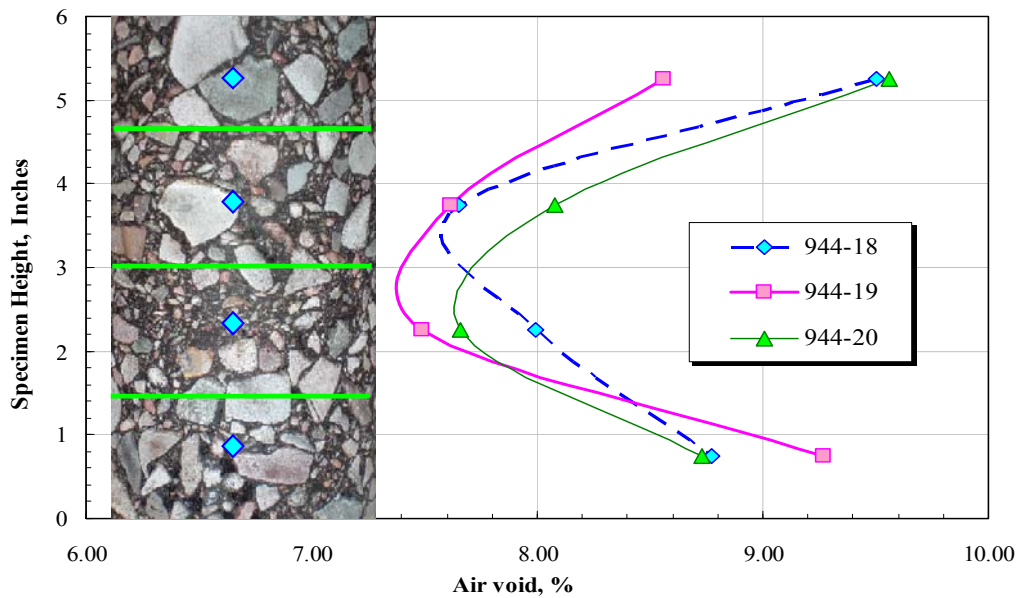
FIGURE 107 Air voids distribution along the specimen height for 6.7-inch height at 8.0% Va.
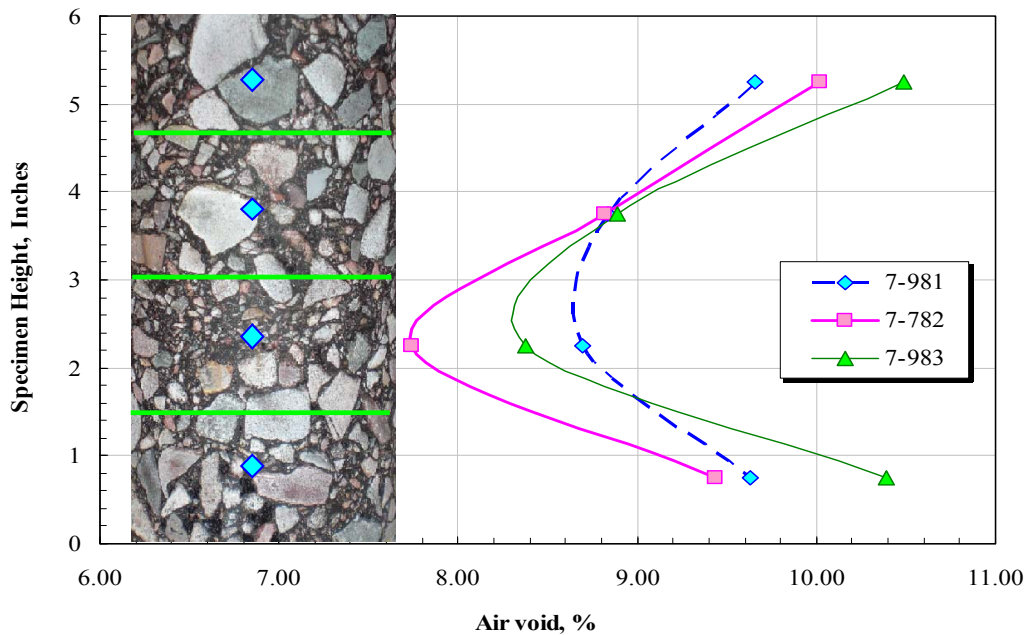
FIGURE 108 Air voids distribution along the specimen height for 7.1-inch height at 9.5% Va.

161
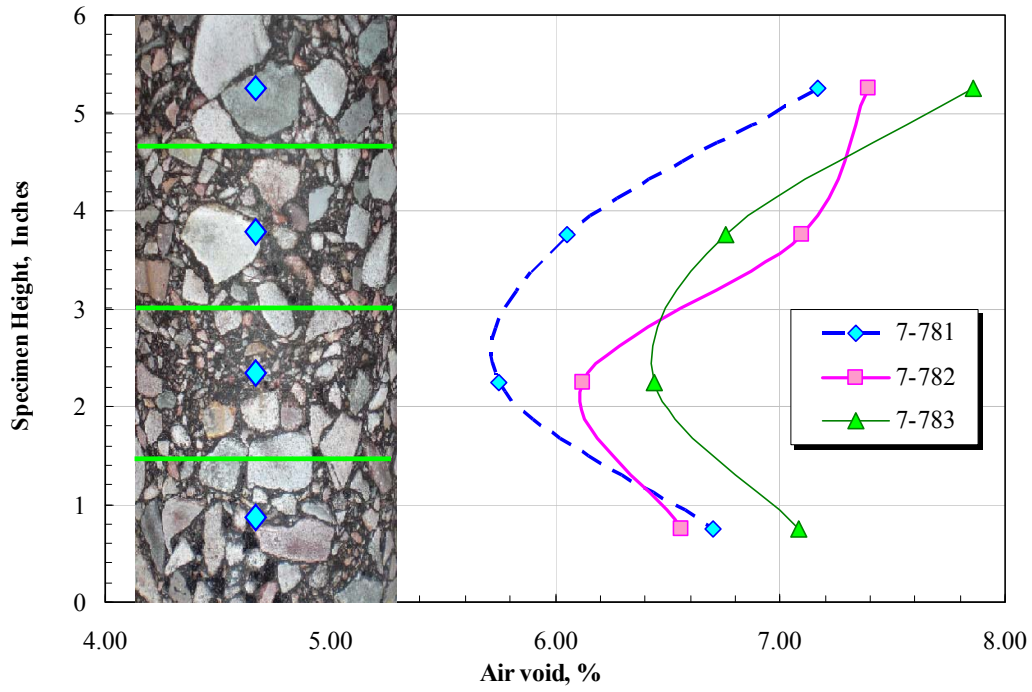
FIGURE 109 Air voids distribution along the specimen height for 7.1-inch height at 7.0% Va.
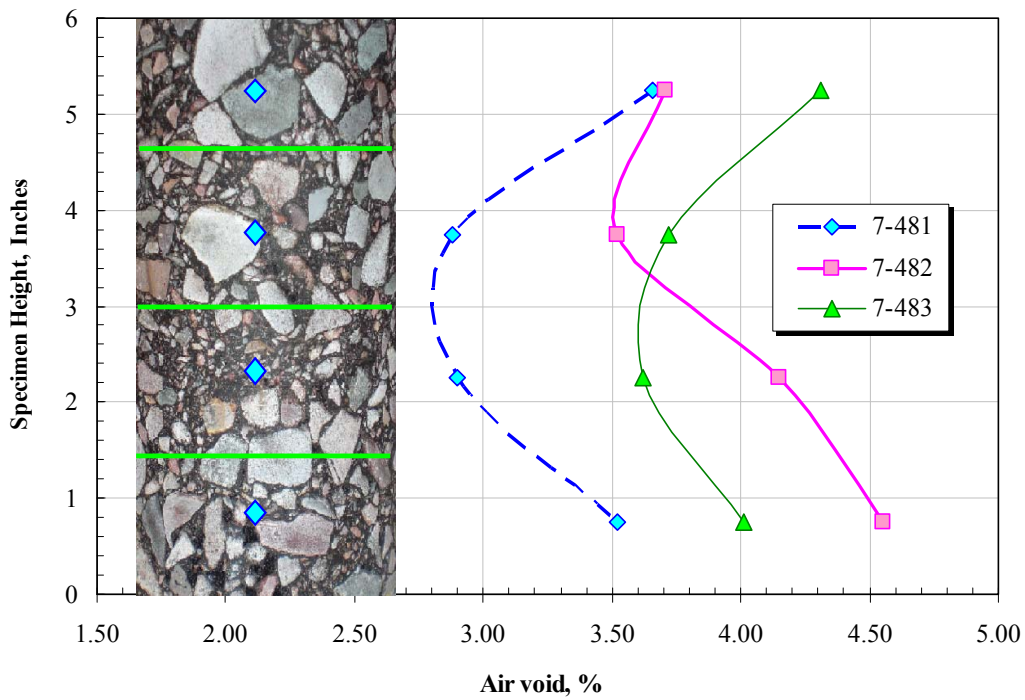
FIGURE 110 Air voids distribution along the specimen height for 7.1-inch height at 4.5% Va.

162
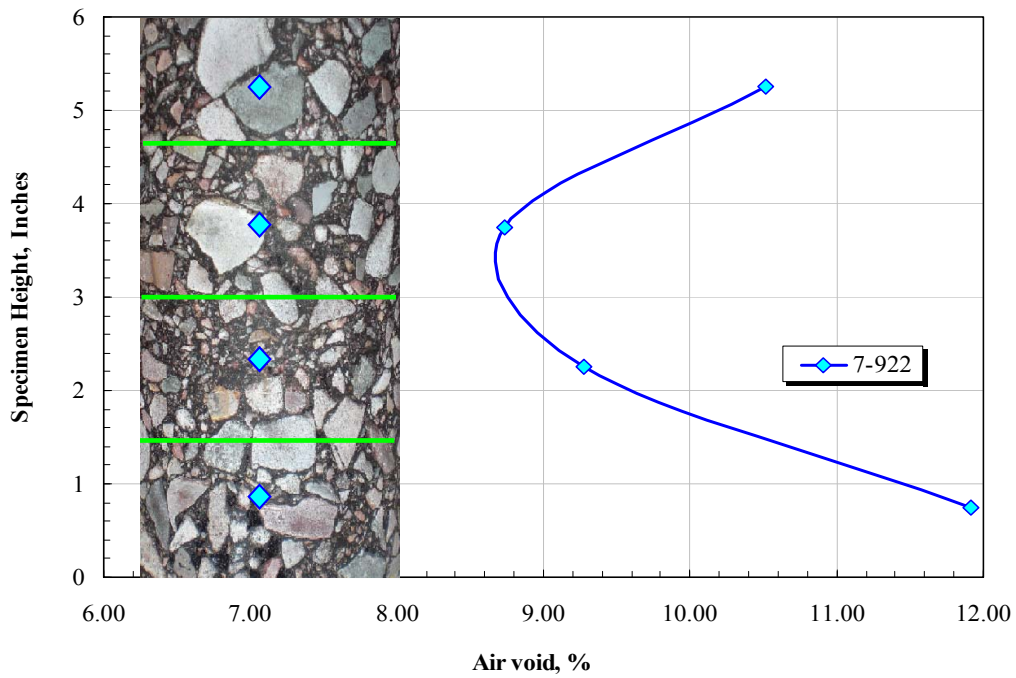
FIGURE 111 Air voids distribution along the specimen height for 7.9-inch height at 9.5% Va.

TABLE 41 Locations of failure for specimens with different compaction heights

Specimen ID	Compaction Height (inches)	Target Air Voids (%)	Actuator Displacement (mm)	Failure Location	Fatigue Life Analysis
MC944A-17			±0.3	At top of specimen	Not applied
MC944A-21			±0.3	At bottom of specimen	Not applied
MC944A-22	6.7	7.0	±0.3	In the LVDT gauge length near top	Applied
MC944A-23			±0.3	At bottom of specimen	Not applied
MC944A-25			±0.3	At bottom of specimen	Not applied
944A-7-984			±0.2	In the LVDT gauge length near top	Applied
944A-7-985		9.5	±0.2	In the LVDT gauge length at middle exactly	Applied
944A-7-986	7.1		±0.2	In the LVDT gauge length near bottom	Applied
944A-7-484			±0.25	In the LVDT gauge length near bottom	Applied
944A-7-485		4.5	±0.25	At top of specimen	Not applied
944A-7-486			±0.25	In the LVDT gauge length near top	Applied
944A-7-921	7.9	9.5	±0.25	In the LVDT gauge length near top	Applied

Investigation of Strain Controlled Methods

A preliminarily controlled-strain tension-compression (Push-Pull) uniaxial fatigue test was performed to compare crosshead (actuator) strain control and on-specimen LVDT strain control. The description of each test is presented below.

Crosshead Controlled-Strain Test

In this test, the strain was controlled by the actuator while the strain values of on-specimen LVDTs were used for the analysis. In this case, the actuator displacement amplitude is maintained constant during the test, while the on-specimen LVDT displacement amplitude varied during the test. Several tests have been conducted using both the GCTS Universal software and the IPC user programmable software (UTS-019, V1.07b). The following test parameters were used:

- Frequency values: 1, 2, 5and 10 Hz.
- Strain levels: ±300, ±500 and ±750 μs.

On-Specimen LVDT Controlled-Strain Test

In this test, the strain was controlled by the on-specimen LVDTs. The on-specimen displacement amplitude was kept constant during the test, whereas the actuator displacement amplitude varied during the test. Controlling the on-specimen LVDT displacements were achieved through a channel created to represent the average displacement from the four on-specimen LVDTs. In this test, ±300 μs amplitude was applied to the on-specimen LVDTs at 10 Hz frequency.

Based on the results obtained from the two tests, the following conclusions were made.

- The on-specimen strain values using the crosshead-control constant strain method cannot be maintained constant, but actually increased during the test. This is mainly because a decrease of the machine compliance factor with time due to the gradual decease in specimen stiffness as illustrated in FIGURE 112.

- It was observed that controlling the strain directly from the on-specimen LVDTs is unsafe as the actuator strain can go too high as it attempts to transfer the assigned amount of strain to the specimen and especially when the machine compliance factor is high. Another issue is that the shape of the load and strain waveform became distorted as the final strain wave was based on the average of the four on-specimen LVDTs (FIGURE 113).

- Since it is important to maintain constant on-specimen strain and to ensure machine safety at the same time, it is recommended to perform a crosshead strain-controlled test and continuously adjust the wave form during the test. This can be done by having a continuous feedback between the actuator and the on-specimen LVDTs.
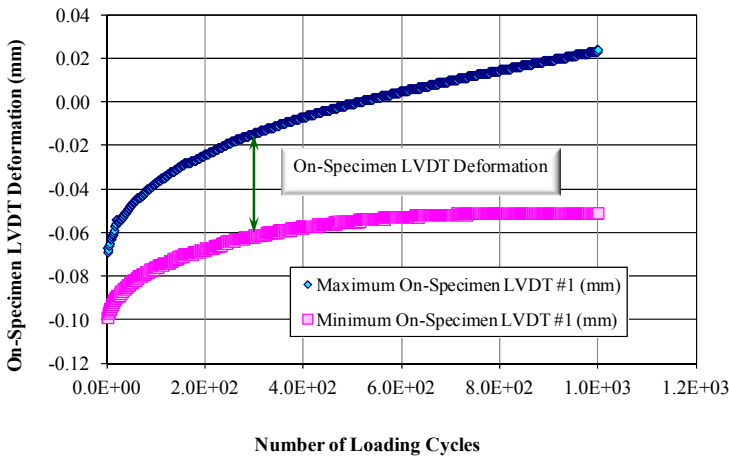
FIGURE 112 On-specimen LVDT deformation using crosshead controlled-strain test.
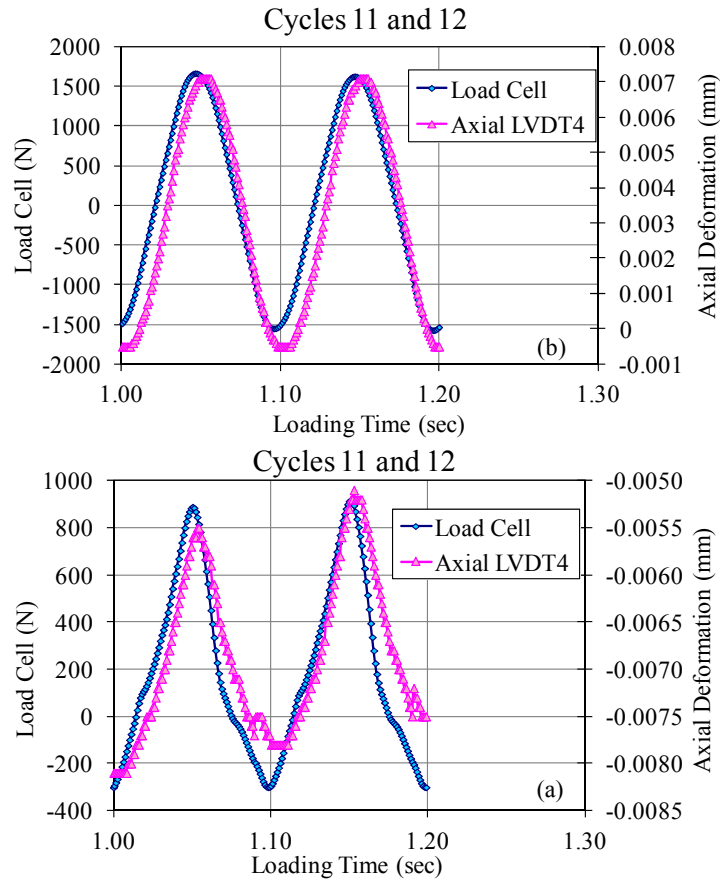
FIGURE 113 Comparison of waveform shape: (a) On-specimen LVDTs controlled- strain test, (b) crosshead controlled-strain test.

DEVELOPMENT OF ARIZONA STATE UNIVERSITY UNIAXIAL FATIGUE TEST SOFTWARE

Since the beginning of this research, it was obvious that running the uniaxial fatigue test presented a big challenge because of the unavailability of the proper commercial software and the limited literature on hardware setup, test parameters, test procedure, and data acquisition system. After conducting several preliminary studies as discussed above, most of the issues regarding the uniaxial fatigue test were solved except two. The first issue was that none of the available software was able to conduct the tension-compression fatigue test with rest period inserted after each loading cycle. The second issue was the ability to maintain the target value of the on-specimen LVDT strain constant during the test.

Through a collaborating effort, IPC Company delivered two new software programs. The first was developed to run the test without rest period so that it can achieve the target on-specimen strain value and to keep it constant throughout the entire test. This issue was critical to determining the endurance limit. The second program developed for this study ensured that the test conducted with the rest period had identical features to that of the test with rest period.

Software without Rest Period

IPC developed the software without rest period by modifying and adding additional features to the NCSU software discussed above. The software is designated "UTS-032 V1.01b S-VECD Fatigue Test" and has these main features:

- The software is capable of running both the direct tension and the tension-compression uniaxial fatigue tests.
- The software is capable of conducting the test by controlling either the actuator strain or the on-specimen LVDT strain.
- The software is able to run a test up to 999,999,999 loading cycles.
- The test can be stopped according to three different criteria that can be used separately or together (number of loading cycles, stiffness reduction percent, and adaptive strain control limit factor).
- The software is capable of saving the dynamic raw data file for the saved loading cycles.
- The software allows for a varying number of LVDTs (2 to 4).
- The software has a fingerprint test to evaluate the variability between replicates.
- The saved output data can be used for the viscoelastic continuum damage analysis as well as the reduced cycle analysis.

At the beginning, a few tests were conducted to check out the applicability of the software for the test without rest period. It was clear from the first test that the software was able to achieve the target on-specimen strains within a few seconds from the beginning of the test by correcting the actuator strain. The amount of actuator strain correction at the beginning depends on the proximity of the seed dynamic modulus value required by the software to the actual or measured value. The estimated input dynamic modulus value helps the software determine the initial stress value to be applied. The actuator correction (iteration) procedure is achieved through the adaptive strain control (ASC) option in the software.

As the test proceeds, the specimen stiffness reduces with time due to fatigue damage which, in turn, decreases the machine compliance factor and increases the average on-specimen strain compared to the target value. To resolve this issue, the software uses the ASC option to readjust the actuator displacement every 10 cycles to keep the target on-specimen strain constant. FIGURE 114 shows typical relationships of the actuator and on-specimens strain values over time. It can be seen that the actuator strain values decrease over time in order to keep the target on-specimen strain values constant.
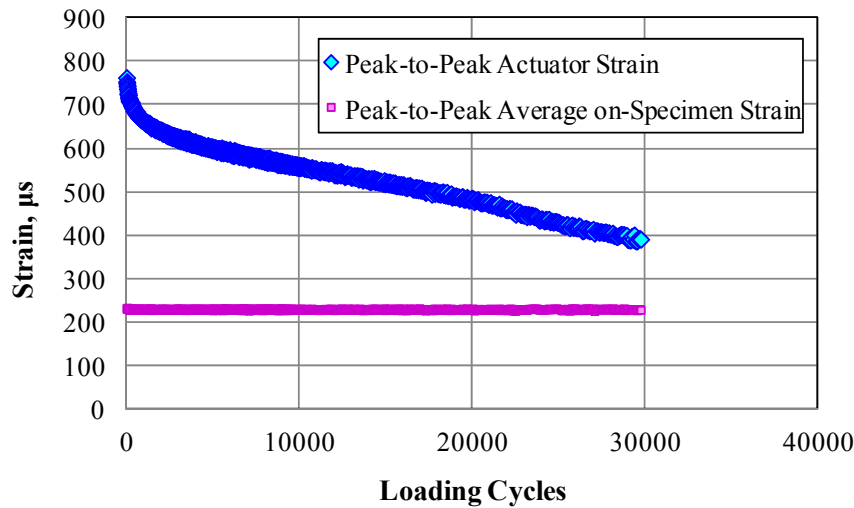
FIGURE 114 Typical actuator and average on-specimen strain over time relationships for test without rest period.

Software with Rest Period

After detailed discussion with the IPC and numerous trials, IPC determined that it was practically impossible to combine the software with and without rest period and that separate software for the test with rest period was needed. The software without a rest period performs a sinusoidal "best fit" of the test data using a prototype equation based on a sinusoidal function. This is basically the approach used in the AASHTO T 342 and PP 61protocols. This best fit was applied over five continuous sine waves dynamically. From this best fit equation, the amplitude and phase angle were determined. Therefore, the best fit technique cannot be applied in the case of rest periods as the sinusoidal wave shape will be broken by straight lines representing the rest periods as shown in FIGURE 115.

To resolve this problem, IPC produced IPC a separate software program incorporating a rest period, which is designated as "UTS-320 V1.00b S-VECD Fatigue Test with Rest Period," and has these main features:

- The software is capable of running the tension-compression uniaxial fatigue tests, but not the direct-tension test.
- The software is capable of conducting the test by controlling either the actuator strain or the on-specimen LVDTs strain.
- The software is able to run a test up to 999,999,999 loading cycles.
- Software is able to apply rest periods ranging from 0 to 10 seconds.
- The test can be stopped according to three different criteria that can be used separately or together (number of loading cycles, stiffness reduction percent, and adaptive strain control limit factor).
- The software is able to save a dynamic raw data file for the saved loading cycles.
- The software allows for a varying number of LVDTs (2 to 4).
- The software has a fingerprint test to evaluate the variability between replicates.

168

- The saved output data can be used for the viscoelastic continuum damage analysis as well as the reduced cycle analysis.
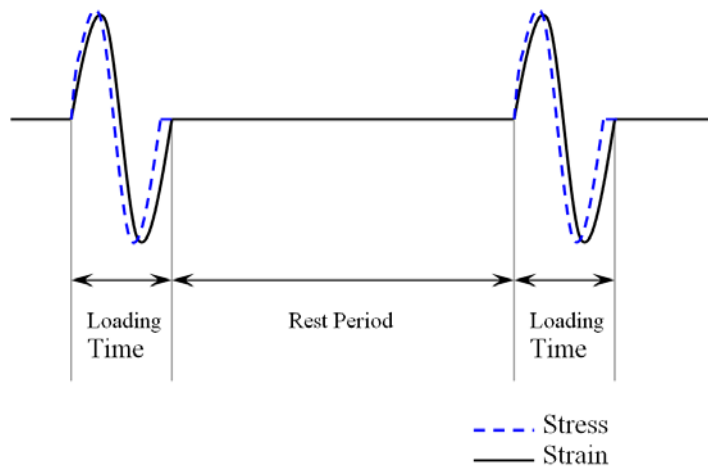
FIGURE 115 Uniaxial tension-compression fatigue test with rest period.

It was determined that the software with rest period was able to reach the target on-specimen strain and to maintain this value over time as shown in FIGURE 116. To capture the real healing due to the rest period, it is very important to insure that the specimen is not subjected to any load during the rest period. One great advantage of that software is that loads and deformations can be recorded not only during the loading time but also during the rest period. These output data were used to check if there is any remaining stress applied on the specimen during the rest period due to the viscoelastic nature of the HMA mixture, thus subjecting the specimen to damage during the rest period. FIGURE 117 illustrates that the software releases any loads or stresses from the specimen during the rest time so that the load is almost zero during that interval.
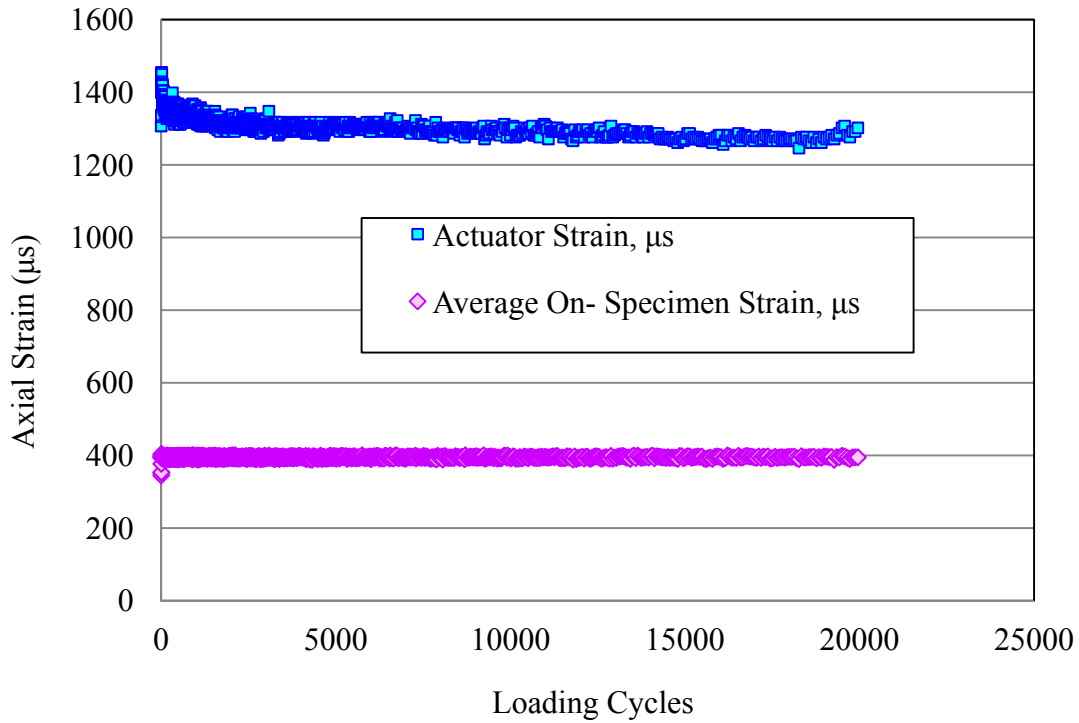
FIGURE 116 Average on-specimen strain and actuator strain over time relationships for test with rest period.
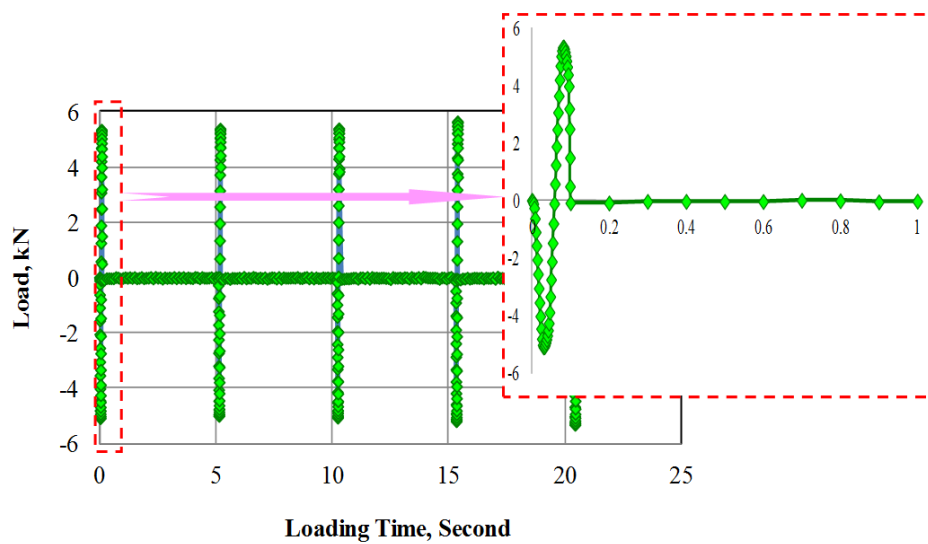
FIGURE 117 Load cell during loading and rest time with a close up of one loading cycle.

170

WHY THE TENSION-COMPRESSION FATIGUE TEST?

Uniaxial tension-compression test was proposed for this research as a fatigue test instead of the uniaxial direct tension test to validate the endurance limit for HMA. The main reason was the results of previous studies as shown in FIGURE 118 (Daniel and Kim, 2002). In case of the direct tension test, the specimen tends to accumulate a significant amount of permanent deformation during the test as the specimen is pulled in only one direction. It was anticipated that the tension-compression fatigue test would decrease the amount of permanent deformation significantly compared to the direct tension fatigue test.
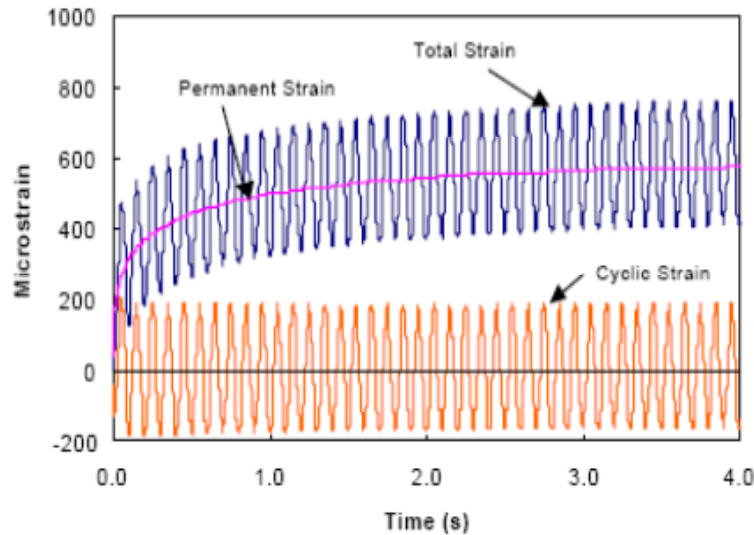
FIGURE 118 Total, permanent, and cyclic strain for cyclic direct tension fatigue test (Daniel and Kim, 2002).

To evaluate the behavior of asphalt concrete mixture in the uniaxial fatigue test in case of direct tension versus tension-compression conditions, two replicates (5.2% AC and 9.5% Va) were tested under each condition using the software for the test without rest period. Both uniaxial fatigue tests were conducted at 70°F (21.1°C) using a peak to peak on-specimen strain of 310 µs.
FIGURE 119 shows the actuator deformation over time for both direct tension and tension-compression uniaxial fatigue tests. It can be observed that there is no difference between wave amplitude for both tests as the two specimens belong to the same mixture. The only difference arose in the wave shape that is haversine in case of direct-tension and sinusoidal for tension-compression test. Examining the on-specimen deformation or strain, it was clear that the specimen exhibited permanent deformation at the beginning for the direct tension test before it disappeared after about 10 loading cycles. At the same time, the tension-compression test showed some minimal permanent deformation (FIGURE 120), as expected from the fact that the behavior of HMA in tension is slightly different than that in compression, with the asphalt concrete mixture strained in tension slightly more than in compression (Kallas, 1970).
To further understand this behavior, the wave shape of the applied stress for both tests over time was plotted in FIGURE 121. It is obvious that the stress wave shape in case of the

direct tension test changed very quickly after only about 10 cycles from haversine to sinusoidal which seems to be the equilibrium condition for the asphalt mixture. The main reason for that is the permanent deformation that the specimen experienced over the first 10 cycles which increased the height of the specimen and shifted the neutral axis of the stress wave to sinusoidal. This shift would cause erroneous fatigue results as the amplitude of the tensile stress and strain are considered to be the peak-to-peak values in case of direct-tension fatigue test. However, the actual direct-tension test results showed that only half of the peak-to-peak stress and strain are in tension. For the tension-compression test, it was observed that the stress wave shape remained the same as sinusoidal.

Based on these outcomes, the tension-compression test was selected instead of the direct tension, as the direct tension test switched to tension-compression due to the viscoelastic behavior of the asphalt mixture. For the strain-controlled uniaxial fatigue test, it is not possible to maintain the haversine test condition, which quickly switches to a sinusoidal wave shape. This conclusion was also supported by previous studies with the beam fatigue test (Pronk et al., 2010 and Mamlouk et al., 2012).
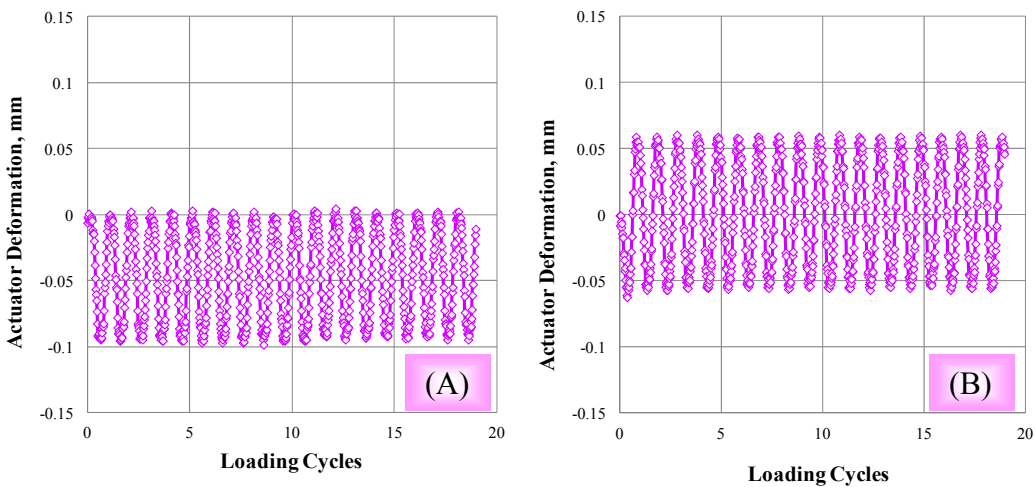
FIGURE 119 Actuator deformation wave shape over time: (A) direct tension and (B) tension-compression.

172
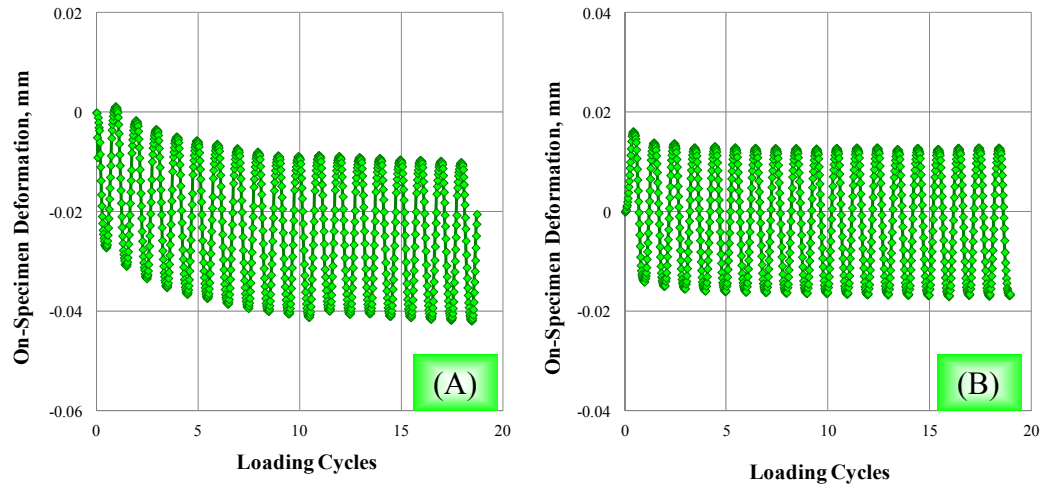
FIGURE 120 On-specimen deformation wave shape over time: (A) direct tension and (B) tension-compression.
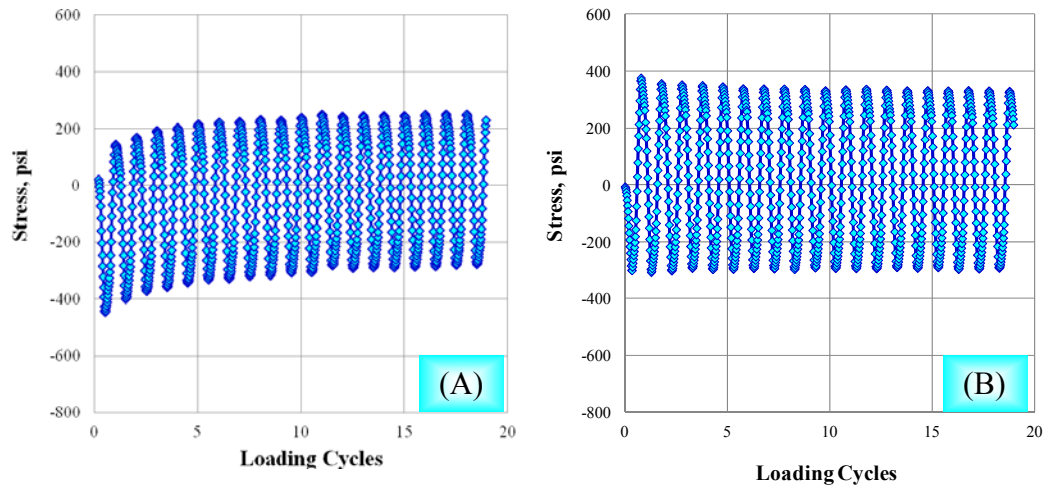
FIGURE 121 Stress wave shape over time: (A) direct tension and (B) tension-compression.

173

CHAPTER 7

ENDURANCE LIMIT METHODOLOGY AND RESULTS OF EXPERIMENTS

BACKGROUND

Many recent studies shown that HMA mixtures exhibit an endurance limit. All these studies are based on the concept that the endurance limit is a strain level below which there is no cumulative fatigue damage, or that the HMA will last for an indefinite number of load cycles. The methodology proposed herein to study the endurance limit is based on the phenomenon of fatigue damage healing. The endurance limit in this situation does not reflect an absence of HMA fatigue damage, but it represents a state where there is a balance of damage induced by loading and healing, or damage recovery that occurs during rest periods. Thus, the endurance limit for HMA is, typically, not a single value, but it will change depending on the material properties, traffic loading, and environmental conditions.

METHODOLOGY DEVELOPMENT

As mentioned earlier, the methodology developed for predicting the HMA endurance limit is based mainly on fatigue healing using viscoelastic and continuum damage analysis. To evaluate the fatigue healing, two uniaxial tension-compression fatigue tests were conducted. The first test was conducted under continuous loading and is referred to as the test without rest period. The second test introduced rest periods between loading cycles and is referred to as the test with rest period. The inclusion of the rest periods lessens the deterioration of the stiffness through partial healing of fatigue damage. That is, the stiffness tends to deteriorate at a slower rate compared to the test without rest period.

Based on the above, the healing of fatigue damage is expressed as a healing ratio difference (HRD), which is expressed as the mathematical difference between the pseudo stiffness ratios of the tests without and with rest period at a certain loading cycle, N. The main advantage of using the pseudo stiffness is to separate healing caused by cracks re-bonding from time-dependant healing due to the material relaxation or viscoelasticity. FIGURE 122 shows Pseudo Stiffness Ratio (PSR) versus time relationship for two tests conducted using 0 and 5 seconds rest periods. Because the initial pseudo stiffness varies between replicates, the PSR is used. The PSR is the pseudo stiffness value at any cycle (PS_n) normalized to the initial stiffness (PS_o), the stiffness value at the initial cycle number.

$$PSR_n = PS_n/PS_o \qquad (106)$$

To determine the effect of applying rest period, two different healing parameters are measured. The first healing parameter is the healing ratio difference (HRD), which is simply the arithmetic difference between the stiffness ratios with and without rest period measured at any number of cycles.

$$HRD = PSR_{WRP} - PSR_{W/ORP} \qquad (107)$$

where,

PSR_{WRP}= Pseudo stiffness ratio with rest period at loading cycle N, and

$PSR_{W/ORP}$= Pseudo stiffness ratio without rest period at the same N.

The other healing parameter is the healing index (HI), which is the healing ratio difference divided by full healing $(1 - SR_{W/ORP})$.

$$HI = (PSR_{WRP} - PSR_{W/ORP})/(1 - PSR_{W/ORP}) \tag{108}$$
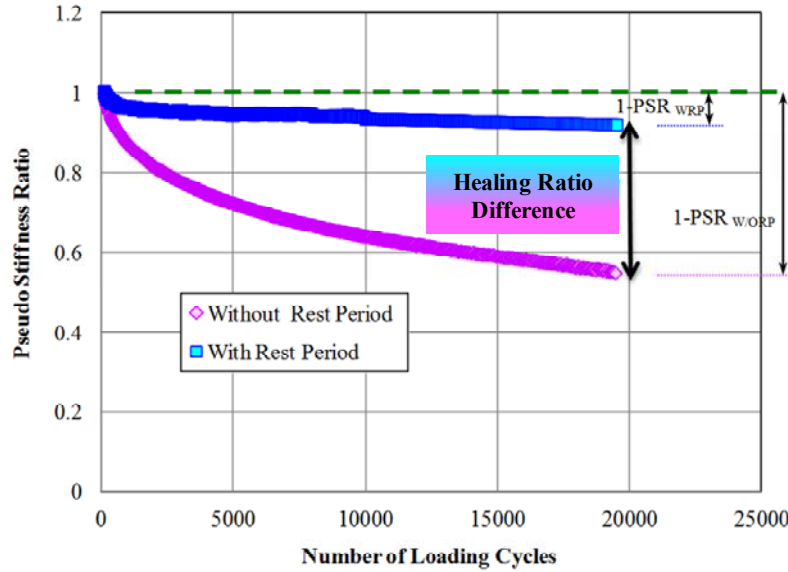
FIGURE 122 Pseudo stiffness ratio versus time relationship for with and without tests.

Note that several definitions of the healing index (HI) are available in the literature. For example, the HI defined in this uniaxial fatigue study is different from that defined in the beam fatigue study described in Appendix 1 (Souliman, 2012).

As mentioned previously, the design of experiment for the uniaxial tension-compression test main experiment consisted of five main factors. The partial factorial design required 32 different combinations to be tested with 3 replicates for each combination. This design would require a total of 96 tests. The experimental factors are as follows:

➢ Binder content (2 levels: 4.2, 5.2 %)
➢ Air voids (2 levels: 4.5, 9.5 %)
➢ Strain Level (2 levels: medium to fail the specimen at 20,000 cycles and low to fail the specimen at 100,000 cycles for the tests without rest period). (Note that a high strain level was added as discussed below)
➢ Temperature (3 levels: 40, 70, 100°F)
➢ Rest period (2 levels: 0, 5 sec)

To determine the strain levels at different temperatures that correspond to the two levels of $N_{f\ W/ORP}$, fatigue tests were performed for the four asphalt mixtures at the three temperatures of 40, 70 and 100°F as shown in FIGURE 123. These fatigue curves were used to determine the recommended strain levels at each temperature. The criterion for selecting the two strain levels at each temperature was to reach an N_f value (for tests without rest period) of 20,000 and 100,000 cycles at the medium and low strain levels, respectively. For the fatigue tests with rest period, all the tests were stopped at 20,000 cycles because of time limitations. The test would take 50 times longer to reach $N_{fw\ RP}$ due to incorporation of the rest period between loading cycles. . In

addition, it was anticipated that the $N_{f\,WRP}$ would be much higher than that without rest period due to the damage healing.
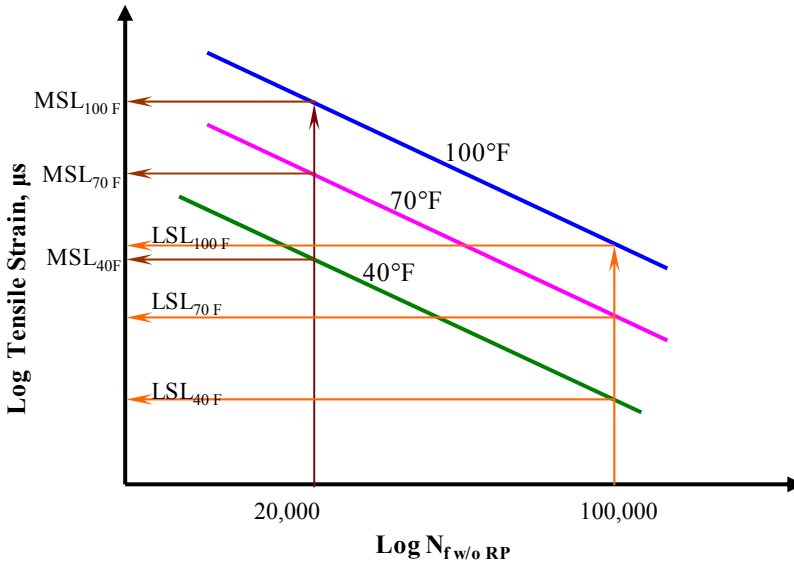
FIGURE 123 Determination of the high and low strain levels at each temperature.

Determination of Fatigue Endurance Limit

The first step in calculating the fatigue endurance limit was to determine the PSR values for the main experiment combinations. A regression model was then established to correlate PSR to the five factors. The PSR model can take the following form:

$$PSR = a_0 + a_1\,T + a_2\,AC + a_3\,Va + a_4\,\varepsilon_t + A_5\,RP + A_6\,N$$
$$+ \text{2-factor interactions} \qquad\qquad (109)$$

where

- PSR = Pseudo stiffness ratio
- $a_o, a_1 \ldots a_n$ = Regression coefficients
- AC = Percent asphalt content
- Va = Percent air voids
- RP = Rest period (sec)
- T = Temperature (°F)
- ε_t = Tensile Strain, μs
- N = Number of loading cycles

To consider the nonlinear effect of N on the PSR value, several PSR values were measured at different N along the same PSR-Time relationship. As the tests with rest period are more of interest in the calculation of the endurance limit, PSR values were selected at four N values for this test. For the test without rest period, only one PSR value was considered, which is that at failure where PSR is equal to 0.5 (FIGURE 124). This arrangement would also help reduce the regression model bias toward the tests conducted at zero rest periods as it represents

176

almost 50% of the tests, with tests with 1, 5, and 10 second rest periods representing the rest of the overall tests. It also prevents overlap of the PSR ranges for tests with and without rest periods and provides a better regression model.
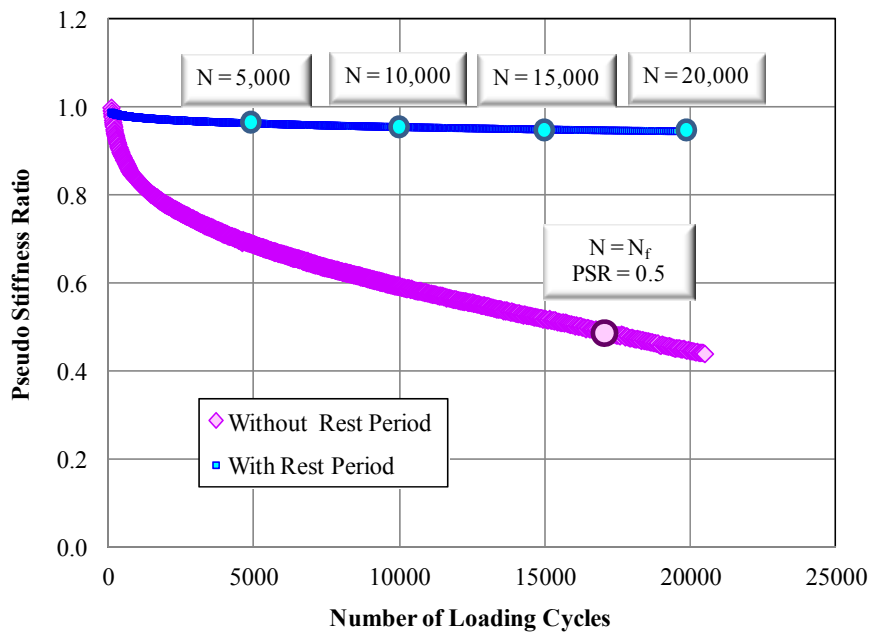
FIGURE 124 Pseudo stiffness ratio at four different numbers of cycles.

Two methods can be followed to determine the fatigue endurance limit. The first method uses the HI parameter while the second uses the PSR regression model.

Healing Index Method

The first step in this method is to calculate the HI values for all test combinations (i.e., at different tensile strains and temperatures). HI can be calculated by running the regression model for each test combination two times. On the first run $PSR_{W/ORP}$ is calculated using a rest period value equal to zero. On the second run, $PSR_{W/ORP}$ is calculated using a specific rest period value for the same test condition and volumetric properties. The second step is to plot the HI values versus the tensile strain at each temperature and for each mixture type. This is done in anticipation of having different endurance limit values for each mixture at each temperature. The expected relationship between the strain level and the HI is shown in FIGURE 125. In the figure, the HI values increases as the tensile strain decreases. Because the main experiment has only two strain levels, the HI-tensile strain relationships must be assumed to be linear.
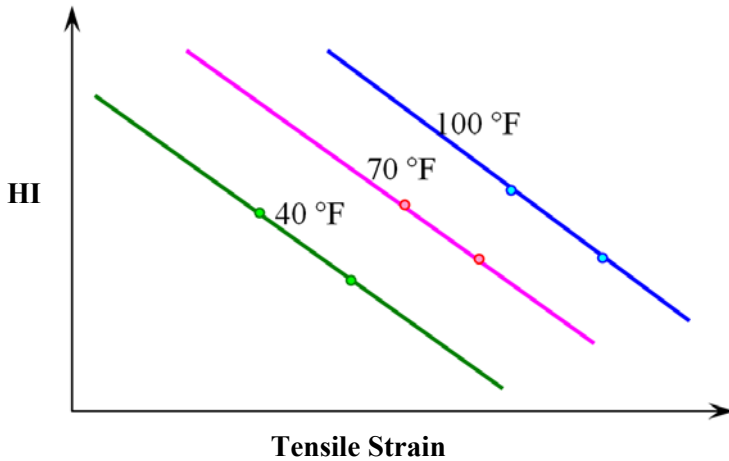
FIGURE 125 Healing parameters versus strain levels at different temperatures.

As proposed, the endurance limit will occur when complete healing happens during the rest period. In this case, the endurance limit is estimated at an HI value of 1.0, as the PSR_{WRP} is equal to 1.0, which is the healing ratio at no damage with rest period (FIGURE 126). This method can be used for any mixture even without using the PSR regression model, as long as the mixture is tested at at least two strain levels, with and without rest periods, and at a certain temperature. This analysis is usually done at a single N value. If the N value is considered as the number of cycles until failure for the test without rest period ($N_{fW/ORP}$), the $PSR_{W/ORP}$ will be equal to 0.5. In this case, the endurance limit can be determined at HRD = 0.5, with HRD plotted against the tensile strain instead of the healing index as the PSR_{WRP} is equal to 1.0 (HRD = 1.0 - 0.5 = 0.5).
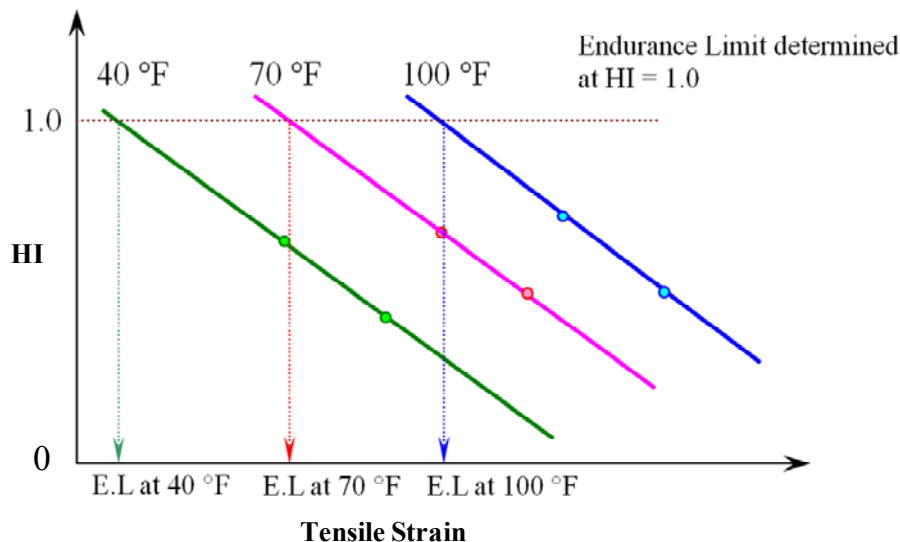
FIGURE 126 Determination of endurance limit at each temperature using HI parameter.

178

Pseudo Stiffness Ratio Method

This method depends on using the PSR regression model to calculate the PSR values at two different strain levels for the same test conditions, same volumetric properties, and any rest period. For any values of rest period and N, the PSR is expected to decrease as the strain level increases (FIGURE 127). The endurance limit in this case can be defined as the strain level where the PSR equals 1.0, when the relationship between the PSR and the strain level is plotted as shown in FIGURE 128. This method is recommended when a PSR regression model is established for the nonlinear effect between N and PSR. The power of this method is that, for the endurance limit case, PSR is independent of N as the PSR is equal to 1.0 at any value of N. A second advantage is that this method can be used to determine the value of EL for the continuous test condition. Based on this discussion, the second method was adopted for this study as a regression model can be developed over a reasonable range of volumetric properties, rest periods, and strain values.
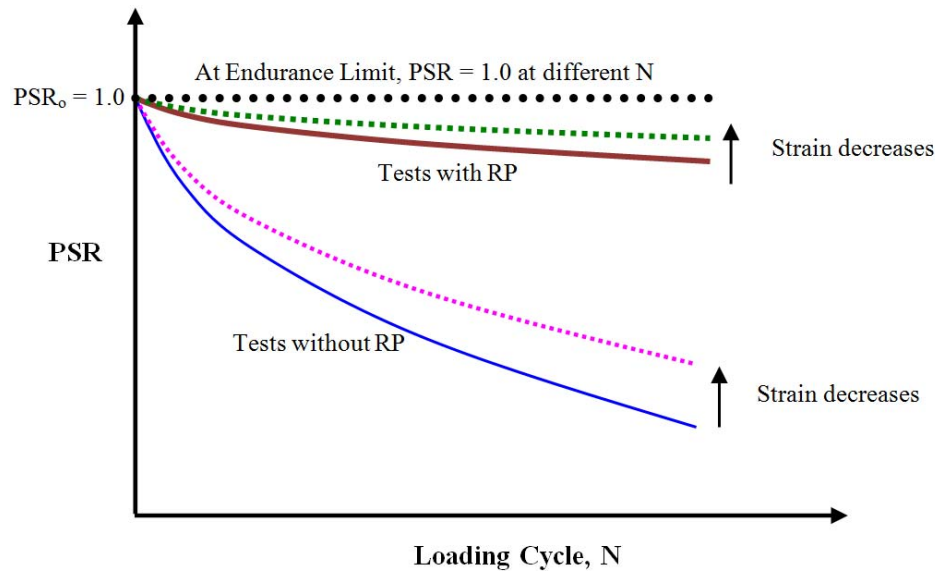
FIGURE 127 Effect of strain and rest period of the PSR as a function of the loading cycles.
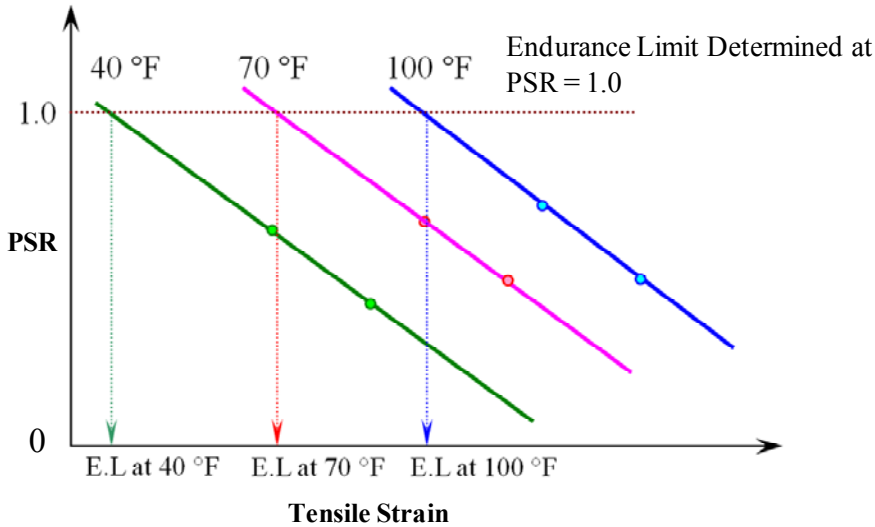
FIGURE 128 Determination of endurance limit at each temperature using PSR parameter.

Effect of Different Strain Levels and Rest Periods

As only two strain levels were considered in this study, the relationship between the HI and the strain levels must be assumed to be linear, though the true relationship may not be. The same assumption must be made for the rest period as only two rest periods were applied (0 and 5 seconds). As was mentioned in Chapter 2, the rest period may not have a significant effect on the fatigue life or healing parameters past a certain value as is shown in FIGURE 129. Therefore, the relationship between the PSR and the rest period is not linear and it is important to conduct additional tests at different rest periods to validate the true relationship. For the additional tests, another strain level (high) and two more rest periods (1 and 10 seconds) were added. The selection of the required combinations is justified using a fractional factorial statistical technique considering two levels of interaction. Based on this factorial design, 18 more combinations were required for testing. The regression analysis was repeated again by compiling the whole dataset to get an integrated regression model that accounts for the nonlinear effect of strain level and rest period.
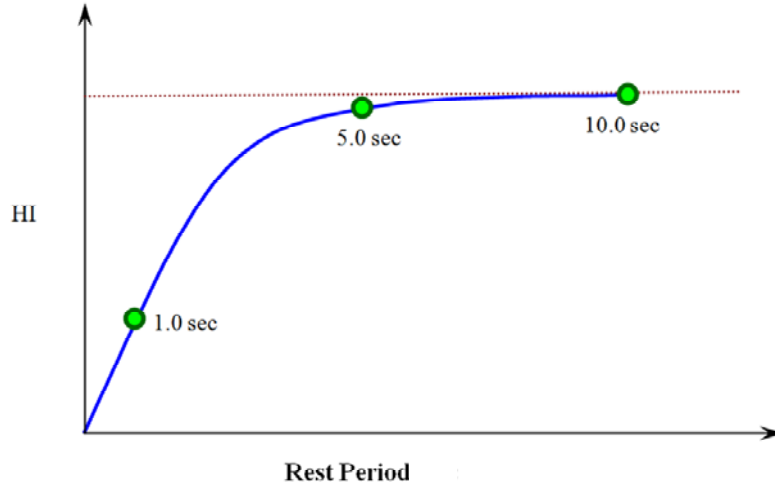
FIGURE 129 Expected rest period versus healing parameters relationship.

DETERMINATION OF PSEUDO STIFFNESS

The calculation of the pseudo stiffness (PS) requires the calculation of pseudo strain (ε^R). The pseudo strain can be calculated rigorously using Equation 110, where ε is the measured strain, $E(t)$ is the linear viscoelastic relaxation modulus, and E_R is the reference modulus (typically taken as 1) used for dimensional compatibility (Schapery, 1984). Equation 110 was used to calculate the pseudo strain for the first loading cycle.

$$\varepsilon^R = \frac{1}{E_R} \int_0^t E(t-\tau)\frac{d\varepsilon}{d\tau}d\tau \tag{110}$$

The pseudo strains for the rest of the loading cycles were calculated using Equation 111 proposed by Kim et al. (2003) using a simplified approach for the steady-state assumption to calculate the pseudo strain. This equation is based on the assumption that fatigue damage accumulates only under the tensile loading condition, the pseudo strain tension amplitude, $\varepsilon^R_{0,ta}$. In such conditions, the pseudo strain can be rigorously computed as the product of strain and dynamic modulus, $|E^*|_{LVE}$ (at temperature and frequency matching those of the test under investigation).

$$\left(\varepsilon^R_{0,ta}\right)_i = \frac{1}{E_R}\cdot\frac{\beta+1}{2}\left(\left(\varepsilon_{0,pp}\right)_i\cdot|E^*|_{LVE}\right) \tag{111}$$

where β is a factor used to quantify the duration that a given stress cycle is tensile (1 means always tensile, 0 means fully reversed loading and -1 means always compressive), and $\varepsilon_{0,pp}$ stands for the peak-to-peak strain amplitude.

Once the pseudo strain is calculated, the pseudo stiffness is calculated with Equation 112 using the pseudo strain as defined in Equations 110 and 111 (Underwood et al., 2010).

$$C = \begin{cases} \dfrac{\sigma}{\varepsilon^R \times DMR} & \textit{first cycle} \\[2ex] \dfrac{\sigma}{\varepsilon^R_{0,ta} \times DMR} & \textit{rest of cycles} \end{cases} \qquad (112)$$

where the DMR is the dynamic modular ratio to account for specimen-to-specimen variability (Underwood et al., 2010) and is defined as shown in Equation 113. In this equation $|E^*|_{LVE}$ is the linear viscoelastic dynamic modulus of the material at the particular temperature and frequency of the test; it can be determined from $|E^*|$ master curve. $|E^*|_{fp}$ is the fingerprint dynamic modulus that is measured from a fingerprint experiment which is performed before the uniaxial fatigue test.

$$DMR = \frac{|E^*|_{fp}}{|E^*|_{LVE}} \qquad (113)$$

FATIGUE LIFE EXPERIMENT

Fatigue Failure Criterion

As discussed in Chapter 2, several criteria are available to define fatigue failure. Based on the results of the initial tests in this study, it was concluded that determining the fatigue life based on 50% reduction of the initial stiffness was feasible at the different test conditions, especially at different temperatures. On the other hand, using the phase angle relationship to determine the fatigue life (Reese, 1997) was not possible, especially for tests conducted at 100°F, as the point where the phase angle relationship has a sharp decrease is not found compared to tests conducted at 40 and 70°F (FIGURES 130 to 132).
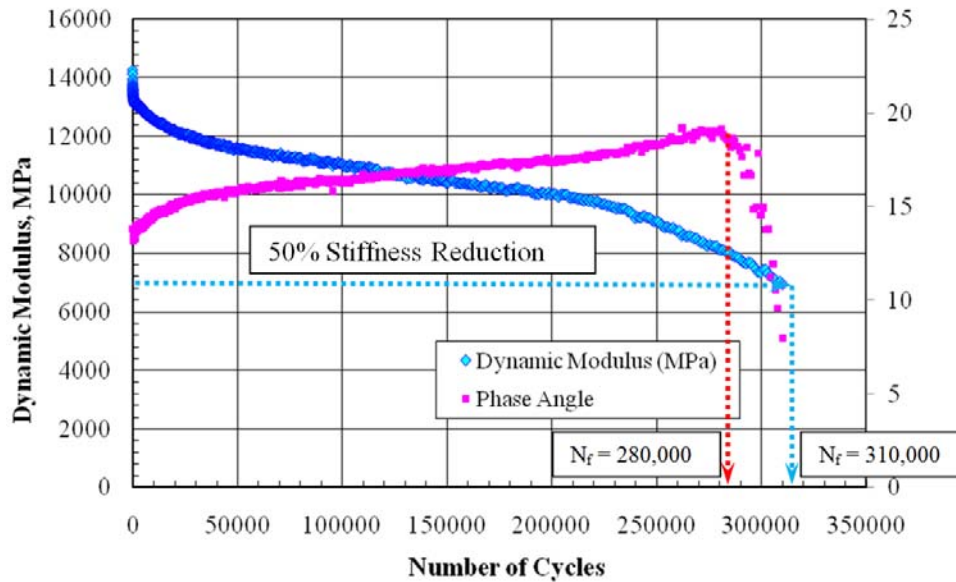
FIGURE 130 Typical phase angle versus loading cycle relationship at 40°F.

182
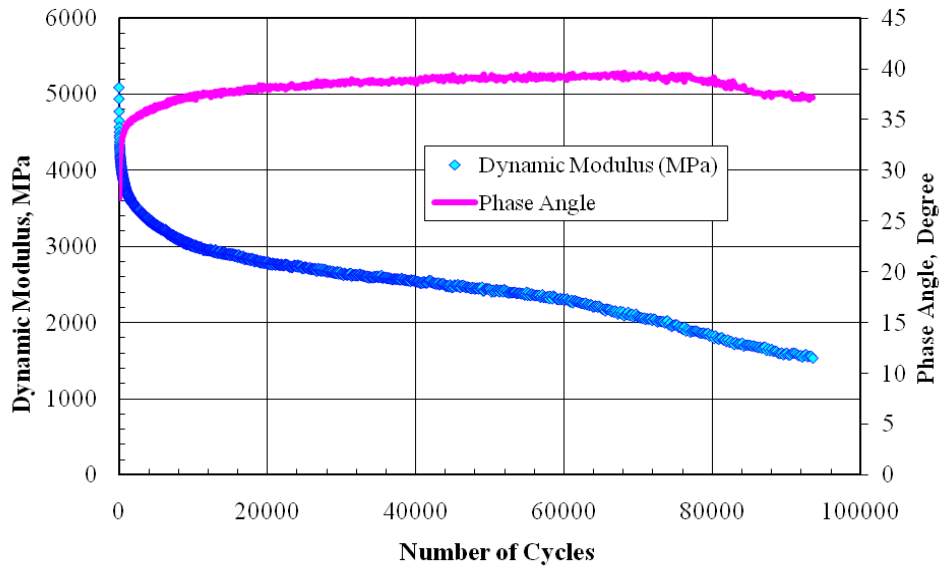
FIGURE 131 Typical phase angle versus loading cycle relationship at 70°F.
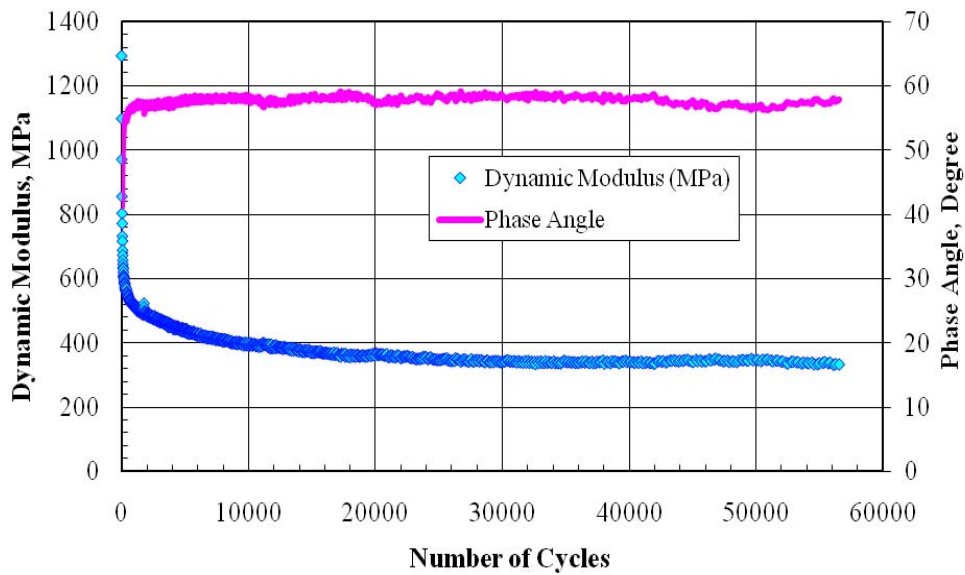
FIGURE 132 Typical phase angle versus loading cycle relationship at 100°F.

Definition of the Initial Number of Cycles

In this study, specimens were manufactured only at the optimum mix design conditions (4.7% asphalt content and 7% air voids). A series of tests without rest periods were conducted at

183

different strain levels at 40, 70 and 100°F. The 50% reduction in the initial stiffness criterion was used to determine the fatigue lives for the different test conditions.

As per AASHTO T 321, the initial stiffness is the stiffness at the 50th cycle for the beam fatigue test. Consequently, the fatigue life values were initially calculated using initial stiffness at the 50th cycle. It was noticed that there is a significant drop of stiffness at the beginning of tests conducted at 100°F compared to those conducted at 40 and 70°F as shown previously in FIGURES 130 to 132. This means that using the stiffness at the 50th cycle as an initial stiffness at 100°F will notably decrease the calculated fatigue life. For that reason, two different initial numbers of cycles were investigated.

Fatigue analysis using initial stiffness values at both the 50th and the 100th cycles are illustrated in FIGURES 133 and 134, respectively. The fitting of fatigue life at 100°F improved significantly using the initial stiffness at the 100th cycle compared to the 50th cycle. Therefore, the fatigue life determination in this research was based on an initial stiffness measured at the 100th cycle.
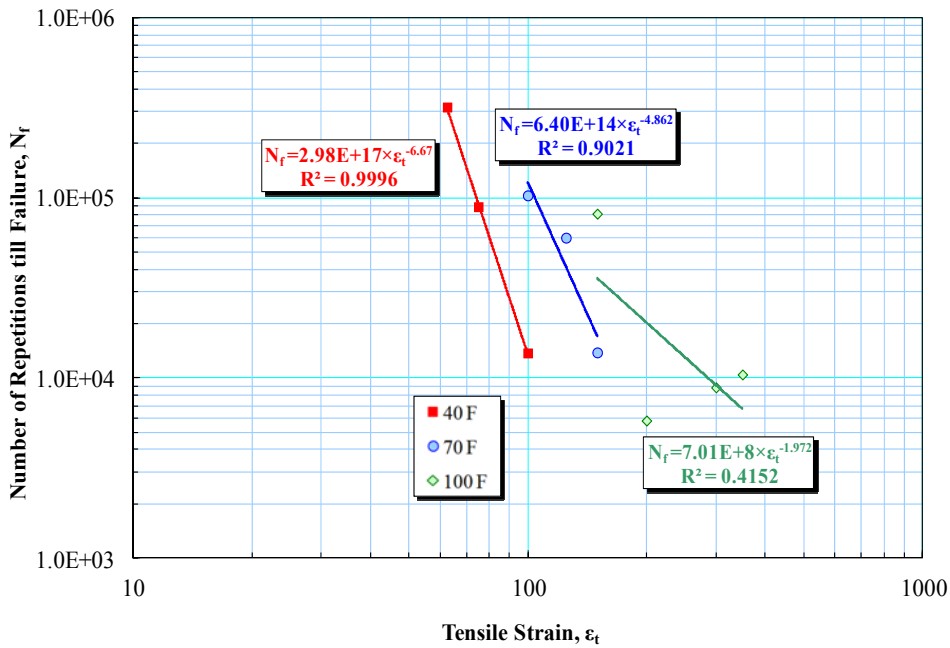
FIGURE 133 Fatigue lines at different temperatures using 50th cycle initial stiffness.

184

Legend:
- 40 F
- 70 F
- 100 F

$N_f = 1.17E+12 \times \varepsilon_t^{-3.162}$
$R^2 = 0.9623$

$N_f = 2.34E+17 \times \varepsilon_t^{-6.61}$
$R^2 = 0.9996$

$N_f = 1.11E+14 \times \varepsilon_t^{-4.45}$
$R^2 = 0.9459$

Y-axis: Number of Repetitions till Failure, N_f
X-axis: Tensile Strain, ε_t
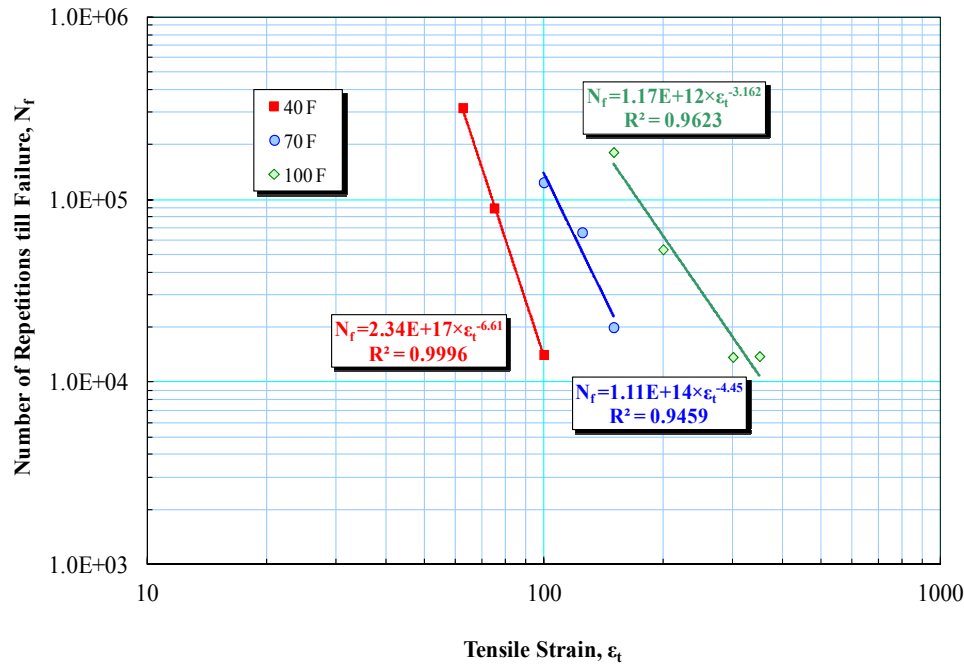
FIGURE 134 Fatigue lines at different temperatures using 100th cycle initial stiffness.

Fatigue Life Experiment Results

As stated earlier, the criterion for selecting the two strain levels at each temperature for the main experiment was to reach a fatigue life of 20,000 cycles for the medium strain level, and 100,000 cycles for the low strain level. To construct the fatigue lives for the four tested mixtures (4.2% AC & 4.5 %Va, 5.2% AC & 4.5 %Va, 4.2% AC & 9.5 %Va, and 5.2% AC & 9.5 %Va), three to four tests without rest period were conducted at different strain levels and temperatures. The results of the fingerprint as well as the uniaxial tension-compression fatigue tests are tabulated for the four mixtures in TABLES 42 to 45.

TABLE 42 Fingerprint and uniaxial fatigue tests results at 9.5% Va and 4.2% AC

Temp (°F)	Specimen ID	Air Voids (%)	Peak to Peak Strain (μs)	Tensile Strain (μs)	FP Modulus (psi)	Phase Angle φ Degree	MCF	Initial Stiffness (psi)	Initial φ Degree	Cycles to Failure (Nf)
100	D-960	10.28	300	150.0	141,890	34.8	2.25	83,194	51.7	469,540
	D-962	9.28	450	225.0	152,300	31.4	2.10	70,546	50.3	32,030
	D-964	9.49	350	175.0	164,200	38.0	2.03	86,892	49.1	168,530
	D-963	9.91	550	275.0	145,500	34.8	1.95	65,949	51.5	7,100
70	D-945	9.60	210	105.0	669,784	26.6	3.62	500,815	32.4	14,270
	D-946	9.22	175	87.5	648,028	27.5	3.50	514,739	29.9	94,770
	D-947	8.52	250	125.0	827,585	25.2	3.46	617,135	29.7	22,260
	D-951	9.31	200	100.0	724,318	25.4	3.90	596,830	29.0	84,000
	D-957	9.00	125	62.5	740,708	24.6	4.13	661,923	26.7	1,280,000
	D-955	9.26	200	100.0	638,746	24.0	3.20	539,540	27.9	73,570
40	D-959	9.65	150	75.0	1,936,543	13.0	12.92	1,701,002	13.5	17,920
	D-965	9.52	125	62.5	2,404,145	14.6	11.61	2,031,978	16.0	132,340
	D-968	9.31	175	87.5	1,589,613	13.2	7.88	1,355,087	14.0	10,500
	D-972	9.49	140	70.0	1,595,270	14.4	7.38	1,478,514	14.4	57,250

TABLE 43 Fingerprint and uniaxial fatigue tests results at 4.5% Va and 4.2% AC

Temp (°F)	Specimen ID	Air Voids (%)	Peak to Peak Strain (μs)	Tensile Strain (μs)	FP Modulus (psi)	Phase Angle φ Degree	MCF	Initial Stiffness (psi)	Initial φ Degree	Cycles to Failure (Nf)
100	D-406	4.63	350	175.0	316,617	41.6	2.46	147,895	53.1	184,080
	D-407	4.09	510	255.0	346,785	39.8	2.45	140,687	53.0	15,930
	D-408	4.56	350	175.0	321,259	31.9	2.30	163,167	48.2	261,000
	D-414	4.24	510	255.0	427,426	34.1	2.52	195,018	45.8	12,120
70	D-401	3.77	150	75.0	984,226	29.3	5.74	984,226	29.2	431,740
	D-402	4.72	290	145.0	1,101,996	28.5	5.29	851,154	31.3	9,070
	D-404	4.08	290	145.0	1,307,370	33.0	6.23	1,105,767	40.6	3,430
	D-405	4.33	210	105.0	1,333,332	31.9	6.03	1,020,630	31.5	26,300
	D-432	4.03	210	105.0	1,344,064	22.6	6.74	1,099,821	25.7	27,340
40	D-411	4.48	140	70.0	2,986,906	8.5	14.87	2,808,510	10.3	172,460
	D-412	4.84	190	95.0	2,573,694	9.3	11.89	2,393,992	10.5	9,470
	D-434	4.53	150	75.0	2,770,800	10.8	11.96	2,519,595	13.5	149,630
	D-435	4.49	175	87.5	2,801,548	13.7	14.83	2,498,274	14.3	23,000

TABLE 44 Fingerprint and uniaxial fatigue tests results at 9.5% Va and 5.2% AC

Temp (°F)	Specimen ID	Air Voids (%)	Peak to Peak Strain (µs)	Tensile Strain (µs)	FP Modulus (psi)	Phase Angle φ Degree	MCF	Initial Stiffness (psi)	Initial φ Degree	Cycles to Failure (N_f)
100	D+952	9.66	400	200.0	110,230	34.3	1.59	54,389	49.7	357,550
	D+956	9.77	500	250.0	107,210	30.3	1.78	52,591	51.0	74,140
	D+957	10.25	600	300.0	109,095	33.1	1.78	50,908	52.5	71,340
	D+953	10.37	700	350.0	99,694	37.1	1.76	41,959	53.2	13,560
70	D+943	9.52	190	95.0	516,624	28.3	2.85	409,296	31.4	372,300
	D+944	8.90	250	125.0	643,532	24.1	3.57	483,121	31.3	63,910
	D+948	9.34	400	200.0	613,219	26.8	3.93	356,938	36.3	4,070
	D+949	9.99	375	187.5	501,250	31.8	2.97	328,365	39.0	9,740
40	D+949	10.15	150	75.0	1,691,430	15.7	7.86	1,476,194	16.5	151,360
	D+959	9.10	200	100.0	1,443,415	12.2	7.92	1,332,316	13.6	53,760
	D+958	8.80	225	112.5	1,777,437	14.4	8.19	1,423,545	14.4	17380
	D+962	9.40	260	130.0	1,610,644	14.1	8.15	1,434,713	15.4	8,320

TABLE 45 Fingerprint and uniaxial fatigue tests results at 4.5% Va and 5.2% AC

Temp (°F)	Specimen ID	Air Voids (%)	Peak to Peak Strain (µs)	Tensile Strain (µs)	FP Modulus (psi)	Phase Angle φ Degree	MCF	Initial Stiffness (psi)	Initial φ Degree	Cycles to Failure (N_f)
100	D+432	4.57	300	150.0	220,457	35.8	1.99	103,412	51.0	460,610
	D+430	4.89	500	250.0	149,389	47.6	1.75	72,475	59.4	64,570
	D+438	3.99	900	450.0	201,167	45.7	1.77	79,597	58.2	8,810
	D+439	3.91	850	425.0	238,442	43.4	2.01	81,946	57.8	9,670
	D+440	4.46	400	200.0	157,656	49.8	1.74	94,420	57.0	245,470
70	D+402	3.46	210	105.0	1,038,905	28.2	4.80	842,988	31.2	218,000
	D+403	3.63	290	145.0	1,049,058	30.5	5.25	756,981	33.0	50,500
	D+404	3.37	350	175.0	924,035	30.2	4.41	670,669	34.3	30,000
	D+406	3.54	150	75.0	982,630	31.4	4.80	845,309	32.5	476,800
40	D+418	4.07	140	70.0	2,716,846	12.3	12.03	2,481,624	13.5	280,000
	D+419	4.32	140	70.0	2,341,489	10.7	10.86	2,319,385	10.8	135,420
	D+442	4.79	175	87.5	2,129,444	11.8	9.67	2,044,741	11.6	130,320
	D+443	4.20	200	100.0	2,440,549	12.8	14.21	2,164,253	12.7	74,710
	D+445	4.37	275	137.5	2,648,388	13.2	11.99	2,263,603	13.1	9,470

Based on the uniaxial fatigue test results for the four mixtures, the fatigue lives were determined at the three test temperatures (40, 70, and 100 ºF) as shown in FIGURES 135 to 138 The fatigue life at each temperature is represented by a linear relationship between the number of cycles to failure (N_f) and the applied tensile strain levels (ε_t) on a log-log scale. This relationship is represented by the form of Equation 114.

$$N_f = k_1 \times (1/\varepsilon_t)^{k_2} \tag{114}$$

where k_1 and k_2 are the intercept and slope of the fatigue life relationship, respectively, as was shown in FIGURES 135 to 138. It is noted that as the binder content increases, the k_2 value decreases. This means that adding more binder to the asphalt mixtures would reduce the fatigue deterioration of that mixture. On the other hand, the effect of air voids on k_2 values appears insignificant, especially at lower asphalt contents. At higher asphalt contents, it is clear that decreasing the air voids results in decreasing the k_2 values. Indeed, changing the asphalt content by 1% has more effect on the k_2 values than changing the air voids by 5%.
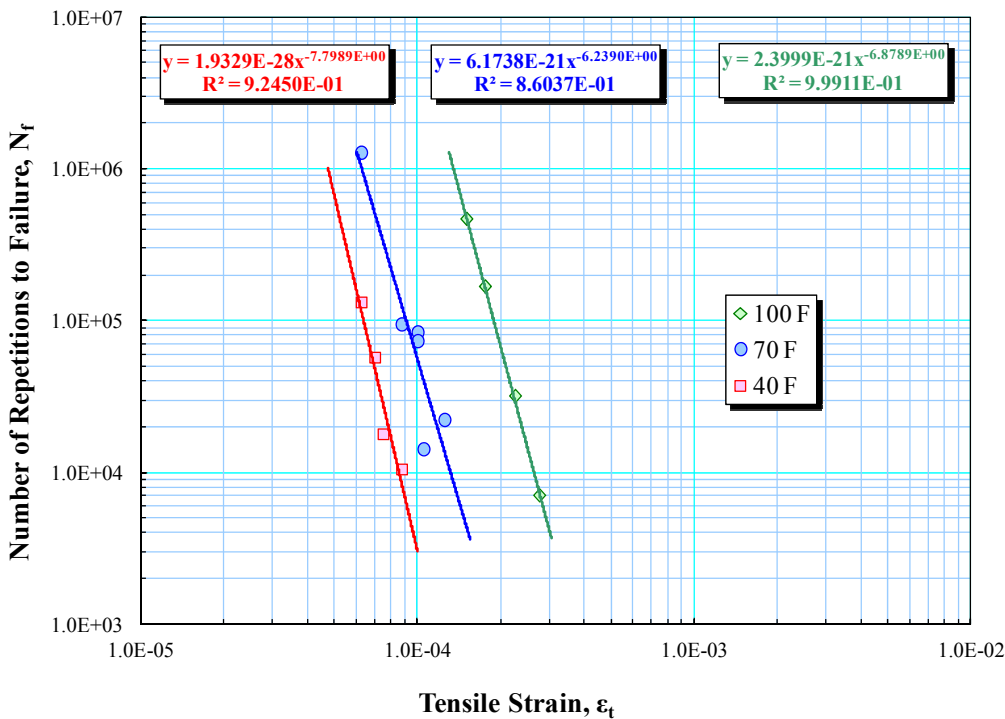
FIGURE 135 Fatigue lives at different temperatures (9.5% Va and 4.2% AC).
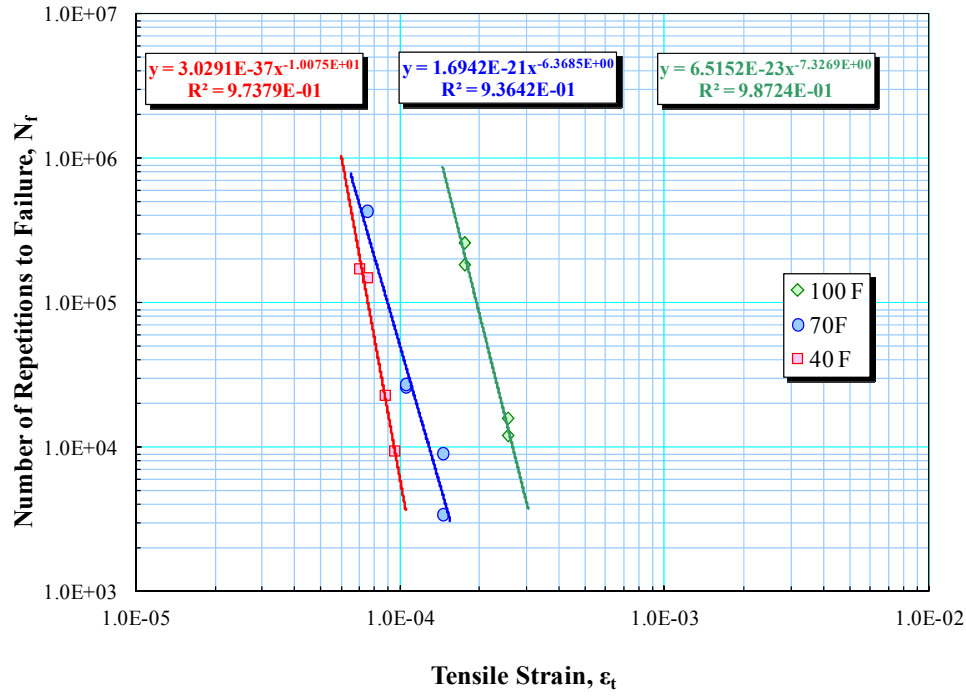
FIGURE 136 Fatigue lives at different temperatures (4.5% Va and 4.2% AC).
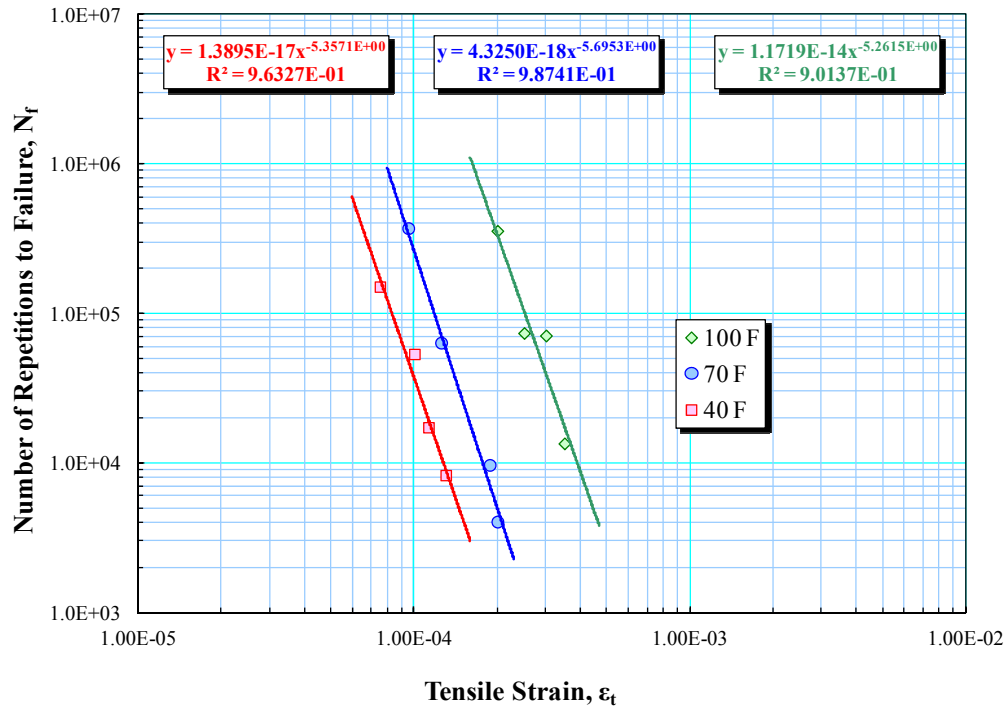
FIGURE 137 Fatigue lives at different temperatures (9.5% Va and 5.2% AC).
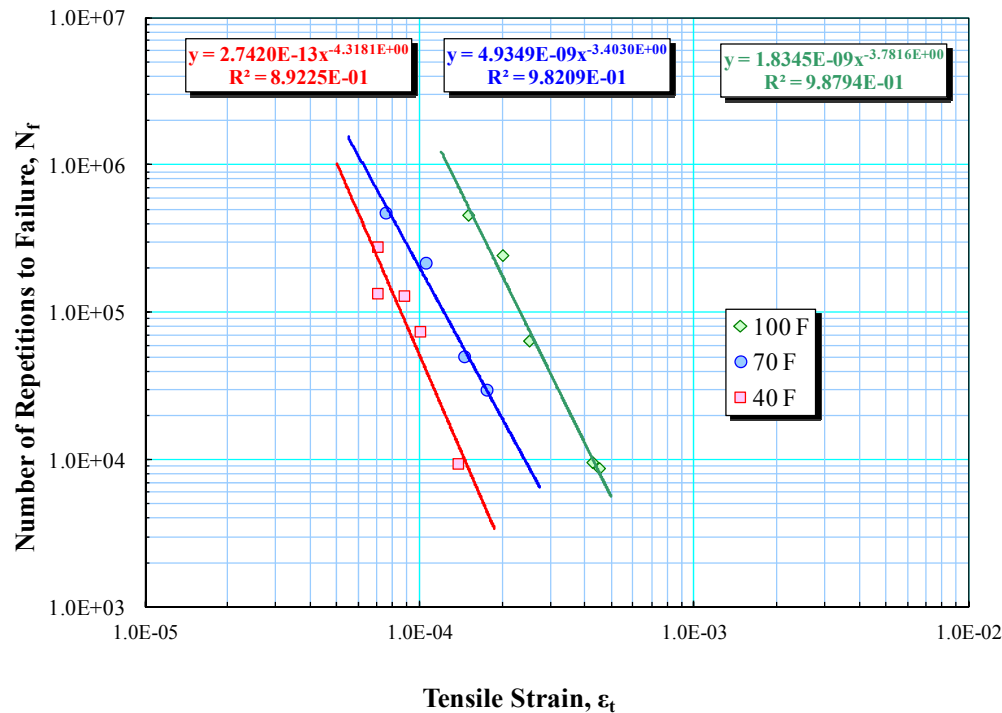
FIGURE 138 Fatigue lives at different temperatures (9.5% Va and 5.2% AC).

Using the k_1 and k_2 values, the low and medium strain levels at each temperature for the four mixtures were determined at fatigue lives of 100,000 and 20,000 loading cycles, respectively. TABLE 46 contains the low and medium strain levels at different temperatures for all mixtures.

The fatigue test results for each mixture at different test temperatures were used to generate the generalized fatigue model coefficients (k_1, k_2, and k_3) as in Equation 115.

$$N_f = k_1 \times (1/\varepsilon_t)^{k_2} \times (1/E)^{k_3} \tag{115}$$

where k_1, k_2, and k_3 are regression coefficients and E is the initial stiffness in psi. TABLE 47 shows the k_1, k_2, and k_3 values for the four mixtures. In addition, all the test results of the four mixtures were pooled together in one data set and used to get regression coefficients for all mixtures together (TABLE 47). It can be easily recognized that the lower the air voids, the lower the k_2 and k_3 values. Also, increasing the asphalt content reduces both k_2 and k_3 values. It can be concluded that high binder content and lower air voids increase the resistance of the asphalt mixture to fatigue damage, which agrees with previous fatigue research. All the generalized fatigue models showed excellent to good levels of goodness of fit measured by a coefficient of determination (R^2) ranging from 98.7% to 88.43% for the individual mixtures. When combining the test results for all the mixtures, the R^2 value was reduced slightly to 82.2%, which still shows a good level of prediction.

In order to evaluate the accuracy of the generalized fatigue models, the fatigue lives predicted from these models were compared to the corresponding measured values. FIGURE 139 shows a comparison of the measured to the predicted fatigue lives based on the individual models for each mixture while FIGURE 140 shows the same comparison using the all-data

190

model. As discussed earlier, the individual models showed better predictions as compared to the combined model. However, the combined data model very reasonably describes the behavior of the different mixtures. Thus, the effect of using different binder contents and air voids can be easily captured by considering their effect on the corresponding stiffness values, which are represented in the generalized fatigue model.

TABLE 46 Low and medium tensile strain values for all mixtures at different temperatures

Temp (°F)	4.2% AC				5.2% AC			
	9.5% Va		4.5% Va		9.5% Va		4.5% Va	
	Low (100,000)	Medium (20,000)	Low (100,000)	Medium (20,000)	Low (100,000)	Medium (20,000)	Low (100,000)	Medium (20,000)
100	187.5	237.5	195	242.5	252.5	342.5	232.5	357.5
70	90	115	90	115	112.5	155	122.5	197.5
40	62.5	80	70	87.5	82.5	112.5	85	112.5

TABLE 47 k_1, k_2 and k_3 values for each individual mixture and all mixtures together

Air voids Va (%)	Asphalt content AC (%)	k_1	k_2	k_3	R^2 (%)
9.5	4.2	2.901E-11	7.930	2.869	98.68
4.5	4.2	0.000514	4.599	1.674	88.43
9.5	5.2	1.682E-05	5.114	1.819	97.73
4.5	5.2	0.0424	3.172	1.016	93.19
All mixtures		1.246E-05	4.882	1.633	83.54

*$N_f = k_1 \times (1/\varepsilon_t E)^{k_2} \times (1/E)^{k_3}$
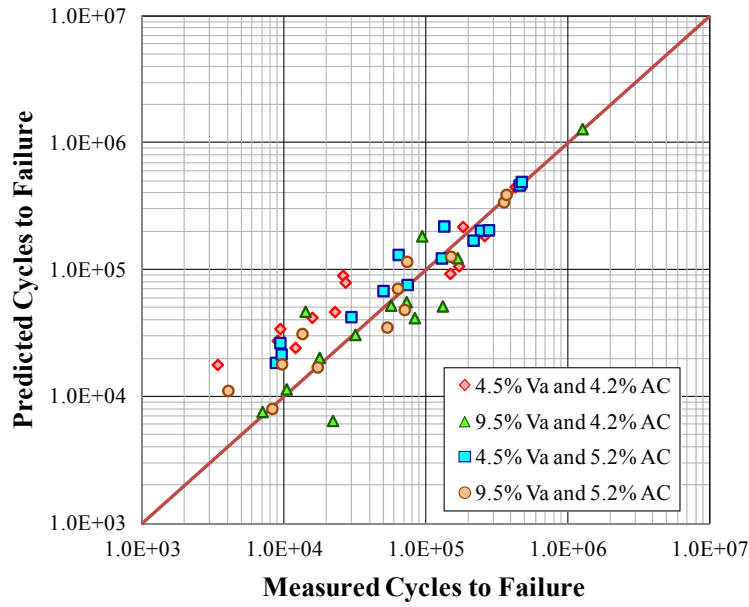
FIGURE 139 Measured versus predicted cycles to failure based on individual generalized fatigue models.
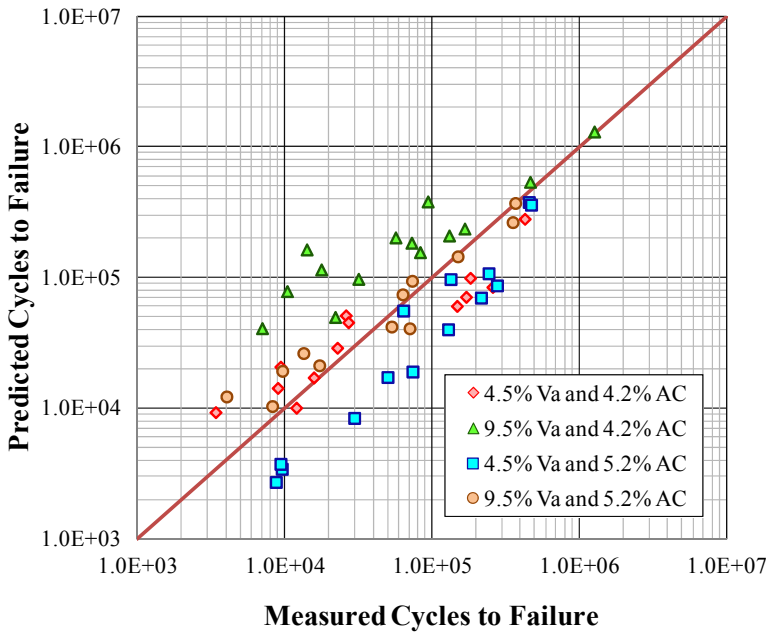
FIGURE 140   Measured versus predicted cycles to failure based on generalized fatigue model for all mixtures together.

Main Experiment Results

As explained earlier, the main objective of this experiment is to investigate the effect of five main factors on the fatigue damage and healing of HMA mixtures. These five factors are:

- Asphalt content (AC)
- Air voids (Va)
- Tensile strain level (ε_t)
- Temperature (T)
- Rest period (RP)

The main experiment included two levels for each factor except the temperature, where three levels were included. Thirty two (32) combinations were included as a result of the fractional factorial statistical design. Each combination was tested using three replicates. The 32 combinations include 15 combinations at zero rest period and 17 combinations at five second rest period. Two different tests were used for each combination group. The first was without rest period (damage test) while the second with rest period (healing test). Two different software programs were developed to conduct the tests. The main idea was to trace the change of the PS over time for the tests "without" and "with" rest periods. The calculated differences of the PS between the "with" and "without" rest period tests for each combination represent the fatigue healing.

Results of Tests without Rest Period

Using three replicates, 45 specimens were tested without rest period in the main experiment for all PG 64-22 mixtures. Each mixture was tested using two selected strain levels at test temperatures of 40, 70 and 100°F. The criterion of selecting the two strain levels at each temperature was to reach a fatigue life of 20,000 cycles for the medium strain level, and 100,000 cycles for the low strain level. Prior to the uniaxial fatigue test, a dynamic modulus fingerprint test was conducted at 10 Hz to determine the dynamic modulus (E*) value as well as the Machine Compliance Factor (MCF). The 50% reduction in the initial stiffness criterion was used to determine the fatigue life of material. The initial stiffness is the stiffness at the 100th cycle.

The results of the fingerprints as well as the uniaxial tension-compression fatigue tests are tabulated for each mixture in TABLES 48 to 51.

TABLE 48 Fingerprint and uniaxial fatigue test results at 9.5% Va and 4.2% AC

Temp °F)	Specimen ID	Air Voids (%)	Tensile Strain (µs)	FP Modulus (psi)	Phase Angle φ Degree	MCF	Initial Stiffness (psi)	Initial φ Degree	Cycles to Failure	Average Cycles	Standard Deviation	Coefficient of Variation (%)
100	D-985	8.84	237.5	130.5	51.65	1.29	72.4	56.7	9,810	13,897	3,563	25.6
	D-986	9.17	237.5	120.7	49.30	1.25	67.3	56.0	15,530			
	D-992	9.05	237.5	169.7	46.54	1.37	98.0	52.0	16,350			
70	D-969	9.52	115	538.4	24.58	2.83	433.6	28.1	31,150	25,753	4,793	18.6
	D-984	8.76	115	720.8	24.46	3.56	551.1	30.1	21,990			
	D-981	8.73	115	729.5	28.92	3.58	583.2	31.5	24,120			
	D-977	9.25	90	716.6	23.16	3.36	627.9	25.8	146,780	86,893	52,092	59.9
	D-978	9.45	90	672.8	24.26	3.45	557.3	28.2	61,820			
	D-983	9.32	90	768.8	27.53	4.26	572.5	32.3	52,080			
40	D-993	9.14	62.5	1,735	10.84	8.25	1,674	11.8	86,210	101,610	23,238	22.9
	D-988	8.39	62.5	2,175	12.95	9.29	2,175	13.6	90,280			
	D-987	9.01	62.5	2,066	12.66	9.13	1,960	13.4	128,340			

TABLE 49 Fingerprint and uniaxial fatigue test results at 4.5% Va and 4.2% AC

Temp °F)	Specimen ID	Air Voids (%)	Tensile Strain (µs)	FP Modulus (psi)	Phase Angle φ Degree	MCF	Initial Stiffness (psi)	Initial φ Degree	Cycles to Failure	Average Cycles	Standard Deviation	Coefficient of Variation (%)
100	D-427	3.85	195	295.6	42.37	1.77	183.1	49.9	85,770	77,083	7,652	9.9
	D-467	4.12	195	244.7	51.49	1.77	140.3	56.1	71,340			
	D-466	4.50	195	203.6	50.02	1.51	132.9	55.4	74,140			
70	D-436	4.92	115	974.9	23.89	4.33	814.0	27.5	12,090	15,253	6,401	42.0
	D-437	5.09	115	1,133.2	26.63	5.53	862.0	30.1	22,620			
	D-488	4.99	115	1,220.3	23.34	5.01	901.2	28.3	11050			
40	D-442	3.81	87.5	3,145	11.52	12.70	2,712	13.1	21,660	16,147	5,353	33.2
	D-440	4.39	87.5	2,701	10.74	12.21	2,394	12.9	15,810			
	D-446	4.82	87.5	2,956	2,956	14.42	2,354	15.2	10,970			
	D-443	4.06	70	3,050	12.72	13.40	2,751	13.3	71,160	57,903	13,300	23.0
	D-452	4.52	70	2,969	10.64	12.95	2,756	11.7	44,560			
	D-455	4.46	70	3,137	12.22	13.09	2,823	14.4	57,990			

TABLE 50 Fingerprint and uniaxial fatigue test results at 9.5% Va and 5.2% AC

Temp (°F)	Specimen ID	Air Voids (%)	Tensile Strain (μs)	FP Modulus (psi)	Phase Angle φ Degree	MCF	Initial Stiffness (psi)	Initial φ Degree	Cycles to Failure	Average Cycles	Standard Deviation	Coefficient of Variation (%)
100	D+985	9.41	252.5	129.8	43.41	1.33	78.6	51.2	126,870	97,217	35,115	36.1
	D+989	9.89	252.5	80.0	56.86	1.21	48.4	59.1	58,440			
	D+984	9.39	252.5	122.3	44.21	1.21	76.4	49.5	106,340			
70	D+961	9.66	155	603.4	30.02	3.51	433.1	34.6	25,910	20,377	4,813	23.6
	D+974	9.61	155	459.6	29.08	2.55	368.3	34.1	18,060			
	D+9B2	9.34	155	540.3	27.94	2.66	412.9	33.5	17,160			
40	D+971	9.16	112.5	1,629	12.51	6.92	1,490	13.0	20,580	14,723	5,105	34.7
	D+968	9.98	112.5	1,471	12.21	6.73	1,348	13.1	11,220			
	D+967	9.04	112.5	1,612	11.74	7.72	1,510	14.2	12,370			
	D+965	9.38	82.5	1,380	12.16	5.97	1,334	12.5	93,810	119,010	32,788	27.6
	D+936	9.79	82.5	1,408	12.36	6.37	1,345	12.5	156,080			
	D+935	9.26	82.5	1,599	11.87	7.90	1,531	12.2	107,140			

TABLE 51 Fingerprint and uniaxial fatigue test results at 4.5% Va and 5.2% AC

Temp (°F)	Specimen ID	Air Voids (%)	Tensile Strain (μs)	FP Modulus (psi)	Phase Angle φ Degree	MCF	Initial Stiffness (psi)	Initial φ Degree	Cycles to Failure	Average Cycles	Standard Deviation	Coefficient of Variation (%)
100	D+457	4.63	357.5	142.7	51.90	1.26	75.4	59.6	29,520	24,897	7,060	28.4
	D+465	4.78	357.5	140.7	50.89	1.26	77.0	57.0	28,400			
	D+463	4.86	357.5	155.3	49.98	1.32	81.5	58.6	16,770			
70	D+449	4.79	122.5	872.0	30.02	4.31	679.4	33.0	129,320	92,577	31,918	34.5
	D+455	4.01	122.5	959.1	24.88	4.84	784.7	28.7	71,710			
	D+492	4.63	122.5	1,036	26.13	4.27	824.1	29.5	76.700			
40	D+459	4.79	112.5	2,291	11.17	10.86	2,095	13.0	23,270	17,270	6,035	34.9
	D+452	3.75	112.5	2,386	10.92	11.97	2,184	12.2	17,340			
	D+453	4.51	112.5	2,542	13.34	11.16	2,139	13.2	11,200			

Results of Tests with Rest Period

The main experiment included 17 different combinations of the tests with rest period. Using three replicates for each combination, 51 specimens were tested. Considering the long time needed for tests with rest period, all the tests were stopped after 20,000 cycles, which was

195

reasonable to demonstrate a clear behavior of the mixtures tested with rest period. It takes 28 hours to complete one test with 5 seconds rest period run until 20,000 cycles. The results of the tests with rest periods for the different mixtures are summarized in TABLES 52 to 55.

TABLE 52 Fingerprint and uniaxial fatigue test results at 9.5% Va and 4.2% AC

Temp (°F)	Specimen ID	Air Voids (%)	Tensile Strain (μs)	Rest Period (sec)	FP Modulus (psi)	Phase Angle φ Degree	MCF	Initial Stiffness (psi)	Cycles N	PSR at N
100	D-996	9.28	187.5	5.0	135.2	47.45	1.35	113.0	20,000	0.934
	D-999	9.47	187.5	5.0	151.9	46.67	1.46	122.1	20,000	0.976
	D-9C9	8.64	187.5	5.0	145.9	50..02	1.37	122.9	20,000	0.899
	D-995	9.08	237.5	5.0	132.4	50.69	1.24	103.4	20,000	0.890
	D-9A2	9.48	237.5	5.0	126.0	48.24	1.21	92.0	20,000	0.853
	D-9C7	9.35	237.5	5.0	126.3	47.27	1.13	102.6	20,000	0.894
70	D-997	9.25	90.0	5.0	772.9	24.22	3.61	682.8	20,000	0.939
	D-9A1	9.29	90.0	5.0	699.1	25.54	2.34	636.1	20,000	0.957
	D-9C5	9.10	90.0	5.0	728.2	25.49	3.31	652.4	20,000	0.952
40	D-9A4	9.05	80.0	5.0	1,665.5	10.81	6.92	1,527.8	20,000	0.842
	D-9B9	9.29	80.0	5.0	1,720.4	11.68	7.13	1,604.8	20,000	0.890
	D-9C8	9.04	80.0	5.0	1,608.9	12.28	6.52	1,492.8	20,000	0.944

TABLE 53 Fingerprint and uniaxial fatigue test results at 4.5% Va and 4.2% AC

Temp (°F)	Specimen ID	Air Voids (%)	Tensile Strain (μs)	Rest Period (sec)	FP Modulus (psi)	Phase Angle φ Degree	MCF	Initial Stiffness (psi)	Cycles N	PSR at N
100	D-472	4.25	242.5	5.0	213.9	45.34	1.48	166.6	20,000	0.900
	D-474	4.68	242.5	5.0	226.1	47.19	1.56	163.3	20,000	0.872
	D-497	5.00	242.5	5.0	182.0	46.39	1.28	145.4	20,000	0.853
70	D-465	4.54	90.0	5.0	1,126.1	22.43	5.01	1,036.4	20,000	0.927
	D-468	3.95	90.0	5.0	1,343.3	24.12	5.81	1,183.2	20,000	0.948
	D-493	4.25	90.0	5.0	1,261.7	23.77	5.03	1,110.0	20,000	0.932
	D-471	4.66	115.0	5.0	1,208.7	26.62	5.25	987.8	20,000	0.905
	D-473	4.83	115.0	5.0	1,095.5	25.15	4.77	975.4	20,000	0.919
	D-494	4.34	115.0	5.0	1,195.7	20.98	4.75	1,066.6	20,000	0.882
40	D-475	4.62	70.0	5.0	3,145.4	11.51	14.20	2,731.2	20,000	1.000
	D-478	4.26	70.0	5.0	2,691.0	11.37	10.63	2,567.8	20,000	0.976
	D-495	3.99	70.0	5.0	2,763.7	9.85	10.20	2,763.7	20,000	0.956

TABLE 54 Fingerprint and uniaxial fatigue test results at 9.5% Va and 5.2% AC

Temp (°F)	Specimen ID	Air Voids (%)	Tensile Strain (µs)	Rest Period (sec)	FP Modulus (psi)	Phase Angle φ Degree	MCF	Initial Stiffness (psi)	Cycles N	PSR at N
100	D+993	9.43	342.5	5.0	84.9	54.36	1.20	66.2	20,000	0.860
	D+999	9.43	342.5	5.0	103.7	52.46	1.27	73.2	20,000	0.842
	D+9B8	8.98	342.5	5.0	77.6	51.23	1.14	59.3	20,000	0.810
70	D+991	8.73	112.5	5.0	656.7	26.28	3.13	584.1	20,000	0.940
	D+992	8.97	112.5	5.0	543.3	26.54	2.77	491.4	20,000	0.940
	D+9B4	9.35	112.5	5.0	570.7	27.69	2.77	501.2	20,000	0.950
	D+983	9.77	155.0	5.0	606.7	25.46	2.93	494.4	20,000	0.920
	D+988	8.76	155.0	5.0	782.0	20.20	3.65	676.8	20,000	0.895
	D+9B1	9.65	155.0	5.0	509.8	27.66	2.53	433.4	20,000	0.912
40	D+996	8.84	82.5	5.0	2,009.5	13.08	8.37	1,807.2	20,000	0.968
	D+9A0	9.06	82.5	5.0	1,616.3	10.55	7.08	1,552.9	20,000	0.974
	D+9C0	9.32	82.5	5.0	1,427.9	12.31	5.65	1,350.5	20,000	0.967
	D+995	9.66	112.5	5.0	1,443.9	13.08	5.96	1,336.3	20,000	0.960
	D+997	9.54	112.5	5.0	1,704.5	10.00	7.10	1,614.1	20,000	0.936
	D+9B0	8.77	112.5	5.0	1,543.5	12.23	5.98	1,427.1	20,000	0.921

TABLE 55 Fingerprint and uniaxial fatigue test results at 4.5% Va and 5.2% AC

Temp (°F)	Specimen ID	Air Voids (%)	Tensile Strain (µs)	Rest Period (sec)	FP Modulus (psi)	Phase Angle φ Degree	MCF	Initial Stiffness (psi)	Cycles N	PSR at N
100	D+466	4.57	232.5	5.0	151.6	51.59	1.44	124.3	20,000	0.941
	D+470	4.13	232.5	5.0	209.6	48.89	1.71	149.0	20,000	0.893
	D+493	4.70	232.5	5.0	165.9	52.00	1.41	135.1	20,000	0.906
70	D+468	4.39	197.5	5.0	1,155.8	24.00	5.15	865.7	20,000	0.873
	D+471	4.61	197.5	5.0	883.4	26.83	4.10	719.9	20,000	0.912
	D+495	4.68	197.5	5.0	907.5	24.99	3.82	761.8	20,000	0.877
40	D+473	4.57	82.5	5.0	2,268.8	10.51	11.49	2,168.4	20,000	0.997
	D+476	4.22	82.5	5.0	2,889.4	11.81	13.29	2,540.8	20,000	1.001
	D+491	4.95	82.5	5.0	2,402.4	12.55	9.21	2,180.0	20,000	0.963
	D+464	5.00	112.5	5.0	2,275.6	12.25	8.80	2,090.4	20,000	0.969
	D+477	4.54	112.5	5.0	2,664.1	11.86	11.30	2,330.6	20,000	0.968
	D+489	4.36	112.5	5.0	2,299.3	11.18	8.90	2,147.2	20,000	0.940

Additional Experimental Results

An additional experiment was conducted to study the nonlinear effect of the strain level and the rest period on the fatigue healing. The additional experiment included two additional rest periods and one additional strain level. The additional experiment included five combinations for tests without rest period and 13 combinations for tests with rest period. Considering two replicates for each combination, 36 tests were conducted in the additional experiment.

The new rest period levels were 1 and 10 seconds. The new strain level was high enough to fail the specimen at 5,000 loading cycles. The fatigue life relationships were improved by adding the data of the tests without rest period from the main experiment to the existing fatigue life relationships. Consequentially, the fatigue life relationships can be fitted using more data points (7 to 12 data points). The improved fatigue life relationships for each mixture at different temperatures are shown in FIGURES 141 to 144. The new k_1 and k_2 values at different temperatures are shown in the figures for each mixture.

The equations shown on the figure:

$$y = 1.3590E\text{-}26x^{-7.3478E+00}$$
$$R^2 = 9.2949E\text{-}01$$

$$y = 1.2498E\text{-}19x^{-5.9067E+00}$$
$$R^2 = 8.3246E\text{-}01$$

$$y = 4.4773E\text{-}23x^{-7.3296E+00}$$
$$R^2 = 9.7216E\text{-}01$$
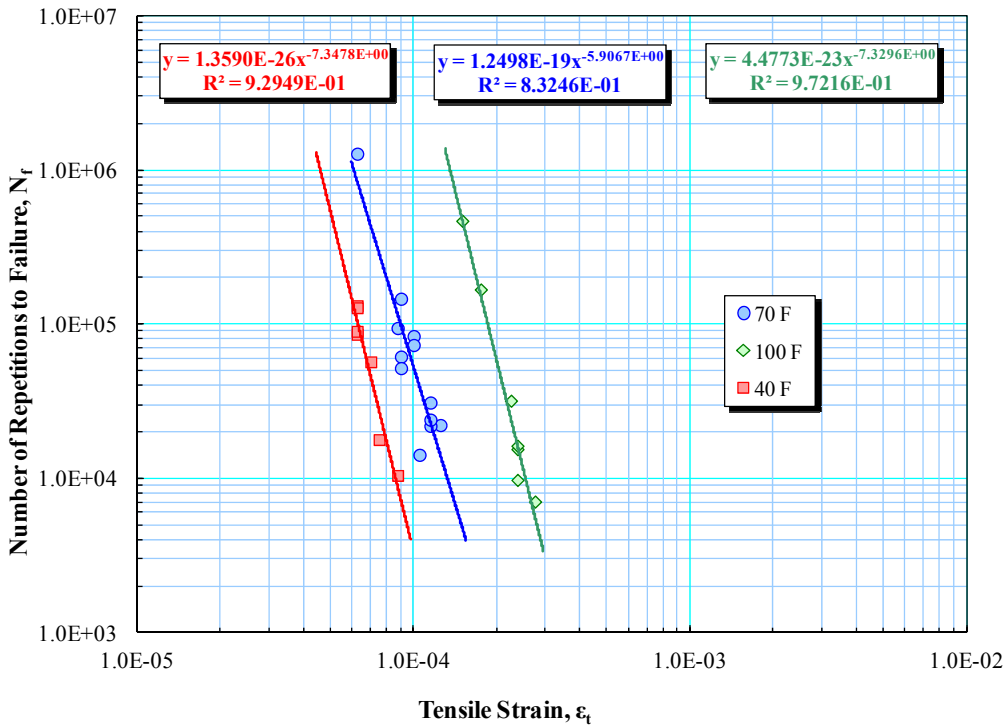
FIGURE 141 Updated fatigue lives at different temperatures (9.5% AV and 4.2% AC).
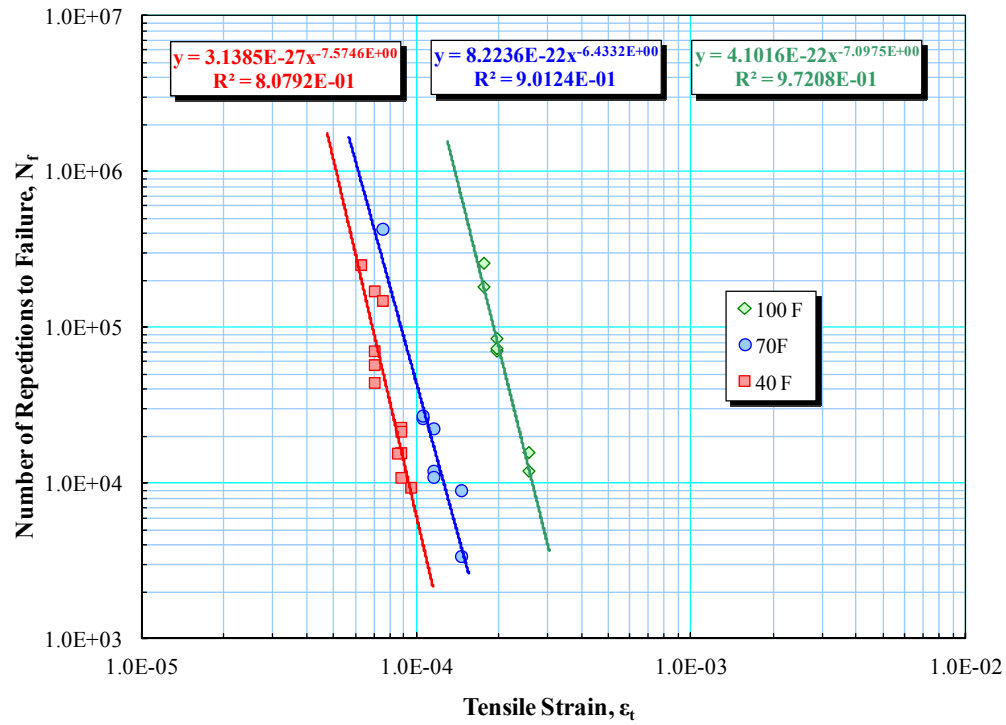
FIGURE 142 Updated fatigue lives at different temperatures (4.5% AV and 4.2% AC).
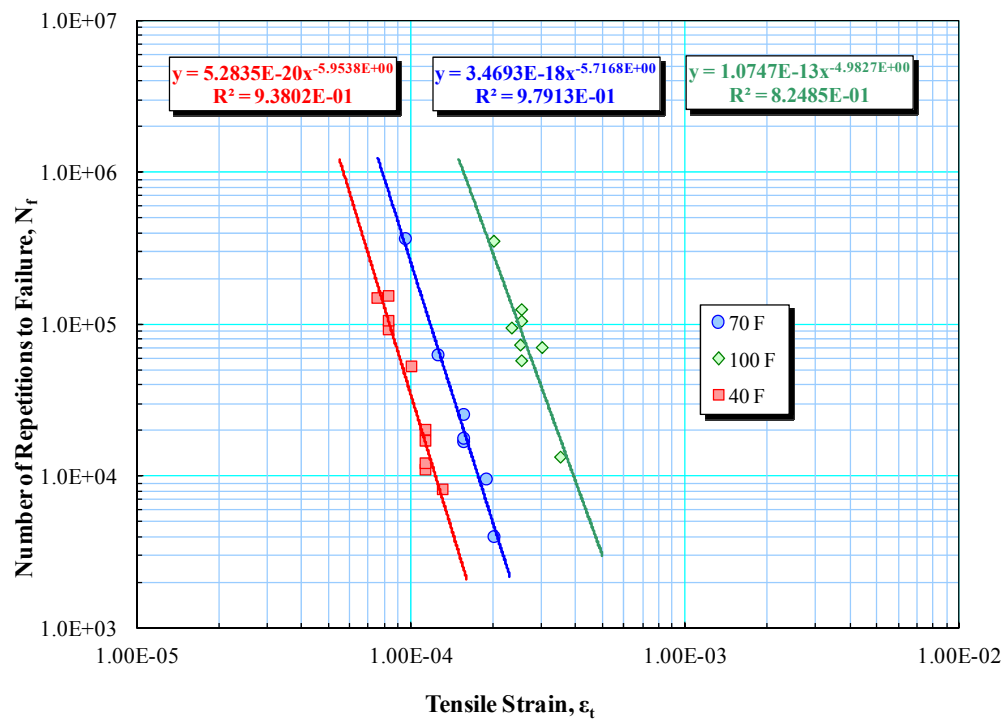
FIGURE 143 Updated fatigue lives at different temperatures (9.5% AV and 5.2% AC).

199
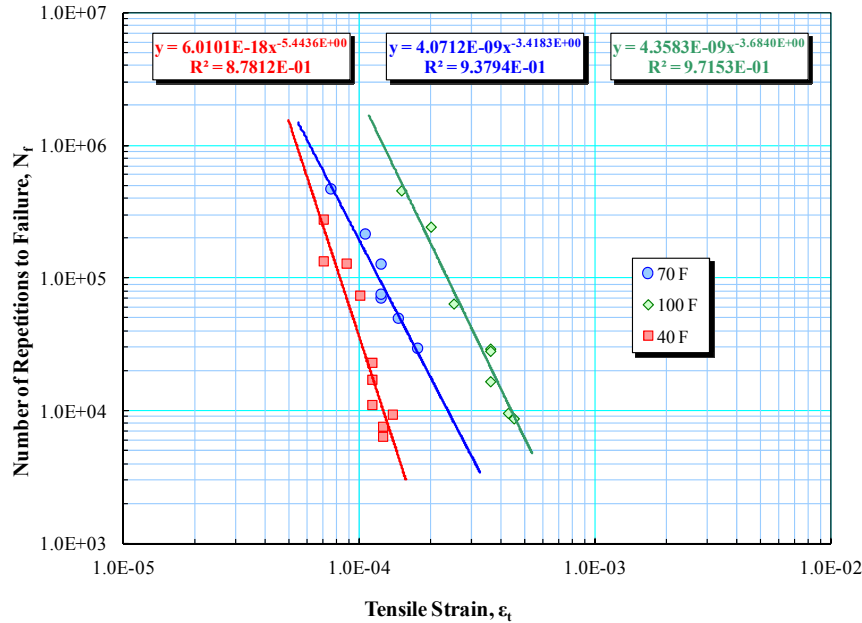
FIGURE 144 Updated fatigue lives at different temperatures (4.5% AV and 5.2% AC).

Based on a fatigue life criterion of 5,000 loading cycles, the high strain values for the asphalt mixtures at different temperatures were calculated as shown in TABLE 56. Using the combined data set for each mixture, the fatigue test results at different test temperatures were used to generate the generalized fatigue model coefficients (k_1, k_2, and k_3). TABLE 57 shows the k_1, k_2, and k_3 values for the four mixtures. In addition, all the test results for the four mixtures were pooled together in one generalized data set and used to get regression coefficients for all mixtures (TABLE 57). FIGURE 145 shows a comparison of the measured to the predicted fatigue lives based on the individual models for each mixture. FIGURE 146 displays the same comparison but using the generalized fatigue model for all mixtures together.

For the additional experiment, TABLE 58 contains a summary of the test results without rest period. For the tests with rest period, all the tests were stopped at 20,000 loading cycles. As stated before, this was a reasonable number of cycles due to time constrains; a test with 10 seconds rest period required 56 hours of testing. The results of the tests with rest period were summarized in

TABLE 59. It is worthwhile to mention that the results for four tests without rest period and two tests with rest period at the lowest temperature (40°F) could not be obtained even with many trials. The reason for this failure was that all test specimens failed quickly as the specimens were subjected to extreme levels of stress.

TABLE 56 High tensile strain values for all mixtures at different temperatures

Temp. (ºF)	4.2% AC		5.2% AC	
	9.5% Va	4.5% Va	9.5% Va	4.5% Va
	(5000 Cycles)	(5000 Cycles)	(5000 Cycles)	(5000 Cycles)
100 ºF	280	290	450	532.5
70 ºF	145	142.5	207.5	302.5
40 ºF	95	100	140	142.5

TABLE 57 Updated k_1, k_2 and k_3 values for each individual mixture and all mixtures together

Air voids Va%	Asphalt content AC%	k_1	k_2	k_3	R^2%
9.5	4.2	3.7904E-11	7.8325	2.8178	97.71
4.5	4.2	4.0851E-06	5.5693	1.9891	82.87
9.5	5.2	1.4200E-05	4.9422	1.6812	88.23
4.5	5.2	0.009953	3.4648	1.1127	93.35
All Mixtures		3.2761E-06	5.2812	1.8259	77.55

$$*N_f = k_1 \times (1/E)^{k_2} \times (1/\varepsilon_t)^{k_3}$$
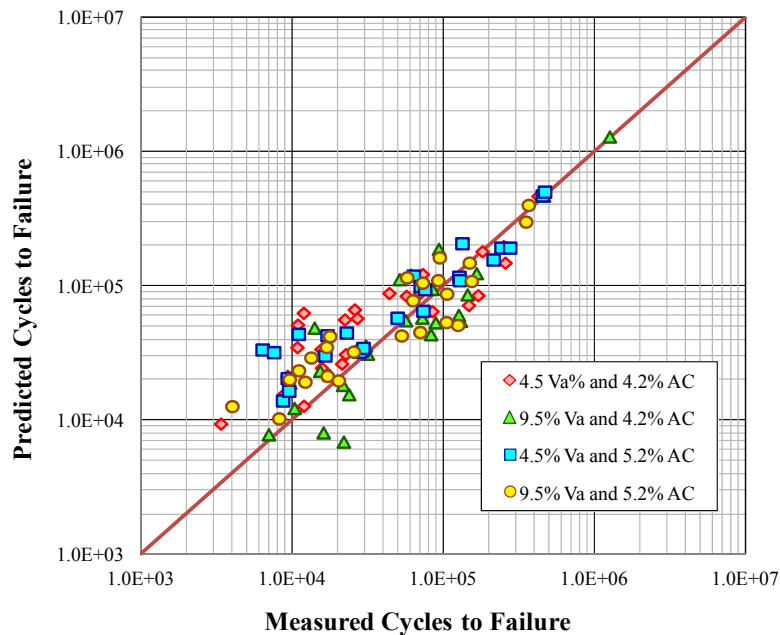
FIGURE 145 Measured versus predicted cycles to failure based on individual generalized fatigue models.
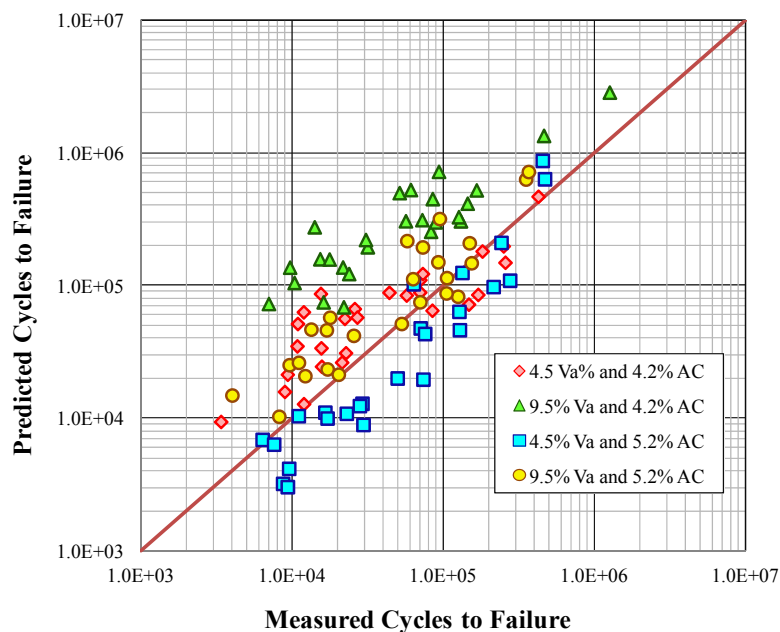
FIGURE 146   Measured versus predicted cycles to failure based on generalized fatigue model for all mixtures together.

TABLE 58 Summary results of uniaxial fatigue test without rest period for all mixtures

Temp ºF)	Specimen ID	Air Voids (%0	Tensile Strain (μs)	FP Modulus (psi)	Phase Angle φ Degree	MCF	Initial Stiffness (psi)	Initial φ Degree	Cycles to Failure	Average Cycles	Standard Deviation	Coefficient of Variation (%)
100	D-9A7	8.87	280.0	214.2	38.94	1.51	110.0	49.01	5,990	6,360	523	8.23
	D-9B3	8.83	280.0	152.7	46.54	1.44	80.0	55.6	6,730			
100	D+9B3	8.87	342.5	84.6	51.32	1.17	46.0	58.96	16,350	14,175	3,076	21.70
	D+9B5	8.83	343.5	90.0	52.38	1.41	46.1	58.24	12,000			
70	D-490	4.44	90.0	1,118.4	26.32	4.55	961.4	27.92	53,840	50,550	4,653	9.20
	D-491	4.48	90.0	1,058.1	23.50	4.50	896.7	26.82	47,260			

203

TABLE 59 Summary results of uniaxial fatigue test with rest period for all mixtures

Temp (°F)	Specimen ID	Air Voids (%)	Tensile Strain (μs)	Rest Period (sec)	FP Modulus (psi)	Phase Angle ϕ (Degree)	MCF	Initial Stiffness (psi)	Cycles N	PSR at N
40	D-484	4.11	100.0	5.0	2,928.6	11.17	11.10	2,586.5	20,000	0.863
100	D-476	4.07	195.0	1.0	298.6	39.64	1.97	221.8	20,000	0.791
	D-482	4.35	195.0	1.0	199.0	47.06	1.37	156.1	20,000	0.803
40	D+478	4.33	112.5	10.0	2,456.8	10.77	9.37	2,338.2	20,000	0.977
	D+483	4.44	112.5	10.0	2,528.3	11.16	9.72	2,277.3	20,000	0.992
	D+485	4.70	125.0	1.0	2,130.5	10.98	8.47	1,991.3	20,000	0.610
70	D+472	4.24	197.5	1.0	995.2	25.12	4.26	758.5	20,000	0.811
	D+475	4.18	197.5	1.0	991.3	24.17	4.27	783.8	20,000	0.750
	D+474	4.24	122.5	10.0	967.5	24.86	4.24	845.6	20,000	0.946
	D+479	4.17	122.5	10.0	977.0	29.22	4.56	807.9	20,000	0.946
40	D-9B2	9.32	62.5	5.0	1,790.5	13.25	7.38	1,699.1	20,000	0.976
	D-9B6	9.08	62.5	5.0	1,896.4	11.26	7.52	1,759.4	20,000	0.961
	D-9B8	9.30	80.0	1.0	1,520.3	13.21	6.14	1,369.7	20,000	0.689
	D-9C0	9.13	80.0	1.0	1,610.5	12.07	6.42	1,497.5	20,000	0.702
70	D-9A8	9.69	115.0	5.0	737.4	23.00	3.46	651.3	20,000	0.922
	D-9B0	9.76	115.0	5.0	678.1	23.90	3.29	599.3	20,000	0.940
100	D-9B5	9.46	237.5	10.0	122.0	47.36	1.37	98.3	20,000	0.909
	D-9C1	9.13	237.5	10.0	118.8	46.88	1.34	102.7	20,000	0.858
70	D+9A5	9.35	207.5	1.0	516.2	27.11	2.55	412.2	20,000	0.795
	D+997	9.54	207.5	1.0	548.2	27.59	2.78	440.2	20,000	0.757
100	D+9A6	9.42	450.0	5.0	82.1	50.96	1.13	56.3	20,000	0.729
	D+9A7	8.91	450.0	5.0	81.0	49.30	1.21	55.8	20,000	0.676
	D+9A8	9.06	252.5	1.0	86.4	51.22	1.15	69.3	20,000	0.802
	D+9A9	9.11	252.5	1.0	93.2	51.05	1.47	67.4	20,000	0.758

CHAPTER 8

ENDURANCE LIMIT MODEL DEVELOPMENT AND SENSITIVITY ANALYSIS

BACKGROUND

This chapter includes the methodology and implementation of the endurance limits developed using test results from the laboratory experiments. The developed methodology incorporates one important aspect—the healing of fatigue damage—into the endurance limit estimation. This methodology is an unique approach compared to other current methods. Healing of the fatigue damage is believed to be the main reason for the existence of asphalt mixture endurance limits.

As explained Chapter 7, there are two scenarios to determine the endurance limit values. In the first scenario, the endurance limit is calculated using the HI parameter where the endurance limit occurs at HI equal to one, or when all the fatigue micro-cracks are healed at certain number of cycles. In the second scenario, the PSR parameter is calculated at two different strain levels for the same test conditions, same volumetric properties, and any rest period. As discussed earlier, the PSR method was used in this study to determine the endurance limit. Both methods entailed the development of PSR regression model. Five main factors that affect the fatigue behavior of asphalt mixtures were considered in this study: air voids, binder content, temperature, tensile strain, and rest period.

This chapter also includes a comparison of the endurance limit values obtained from the uniaxial tension-compression fatigue study to those obtained from the beam fatigue study that was conducted as a part of the NCHRP Project 9-44A (Souliman, 2012) and described in Appendix 1.

DEVELOPMENT OF THE FIRST GENERATION PSR MODEL

The test results from all uniaxial fatigue experiments were combined together to develop the first generation PSR model for the PG 64-22 mixtures. For each test with rest period, four PSR values were measured at different N values to represent the nonlinear change of PSR over time. Only the PSR values at N_f were considered for the tests without rest period. A total number of 161 test results were used in the model development that included 385 data points. All data points are presented in Appendix C. The first PSR model includes the main five factors plus one additional factor, which is N where PSR values were measured.

One- and two-factor interactions were used in the statistical model. Two statistical techniques were used to develop the PSR model. The first technique was the regression analysis using the Minitab® software. The second technique was a nonlinear optimization technique. The nonlinear optimization analysis can be done using the Solver function in Excel® or other statistical software like Statistica® and Minitab®,. These different software programs use the Generalized Reduced Gradient (GRG) Algorithm for optimizing nonlinear problems. The only issue with this technique is that once a solution is found that seems to produce favorable results, it will stop trying for new solutions. Another issue is the difficulty of getting a reasonable solution when the number of adjustable parameters is quite large, which was the case for this

model where one- and two-factor interactions between six different factors were considered. A more powerful nonlinear optimization technique that uses innovative Genetic Algorithm (GA) technology provides a more accurate optimization solution. Evolver®, one of the GA technology based software that is well-suited to find the best overall answer by exploring the entire universe of possible answers, was used in this study to develop the PSR model. The Evolver® software is completely compatible with Microsoft Excel®.

The Evolver® optimization technique requires the main form of the regression model as an input. To construct a more rational model from, the relationship between the PSR and each factor was investigated to choose the best mathematical function to fit this relationship by an iteration process. It was found that there is a need for a logarithmic transformation for strain and number of loading cycles, while a second degree polynomial function was proper for temperature. For the rest period, a special function was used to fit its relationship with the PSR. It was noticed that by increasing the rest period, the PSR increases, indicating more healing. The rate of increase of PSR decreases as the rest period increases up to a certain value above which there is no more PSR increase. This value of rest period is called the optimum rest period. Using the tangent hyperbolic (tanh) function to fit the PSR and RP relationship, the optimum rest period can be found. The shape and form of the tanh function to fit the PSR and RP relationship is presented in FIGURE 147.

$$SPR = x + y \times Tanh (z \times RP)$$
x, y, and z are regression coefficients.
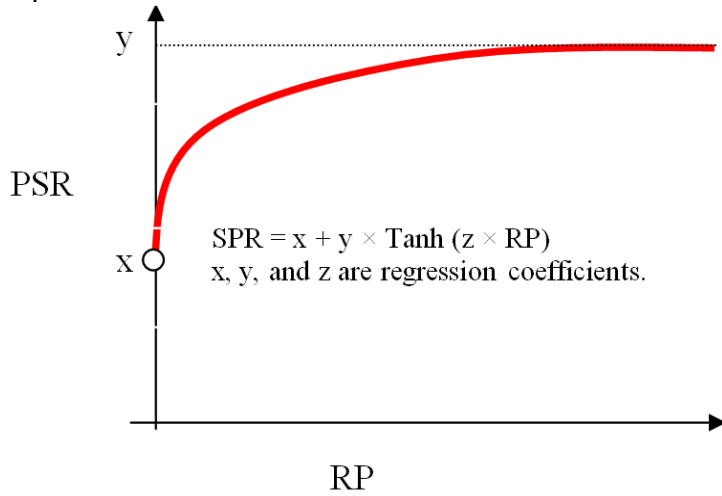
FIGURE 147   PSR and RP relationship fitted by tanh function.

Based on the statistical accuracy, precision measurements, and the rationality of the sensitivity analysis, it was clear that the PSR models developed by the nonlinear optimization technique were more accurate compared to the regression analysis technique. The regression analysis technique, however, was not able to include some of the essential function forms used by the nonlinear optimization technique.

The form of the PSR model can be expressed as shown in Equation 116.

$$PSR = a_0 + (a_1 T^2 + a_2 T) + a_3 AC + a_4 Va + a_5 \log \varepsilon_t + (a_6 Tanh(a_7 RP) + a_8 \log N + a_9 T^2*AC + a_{10} T*AC + a_{11} T^2*Va + a_{12} T*Va + a_{13} T^2*\log \varepsilon_t + a_{14} T*\log \varepsilon_t + a_{15} T^2*Tanh(a_{16} RP) + a_{17} T*Tanh(a_{18} RP) + a_{19} T^2*\log N + a_{20} T*\log N + a_{21} AC * Va + a_{22} AC * \log \varepsilon_t + a_{23} AC* Tanh(a_{24} RP) + a_{25} AC * \log N + a_{26} Va * \log \varepsilon_t + a_{27} Va* Tanh(a_{28} RP) + a_{29} Va *$$

$$\log N + a_{30} \log \varepsilon_t * \text{Tanh}(a_{31} RP) + a_{32} \log \varepsilon_t * \log N + a_{33} \log N * \text{Tanh}(a_{34} RP)$$

$$(116)$$

where,

AC	= Percent asphalt content by weight
Va	= Percent air voids
ε_t	= Tensile strain, microstrain
T	= Temperature (°F)
RP	= Rest period (seconds)

To reduce the analysis time using the Evolver® optimization function, the Solver® function was used to find reasonable initial values for the regression coefficients (a_0 to a_{34}). The Evolver® optimization function was used then to further reduce the sum of squared errors. The analysis was usually run for 12 hours and the best reasonable solution that has the least sum of squared errors was then considered. To have a non-biased regression model, the sum of errors was constrained to be zero. The model was further improved by removing two outlier data points using the method suggested by Montgomery (2008). The analysis was then repeated based on the remaining 383 data points and the following regression coefficients values were obtained (TABLE 60).

TABLE 60 Regression coefficient values of first generation model

Coefficient	Value	Coefficient	Value
a_0	1.128166247	a_{18}	0.000000000
a_1	0.000013877	a_{19}	0.000000485
a_2	-0.001196544	a_{20}	0.000106845
a_3	0.044418678	a_{21}	0.000032361
a_4	-0.004845287	a_{22}	0.000008648
a_5	-0.318423391	a_{23}	0.000000000
a_6	0.415230129	a_{24}	0.000000000
a_7	0.899087837	a_{25}	-0.000084625
a_8	-0.046120564	a_{26}	-0.000050235
a_9	-0.000003538	a_{27}	0.000000000
a_{10}	0.000135597	a_{28}	0.000000000
a_{11}	-0.000001893	a_{29}	-0.000799796
a_{12}	0.000231228	a_{30}	0.000000000
a_{13}	0.000007109	a_{31}	0.000000000
a_{14}	-0.000047641	a_{32}	-0.000104153
a_{15}	0.000000000	a_{33}	0.000000000
a_{16}	0.000000000	a_{34}	0.000000000
a_{17}	0.000000000		

From the analysis of the results, it was noticed that there is no interaction between the rest period and other factors. The resulting first generation regression model is shown in Equation 117.

$$PSR = 1.1282 + 0.00001388\ T^2 - 0.0011197\ T + 0.04442\ AC - 0.004845\ Va - 0.3184\ \log \varepsilon_t +$$
$$0.4152\ Tanh(0.8991\ RP) - 0.04612\ \log N - 0.00000354\ T^2*AC + 0.000136\ T*AC -$$
$$0.00000189\ T^2*Va + 0.000231\ T*Va + 0.00000711\ T^2*\log \varepsilon_t - 0.0000476\ T*\log \varepsilon_t +$$
$$0.000000485\ T^2*\log N + 0.000107\ T*\log N + 0.0000324\ AC * Va + 0.00000865\ AC *$$
$$\log \varepsilon_t - 0.0000846\ AC * \log N - 0.0000502\ Va * \log \varepsilon_t - 0.000800\ Va * \log N -$$
$$0.000104\ \log \varepsilon_t * \log N$$

$$(117)$$

The above model shows good predictions when compared with the measured PSR values. This also was supported by the excellent statistical measures of accuracy terms ($R^2_{adj} = 0.9563$ and $S_e/S_y = 0.291$).

The measured versus predicted PSR is shown in FIGURE 148. FIGURE 149 shows the model's adequacy using the residual versus raw data plot. The fitting model meets the requirement of normal distribution with constant variance. FIGURE 150 shows standardized error versus the measured PSR after deleting the two outlier data points.
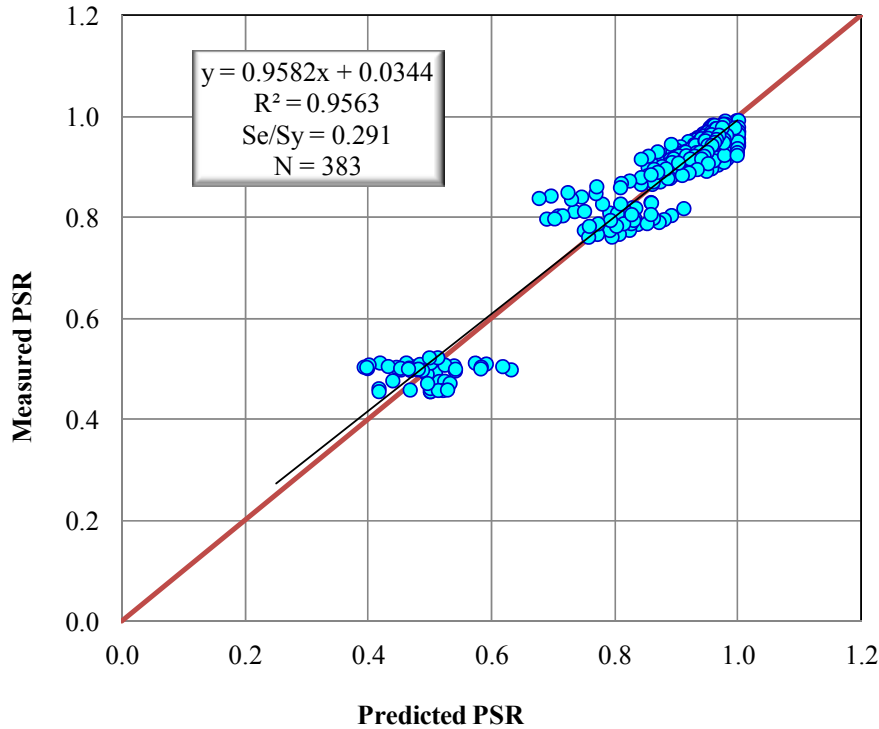
FIGURE 148 Measured versus predicted PSR for the first generation model.

208
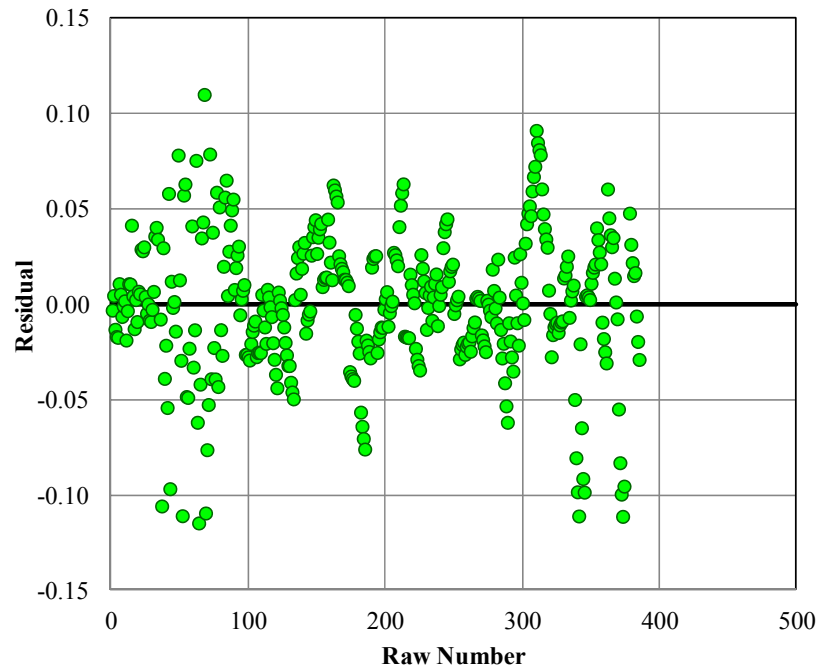
FIGURE 149 Residual versus raw number for the first generation model.
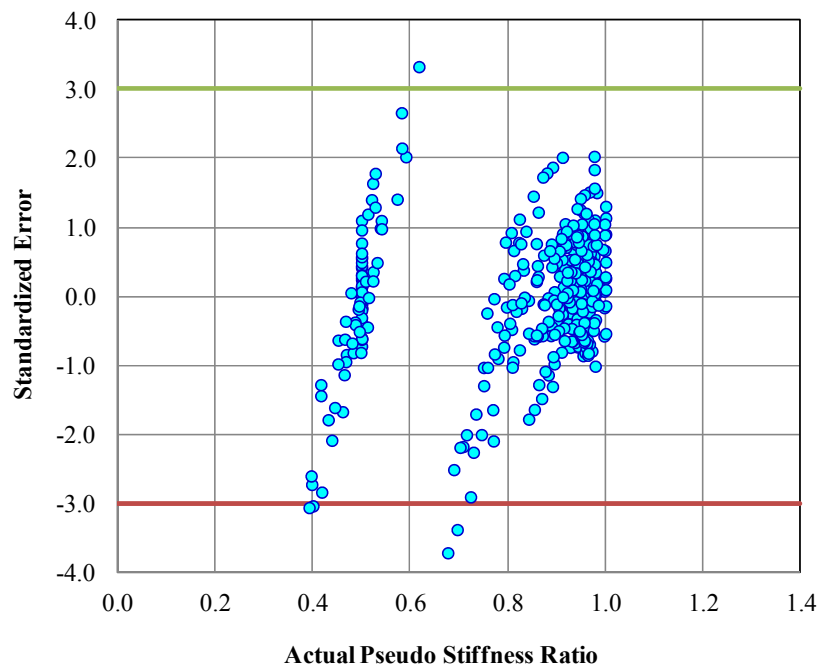
FIGURE 150 Standerdized error versus measured PSR values.

Effect of Rest Period on PSR

The effect of rest period on the PSR for all mixtures at different temperatures is shown in FIGURE 151. For all the cases presented, it is clear that the PSR increases as the rest period increases until a certain value, after which the PSR is constant. This observed trend is supported by all the literature studies regarding the effect of rest period on fatigue behavior. The previous studies showed that there is an optimum rest period value beyond which there is no more enhancement of fatigue behavior. The optimum rest period values for all the cases (in FIGURE 151) are 3 seconds (loading ratio of 30), which almost fit in the middle range of optimum rest periods (1 to 5 seconds) reported in the literature and discussed earlier.
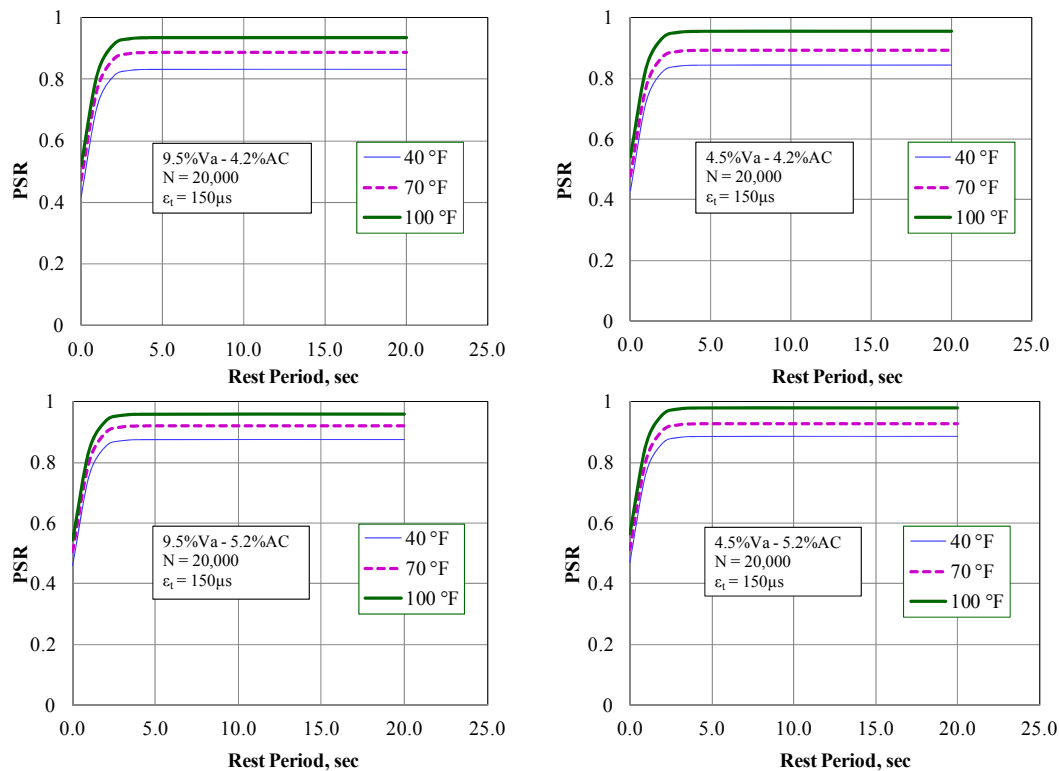
FIGURE 151 Effect of rest period on PSR for all mixtures.

Effect of N on PSR

To investigate the effect of N on the PSR and consequently on the endurance limit, a sensitivity analysis study was performed. In this analysis, the PSR versus the tensile strain relationships were investigated at rest periods of 1 and 10 seconds, N values of 25,000, 50,000, and 100,000 loading cycles, and temperatures of 40, 70, and 100°F. The results of the sensitivity analysis is shown in FIGURE 152 for only one asphalt mixture (4.5% Va-4.2%AC) as the other asphalt mixtures showed similar trends. Based on the sensitivity analysis results, N has small or almost no effect on the SR value for tests with rest period, where there is a trivial increase on the PSR by increasing N values. Consequentially, a rational N value of 20,000 loading cycles is

210

recommended for the endurance limit calculation as it represents the end of all the uniaxial fatigue tests with rest period in this study.
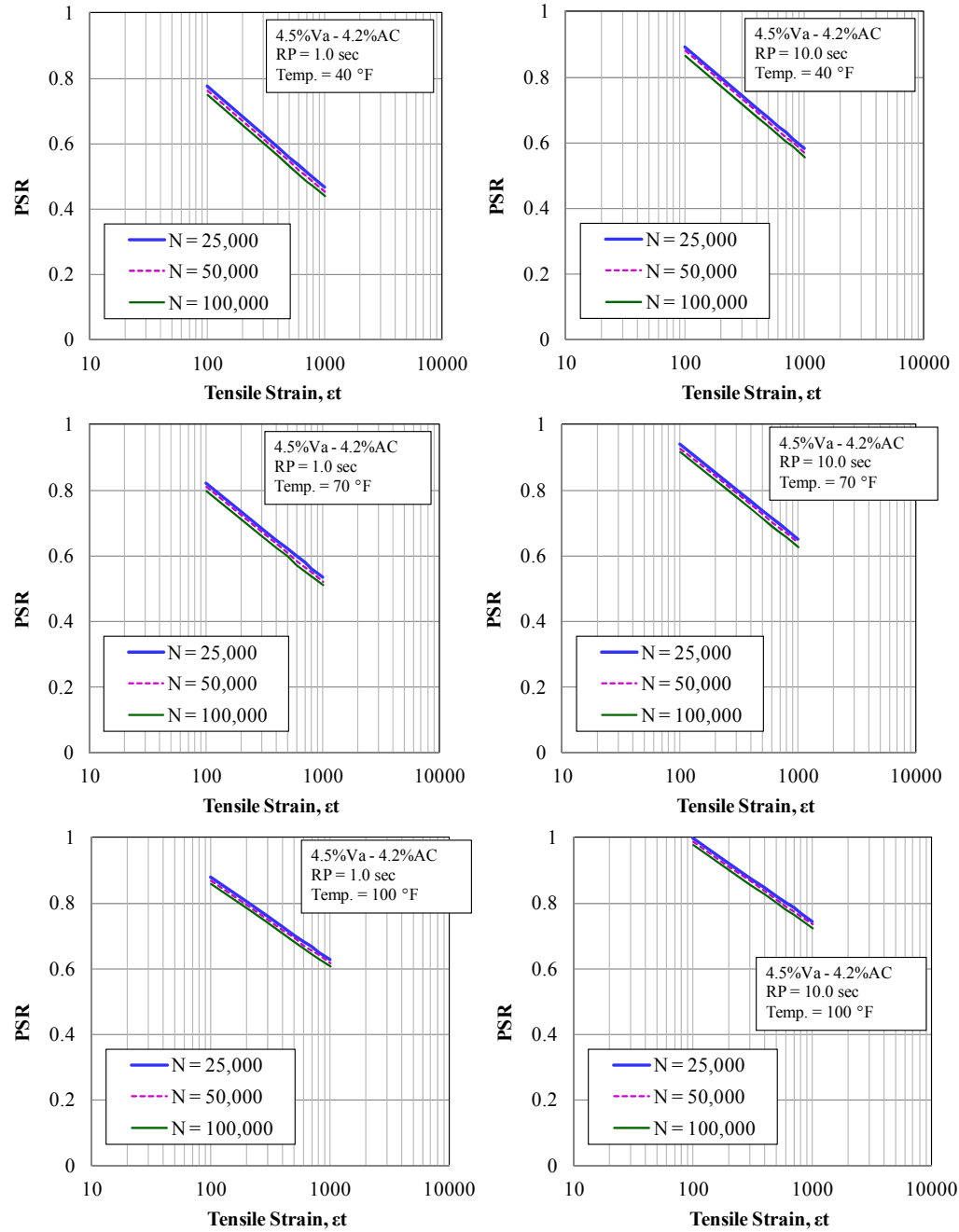
FIGURE 152 Effect of N on PSR-ε_t relationship at different RP and temperatures for the 4.5%Va-4.2%AC mixture.

Estimating Endurance Limits Using the First Generation PSR Model

The above model was used to predict the PSR values at different tensile strains values for each mixture type at different temperatures (4 mixtures × 3 temperatures). FIGURES 153 to 155 illustrate the relationship between the PSR and the tensile strain for different mixtures. In general, it is observed that the mixtures with higher asphalt contents showed considerably higher PSR values, especially at 40 and 70°F. At 100 °F, the effect of the asphalt content was less. This totally agrees with typical asphalt mixture behavior, where the asphalt binder dominates the mix behavior at low and medium temperatures. The opposite trend was observed for air voids, where the mixtures with high and low air voids (4.5 and 9.5% Va) showed comparable PSR values at 40 and 70°F. At 100°F, the mixtures with 4.5% Va showed higher PSR values than the mixtures with 9.5% Va. The effect of both air voids and asphalt content on the healing of fatigue damage described by the PSR values emulates the fatigue behavior of the different mixtures under the uniaxial fatigue test conditions.

To estimate the endurance limit for each mixture, the endurance limit values were calculated at different temperatures where the PSR-tensile strain relationship intersects the line and the PSR is equal to 1.0. FIGURE 156 shows the endurance limit values of the asphalt mixtures at different temperatures for the 5 second rest period using an N value of 20,000 cycles. As expected, the mixtures with higher binder contents and lower air voids exhibited high endurance limit values at all test temperatures. It is also noticed that the effect of asphalt content is much more significant than the effect of air voids on the fatigue micro-cracks healing. This is hypothesized to be due to the fact that healing of micro-cracks occurs mainly due to the diffusivity of the asphalt binder along the surface of the microcrack. Higher asphalt content increases the ability of the micro-cracks to heal. The same endurance limit trend was found at different rest periods.
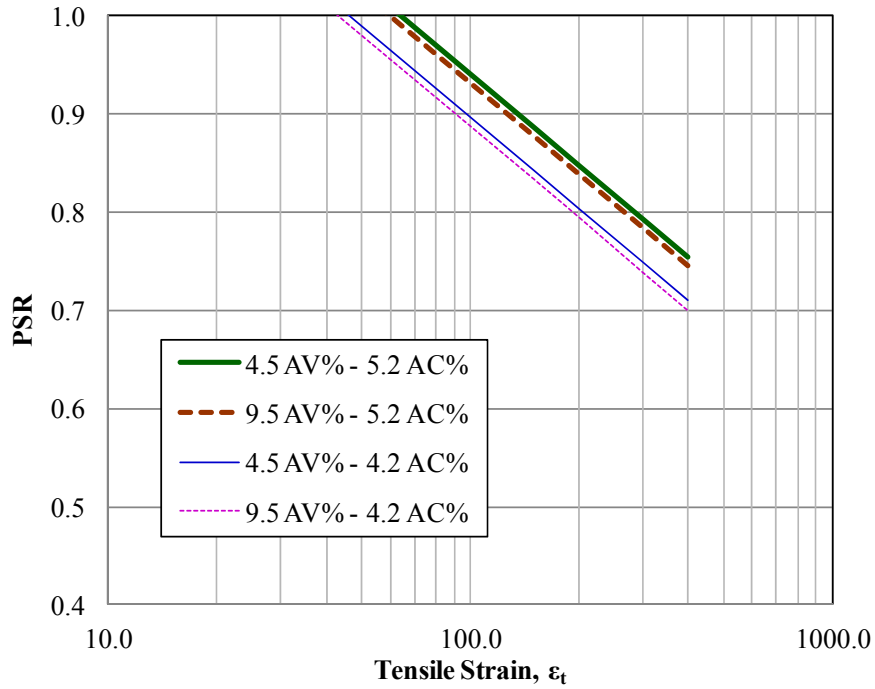
FIGURE 153 PSR versus tensile strain for all mixtures at 40°F (RP = 5.0 sec, and N = 20,000).
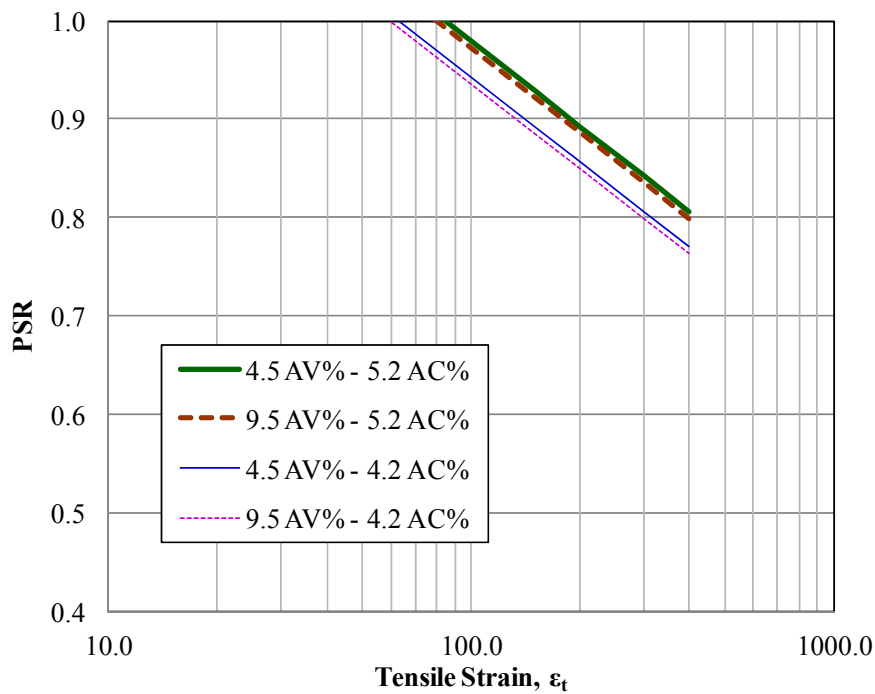
FIGURE 154 PSR versus tensile strain for all mixtures at 70°F (RP = 5.0 sec, and N = 20,000).

213
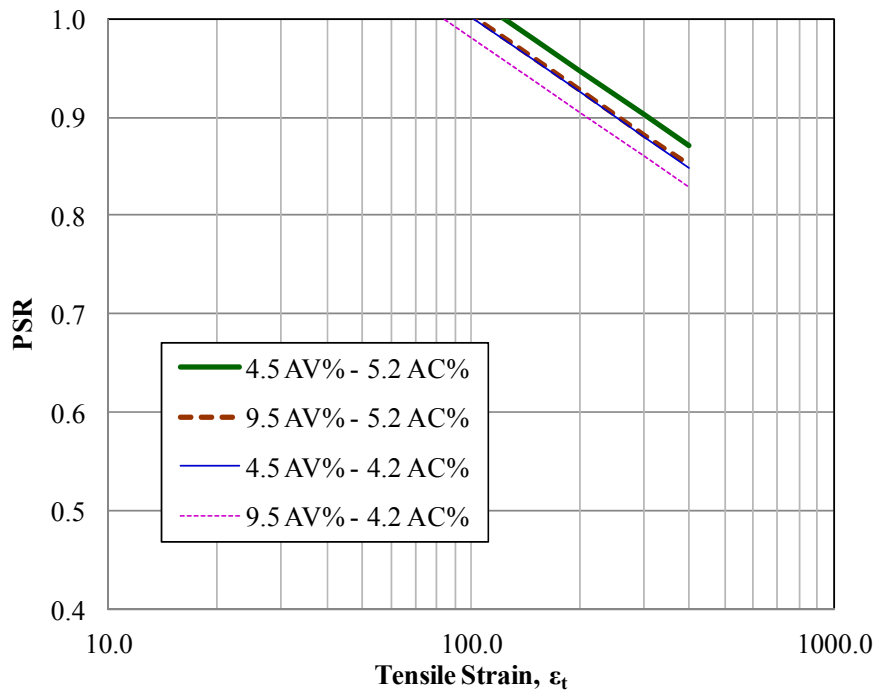
FIGURE 155 PSR versus tensile strain for all mixtures at 100°F (RP = 5.0 sec, and N = 20,000).
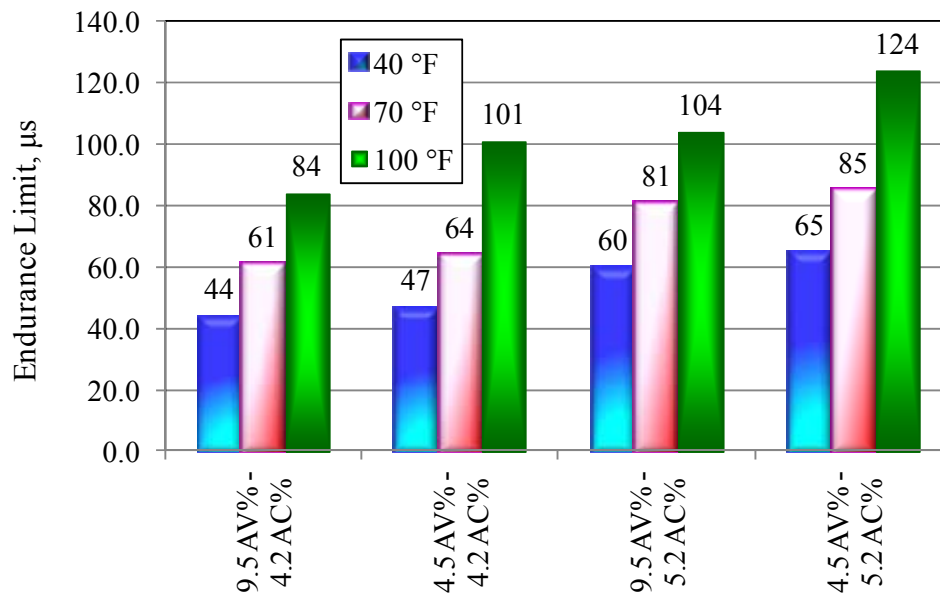
FIGURE 156 Endurance limit values for all mixtures at different temperatures using the first generation PSR model.

DEVELOPMENT OF A SECOND GENERATION PSR MODEL

In the second generation model, the initial stiffness of the mixtures was used as a replacement for three factors that mainly affect the stiffness value. These factors are asphalt content, air voids, and temperatures. Two main advantages can be achieved by this modification. The first advantage is to simplify the PSR model. The second advantage is to develop a PSR model that is more compatible with the AASHTOWare Pavement ME Design software, where the pavement performance prediction is mainly driven by the dynamic modulus of the HMA mixture. The development of the second generation PSR model followed the same procedure used to develop the first generation model. Logarithmic transformation was required for the initial stiffness. In addition to the main factor effects, one- and two-factor interactions were considered. The structure of the second generation model is shown in Equation 118.

$$PSR = a_0 + a_1 * \log E_o + a_2 * \log \varepsilon_t + (a_3 * Tanh (a_4 * RP) + a_5 * \log N$$
$$+ a_6 * \log E_o * \log \varepsilon_t + a_7 * \log E_o * Tanh (a_8*RP) + a_9 * \log E_o * \log N$$
$$+ a_{10} * \log \varepsilon_t * Tanh (a_{11}* RP) + a_{12} * \log \varepsilon_t * \log N + a_{13} * \log N * Tanh$$
$$(a_{14}* RP) \tag{118}$$

where E_o is the initial stiffness measured at the 100th cycle in ksi.

Both Excel Solver® and Evolver® software were used to minimize the sum of the squared errors using a nonlinear optimization technique to estimate the regression analysis coefficients (a_0 to a_{14}). The model was further improved by removing the outliers using the method suggested by Montgomery (2008). Only two outlier data points were removed out of the 385 data points. The analysis was then repeated based on the remaining 383 data points which improved the R^2_{adj} from 0.9425 to 0.9511. The final regression coefficient values were obtained as tabulated in TABLE 61. The second generation regression model is shown in Equation 119.

TABLE 61 Regression coefficient values of second generation model

Coefficient	Value	Coefficient	Value
a_0	0.459539	a_8	0.000000
a_1	-0.090917	a_9	-0.041502
a_2	-0.104389	a_{10}	0.000000
a_3	0.417028	a_{11}	0.000000
a_4	0.875884	a_{12}	-0.077377
a_5	0.238893	a_{13}	0.000000
a_6	0.120018	a_{14}	0.000000
a_7	0.000000		

$$PSR = 0.459539 - 0.090917 * \log E_o - 0.104389 * \log \varepsilon_t + 0.417028 * Tanh (0.875884 * RP) +$$
$$0.238893 * \log N + 0.120018 * \log E_o * \log \varepsilon_t - 0.041502 * \log E_o * \log N - 0.077377 * \log$$
$$\varepsilon_t * \log N \tag{119}$$

FIGURE 157 presents the measured versus predicted PSR using the second generation model. The residual versus raw data plot is shown in FIGURE 158, which indicates that the

fitting model meets the requirement of normal distribution with constant variance. The standardized error versus the measured PSR plot is illustrated in FIGURE 159.

y = 0.9501x + 0.0411
R² = 0.9511
Se/Sy = 0.2253
N = 383
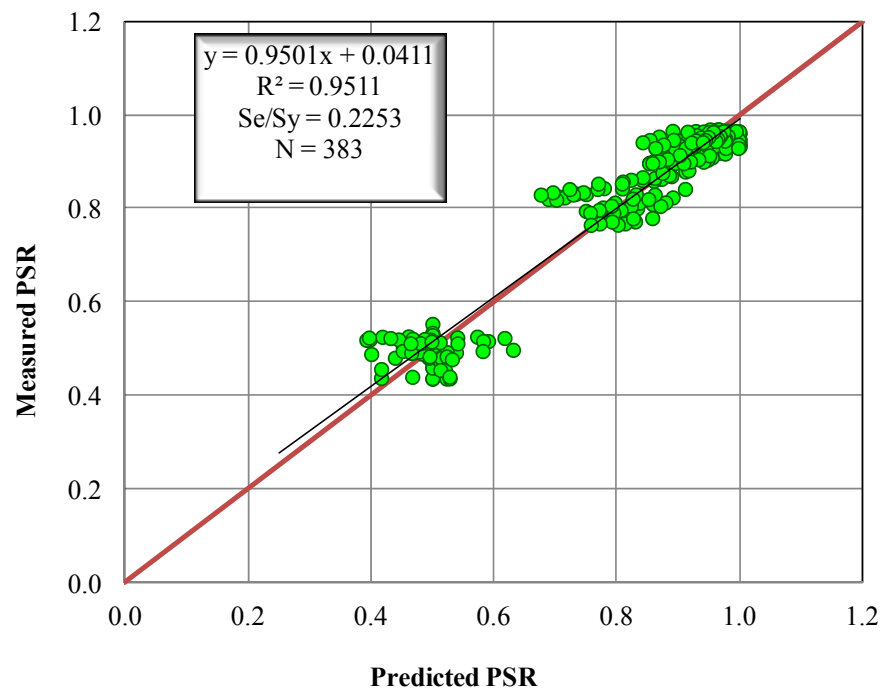
FIGURE 157 Measured versus predicted PSR for the second generation model.
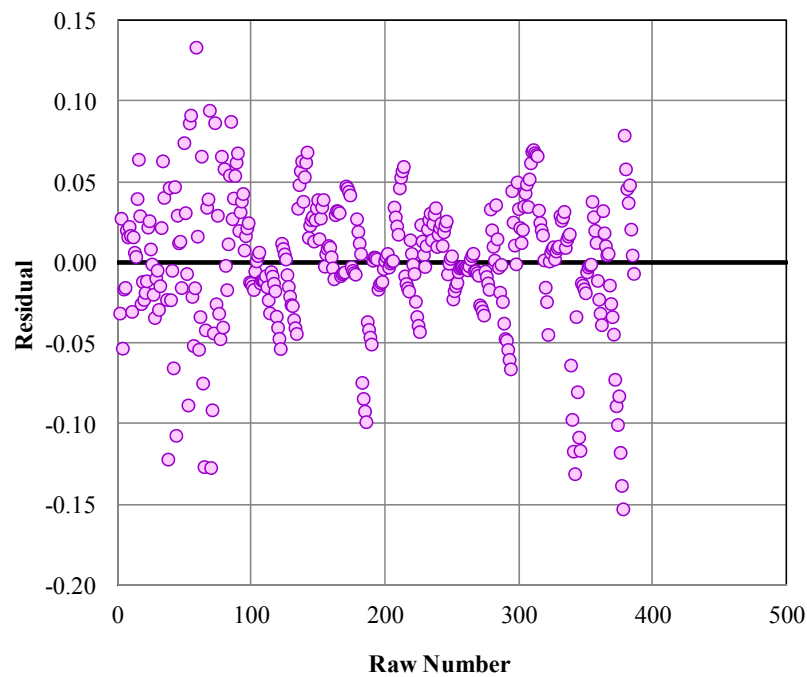
FIGURE 158 Residual versus raw number for the second generation model.
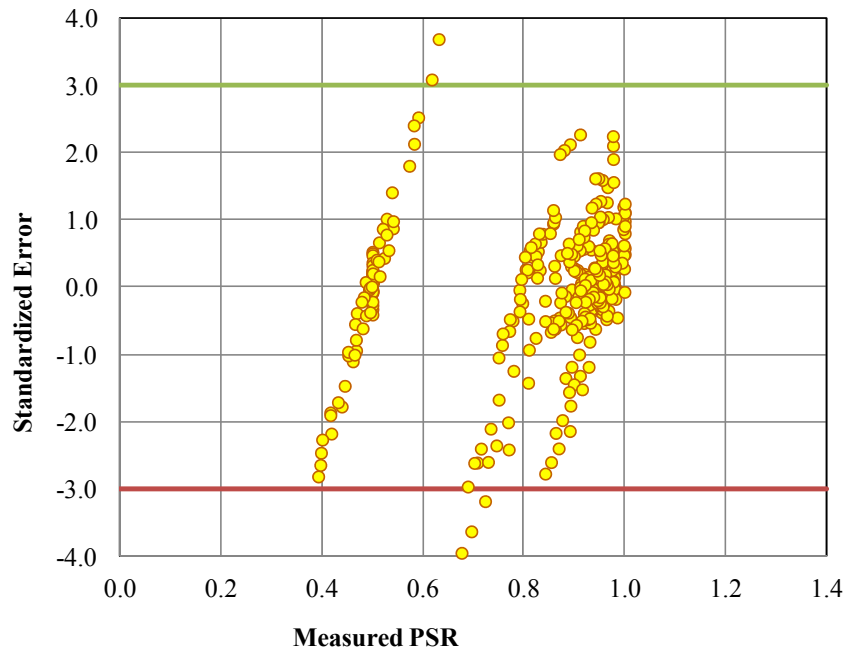
FIGURE 159 Standardized error versus measured PSR values.

Effect of Rest Period on PSR

FIGURE 160 shows the effect of rest period on the PSR, initial stiffness, and N values. The second generation model shows a similar trend for the effect of rest period compared to the first generation model. It is observed that increasing the rest period would increase the PSR until it reaches a maximum value, with no further change with increasing rest period. An optimum rest period of 3 seconds (loading ratio of 30) for all the cases was obtained, which is the same as that generated by the first generation model.

Effect of N on PSR

Further analysis was conducted to investigate the effect of N on the PSR for the second generation model. The sensitivity analysis included plotting the PSR versus the tensile strain for different mixtures represented by the initial stiffness at rest periods of 1 and 10 seconds and N values of 25,000, 50,000, 100,000, and 200,000 loading cycles. The PSR-tensile strain relationships are presented in FIGURE 161 for the different cases. The analysis showed that PSR-tensile strain relationships are not perfectly parallel at different N values when compared to the first generation model. Therefore, the effect of N will depend on the point of intersection. If the point of intersection is close enough to the horizontal line where PSR = 1.0, N will not have any effect on the PSR and the calculation of the endurance limit. The N value seems to have an effect on the PSR if the intersecting point is distant from a PSR value of 1.0. An N value of 20,000 cycles is recommended for the second generation PSR model.
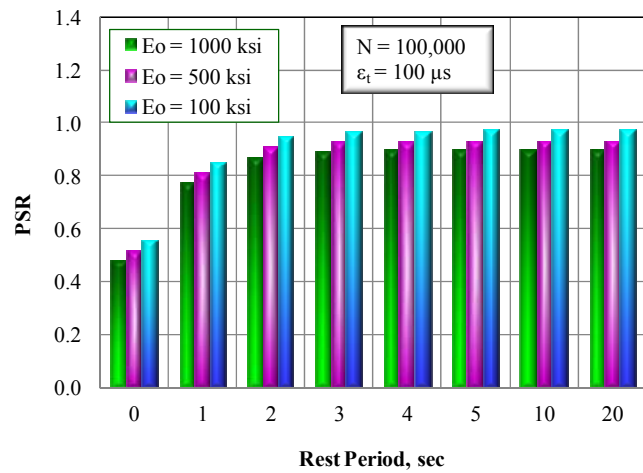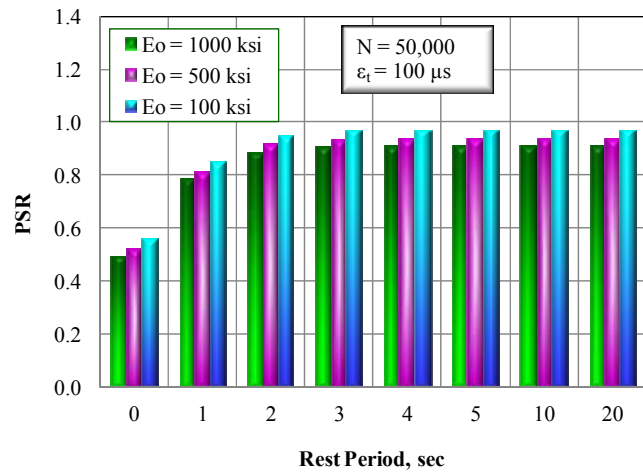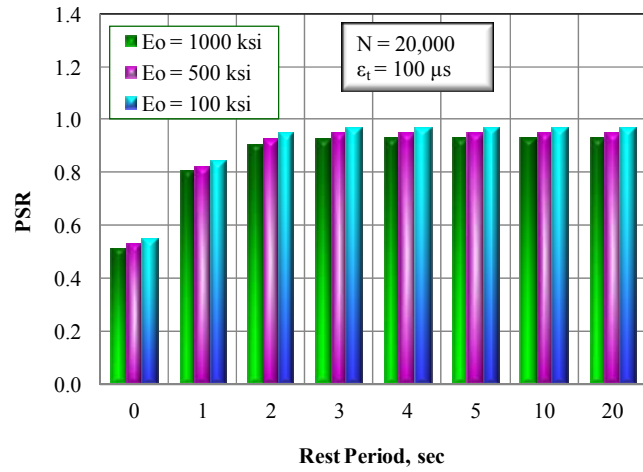
FIGURE 160 Effect of rest period on PSR at different N values.
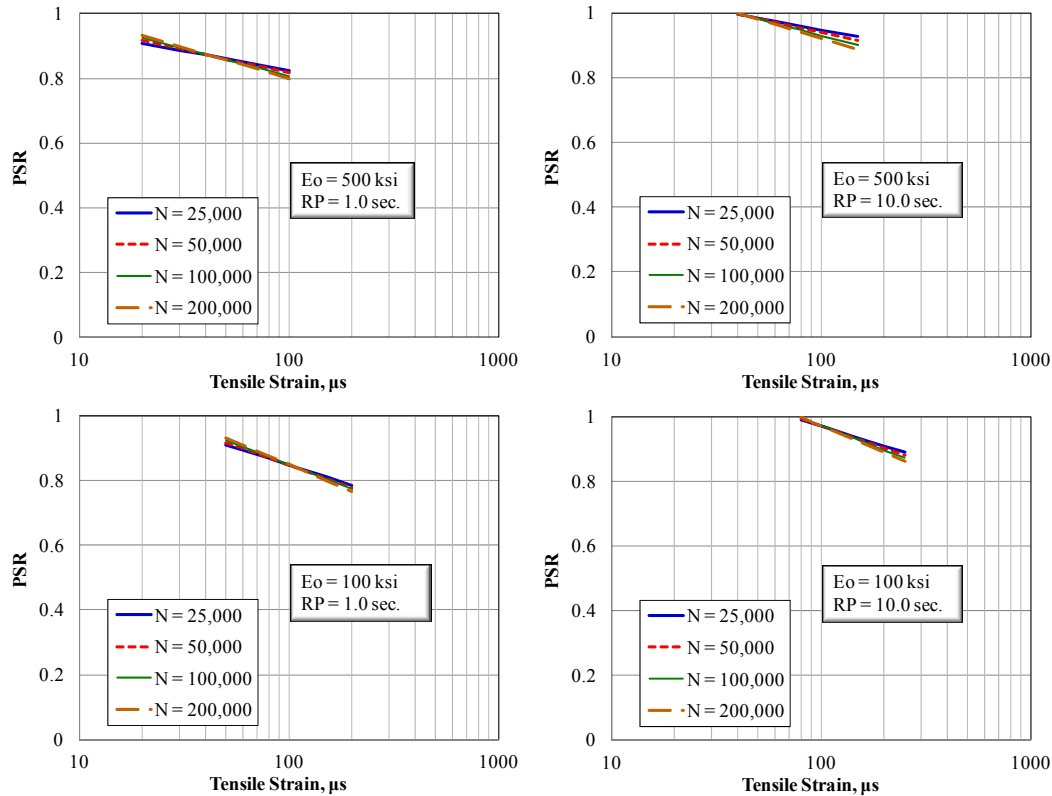
FIGURE 161 Effect of N on PSR at different initial stiffness and RP values.

Estimating Endurance Limits Using Second Generation PSR Model

Using the second generation PSR model, PSR versus tensile strain plots were established using several stiffness and rest period values at N of 200,000 loading cycles (FIGURES 162 to 166). It was observed that the relationship lines in case of the second model are intersecting, where they appeared parallel for the first model. This difference is mainly due to the use of the stiffness in the model. Mixtures with high and low binder contents have a slight stiffness difference; however, their performance could be notably different. In addition, mixtures with high binder content and low air voids showed similar stiffness to those that have high air voids and low binder content, even though their performance could be relatively dissimilar. Despite this concern, the model shows rational results and relationships. In addition, the simplicity of the model itself is an advantage compared to the form of the first generation PSR model. Based on relationships in FIGURES 162 to 166, the endurance limit is calculated as the tensile strain value where the PSR-tensile strain relationship meets a PSR value of 1.0.
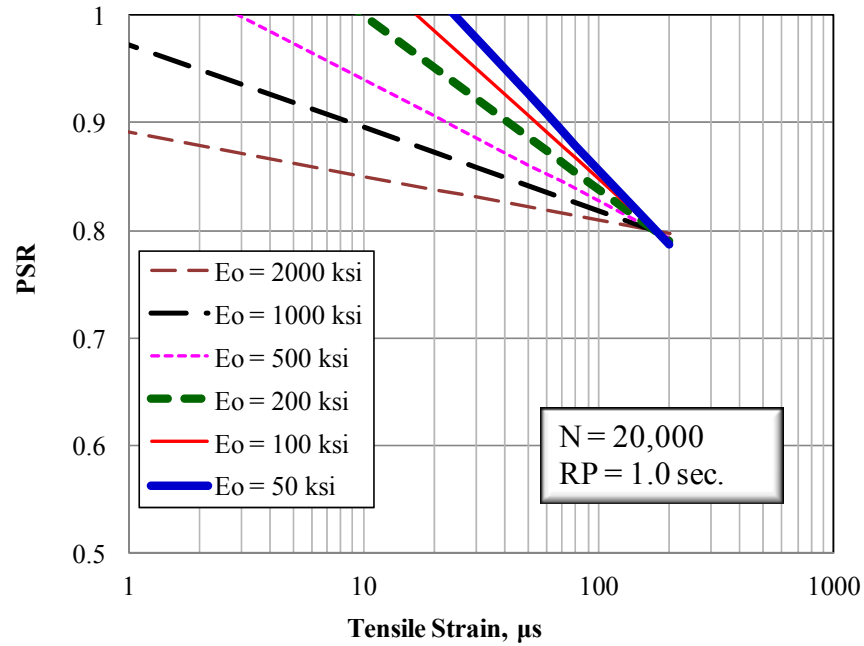
FIGURE 162 PSR versus tensile strain at different initial stiffness values (RP = 1.0 sec, N=20,000 cycles).
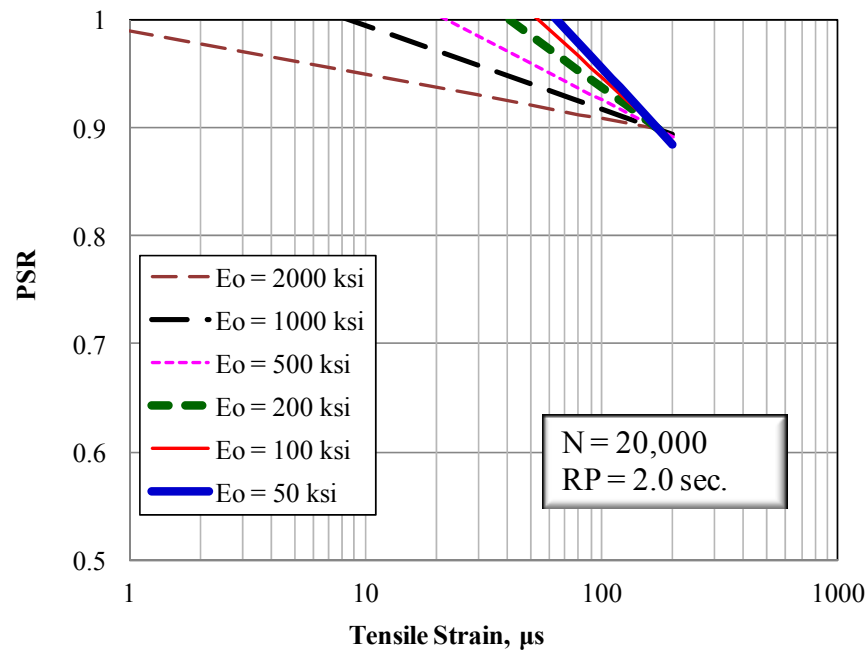
FIGURE 163 PSR versus tensile strain at different initial stiffness values (RP = 2.0 sec, N=20,000 cycles).
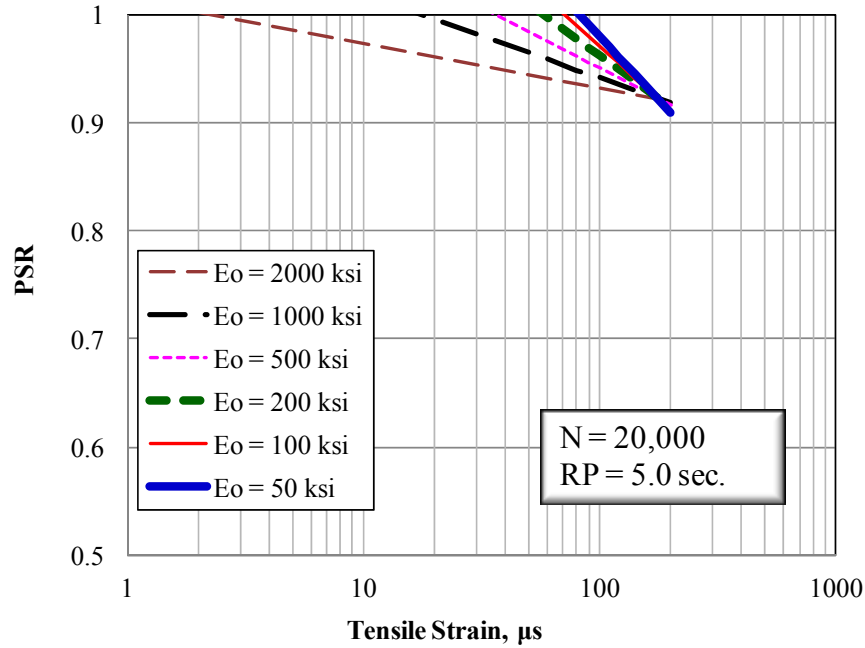
FIGURE 164 PSR versus tensile strain at different initial stiffness values (RP = 5.0 sec, N=20,000 cycles).
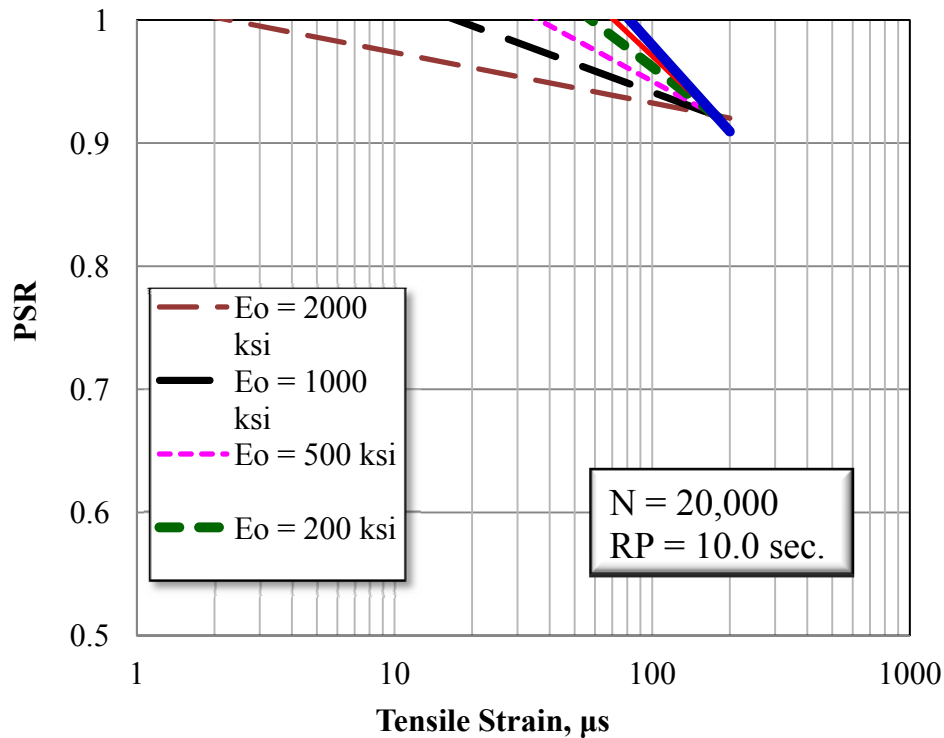
FIGURE 165 PSR versus tensile strain at different initial stiffness values (RP = 10.0 sec, N=20,000 cycles).
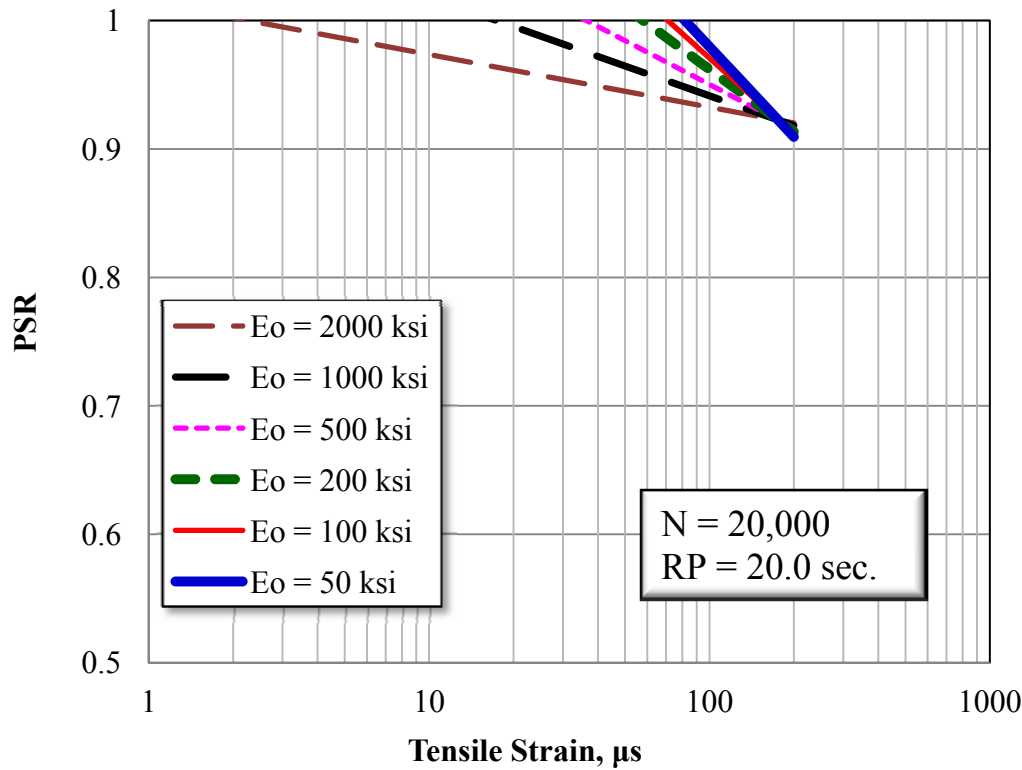
FIGURE 166 PSR versus tensile strain at different initial stiffness values (RP = 20.0 sec, N=20,000 cycles).

FIGURES 167 and 168 demonstrate the endurance limit values for different stiffness and rest period values at N = 20,000 and 100,000 cycles, respectively. It can be observed that the mixtures with higher stiffness showed a lower endurance limit as expected. In addition, the endurance limit values were stable after 5 seconds rest period (loading ratio of 50). N has a slight effect on the endurance limit values, with higher N showing higher endurance limit values. The endurance limit values computed from the second model are slightly less than those computed from the first generation model at a comparable stiffness.
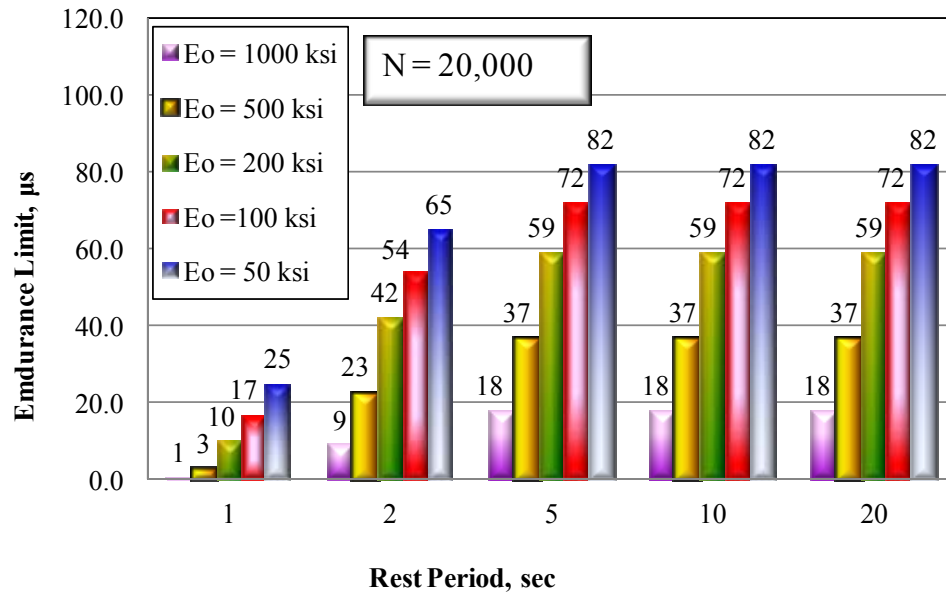
FIGURE 167 Endurance limit values at different rest periods and stiffness values using second generation model (N = 20,000).
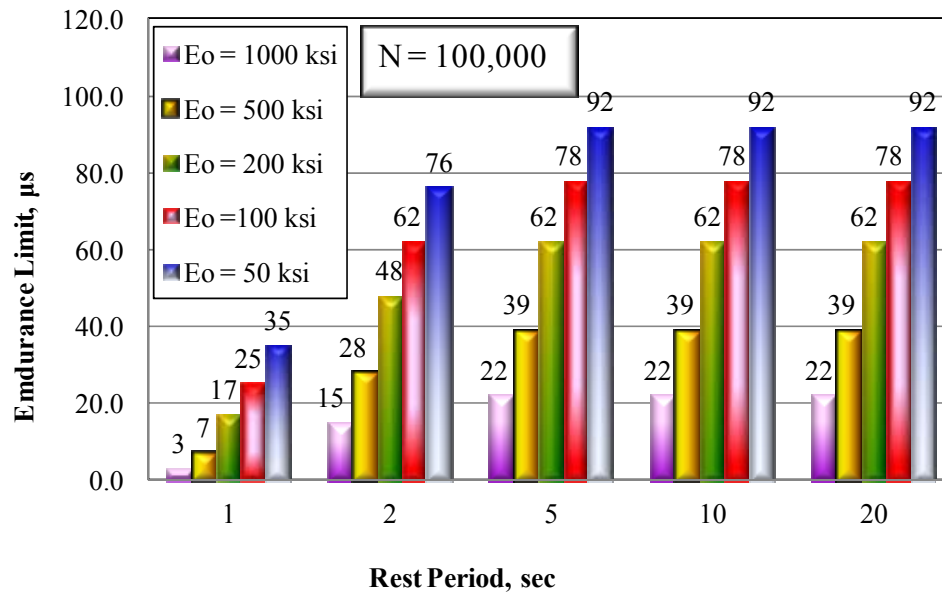
FIGURE 168 Endurance limit values at different rest periods and stiffness values using second generation model (N = 100,000).

COMPARISON WITH ENDURANCE LIMITS COMPUTED FROM THE BEAM FATIGUE EXPERIMENT

The beam fatigue data for the PG 64-22 mixtures (Souliman, 2012) were used to develop the beam fatigue model to predict the Stiffness Ratio (SR). The procedure was similar to that of the first generation PSR model except that the initial stiffness identified from the beam fatigue results at the 50th cycle. The model was developed with the nonlinear optimization techniques provided by the Solver® and Evolver® software. The sum of the squares errors was minimized and the regression coefficients were determined. The regression coefficients are listed in
TABLE 62 and the model form is presented in Equation 120.
FIGURE 169 presents the measured versus predicted SR using the SR model generation. FIGURE 170 shows the residual versus raw data plot. The standardized error versus the measured PSR plot is shown in FIGURE 171.
The model shows a highly accurate predictive capability based on its R^2_{adj} of 0.9471 and Se/Sy of 0.2502 using 231 data points.

TABLE 62 Regression coefficient values of first generation SR model using beam fatigue data for the PG 64-22 mixtures

Coefficient	Value	Coefficient	Value
a_0	1.46723575	a_{18}	0.00000000
a_1	-0.00000627	a_{19}	0.00000449
a_2	0.00062326	a_{20}	-0.00018445
a_3	0.04017422	a_{21}	-0.00011536
a_4	-0.00592721	a_{22}	-0.00001510
a_5	-0.40039632	a_{23}	0.00000000
a_6	0.31492804	a_{24}	0.00000000
a_7	1.33934526	a_{25}	-0.00003475
a_8	-0.05944687	a_{26}	-0.00006440
a_9	0.00000000	a_{27}	0.00000000
a_{10}	0.00002984	a_{28}	0.00000000
a_{11}	-0.00000240	a_{29}	-0.00012923
a_{12}	0.00022569	a_{30}	0.00000000
a_{13}	0.00000388	a_{31}	0.00000000
a_{14}	-0.00021350	a_{32}	-0.00002508
a_{15}	0.00000000	a_{33}	0.00000000
a_{16}	0.00000000	a_{34}	0.00000000
a_{17}	0.00000000		

$$SR = 1.46723575 - 0.00000627\ T^2 + 0.00062326\ T + 0.04017422\ AC - 0.00592721\ Va -$$
$$0.40039632\ \log \varepsilon_t + 0.31492804\ \mathrm{Tanh}(1.33934526\ RP) - 0.05944687\ \log N +$$
$$0.00002984\ T*AC - 0.00000240\ T^2*Va + 0.00022569\ T*Va + 0.00000388\ T^2*\log \varepsilon_t -$$
$$0.00021350\ T*\log \varepsilon_t + 0.00000449\ T^2*\log N - 0.00018445\ T*\log N - 0.00011536\ AC *$$
$$Va - 0.00001510\ AC * \log \varepsilon_t - 0.00003475\ AC * \log N - 0.00006440\ Va * \log \varepsilon_t -$$
$$0.00012923\ Va * \log N - 0.00002508\ \log \varepsilon_t * \log N \qquad\qquad (120)$$

The plot contains the text box:
$y = 0.9272x + 0.0533$
$R^2 = 0.9471$
$Se/Sy = 0.2502$
$N = 231$

with axes "Measured SR" (vertical) and "Predicted SR" (horizontal).
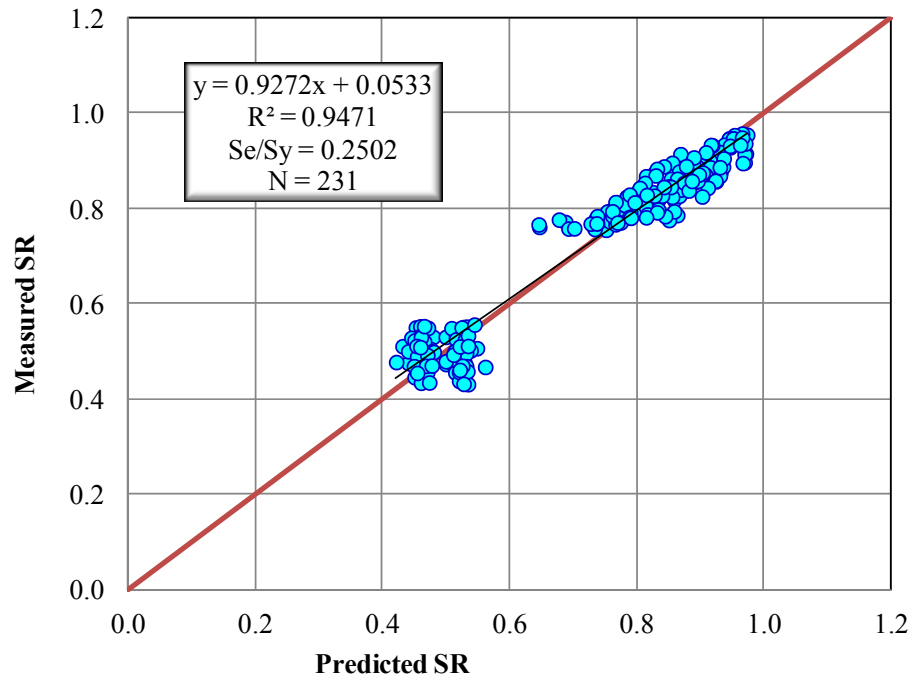
FIGURE 169 Measured versus predicted SR using the beam fatigue, PG 64-22 model.
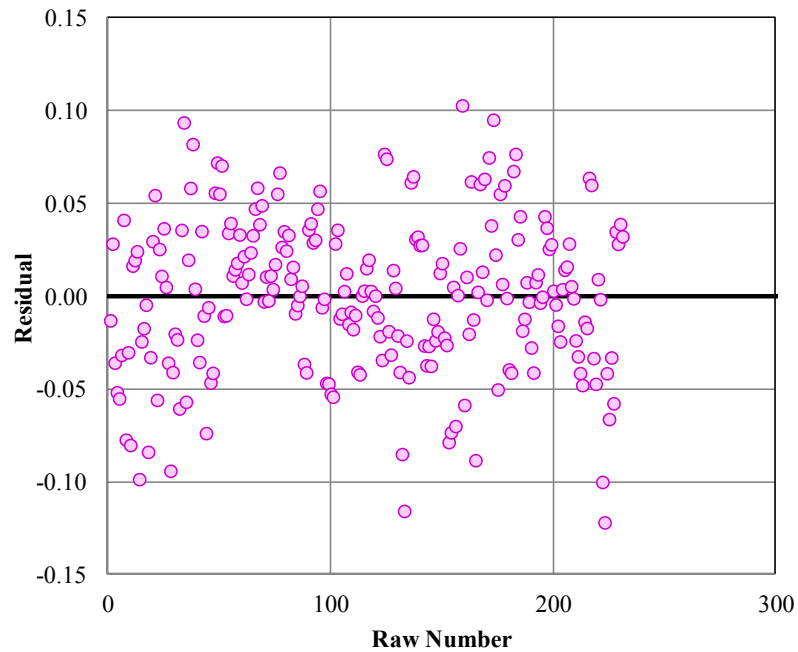
FIGURE 170 Residual versus raw number using the beam fatigue, PG 64-22 SR model.
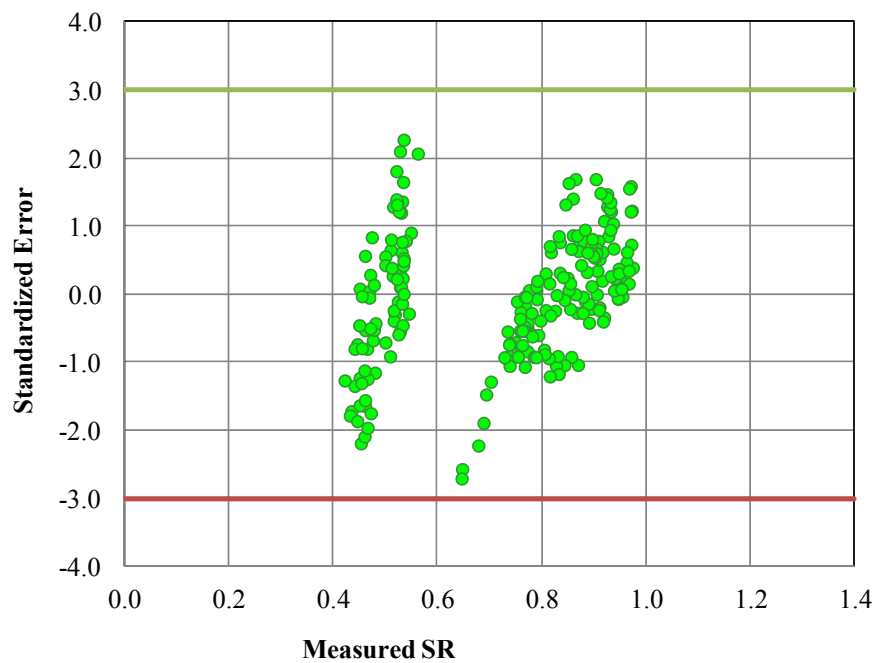
FIGURE 171 Standerdized error versus measured SR values using the beam fatigue, PG 64-22 SR mode.

226

The effect of rest period on the SR values at different temperatures is shown in FIGURE 172. The optimum rest period is 2.5 seconds (loading ratio of 25) compared to 3.0 seconds (loading ratio of 30) for the uniaxial fatigue test. The effect of N on the SR for the beam fatigue test is minimal especially at 100°F as shown in FIGURE 173. A value of N of 20,000 is recommended to avoid extrapolations as it represents the end of the fatigue tests with rest period.
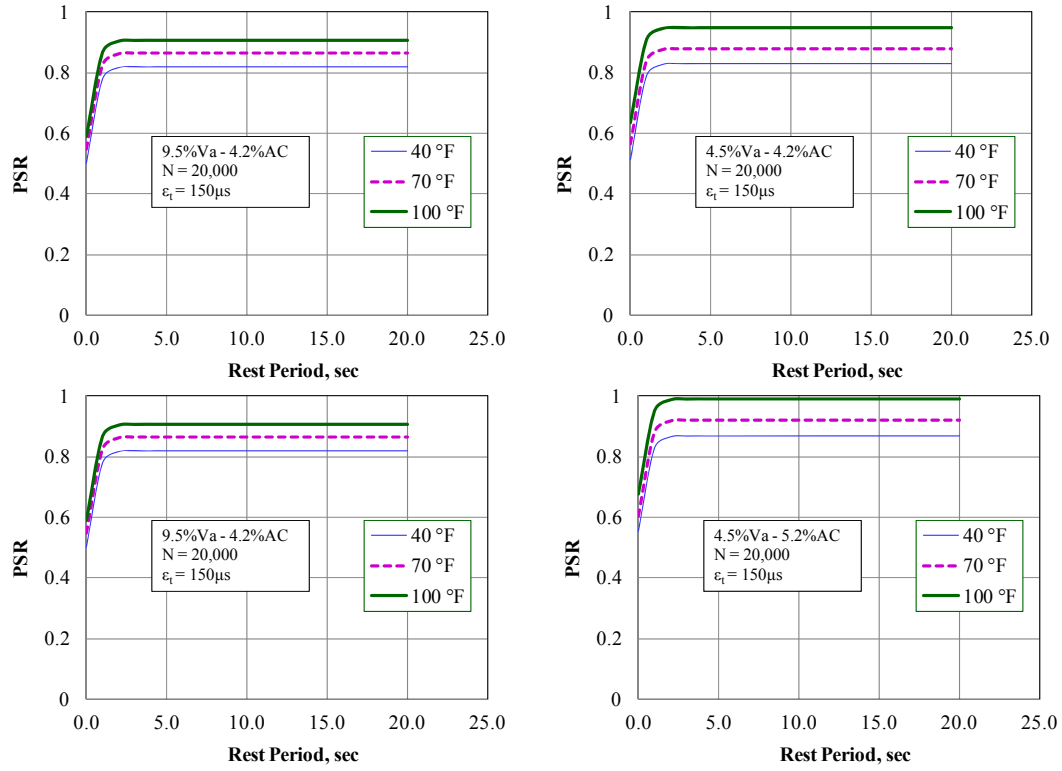
FIGURE 172 Effect N on SR-ε_t relationship at different RP and temperatures for the beam fatigue, PG 64-22, 4.5Va-4.2AC mixture.
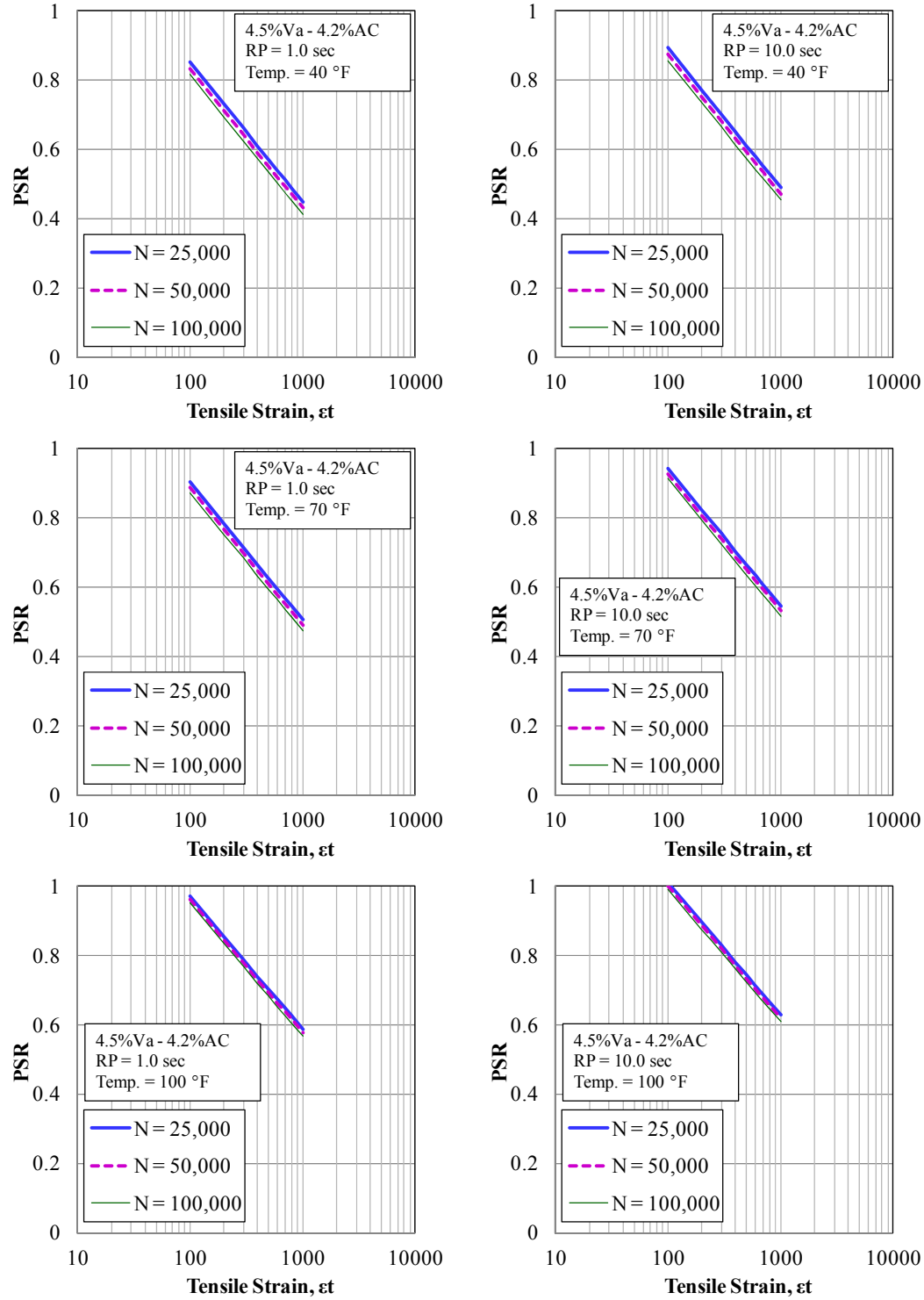
FIGURE 173 Effect N on SR-ε_t relationship at different RP and temperatures for the beam fatigue test, PG 64-22, 4.5%Va-4.2%AC mixture.

The beam fatigue model was also used to predict the PSR values at different tensile strains for each mixture type at different temperatures (4 mixtures × 3 temperatures). FIGURES 174 to 176 show the relationship between the SR and the tensile strain for different mixtures. It is interesting that the SR-ε_t relationships of the beam fatigue tests show similar trends compared to those obtained in the uniaxial fatigue test. The mixtures with higher asphalt contents and lower air voids showed higher SR. In addition, the effect of asphalt content is higher compared to the effect of air voids.

The endurance limit values are calculated for mixtures at different temperatures where the SR-ε_t relationships intersect a SR value of 1.0. FIGURE 177 shows the endurance limit values at different temperatures for the 5 second rest period at 20,000 loading cycles. The mixtures with higher binder contents and lower air voids exhibited high endurance limit values at all test temperatures. The endurance limit values from the beam fatigue test exhibits similar trends to those from the uniaxial fatigue test. However, the endurance limit values from beam fatigue are about 12% higher than those from the uniaxial fatigue test. This is an interesting finding considering that the fatigue life using the beam fatigue test is much higher compared to the uniaxial fatigue test. This difference is mainly due to the fact that the calculation of the endurance limit is based on healing, i.e., on the changes of the stiffness or the pseudo stiffness and not the fatigue life extension. In addition, this comparison showed that, regardless of the fatigue test type, the asphalt mixtures are prone to heal in a similar fashion if allowed to rest.
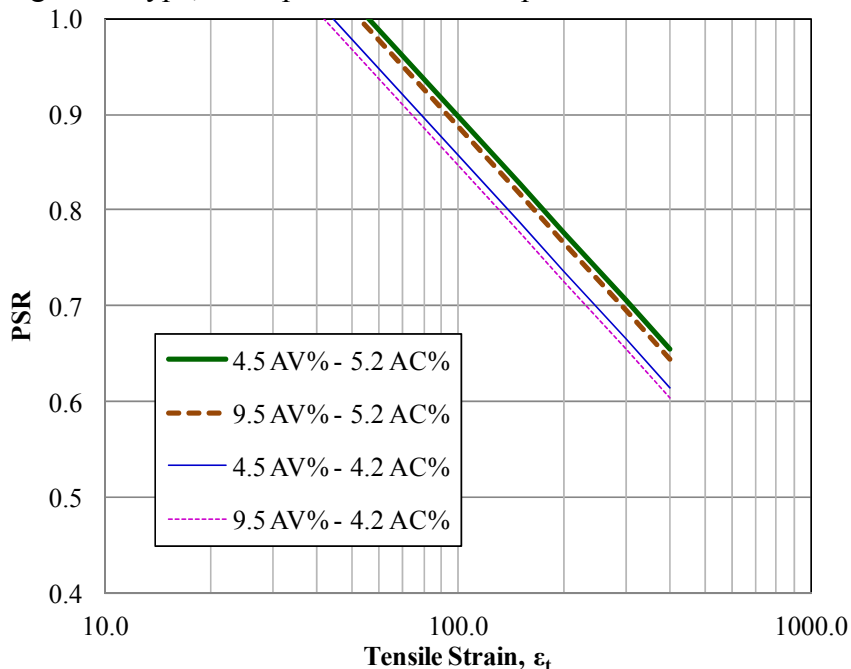
FIGURE 174 SR versus tensile strain for the beam fatigue test, PG 64-22 mixtures at 40°F (RP = 5.0 sec, and N = 20,000).
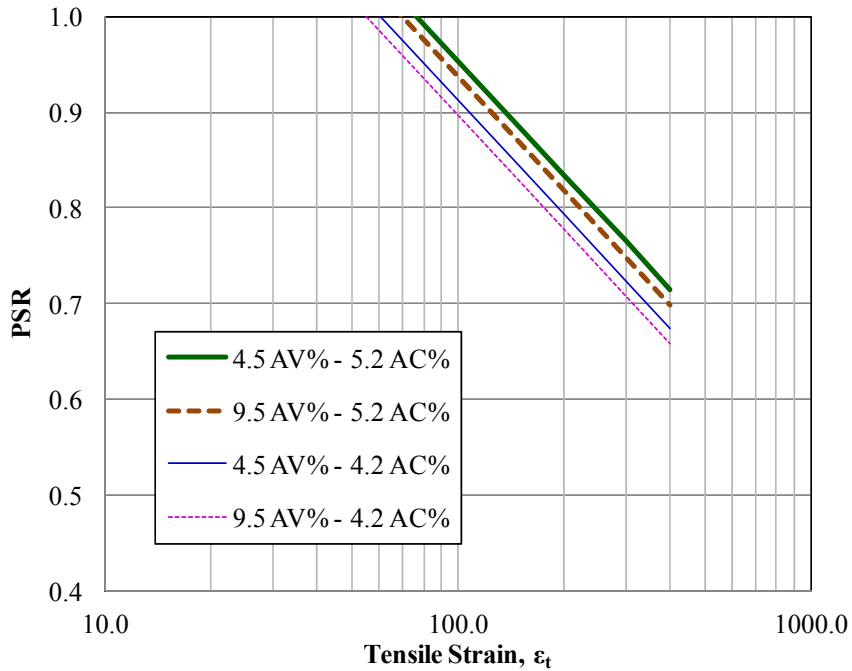
FIGURE 175 SR versus tensile strain for the beam fatigue test, PG 64-22 mixtures at 70°F (RP = 5.0 sec, and N = 20,000).
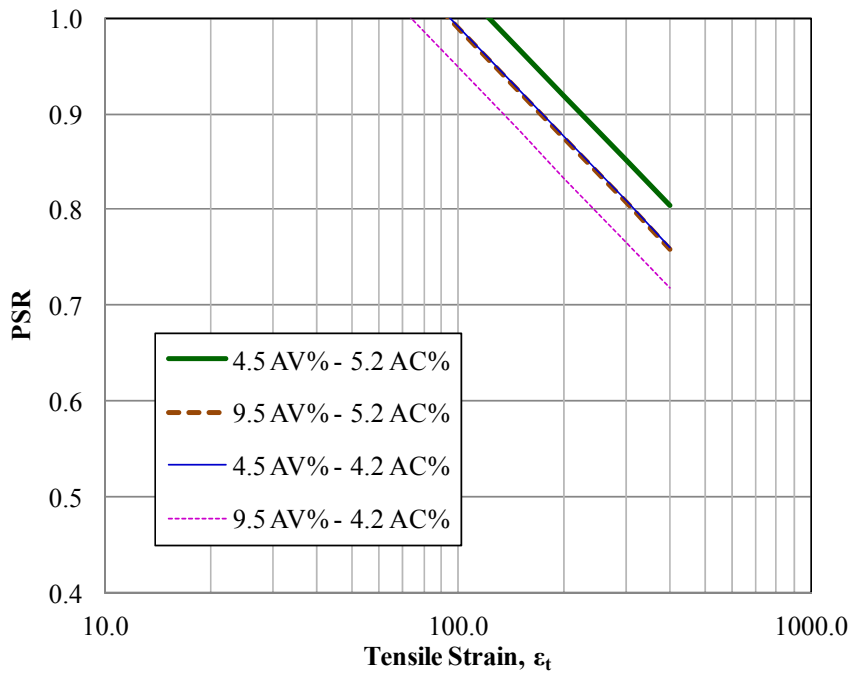
FIGURE 176 SR versus tensile strain for the beam fatigue test, PG 64-22 mixtures at 100°F (RP = 5.0 sec, and N = 20,000).

231
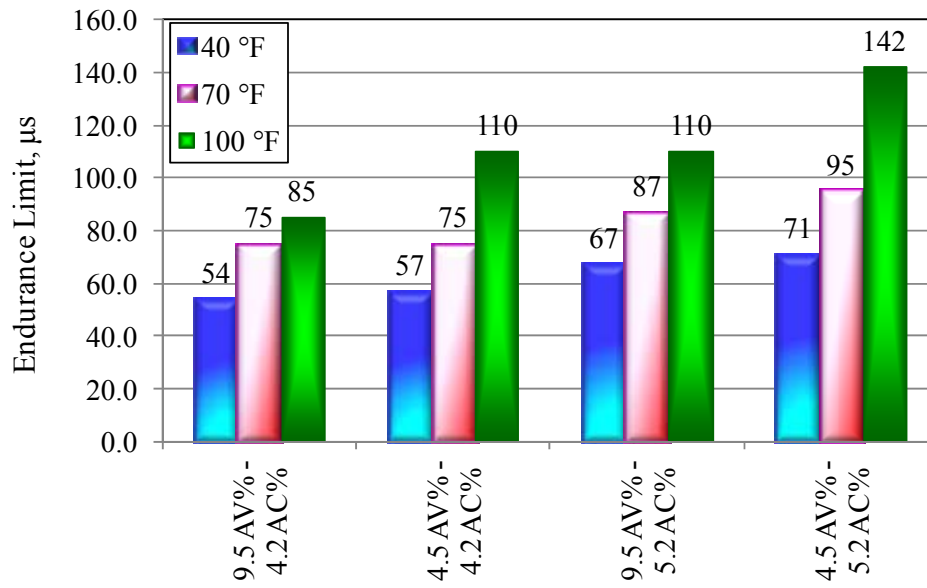
FIGURE 177 Endurance limit values for the beam fatigue test, PG 64-22 mixtures at different temperatures using SR model (RP = 5 sec and N = 20,000 cycle).

FIGURE 178 directly compares the endurance limit values obtained from the uniaxial fatigue model to those from the beam fatigue model. These values were estimated for all mixtures at 5 seconds rest period, 200,000 loading cycles, and three temperatures (40, 70, and 100°F). It is clear that there is a good correlation between the endurance limit values from both tests, which assures the robustness of the developed methodology to estimate the endurance limit of asphalt mixtures. The relationship between the two data groups showed that the endurance limit calculated from the uniaxial fatigue test is about 90% of the beam fatigue test values.
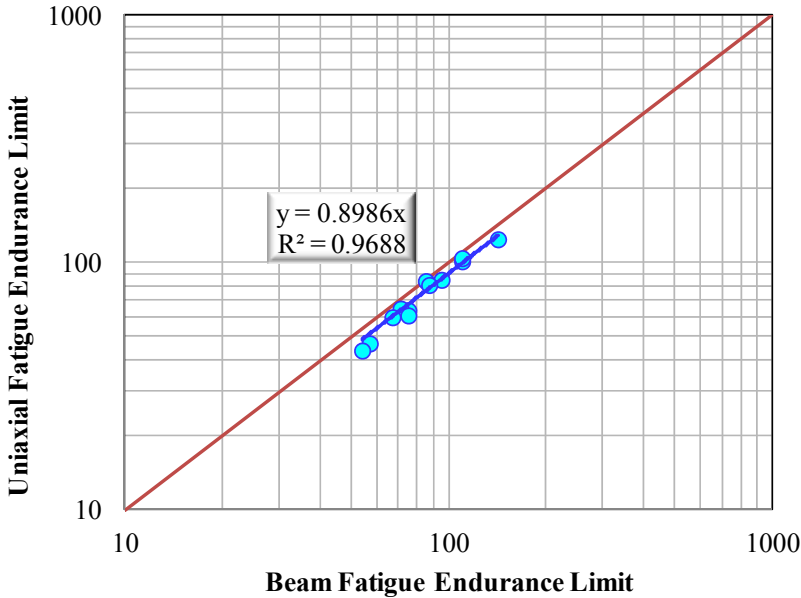
FIGURE 178 Comparison of endurance limit values for all mixtures using beam fatigue versus uniaxial fatigue test (PG 64-22, RP = 5 sec, N = 20,000 cycles).

METHODOLOGY FOR INCORPORATING THE ENDURANCE LIMIT INTO THE AASHTOWARE PAVEMENT ME DESIGN

Based on findings from NCHRP Project 9-44A, the fatigue endurance limit varies with and depends on mixture volumetric properties, HMA stiffness, and the frequency of truck distribution. In other words, there is no single value of the endurance limit that can be input into the Pavement ME Design software for all conditions. The present implementation of the fatigue endurance limit in Pavement ME Design requires the input of a single value for all different conditions. Therefore, implementation of the endurance limit formalism developed in this research will require an additional subroutine that calculates the endurance limit for the project conditions used in the simulation and provides it to the proper main routine during the analysis process. The sections below discuss a framework for achieving this implementation.

Calculation of Endurance Limit

The PSR model developed in the NCHRP Project 9-44A to estimate the endurance limit consists of five parameters as follows:

$$PSR = f(\varepsilon_t, E_o, N, RP) \qquad (121)$$

where:
PSR = Pseudo stiffness ratio at number of cycles N
ε_t = Tensile strain, µs
E_o = Initial stiffness, ksi
N = Number of load cycles

RP   = Rest period between load application, seconds

In Equation 121, when the PSR stiffness ratio is substituted with 1, the tensile strain becomes the endurance limit below which no fatigue damage occurs in the HMA layer. Although N is included in the PSR model, the results showed that N has little or no effect on the endurance limit values. N = 20,000 loading cycles is recommended as a reasonable value.

The model parameters are dynamic and must be calculated by the Pavement ME Design software for each simulation period during the pavement service life. The parameters included in the model are discussed below.

Pseudo Stiffness Ratio (PSR)

For the analysis of the fatigue endurance limit, the PSR value is always assumed to be 1.0 indicating full healing of the fatigue damage.

Initial Stiffness or Modulus (E_o)

The E_o value is a changeable parameter as the dynamic modulus (E^*) depends on the loading rate, temperature, and volumetric properties. One of the differences between E_o and E^* is that E^* is measured at a strain range low enough not to induce damage (or permit complete healing during the rest period), whereas E_o is measured through a "damage" test with higher strain values. Due to damage that takes place in fatigue tests, E_o is always lower than the E^* for the same mixture. The difference between both parameters increases with increasing temperature and strain values. As E^* is a key parameter in the calculations of Pavement ME Design, it is more convenient and powerful to develop a correlation between E_o and E^*. Fortunately, and as explained before, the E^* values were measured for all the tests using the fingerprint test before the uniaxial fatigue test. Using available data, an excellent relationship was found between E_o and E^* as shown in FIGURE 179. This relationship can be used to predict E_o from E^* values with high level of precision ($R^2 = 0.9875$).
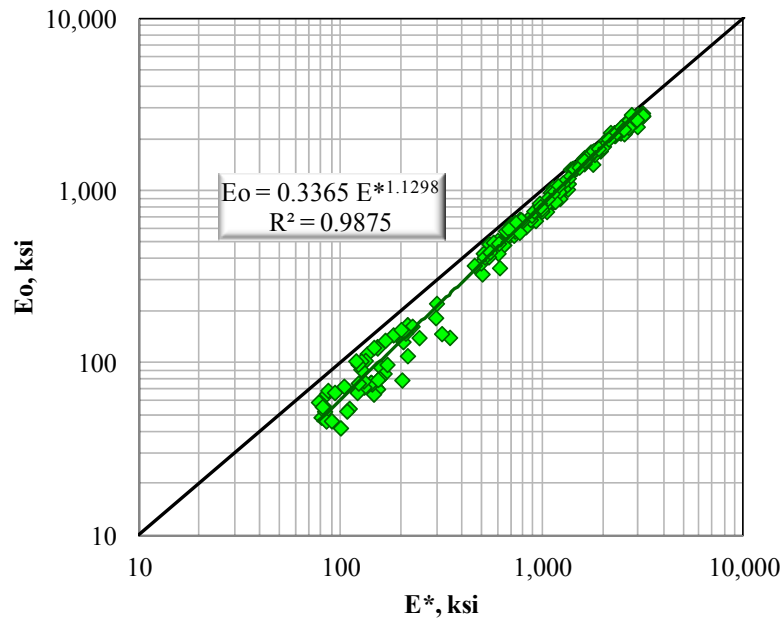
FIGURE 179 Relationship between initial stiffness and dynamic modulus using the uniaxial fatigue results.

Rest Period (RP)

The rest period between truck axles in seconds is calculated as an average value every analysis period in the Pavement ME Design simulations. This requires calculation of the actual truck spectrum every 2 hours as shown in FIGURE 180.
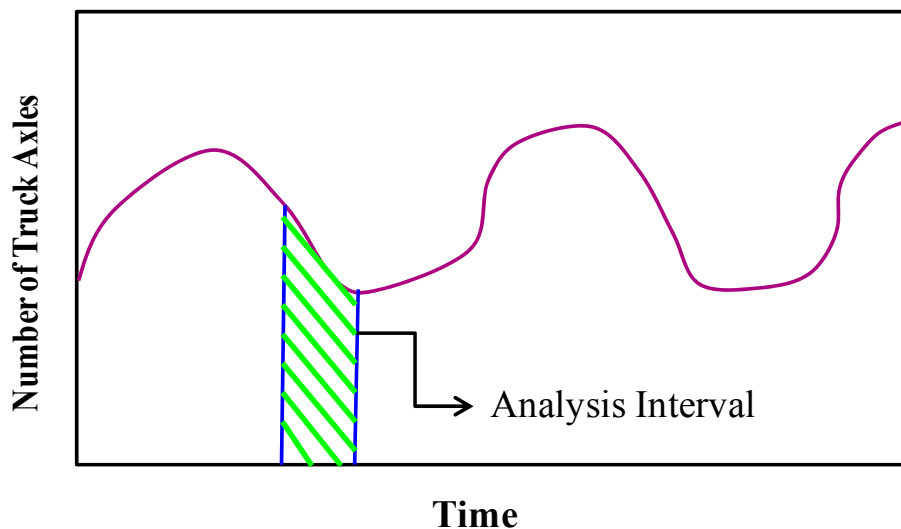
FIGURE 180 Assumed truck axle distribution during the 24 hours of the day.

The value of RP in this case can be calculated as follows:

235

$$RP = 3,600/\sum(NT*NA) \hspace{4cm} (122)$$

where

NT = Number of trucks in the analysis period increment considered in the simulations

NA = Average number of axles in each truck.

Once all the different parameters are calculated, the model in Equation 121 can be solved for the endurance limit, which is the strain at a stiffness ratio of 1. This calculation will be done every analysis period during the Pavement ME Design simulations.

Incorporating Endurance Limit into Fatigue Relationships

The model used for the calculation of the fatigue damage in Pavement ME Design is as follows:

$$N_f = C \times k_1 (1/\varepsilon_t)^{k_2} (1/E_o)^{k_3} \hspace{3cm} (123)$$

where:

N_f = Number of repetitions to fatigue failure,

ε_t = Tensile strain at the critical location,

E_o = Initial stiffness of the HMA,

k_1, k_2, k_3 = Laboratory regression coefficients, and

C = Laboratory to field adjustment factor.

Pavement ME Design divides the structural layers of the HMA layer into sub-layers. The JULEA program then calculates the critical tensile strain analysis period. The values k_1, k_2, k_3, calculated and calibrated based on the fatigue tests without rest period, are used to determine the fatigue lives at different temperatures. The endurance limit approach developed in this study is based mainly on the fatigue healing using the results of the fatigue test with rest period. To incorporate the endurance limit concept with the fatigue lives used to calculate the fatigue damage in the Pavement ME Design simulations, the fatigue lives are considered to be infinity when the strain level is equal to the endurance limit. This means the fatigue life versus the tensile strain relationship becomes a horizontal line at a strain value equal to the endurance limit. For each fatigue relationship, a corresponding endurance limit value is calculated at the same E_o but at different rest periods using the second generation PSR model, which is a function of E_o. FIGURES 181 to 183 show examples of incorporating of the endurance limit with fatigue relationships using different rest periods.
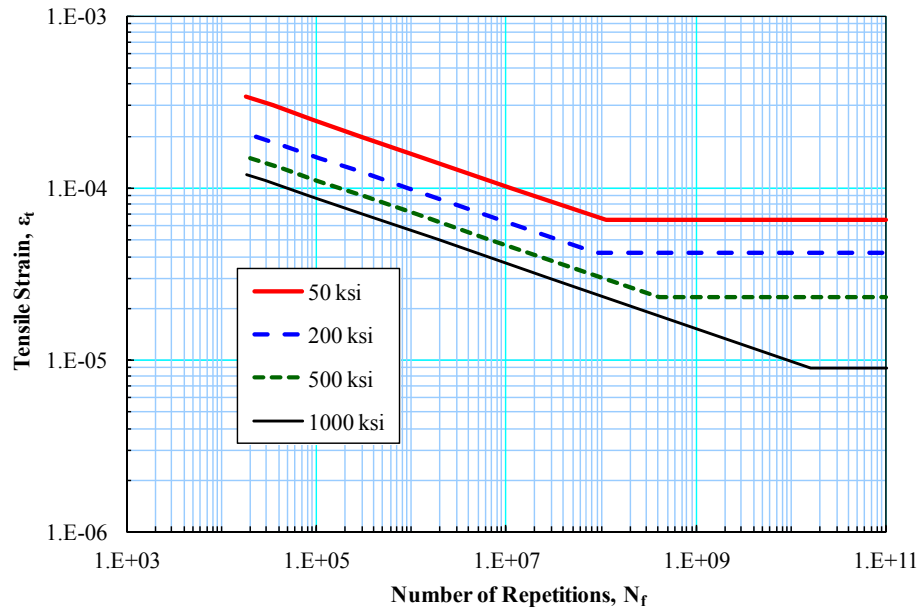
FIGURE 181 Fatigue relationships for different stiffness values at 2 second rest period.
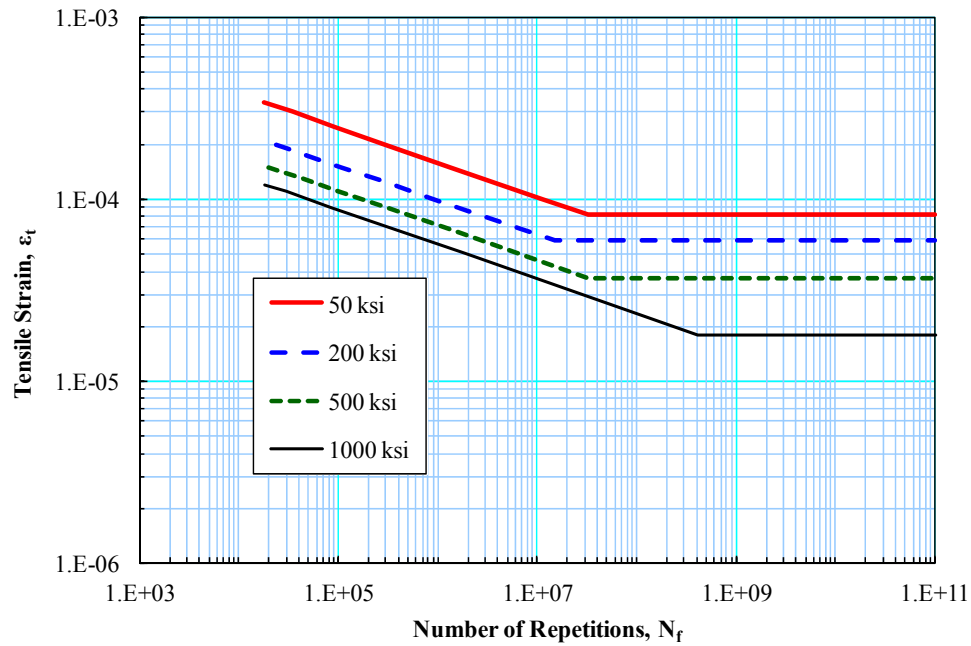
FIGURE 182 Fatigue relationships for different stiffness values at 5 second rest period.
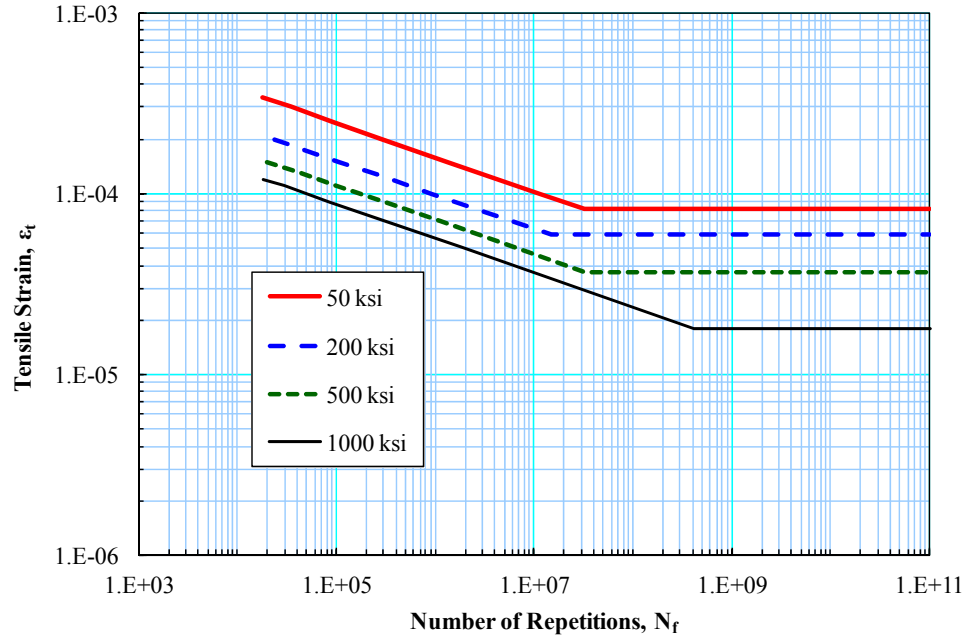
FIGURE 183 Fatigue relationships for different stiffness values at 20 second rest period.

Incorporating Endurance Limit into Fatigue Damage

The estimation of the fatigue damage in the Pavement ME Design is based on Miner's law given by Equation 124.

$$D_i = \Sigma (n_i / N_i) \tag{124}$$

where:

    D = Damage,

    n_i = Actual traffic for period i, and

    N_i = Traffic allowed under conditions prevailing in period i.

The endurance limit is calculated for every analysis period as discussed before. At the same time, the critical strain value of the HMA layer (or sub-layer) for each truck axle is calculated using the JULEA program. If the critical strain calculated from the JULEA program is less than or equal to the fatigue endurance limit, the value of N_i calculated from the fatigue life relationships approaches infinity, which means that n_i/N_i approaches zero and the fatigue damage induced by that axle load is not counted in the analysis. However, if the critical strain is greater than the fatigue endurance limit, the axle is counted as causing fatigue damage.

CHAPTER 9

SUMMARY, FINDINGS, AND SUGGESTIONS FOR FUTURE RESEARCH

SUMMARY

The main objective of this research described in his appendix was to develop and validate fatigue endurance limit models based on uniaxial fatigue tests that can be used as input into the AASHTOWare Pavement ME Design software.

This study included testing of four HMA mixtures using two levels each of air voids and asphalt contents. Three asphalt binders (PG 58-28, PG 64-22, and PG 76-16) were used for the dynamic modulus test and one binder (PG 64-22) was used in the uniaxial fatigue test. One aggregate type and gradation were used in the study.

The endurance limit was defined as the allowable tensile strain at which the micro-cracks damage due to load is balanced with the healing during the rest periods. To account for the damage and healing due to fatigue, the viscoelastic continuum damage analysis was applied. To determine the viscoelastic properties required for the viscoelastic continuum damage analysis, dynamic modulus tests were conducted according to the AASHTO T 342 procedure, and the Prony series coefficients were determined for the tested mixtures. Several ancillary studies were conducted to develop a proposed uniaxial fatigue test protocol that permits testing with and without rest periods. These studies included: specimen preparation and fixture adjustments, specimen geometry and air voids distribution, strain control, and machine compliance. In addition, two new test control and analysis software programs were developed through collaboration with IPC Company to conduct the tests with and without rest period.

Three major uniaxial fatigue test experiments were conducted. The first experiment was the fatigue life experiment. The main objective of this experiment was to establish the N_f-ε_t relationships at different temperatures to determine the proper strain levels for each asphalt mixtures that would fail specimens at 20,000 and 100,000 loading cycles. The second experiment was the main experiment to study the effect of five factors on the fatigue damage and healing by conducting uniaxial fatigue tests with and without rest periods. These factors were asphalt content, air voids, strain, rest period, and temperature. Each factor was represented by two levels except for temperature, where three levels were used. A third uniaxial fatigue experiment was introduced to account for additional strain levels and rest periods to study non-linearity effects. A total of 54 dynamic modulus tests and 182 uniaxial fatigue tests were performed.

The data for the three uniaxial fatigue experiments were combined together to develop Pseudo Stiffness Ratio (PSR) models using a total number of 161 test results. Two PSR regression models were developed. The first PSR model included the main five factors plus one additional factor, the number of loading cycles N at which the PSR values were measured. The second PSR regression model was developed by replacing three factors (air voids, asphalt content, and temperature) with the initial stiffness. The endurance limit was estimated using both models as the allowable tensile strain when PSR is equal to 1.0.

To compare the endurance limits from the uniaxial fatigue tests to those obtained from the beam fatigue tests, a stiffness ratio (SR) model was developed based on beam fatigue tests conducted in a companion study. The beam fatigue SR regression model included six factors

similar to those of the uniaxial PSR regression model and the endurance limits were determined. The last task of this study was to provide a framework for implementing the endurance limit calculated from the PSR model into fatigue analysis and damage using the Pavement ME Design software.

FINDINGS

The following are key findings from this research.

Viscoelastic Properties

- The effect of air voids on the dynamic modulus master curves was clear within the selected ranges, in which dynamic modulus master curves were shifted from each other in a parallel pattern. Increasing the air voids resulted in lowering the dynamic modulus master curves.
- There was no common trend for the effect of the binder content on the E* master curves for all tested mixtures. However, a certain trend (or absence of such) was evident for each PG binder mixture separately. For the PG 64-22 mixtures, the E* master curves at different binder contents overlapped with no specific trend. In the case of PG 58-28 mixtures, the lower the binder content, the higher the E* values. The master curves of the PG 76-16 mixtures at the optimum asphalt content (OAC) showed higher E* values compared to those with OAC ±0.5%.
- The effect of the asphalt content (OAC and OAC±0.5%) on the dynamic modulus master curves was less compared to the effect of the air voids range (design value ± 2.5% or ± 3.0%).
- The effect of changing air voids and binder content on the E* master curves was very accurately predicted using regression models that correlate both volumetric and sigmoidal parameters.
- The approach developed in this study can be applied to quality assurance, especially if the project contract considered the pavement performance predicted by the MEPDG as a basis for penalties or bonuses. In this case, this approach would save extensive testing, and at the same time would accurately predict the dynamic modulus values due volumetric changes.
-

Development of the Uniaxial Fatigue Protocol and Software

- Aluminum platens provide better adhesion to specimens than steel platens.
- Loctite Epoxy Metal/Concrete, Loctite Fixmaster Superior Metal, and Davcon Plastic Steel Liquid (10210) are appropriate for 3-inch diameter specimens. ACE Plastic repair epoxy is suitable for 4-inch diameter specimens.
- Three-inch diameter specimens have greater tendency to fail within the middle of the specimen, while the 4-inch diameter specimens usually fail more frequently near to the end platens.
- The thread locked joint is better that the slipped locked joint to decrease the machine compliance factor.

- Increasing the compaction height from 6.7-inch (170-mm) to 7.1-inch (180-mm) increases from 20 % to 83% the chances of having a successful test where failure takes place in the middle of the specimen.
- The on-specimen strain values using the crosshead controlled-strain method cannot be kept constant, but increase with time.
- Controlling the strain directly from the on-specimen LVDTs is undesirable. The wave shape of the load and strain waveform becomes distorted when the test is controlled by the average on-specimen LVDTs.
- The tension-compression test (sinusoidal) diminishes specimen permanent deformation compared to the direct-tension test (haversine).
- For the strain controlled uniaxial fatigue test, the haversine test condition cannot be maintained during the test, as it will switch quickly to a sinusoidal wave shape.
-

Results of the Uniaxial Fatigue Experiments

- The 50% stiffness reduction or pseudo stiffness reduction criterion seems to be an appropriate definition for fatigue failure at all test temperatures. On the other hand, the definition of fatigue failure as the point where there is a sharp decrease of the phase angle is not usually valid, as the test results at high temperatures (e.g., 100°F) did not show a sharp drop in the phase angle.
- The selection of initial stiffness to be at the 100th cycle significantly improved the fitting of the fatigue life relationships especially at 100°F compared to the initial stiffness at the 50th cycle.
- For all test temperatures, increasing the asphalt content by 1% (from 4.2 to 5.2) had a greater effect on the fatigue life and k_2 values than decreasing the air voids by 5% (from 9.5% to 4.5%).
- For the generalized fatigue model, the lower the air voids the lower the k_2 and k_3 values. Also, increasing the asphalt content reduces both k_2 and k_3 values.
- For the individual fatigue lives, the k_2 values for the uniaxial tension-compression fatigue test were higher compared to the historical beam fatigue test. This means that the fatigue damage caused by the uniaxial fatigue test is greater than that of the beam fatigue test.
- Based on test results, increasing the rest period from 5 to 10 seconds (50 to 100 loading ratio) did not show an increase in the healing value when comparing the PSR values for both rest periods.
- Introducing a 1-second rest period increased the PSR by 50% compared to the test without rest period.

Development of PSR Regression Models and Endurance Limit Analysis

- PSR Regression models developed by the nonlinear optimization approach showed more accurate prediction compared to the models developed by the nonlinear regression analysis.
- The Evolver® software reduced the sum of squares error and increases the accuracy of the regression models compared to using Solver® function and Statistica® Software to perform nonlinear optimization analysis.

241

- Using the tangent hyperbolic (tanh) function to fit the PSR and rest period relationship increased the accuracy of the models.
- For the first and second generation PSR models, the optimum rest period values for all tested mixtures were 3 seconds (loading ratio of 30) for all test temperatures. This optimum rest period fits in the middle range of optimum rest periods (1 to 5 seconds or 10 to 50 loading ratio) collected from a review of the literature.
- The effect of N on the endurance limit value when PSR is equal to 1.0 was minimal.
- Mixtures with higher asphalt content and lower air voids exhibit higher endurance limit values.
- The effect of asphalt content is much more significant than the air voids on the fatigue healing and endurance limit.
- The endurance limits almost doubled when the temperature was increased from 40 to 70°F for the four asphalt mixtures.
- For the second generation PSR model, significant simplification was achieved by replacing the air voids, asphalt content, and temperature with the initial stiffness. In addition, the second generation PSR model is more compatible with the Pavement ME Design software, where the pavement performance prediction is mainly driven by the dynamic modulus of the HMA mixture.
- The only concern in replacing the stiffness with the volumetric parameters is that a mixture with very high asphalt content that is stiff would show the same modulus as a mixture with very low asphalt binder that is soft. However, the expected fatigue damage and healing could be totally different. At the extreme, two such mixtures could have the same stiffness, with the first very rich with asphalt and well compacted while the second has a low asphalt content and is poorly compacted. The first mixture represents the best condition for fatigue resistance and healing, although the fatigue and healing performance of the second mixture should be the worst. This irregular stiffness effect can be reduced by having a larger experimental database to refine the models.
- The endurance limits estimated by the second PSR model were 25% less than those estimated by the first model.
- The endurance limit values determined from uniaxial and beam fatigue tests showed very high correlation with the uniaxial fatigue endurance limit about 10% less than the beam fatigue endurance limit.
- A reasonable framework for implementation of the developed methodology into Pavement ME Design was described.

SUGGESTED FUTURE RESEARCH

Based on the main outcomes of this study, the following future research is suggested:
1. The laboratory experimental work of this study was conducted using only the PG 64-22 binder. Further testing of mixtures prepared with other PG binders, especially binders modified with polymers, crumb rubber, warm mix technologies, etc., is important to define the effect of the binder type on the fatigue healing and endurance limit. In addition, the effect of aggregate type and gradation requires further investigation.

2. The effect of specimen geometry on the fatigue damage, healing, and endurance limit should be investigated further.
3. The current study was based on laboratory tests only. Verification and calibration are still needed through full-scale field or accelerated pavement testing.

REFERENCES

American Association of State Highway and Transportation Officials. Bulk Specific Gravity of Bituminous Mixtures Using Saturated Surface Dry Specimens, Test Method AASHTO T 166 – 00, Standard Specifications for Transportation Materials and Methods of Sampling and Testing, *Part II – Tests*, Twentieth Edition, 2000.

American Association of State Highway and Transportation Officials. Determining the Fatigue Life of Compacted Hot-Mix Asphalt (HMA) Subjected to Repeated Flexural Bending, Test Method T321-03, *AASHTO Provisional Standards*, Washington, D.C., 2003.

American Association of State Highway and Transportation Officials. Determining Dynamic Modulus of Hot-Mix Asphalt Concrete Mixtures, Test Method AASHTO TP 62-03, *AASHTO Provisional Standards*, Washington D.C., 2006.

American Association of State Highway and Transportation Officials. Theoretical Maximum Specific Gravity of Bituminous Mixtures, Test Method AASHTO T 209 – 00, Standard Specifications for Transportation Materials and Methods of Sampling and Testing, *Part II – Tests*, Twentieth Edition, 2000.

Abojaradeh, M. *Predictive Fatigue Models for Arizona Asphalt Concrete Mixtures*, Ph.D. Dissertation, Arizona State University, Tempe AZ, December 2003.

Advanced Asphalt Technologies, LLC, *Hot Mix Asphalt Endurance Limit Workshop*: Executive Summary, National Cooperative Highway Research Program Project 9-44, 2007.

Aglan, H., and Figueroa, L. Technical Report, U.S Corps of Engineer, *Waterways Experiment Station*, Contact No: DACA39-90-K0023, December, 1991.

Al-Khateeb, G., and Shenoy, A. A Simple Quantitative Method for Identification of Failure due to Fatigue Damage, *International Journal of Damage Mechanics,* Vol. 20, pp 3-21, 2011.

Al-Khateeb, G., and Shenoy, A. *A Distinctive Fatigue Failure Criterion*, Journal of the Association of Asphalt Paving Technologists (AAPT), Vol. 73, pp. 585-622, 2004.

Anderson, D.A., Christensen, D.W. and Bahia, H. Physical Properties of Asphalt Cement and the Development of Performance Related Specifications, *Journal of the Association of Asphalt Paving Technologists (AAPT)*, Vol. 60, pp. 437-475, 1991.

Anderson, T.L. *Fracture Mechanics: Fundamentals and Applications*, CRC, Pr, 2nd Edition, February, 1995.

Asphalt Pavement Alliance (APA). *Perpetual Pavements: A Synthesis*, APA 101, Asphalt Pavement Alliance, Lanham, MD, 2002.

Bahia, H., Zhai, H., Bonnetti, K., and Kose, S. Non-linear viscoelastic and fatigue properties of asphalt binders, *Journal of the Association of Asphalt Paving Technologists (AAPT)*, Vol. 68, pp. 1–34, 1999.

Balbissi, A.H. *A comparative Analysis of the Fracture and Fatigue Properties of Asphalt Concrete and Sulphex*, Ph.D. Dissertation, Texas A&M University, College Station, Texas, 1983.

Barksdale, R.D. and Miller, J. H., III. *Development of Equipment and Techniques for Evaluating Fatigue and Rutting Characteristics of Asphalt Concrete Mixes*, Report SCEGIT-77-147, School of Civil Engineering, Georgia Institute of Technology, Atlanta, 1977.

Bazin, P., and Saunier, J. Deformability, Fatigue and Healing Properties of Asphalt Mixes, *Proceedings of the 2nd International Conference of Structural Design of Asphalt Pavements*, Ann Arbor, Michigan, pp. 553-569, 1967.

Bhattacharjee, S., Swamy, A.K., and Daniel, J.S. *Application of the Elastic-Viscoelastic Correspondence Principle to Determine the Fatigue Endurance Limit of Hot Mix Asphalt,* Transportation Research Record 2126, Transportation Research Board of the National Academies, pp. 12-18, Washington D.C, 2009.

Biligiri, K.P., Kaloush, K.E, and Uzan, j. Evaluation of Asphalt Mixtures' Viscoelastic Properties Using Phase Angle Relationships, *International Journal of Pavement Engineering*, Vol. 11, Issue 2, pp. 143-152, April 2010.

Bonaquist, R.F. *Developing a Plan for Validating an Endurance Limit for HMA Pavements*, NCHRP 9-44, National Cooperative Highway Research Program, HMA Workshop Executive Summary, 2007.

Bonnaure, F., Gravois A., and Udron, J. A New Method for Predicting The Fatigue Life of Bituminous Mixes, *Journal of the Association of Asphalt Paving Technologists (AAPT)*, Vol. 49 Proc., Louisville, KY, February 1980.

Bonnaure, F., Huibers, A., and Boonders, A. A Laboratory Investigation of the Influence of Rest Periods on the Fatigue Characteristics of Bituminous Mixes, *Journal of the Association of Asphalt Paving Technologists (AAPT),* Kansas City, Missouri, Vol.51, pp.104-128, 1982.

Bonnot, J. *Asphalt Aggregate Mixtures*, Transportation Research Record 1096, Transportation Research Board of the National Academies, Washington, D. C., pp. 42-50, 1986.

Breysse, D., Roche, C.D.L., Domee, V., and Chauvin, J. J. *Influence of Rest Time on Recovery and Damage during Fatigue Tests on Bituminous Composites*, Proceedings of 6th RILEM Symposium PTEBM' 03, Vol. 36, pp. 648-651, Zurich, 2003.

Brown, E., Cooley, L., Hanson, D., Lynn, C., Powell, B., Prowell, B., and Watson, D. *NCAT Test Track Design, Construction, and Performance*, NCAT Report 2002-12, National Center for Asphalt Technology, Auburn University, 2002.

Button, J.W., Little, D.N., Kim, Y., and Ahmed, S.J. Mechanistic evaluation of selected asphalt mixes, *Journal of the Association of Asphalt Paving Technologists (AAPT)*, Vol. 56, pp. 62-90, 1987.

Carpenter, S. H., Ghuzlan, K, and Shen, S. *Fatigue Endurance Limit for Highway and Airport Pavements*, Transportation Research Record 1832, Journal of the Transportation Research Board, pp. 131-138, National Research Council, Washington D.C., 2003.

Carpenter, S.H. *Fatigue Performance of IDOT Mixtures*, Civil Engineering Studies, Illinois Center for Transportation Series No 07.-007, University of Illinois at Urbana-Champaign, July, 2006.

Carpenter, S.H., and Jansen, M. *Fatigue Behavior Under New Aircraft Loading Conditions*, Proceedings of Aircraft Pavement Technology in the Midst of Change, pp. 259- 271, 1997.

Carpenter, S.H., and Shen, S. *Application of the Dissipated Energy Concept in Fatigue Endurance Limit Testing*, Transportation Research Record 1929, Transportation Research Board of National Academies, pp. 165-173, 2005.

Carpenter, S.H., and Shen, S. *Dissipated Energy Approach to Study Hot-Mix Asphalt Healing in Fatigue*, Transportation Research Record 1970, Transportation Research Board of National Academies, Washington, D.C., 2006.

Carpenter, S.H., Ghuzlan, K., and Shen, S. *Fatigue Endurance Limit for Highway and Airport Pavements*, Transportation Research Record 1832, Transportation Research Board of National Academies, Washington, DC., pp. 131-138, 2003.

Castro, M. and Sanchez, J.A. Fatigue and Healing of Asphalt Mixtures: Discriminate Analysis of Fatigue Curves, *Journal of Transportation Engineering*, ASCE, Vol. 132, No. 2, pp. 168-174, 2006.

Chehab, G., Kim, Y.R., Schapery, R.A., Witczack, M., and Bonaquist, R. Time-Temperature Superposition Principle for Asphalt Concrete Mixtures with Growing Damage in Tension State, *Journal of the Association of Asphalt Paving Technologists (AAPT)*, Vol. 71, pp. 559-593, 2002.

Chehab, G.R. *Characterization of Asphalt Concrete in Tension Using a Viscoelastoplastic Model*, PhD Thesis, North Carolina State University, Raleigh, North Carolina, USA, 2002.

Chehab, G.R., O'Quinn, E., and Kim, Y.R. *Specimen Geometry Study for Direct Tension Test Based on Mechanical Tests and Air Void Variation in Asphalt Concrete Specimens Compacted by SGC.* In Transportation Research Record 1723, Transportation Research Board of National academies, Washington D.C., pp. 125-1332, 2000.

Chen, C.W. *Mechanistic Approach to The Evaluation of Microdamage in Asphalt Mixes*, PhD thesis, Texas A&M University, College Station, Texas, 1997.

Shen, Shihui, Ho-Ming Chiu, and Hai Huang. Fatigue and healing in asphalt binders. Transportation Research Board 88th Annual Meeting, Washington, DC., No. 09-1338, 2009.

Chomton, J.S., and Valayer, P.J. *Applied Rheology of Asphalt Mixes, Practical Applications*, Proceedings of 3rd International Conference on the Structural Design of Asphalt Pavements, London, vol. I, 1972.

Chowdary, V. *Experimental Studies on Healing Of Asphalt Mixtures*, International Symposium of Research Students on Materials Science and Engineering, Department of Metallurgical and Materials Engineering, Indian Institute of Technology Madras, India, 2004.

Christensen, D.W., and Bonaquist, R.F. Practical Application of Continuum Damage Theory to Fatigue Phenomena in Asphalt Concrete Mixtures, *Journal of the Association of Asphalt Paving Technologists (AAPT)*, Vol. 74, , pp. 963–1002, 2005.

Christensen, D.W., and Bonaquist, R.F. Analysis of HMA Fatigue Data Using the Concepts of Reduced Loading Cycles and Endurance Limit, *Journal of the Associations of Asphalt Paving Technologists (AAPT)*, vol. 78, pp. 377-416, 2009.

Cowher, K. *Cumulative Damage of Asphalt Materials under Repeated-Load Indirect Tension*, Research Report Number 183-3, Center for Highway Research – University of Texas at Austin, Austin, TX, 1975.

Cox W.P., and Merz, E.H. *Correlation of Dynamic and Steady Flow Viscosities*. Journal of Polymer Sciences, Vol. 28, pp. 619-622, 1958.

Daniel, J.S., and Kim, Y.R. *Development of a Simplified Fatigue Test and Analysis Procedure Using a Viscoelastic, Continuum Damage Model*, Journal of the Association of Asphalt Paving Technologists, Vol. 71, Pp. 619–650, 2002.

Daniel, J.S., and Kim, Y.R. *Laboratory Evaluation of Fatigue Damage and Healing of Asphalt Mixtures,* Journal of Materials in Civil Engineering, Vol. 13, No. 6, pp. 434–440, 2001.

Daniel, J.S. *Development of a simplified fatigue test and analysis procedure using a viscoelastic, continuum damage model and its implementation to WesTrack mixtures*, Ph.D. dissertation, North Carolina State University, Raleigh, 2001.

Douglas, R.A., and Holt, J.D. *Determining Length of Installed Timber Pilings by Dispersive Wave Propagation Methods*, Final Report Research Project 23241-92-2. North Carolina Department of Transportation, FHWA, U.S. Department of Transportation, June 1993.

El-Basyouny, M., and Witczak, M. *Development of the Fatigue Cracking Models for the 2002 Design Guide*, Presented at the 84th Annual Meeting of the Transportation Research Board, January 2005.

Elliot, R.P., and Thompson, M.R. *Mechanistic Design Concepts for Conventional Flexible Pavements*, Transportation Engineering Series No. 42, University of Illinois, Urbana, IL, February 1986.

Epps, J.A. and Monismith, C.L. Influence of Mixture Variables on the Flexural Fatigue Properties of Asphaltic Concrete, *Journal of the Association of Asphalt Paving Technologists (AAPT)*, Vol. 38, pp. 423-464, 1969.

Evolver Software, http://www.palisade.com/evolver/

Ferne, B. *Long-Life Pavements* – A European Study by ELLPAG, *International Journal of Pavement Engineering*, Vol. 7, No. 2, pp 91-100, 2006.

Ferry, J.D. *Viscoelastic Properties of Polymers*, 3rd edn. John Wiley and Sons, New York, 1980.

Finn, F., Saraf, C.L., Kulkarni, K., Nair, K., Smith, W., and Abdullah, A. *Development of Pavement Structural Subsystems*, Final Report, Project 1-10B, February 1977.

Franken, L. *Fatigue Performance of a Bituminous Road Mix under Realistic Test Condition*, Transportation Research Record 712, Transportation Research Board of National Academies, Washington D.C., pp. 30-36, 1979.

Freund, L.B., and Suresh, S. *Thin Film Materials: Stress, Defect Formation and Surface Evolution*, Cambridge, UK, Cambridge University Press, 2003.

Germann, F.P., and Laytton, R.L. *Methodology for Predicting the Reflective Cracking Life of Asphalt Concrete Overlays*, Texas Transportation Institute, TTI-2-8-75-207-5, 1979.

Ghuzlan, K.A. *Fatigue Damage Analysis in Asphalt Concrete Mixtures Based Upon Dissipated Energy Concepts*, Ph.D. Dissertation, University of Illinois at Urbana-Champaign, August 2001.

Ghuzlan, K., and Carpenter, S.H. *An Energy-Derived/Damage-Based Failure Criteria for Fatigue Testing*, Transportation Research Record 1723, Transportation Research Board of the National Academies, pp. 131- 141, 2000.

Griffith, A.A. *The Phenomena of Rupture and Flaw in Solids*, Philosophical Transactions of the Royal Society, London, Series A, Vol. 221, 1921.

Harvey, J.T., Deacon, J.A., Taybali, A.A. , and Leahy, R.B. *A Reliability-Based Mix Design and Analysis System for Mitigating Fatigues Distress.* Proceedings of the 8th International Conference on Asphalt Pavements, Vol. 1. University of Washington, Seattle, WA, pp. 301-323, August 1997.

Hilton, H.H., and Yi., S. Analytical Formulation of Optimum Material Properties for Viscoelastic Damping, *Journal of Smart Materials and Structures*, Vol. 1, pp. 113–122, 1992.

Hopman, P.C., Kunst, P.A.J.C. and Pronk, A.C. *A Renewed Interpretation Method for Fatigue Measurements, Verification of Miner's Rule*, Proceedings of 4th Eurobitume Symposium in Madrid, Vol. 1, pp. 557-561, 1989.

Hou, T. *Fatigue Performance Prediction of North Carolina Mixtures Using Simplified Viscoelastic Continuum Damage Model*, Ms.C Thesis, North Carolina State University, Raleigh, North Carolina, 2009.

Hou, T., Underwood, B.S., and Kim, Y.R. Fatigue Performance Prediction of North Carolina Mixtures Using the Simplified Viscoelastic Continuum Damage Model, *Journal of the Association of Asphalt Paving Technologists (AAPT)*, Vol. 79, pp. 35-73, 2010.

Hsu, T.W., and Tseng, K.H. Effect of Rest Periods on Fatigue Response of Asphalt Concrete Mixtures, *Journal of Transportation Engineering*, American Society of Civil Engineering, Vol. 122, No. 4, PP. 316-322, 1996.

Huang, Y.H. *Material Characterization and Performance Properties of Superpave Mixtures*, Ph.D. Dissertation, North Carolina State University, Raleigh, 2004.

Huang, Y.H. *Pavement Analysis and Design*. Prentice-Hall Englewood Cliffs, NJ, 1993.

Jacobs, M. M. J. *Crack Growth in Asphaltic Mixes*, Ph.D. Thesis, Delft University of Technology, the Netherlands, 1995.

Jacobs, M.M.J., Hopman, P. C. and Molenaar, A.A.A. Application of Fracture Mechanics Principles to Analyze in Asphalt Concrete, *Journal of the Association of Asphalt Paving Technologists (AAPT)*, Vol. 65, pp. 1-39, 1996.

Jeong M.G. *Implementation of Simple Performance Test Procedure in Hot Mix Asphalt Quality Assurance Program*. Ph.D. Thesis, Arizona State University, Tempe, Arizona, 2010.

JMP software, SAS Institute Inc, http://www.jmp.com/.

Kallas, B. Dynamic Modulus of Asphalt Concrete in Tension and Tension-Compression, *Journal of the Association of Asphalt Paving Technologists (AAPT)*, vol. 39, pp. 1-20, 1970.

Kaloush, K.E., Mello, L.G. *Continuum Damage Theory Applied for Asphalt Rubber Mixtures*, Report No. FHWA-AZ-08-644, Final Report Submitted to Arizona Department of Transportation, Arizona State University, Tempe, Arizona, USA, 2009.

Kennedy, T.W. Characterization of asphalt pavement material using the indirect tensile test, *Journal of the Association of Asphalt Paving Technologists (AAPT)*, Vol. 46, 1977.

Kim, Y. and Kim, Y.R. *In-Situ Evaluation of Fatigue Damage Growth and Healing of Asphalt Concrete Pavements Using Stress Wave Method*, Transportation Research Record 1568, National Research Council, Washington, D.C., pp. 106-113, 1997.

Kim, Y.R. *Evaluation of Healing and Constitutive modeling of Asphalt Concrete by Means of the Theory of Nonlinear Viscoelasticity and Damage Mechanics*, Ph.D Dissertation, Texas A&M University, College Station, Tex, 1988.

Kim, Y.R. *Mechanistic Fatigue Characterization and Damage Modeling of Asphalt Mixtures*, Ph.D. Dissertation, Texas A&M University, College Station, Texas, August 2003

Kim, Y.R., Lee, H.J, Kim, Y, and Little, D.N. *Mechanistic Evaluation of Fatigue Damage Growth and Healing of Asphalt Concrete: Laboratory and field experiments*, Proceedings of the 8th International Conference on Asphalt Pavements, ISAP, Seattle, Washington, pp. 1089-1107, August 1997b.

Kim, Y.R., Lee, H.J., and Little, D.N. Fatigue Characterization of Asphalt Concrete Using Visco-elasticity and Continuum Damage Theory, *Journal of the Association of Asphalt Paving Technologists (AAPT),* Vol. 66, pp. 520-569, 1997a.

Kim, Y.R., Little, D.N., and Benson, F. Chemical and Mechanical Evaluation on Healing Mechanism of Asphalt Concrete, *Journal of the Association of Asphalt Paving Technologists (AAPT),* Vol. 59, pp.240-276, 1990.

Kim, Y.R., Little, D.N., and Lytton, R.L. Fatigue and healing characterization of asphalt mixtures, *Journal of Materials in Civil Engineering*, ASCE, Vol. 15, No. 1, pp. 75-83, 2003.

Kim, Y.R. *Modeling of Asphalt Concrete*, American Society of Civil Engineers (ASCE) Press, Reston, Virginia, 2009.

Kim, Y.S. *Evaluation of Healing and Constitutive Modeling of Asphalt Concrete by Means of the Theory of Nonlinear Viscoelasticity and Damage Mechanics*, Ph.D. Dissertation, Texas A&M University, College Station, Texas, 1988.

Kunst, P.A.J.C. *Surface Cracking on Asphalt Layers*, Working Committee B12, Hoevelaken, Holland, 1989.

Leahy, R.B., Hicks, R.G., Monismith, C.L., and Finn, F.N. Framework for Performance—Based Approach to Mix Design and Analysis, *journal of the Association of Asphalt Paving Technologists (AAPT)*, Vol. 64, pp. 431–473, Minneapolis, MN, 1995.

Lee, H.J., and Kim, Y.R. A Uniaxial Viscoelastic Constitutive Model for Asphalt Concrete under Cyclic Loading, *ASCE Journal of Engineering Mechanics*, Vol. 124, No. 11, Pp. 1224-1232, 1998a.

Lee, H.J., and Kim, Y.R. A Viscoelastic Continuum Damage Model of Asphalt Concrete with Healing, A*SCE Journal of Engineering Mechanics*, Vol. 124, No. 11, Pp. 1-9, 1998b.

Lee, H.J. *Viscoelastic Constitutive Modeling of Asphalt Concrete Using Viscoelasticity and Continuum Damage Theory*, Ph.D. Dissertation, North Carolina State University, Raleigh, North Carolina, 1996.

Lee, S. *Investigation of the Effects of Lime on the Performance of HMA using Advanced Testing and Modeling Techniques*, Ph.D. dissertation, North Carolina State University, Raleigh, North Carolina, USA, 2007.

Liang, R.Y., and Zhou, J. Prediction of Fatigue Life of Asphalt Concrete Beams, *International Journal of Fatigue*, 19 (2), pp. 117-124, 1997.

Little, D.N. *Investigation of Microdamage Healing in Asphalt and Asphalt Concrete,* Task K, Semi-Annual Technical Report Western research Institute, FHWA project DTFH61-92-C-00170- Fundamental Properties of Asphalts and Modified Asphalts, October, 1995.

Little, D.N., Lytton, R.L., Williams, D., and Chen, C.W. *Microdamage Healing in Asphalt and Asphalt Concrete, Volume I: Microdamage and Microdamage Healing Project Summary Report*, Report Number FHWA-RD-98-141, Federal Highway Administration, Washington, D.C., June 2001.

Little, D.N., R.L. Lytton, et al. An Analysis of the Mechanism of Microdamage Healing Based on the Applications of Micromechanics First Principles of Fracture and Healing, *Journal of the Association of Asphalt Paving Technologists (AAPT)*, Chicago, Illinois, Vol. 68, pp. 501 – 542, 1999.

Lytton, R.L. *Characterizing asphalt pavements for performance*, Transportation Research Record 1723, TRB, National Research Council, pp. 5-16, 2000.

Lytton, R.L., Chen, C.W., and Little, D.N. *Microdamage Healing in Asphalt and Asphalt Concrete, Volume III: A Micromechanics Fracture and Healing Model for Asphalt Concrete*, FHWA-RD-98-143, Texas A&M University, College Station, TX, 2001.

Mahoney, J.P. *Study of Long-Lasting Pavements in Washington State, Perpetual Bituminous Pavements*, Transportation Research Circular 503. Transportation Research Board, National Research Council. Washington, D.C., pp. 88-95, 2001.

Majidzadah, K., Kaufmann, E.M., and Saraf, C.L. Analysis of Fatigue of Paving Mixtures From the Fracture Mechanics Viewpoint, *Journal of Fatigue of Compacted Bituminous Aggregate Mixtures*, ASTM STP 508, pp. 67-83, 1972.

Majidzadeh, K., Kauffmann, E.M., and Ramsamooj, D.V. Application of Fracture Mechanics in the Analysis of Pavement Fatigue, *Journal of Association of Asphalt Paving Technologists (AAPT)*, pp. 227-246, 1971.

Mamlouk, M.S., Souliman, M.I., and Zeiada, W.A. *Optimum Testing Conditions to Measure HMA Fatigue and Healing Using Flexural Bending Test*. CR-ROM, Transportation Research Record 1266, Transportation Research Board of National Academies, Washington, DC, January 2012.

Maupin, G.W. Jr. and J.R. Freeman, Jr. *Simple Procedure for Fatigue Characterization of Bituminous Concrete*, Final Report No. FHWA-RD-76-102, Federal Highway Administration, Washington, DC, 1976.

McElvaney, J., and Pell, P.S. Fatigue Damage of Asphalt-Effect of Rest Periods, *Highway and Road Construction*, Vol. 41, No. 1776, pp. 16-20, 1973.

Mello, L.G.R., Kaloush, K.E., and Farias, M.M. Damage Theory Applied to Flexural Fatigue Tests on Conventional and Asphalt Rubber Hot Mixes, *International Journal on Road Materials and Pavement Design,* Vol. 11(3), pp. 681-700, 2010.

Minitabe software, http://www.minitab.com/en-US/default.aspx

Monismith, C.L., and McLean, D.B. Structural Design Considerations, *Proceedings of the Association of Asphalt Paving Technologists (AAPT)*, Vol. 41, pp. 258-304, 1972.

Monismith, C.L., Epps, J.A., Kasianchuk, D.A., and Mclean, D.B. *Asphalt Mixture Behavior in Repeated Flexure*, Report No. TE 70-5, Institute of Transportation and Traffic Engineering, University of California, Berkeley, 1970.

Monismith, C.L., Secor, K.E., and Blackner, E.W. Asphalt Mixture Behavior in Repeated Flexure, *Proceedings of the Association of Asphalt Paving Technologists (AAPT)*, Vol. 30, pp. 188-222, 1961.

Monismith, C.L. *Fatigue of Asphalt Paving Mixtures*, Paper prepared for presentation at the First Annual Street and Highway Conference, University of Nevada, March 1966b..

Monismith, C.L., Epps, J.A., Kasianchuk, D.A., and McLean, D.B. *Asphalt Mixture Behavior in Repeated Flexure*, Report No. TE 70-5, Institute of Transportation and Traffic Engineering, University of California, Berkeley, 1970.

Montgomery, Douglas C., *Design and Analysis of Experiments*, Wiley, 2008.

Moore, R.K. and Kennedy, T. W. *Tensile Behavior of Subbase Materials under Repetitive Loading*, Research Report 98-12, Center for Highway Research, University of Texas at Austin, Austin, TX, 1971.

Navarro, D. and Kennedy, T. W. *Fatigue and Repeated-Load Elastic Characteristics of In-service Asphalt-Treated Pavement*, Research Report No.183-2, Center for Highway Research, the University of Texas at Austin, Austin, TX, 1975.

NCHRP Project 9-44A. *Validating an Endurance Limit for HMA Pavements: Laboratory Experiment and Algorithm Development*, Quarterly Progress Report, Arizona State University, Tempe, Arizona, June, 2010.

Nishizawa, T., Shimeno, S., and Sekiguchi, M. *Fatigue Analysis of Asphalt Pavements with Thick Asphalt Mixture Layer*, Proceedings of the 8th International Conference on Asphalt Pavements, Vol. 2, pp. 969–976, University of Washington, Seattle, WA, August 1996.

Nunn, M. *Long-life Flexible Roads*. Proceedings of the 8th International Conference on Asphalt Pavements, Vol. 1, pp. 3–16, University of Washington, Seattle, WA, August 1997.

Paris, P.C and Erdogan, F. A Critical Analysis of Crack Propagation Laws, *Journal of Basic Engineering, Transactions of ASME*, Series D, Vol.85, pp.528–534, 1963.

Park, S.W. and Kim, Y.R. Fitting Prony-Series Viscoelastic Models with Power-Law Presmoothing, *Journal of Materials in Civil Engineering*, pp. 26-32, January/February 2001.

Park, S.W., Kim, Y.R., and Schapery, R.A. A Viscoelastic Continuum Damage Model and Its Application to Uniaxial Behavior of Asphalt Concrete, *Mechanics of Materials*, No. 24, pp. 241-255, 1996.

Park, S.W, and Schapery, R.A. Methods of Interconversion between Linear Viscoelastic Material Functions. Part I- a numerical method based on Prony series, *International Journal of Solids and Structures*, Vol. 36, pp. 1653-1675, 1999.

Pell, P.S. and Hanson, J.M. Behavior of Bituminous Road Base Materials under Repeated Loading, *Proceedings of Association of Asphalt Paving Technologists (AAPT),* pp. 201-229, 1973.

Pell, P.S. *Fatigue of Asphalt Pavement Mixes*, Proceeding of the Second international Conference on the Structural Design of Asphalt Pavements, Ann Arbor, Michigan, pp. 577-594, 1967.

Pell, P.S. and Cooper, K.E. The Effect of Testing and Mix Variables on The Fatigue Performance of Bituminous Materials, *Journal of the Association of Asphalt Paving Technologists (AAPT)*, Vol. 44, pp. 1-37, 1975.

Pell, P.S. *Characterization of Fatigue Behavior*, Highway Research board Special Report No. 140, National Research Council, Washington, D.C., pp. 49-64, 1973.

Pell, P.S. *Pavement Materials*, Sixth International Conference on the Structural Design of Asphalt Pavements, Vol. 2 Proceedings, Ann Arbor, Michigan, July 1987.

Pellinen, T.K. *Investigation of the Use of Dynamic Modulus as an Indicator of Hot-Mix Asphalt Performance*, Ph.D. Dissertation, Arizona State University, Tempe, AZ, May 2001.

Petersen, J.C. *Chemical Composition of Asphalt as Related to Asphalt Durability: State of Art*, Transportation Research Record 999, Transportation Research Board, Washington D.C., pp. 13-30, 1984.

Peterson, R.L., Turner, P., Anderson, M., and Buncher, M. *Determination of Threshold Strain Level for Fatigue Endurance Limit in Asphalt Mixtures*, Proceedings of International Symposium on Design and Construction of Long Lasting Asphalt Pavements, National Center for Asphalt Technology, Auburn, pp. 385–410, AL, 2004.

Phillips, M.C. *Multi-Step Models for Fatigue and Healing, and Binder Properties Involved in Healing*, Proceedings of Eurobitume Workshop on Performance Related Properties for Bituminous, Luxembourg, No. 115, 1998.

Powell, W.D., Potter, J. F., Mayhew, H.C., and Nunn, M. E. *The Structural Design of Bituminous Roads*, Transportation and Road Research Laboratory (TRRL), Report No. 1132, pp. 62, 1984.

Priest, A.L., and Timm, D.H. *Methodology and Calibration of Fatigue Transfer Functions for Mechanistic-Empirical Flexible Pavement Design*, Publication NCAT 06-03. National Center for Asphalt Technology, Auburn University, Auburn, Alabama, 2006.

Pronk A.C., Poot, M. R., M. M. J. Jacobs, y R. F. Gelpke. *Haversine Fatigue Testing in Controlled Deflection Mode. Is it Possible?*, 89th Annual Meeting of the Transportation Research Board, Transportation Research Board of National Academies, Washington, DC, 2010.

Pronk, A.C. Partial Healing in Fatigue tests on Asphalt Specimens, *International Journal of Road, Materials and Pavement Design (IJRMPD)*, Vol.4, No.4, 2001.

Pronk, A.C. Partial Healing, A new approach for damage process during fatigue testing of asphalt specimen, *ASCE*, Geotechnical Special Publication No.146, pp. 83-94, Baton Rouge, 2005.

Pronk, A.C. *PH* Model in 4PB Tests with Rest Periods, *International Journal of Road, Materials and Pavement Design (IJRMPD)*, Vol.10, No.2, pp. 417-426, 2009.

Pronk, A.C. *Comparison of 2 and 4 point fatigue tests and healing in 4 point dynamic bending test based on the dissipated energy concept*, Proceedings of the 8th international conference on asphalt pavements, Seattle, Washington, pp. 987-994, 1997.

Prowell B.D. and Brown, E.R. *Method of Determining Endurance Limit Using Beam Fatigue Tests*, International Conference on Perpetual Pavement. CD ROM 2006.

Prowell, B., Brown, E.R., Anderson, R.M., Daniel, J.S., Swamy, A.K., Von Quintus, H., , Shen, S., Carpenter, S.H., Bhattacharjee, S., and Maghsoodloo, S. *Validating the Fatigue Endurance Limit for Hot Mix Asphalt*, Final NCHRP Report 646, NCHRP 9-38 Project, National Cooperative Highway Research Program, Washington, D.C., 2010.

Raithby, K.D. and Ramshaw, J.T. *Effect of Secondary Compaction on the Fatigue Performance of a Hot-Rolled Asphalt*, Transportation and Road Research Laboratory TRRL-LR 471, Crowthorne, England, 1972.

Raithby, K.D. and Sterling, A.B. *Some effects of loading history on the fatigue performance of rolled asphalt,* Transport and Road Research Laboratory (TRRL), Report No. LR 496, Crowthorne, U.K, 1972.

Raithby, K.D. and Sterling, A.B. The Effect of Rest Periods on the Fatigue Performance of Hot-Rolled Asphalt under Reversed Axial Loading, *Proceedings, The Association of Asphalt Paving Technologists (AAPT)*, Vol. 39, pp. 134-147, 1970.

Reese, R. Properties of Aged Asphalt Binder Related to Asphalt Concrete Fatigue Life, *Journal of the Association of Asphalt Paving Technologists (AAPT)*, Vol. 66, pp. 604-632, 1997.

Romanoschi S.A., Gisi, A. and Dumitru, C. *The dynamic response of Kansas Perpetual Pavements under vehicle loading*, Proceeding of the International Conference on Perpetual Pavement, Columbus, OH, September 13-15, 2006.

Rowe, G.M. and Bouldin, M.G. *Improved Techniques to Evaluate the Fatigue Resistance of Asphaltic Mixtures*, Proceedings of 2nd Eurasphalt & Eurobitume Congress, Book 1, pp. 754-763, Barcelona, Spain, September, 2000.

Rowe, G.M. Performance of Asphalt Mixtures in the Trapezoidal Fatigue Test, *Proceedings of Associations of Asphalt Paving Technologists (AAPT),* Vol. 62, pp. 344-384, 1993.

Rowe, G.M. Performance of Asphalt Mixtures in the Trapezoidal Fatigue Test, *Journal of the Association of Asphalt Paving Technologists (AAPT)*, Vol. 62, pp. 334-384, 1993.

Said, S.F. *Variable in Roadbase Layer Properties Conducting Indirect Tensile Test*, 8th International Conference on The Structural Design of Asphalt Pavements, Vol. 2, Seattle, Washington, August 1997.

Schapery, R.A. A Method for Predicting Crack Growth in Nonhomogeneous Visco-Elastic Media, *International Journal of Fracture*, Vol. 14, No. 3, pp. 293-309., 1978.

Schapery, R.A. *A Theory of Crack Growth in Viscoelastic Media*, Research Report MM 2764-73-1, Mechanics and Materials Research Center, Texas A&M University, College Station, Texas,1973.

Schapery, R.A. Analysis of Damage Growth in Particulate Composites Using a Work Potential, *Composite Engineering*, Vol. 1(3) , pp. 167-182., 1991.

Schapery, R.A. Correspondence Principles and a Generalized J Integral for Large Deformation and Fracture Analysis of Viscoelastic Media, *International Journal of Fracture*, Vol. 25, pp. 195-223., 1984.

Schapery, R.A. A Theory of Mechanical Behavior of Elastic Media with Growing Damage and Other Changes in Structure, *Journal of Mechanics and Physics of Solids*, Vol. 38, pp.215-253, 1990.

Schapery, R.A. *On The Mechanics of Crack Closing and Bonding in Linear Viscoelastic Media*, International Journal of Fracture, Vol. 39, pp. 163-189, 1989.

Schapery, R.A., Park, S.W. Methods of Interconversion between Linear Viscoelastic Material Functions. Part II- An Approximate Analytical Method, *International Journal of Solids and Structures*, Vol. 36, pp. 1677-1699, 1999.

Schutz, W. A history of fatigue, *Engineering Fracture Mechanics*, Vol. 54, No. 2, pp. 263-300, 1996

Seo, Youngguk, and Kim, Y.R. Using Acoustic Emission to Monitor Fatigue Damage and Healing in Asphalt Concrete, *KSCE Journal of Civil Engineering*, Vol. 12, No. 4, pp. 237-243, 2008.

Shell Pavement Design Manual. *Asphalt Pavements and Overlay for Road Traffic*, Shell International Petroleum Company Limited, London, 1978.

Shen, S. and Carpenter, S.H. Development of an Asphalt Fatigue Model Based on Energy Principles, *Proceedings of The Association of Asphalt Paving Technologists (AAPT)*, Vol. 76, pp. 525- 574, 2007.

Shen, S., and Carpenter, S.H. *Application of Dissipated Energy Concept in Fatigue Endurance Limit Testing*, Transportation Research Record 1929, Journal of Transportation Research Board, pp. 165-173, National Research Council, Washington D.C 2005.

Shen, S. *Dissipated Energy Concepts for HMA Performance: Fatigue and Healing*, Ph.D. Dissertation, University of Illinois at Urban-Champaign, IL, 2006.

Shen, S., Chiu, H., Huang, H. *Fatigue and Healing of Asphalt binders*, Transportation Research Record 1338, Transportation Research Board of National Academies, Washington, D.C., 2009.

SHRP A_404, *Fatigue Characteristics of Bitumen and Bituminous Mixes*, Asphalt research Program, Institute of transportation studies, University of California, Berkeley, Strategic Highway research Program, national research Council, 1994.

SHRP Designation: M-009. *Standard Method of Test for Determining the Fatigue Life of Compacted Bituminous Mixtures Subjected to Repeated Flexural Bending*.

SHRP, *Direct Tension Test Experiments*, SHRP–A –641, Strategic Highway Research Program, National Research Council, Washington, D.C. 1993.

Si, Z., Little, D.N., and Lytton, R.L. Characterization of Microdamage and Healing of Asphalt Concrete Mixtures. *Journal of Materials in Civil Engineering, ASCE*, Vol. 14, No. 6, pp. 461-470, 2002.

Si, Z. *Characterization of Microdamage and Healing of Asphalt Concrete Mixtures*, Ph.D. Dissertation, Texas A&M University, College Station, Texas, 2001

Soltani, A., and Anderson, D.A. New Test Protocol to Measure Fatigue Damage in Asphalt Mixtures, *Journal of Road Materials and Pavement Design*, Vol. 6, pp. 485-514, 2005.

Souliman, M.I. *Integrated Predictive Model for Healing and Fatigue Endurance Limit for Asphalt Concrete*. Ph.D. Dissertation, Arizona State University, Tempe AZ, May 2012.

Soltani, A., Solaimanian, M., and Anderson, D.A. *An Investigation of the Endurance Limit of Hot-Mix Asphalt Concrete Using a New Uniaxial Fatigue Protocol*. Final Report, Report Number FHWA-HIF-07-002, Federal Highway Administration (FHWA), Washington, D.C., 2006.

Sousa, J.B. *Dynamic Properties of Pavement Materials*, Ph.D. Thesis, University of California, Berkeley, 1986.

STATISTICA software, StatSoft, http://www.statsoft.com/#.

Suresh, S. *Fatigue of materials*. 2nd edition, Cambridge University Press, Cambridge, UK, 1998.

Tangella, S.R., Craus, J., Deacon, J.A., and Monismith, C.L. *Summary Report of Fatigue Response of Asphalt Mixture*s, Technical Memorandum No. TM-UCB-A-003A-89-3M, prepared for SHRP Project A-003A, Institute of Transportation Studies, University of California, Berkeley, 1990.

Tayebali, A.A., Coplantz, J.S., Harvey, J.T., and Monismith, C.L. *Interim Report on Fatigue Response of Asphalt-Aggregate Mixtures,* SHRP project A-003A, TM-UCB-A-003A-92-1, Asphalt Research Program, Institute of Transportation Studies, University of California-Berkeley, Berkeley, CA, 1992.

Tayebali, A.A., Deacon, J.A., Coplantz, J.S., Harvey, J.T., and Monismith, C.L. Mix and Mode-of Loading Effects on Fatigue Response of Asphalt-Aggregate Mixes, Proceedings of the Association of Asphalt Paving Technologists (AAPT), Vol. 63, pp. 118- 151, 1994.

Tayebali, A.A., Rowe, G.M. and Sousa, J.B. Fatigue Response of Asphalt-Aggregate Mixtures, *Journal of the Association of Asphalt Paving Technologists (AAPT)*, Vol. 61, pp. 333-360, 1992.

The Asphalt Institute. *Research and Development of The Asphalt Institute's Thickness Design Manual (MS-1) Ninth Edition*, Research Report No. 82-2, August 1982.

Thompson, M.R., and Carpenter, S.H. *Considering Hot-Mix-Asphalt Fatigue Endurance Limit in Full-Depth Mechanistic-Empirical Pavement Design*. CD-ROM, Proceedings of the International Conference on Perpetual Pavements. Columbus, Ohio, September 13-15, 2006.

Tsai, B.W., Harvey, J.T., and Monismith, C.L. High Temperature Fatigue and Fatigue Damage Process of Aggregate-Asphalt Mixes, *Journal of the Association of Asphalt Paving Technologists (AAPT)*, Vol. 71, pp. 345–385, 2002.

Tsai, B.W., Harvey, J.T., and Monismith, C.L. *Using the Three- Stage Weibull Equation and Tree-Based Model to Characterize the Mix Fatigue Damage Process*, Transportation Research Record1929, Journal of Transportation Research Board, pp. 227-237, National Research Council, Washington D.C, 2005.

Tsai, B., Harvey, J.T., and Monismith, C.L. Two-Stage Weibull Approach for Asphalt Concrete Fatigue Performance Prediction, *Proceedings of the Association of Asphalt Paving Technologists (AAPT)*, Vol. 73, pp. 200-228, 2004.

Tschoegl, N.W. *The Phenomenological Theory of Linear Viscoelastic Behavior*, Springer-Verlag, Berlin, 1989.

Underwood, B.S., Kim, Y.R., and Guddati, M.N. Characterization and Performance Prediction of ALF Mixtures Using a Viscoelastoplastic Continuum Damage Model, *Proceedings of the Association of Asphalt Paving Technologists (AAPT)*, Vol. 75, pp. 577-636, 2006.

Underwood, B.S. and Kim, Y.R. *Analytical Techniques for Determining the Endurance Limit of Hot Mix Asphalt Concrete*, CD-ROM, International Conference on Perpetual Pavement, Columbus, Ohio, 2009.

Underwood, B.S., Kim, Y.R., and Guddati, M.N. Improved Calculation Method of Damage Parameter in Viscoelastic Continuum Damage Model, *International Journal of Pavement Engineering*, Vol. 11, Issue 6, pp. 459 – 476, December 2010.

Van Dijk, W. Practical Fatigue Characterization of Bituminous Mixes, Proceedings, *Journal of the Association of Asphalt Paving Technologists (AAPT)*, Vol. 44, p.38, Phoenix, Arizona, 1975.

Van Dijk, W., and Visser, W. The Energy Approach to Fatigue for Pavement Design, *Proceedings of the Association of Asphalt Paving Technologists (AAPT)*, Vol. 46, pp.1-40, 1977.

Van Dijk, W., Moreaud, H., Quedeville, A., and Uge, P. *The Fatigue of Bitumen and Bituminous Mixes,* Proceedings, Third International Conference of Structural Design of Asphalt Pavements, London, Vol. 1, pp. 354-366, September 1972.

Verstraeten, j. *Aspects Divers de la Fatigue des Mélanges Bitumineux*. Report No. 170/Jv(1976), Center de Recherche Routiéres, Bruxelles, 1976.

Walubita, L.F., Liu, W., Scullion, T., and Leidy, J. *Modeling Perpetual Pavements Using the Flexible Pavement System (FPS) Software*, CD-ROM, Transportation Research Record 2311, Transportation Research Board, Annual Meeting, Washington, D.C., 2008.

Willis, J.R. *Field Based Strain Thresholds for Flexible Perpetual Pavement Design*. Ph.D. Dissertation, Auburn University, Auburn, Alabama, 2009.

Witczak, M.W. *Development of relationships between binder viscosity and stiffness*. SUPERPAVE Support and Performance Models Contract, FHWA No. DTFH 61-94-R-00045, Team Technical Rep., University of Maryland, College Park, Md, 1998.

Witczak, M.W., Hafez, I., Qi, X. *Laboratory characterization of Elvaloy modified asphalt mixtures: vol. I – Technical report*, College Park, Maryland, University of Maryland, 1995. Available from: http://www.dupont.com/asphalt/link5.html.

Witczak, M.W., K. Kaloush, T.K. Pellinen, M. El-Basyouny, and H. Von Quintus. *Simple Performance Test for Superpave Mix Design*, NCHRP Report 465, National Cooperative Highway Research Program, Washington D.C, 2002.

Witczak, M.W., Mamlouk, M., and Abojaradeh, M. *Flexural Fatigue Tests,. NCHRP 9-19, Subtask F6 Evaluation Tests*, *Task F Advanced Mixture Characterization*. Interim Report, Arizona State University, Tempe, Arizona, July 2001.

Wu, Z., Siddique, Z.Q. and Gisi, A.J. Kansas Turnpike—*An Example of Long Lasting Asphalt Pavement*, International Symposium on Design and Construction of Long Lasting Asphalt Pavements, pp. 859–879, International Society for Asphalt Pavements, Auburn, Alabama, 2004.

Zhang, Z., Roque, R., Birgisson, B., and Sangpetngam, B. Identification and Verification of a Suitable Crack Growth Law, *Journal of the Association of Asphalt Paving Technologists (AAPT)*, Vol. 70, pp.206-241, 2001.

APPENDIX A

SUMMARY OF DYNAMIC MODULUS TEST RESULTS

This Appendix A includes the complex modulus test results (dynamic modulus and phase angle) of three different mixtures based on the binder type. These binder types are PG 58-28, PG 64-22, and PG 76-16. For each mixture, a total of nine different mixtures was tested, which represent nine different combinations of air voids and asphalt content. The test results for each mixture combination were based on two replicates. The air voids and asphalt content levels varied according to the mix design. For the PG 64-22 mixture, the air voids values were the design AV± 3% (7-3, 7, and 7+3 = 4, 7, and 10). The asphalt content values were the optimum AC±0.5% (4.5-0.5, 4.5, and 4.5+0.5 = 4.0, 4.5, and 5). For both the PG 58-28 and PG 76-16 mixtures, the air voids values were the design AV±2.5% (7-2.5, 7, and 7+2.5 = 4.5, 7, and 9.5). The asphalt content values were fixed for these two mixtures at 4.2, 4.7, and 5.2%.

TABLES A1 to A27 summarize the complex modulus test results for a total of 27 different mixtures; nine for each mixture type representing nine different combinations of air voids and asphalt cement contents. Each table contains the dynamic modulus and phase angle of each replicate and the averages as well. To show the amount of variability between the replicates at different test temperatures and frequencies, standard deviation and coefficient of variation are also presented.

TABLE A1 E* test results of PG 64-22 mixture at 4.0% AC and 10.0% Va

Temp (°F)	Freq (Hz)	Dynamic Modulus, E*					Phase Angle, φ				
		Repl. 1 6-105 (ksi)	Repl. 2 6-106 (ksi)	Average (ksi)	Std. Dev. (ksi)	Coeff. of Var.	Repl. 1 6-105 (Deg.)	Repl. 2 6-106 (Deg.)	Average (Deg.)	Std. Dev. (Deg.)	Coeff. of Var.
14	25	2482	2585	2533	73	2.9	5.0	5.2	5.1	0.1	2.1
	10	2381	2484	2432	73	3.0	6.0	7.7	6.8	1.2	17.9
	5	2268	2346	2307	55	2.4	6.3	8.7	7.5	1.7	22.7
	1	2104	2167	2136	45	2.1	7.3	9.1	8.2	1.3	15.8
	0.5	1997	2147	2072	106	5.1	7.8	11.0	9.4	2.2	23.5
	0.1	1764	1880	1822	82	4.5	9.2	11.1	10.1	1.3	13.3
40	25	1720	1691	1706	20	1.2	10.5	8.5	9.5	1.4	15.3
	10	1568	1573	1570	4	0.2	12.1	10.1	11.1	1.4	13.0
	5	1436	1460	1448	17	1.2	13.2	11.1	12.1	1.5	12.3
	1	1182	1218	1200	26	2.1	15.6	14.9	15.2	0.5	3.4
	0.5	1086	1096	1091	7	0.7	16.7	15.2	15.9	1.1	6.7
	0.1	848	851	849	2	0.3	20.3	16.4	18.4	2.7	14.9
70	25	862	903	882	29	3.3	18.5	19.2	18.9	0.5	2.8
	10	709	770	739	43	5.9	21.9	20.1	21.0	1.3	6.0
	5	610	673	642	44	6.9	23.2	23.0	23.1	0.1	0.5
	1	425	468	446	30	6.8	28.4	27.1	27.7	0.9	3.3
	0.5	359	408	383	35	9.1	30.8	28.1	29.4	1.9	6.4
	0.1	236	275	255	27	10.8	34.6	30.9	32.7	2.6	7.9
100	25	332	356	344	17	5.0	35.2	29.1	32.2	4.3	13.3
	10	245	285	265	28	10.5	34.6	29.0	31.8	4.0	12.5
	5	192	233	213	28	13.4	32.7	29.1	30.9	2.6	8.3
	1	120	153	137	23	17.2	30.7	26.8	28.7	2.8	9.6
	0.5	101	131	116	22	18.7	29.2	26.2	27.7	2.1	7.6
	0.1	76	77	77	1	1.0	27.6	23.3	25.5	3.1	12.0
130	25	113	120	117	5	4.4	32.4	25.2	28.8	5.1	17.6
	10	86	93	89	5	6.0	25.6	20.8	23.2	3.4	14.7
	5	68	77	72	6	8.3	25.2	18.2	21.7	5.0	22.9
	1	43	48	46	4	8.5	21.1	16.1	18.6	3.5	18.8
	0.5	35	40	37	3	8.6	17.8	14.3	16.0	2.5	15.7
	0.1	22	25	24	2	8.9	15.6	13.5	14.6	1.5	10.2

TABLE A2 E* test results of PG 64-22 mixture at 4.0% AC and 7.0% Va

Temp (°F)	Freq (Hz)	Dynamic Modulus, E*					Phase Angle, φ				
		Repl. 1 6-703 (ksi)	Repl. 2 6-704 (ksi)	Average (ksi)	Std. Dev. (ksi)	Coeff. of Var.	Repl. 1 6-703 (Deg.)	Repl. 2 6-704 (Deg.)	Average (Deg.)	Std. Dev. (Deg.)	Coeff. of Var.
14	25	3265	3324	3295	42	1.3	4.8	5.2	5.0	0.3	5.4
	10	3218	3236	3227	13	0.4	7.7	6.2	7.0	1.1	15.7
	5	3145	3153	3149	6	0.2	8.3	8.4	8.3	0.0	0.3
	1	2918	2916	2917	1	0.0	8.8	8.5	8.6	0.3	2.9
	0.5	2859	2817	2838	30	1.0	9.0	7.7	8.4	0.9	10.7
	0.1	2553	2537	2545	11	0.4	8.1	9.8	8.9	1.2	13.4
40	25	2443	2237	2340	145	6.2	7.7	11.7	9.7	2.8	29.3
	10	2480	2261	2370	155	6.5	9.6	11.2	10.4	1.1	10.3
	5	2359	2171	2265	133	5.9	10.1	13.2	11.7	2.2	18.6
	1	2045	1886	1965	112	5.7	12.1	14.1	13.1	1.4	10.9
	0.5	1929	1778	1854	106	5.7	13.4	14.7	14.1	1.0	6.9
	0.1	1642	1520	1581	87	5.5	17.4	17.2	17.3	0.1	0.7
70	25	1311	1437	1374	89	6.5	13.1	11.8	12.4	0.9	7.6
	10	1255	1312	1283	40	3.1	16.3	14.2	15.2	1.5	9.9
	5	1118	1166	1142	34	3.0	17.5	17.2	17.3	0.2	1.3
	1	859	922	891	45	5.0	23.2	23.0	23.1	0.2	0.7
	0.5	767	762	764	3	0.5	26.3	25.6	25.9	0.5	1.8
	0.1	555	570	562	11	1.9	31.1	30.9	31.0	0.1	0.4
100	25	524	461	493	44	9.0	36.7	31.2	33.9	3.9	11.5
	10	381	344	362	26	7.3	35.5	32.4	34.0	2.1	6.3
	5	297	274	285	16	5.6	34.4	31.9	33.2	1.8	5.5
	1	183	170	176	10	5.5	34.0	31.7	32.8	1.7	5.0
	0.5	180	142	161	26	16.4	32.1	31.1	31.6	0.8	2.4
	0.1	113	103	108	7	6.6	29.7	29.1	29.4	0.4	1.3
130	25	190	145	167	31	18.7	26.5	30.0	28.2	2.4	8.6
	10	134	118	126	11	8.7	21.5	23.6	22.6	1.5	6.6
	5	108	107	107	1	0.7	19.8	21.4	20.6	1.2	5.6
	1	62	59	60	2	3.2	16.9	20.5	18.7	2.5	13.6
	0.5	49	47	48	1	2.9	15.3	19.2	17.3	2.8	16.1
	0.1	30	29	29	1	2.1	15.1	18.8	16.9	2.6	15.4

TABLE A3 E* test results of PG 64-22 mixture at 4.0% AC and 4.0% Va

Temp (°F)	Freq (Hz)	Dynamic Modulus, E*					Phase Angle, φ				
		Repl. 1 6-404 (ksi)	Repl. 2 6-405 (ksi)	Average (ksi)	Std. Dev. (ksi)	Coeff. of Var.	Repl. 1 6-404 (Deg.)	Repl. 2 6-405 (Deg.)	Average (Deg.)	Std. Dev. (Deg.)	Coeff. of Var.
14	25	4642	5144	4893	355	7.3	5.4	4.3	4.8	0.8	16.2
	10	4526	5054	4790	373	7.8	6.8	7.6	7.2	0.5	7.4
	5	4395	4964	4679	403	8.6	7.0	7.5	7.3	0.4	5.4
	1	4041	4656	4349	434	10.0	5.5	6.6	6.0	0.8	13.4
	0.5	3976	4484	4230	359	8.5	7.5	7.9	7.7	0.3	3.7
	0.1	3569	4012	3790	313	8.3	9.1	8.2	8.6	0.7	7.8
40	25	3023	4839	3931	1284	32.7	8.9	5.0	6.9	2.8	40.1
	10	2953	4578	3766	1150	30.5	9.9	8.2	9.1	1.2	13.2
	5	2742	4235	3489	1056	30.3	11.6	10.9	11.3	0.5	4.1
	1	2411	3546	2978	803	27.0	12.2	11.4	11.8	0.6	4.7
	0.5	2251	3298	2775	740	26.7	14.3	12.6	13.5	1.3	9.3
	0.1	1794	2678	2236	625	28.0	16.1	15.3	15.7	0.6	3.8
70	25	1706	3133	2420	1009	41.7	15.3	14.5	14.9	0.6	3.9
	10	1485	2875	2180	983	45.1	19.4	18.6	19.0	0.6	2.9
	5	1317	2552	1935	873	45.1	21.0	21.1	21.1	0.0	0.2
	1	954	1875	1415	651	46.0	24.6	26.6	25.6	1.4	5.5
	0.5	820	1583	1202	539	44.9	27.3	29.9	28.6	1.9	6.5
	0.1	550	1106	828	393	47.5	29.4	30.4	29.9	0.7	2.3
100	25	654	758	706	73	10.4	29.1	31.7	30.4	1.8	6.1
	10	489	573	531	59	11.1	30.3	30.0	30.1	0.2	0.8
	5	388	454	421	47	11.1	29.9	30.6	30.3	0.5	1.6
	1	232	269	250	26	10.5	29.8	31.9	30.9	1.5	4.8
	0.5	186	217	201	22	10.8	29.5	31.0	30.2	1.1	3.5
	0.1	120	140	130	14	11.0	26.0	27.2	26.6	0.9	3.3
130	25	205	194	199	8	3.9	31.8	35.1	33.4	2.3	6.9
	10	148	139	144	7	4.7	29.5	29.9	29.7	0.2	0.8
	5	119	115	117	3	2.4	25.2	26.4	25.8	0.8	3.2
	1	69	68	68	0	0.3	20.8	20.3	20.6	0.3	1.7
	0.5	55	55	55	0	0.3	19.4	18.1	18.8	0.9	4.8
	0.1	34	34	34	0	0.3	14.8	15.7	15.2	0.7	4.5

TABLE A4 E* test results of PG 64-22 mixture at 4.5% AC and 10.0% Va

Temp (°F)	Freq (Hz)	Dynamic Modulus, E*					Phase Angle, φ				
		Repl. 1 6O103 (ksi)	Repl. 2 6O104 (ksi)	Average (ksi)	Std. Dev. (ksi)	Coeff. of Var.	Repl. 1 6O103 (Deg.)	Repl. 2 6O104 (Deg.)	Average (Deg.)	Std. Dev. (Deg.)	Coeff. of Var.
14	25	2623	1769	2196	604	27.5	7.1	8.2	7.7	0.8	10.2
	10	2492	1802	2147	488	22.7	7.8	8.5	8.2	0.5	6.5
	5	2409	1741	2075	472	22.8	8.5	9.1	8.8	0.4	4.3
	1	2178	1569	1874	431	23.0	9.4	10.0	9.7	0.4	4.6
	0.5	2106	1504	1805	426	23.6	9.4	9.8	9.6	0.3	3.0
	0.1	1861	1347	1604	363	22.6	10.5	10.6	10.6	0.1	0.5
40	25	1424	1211	1318	150	11.4	10.5	10.9	10.7	0.3	2.7
	10	1319	1138	1229	128	10.4	12.2	13.0	12.6	0.6	4.9
	5	1221	1082	1152	98	8.5	14.2	14.0	14.1	0.1	1.0
	1	973	872	922	72	7.8	16.8	16.5	16.7	0.2	1.2
	0.5	880	793	836	61	7.3	17.2	18.2	17.7	0.7	4.1
	0.1	673	615	644	41	6.4	20.5	20.9	20.7	0.3	1.3
70	25	642	693	667	36	5.4	20.3	20.0	20.2	0.2	1.2
	10	533	565	549	23	4.2	23.0	23.5	23.2	0.4	1.6
	5	461	485	473	17	3.6	25.1	24.7	24.9	0.3	1.2
	1	315	336	326	15	4.5	29.6	29.0	29.3	0.5	1.6
	0.5	272	287	280	11	3.9	32.2	31.5	31.8	0.5	1.7
	0.1	186	197	191	8	4.1	37.5	36.5	37.0	0.7	2.0
100	25	271	258	264	10	3.6	30.4	33.3	31.8	2.1	6.6
	10	201	196	199	4	2.1	28.9	30.8	29.9	1.3	4.4
	5	169	160	165	7	4.2	29.0	30.2	29.6	0.8	2.9
	1	113	110	111	2	1.8	28.2	30.7	29.5	1.8	6.1
	0.5	102	95	98	4	4.4	26.6	29.6	28.1	2.1	7.5
	0.1	63	63	63	0	0.2	22.4	32.3	27.4	7.0	25.8
130	25	97	96	96	0	0.3	30.5	28.0	29.3	1.8	6.1
	10	76	76	76	0	0.0	23.8	23.2	23.5	0.4	1.6
	5	63	63	63	0	0.2	20.2	21.9	21.0	1.2	5.7
	1	41	41	41	0	0.7	16.6	20.2	18.4	2.6	13.9
	0.5	34	34	34	0	0.9	15.3	19.4	17.3	2.9	16.9
	0.1	22	22	22	0	1.4	12.7	17.3	15.0	3.2	21.7

TABLE A5 E* test results of PG 64-22 mixture at 4.5% AC and 7.0% Va

Temp (°F)	Freq (Hz)	Dynamic Modulus, E*					Phase Angle, φ				
		Repl. 1 6O701 (ksi)	Repl. 2 6O702 (ksi)	Average (ksi)	Std. Dev. (ksi)	Coeff. of Var.	Repl. 1 6O701 (Deg.)	Repl. 2 6O702 (Deg.)	Average (Deg.)	Std. Dev. (Deg.)	Coeff. of Var.
14	25	4314	2714	3514	1131	32.2	6.6	5.9	6.2	0.5	7.6
	10	4053	2604	3328	1024	30.8	7.7	7.5	7.6	0.1	2.0
	5	3878	2498	3188	976	30.6	7.3	7.7	7.5	0.3	3.9
	1	3574	2318	2946	888	30.1	7.6	7.7	7.7	0.1	0.8
	0.5	3427	2232	2830	845	29.9	8.3	8.4	8.3	0.1	1.4
	0.1	2985	2018	2501	684	27.3	8.9	9.4	9.1	0.3	3.6
40	25	2971	2862	2917	77	2.6	11.5	9.8	10.7	1.2	11.3
	10	2783	2566	2674	153	5.7	13.8	13.5	13.6	0.3	1.9
	5	2568	2390	2479	126	5.1	14.1	14.3	14.2	0.2	1.1
	1	2122	1989	2056	94	4.6	15.3	15.3	15.3	0.0	0.2
	0.5	1956	1832	1894	88	4.6	16.0	16.3	16.1	0.2	1.2
	0.1	1524	1472	1498	36	2.4	19.4	19.4	19.4	0.0	0.1
70	25	1212	1140	1176	51	4.4	15.8	18.0	16.9	1.5	9.0
	10	1006	1028	1017	15	1.5	20.2	20.3	20.2	0.0	0.1
	5	884	920	902	25	2.8	21.5	21.8	21.6	0.2	1.0
	1	638	661	650	16	2.5	27.4	26.6	27.0	0.6	2.0
	0.5	551	571	561	14	2.5	30.5	28.9	29.7	1.1	3.9
	0.1	372	399	385	19	4.9	35.6	33.2	34.4	1.7	5.0
100	25	510	482	496	20	4.0	29.9	29.7	29.8	0.1	0.5
	10	372	349	360	16	4.5	28.1	28.4	28.3	0.2	0.8
	5	305	277	291	20	6.8	25.9	29.0	27.5	2.2	7.9
	1	189	171	180	13	7.2	23.9	29.6	26.7	4.0	15.1
	0.5	154	141	148	9	6.2	22.0	28.2	25.1	4.3	17.2
	0.1	95	100	98	3	3.5	22.5	25.9	24.2	2.4	9.9
130	25	154	148	151	4	2.6	29.7	26.9	28.3	1.9	6.9
	10	117	109	113	6	5.2	26.5	23.3	24.9	2.3	9.1
	5	95	92	94	2	1.8	22.2	21.3	21.7	0.7	3.0
	1	58	55	56	2	3.9	16.4	19.1	17.7	1.9	10.7
	0.5	47	44	45	2	3.8	12.3	17.7	15.0	3.9	25.7
	0.1	29	27	28	1	3.6	10.8	15.7	13.2	3.5	26.1

TABLE A6 E* test results of PG 64-22 mixture at 4.5% AC and 4.0% Va

Temp (°F)	Freq (Hz)	Dynamic Modulus, E*					Phase Angle, φ				
		Repl. 1 6O401 (ksi)	Repl. 2 6O402 (ksi)	Average (ksi)	Std. Dev. (ksi)	Coeff. of Var.	Repl. 1 6O401 (Deg.)	Repl. 2 6O402 (Deg.)	Average (Deg.)	Std. Dev. (Deg.)	Coeff. of Var.
14	25	4591	4886	4738	208	4.4	5.7	8.0	6.8	1.6	23.5
	10	4515	4852	4684	238	5.1	8.9	8.0	8.4	0.7	7.9
	5	4451	4913	4682	327	7.0	8.8	11.9	10.4	2.2	21.2
	1	4115	4289	4202	123	2.9	8.7	12.4	10.5	2.6	24.7
	0.5	3970	4114	4042	102	2.5	9.4	13.4	11.4	2.8	24.5
	0.1	3542	3455	3499	62	1.8	9.0	14.1	11.6	3.6	31.1
40	25	4139	3109	3624	728	20.1	6.3	7.5	6.9	0.9	12.7
	10	3886	2953	3419	660	19.3	8.5	11.2	9.8	1.9	19.5
	5	3660	2821	3241	593	18.3	9.4	12.2	10.8	2.0	18.9
	1	3135	2338	2737	563	20.6	11.9	15.2	13.5	2.3	17.3
	0.5	2935	2176	2556	537	21.0	13.3	15.8	14.6	1.8	12.4
	0.1	2386	1774	2080	432	20.8	16.3	18.6	17.4	1.6	9.1
70	25	2191	2088	2139	73	3.4	15.5	14.4	15.0	0.8	5.3
	10	2035	1843	1939	136	7.0	20.4	23.0	21.7	1.8	8.5
	5	1798	1562	1680	167	9.9	22.9	25.0	23.9	1.5	6.4
	1	1311	1070	1190	170	14.3	29.7	29.5	29.6	0.2	0.6
	0.5	1087	904	995	129	13.0	32.5	31.1	31.8	1.0	3.0
	0.1	711	593	652	83	12.8	38.2	35.5	36.8	1.9	5.1
100	25	730	659	694	50	7.1	27.2	32.9	30.0	4.1	13.5
	10	523	473	498	35	7.1	27.6	35.1	31.3	5.3	16.8
	5	413	373	393	28	7.2	28.9	34.3	31.6	3.8	12.0
	1	257	214	236	31	13.1	30.0	35.5	32.7	3.9	11.9
	0.5	214	171	193	31	15.9	28.8	34.0	31.4	3.7	11.7
	0.1	151	122	136	21	15.5	25.9	29.2	27.6	2.3	8.3
130	25	164	162	163	2	0.9	34.4	40.6	37.5	4.4	11.6
	10	115	108	112	5	4.3	29.0	34.7	31.8	4.0	12.7
	5	97	89	93	6	6.1	24.7	31.9	28.3	5.1	18.1
	1	64	64	64	0	0.0	20.0	24.8	22.4	3.4	15.1
	0.5	52	52	52	0	0.0	16.5	22.1	19.3	4.0	20.5
	0.1	32	32	32	0	0.0	14.1	21.6	17.8	5.3	29.8

TABLE A7 E* test results of PG 64-22 mixture at 5.0% AC and 10.0% Va

Temp (°F)	Freq (Hz)	Dynamic Modulus, E*					Phase Angle, φ				
		Repl. 1 6+105 (ksi)	Repl. 2 6+106 (ksi)	Average (ksi)	Std. Dev. (ksi)	Coeff. of Var.	Repl. 1 6+105 (Deg.)	Repl. 2 6+106 (Deg.)	Average (Deg.)	Std. Dev. (Deg.)	Coeff. of Var.
14	25	1933	1778	1855	110	5.9	4.8	7.1	5.9	1.6	27.9
	10	1982	1709	1845	193	10.5	7.4	8.4	7.9	0.7	8.7
	5	1924	1673	1799	178	9.9	7.4	9.5	8.5	1.5	18.2
	1	1776	1543	1659	164	9.9	8.1	11.2	9.6	2.1	22.1
	0.5	1714	1483	1598	163	10.2	9.2	11.2	10.2	1.4	13.7
	0.1	1529	1338	1434	135	9.4	10.9	12.3	11.6	1.0	8.7
40	25	1575	1468	1522	75	4.9	13.9	14.0	14.0	0.0	0.2
	10	1544	1321	1433	158	11.0	17.7	15.3	16.5	1.7	10.4
	5	1495	1231	1363	186	13.7	18.6	20.0	19.3	1.0	5.2
	1	1192	1030	1111	114	10.3	21.0	23.9	22.5	2.0	9.1
	0.5	1090	934	1012	110	10.9	23.0	24.9	24.0	1.4	5.7
	0.1	869	819	844	35	4.2	27.7	27.2	27.5	0.4	1.4
70	25	788	912	850	87	10.3	21.0	33.6	27.3	8.9	32.6
	10	735	823	779	62	8.0	24.8	36.5	30.6	8.2	26.8
	5	665	775	720	78	10.8	25.7	35.4	30.5	6.8	22.3
	1	449	585	517	97	18.7	31.5	39.5	35.5	5.6	15.9
	0.5	380	487	434	76	17.5	34.3	40.9	37.6	4.6	12.2
	0.1	244	298	271	38	14.0	42.0	43.0	42.5	0.7	1.7
100	25	300	307	304	5	1.6	37.7	37.9	37.8	0.1	0.4
	10	208	202	205	4	2.1	34.9	38.1	36.5	2.3	6.3
	5	173	161	167	8	4.8	31.4	35.1	33.2	2.6	7.8
	1	117	103	110	10	8.9	27.5	34.3	30.9	4.8	15.5
	0.5	106	89	97	12	12.2	24.6	32.2	28.4	5.4	19.1
	0.1	62	69	66	5	7.4	24.2	31.5	27.9	5.2	18.6
130	25	100	102	101	2	1.9	30.2	33.7	31.9	2.4	7.6
	10	76	78	77	1	1.7	26.3	31.8	29.0	3.9	13.5
	5	62	64	63	1	1.6	25.2	29.8	27.5	3.2	11.7
	1	38	39	39	0	1.2	24.2	26.4	25.3	1.5	6.1
	0.5	31	32	31	0	1.1	22.5	23.7	23.1	0.9	3.9
	0.1	19	20	19	0	0.8	20.5	21.9	21.2	1.0	4.8

TABLE A8 E* test results of PG 64-22 mixture at 5.0% AC and 7.0% Va

Temp (°F)	Freq (Hz)	Dynamic Modulus, E*					Phase Angle, φ				
		Repl. 1 6+705 (ksi)	Repl. 2 6+706 (ksi)	Average (ksi)	Std. Dev. (ksi)	Coeff. of Var.	Repl. 1 6+705 (Deg.)	Repl. 2 6+706 (Deg.)	Average (Deg.)	Std. Dev. (Deg.)	Coeff. of Var.
14	25	3094	3593	3344	353	10.6	9.3	6.3	7.8	2.1	27.3
	10	3073	3450	3261	266	8.2	10.7	9.6	10.2	0.8	8.2
	5	2881	3327	3104	315	10.1	10.5	9.2	9.8	0.9	8.9
	1	2582	3001	2792	297	10.6	10.3	11.1	10.7	0.6	5.7
	0.5	2376	2848	2612	334	12.8	10.6	11.6	11.1	0.7	6.6
	0.1	2070	2495	2282	301	13.2	10.6	13.1	11.8	1.7	14.8
40	25	1633	2668	2151	732	34.0	8.5	14.3	11.4	4.1	35.5
	10	1580	2498	2039	649	31.8	10.2	16.9	13.5	4.7	35.0
	5	1493	2313	1903	580	30.5	11.3	17.9	14.6	4.7	31.9
	1	1251	1889	1570	451	28.7	13.7	20.5	17.1	4.8	28.2
	0.5	1159	1701	1430	383	26.8	15.4	21.5	18.5	4.3	23.2
	0.1	936	1296	1116	255	22.9	19.1	25.2	22.1	4.3	19.3
70	25	1058	1360	1209	214	17.7	24.9	16.0	20.5	6.3	30.8
	10	939	1137	1038	140	13.5	28.0	18.2	23.1	6.9	29.8
	5	849	1003	926	109	11.7	29.6	19.9	24.7	6.9	27.7
	1	594	739	667	103	15.4	35.7	26.7	31.2	6.4	20.5
	0.5	520	639	579	85	14.6	38.7	29.4	34.0	6.6	19.4
	0.1	349	422	386	52	13.4	43.2	36.5	39.8	4.8	11.9
100	25	423	432	428	7	1.5	37.0	39.0	38.0	1.4	3.6
	10	285	313	299	20	6.6	35.4	34.5	34.9	0.6	1.6
	5	227	251	239	17	7.1	34.0	32.1	33.0	1.3	4.0
	1	142	161	151	13	8.9	34.7	32.9	33.8	1.3	3.8
	0.5	117	139	128	15	12.1	31.7	30.3	31.0	1.0	3.2
	0.1	87	93	90	4	4.5	32.8	32.0	32.4	0.6	1.7
130	25	137	149	143	8	5.5	33.5	28.4	31.0	3.6	11.7
	10	108	113	111	4	3.8	26.8	22.2	24.5	3.3	13.3
	5	89	92	91	2	2.4	22.9	21.3	22.1	1.1	5.0
	1	57	57	57	0	0.9	18.7	20.8	19.7	1.5	7.8
	0.5	47	46	47	1	2.3	14.1	14.0	14.0	0.1	0.8
	0.1	31	28	29	2	5.5	13.2	13.5	13.4	0.2	1.4

TABLE A9 E* test results of PG 64-22 mixture at 5.0% AC and 4.0% Va

Temp (°F)	Freq (Hz)	Dynamic Modulus, E*					Phase Angle, φ				
		Repl. 1 6+405 (ksi)	Repl. 2 6+406 (ksi)	Average (ksi)	Std. Dev. (ksi)	Coeff. of Var.	Repl. 1 6+405 (Deg.)	Repl. 2 6+406 (Deg.)	Average (Deg.)	Std. Dev. (Deg.)	Coeff. of Var.
14	25	4023	4197	4110	123	3.0	9.6	7.1	8.3	1.8	21.7
	10	3673	3737	3705	45	1.2	10.9	9.2	10.0	1.2	11.8
	5	3392	3445	3418	38	1.1	10.3	6.1	8.2	3.0	36.3
	1	3140	3245	3193	74	2.3	10.6	9.6	10.1	0.7	7.1
	0.5	3023	3061	3042	27	0.9	8.6	6.5	7.5	1.5	20.2
	0.1	2988	3022	3005	24	0.8	8.9	7.7	8.3	0.9	10.3
40	25	2649	2763	2706	81	3.0	13.0	9.8	11.4	2.3	19.8
	10	2517	2709	2613	135	5.2	14.6	13.0	13.8	1.1	8.2
	5	2351	2538	2445	132	5.4	16.1	13.8	14.9	1.6	10.8
	1	2005	2213	2109	147	7.0	17.2	15.3	16.2	1.3	8.1
	0.5	1853	2083	1968	163	8.3	17.4	16.0	16.7	1.0	6.1
	0.1	1508	1832	1670	229	13.7	19.5	18.7	19.1	0.6	3.1
70	25	1588	1756	1672	119	7.1	13.3	12.3	12.8	0.7	5.8
	10	1382	1602	1492	156	10.4	16.2	15.7	16.0	0.4	2.2
	5	1245	1458	1351	151	11.1	17.4	18.5	18.0	0.8	4.4
	1	919	1106	1012	132	13.0	23.5	23.9	23.7	0.3	1.2
	0.5	798	975	886	126	14.2	25.9	26.2	26.0	0.2	0.7
	0.1	542	712	627	120	19.2	32.7	32.6	32.7	0.1	0.2
100	25	622	650	636	20	3.2	32.9	31.2	32.1	1.2	3.7
	10	442	508	475	47	9.9	32.1	31.4	31.8	0.5	1.5
	5	358	387	373	20	5.4	30.6	29.9	30.2	0.5	1.8
	1	215	244	229	21	9.2	29.1	28.1	28.6	0.7	2.5
	0.5	174	199	186	17	9.4	27.6	24.6	26.1	2.1	8.0
	0.1	118	130	124	9	7.2	23.2	21.6	22.4	1.1	5.0
130	25	186	195	191	7	3.6	36.5	34.2	35.3	1.6	4.5
	10	139	155	147	11	7.3	35.2	26.0	30.6	6.5	21.3
	5	112	125	118	9	7.8	27.5	23.7	25.6	2.7	10.4
	1	67	77	72	7	10.4	21.3	20.0	20.6	0.9	4.4
	0.5	53	62	58	6	10.4	19.5	18.6	19.0	0.6	3.4
	0.1	32	37	34	4	10.4	16.6	17.7	17.2	0.7	4.3

TABLE A10 E* test results of PG 58-28 mixture at 4.2% AC and 9.5% Va

Temp (°F)	Freq (Hz)	Dynamic Modulus, E*					Phase Angle, φ				
		Repl. 1 5-901 (ksi)	Repl. 2 5-902 (ksi)	Average (ksi)	Std. Dev. (ksi).	Coeff. of Var.	Repl. 1 5-901 (Deg.)	Repl. 2 5-902 (Deg.)	Average (Deg.)	Std. Dev. (Deg.)	Coeff. of Var.
14	25	3024	2259	2642	541	20.5	4.6	7.8	6.2	2.2	35.8
	10	2832	2222	2527	431	17.1	6.9	10.1	8.5	2.2	26.3
	5	2709	2111	2410	423	17.5	8.8	10.0	9.4	0.8	8.7
	1	2465	1904	2185	396	18.1	10.6	11.0	10.8	0.3	2.8
	0.5	2324	1835	2080	346	16.6	11.1	13.2	12.1	1.5	12.2
	0.1	1972	1642	1807	233	12.9	12.9	14.3	13.6	1.0	7.1
40	25	1801	1662	1732	98	5.7	11.5	8.8	10.2	1.9	18.6
	10	1601	1602	1602	1	0.0	17.3	11.3	14.3	4.2	29.7
	5	1459	1504	1482	31	2.1	20.1	13.7	16.9	4.6	27.1
	1	1129	1239	1184	78	6.5	22.0	14.8	18.4	5.1	27.9
	0.5	1016	1128	1072	79	7.4	22.9	16.6	19.7	4.4	22.3
	0.1	745	877	811	93	11.5	26.7	19.9	23.3	4.8	20.7
70	25	798	969	884	121	13.7	21.8	17.6	19.7	2.9	14.9
	10	675	786	730	78	10.7	23.0	21.7	22.3	1.0	4.3
	5	604	661	633	41	6.4	26.3	22.8	24.6	2.5	10.1
	1	413	451	432	27	6.3	31.2	28.1	29.7	2.2	7.4
	0.5	351	378	364	19	5.3	33.5	30.7	32.1	2.0	6.3
	0.1	232	244	238	8	3.4	34.4	33.4	33.9	0.7	2.1
100	25	283	243	263	29	10.9	31.0	32.6	31.8	1.1	3.5
	10	205	178	191	19	9.9	29.8	31.3	30.5	1.1	3.7
	5	167	142	154	18	11.4	29.3	30.6	30.0	0.9	2.9
	1	107	94	101	10	9.5	26.8	25.1	26.0	1.2	4.6
	0.5	91	83	87	6	6.5	24.8	23.0	23.9	1.2	5.2
	0.1	56	58	57	2	3.4	22.1	18.9	20.5	2.3	11.0
130	25	88	98	93	7	7.6	18.5	27.8	23.1	6.6	28.6
	10	65	75	70	8	10.8	19.3	26.9	23.1	5.4	23.2
	5	55	62	58	4	7.4	15.7	22.9	19.3	5.1	26.2
	1	36	38	37	2	4.5	12.2	19.6	15.9	5.2	32.8
	0.5	29	31	30	2	5.1	12.3	17.5	14.9	3.7	24.9
	0.1	18	20	19	1	6.3	11.4	17.6	14.5	4.3	30.0

TABLE A11 E* test results of PG 58-28 mixture at 4.2% AC and 7.0% Va

Temp (°F)	Freq (Hz)	Dynamic Modulus, E*					Phase Angle, φ				
		Repl. 1 5-701 (ksi)	Repl. 2 5-702 (ksi)	Average (ksi)	Std. Dev. (ksi)	Coeff. of Var.	Repl. 1 5-701 (Deg.)	Repl. 2 5-702 (Deg.)	Average (Deg.)	Std. Dev. (Deg.)	Coeff. of Var.
14	25	3386	2399	2893	698	24.1	4.7	6.7	5.7	1.4	24.6
	10	3171	2365	2768	570	20.6	5.9	9.3	7.6	2.4	31.4
	5	3046	2274	2660	546	20.5	7.5	9.5	8.5	1.4	16.3
	1	2704	2029	2366	477	20.2	9.1	10.7	9.9	1.1	11.2
	0.5	2458	1929	2193	374	17.1	8.6	12.2	10.4	2.6	24.7
	0.1	2106	1645	1875	326	17.4	12.3	11.2	11.7	0.7	6.4
40	25	2654	2069	2361	413	17.5	10.8	8.4	9.6	1.7	17.6
	10	2486	2003	2244	342	15.2	14.9	11.2	13.1	2.7	20.3
	5	2227	1900	2063	231	11.2	18.1	13.0	15.5	3.6	23.2
	1	1685	1598	1641	62	3.7	20.7	14.7	17.7	4.2	24.0
	0.5	1486	1458	1472	20	1.3	21.8	15.2	18.5	4.6	25.1
	0.1	1050	1154	1102	73	6.6	26.6	19.9	23.3	4.7	20.4
70	25	1333	1173	1253	113	9.0	20.9	19.5	20.2	1.0	4.9
	10	1116	985	1051	92	8.8	24.1	21.7	22.9	1.7	7.4
	5	970	858	914	79	8.6	27.5	24.5	26.0	2.1	8.1
	1	643	586	614	40	6.5	33.8	30.2	32.0	2.6	8.0
	0.5	528	491	510	27	5.2	35.7	32.0	33.8	2.6	7.8
	0.1	329	321	325	6	1.9	39.3	35.0	37.2	3.0	8.0
100	25	347	295	321	37	11.5	37.3	31.9	34.6	3.9	11.1
	10	251	213	232	27	11.6	36.3	30.2	33.3	4.3	12.9
	5	194	171	183	17	9.2	35.3	30.2	32.7	3.6	10.9
	1	128	108	118	14	11.7	31.0	26.2	28.6	3.4	12.0
	0.5	108	91	100	12	12.1	27.9	24.5	26.2	2.4	9.2
	0.1	73	67	70	4	6.2	23.8	19.7	21.8	2.9	13.4
130	25	127	121	124	4	3.2	23.3	27.5	25.4	2.9	11.5
	10	96	94	95	2	1.8	21.1	22.9	22.0	1.2	5.6
	5	78	77	77	1	0.7	17.5	20.5	19.0	2.1	11.1
	1	47	49	48	1	1.9	14.9	15.6	15.2	0.5	3.1
	0.5	38	40	39	1	3.0	12.6	13.7	13.1	0.8	6.2
	0.1	24	25	24	1	5.5	7.2	13.0	10.1	4.1	40.2

TABLE A12 E* test results of PG 58-28 mixture at 4.2% AC and 4.5% Va

Temp (°F)	Freq (Hz)	Dynamic Modulus, E*					Phase Angle, φ				
		Repl. 1 5-401 (ksi)	Repl. 2 5-402 (ksi)	Average (ksi)	Std. Dev. (ksi)	Coeff. of Var.	Repl. 1 5-401 (Deg.)	Repl. 2 5-402 (Deg.)	Average (Deg.)	Std. Dev. (Deg.)	Coeff. of Var.
14	25	3447	3730	3588	200	5.6	7.0	6.6	6.8	0.3	4.8
	10	3281	3614	3448	235	6.8	8.9	8.6	8.8	0.2	2.7
	5	3215	3482	3348	189	5.6	9.6	9.2	9.4	0.2	2.6
	1	2856	3109	2982	179	6.0	11.8	9.4	10.6	1.7	16.3
	0.5	2725	2978	2852	179	6.3	11.4	10.3	10.8	0.8	7.5
	0.1	2361	2600	2480	169	6.8	11.8	11.3	11.6	0.4	3.4
40	25	2864	2934	2899	49	1.7	9.7	9.1	9.4	0.4	4.6
	10	2488	2691	2590	143	5.5	12.0	11.5	11.8	0.3	2.8
	5	2270	2554	2412	201	8.3	13.5	13.8	13.6	0.2	1.5
	1	1864	2136	2000	192	9.6	15.8	15.7	15.7	0.1	0.5
	0.5	1703	1956	1830	179	9.8	17.3	16.1	16.7	0.8	5.1
	0.1	1317	1559	1438	171	11.9	19.2	20.7	19.9	1.1	5.3
70	25	1536	1581	1559	32	2.1	14.3	18.4	16.4	2.9	17.5
	10	1311	1417	1364	75	5.5	18.4	24.0	21.2	4.0	18.9
	5	1155	1271	1213	82	6.8	20.5	27.1	23.8	4.7	19.6
	1	814	858	836	31	3.7	25.3	31.3	28.3	4.3	15.1
	0.5	693	725	709	23	3.2	27.5	33.3	30.4	4.1	13.6
	0.1	462	472	467	7	1.6	30.6	37.0	33.8	4.5	13.3
100	25	437	454	445	12	2.8	30.3	32.5	31.4	1.6	5.0
	10	329	336	333	5	1.4	29.6	31.0	30.3	0.9	3.1
	5	263	268	266	4	1.5	29.8	30.4	30.1	0.4	1.4
	1	165	169	167	2	1.5	28.4	28.1	28.2	0.1	0.5
	0.5	137	142	140	3	2.3	26.6	25.9	26.3	0.4	1.7
	0.1	99	108	103	6	6.1	23.6	20.4	22.0	2.2	10.2
130	25	168	167	168	0	0.2	29.9	30.9	30.4	0.7	2.4
	10	128	127	127	1	0.8	25.0	25.6	25.3	0.5	1.8
	5	104	102	103	1	1.3	22.9	23.5	23.2	0.4	1.9
	1	64	62	63	1	2.3	17.9	18.0	18.0	0.1	0.5
	0.5	52	50	51	1	2.8	15.3	16.3	15.8	0.7	4.4
	0.1	33	31	32	1	3.9	12.8	12.3	12.6	0.4	3.2

TABLE A13 E* test results of PG 58-28 mixture at 4.7% AC and 9.5% Va

Temp (°F)	Freq (Hz)	Dynamic Modulus, E*					Phase Angle, ϕ				
		Repl. 1 5O901 (ksi)	Repl. 2 5O902 (ksi)	Average (ksi)	Std. Dev. (ksi)	Coeff. of Var.	Repl. 1 5O901 (Deg.)	Repl. 2 5O902 (Deg.)	Average (Deg.)	Std. Dev. (Deg.)	Coeff. of Var.
14	25	2222	1734	1978	345	17.4	5.7	9.2	7.4	2.4	32.6
	10	2146	1717	1932	303	15.7	9.0	10.2	9.6	0.9	9.2
	5	2045	1661	1853	272	14.7	9.3	12.3	10.8	2.1	19.8
	1	1826	1508	1667	225	13.5	11.3	11.8	11.6	0.3	2.9
	0.5	1732	1409	1570	228	14.5	9.9	13.9	11.9	2.8	23.5
	0.1	1496	1235	1366	184	13.5	12.8	13.5	13.1	0.5	4.1
40	25	1712	1230	1471	341	23.2	14.3	12.9	13.6	1.0	7.1
	10	1549	1173	1361	266	19.6	16.5	15.0	15.7	1.1	6.7
	5	1409	1106	1258	214	17.0	19.2	16.4	17.8	2.0	11.2
	1	1078	859	969	155	16.0	22.8	18.6	20.7	3.0	14.4
	0.5	968	789	879	126	14.3	23.4	20.7	22.0	1.9	8.8
	0.1	679	592	636	62	9.8	28.3	24.3	26.3	2.8	10.8
70	25	845	743	794	72	9.1	21.2	24.4	22.8	2.2	9.7
	10	688	627	657	43	6.6	24.4	25.2	24.8	0.6	2.4
	5	578	531	554	34	6.1	28.1	28.9	28.5	0.6	2.1
	1	383	362	373	15	4.0	31.9	32.6	32.2	0.5	1.5
	0.5	320	303	311	12	3.8	33.4	35.1	34.2	1.2	3.5
	0.1	202	201	202	1	0.4	37.2	37.7	37.5	0.4	1.1
100	25	215	238	226	17	7.4	33.4	30.4	31.9	2.1	6.6
	10	160	182	171	15	8.9	33.8	29.6	31.7	3.0	9.4
	5	125	145	135	14	10.6	30.6	27.4	29.0	2.3	7.8
	1	82	102	92	14	15.3	28.2	26.2	27.2	1.5	5.4
	0.5	69	89	79	14	18.3	25.4	25.2	25.3	0.1	0.6
	0.1	51	58	54	5	9.0	20.5	24.7	22.6	3.0	13.1
130	25	93	96	94	2	2.2	30.6	23.3	27.0	5.2	19.1
	10	68	74	71	4	6.0	25.9	23.2	24.5	1.9	7.7
	5	59	61	60	2	2.6	22.6	21.3	22.0	0.9	4.2
	1	33	38	36	4	11.1	20.7	21.3	21.0	0.4	2.0
	0.5	27	32	29	3	11.7	18.0	19.7	18.9	1.2	6.1
	0.1	17	20	18	2	13.1	15.9	16.3	16.1	0.3	1.8

TABLE A14 E* test results of PG 58-28 mixture at 4.7% AC and 7.0% Va

Temp (°F)	Freq (Hz)	Dynamic Modulus, E*					Phase Angle, φ				
		Repl. 1 5O702 (ksi)	Repl. 2 5O703 (ksi)	Average (ksi)	Std. Dev. (ksi)	Coeff. of Var.	Repl. 1 5O702 (Deg.)	Repl. 2 5O703 (Deg.)	Average (Deg.)	Std. Dev. (Deg.)	Coeff. of Var.
14	25	2986	3006	2996	14	0.5	9.7	4.4	7.0	3.7	53.0
	10	2868	2889	2878	15	0.5	11.2	6.3	8.8	3.5	40.0
	5	2771	2788	2779	12	0.4	10.9	7.0	9.0	2.8	31.3
	1	2447	2499	2473	37	1.5	11.1	8.4	9.8	1.9	19.5
	0.5	2358	2373	2365	11	0.5	11.6	9.0	10.3	1.8	17.5
	0.1	2043	2059	2051	11	0.6	13.4	10.8	12.1	1.8	14.7
40	25	2176	2079	2127	69	3.2	11.5	10.8	11.2	0.5	4.2
	10	1931	1861	1896	49	2.6	12.8	13.3	13.1	0.4	3.0
	5	1784	1677	1730	76	4.4	14.4	15.1	14.8	0.5	3.4
	1	1437	1320	1378	83	6.0	18.7	18.3	18.5	0.3	1.4
	0.5	1301	1177	1239	88	7.1	18.4	20.8	19.6	1.7	8.9
	0.1	994	856	925	98	10.6	23.1	24.2	23.7	0.7	3.1
70	25	1010	908	959	72	7.5	20.3	21.9	21.1	1.1	5.4
	10	836	735	785	71	9.1	23.2	25.7	24.4	1.7	7.1
	5	722	634	678	62	9.1	25.0	29.3	27.2	3.0	11.2
	1	486	390	438	68	15.4	29.7	33.3	31.5	2.6	8.2
	0.5	411	324	368	62	16.8	30.4	34.3	32.4	2.8	8.5
	0.1	272	198	235	52	22.1	31.4	35.6	33.5	3.0	9.0
100	25	373	258	316	81	25.8	31.8	32.4	32.1	0.4	1.2
	10	280	187	233	66	28.2	28.3	31.2	29.8	2.1	7.0
	5	227	149	188	55	29.5	28.5	30.2	29.4	1.2	4.1
	1	151	93	122	41	33.8	24.0	25.6	24.8	1.1	4.4
	0.5	123	79	101	31	31.2	22.6	23.4	23.0	0.5	2.4
	0.1	78	60	69	13	18.8	17.5	18.4	17.9	0.7	3.6
130	25	130	102	116	20	16.9	23.3	29.5	26.4	4.4	16.6
	10	100	78	89	16	17.7	20.5	24.3	22.4	2.7	12.0
	5	82	63	73	13	18.3	20.2	20.5	20.3	0.2	0.9
	1	52	39	45	9	19.6	16.9	16.2	16.5	0.5	3.2
	0.5	42	32	37	7	20.2	13.6	13.3	13.4	0.2	1.5
	0.1	27	20	23	5	21.6	13.3	7.7	10.5	4.0	37.9

TABLE A15 E* test results of PG 58-28 mixture at 4.7% AC and 4.5% Va

Temp (°F)	Freq (Hz)	Dynamic Modulus, E*					Phase Angle, ϕ				
		Repl. 1 5O402 (ksi)	Repl. 2 5O403 (ksi)	Average (ksi)	Std. Dev. (ksi)	Coeff. of Var.	Repl. 1 5O402 (Deg.)	Repl. 2 5O403 (Deg.)	Average (Deg.)	Std. Dev. (Deg.)	Coeff. of Var.
14	25	3387	3306	3347	57	1.7	6.7	7.1	6.9	0.3	4.3
	10	3326	3240	3283	61	1.9	9.9	9.0	9.5	0.6	6.7
	5	3150	3153	3152	2	0.1	10.4	9.9	10.1	0.3	3.2
	1	2745	2847	2796	72	2.6	11.8	10.2	11.0	1.1	10.2
	0.5	2608	2733	2670	88	3.3	12.2	11.4	11.8	0.6	4.9
	0.1	2438	2408	2423	21	0.9	13.7	12.6	13.1	0.8	6.0
40	25	3265	1720	2493	1093	43.8	9.1	12.3	10.7	2.2	20.9
	10	3135	1701	2418	1014	41.9	11.2	14.2	12.7	2.1	16.8
	5	2942	1613	2277	939	41.2	13.7	15.6	14.6	1.3	9.1
	1	2373	1296	1835	761	41.5	16.6	18.1	17.4	1.1	6.1
	0.5	2118	1188	1653	658	39.8	16.6	19.8	18.2	2.3	12.5
	0.1	1701	915	1308	556	42.5	22.9	23.1	23.0	0.2	0.9
70	25	1759	1096	1427	468	32.8	20.1	23.0	21.6	2.1	9.5
	10	1500	907	1204	419	34.8	23.0	26.3	24.6	2.4	9.7
	5	1299	780	1039	367	35.3	26.2	27.1	26.6	0.7	2.5
	1	889	517	703	263	37.4	34.0	31.7	32.8	1.6	4.9
	0.5	731	420	576	220	38.2	34.8	31.6	33.2	2.2	6.7
	0.1	460	277	369	130	35.1	34.8	33.0	33.9	1.3	3.8
100	25	475	396	436	55	12.7	28.1	34.1	31.1	4.2	13.7
	10	345	301	323	31	9.6	28.5	31.9	30.2	2.4	8.1
	5	272	241	256	22	8.4	27.9	32.0	29.9	2.9	9.7
	1	176	161	169	10	6.1	25.1	29.3	27.2	3.0	10.9
	0.5	146	139	142	5	3.8	22.8	29.0	25.9	4.4	17.0
	0.1	88	81	85	5	6.2	17.8	24.5	21.2	4.7	22.4
130	25	163	137	150	19	12.5	26.0	28.9	27.4	2.0	7.3
	10	119	105	112	10	9.3	22.9	27.3	25.1	3.1	12.3
	5	94	85	90	6	6.8	20.8	22.2	21.5	1.0	4.5
	1	54	53	54	1	1.1	14.3	15.6	15.0	0.9	6.2
	0.5	43	43	43	1	1.3	12.4	14.0	13.2	1.1	8.6
	0.1	25	27	26	2	6.9	10.2	12.2	11.2	1.4	12.7

TABLE A16 E* test results of PG 58-28 mixture at 5.2% AC and 9.5% Va

Temp (°F)	Freq (Hz)	Dynamic Modulus, E*					Phase Angle, φ				
		Repl. 1 5+901 (ksi)	Repl. 2 5+902 (ksi)	Average (ksi)	Std. Dev. (ksi)	Coeff. of Var.	Repl. 1 5+901 (Deg.)	Repl. 2 5+902 (Deg.)	Average (Deg.)	Std. Dev. (Deg.)	Coeff. of Var.
14	25	1883	1735	1809	104	5.7	6.8	7.1	6.9	0.2	2.7
	10	1791	1613	1702	126	7.4	8.2	8.6	8.4	0.3	3.8
	5	1710	1537	1624	122	7.5	10.5	8.2	9.4	1.6	17.1
	1	1503	1345	1424	111	7.8	11.4	11.9	11.7	0.4	3.1
	0.5	1420	1260	1340	113	8.4	11.8	11.6	11.7	0.2	1.3
	0.1	1187	1067	1127	85	7.5	14.8	14.3	14.5	0.3	2.4
40	25	1202	1242	1222	28	2.3	13.9	11.6	12.7	1.6	12.8
	10	1073	1207	1140	95	8.3	16.2	16.8	16.5	0.4	2.6
	5	978	1131	1055	108	10.2	18.6	20.4	19.5	1.3	6.7
	1	748	886	817	98	12.0	23.3	21.6	22.5	1.2	5.3
	0.5	662	791	727	91	12.6	24.7	23.3	24.0	0.9	3.9
	0.1	464	572	518	76	14.8	29.9	30.3	30.1	0.3	0.9
70	25	478	680	579	143	24.7	25.2	25.1	25.2	0.0	0.1
	10	376	602	489	160	32.7	27.7	26.2	26.9	1.1	4.1
	5	308	504	406	139	34.1	29.5	29.3	29.4	0.1	0.4
	1	194	331	262	96	36.7	33.4	35.7	34.5	1.6	4.6
	0.5	156	265	211	77	36.5	32.9	37.3	35.1	3.1	8.8
	0.1	95	166	131	50	38.1	32.5	41.9	37.2	6.6	17.9
100	25	150	152	151	1	0.6	31.7	34.0	32.8	1.6	4.9
	10	102	123	112	15	13.6	31.1	32.6	31.8	1.1	3.4
	5	82	114	98	22	22.7	27.8	29.4	28.6	1.1	3.9
	1	51	90	70	28	39.9	22.6	28.5	25.6	4.2	16.4
	0.5	44	85	64	29	45.5	21.5	27.5	24.5	4.3	17.5
	0.1	36	52	44	11	25.5	18.1	24.5	21.3	4.5	21.0
130	25	52	85	68	23	34.1	21.6	22.5	22.1	0.7	3.0
	10	39	66	53	19	36.3	20.2	19.1	19.7	0.7	3.7
	5	31	55	43	16	38.0	19.5	17.4	18.4	1.4	7.8
	1	19	35	27	11	41.8	17.1	14.5	15.8	1.8	11.6
	0.5	15	29	22	10	43.5	16.2	13.2	14.7	2.2	14.7
	0.1	9	19	14	7	47.2	14.5	11.5	13.0	2.1	16.5

TABLE A17 E* test results of PG 58-28 mixture at 5.2% AC and 7.0% Va

Temp (°F)	Freq (Hz)	Dynamic Modulus, E*					Phase Angle, φ				
		Repl. 1 5+703 (ksi)	Repl. 2 5+704 (ksi)	Average (ksi)	Std. Dev. (ksi)	Coeff. of Var.	Repl. 1 5+703 (Deg.)	Repl. 2 5+704 (Deg.)	Average (Deg.)	Std. Dev. (Deg.)	Coeff. of Var.
14	25	2883	2059	2471	582	23.6	8.1	9.3	8.7	0.9	10.2
	10	2728	1971	2350	536	22.8	10.5	12.3	11.4	1.3	11.4
	5	2624	1898	2261	513	22.7	11.0	14.1	12.6	2.2	17.5
	1	2321	1661	1991	467	23.5	12.0	13.9	12.9	1.3	10.3
	0.5	2234	1569	1901	470	24.7	12.4	13.7	13.1	0.9	6.6
	0.1	1897	1287	1592	431	27.1	15.0	15.1	15.0	0.1	0.6
40	25	1700	1340	1520	255	16.8	13.2	13.7	13.4	0.4	2.7
	10	1574	1224	1399	247	17.7	16.1	15.2	15.6	0.7	4.3
	5	1437	1136	1286	213	16.5	17.9	17.8	17.8	0.0	0.2
	1	1125	880	1003	173	17.2	21.2	20.2	20.7	0.7	3.5
	0.5	1000	789	894	149	16.6	23.9	22.4	23.1	1.0	4.3
	0.1	729	590	660	99	15.0	29.2	27.6	28.4	1.1	4.0
70	25	769	596	683	122	17.9	25.6	25.6	25.6	0.0	0.0
	10	619	498	559	86	15.4	26.6	28.3	27.5	1.2	4.5
	5	517	430	473	62	13.0	29.0	29.3	29.2	0.2	0.7
	1	335	278	306	40	13.1	34.2	32.7	33.4	1.1	3.3
	0.5	276	233	254	30	11.9	34.8	33.4	34.1	0.9	2.8
	0.1	181	161	171	14	8.0	33.6	34.5	34.0	0.6	1.9
100	25	235	219	227	11	5.0	30.6	31.6	31.1	0.7	2.2
	10	162	176	169	10	6.0	27.7	30.2	28.9	1.7	6.0
	5	132	152	142	14	9.6	26.3	27.5	26.9	0.9	3.3
	1	86	110	98	17	16.9	21.2	22.8	22.0	1.1	5.2
	0.5	77	102	90	18	19.7	19.3	20.4	19.8	0.7	3.7
	0.1	67	61	64	4	6.4	17.3	15.8	16.5	1.0	6.3
130	25	104	97	101	5	4.9	19.7	20.7	20.2	0.7	3.5
	10	79	77	78	2	2.2	18.5	16.4	17.4	1.5	8.8
	5	64	64	64	0	0.1	16.3	15.2	15.7	0.8	5.2
	1	39	42	41	2	4.8	18.0	14.0	16.0	2.8	17.5
	0.5	32	35	33	2	6.9	17.2	13.2	15.2	2.9	18.8
	0.1	20	23	21	3	11.7	14.5	11.5	13.0	2.1	15.8

TABLE A18 E* test results of PG 58-28 mixture at 5.2% AC and 4.5% Va

Temp (°F)	Freq (Hz)	Dynamic Modulus, E*					Phase Angle, φ				
		Repl. 1 5+401 (ksi)	Repl. 2 5+402 (ksi)	Average (ksi)	Std. Dev. (ksi)	Coeff. of Var.	Repl. 1 5+401 (Deg.)	Repl. 2 5+402 (Deg.)	Average (Deg.)	Std. Dev. (Deg.)	Coeff. of Var.
14	25	3444	3171	3307	193	5.8	8.1	5.2	6.7	2.0	30.4
	10	3340	3077	3208	186	5.8	12.1	7.7	9.9	3.1	31.7
	5	3253	2970	3111	200	6.4	13.3	7.9	10.6	3.8	35.4
	1	2880	2661	2771	155	5.6	14.5	9.3	11.9	3.7	31.1
	0.5	2689	2547	2618	100	3.8	15.3	10.6	12.9	3.3	25.7
	0.1	2304	2208	2256	67	3.0	14.4	12.3	13.4	1.5	11.0
40	25	2828	2482	2655	244	9.2	13.4	8.8	11.1	3.2	28.9
	10	2481	2353	2417	90	3.7	16.0	12.2	14.1	2.7	18.9
	5	2259	2080	2169	126	5.8	16.9	15.3	16.1	1.2	7.2
	1	1775	1664	1719	79	4.6	19.8	18.1	19.0	1.2	6.2
	0.5	1599	1496	1548	73	4.7	21.0	22.5	21.7	1.1	5.0
	0.1	1179	1070	1124	77	6.9	23.9	26.6	25.2	1.9	7.4
70	25	1294	1307	1300	10	0.7	22.5	25.6	24.1	2.2	9.1
	10	1188	1122	1155	47	4.0	27.9	29.6	28.8	1.2	4.3
	5	991	914	953	54	5.7	30.3	32.1	31.2	1.3	4.1
	1	631	568	600	45	7.4	35.3	36.6	36.0	0.9	2.5
	0.5	511	459	485	37	7.6	35.8	38.2	37.0	1.6	4.4
	0.1	322	275	298	33	11.1	37.9	40.3	39.1	1.7	4.2
100	25	344	312	328	22	6.9	31.5	34.3	32.9	2.0	6.1
	10	250	220	235	21	9.1	31.6	31.7	31.7	0.1	0.2
	5	203	173	188	22	11.5	29.9	30.2	30.0	0.2	0.6
	1	134	115	124	14	11.0	26.8	27.7	27.3	0.6	2.3
	0.5	120	100	110	14	12.7	24.1	24.8	24.5	0.5	1.9
	0.1	79	82	81	2	2.9	19.7	21.9	20.8	1.6	7.6
130	25	134	120	127	10	7.8	24.7	21.7	23.2	2.1	9.2
	10	103	92	97	8	8.0	20.9	18.1	19.5	2.0	10.1
	5	83	74	79	6	8.2	20.2	17.1	18.7	2.2	11.7
	1	51	46	49	4	8.6	18.5	17.0	17.7	1.0	5.8
	0.5	42	37	39	3	8.8	17.9	14.7	16.3	2.3	14.2
	0.1	26	23	25	2	9.2	16.6	13.5	15.0	2.2	14.5

TABLE A19 E* test results of PG 76-16 mixture at 4.2% AC and 9.5% Va

Temp (°F)	Freq (Hz)	Dynamic Modulus, E*					Phase Angle, φ				
		Repl. 1 7-901 (ksi)	Repl. 2 7-902 (ksi)	Average (ksi)	Std. Dev. (ksi)	Coeff. of Var.	Repl. 1 7-901 (Deg.)	Repl. 2 7-902 (Deg.)	Average (Deg.)	Std. Dev. (Deg.)	Coeff. of Var.
14	25	3888	3225	3556	468	13.2	3.7	5.0	4.3	1.0	22.6
	10	3803	3153	3478	460	13.2	5.7	8.0	6.9	1.6	23.3
	5	3767	3035	3401	518	15.2	5.8	8.2	7.0	1.7	23.7
	1	3490	2820	3155	474	15.0	7.4	7.2	7.3	0.2	2.1
	0.5	3478	2721	3100	535	17.3	7.1	6.7	6.9	0.3	3.9
	0.1	3233	2446	2840	556	19.6	7.6	7.8	7.7	0.1	1.6
40	25	2961	2458	2709	356	13.1	5.9	8.2	7.1	1.6	23.2
	10	2824	2384	2604	311	12.0	6.3	9.6	7.9	2.3	29.1
	5	2710	2220	2465	346	14.1	8.4	10.5	9.5	1.5	15.7
	1	2420	1895	2158	372	17.2	9.5	11.9	10.7	1.7	15.6
	0.5	2278	1785	2031	349	17.2	10.1	13.1	11.6	2.1	17.8
	0.1	1990	1455	1723	378	22.0	13.5	14.6	14.0	0.8	5.8
70	25	1693	1585	1639	77	4.7	14.3	18.1	16.2	2.7	16.4
	10	1521	1330	1426	135	9.5	16.3	21.0	18.6	3.3	17.7
	5	1384	1177	1281	147	11.5	18.8	23.7	21.3	3.5	16.2
	1	1067	855	961	150	15.6	23.3	25.0	24.2	1.2	4.9
	0.5	933	749	841	130	15.4	25.4	27.3	26.3	1.3	4.9
	0.1	635	526	581	77	13.3	29.9	30.9	30.4	0.7	2.2
100	25	717	575	646	100	15.5	33.1	27.1	30.1	4.2	14.0
	10	507	441	474	46	9.8	35.3	28.7	32.0	4.7	14.7
	5	398	355	376	30	8.0	35.7	29.0	32.4	4.7	14.6
	1	226	223	225	2	1.0	35.9	29.4	32.6	4.6	14.1
	0.5	180	185	182	4	2.0	34.7	28.8	31.7	4.2	13.2
	0.1	113	126	120	9	7.5	29.9	27.5	28.7	1.7	6.1
130	25	223	177	200	33	16.4	32.5	34.4	33.5	1.3	3.9
	10	161	133	147	20	13.5	30.0	30.0	30.0	0.0	0.0
	5	136	112	124	17	13.9	26.9	27.6	27.3	0.5	1.8
	1	78	76	77	1	1.1	21.9	24.2	23.1	1.7	7.3
	0.5	62	59	61	2	3.4	20.7	22.5	21.6	1.3	5.8
	0.1	37	36	36	1	1.8	20.1	20.9	20.5	0.6	2.9

TABLE A20 E* test results of PG 76-16 mixture at 4.2% AC and 7.0% Va

Temp (°F)	Freq (Hz)	Dynamic Modulus, E*					Phase Angle, ϕ				
		Repl. 1 7-703 (ksi)	Repl. 2 7-704 (ksi)	Average (ksi)	Std. Dev. (ksi)	Coeff. of Var.	Repl. 1 7-703 (Deg.)	Repl. 2 7-704 (Deg.)	Average (Deg.)	Std. Dev. (Deg.)	Coeff. of Var.
14	25	4015	4089	4052	52	1.3	5.8	5.2	5.5	0.5	8.6
	10	3934	4042	3988	76	1.9	6.9	7.3	7.1	0.3	4.5
	5	3857	3931	3894	52	1.3	7.0	7.6	7.3	0.4	5.6
	1	3633	3682	3658	35	1.0	6.7	7.5	7.1	0.5	7.7
	0.5	3518	3583	3550	46	1.3	7.1	8.1	7.6	0.7	9.6
	0.1	3266	3382	3324	82	2.5	6.9	10.7	8.8	2.6	29.8
40	25	2974	3107	3041	95	3.1	8.3	8.2	8.2	0.1	0.9
	10	2853	2936	2895	59	2.0	10.7	10.1	10.4	0.4	3.6
	5	2735	2717	2726	13	0.5	11.6	11.2	11.4	0.2	2.0
	1	2412	2386	2399	18	0.8	12.7	13.4	13.1	0.5	4.1
	0.5	2282	2245	2264	26	1.2	13.2	14.2	13.7	0.7	5.4
	0.1	1941	1977	1959	26	1.3	14.2	15.6	14.9	1.0	6.7
70	25	1647	2198	1922	390	20.3	12.2	11.9	12.0	0.2	1.6
	10	1476	1953	1715	338	19.7	15.0	15.9	15.4	0.6	4.1
	5	1337	1759	1548	298	19.3	16.7	16.2	16.4	0.3	2.1
	1	1029	1305	1167	195	16.7	21.1	21.7	21.4	0.4	1.9
	0.5	913	1141	1027	161	15.7	23.1	23.9	23.5	0.6	2.6
	0.1	655	801	728	104	14.2	28.0	29.0	28.5	0.7	2.3
100	25	789	945	867	110	12.7	25.9	27.6	26.7	1.2	4.6
	10	690	736	713	33	4.6	28.0	29.4	28.7	1.0	3.6
	5	569	608	588	27	4.6	29.2	30.4	29.8	0.8	2.8
	1	355	369	362	10	2.7	32.7	33.3	33.0	0.4	1.2
	0.5	282	292	287	7	2.5	33.5	34.5	34.0	0.7	2.2
	0.1	171	161	166	7	4.4	34.0	35.3	34.6	0.9	2.6
130	25	252	283	268	22	8.2	34.3	35.2	34.8	0.6	1.8
	10	196	216	206	14	7.0	31.8	33.3	32.6	1.1	3.3
	5	160	175	168	10	6.0	30.5	31.8	31.1	0.9	3.0
	1	100	105	102	4	3.7	26.6	28.0	27.3	1.0	3.8
	0.5	81	84	82	2	2.7	24.5	25.0	24.8	0.4	1.5
	0.1	49	50	50	0	0.3	19.6	20.3	19.9	0.5	2.7

TABLE A21 E* test results of PG 76-16 mixture at 4.2% AC and 4.5% Va

Temp (°F)	Freq (Hz)	Dynamic Modulus, E*					Phase Angle, φ				
		Repl. 1 7-403 (ksi)	Repl. 2 7-404 (ksi)	Average (ksi)	Std. Dev. (ksi)	Coeff. of Var.	Repl. 1 7-403 (Deg.)	Repl. 2 7-404 (Deg.)	Average (Deg.)	Std. Dev. (Deg.)	Coeff. of Var.
14	25	4649	5325	4987	478	9.6	4.0	3.1	3.5	0.6	17.4
	10	4416	5060	4738	455	9.6	6.0	4.5	5.3	1.1	20.7
	5	4325	4892	4608	400	8.7	5.7	4.9	5.3	0.5	10.1
	1	4094	4597	4345	356	8.2	5.4	5.7	5.6	0.2	3.1
	0.5	3976	4503	4240	372	8.8	5.8	6.2	6.0	0.3	4.6
	0.1	3668	4083	3875	293	7.6	7.1	7.1	7.1	0.0	0.2
40	25	3476	3886	3681	290	7.9	6.2	5.4	5.8	0.6	10.0
	10	3288	3682	3485	279	8.0	8.7	7.8	8.3	0.7	8.2
	5	3148	3451	3299	215	6.5	7.3	8.3	7.8	0.7	8.7
	1	2760	2964	2862	145	5.1	10.1	10.4	10.3	0.2	2.1
	0.5	2551	2727	2639	124	4.7	11.0	11.8	11.4	0.6	4.8
	0.1	2168	2185	2176	12	0.6	13.6	14.8	14.2	0.9	6.0
70	25	2136	2207	2172	50	2.3	11.7	13.2	12.4	1.1	8.8
	10	1918	1886	1902	23	1.2	16.1	17.2	16.6	0.8	4.5
	5	1731	1667	1699	45	2.7	18.3	19.6	19.0	0.9	5.0
	1	1338	1221	1280	83	6.5	21.3	25.7	23.5	3.1	13.4
	0.5	1184	1044	1114	99	8.8	23.5	28.5	26.0	3.6	13.7
	0.1	857	705	781	108	13.8	30.3	34.7	32.5	3.1	9.4
100	25	940	894	917	33	3.6	26.6	29.3	27.9	1.9	6.8
	10	720	669	694	36	5.2	28.9	29.7	29.3	0.6	1.9
	5	591	553	572	27	4.7	29.8	28.8	29.3	0.7	2.3
	1	354	332	343	16	4.5	31.8	32.0	31.9	0.1	0.3
	0.5	284	267	275	12	4.5	31.4	32.8	32.1	1.0	3.1
	0.1	173	182	177	6	3.4	29.6	30.0	29.8	0.2	0.8
130	25	268	295	282	19	6.9	33.8	34.2	34.0	0.2	0.7
	10	201	234	218	23	10.7	28.3	32.0	30.2	2.7	8.8
	5	165	198	182	24	13.0	26.2	30.8	28.5	3.3	11.5
	1	115	111	113	3	2.5	20.1	24.3	22.2	3.0	13.4
	0.5	93	89	91	3	2.9	17.7	21.9	19.8	2.9	14.9
	0.1	57	54	56	2	3.9	13.0	22.1	17.5	6.4	36.5

TABLE A22 E* test results of PG 76-16 mixture at 4.7% AC and 9.5% Va

Temp (°F)	Freq (Hz)	Dynamic Modulus, E*					Phase Angle, ϕ				
		Repl. 1 7O903 (ksi)	Repl. 2 7O904 (ksi)	Average (ksi)	Std. Dev. (ksi)	Coeff. of Var.	Repl. 1 7O903 (Deg.)	Repl. 2 7O904 (Deg.)	Average (Deg.)	Std. Dev. (Deg.)	Coeff. of Var.
14	25	2898	3814	3356	648	19.3	4.2	5.9	5.0	1.2	23.0
	10	2763	3649	3206	627	19.6	6.3	10.2	8.2	2.8	34.0
	5	2719	3537	3128	578	18.5	8.3	9.4	8.8	0.8	8.6
	1	2537	3339	2938	567	19.3	8.9	10.9	9.9	1.4	14.3
	0.5	2445	3189	2817	527	18.7	9.1	10.4	9.8	0.9	9.7
	0.1	2180	2882	2531	496	19.6	9.3	10.6	10.0	0.9	9.0
40	25	2722	2721	2722	1	0.0	8.4	8.0	8.2	0.3	3.2
	10	2543	2553	2548	7	0.3	11.2	10.2	10.7	0.7	6.3
	5	2410	2423	2417	9	0.4	11.9	11.7	11.8	0.1	1.1
	1	2065	2124	2094	41	2.0	13.8	11.5	12.7	1.6	12.8
	0.5	1925	2003	1964	55	2.8	12.9	13.0	13.0	0.1	0.5
	0.1	1603	1695	1649	64	3.9	14.6	14.5	14.6	0.0	0.2
70	25	1490	1445	1468	32	2.2	12.0	13.5	12.8	1.1	8.6
	10	1317	1290	1303	19	1.4	14.9	15.9	15.4	0.7	4.6
	5	1197	1160	1178	26	2.2	16.2	17.8	17.0	1.1	6.4
	1	920	895	907	17	1.9	20.4	21.9	21.1	1.0	4.9
	0.5	798	787	793	8	1.0	23.3	24.6	24.0	1.0	4.0
	0.1	557	564	561	5	1.0	27.4	30.7	29.0	2.3	7.9
100	25	548	584	566	25	4.4	25.1	29.0	27.0	2.8	10.4
	10	427	452	439	18	4.1	26.7	30.3	28.5	2.5	8.9
	5	354	372	363	13	3.5	28.8	30.9	29.9	1.5	5.0
	1	229	234	231	3	1.3	32.4	34.1	33.2	1.1	3.4
	0.5	190	192	191	1	0.8	33.1	33.3	33.2	0.1	0.3
	0.1	131	131	131	1	0.4	33.4	35.2	34.3	1.3	3.7
130	25	204	209	206	4	1.9	28.1	31.1	29.6	2.2	7.3
	10	159	166	162	5	2.9	28.5	29.4	29.0	0.6	2.1
	5	131	130	131	1	0.6	26.9	28.3	27.6	1.0	3.6
	1	82	77	80	4	4.7	22.2	26.5	24.3	3.1	12.6
	0.5	67	62	65	4	5.5	19.5	25.9	22.7	4.6	20.1
	0.1	42	37	40	3	7.5	17.1	25.6	21.3	6.0	28.2

TABLE A23 E* test results of PG 76-16 mixture at 4.7% AC and 7.0% Va

Temp (°F)	Freq (Hz)	Dynamic Modulus, E*					Phase Angle, φ				
		Repl. 1 7O701 (ksi)	Repl. 2 7O702 (ksi)	Average (ksi)	Std. Dev. (ksi)	Coeff. of Var.	Repl. 1 7O701 (Deg.)	Repl. 2 7O702 (Deg.)	Average (Deg.)	Std. Dev. (Deg.)	Coeff. of Var.
14	25	4752	3803	4277	671	15.7	7.5	6.6	7.1	0.7	9.4
	10	4528	3529	4028	707	17.5	10.8	8.6	9.7	1.6	16.0
	5	4359	3441	3900	649	16.6	12.4	9.1	10.8	2.4	22.1
	1	3800	3166	3483	449	12.9	13.4	9.9	11.6	2.5	21.6
	0.5	3609	3047	3328	397	11.9	14.8	8.8	11.8	4.2	36.2
	0.1	3134	2791	2963	242	8.2	14.9	10.6	12.8	3.0	23.7
40	25	3040	3094	3067	38	1.3	10.6	8.5	9.5	1.5	15.5
	10	2860	2828	2844	22	0.8	14.8	11.1	12.9	2.6	20.1
	5	2788	2633	2710	110	4.0	15.9	13.0	14.4	2.1	14.4
	1	2325	2281	2303	31	1.3	17.4	12.6	15.0	3.5	23.1
	0.5	2132	2142	2137	7	0.3	18.7	13.3	16.0	3.8	23.7
	0.1	1752	1857	1805	74	4.1	19.9	12.8	16.3	5.0	30.5
70	25	2246	1825	2035	298	14.6	18.3	10.7	14.5	5.4	37.0
	10	2072	1737	1905	237	12.5	21.9	13.6	17.7	5.9	33.2
	5	1790	1602	1696	133	7.9	23.4	17.2	20.3	4.4	21.9
	1	1238	1259	1249	15	1.2	28.4	20.9	24.7	5.3	21.3
	0.5	1100	1106	1103	4	0.4	30.1	22.3	26.2	5.5	21.1
	0.1	748	823	786	53	6.7	33.7	26.1	29.9	5.4	18.0
100	25	921	633	777	204	26.3	31.9	24.6	28.2	5.1	18.2
	10	711	488	600	158	26.3	33.9	28.7	31.3	3.7	11.8
	5	596	411	503	130	25.9	34.5	28.4	31.4	4.3	13.6
	1	342	267	305	53	17.4	39.4	30.0	34.7	6.7	19.2
	0.5	289	227	258	43	16.8	39.4	29.6	34.5	6.9	20.1
	0.1	200	162	181	27	14.8	39.9	28.2	34.0	8.3	24.4
130	25	284	231	257	38	14.6	33.2	29.2	31.2	2.8	9.0
	10	215	175	195	28	14.5	29.0	25.5	27.2	2.5	9.3
	5	173	148	161	18	11.3	28.5	24.9	26.7	2.6	9.7
	1	103	97	100	4	4.2	24.8	20.1	22.4	3.3	14.8
	0.5	82	79	81	2	2.7	21.4	18.8	20.1	1.8	9.1
	0.1	48	49	48	0	0.9	20.9	19.0	19.9	1.3	6.7

TABLE A24 E* test results of PG 76-16 mixture at 4.7% AC and 4.5% Va

Temp (°F)	Freq (Hz)	Dynamic Modulus, E*					Phase Angle, φ				
		Repl. 1 7O401 (ksi)	Repl. 2 7O403 (ksi)	Average (ksi)	Std. Dev. (ksi)	Coeff. of Var.	Repl. 1 7O401 (Deg.)	Repl. 2 7O403 (Deg.)	Average (Deg.)	Std. Dev. (Deg.)	Coeff. of Var.
14	25	4641	5346	4994	498	10.0	5.0	2.5	3.8	1.8	46.5
	10	4620	5260	4940	453	9.2	7.8	3.8	5.8	2.8	48.4
	5	4513	5183	4848	474	9.8	8.6	4.3	6.4	3.1	47.7
	1	4100	4870	4485	545	12.1	8.0	6.7	7.4	0.9	12.9
	0.5	3971	4709	4340	522	12.0	8.9	7.4	8.2	1.1	12.9
	0.1	3591	4324	3957	518	13.1	7.8	9.1	8.4	0.9	10.8
40	25	3404	3979	3692	407	11.0	7.1	5.6	6.3	1.1	16.9
	10	3192	3783	3487	418	12.0	8.9	7.6	8.2	0.9	11.3
	5	3028	3597	3313	403	12.2	9.6	8.1	8.9	1.0	11.8
	1	2663	3310	2987	458	15.3	10.5	10.2	10.4	0.2	2.2
	0.5	2529	3049	2789	368	13.2	11.0	12.1	11.6	0.8	7.2
	0.1	2183	2548	2365	258	10.9	12.6	15.7	14.1	2.2	15.6
70	25	2338	2115	2226	158	7.1	11.4	11.9	11.6	0.4	3.0
	10	2316	1944	2130	263	12.3	14.4	16.0	15.2	1.1	7.5
	5	2147	1690	1918	323	16.9	14.0	17.9	15.9	2.8	17.5
	1	1623	1264	1443	254	17.6	17.9	23.6	20.8	4.0	19.3
	0.5	1441	1112	1276	232	18.2	20.0	25.1	22.6	3.6	15.9
	0.1	1035	763	899	192	21.4	24.3	30.9	27.6	4.6	16.7
100	25	1074	1079	1077	4	0.4	23.7	25.8	24.8	1.5	5.9
	10	893	824	858	49	5.7	24.8	28.4	26.6	2.5	9.4
	5	776	682	729	67	9.2	25.8	28.6	27.2	2.0	7.4
	1	518	413	465	75	16.0	29.2	35.6	32.4	4.6	14.1
	0.5	439	325	382	80	20.9	30.0	36.3	33.2	4.5	13.4
	0.1	299	193	246	75	30.5	26.7	32.2	29.4	3.9	13.1
130	25	389	386	387	2	0.6	25.3	35.6	30.5	7.3	24.0
	10	313	270	291	30	10.3	24.6	32.9	28.8	5.9	20.5
	5	270	209	240	43	17.9	23.3	31.3	27.3	5.7	20.9
	1	167	125	146	30	20.3	20.3	25.1	22.7	3.4	15.0
	0.5	136	106	121	21	17.7	18.4	21.1	19.7	1.9	9.5
	0.1	84	68	76	11	14.7	15.9	15.0	15.4	0.6	4.1

TABLE A25 E* test results of PG 76-16 mixture at 5.2% AC and 9.5% Va

Temp (°F)	Freq (Hz)	Repl. 1 7+903 (ksi)	Repl. 2 7+904 (ksi)	Average (ksi)	Std. Dev. (ksi)	Coeff. of Var.	Repl. 1 7+903 (Deg.)	Repl. 2 7+904 (Deg.)	Average (Deg.)	Std. Dev. (Deg.)	Coeff. of Var.
		Dynamic Modulus, E*					Phase Angle, φ				
14	25	2724	2331	2527	278	11.0	3.5	8.4	6.0	3.5	58.3
	10	2691	2222	2457	331	13.5	5.7	9.7	7.7	2.9	37.2
	5	2659	2140	2399	367	15.3	6.1	10.2	8.2	2.9	35.4
	1	2448	1975	2211	334	15.1	7.3	9.6	8.4	1.6	19.1
	0.5	2391	1923	2157	331	15.4	7.5	9.9	8.7	1.7	19.5
	0.1	2203	1725	1964	338	17.2	8.3	10.7	9.5	1.6	17.2
40	25	1999	1427	1713	404	23.6	7.7	8.3	8.0	0.4	5.6
	10	1921	1384	1652	380	23.0	10.8	9.0	9.9	1.3	12.7
	5	1825	1314	1570	362	23.1	12.3	11.5	11.9	0.6	4.9
	1	1571	1132	1351	311	23.0	13.1	11.9	12.5	0.8	6.6
	0.5	1490	1127	1309	256	19.6	13.2	12.1	12.7	0.7	5.9
	0.1	1233	886	1060	245	23.1	15.7	16.6	16.1	0.7	4.1
70	25	1101	774	937	231	24.6	13.9	17.6	15.7	2.6	16.6
	10	992	733	863	183	21.2	15.9	22.0	18.9	4.3	22.6
	5	910	672	791	168	21.3	18.0	22.8	20.4	3.4	16.7
	1	679	497	588	128	21.8	22.3	28.2	25.2	4.1	16.3
	0.5	591	430	511	114	22.2	24.3	31.4	27.8	5.0	18.1
	0.1	413	293	353	85	24.0	29.6	36.0	32.8	4.6	13.9
100	25	524	359	441	117	26.4	27.2	30.2	28.7	2.1	7.4
	10	398	278	338	85	25.0	28.2	29.6	28.9	1.0	3.4
	5	322	226	274	68	25.0	31.5	30.0	30.8	1.1	3.4
	1	193	140	166	38	22.8	32.5	31.6	32.0	0.6	2.0
	0.5	157	116	137	29	21.3	30.9	31.9	31.4	0.7	2.3
	0.1	104	80	92	17	18.4	29.4	32.7	31.0	2.3	7.5
130	25	165	142	154	16	10.4	33.3	34.3	33.8	0.7	2.1
	10	119	104	112	11	9.8	29.9	31.1	30.5	0.8	2.6
	5	96	87	91	6	6.7	27.8	27.4	27.6	0.3	1.2
	1	68	51	59	12	20.4	24.2	23.4	23.8	0.6	2.4
	0.5	60	41	51	14	26.6	22.8	21.2	22.0	1.1	5.2
	0.1	36	26	31	8	24.3	21.5	18.5	20.0	2.1	10.5

TABLE A26 E* test results of PG 76-16 mixture at 5.2% AC and 7.0% Va

Temp (°F)	Freq (Hz)	Dynamic Modulus, E*					Phase Angle, φ				
		Repl. 1 7+703 (ksi)	Repl. 2 7+704 (ksi)	Average (ksi)	Std. Dev. (ksi)	Coeff. of Var.	Repl. 1 7+703 (Deg.)	Repl. 2 7+704 (Deg.)	Average (Deg.)	Std. Dev. (Deg.)	Coeff. of Var.
14	25	4181	3192	3687	699	19.0	4.5	5.4	4.9	0.7	13.6
	10	3983	3104	3543	622	17.5	5.0	7.8	6.4	1.9	30.2
	5	3863	2968	3415	633	18.5	5.7	8.2	7.0	1.8	25.3
	1	3578	2741	3160	592	18.7	6.9	9.8	8.3	2.0	24.1
	0.5	3442	2617	3029	584	19.3	6.8	9.3	8.0	1.8	22.8
	0.1	3043	2395	2719	458	16.8	6.8	10.0	8.4	2.3	27.0
40	25	2846	2333	2589	363	14.0	5.8	8.6	7.2	1.9	26.8
	10	2693	2268	2481	300	12.1	8.6	12.3	10.4	2.6	25.2
	5	2543	2137	2340	287	12.3	9.8	13.6	11.7	2.7	23.1
	1	2194	1840	2017	250	12.4	10.4	14.7	12.5	3.1	24.5
	0.5	2041	1717	1879	229	12.2	11.0	15.1	13.0	2.9	22.6
	0.1	1707	1422	1564	201	12.9	13.0	16.9	14.9	2.7	18.1
70	25	1684	1787	1735	73	4.2	13.1	14.8	14.0	1.2	8.4
	10	1494	1532	1513	27	1.8	17.9	20.0	18.9	1.5	7.9
	5	1340	1371	1356	22	1.6	18.3	22.2	20.2	2.8	13.7
	1	1005	979	992	18	1.8	24.2	27.1	25.7	2.1	8.0
	0.5	873	851	862	15	1.8	26.7	29.7	28.2	2.1	7.3
	0.1	596	558	577	27	4.6	32.9	34.5	33.7	1.1	3.3
100	25	702	715	709	10	1.3	26.6	29.4	28.0	2.0	7.1
	10	546	538	542	6	1.0	29.2	31.9	30.5	1.9	6.1
	5	444	427	435	12	2.7	30.4	32.5	31.4	1.5	4.7
	1	272	252	262	14	5.5	34.0	36.3	35.2	1.6	4.6
	0.5	218	199	209	14	6.5	34.5	35.7	35.1	0.9	2.5
	0.1	139	124	132	10	7.9	34.4	36.2	35.3	1.2	3.5
130	25	201	208	204	5	2.4	33.5	35.8	34.7	1.7	4.8
	10	147	147	147	0	0.2	30.8	32.7	31.8	1.4	4.3
	5	115	114	115	0	0.3	27.5	29.9	28.7	1.7	6.0
	1	77	75	76	1	1.4	22.5	25.7	24.1	2.3	9.4
	0.5	66	68	67	1	1.7	20.4	23.3	21.8	2.1	9.5
	0.1	38	42	40	2	6.2	17.7	23.6	20.6	4.2	20.2

TABLE A27 E* test results of PG 76-16 mixture at 5.2% AC and 4.5% Va

Temp (°F)	Freq (Hz)	Repl. 1 7+401 (ksi)	Repl. 2 7+402 (ksi)	Average (ksi)	Std. Dev. (ksi)	Coeff. of Var.	Repl. 1 7+401 (Deg.)	Repl. 2 7+402 (Deg.)	Average (Deg.)	Std. Dev. (Deg.)	Coeff. of Var.
		Dynamic Modulus, E*					Phase Angle, φ				
14	25	4765	4031	4398	519	11.8	6.1	5.6	5.8	0.4	6.2
	10	4742	3908	4325	590	13.6	6.4	6.6	6.5	0.2	2.5
	5	4613	3770	4191	596	14.2	6.2	7.3	6.7	0.8	11.2
	1	4322	3446	3884	619	15.9	7.6	6.7	7.1	0.7	9.4
	0.5	4175	3292	3733	624	16.7	8.3	6.7	7.5	1.2	15.4
	0.1	3821	3026	3423	562	16.4	9.5	8.2	8.9	0.9	10.4
40	25	3874	3498	3686	265	7.2	8.6	7.6	8.1	0.7	8.3
	10	3769	3488	3628	199	5.5	10.6	9.0	9.8	1.1	11.7
	5	3580	3341	3461	170	4.9	11.8	10.5	11.1	1.0	8.6
	1	3109	2954	3032	109	3.6	13.2	11.0	12.1	1.6	13.1
	0.5	2931	2775	2853	110	3.9	13.9	11.8	12.9	1.5	11.3
	0.1	2561	2373	2467	133	5.4	16.4	13.6	15.0	2.0	13.2
70	25	1778	1744	1761	24	1.3	14.5	10.7	12.6	2.6	20.9
	10	1567	1538	1552	21	1.3	18.7	14.1	16.4	3.2	19.7
	5	1413	1387	1400	19	1.3	19.9	14.9	17.4	3.5	20.4
	1	1081	1061	1071	14	1.3	24.5	18.2	21.4	4.5	21.0
	0.5	951	934	943	13	1.3	26.8	20.4	23.6	4.5	19.3
	0.1	687	674	680	9	1.3	31.9	25.5	28.7	4.5	15.7
100	25	795	711	753	60	8.0	29.4	27.6	28.5	1.2	4.3
	10	609	565	587	31	5.3	29.2	27.8	28.5	1.0	3.4
	5	481	469	475	9	1.8	29.9	29.1	29.5	0.6	2.0
	1	299	292	296	5	1.6	32.7	30.5	31.6	1.6	5.0
	0.5	244	242	243	2	0.7	31.3	30.9	31.1	0.3	0.9
	0.1	173	159	166	9	5.6	29.3	28.5	28.9	0.6	1.9
130	25	223	256	240	23	9.8	32.7	33.4	33.1	0.5	1.6
	10	159	184	172	18	10.3	27.7	30.5	29.1	2.0	6.8
	5	128	146	137	12	9.1	25.8	28.9	27.3	2.2	8.1
	1	94	97	96	2	2.4	20.3	24.6	22.4	3.0	13.6
	0.5	75	85	80	7	8.8	18.4	22.4	20.4	2.9	14.1
	0.1	44	49	47	4	8.3	16.6	18.4	17.5	1.3	7.3

APPENDIX B

PROPOSED UNIAXIAL FATIGUE TEST PROTOCOL

Proposed Standard Practice For

UNIAXIAL REPEATED FATIGUE TEST OF COMPACTED HOT-MIX ASPHALT (HMA)

AASHTO Designation: PP XX-XX

1. SCOPE

1.1. This test method covers procedures for preparing and testing asphalt concrete mixtures through the uniaxial cyclic fatigue tests.

1.2. This standard is applicable to laboratory-prepared specimens of mixtures with nominal maximum size aggregate less than or equal to 37.5 mm (1.5 in.).

1.3. This standard may involve hazardous materials, operations, and equipment. This standard does not purport to address all of the safety problems associated with its use. It is the responsibility of the user of this procedure to establish appropriate safety and health practices and to determine the applicability of regulatory limitations prior to its use.

2. REFERENCED DOCUMENTS

2.1. AASHTO Standards:

- TP-62 Determining Dynamic Modulus of Hot Mix Asphalt Concrete Specimens

- R-30 Practice for Mixture Conditioning of Hot Mix Asphalt (HMA)

- NCHRP 9-20 PP 01 Preparation of Cylindrical Performance Test Specimen using the Superpave Gyratory Compactor

2.2. ASTM Standards:

- E4, Standard Practice for Force Verification and Testing Machine.

2.3. Other Documents:

- NCHRP 9-29 Equipment Specification for the Simple Performance Tester Version 3.

3. DEFINITIONS

3.1. Complex modulus (E^*)—a complex number that defines the relationship between stress and strain for a linear viscoelastic material where there is no or minimal damage takes place.

3.2. *Dynamic modulus (|E*|)*—the normal value of the complex modulus calculated by dividing the maximum (peak-to-peak) stress by the recoverable (peak-to-peak) axial strain for a material subjected to sinusoidal loading.

3.3. *Phase angle (ϕ)*—the angle in degrees between a sinusoidal applied peak stress and the resulting peak strain in a controlled stress test.

3.4. *Stiffness (E)*—the measured moduli during the uniaxial fatigue test where the specimen is subjected to fatigue damage. The stiffness value at any cycle N is calculated by dividing the peak-to-peak stress by the recoverable peak-to-peak strain.

3.5. *Initial Stiffness (E$_o$)*—the stiffness measured at cycle number 100th.

3.6. *Fatigue life (N$_f$)*—the number of loading cycles until fatigue failure.

4.   SUMMARY OF METHOD

4.1. The uniaxial fatigue test is strain-controlled and repeated sinusoidal cyclic loading that applied to a cylindrical asphalt concrete specimen until failure so that the average on-specimen axial strain is kept constant during the test. The applied stress and on-specimen axial strain response are measured and used to calculate the stiffness and the phase angle until failure. Figure 3.B1 presents a schematic of the test setup for the fatigue test.
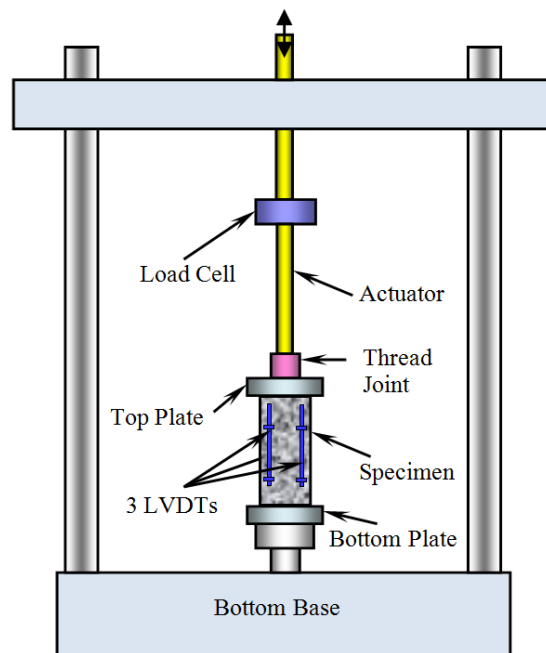
Figure 3.B1—General schematic of the cyclic uniaxial fatigue test setup.

5.   SIGNIFICANCE AND USE

5.1. This practice describes the procedure to run the uniaxial tension-compression (pull-push) fatigue test under a constant on-specimen strain-controlled condition until failure.

286

6.   APPARATUS

6.1.   *Uniaxial fatigue test system*—consists of a testing machine, environmental chamber, and measurement system.

6.2.   *Testing machine*—A servo-hydraulic testing machine capable of producing controlled sinusoidal tensile-compressive loading. The testing machine should have a capability of applying load over a range of frequencies from 1 to 10 Hz and stress level up to 2,800 kPa (400 psi).

6.3. *Conditioning chamber*—A chamber for controlling the test specimens to the desired testing temperature. The chamber shall be capable of controlling the temperature of the specimen over a temperature range of 0° to 40°C (32° to 104°F) to within ± 0.5°C (1°F). The chamber shall be large enough to accommodate at least a single test specimen and a dummy specimen with a temperature sensor mounted at the center and on the surface for temperature verification.

6.4.   *Control and data acquisition system*—The system shall be fully computer controlled and capable of measuring and recording the time history of the applied load and axial deformations. The user shall be able to provide the machine with the target strain level for the test and the machine shall be capable of adjusting the actuator deformation in order to keep the average on-specimen strain constant within +/- 0.5% of the target strain throughout the experiment. The test system shall meet the minimum requirements specified in Table 3.B1.

Table 3.B1—Test System Minimum Requirements.

Measurement	Range	Accuracy	Resolution
Load	± 0.12 to ± 25 kN (± 25 to ± 5600 lb)	Error ≤ 1.0%	≤ 0.0012 kN
Deformation	At least 12 mm (0.5 in)	Error ≤ 0.03 mm	≤ 0.0025 mm
On-specimen Deformation	At least 7000 $\mu\varepsilon$	Error ≤ 1.0%	≤ 7.5 $\mu\varepsilon$
Frequency	1 to 10 Hz	≤ 0.01 Hz	≤ 0.005 Hz
Temperature	0° to 40°C (32° to 104°F)	± 0.5°C (± 1.0°F)	± 0.25°C (± 0.5°F)
Phase Lag between Load and Deformation	Not specified	Error ≤ 1.0 degree	Not specified

6.5.   *Axial deformation measurements*—axial deformations shall be measured using linear variable differential transformers (LVDTs) mounted between gauge points glued to the specimen.

> **Note 1 –** A gauge length range of 70 to 100 mm can be used. Longer gauge length improves the likelihood that cracking will develop within the gauge length

range. Using three LVDTs set at 120° apart has an advantage over using only two LVDTs, and cheaper than using 4 LVDTs.

Note 2 – The LVDTs shall have a span length of ± 2.5 mm ± 0.01mm. This span length is appropriate to cover a wide range of test temperatures and asphalt mixtures (Conventional and modified).

6.6. *Load measurement*—An electronic load cell shall be used to measure the load. The load measuring system shall have a minimum range of ± 25 kN (± 5600 lb).

6.7. *Loading platens*—Top and bottom loading platens are glued to the specimen to transfer the load from the testing machine to the specimen. Loading platens should be made of hardened or plated steel, or anodized high strength aluminum. Softer materials will require more frequent replacement. Materials that have linear elastic modulus properties and hardiness properties lower than that of 6061-T6 aluminum shall not be used. To insure a better adhesion between the glue and the end platens, the face of each load platen shall be slightly ridged. The end platen shall be designed to be easily attached to the gluing jig and the loading machine.

6.8. *End plate gluing jig*—Gluing jig for gluing the end plates to the asphalt concrete specimen is crucial to achieve a good quality test results. The device should take care of centering the specimen within the end plates and ensure that no eccentricity exists between the specimen and end plates. The gluing jig shall have an alignment system to hold the specimen in an absolute vertical direction during the gluing. Figure 3.B2 shows an example of a well-designed gluing jig.

6.9. *Compaction Machine*—Superpave Gyratory Compactor or any other standard compaction apparatus shall be used prepare laboratory specimens. The compactor shall be capable of compacting 180-mm (7.1-inch) high specimen.

6.10. *Coring Machine*—A coring machine with a cooling system and a diamond bit for coring 75-mm (3-inch) or 100-mm (4-inch) diameter shall be used. A vertical feed speed of 0.5 mm/rev (0.002 inch/rev) and a rotational speed of 450RPM has been found to be satisfactory.

6.11. *Sawing Machine*—A saw with a cooling system shall be used to trim the specimen ends to the appropriate length. The saw shall have a diamond cutting edge and that appropriate for asphalt mixtures.

Note 3 – A cutting jig shall be used to hold the specimen tight and to ensure the cutting blade is perpendicular to the specimen edge.
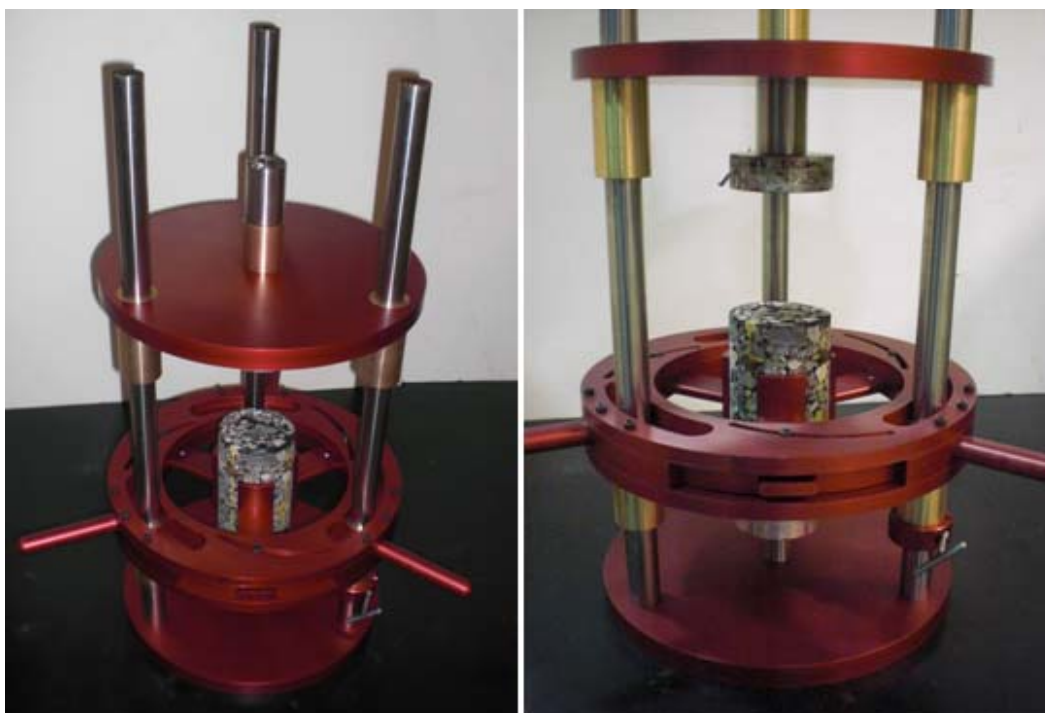
Figure 3.B2—Axial gluing jig.

7. HAZARDS

7.1. This practice and associated standards involve handling of hot asphalt binder, aggregates and asphalt mixtures. It also includes the use of sawing and coring machinery and servo-hydraulic or pneumatic testing equipment. Use standard safety precautions, equipment, and clothing when handling hot materials and operating machinery.

8. TESTING EQUIPMENT CALIBRATION

8.1. The signal conditioning and data acquisition device of the testing system shall be verified to ensure that there is no excess phase shift between load and displacement channels.

8.2. The testing system shall be calibrated prior to initial use and at least once a year thereafter or per manufacturer requirements.

8.3. Check the capability of the environmental chamber to maintain the required temperature within the accuracy specified shall be verified.

8.4. The calibration of all the measurement components (such as the load cell and specimen deformation measurement device) of the testing system shall be verified.

8.5. If any of the verifications yield data that do not comply with the accuracy specified, the problem must be corrected prior to further testing.

289

9.   TEST SPECIMEN

9.1.   *Aging*—Laboratory-prepared mixtures shall be temperature-conditioned in accordance with the 4-hour short-term oven conditioning procedure outlined in AASHTO R-30. Field mixtures need not be aged prior to testing.

9.2.   *Size*—Laboratory uniaxial tension-compression fatigue testing shall be performed on test specimens cored and cut from larger Superpave gyratory compacted specimens. Proper specimens for uniaxial fatigue test have been obtained from gyratory samples 150-mm (6-inch) in diameter and 180-mm (7.1-inch) in height. Test specimens shall be 75 ± 0.5 mm (3 ± 0.02 inch) or 100 ± 0.5 mm (4 ± 0.02 inch) in diameter with a standard deviation of 1.0 mm (0.04 inch). The average height of the test specimens shall be 150 ± 2.5 (6 ± 0.1 inch).

> **Note 4 –** Specimens compacted using gyratory compactors tend to have non-uniform air voids distribution with higher air voids at the core ends compared to the middle part. In addition, the top side of the cored specimen usually has higher air voids compared to the bottom side. The bottom side of the specimen refers to the bottom of the gyratory compaction mold. In order to have a more homogeneous air voids distribution through the height of the specimen, certain portions have to be cut from the top and the bottom side of the cored specimen. For specimens compacted to a height of 180 mm, 18 mm should be cut from the top side of the specimen and 12 mm should be cut from the bottom side.
>
> **Note 5 –** The target air voids content should be representative of that expected to be obtained in the field with a reasonable air voids tolerance for test specimen fabrication of ± 0.5 %.

9.3.   *Replicates*—Two replicate specimens should be tested at each strain level.

9.4.   *Sample storage*—If test specimens will not be tested within two days, the specimens shall be wrapped in polyethylene and stored in an environmentally protected storage area at temperatures between 5° and 25°C (40° and 77°F). Specimens shall not be stacked during storage.

> **Note 6 –** To eliminate the effects of aging on the test results, it is recommended that specimens be stored no longer than one month prior to testing.

10.   TEST SPECIMEN INSTRUMENTATION PROCEDURE

10.1.   Clean the loading platens and the ends of the specimen from any residual dust using a towel or a brush. Screw the top and the bottom end platens into the gluing jig. Place the specimen roughly on the center of the bottom end platens. Tighten the gluing jig to hold the specimen vertically and to place it exactly into the center of the bottom end platen. Move the upper part of the jig upward.

10.2.   Weigh out an appropriate amount of epoxy for only the top end of the specimen.

> **Note 7 –** The following epoxy types were found to be satisfactory for gluing the specimens without having any failure between the platens and the glue:

- Devcon plastic steel 5 minutes putty 10240 (2026 psi strength)
- Devcon plastic steel putty 10110 (2800 Psi strength)
- Loctite epoxy metal /concrete 1405605 (3200 psi strength)
- Loctite Fixmaster Superior Metal 442-97473 (5500 psi strength)
- ACE plastic repair epoxy (3431 psi strength)

Note 8 – Approximately 35 grams epoxy was found to be enough for one side of 75 mm diameter specimen.

10.3. Mix the two components of the epoxy by the required percentages very well for 30 seconds until a homogeneous material is obtained.

10.4. Take approximately 60% of the epoxy and spread it at the top surface of the specimen.

10.5. Move the top part of the jig downward until the upper end platens rest on the upper surface of the specimen.

10.6. Apply a sufficient amount of pressure on the top part of the jig until at least some epoxy has been squeezed to the edge around the entire circumference of the specimen.

10.7. Use the remaining epoxy plus the epoxy that was squeezed to the edge to glue the outer surface of the top end of the specimen (approximately 10 mm) and the top end platen (approximately 10 mm).

Note 9 – Gluing about 10 mm from the outer surface at top and bottom of the specimen was found to decrease the opportunity of having edge failure.

10.8. Allow the adhesive to reach its initial set.

Note 10 – The time necessary to initial set will depend on the epoxy chosen. Refer to the manufacturers' documentation for this information.

10.9. Release the gluing jig then move the upper part upward with the upper end patens and the specimen.

10.10. Prepare the epoxy amount for the bottom side of the specimen as done in step 10.3.

10.11. Spread 60% of the epoxy amount on the top of the lower end platens. Move down the upper part of the jig till the specimen rests on the upper end platen and finish the gluing of the lower end of the specimen as explained in steps 10.6 and 10.7.

10.12. Leave the specimen until the initial set is reached then remove the specimen from the gluing jig.

10.13. After approximately two hours, attach the mounting studs for the axial LVDTs to the sides of the specimen using epoxy cement.

Note 11 – Devcon plastic steel 5 minutes putty 10240 was found to be efficient at the expected testing temperature range (4.4 to 37.8 °C).

10.14. The gauge length for measuring axial deformations of samples may include any value between 100 mm ± 1 mm and 70 mm ± 1 mm (between 4 in. ± 0.04 in. and 2.75 in. ± 0.04 in.). The gauge length shall be measured between the stud centers.

10.15. Allow the glue to reach full cure before testing. Follow the manufacturer's recommendation to determine the time needed to full cure.

11. PROCEDURE

11.1. The test procedure consists of two tests. The first test is the non-destructive test to obtain fingerprint modulus at a specific temperature and frequency under the stress-controlled mode of loading. The second test is fatigue test, which is conducted under a constant on-specimen strain-control mode of loading at 10 Hz frequency until failure.

11.2. Insert the specimen into the environmental chamber of the test equipment.

11.3. Allow enough conditioning time for the specimen to reach the desired temperature ±0.5°C (±1°F) by monitoring the temperature probe instrumented on the dummy specimen.

> **Note 12 –** When the dummy specimen is instrumented with only a core temperature probe, allow 30 minutes after a constant temperature is reached to ensure sample equilibrium. If the dummy specimen has both a surface and a core temperature probe, monitor the specimen until the core probe temperature has equilibrated at the target temperature and the temperature difference between both probes is not more than ±1°C (±2°F).

11.4. Zero the load cell in case it is showing any readings due to the weight of the actuator and the attachment joint.

11.5. Tighten the specimen securely to the bottom support and tighten the inner screw joint into the upper end platen. Bring the actuator to the specimen until the inner screw joint contacts with the outer screw joint attached to the end of the actuator. Tighten the inner and outer screw joints firmly.

> **Note 13 –** After the specimen is tightened to the bottom base; if the testing machine has a mobile bottom base that can move up and down manually by hand or automatically by a motor, move the bottom base upward till the outer screw joint contacts with the inner screw joint and then tighten them together. In this case, keep moving the bottom base upward during the tightening process so that there is no compressive or tensile force applied to the specimen. In case the testing machine has a fixed bottom base, switch the loading mode to a stress control with a compressive force of 10 Newton (20 lbs). When the inner screw joint contacts the outer screw joint, tighten both joints together firmly.

11.6. Attach the LVDTs to the specimen and make any adjustments so that they are as close as possible to the zero reading.

11.7. Reduce the equipment set point load to 0 Newton.

11.8. Allow the specimen time to come to equilibrium with the air temperature.

11.9.   Perform a dynamic modulus fingerprint test at the target test temperature and at 10 Hz.

11.10. The fingerprint test shall be performed in tension-compression mode with a total peak-to-peak strain magnitude of 50–75 microstrain. A total of 50 cycles should be applied. In the first 10 cycles the load level can be adjusted automatically by the machine control software so that the on-specimen strains are 50–75 microstrain and in the final 40 cycles. The obtained stress levels shall then fixed the remaining 40 cycles.

> **Note 14 –** Alternatively one may apply a total of 50 cycles at a known stress input value (again tension-compression). This stress input value should yield on-specimen strain amplitude of 50-75 microstrain. If it does not then one may iterate until 50-75 microstrain is reached. At no time during these trials should the on-specimen strain magnitude exceed 150 microstrain. The specimen should be allowed to rest for at least 2 minutes between each trial.

11.11. Compute the dynamic modulus using the technique recommended in AASHTO TP-62 and by using the measured stresses and strains from the final 5 test cycles.

11.12. Return the dynamic modulus value, the phase angle value, and the machine compliance factor which should be calculated from Equation 1.

$$MCF = \frac{\varepsilon_{act}}{\varepsilon_{on-sp}} \tag{1}$$

where:

ε_{on-sp} =   the peak-to-peak average on-specimen strain,

ε_{act} =   the peak-to-peak actuator strain, calculated from Equation 2, and

MCF =   the machine compliance factor.

$$\varepsilon_{act} = \frac{\Delta_{act}}{H_o} \tag{2}$$

where:

Δ_{act} =   the peak-to-peak actuator displacement, and

H_o =   the initial height of the specimen (150 mm).

$$\varepsilon_{on-sp} = \frac{\Delta_{on-sp}}{L_g} \tag{3}$$

where:

Δ_{on-sp} =   the peak-to-peak average on-specimen displacement, and

L_g =   Gauge length (70 to 100 mm).

11.13. Allow the specimen to rest for a period of 5 to 15 minutes with a set load level of 0 Newton before conducting the uniaxial tension-compression fatigue test.

11.14. Enter the target on-specimen strain into the software.

11.15. Perform a strain-control actuator oscillation fatigue test at a frequency of 10 Hz.

11.16. The load shape for the actuator displacement will be repeating sinusoidal with positive-negative (tension-compression) movement.
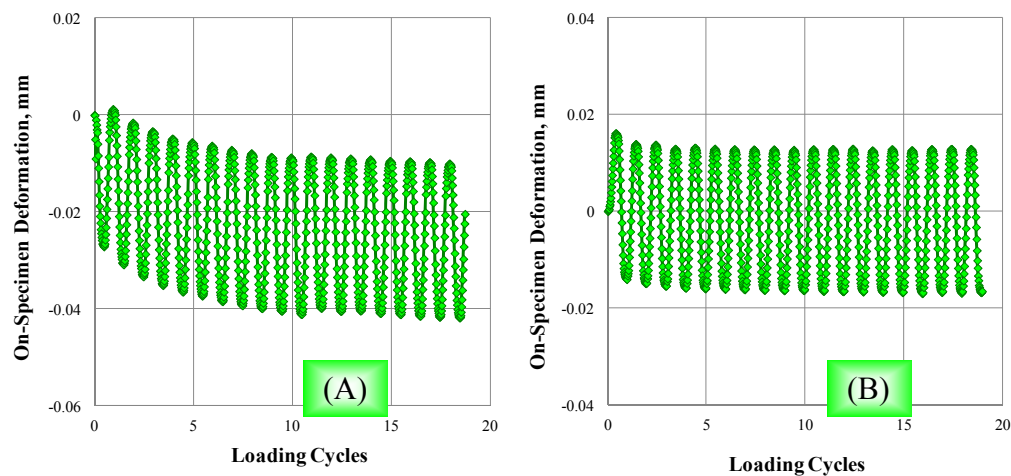
Figure 3.B3—Typical on-specimen deformation wave shape over time; A) direct- tension and B) tension-compression.
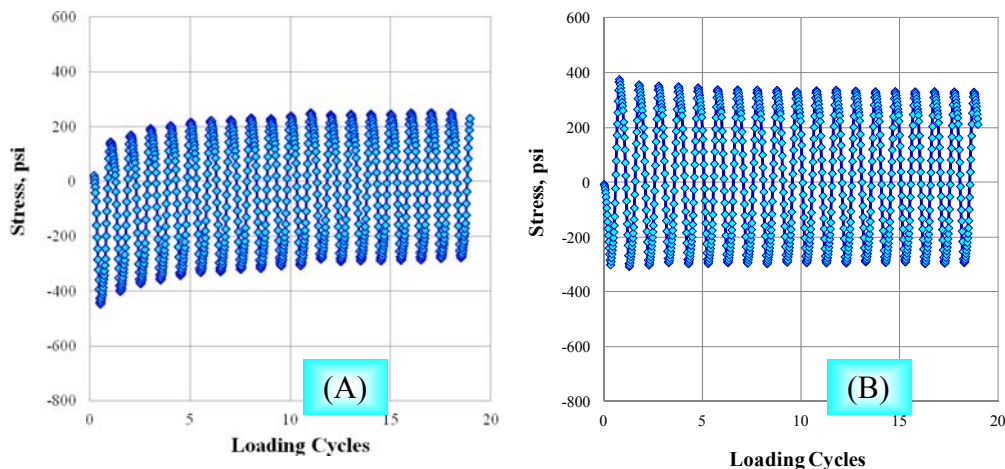
Figure 3.B4 —Typical stress wave shape over time; A) direct- tension and B) tension-compression.

294

11.17. At the first cycle, the software shall convert the initial target on-specimen strain (ε_{ost}) into actuator displacement (Δ_{act}) by using Equation 4.

$$\Delta_{act} = MCF \times L_g \times \varepsilon_{ost} \qquad\qquad (4)$$

11.18. Based on the calculated initial average on-specimen strain from the first cycle, the software shall have the capability to adjust the actuator strain to achieve the target average on-specimen strain by using a correction factor within the first 10 cycles.

> **Note 17 –** Due to the fatigue damage as the test proceeds, the specimen stiffness will change over time and thus change the machine compliance factor and increase the average on-specimen strain compared to the target value. To solve this issue, the software shall keep adjusting the actuator displacement every cycle to keep the target on-specimen strain constant. Figure 3.B5 shows typical relationships of actuator strain and on-specimen LVDTs strain versus loading cycles.
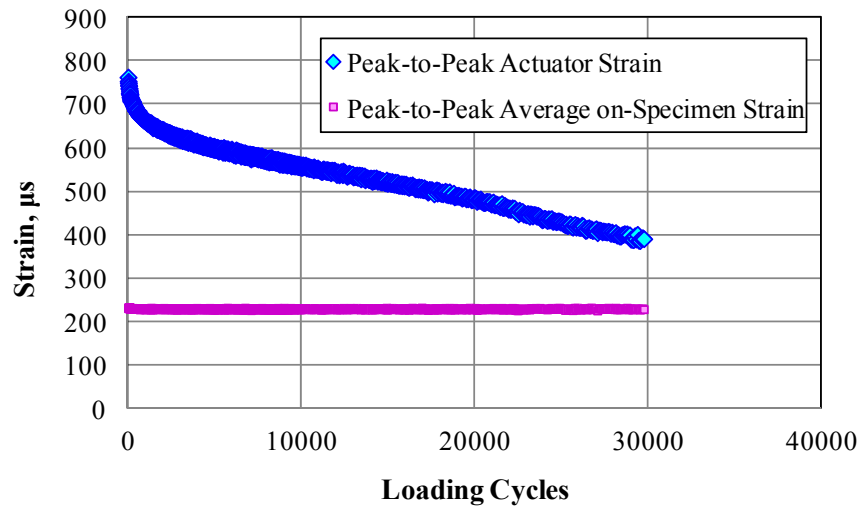
Figure 3.B5 —Typical actuator strain and average on-specimen strain versus loading cycles relationships.

> **Note 18 –** An Adaptive Strain Control (ALC) correction factor of 0.5 to the actuator strain was found to be good. The software shall automatically stop the test if the correction factor suddenly increased to 2.5, which mean that there is an issue with the test with it continuing the test is considered unsafe. These issues can be like a sudden failure of the specimen or one or more LVDTs might get stocked and stopped moving.

11.19. The test shall be run until failure or when the test reaches certain terminate condition.

> **Note 19 –** The software shall have more than one option to automatically stop the test. These options are:

- Target number of loading cycles (i.e. 10,000 cycles),

- Target stiffness reduction (i.e. 50% reduction of the initial stiffness), and

- ALC limit factor (i.e. when the ALC correction factor reaches 2.5).

11.20. The on-screen plots should include access to the following parameters as a function of cycle:

- Modulus

- Phase angle

- Stresses (Minimum stress, maximum stress, and peak-to-peak stress)

- Strains (LVDTs individual strains, and the average strain)

11.21. These values can be determined by analysis or fitting of multiple cycles in a group, for example every 5 cycles or every 10 cycles or 20 cycles.

12.   DATA ACQUISITION AND SAVED DATA

12.1. Data should be acquired into three separate files.

12.2. In the first file the data from the dynamic raw data of the first cycle should be acquired at a rate of 1000 samples per second. The file should contain a header row with the column titles. The exact wording of these column headers is not important.

- Column 1 – Time (mseconds)

- Column 2 – Axial Stress (kilopascals)

- Column 3 –Actuator microstrain (mm/mm)

- Column 4 –Axial microstrain # 1 (mm/mm)

- Column 5 –Axial microstrain # 2 (mm/mm)

- Column 6 –Axial microstrain # 3 (mm/mm)

- Column 7 –Temperature (°C)

- Column 8 –Load (kN)

- Column 9 –Actuator (mm)

- Column 10 –Displacement #1 (mm)

- Column 11 –Displacement #2 (mm)

- Column 12 –Displacement #3 (mm)

12.3. In the second file the data from the remaining cycles should be stored. The contents and the order of data file are given below.

- Column 1 – Cycle

- Column 2 – Dynamic Modulus (MPa)

- Column 3 – Phase Angle (Degrees)
- Column 4 – Peak to Peak Stress (kPa)
- Column 5 – Maximum Stress (kPa)
- Column 6 – Minimum Stress (kPa)
- Column 7 – Peak to Peak Actuator Strain (microstrain)
- Column 8 – Peak to Peak Average Strain (microstrain)
- Column 9 – Peak to Peak Strain #1 (microstrain)
- Column 10 – Peak to Peak Strain #2 (microstrain)
- Column 11 – Peak to Peak Strain #3 (microstrain)
- Column 12 – Maximum Actuator Strain (microstrain)
- Column 13 – Minimum Actuator Strain(microstrain)
- Column 14 – Maximum Strain #1 (microstrain)
- Column 15 – Minimum Strain #1 (microstrain)
- Column 16 – Maximum Strain #2 (microstrain)
- Column 17 – Minimum Strain #2 (microstrain)
- Column 18 – Maximum Strain #3 (microstrain)
- Column 19 – Minimum Strain #3 (microstrain)
- Column 20 – Column 7 –Temperature (°C)
- Column 21 – Peak to Peak Load (kN)
- Column 22 – Maximum Load (kN)
- Column 23 – Minimum Load (kN)
- Column 24 – Peak to Peak Actuator (mm)
- Column 25 – Peak to Peak LVDT #1 (mm)
- Column 26 – Peak to Peak LVDT #2 (mm)
- Column 27 – Peak to Peak LVDT #3 (mm)
- Column 29 – Maximum Actuator Displacement (mm)
- Column 30 – Minimum Actuator Displacement (mm)
- Column 31 – Maximum Displacement #1 (mm)
- Column 32 – Minimum Displacement #1 (mm)
- Column 33 – Maximum Displacement #2 (mm)
- Column 34 – Minimum Displacement #2 (mm)

- Column 35 – Maximum Displacement #3 (mm)
- Column 36 – Minimum Displacement #3 (mm)

12.4. The third data file shall be an optional file that contains the raw dynamic data at a rate of 500 samples per second for every cycle in file 2. The contents and the order of data file are given below.

- Column 1 – Cycle #
- Column 2 – Time (msecond)
- Column 3 – load (kN)
- Column 4 – Actuator (mm)
- Column 5 – LVDT #1 (mm)
- Column 6 – LVDT #2 (mm)
- Column 7 – LVDT #3 (mm)

12.5 The user should be able to select the spacing of data in the second and third file on the basis of cycle number.

---

13.   CALCULATIONS

13.1. Phase Angle (Degree):

$$\phi = 360 \times f \times t_l$$

where:

f = load frequency (Hz), and

t_l = time lag between maximum stress and maximum strain (seconds).

13.2. Maximum (Tensile) Stress (Pa, or psi):

$$\sigma_t = \frac{4 \times P_t}{\pi \times D^2}$$

where:

P_t = maximum (tensile) Load (N, or lb), and

D = specimen diameter (m, or inch).

13.3. Maximum (Tensile) Strain:

$$\varepsilon_t = \frac{\Delta_{t-avg}}{L_g}$$

where:

Δ_{t-avg} = Average maximum (tensile) deflection, (mm, or inch), and

298

L_g = gauge length (mm, or inch).

13.4. Stiffness (*Pa, or psi*):

$$E = \frac{\sigma_t}{\varepsilon_t}$$

13.5. Initial Stiffness (*Pa, or psi*): E_o is defined as the stiffness at 100th loading cycle.

> **Note 20 –** It was found that E_o at 100th cycle provided a more accurate fitting of the experimental data to establish the fatigue life (logN_f–logε_t) relationships compared to E_o at 50th cycle.

13.6. Cycles to Failure (*N_f*): Several fatigue failure definition methods were investigated in the NCHRP 9-44A project for uniaxial tension-compression fatigue test. These methods were 50% stiffness reduction, phase angle, and location of damage localization. 50% stiffness reduction method was applicable over a wide temperature range (4.4 to 37.8°C), however it is an approximate and empirical method and did not identify where exactly damage localization occurred. fatigue failure due to a . Phase angle and damage localization methods were only obvious and applicable at low and intermediate temperatures (4.4 to 21.1 °C), but not high temperatures (37.8 °C or above).

> **Note 21 –** Other definitions of fatigue failure need to be investigated as there is no clear evidence about an ultimate definition of fatigue failure. For example, dissipated energy is another recommended parameter to be investigated.

14. REPORT

14.1. HMA Description: Mixture type, binder type, binder content, and air voids.

14.2. Specimen Dimension: Specimen height, and specimen diameter.

14.3. Test Conditions: Temperature, loading mode, and target peak-to-peak strain.

14.4. Fingerprint Test: Dynamic modulus, phase angle, and machine compliance factor.

14.5. Uniaxial Fatigue Test: Initial modulus, initial phase angle, initial stress, cycles until failure, phase angle at failure, and stress at failure.

APPENDIX C

SUMMARY OF UNIAXIAL FATIGUE TEST RESULTS

Appendix C contains the results of the uniaxial tension-compression fatigue test experiments. Three uniaxial experiments were conducted. The first experiment was the fatigue life experiment to determine the strain levels for each asphalt mixtures that fail the specimens at 20,000 and 100,000 loading cycles. The second experiment was the main experiment to study the effect of five factors on the fatigue damage and healing through the results of the tests without and with rest period, respectively. A third uniaxial fatigue experiment was conducted with additional strain levels and rest period to better account for the non-linearity effect of both factors. The data for the three uniaxial fatigue experiments were compiled together to develop the PSR model using a total number of 161 test results. For the tests without rest period, only one PSR value was collected from each test at N_f. For the tests with rest periods, four PSR values were collected from each test at 5000, 10000, 15000, 20000 cycles, respectively, to investigate the effect of N on the PSR for the tests with rest period which are of interest to determine the endurance limit. A total of 385 data point are summarized in TABLE C1.

The uniaxial fatigue experiments included testing of four asphalt mixtures according to their asphalt content and air voids values (4.5 Va%&4.2 AC%, 9.5 Va%&4.2 AC%, 4.5 Va%&5.2 AC%, and 9.5 Va%&5.2 AC%). To estimate the healing of fatigue damage under different conditions, uniaxial fatigue tests were conducted at three temperatures (40, 70, and 100°F) and at different strain values. The uniaxial fatigue software includes two tests. The first test is the non-damage fingerprint test and the second test is the damage fatigue test. The next sections show the parameters of interest measured for each test.

FINGERPRINT (FP) MODULUS TEST RESULTS

➢ Stress-control test
➢ Sinusoidal wave form (tension-compression)
➢ 10 Hz frequency at fatigue test temperature

$$|E*|_{fp} = \frac{\sigma_o}{\varepsilon_o}$$

$$\phi = (t_i / t_p) \times (360°)$$

Where:

    $E*_{fp}$ = fingerprint modulus
    ϕ = phase angle
    σ_o = peak dynamic stress
    ε_o = recoverable axial strain
    t_i = time lag between a cycle of stress and strain (sec).
    t_p = time for a stress cycle (sec).

Machine Compliance factor (MCF) = peak-to-peak actuator strain / average peak-to-peak on-specimen strain

UNIAXIAL TENSION-COMPRESSION FATIGUE TEST RESULTS

➢ On-specimen strain-control test
➢ Tension-compression Sinusoidal wave form
➢ 10 Hz frequency

$|E_o|$ = initial modulus or stiffness measured at cycle number 100

Tensile strain = peak-to-peak on-specimen strain/2

S_o = tensile stress measured at cycle number 100

PSR = pseudo stiffness at cycle i divided by the initial pseudo stiffness at cycle number 100

$$PS = \frac{\sigma}{\varepsilon_{0,ta}^R \times DMR}$$

where:

PS = Psudo stiffness at cycle i,

σ = peak-to-peak stress at cycle i,

$\varepsilon_{0,ta}^R$ = pseudo strain tension amplitude at cycle i,

DMR = Dynamic Modular Ratio.

$$\left(\varepsilon_{0,ta}^R\right)_i = \frac{1}{E_R} \cdot \frac{\beta+1}{2}\left(\left(\varepsilon_{0,pp}\right)_i \cdot |E^*|_{LVE}\right)$$

where:

$\varepsilon_{0,pp}$ = peak-to-peak strain amplitude at cycle i,

$|E^*|_{LVE}$ = the average representative dynamic modulus for the mixture of interest at the temperature and frequency of interest (kPa or psi).

$$\beta = \frac{Stress_{peak} + Stress_{vally}}{\left|Stress_{peak}\right| + \left|Stress_{vally}\right|}$$

$$DMR = \frac{|E^*|_{fp}}{|E^*|_{LVE}}$$

TABLE C1 Summary of uniaxial fatigue test results

Serial Number	Specimen ID	Temperature, °F	PG Binder Grade	Asphalt Content (AC), %	Target Air Voids (Va), %	Actual Air Voids (Va), %	Tensile Strain (ϵ_t), µs	Rest Period (RP), Sec	Fingerprint Test			Uniaxial Tension-Compression Fatigue Test				
									FP Modulus (E_{LVE}), ksi	Phase Angle (ϕ), Degree	Machine Compliance Factor (MCF)	Initial Stiffness (E_o), ksi	Initial Tensile Stress (S_o), psi	Cycles to Failure at SR = 0.5, (N_f)	Cycle Number, N	Pseudo Stiffness Ratio (PSR) at N
1	D-412	40	64-22	4.20	4.50	4.84	95.0	0.0	2,573.7	9.32	11.89	2,394.0	211.5	9,470	9,470	0.500
2	D-449	40	64-22	4.20	4.50	4.48	62.5	0.0	2,624.7	11.51	12.00	2,527.5	156.2	254,100	254,100	0.500
3	D-404	70	64-22	4.20	4.50	4.08	145.0	0.0	1,307.4	32.99	6.23	1,105.8	149.3	3,430	3,430	0.500
4	D-405	70	64-22	4.20	4.50	4.33	105.0	0.0	1,333.3	31.87	6.03	1,020.7	102.8	27,400	27,400	0.500
5	D-432	70	64-22	4.20	4.50	4.03	105.0	0.0	1,344.1	22.59	6.70	1,099.8	111.5	27,340	27,340	0.500
6	D-407	100	64-22	4.20	4.50	4.09	255.0	0.0	346.8	39.76	2.45	140.7	45.2	15,930	15,930	0.500
7	D-408	100	64-22	4.20	4.50	4.63	175.0	0.0	316.6	41.57	2.46	147.9	35.1	147,895	147,895	0.500
8	D+442	40	64-22	5.20	4.50	4.79	87.5	0.0	2,129.4	11.75	9.67	2,044.7	158.2	130,320	130,320	0.500
9	D+443	40	64-22	5.20	4.50	4.20	100.0	0.0	2,440.5	12.84	14.21	2,164.2	197.3	74,710	74,710	0.500
10	D+445	40	64-22	5.20	4.50	4.37	137.5	0.0	2,648.4	13.16	11.99	2,263.6	285.3	9,470	9,470	0.500
11	D+402	70	64-22	5.20	4.50	3.46	105.0	0.0	1,038.9	28.18	4.80	843.0	92.6	218,000	218,000	0.500
12	D+403	70	64-22	5.20	4.50	3.63	145.0	0.0	1,049.1	30.46	5.25	757.0	109.4	50,500	50,500	0.500
13	D+404	70	64-22	5.20	4.50	3.37	175.0	0.0	924.0	30.18	4.41	670.7	119.2	30,000	30,000	0.500
14	D+430	100	64-22	5.20	4.50	4.89	250.0	0.0	149.4	47.59	1.75	72.5	21.9	64,570	64,570	0.500
15	D+438	100	64-22	5.20	4.50	3.99	450.0	0.0	201.2	45.71	1.77	79.6	38.3	8,810	8,810	0.500
16	D+440	100	64-22	5.20	4.50	4.46	200.0	0.0	157.7	49.80	1.74	94.4	21.4	245,470	245,470	0.500
17	D-959	40	64-22	4.20	9.50	9.65	75.0	0.0	1,936.5	12.96	12.92	1,701.0	119.4	17,920	17,920	0.500
18	D-972	40	64-22	4.20	9.50	9.49	70.0	0.0	1,595.3	14.37	7.38	1,478.5	83.9	57,250	57,250	0.500
19	D-946	70	64-22	4.20	9.50	9.22	87.5	0.0	648.0	27.52	3.46	514.7	47.1	94,770	94,770	0.500

302

20	D-947	70	64-22	4.20	9.50	8.52	125.0	0.0	827.6	25.16	4.27	617.1	75.3	22,260	22,260	0.500
21	D-951	70	64-22	4.20	9.50	9.31	100.0	0.0	724.3	25.42	3.86	596.8	59.5	84,000	84,000	0.500
22	D-962	100	64-22	4.20	9.50	9.28	225.0	0.0	152.3	31.39	2.10	70.5	24.9	32,030	32,030	0.500
23	D-963	100	64-22	4.20	9.50	9.91	275.0	0.0	145.5	34.78	1.95	65.9	26.7	7,100	7,100	0.500
24	D-964	100	64-22	4.20	9.50	9.49	175.0	0.0	164.2	37.97	2.03	86.9	24.3	168,530	168,530	0.500
25	D+959	40	64-22	5.20	9.50	9.10	100.0	0.0	1,443.4	12.21	7.92	1,332.3	126.1	53,760	53,760	0.500
26	D+958	40	64-22	5.20	9.50	8.80	112.5	0.0	1,777.4	14.38	8.19	1,423.6	143.3	17,380	17,380	0.500
27	D+962	40	64-22	5.20	9.50	9.40	130.0	0.0	1,610.6	14.10	8.15	1,434.7	172.7	8,320	8,320	0.500
28	D+943	70	64-22	5.20	9.50	9.52	95.0	0.0	516.6	28.26	2.85	409.4	40.2	372,300	372,300	0.500
29	D+944	70	64-22	5.20	9.50	8.92	125.0	0.0	643.5	24.11	3.57	484.05	60.2	63,910	63,910	0.500
30	D+948	70	64-22	5.20	9.50	9.34	200.0	0.0	613.2	26.83	3.93	356.9	71.7	4,070	4,070	0.500
31	D+949	70	64-22	5.20	9.50	9.99	187.5	0.0	502.6	31.81	2.97	328.4	65.1	9,740	9,740	0.500
32	D+952	100	64-22	5.20	9.50	9.66	200.0	0.0	110.2	34.25	1.59	54.4	20.2	357,550	357,550	0.500
33	D+953	100	64-22	5.20	9.50	9.25	350.0	0.0	99.7	37.08	1.76	42.0	24.0	13,560	13,560	0.500
34	D+956	100	64-22	5.20	9.50	9.77	250.0	0.0	107.2	30.34	1.78	52.6	22.7	74,140	74,140	0.500
35	D-442	40	64-22	4.20	4.50	3.81	87.5	0.0	3,144.6	11.52	12.70	2,711.8	237.3	21,660	16,147	0.735
36	D-440	40	64-22	4.20	4.50	4.39	87.5	0.0	2,700.7	10.74	12.21	2,394.1	209.5	15,810	16,147	0.497
37	D-446	40	64-22	4.20	4.50	4.82	87.5	0.0	2,955.7	11.32	14.42	2,353.5	205.9	10,970	16,147	0.398
38	D-443	40	64-22	4.20	4.50	4.06	70.0	0.0	3,049.7	12.72	13.43	2,751.3	192.6	71,160	61,921	0.539
39	D-452	40	64-22	4.20	4.50	4.52	70.0	0.0	2,969.2	10.64	12.95	2,755.8	192.9	56,700	61,921	0.469
40	D-455	40	64-22	4.20	4.50	4.46	70.0	0.0	3,136.6	12.22	13.09	2,823.4	197.6	57,903	61,921	0.487
41	D-436	70	64-22	4.20	4.50	4.92	115.0	0.0	974.9	23.89	4.33	814.0	93.6	12,090	15,253	0.461
42	D-437	70	64-22	4.20	4.50	5.09	115.0	0.0	1,133.2	26.63	5.53	862.0	99.1	22,620	15,253	0.573
43	D-488	70	64-22	4.20	4.50	4.99	115.0	0.0	1,220.3	23.34	5.01	901.2	97.6	11,050	15,253	0.418
44	D-427	100	64-22	4.20	4.50	3.85	195.0	0.0	295.6	42.37	1.77	183.1	35.7	85,770	77,083	0.508
45	D-467	100	64-22	4.20	4.50	4.12	195.0	0.0	244.7	51.49	1.77	140.3	27.3	71,340	77,083	0.493
46	D-466	100	64-22	4.20	4.50	4.50	195.0	0.0	203.6	50.02	1.51	132.9	25.9	74,140	77,083	0.495
47	D+452	40	64-22	5.20	4.50	3.75	112.5	0.0	2,385.6	10.92	11.97	2,183.8	245.7	17,340	17,270	0.501

48	D+453	40	64-22	5.20	4.50	4.51	112.5	0.0	2,542.2	13.34	11.16	2,139.1	240.6	11,200	17,270	0.250
49	D+459	40	64-22	5.20	4.50	4.79	112.5	0.0	2,291.3	11.17	10.86	2,095.3	235.7	23,270	17,270	0.591
50	D+449	70	64-22	5.20	4.50	4.79	122.5	0.0	872.0	30.02	4.31	679.4	83.2	129,320	98,157	0.524
51	D+455	70	64-22	5.20	4.50	4.01	122.5	0.0	959.1	24.88	4.84	784.7	96.1	88,450	98,157	0.483
52	D+492	70	64-22	5.20	4.50	4.63	122.5	0.0	1,035.6	26.13	4.27	824.1	96.8	76,700	98,157	0.400
53	D+457	100	64-22	5.20	4.50	4.63	357.5	0.0	142.7	51.90	1.26	75.4	27.0	29,520	24,897	0.523
54	D+465	100	64-22	5.20	4.50	4.78	357.5	0.0	140.7	50.87	1.26	77.0	27.5	28,400	24,897	0.528
55	D+463	100	64-22	5.20	4.50	4.86	357.5	0.0	155.3	49.98	1.32	81.5	29.1	16,770	24,897	0.417
56	D-993	40	64-22	4.20	9.50	9.14	62.5	0.0	1,734.7	10.84	8.25	1,673.9	104.6	86,210	104,943	0.452
57	D-988	40	64-22	4.20	9.50	8.93	62.5	0.0	2,175.1	12.95	9.29	2,175.1	135.9	90,280	104,943	0.478
58	D-987	40	64-22	4.20	9.50	9.01	62.5	0.0	2,065.9	12.66	9.13	1,960.0	122.5	138,340	104,943	0.631
59	D-969	70	64-22	4.20	9.50	9.52	115.0	0.0	538.4	24.58	2.83	433.6	49.9	31,150	25,753	0.541
60	D-984	70	64-22	4.20	9.50	8.76	115.0	0.0	720.8	24.46	3.56	551.1	63.4	21,990	25,753	0.468
61	D-981	70	64-22	4.20	9.50	8.73	115.0	0.0	729.5	28.92	3.58	583.2	67.1	24,120	25,753	0.487
62	D-977	70	64-22	4.20	9.50	9.25	90.0	0.0	716.6	23.16	3.36	627.9	56.5	146,780	86,893	0.583
63	D-978	70	64-22	4.20	9.50	9.45	90.0	0.0	672.8	24.26	3.45	557.3	50.2	61,820	86,893	0.445
64	D-983	70	64-22	4.20	9.50	9.32	90.0	0.0	768.8	27.53	4.26	572.5	51.5	52,080	86,893	0.393
65	D-985	100	64-22	4.20	9.50	8.84	237.5	0.0	130.5	51.65	1.29	72.4	17.2	9,810	13,897	0.439
66	D-986	100	64-22	4.20	9.50	9.17	237.5	0.0	120.7	49.30	1.25	67.3	16.0	15,530	13,897	0.514
67	D-992	100	64-22	4.20	9.50	9.05	237.5	0.0	169.7	46.54	1.37	98.0	23.3	16,350	13,897	0.523
68	D+971	40	64-22	5.20	9.50	9.16	112.5	0.0	1,628.6	12.51	6.92	1,490.3	167.7	20,580	14,723	0.617
69	D+968	40	64-22	5.20	9.50	9.98	112.5	0.0	1,470.8	12.21	6.73	1,348.4	151.7	11,220	14,723	0.397
70	D+967	40	64-22	5.20	9.50	9.04	112.5	0.0	1,612.1	11.74	7.72	1,510.0	169.9	12,370	14,723	0.432
71	D+965	40	64-22	5.20	9.50	9.38	82.5	0.0	1,379.5	12.16	5.97	1,334.0	110.1	93,810	119,010	0.452
72	D+936	40	64-22	5.20	9.50	9.79	82.5	0.0	1,408.0	12.36	6.37	1,345.4	111.0	156,080	119,010	0.582
73	D+935	40	64-22	5.20	9.50	9.26	82.5	0.0	1,598.6	11.87	7.90	1,531.4	126.3	107,140	119,010	0.466
74	D+961	70	64-22	5.20	9.50	9.66	155.0	0.0	603.4	30.02	3.50	433.1	67.1	25,910	20,377	0.541
75	D+974	70	64-22	5.20	9.50	9.61	155.0	0.0	459.6	29.08	2.55	368.3	57.1	18,060	20,377	0.481

76	D+9B2	70	64-22	5.20	9.50	9.34	155.0	0.0	540.3	27.94	2.66	412.9	62.5	17,160	20,377	0.464
77	D+985	100	64-22	5.20	9.50	9.41	252.5	0.0	129.8	43.41	1.33	78.6	19.8	126,870	97,217	0.521
78	D+989	100	64-22	5.20	9.50	9.89	252.5	0.0	80.0	56.86	1.21	48.4	12.2	58,440	97,217	0.417
79	D+984	100	64-22	5.20	9.50	9.39	252.5	0.0	122.3	44.21	1.21	76.4	19.3	106,340	97,217	0.513
80	D-490	70	64-22	4.20	4.50	4.44	90.0	0.0	1,118.4	26.32	4.55	961.4	83.4	53,570	50,355	0.512
81	D-491	70	64-22	4.20	4.50	4.48	90.0	0.0	1,058.1	23.50	4.50	896.7	76.8	47,140	50,355	0.499
82	D-9A7	100	64-22	4.20	9.50	8.87	280.0	0.0	214.2	38.94	1.51	110.0	32.5	6,050	6,390	0.495
83	D-9B3	100	64-22	4.20	9.50	8.83	280.0	0.0	152.7	46.54	1.44	80.0	24.5	6,730	6,390	0.532
84	D+9B3	100	64-22	5.20	9.50	8.87	342.5	0.0	84.6	51.32	1.17	46.0	17.3	16,350	14,175	0.528
85	D+9B5	100	64-22	5.20	9.50	8.83	343.5	0.0	90.0	52.38	1.41	46.1	17.6	12,000	14,175	0.467
86	D-475	40	64-22	4.20	4.50	4.62	70.0	5.0	3,145.4	11.51	14.20	2,731.2	191.2		5,000	1.000
87	D-475	40	64-22	4.20	4.50	4.62	70.0	5.0	3,145.4	11.51	14.20	2,731.2	191.2		10,000	1.000
88	D-475	40	64-22	4.20	4.50	4.62	70.0	5.0	3,145.4	11.51	14.20	2,731.2	191.2		15,000	1.000
89	D-475	40	64-22	4.20	4.50	4.62	70.0	5.0	3,145.4	11.51	14.20	2,731.2	191.2		20,000	1.000
90	D-478	40	64-22	4.20	4.50	4.26	70.0	5.0	2,691.0	11.37	10.63	2,567.8	179.7		5,000	0.980
91	D-478	40	64-22	4.20	4.50	4.26	70.0	5.0	2,691.0	11.37	10.63	2,567.8	179.7		10,000	0.978
92	D-478	40	64-22	4.20	4.50	4.26	70.0	5.0	2,691.0	11.37	10.63	2,567.8	179.7		15,000	0.977
93	D-478	40	64-22	4.20	4.50	4.26	70.0	5.0	2,691.0	11.37	10.63	2,567.8	179.7		20,000	0.976
94	D-495	40	64-23	4.20	4.50	3.99	70.0	5.0	2,763.7	9.85	10.20	2,763.7	193.5		5,000	0.968
95	D-495	40	64-23	4.20	4.50	3.99	70.0	5.0	2,763.7	9.85	10.20	2,763.7	193.5		10,000	0.962
96	D-495	40	64-23	4.20	4.50	3.99	70.0	5.0	2,763.7	9.85	10.20	2,763.7	193.5		15,000	0.959
97	D-495	40	64-23	4.20	4.50	3.99	70.0	5.0	2,763.7	9.85	10.20	2,763.7	193.5		20,000	0.956
98	D-465	70	64-22	4.20	4.50	4.54	90.0	5.0	1,126.1	22.43	5.01	1,036.4	93.3		5,000	0.955
99	D-465	70	64-22	4.20	4.50	4.54	90.0	5.0	1,126.1	22.43	5.01	1,036.4	93.3		10,000	0.943
100	D-465	70	64-22	4.20	4.50	4.54	90.0	5.0	1,126.1	22.43	5.01	1,036.4	93.3		15,000	0.934
101	D-465	70	64-22	4.20	4.50	4.54	90.0	5.0	1,126.1	22.43	5.01	1,036.4	93.3		20,000	0.927
102	D-468	70	64-22	4.20	4.50	3.95	90.0	5.0	1,343.3	24.12	5.81	1,183.2	106.5		5,000	0.961
103	D-468	70	64-22	4.20	4.50	3.95	90.0	5.0	1,343.3	24.12	5.81	1,183.2	106.5		10,000	0.955

104	D-468	70	64-22	4.20	4.50	3.95	90.0	5.0	1,343.3	24.12	5.81	1,183.2	106.5		15,000	0.951
105	D-468	70	64-22	4.20	4.50	3.95	90.0	5.0	1,343.3	24.12	5.81	1,183.2	106.5		20,000	0.948
106	D-493	70	64-22	4.20	4.50	4.25	90.0	5.0	1,261.7	23.77	5.03	1,110.0	100.0		5,000	0.954
107	D-493	70	64-22	4.20	4.50	4.25	90.0	5.0	1,261.7	23.77	5.03	1,110.0	100.0		10,000	0.944
108	D-493	70	64-22	4.20	4.50	4.25	90.0	5.0	1,261.7	23.77	5.03	1,110.0	100.0		15,000	0.937
109	D-493	70	64-22	4.20	4.50	4.25	90.0	5.0	1,261.7	23.77	5.03	1,110.0	100.0		20,000	0.932
110	D-471	70	64-22	4.20	4.50	4.66	115.0	5.0	1,208.7	26.62	5.25	987.8	113.6		5,000	0.955
111	D-471	70	64-22	4.20	4.50	4.66	115.0	5.0	1,208.7	26.62	5.25	987.8	113.6		10,000	0.935
112	D-471	70	64-22	4.20	4.50	4.66	115.0	5.0	1,208.7	26.62	5.25	987.8	113.6		15,000	0.919
113	D-471	70	64-22	4.20	4.50	4.66	115.0	5.0	1,208.7	26.62	5.25	987.8	113.6		20,000	0.905
114	D-473	70	64-22	4.20	4.50	4.83	115.0	5.0	1,095.5	25.15	4.77	975.4	112.2		5,000	0.958
115	D-473	70	64-22	4.20	4.50	4.83	115.0	5.0	1,095.5	25.15	4.77	975.4	112.2		10,000	0.942
116	D-473	70	64-22	4.20	4.50	4.83	115.0	5.0	1,095.5	25.15	4.77	975.4	112.2		15,000	0.929
117	D-473	70	64-22	4.20	4.50	4.83	115.0	5.0	1,095.5	25.15	4.77	975.4	112.2		20,000	0.919
118	D-494	70	64-22	4.20	4.50	4.34	115.0	5.0	1,195.7	20.98	4.75	1,066.6	122.3		5,000	0.930
119	D-494	70	64-22	4.20	4.50	4.34	115.0	5.0	1,195.7	20.98	4.75	1,066.6	122.3		10,000	0.909
120	D-494	70	64-22	4.20	4.50	4.34	115.0	5.0	1,195.7	20.98	4.75	1,066.6	122.3		15,000	0.894
121	D-494	70	64-22	4.20	4.50	4.34	115.0	5.0	1,195.7	20.98	4.75	1,066.6	122.3		20,000	0.882
122	D-472	100	64-22	4.20	4.50	4.25	242.5	5.0	213.9	45.34	1.48	166.6	40.4		5,000	0.933
123	D-472	100	64-22	4.20	4.50	4.25	242.5	5.0	213.9	45.34	1.48	166.6	40.4		10,000	0.918
124	D-472	100	64-22	4.20	4.50	4.25	242.5	5.0	213.9	45.34	1.48	166.6	40.4		15,000	0.908
125	D-472	100	64-22	4.20	4.50	4.25	242.5	5.0	213.9	45.34	1.48	166.6	40.4		20,000	0.900
126	D-474	100	64-22	4.20	4.50	4.68	242.5	5.0	226.1	47.19	1.56	163.3	39.6		5,000	0.913
127	D-474	100	64-22	4.20	4.50	4.68	242.5	5.0	226.1	47.19	1.56	163.3	39.6		10,000	0.895
128	D-474	100	64-22	4.20	4.50	4.68	242.5	5.0	226.1	47.19	1.56	163.3	39.6		15,000	0.882
129	D-474	100	64-22	4.20	4.50	4.68	242.5	5.0	226.1	47.19	1.56	163.3	39.6		20,000	0.872
130	D-497	100	64-22	4.20	4.50	5.00	242.5	5.0	182.0	46.39	1.28	145.4	31.9		5,000	0.892
131	D-497	100	64-22	4.20	4.50	5.00	242.5	5.0	182.0	46.39	1.28	145.4	31.9		10,000	0.873

132	D-497	100	64-22	4.20	4.50	5.00	242.5	5.0	182.0	46.39	1.28	145.4	31.9		15,000	0.861
133	D-497	100	64-22	4.20	4.50	5.00	242.5	5.0	182.0	46.39	1.28	145.4	31.9		20,000	0.853
134	D+473	40	64-22	5.20	4.50	4.57	82.5	5.0	2,268.8	10.51	11.49	2,168.4	178.9		5,000	0.997
135	D+473	40	64-22	5.20	4.50	4.57	82.5	5.0	2,268.8	10.51	11.49	2,168.4	178.9		10,000	0.997
136	D+473	40	64-22	5.20	4.50	4.57	82.5	5.0	2,268.8	10.51	11.49	2,168.4	178.9		15,000	0.997
137	D+473	40	64-22	5.20	4.50	4.57	82.5	5.0	2,268.8	10.51	11.49	2,168.4	178.9		20,000	0.997
138	D+476	40	64-22	5.20	4.50	4.22	82.5	5.0	2,889.4	11.81	13.29	2,540.8	209.6		5,000	1.000
139	D+476	40	64-22	5.20	4.50	4.22	82.5	5.0	2,889.4	11.81	13.29	2,540.8	209.6		10,000	1.000
140	D+476	40	64-22	5.20	4.50	4.22	82.5	5.0	2,889.4	11.81	13.29	2,540.8	209.6		15,000	1.000
141	D+476	40	64-22	5.20	4.50	4.22	82.5	5.0	2,889.4	11.81	13.29	2,540.8	209.6		20,000	1.000
142	D+491	40	64-22	5.20	4.50	4.95	82.5	5.0	2,402.4	12.55	9.21	2,180.0	196.4		5,000	0.979
143	D+491	40	64-22	5.20	4.50	4.95	82.5	5.0	2,402.4	12.55	9.21	2,180.0	196.4		10,000	0.972
144	D+491	40	64-22	5.20	4.50	4.95	82.5	5.0	2,402.4	12.55	9.21	2,180.0	196.4		15,000	0.967
145	D+491	40	64-22	5.20	4.50	4.95	82.5	5.0	2,402.4	12.55	9.21	2,180.0	196.4		20,000	0.963
146	D+464	40	64-22	5.20	4.50	5.00	112.5	5.0	2,275.6	12.25	8.80	2,090.4	235.2		5,000	0.978
147	D+464	40	64-22	5.20	4.50	5.00	112.5	5.0	2,275.6	12.25	8.80	2,090.4	235.2		10,000	0.973
148	D+464	40	64-22	5.20	4.50	5.00	112.5	5.0	2,275.6	12.25	8.80	2,090.4	235.2		15,000	0.971
149	D+464	40	64-22	5.20	4.50	5.00	112.5	5.0	2,275.6	12.25	8.80	2,090.4	235.2		20,000	0.969
150	D+477	40	64-22	5.20	4.50	4.54	112.5	5.0	2,664.1	11.86	11.30	2,330.6	262.2		5,000	0.979
151	D+477	40	64-22	5.20	4.50	4.54	112.5	5.0	2,664.1	11.86	11.30	2,330.6	262.2		10,000	0.974
152	D+477	40	64-22	5.20	4.50	4.54	112.5	5.0	2,664.1	11.86	11.30	2,330.6	262.2		15,000	0.970
153	D+477	40	64-22	5.20	4.50	4.54	112.5	5.0	2,664.1	11.86	11.30	2,330.6	262.2		20,000	0.968
154	D+489	40	64-22	5.20	4.50	4.36	112.5	5.0	2,299.3	11.18	8.90	2,147.2	243.9		5,000	0.962
155	D+489	40	64-22	5.20	4.50	4.36	112.5	5.0	2,299.3	11.18	8.90	2,147.2	243.9		10,000	0.952
156	D+489	40	64-22	5.20	4.50	4.36	112.5	5.0	2,299.3	11.18	8.90	2,147.2	243.9		15,000	0.945
157	D+489	40	64-22	5.20	4.50	4.36	112.5	5.0	2,299.3	11.18	8.90	2,147.2	243.9		20,000	0.940
158	D+468	70	64-22	5.20	4.50	4.39	197.5	5.0	1,155.8	24.00	5.15	865.7	171.0		5,000	0.964
159	D+468	70	64-22	5.20	4.50	4.39	197.5	5.0	1,155.8	24.00	5.15	865.7	171.0		10,000	0.940

307

160	D+468	70	64-22	5.20	4.50	4.39	197.5	5.0	1,155.8	24.00	5.15	865.7	171.0		15,000	0.922
161	D+468	70	64-22	5.20	4.50	4.39	197.5	5.0	1,155.8	24.00	5.15	865.7	171.0		20,000	0.908
162	D+471	70	64-22	5.20	4.50	4.61	197.5	5.0	883.4	26.83	4.10	719.9	142.2		5,000	0.982
163	D+471	70	64-22	5.20	4.50	4.61	197.5	5.0	883.4	26.83	4.10	719.9	142.2		10,000	0.967
164	D+471	70	64-22	5.20	4.50	4.61	197.5	5.0	883.4	26.83	4.10	719.9	142.2		15,000	0.956
165	D+471	70	64-22	5.20	4.50	4.61	197.5	5.0	883.4	26.83	4.10	719.9	142.2		20,000	0.948
166	D+495	70	64-22	5.20	4.50	4.68	197.5	5.0	907.5	24.99	3.82	761.8	142.7		5,000	0.944
167	D+495	70	64-22	5.20	4.50	4.68	197.5	5.0	907.5	24.99	3.82	761.8	142.7		10,000	0.928
168	D+495	70	64-22	5.20	4.50	4.68	197.5	5.0	907.5	24.99	3.82	761.8	142.7		15,000	0.918
169	D+495	70	64-22	5.20	4.50	4.68	197.5	5.0	907.5	24.99	3.82	761.8	142.7		20,000	0.912
170	D+466	100	64-22	5.20	4.50	4.57	232.5	5.0	151.6	51.59	1.44	124.3	28.9		5,000	0.966
171	D+466	100	64-22	5.20	4.50	4.57	232.5	5.0	151.6	51.59	1.44	124.3	28.9		10,000	0.955
172	D+466	100	64-22	5.20	4.50	4.57	232.5	5.0	151.6	51.59	1.44	124.3	28.9		15,000	0.948
173	D+466	100	64-22	5.20	4.50	4.57	232.5	5.0	151.6	51.59	1.44	124.3	28.9		20,000	0.941
174	D+470	100	64-22	5.20	4.50	4.13	232.5	5.0	209.6	48.89	1.71	149.0	34.6		5,000	0.919
175	D+470	100	64-22	5.20	4.50	4.13	232.5	5.0	209.6	48.89	1.71	149.0	34.6		10,000	0.906
176	D+470	100	64-22	5.20	4.50	4.13	232.5	5.0	209.6	48.89	1.71	149.0	34.6		15,000	0.899
177	D+470	100	64-22	5.20	4.50	4.13	232.5	5.0	209.6	48.89	1.71	149.0	34.6		20,000	0.893
178	D+493	100	64-22	5.20	4.50	4.70	232.5	5.0	165.9	52.00	1.41	135.1	27.5		5,000	0.947
179	D+493	100	64-22	5.20	4.50	4.70	232.5	5.0	165.9	52.00	1.41	135.1	27.5		10,000	0.929
180	D+493	100	64-22	5.20	4.50	4.70	232.5	5.0	165.9	52.00	1.41	135.1	27.5		15,000	0.916
181	D+493	100	64-22	5.20	4.50	4.70	232.5	5.0	165.9	52.00	1.41	135.1	27.5		20,000	0.906
182	D-9A4	40	64-22	4.20	9.50	9.05	80.0	5.0	1,665.5	10.81	6.92	1,527.8	122.2		5,000	0.891
183	D-9A4	40	64-22	4.20	9.50	9.05	80.0	5.0	1,665.5	10.81	6.92	1,527.8	122.2		10,000	0.869
184	D-9A4	40	64-22	4.20	9.50	9.05	80.0	5.0	1,665.5	10.81	6.92	1,527.8	122.2		15,000	0.854
185	D-9A4	40	64-22	4.20	9.50	9.05	80.0	5.0	1,665.5	10.81	6.92	1,527.8	122.2		20,000	0.842
186	D-9B9	40	64.22	4.20	9.50	9.29	80.0	5.0	1,720.4	11.68	7.13	1,604.8	128.4		5,000	0.928
187	D-9B9	40	64.22	4.20	9.50	9.29	80.0	5.0	1,720.4	11.68	7.13	1,604.8	128.4		10,000	0.911

188	D-9B9	40	64.22	4.20	9.50	9.29	80.0	5.0	1,720.4	11.68	7.13	1,604.8	128.4		15,000	0.899
189	D-9B9	40	64.22	4.20	9.50	9.29	80.0	5.0	1,720.4	11.68	7.13	1,604.8	128.4		20,000	0.890
190	D-9C8	40	64.22	4.20	9.50	9.04	80.0	5.0	1,608.9	12.28	6.52	1,492.8	130.6		5,000	0.967
191	D-9C8	40	64.22	4.20	9.50	9.04	80.0	5.0	1,608.9	12.28	6.52	1,492.8	130.6		10,000	0.957
192	D-9C8	40	64.22	4.20	9.50	9.04	80.0	5.0	1,608.9	12.28	6.52	1,492.8	130.6		15,000	0.950
193	D-9C8	40	64.22	4.20	9.50	9.04	80.0	5.0	1,608.9	12.28	6.52	1,492.8	130.6		20,000	0.944
194	D-997	70	64-22	4.20	9.50	9.25	90.0	5.0	772.9	24.22	3.61	682.8	61.5		5,000	0.952
195	D-997	70	64-22	4.20	9.50	9.25	90.0	5.0	772.9	24.22	3.61	682.8	61.5		10,000	0.946
196	D-997	70	64-22	4.20	9.50	9.25	90.0	5.0	772.9	24.22	3.61	682.8	61.5		15,000	0.942
197	D-997	70	64-22	4.20	9.50	9.25	90.0	5.0	772.9	24.22	3.61	682.8	61.5		20,000	0.939
198	D-9A1	70	64-22	4.20	9.50	9.29	90.0	5.0	699.1	25.54	2.34	636.1	57.3		5,000	0.965
199	D-9A1	70	64-22	4.20	9.50	9.29	90.0	5.0	699.1	25.54	2.34	636.1	57.3		10,000	0.961
200	D-9A1	70	64-22	4.20	9.50	9.29	90.0	5.0	699.1	25.54	2.34	636.1	57.3		15,000	0.959
201	D-9A1	70	64-22	4.20	9.50	9.29	90.0	5.0	699.1	25.54	2.34	636.1	57.3		20,000	0.957
202	D-9C5	70	64-22	4.20	9.50	9.10	90.0	5.0	728.2	25.49	3.31	652.4	58.0		5,000	0.966
203	D-9C5	70	64-22	4.20	9.50	9.10	90.0	5.0	728.2	25.49	3.31	652.4	58.0		10,000	0.960
204	D-9C5	70	64-22	4.20	9.50	9.10	90.0	5.0	728.2	25.49	3.31	652.4	58.0		15,000	0.955
205	D-9C5	70	64-22	4.20	9.50	9.10	90.0	5.0	728.2	25.49	3.31	652.4	58.0		20,000	0.952
206	D-996	100	64-22	4.20	9.50	9.28	187.5	5.0	135.2	47.45	1.35	113.0	21.2		5,000	0.965
207	D-996	100	64-22	4.20	9.50	9.28	187.5	5.0	135.2	47.45	1.35	113.0	21.2		10,000	0.952
208	D-996	100	64-22	4.20	9.50	9.28	187.5	5.0	135.2	47.45	1.35	113.0	21.2		15,000	0.942
209	D-996	100	64-22	4.20	9.50	9.28	187.5	5.0	135.2	47.45	1.35	113.0	21.2		20,000	0.934
210	D-999	100	64-22	4.20	9.50	9.47	187.5	5.0	151.9	46.67	1.46	122.1	22.9		5,000	0.977
211	D-999	100	64-22	4.20	9.50	9.47	187.5	5.0	151.9	46.67	1.46	122.1	22.9		10,000	0.977
212	D-999	100	64-22	4.20	9.50	9.47	187.5	5.0	151.9	46.67	1.46	122.1	22.9		15,000	0.977
213	D-999	100	64-22	4.20	9.50	9.47	187.5	5.0	151.9	46.67	1.46	122.1	22.9		20,000	0.976
214	D-9C9	100	64-22	4.20	9.50	8.64	187.5	5.0	145.9	50..02	1.37	122.9	21.9		5,000	0.923
215	D-9C9	100	64-22	4.20	9.50	8.64	187.5	5.0	145.9	50..02	1.37	122.9	21.9		10,000	0.911

216	D-9C9	100	64-22	4.20	9.50	8.64	187.5	5.0	145.9	50..02	1.37	122.9	21.9		15,000	0.904
217	D-9C9	100	64-22	4.20	9.50	8.64	187.5	5.0	145.9	50..02	1.37	122.9	21.9		20,000	0.899
218	D-995	100	64-22	4.20	9.50	9.08	237.5	5.0	132.4	50.69	1.24	103.4	24.5		5,000	0.928
219	D-995	100	64-22	4.20	9.50	9.08	237.5	5.0	132.4	50.69	1.24	103.4	24.5		10,000	0.911
220	D-995	100	64-22	4.20	9.50	9.08	237.5	5.0	132.4	50.69	1.24	103.4	24.5		15,000	0.899
221	D-995	100	64-22	4.20	9.50	9.08	237.5	5.0	132.4	50.69	1.24	103.4	24.5		20,000	0.890
222	D-9A2	100	64-22	4.20	9.50	9.48	237.5	5.0	126.0	48.24	1.21	92.0	21.8		5,000	0.888
223	D-9A2	100	64-22	4.20	9.50	9.48	237.5	5.0	126.0	48.24	1.21	92.0	21.8		10,000	0.870
224	D-9A2	100	64-22	4.20	9.50	9.48	237.5	5.0	126.0	48.24	1.21	92.0	21.8		15,000	0.860
225	D-9A2	100	64-22	4.20	9.50	9.48	237.5	5.0	126.0	48.24	1.21	92.0	21.8		20,000	0.853
226	D-9C7	100	64-22	4.20	9.50	9.35	237.5	5.0	126.3	47.27	1.13	102.6	21.3		5,000	0.937
227	D-9C7	100	64-22	4.20	9.50	9.35	237.5	5.0	126.3	47.27	1.13	102.6	21.3		10,000	0.918
228	D-9C7	100	64-22	4.20	9.50	9.35	237.5	5.0	126.3	47.27	1.13	102.6	21.3		15,000	0.905
229	D-9C7	100	64-22	4.20	9.50	9.35	237.5	5.0	126.3	47.27	1.13	102.6	21.3		20,000	0.894
230	D+996	40	64-22	5.20	9.50	8.84	82.5	5.0	2,009.5	13.08	8.37	1,807.2	149.1		5,000	0.975
231	D+996	40	64-22	5.20	9.50	8.84	82.5	5.0	2,009.5	13.08	8.37	1,807.2	149.1		10,000	0.972
232	D+996	40	64-22	5.20	9.50	8.84	82.5	5.0	2,009.5	13.08	8.37	1,807.2	149.1		15,000	0.969
233	D+996	40	64-22	5.20	9.50	8.84	82.5	5.0	2,009.5	13.08	8.37	1,807.2	149.1		20,000	0.968
234	D+9A0	40	64-22	5.20	9.50	9.06	82.5	5.0	1,616.3	10.55	7.08	1,552.9	128.1		5,000	0.979
235	D+9A0	40	64-22	5.20	9.50	9.06	82.5	5.0	1,616.3	10.55	7.08	1,552.9	128.1		10,000	0.977
236	D+9A0	40	64-22	5.20	9.50	9.06	82.5	5.0	1,616.3	10.55	7.08	1,552.9	128.1		15,000	0.975
237	D+9A0	40	64-22	5.20	9.50	9.06	82.5	5.0	1,616.3	10.55	7.08	1,552.9	128.1		20,000	0.974
238	D+9C0	40	64-22	5.20	9.50	9.32	82.5	5.0	1,427.9	12.31	5.65	1,350.5	119.3		5,000	0.976
239	D+9C0	40	64-22	5.20	9.50	9.32	82.5	5.0	1,427.9	12.31	5.65	1,350.5	119.3		10,000	0.972
240	D+9C0	40	64-22	5.20	9.50	9.32	82.5	5.0	1,427.9	12.31	5.65	1,350.5	119.3		15,000	0.969
241	D+9C0	40	64-22	5.20	9.50	9.32	82.5	5.0	1,427.9	12.31	5.65	1,350.5	119.3		20,000	0.967
242	D+995	40	64-22	5.20	9.50	9.66	112.5	5.0	1,443.9	13.08	5.96	1,336.3	150.3		5,000	0.975
243	D+995	40	64-22	5.20	9.50	9.66	112.5	5.0	1,443.9	13.08	5.96	1,336.3	150.3		10,000	0.968

244	D+995	40	64-22	5.20	9.50	9.66	112.5	5.0	1,443.9	13.08	5.96	1,336.3	150.3		15,000	0.963
245	D+995	40	64-22	5.20	9.50	9.66	112.5	5.0	1,443.9	13.08	5.96	1,336.3	150.3		20,000	0.960
246	D+997	40	64-22	5.20	9.50	9.54	112.5	5.0	1,704.5	10.00	7.10	1,614.1	181.6		5,000	0.957
247	D+997	40	64-22	5.20	9.50	9.54	112.5	5.0	1,704.5	10.00	7.10	1,614.1	181.6		10,000	0.948
248	D+997	40	64-22	5.20	9.50	9.54	112.5	5.0	1,704.5	10.00	7.10	1,614.1	181.6		15,000	0.941
249	D+997	40	64-22	5.20	9.50	9.54	112.5	5.0	1,704.5	10.00	7.10	1,614.1	181.6		20,000	0.936
250	D+9B0	40	64-22	5.20	9.50	8.77	112.5	5.0	1,543.5	12.23	5.98	1,427.1	164.0		5,000	0.941
251	D+9B0	40	64-22	5.20	9.50	8.77	112.5	5.0	1,543.5	12.23	5.98	1,427.1	164.0		10,000	0.931
252	D+9B0	40	64-22	5.20	9.50	8.77	112.5	5.0	1,543.5	12.23	5.98	1,427.1	164.0		15,000	0.925
253	D+9B0	40	64-22	5.20	9.50	8.77	112.5	5.0	1,543.5	12.23	5.98	1,427.1	164.0		20,000	0.921
254	D+991	70	64-22	5.20	9.50	8.73	112.5	5.0	656.7	26.28	3.13	584.1	65.7		5,000	0.958
255	D+991	70	64-22	5.20	9.50	8.73	112.5	5.0	656.7	26.28	3.13	584.1	65.7		10,000	0.950
256	D+991	70	64-22	5.20	9.50	8.73	112.5	5.0	656.7	26.28	3.13	584.1	65.7		15,000	0.944
257	D+991	70	64-22	5.20	9.50	8.73	112.5	5.0	656.7	26.28	3.13	584.1	65.7		20,000	0.940
258	D+992	70	64-22	5.20	9.50	8.97	112.5	5.0	543.3	26.54	2.77	491.4	55.3		5,000	0.960
259	D+992	70	64-22	5.20	9.50	8.97	112.5	5.0	543.3	26.54	2.77	491.4	55.3		10,000	0.951
260	D+992	70	64-22	5.20	9.50	8.97	112.5	5.0	543.3	26.54	2.77	491.4	55.3		15,000	0.945
261	D+992	70	64-22	5.20	9.50	8.97	112.5	5.0	543.3	26.54	2.77	491.4	55.3		20,000	0.940
262	D+9B4	70	64-22	5.20	9.50	9.35	112.5	5.0	570.7	27.69	2.77	501.2	56.0		5,000	0.961
263	D+9B4	70	64-22	5.20	9.50	9.35	112.5	5.0	570.7	27.69	2.77	501.2	56.0		10,000	0.956
264	D+9B4	70	64-22	5.20	9.50	9.35	112.5	5.0	570.7	27.69	2.77	501.2	56.0		15,000	0.952
265	D+9B4	70	64-22	5.20	9.50	9.35	112.5	5.0	570.7	27.69	2.77	501.2	56.0		20,000	0.950
266	D+983	70	64-22	5.20	9.50	9.77	155.0	5.0	606.7	25.46	2.93	494.4	76.6		5,000	0.949
267	D+983	70	64-22	5.20	9.50	9.77	155.0	5.0	606.7	25.46	2.93	494.4	76.6		10,000	0.936
268	D+983	70	64-22	5.20	9.50	9.77	155.0	5.0	606.7	25.46	2.93	494.4	76.6		15,000	0.927
269	D+983	70	64-22	5.20	9.50	9.77	155.0	5.0	606.7	25.46	2.93	494.4	76.6		20,000	0.920
270	D+988	70	64-22	5.20	9.50	8.76	155.0	5.0	782.0	20.20	3.65	676.8	104.9		5,000	0.930
271	D+988	70	64-22	5.20	9.50	8.76	155.0	5.0	782.0	20.20	3.65	676.8	104.9		10,000	0.914

272	D+988	70	64-22	5.20	9.50	8.76	155.0	5.0	782.0	20.20	3.65	676.8	104.9		15,000	0.903
273	D+988	70	64-22	5.20	9.50	8.76	155.0	5.0	782.0	20.20	3.65	676.8	104.9		20,000	0.895
274	D+9B1	70	64-22	5.20	9.50	9.65	155.0	5.0	509.8	27.66	2.53	433.4	65.7		5,000	0.948
275	D+9B1	70	64-22	5.20	9.50	9.65	155.0	5.0	509.8	27.66	2.53	433.4	65.7		10,000	0.932
276	D+9B1	70	64-22	5.20	9.50	9.65	155.0	5.0	509.8	27.66	2.53	433.4	65.7		15,000	0.921
277	D+9B1	70	64-22	5.20	9.50	9.65	155.0	5.0	509.8	27.66	2.53	433.4	65.7		20,000	0.912
278	D+993	100	64-22	5.20	9.50	9.43	342.5	5.0	84.9	54.36	1.20	66.2	22.7		5,000	0.912
279	D+993	100	64-22	5.20	9.50	9.43	342.5	5.0	84.9	54.36	1.20	66.2	22.7		10,000	0.889
280	D+993	100	64-22	5.20	9.50	9.43	342.5	5.0	84.9	54.36	1.20	66.2	22.7		15,000	0.873
281	D+993	100	64-22	5.20	9.50	9.43	342.5	5.0	84.9	54.36	1.20	66.2	22.7		20,000	0.860
282	D+999	100	64-22	5.20	9.50	9.43	342.5	5.0	103.7	52.46	1.27	73.2	25.1		5,000	0.917
283	D+999	100	64-22	5.20	9.50	9.43	342.5	5.0	103.7	52.46	1.27	73.2	25.1		10,000	0.885
284	D+999	100	64-22	5.20	9.50	9.43	342.5	5.0	103.7	52.46	1.27	73.2	25.1		15,000	0.862
285	D+999	100	64-22	5.20	9.50	9.43	342.5	5.0	103.7	52.46	1.27	73.2	25.1		20,000	0.842
286	D+9B8	100	64-22	5.20	9.50	8.98	342.5	5.0	77.6	51.23	1.14	59.3	18.5		5,000	0.874
287	D+9B8	100	64-22	5.20	9.50	8.98	342.5	5.0	77.6	51.23	1.14	59.3	18.5		10,000	0.842
288	D+9B8	100	64-22	5.20	9.50	8.98	342.5	5.0	77.6	51.23	1.14	59.3	18.5		15,000	0.823
289	D+9B8	100	64-22	5.20	9.50	8.98	342.5	5.0	77.6	51.23	1.14	59.3	18.5		20,000	0.810
290	D-484	40	64-22	4.20	4.50	4.11	100.0	5.0	2,928.6	11.17	11.10	2,586.5	261.6		5,000	0.915
291	D-484	40	64-22	4.20	4.50	4.11	100.0	5.0	2,928.6	11.17	11.10	2,586.5	261.6		10,000	0.892
292	D-484	40	64-22	4.20	4.50	4.11	100.0	5.0	2,928.6	11.17	11.10	2,586.5	261.6		15,000	0.876
293	D-484	40	64-22	4.20	4.50	4.11	100.0	5.0	2,928.6	11.17	11.10	2,586.5	261.6		20,000	0.863
294	D-476	100	64-22	4.20	4.50	4.07	195.0	1.0	298.6	39.64	1.97	221.8	41.3		5,000	0.858
295	D-476	100	64-22	4.20	4.50	4.07	195.0	1.0	298.6	39.64	1.97	221.8	41.3		10,000	0.828
296	D-476	100	64-22	4.20	4.50	4.07	195.0	1.0	298.6	39.64	1.97	221.8	41.3		15,000	0.807
297	D-476	100	64-22	4.20	4.50	4.07	195.0	1.0	298.6	39.64	1.97	221.8	41.3		20,000	0.791
298	D-482	100	64-22	4.20	4.50	4.35	195.0	1.0	199.0	47.06	1.37	156.1	26.7		5,000	0.859
299	D-482	100	64-22	4.20	4.50	4.35	195.0	1.0	199.0	47.06	1.37	156.1	26.7		10,000	0.833

312

300	D-482	100	64-22	4.20	4.50	4.35	195.0	1.0	199.0	47.06	1.37	156.1	26.7		15,000	0.816
301	D-482	100	64-22	4.20	4.50	4.35	195.0	1.0	199.0	47.06	1.37	156.1	26.7		20,000	0.803
302	D+478	40	64-22	5.20	4.50	4.33	112.5	10.0	2,456.8	10.77	9.37	2,338.2	261.6		5,000	0.985
303	D+478	40	64-22	5.20	4.50	4.33	112.5	10.0	2,456.8	10.77	9.37	2,338.2	261.6		10,000	0.982
304	D+478	40	64-22	5.20	4.50	4.33	112.5	10.0	2,456.8	10.77	9.37	2,338.2	261.6		15,000	0.979
305	D+478	40	64-22	5.20	4.50	4.33	112.5	10.0	2,456.8	10.77	9.37	2,338.2	261.6		20,000	0.977
306	D+483	40	64-22	5.20	4.50	4.44	112.5	10.0	2,528.3	11.16	9.72	2,277.3	256.9		5,000	0.999
307	D+483	40	64-22	5.20	4.50	4.44	112.5	10.0	2,528.3	11.16	9.72	2,277.3	256.9		10,000	0.999
308	D+483	40	64-22	5.20	4.50	4.44	112.5	10.0	2,528.3	11.16	9.72	2,277.3	256.9		15,000	0.998
309	D+483	40	64-22	5.20	4.50	4.44	112.5	10.0	2,528.3	11.16	9.72	2,277.3	256.9		20,000	0.998
310	D+485	40	64-22	5.20	4.50	4.70	125.0	1.0	2,130.5	10.98	8.47	1,991.3	257.7		5,000	0.911
311	D+485	40	64-22	5.20	4.50	4.70	125.0	1.0	2,130.5	10.98	8.47	1,991.3	257.7		10,000	0.891
312	D+485	40	64-22	5.20	4.50	4.70	125.0	1.0	2,130.5	10.98	8.47	1,991.3	257.7		15,000	0.880
313	D+485	40	64-22	5.20	4.50	4.70	125.0	1.0	2,130.5	10.98	8.47	1,991.3	257.7		20,000	0.871
314	D+472	70	64-22	5.20	4.50	4.24	197.5	1.0	995.2	25.12	4.26	758.5	139.3		5,000	0.862
315	D+472	70	64-22	5.20	4.50	4.24	197.5	1.0	995.2	25.12	4.26	758.5	139.3		10,000	0.837
316	D+472	70	64-22	5.20	4.50	4.24	197.5	1.0	995.2	25.12	4.26	758.5	139.3		15,000	0.822
317	D+472	70	64-22	5.20	4.50	4.24	197.5	1.0	995.2	25.12	4.26	758.5	139.3		20,000	0.811
318	D+475	70	64-22	5.20	4.50	4.18	197.5	1.0	991.3	24.17	4.27	783.8	145.1		5,000	0.831
319	D+475	70	64-22	5.20	4.50	4.18	197.5	1.0	991.3	24.17	4.27	783.8	145.1		10,000	0.797
320	D+475	70	64-22	5.20	4.50	4.18	197.5	1.0	991.3	24.17	4.27	783.8	145.1		15,000	0.778
321	D+475	70	64-22	5.20	4.50	4.18	197.5	1.0	991.3	24.17	4.27	783.8	145.1		20,000	0.750
322	D+474	70	64-22	5.20	4.50	4.24	122.5	10.0	967.5	24.86	4.24	845.6	101.4		5,000	0.963
323	D+474	70	64-22	5.20	4.50	4.24	122.5	10.0	967.5	24.86	4.24	845.6	101.4		10,000	0.955
324	D+474	70	64-22	5.20	4.50	4.24	122.5	10.0	967.5	24.86	4.24	845.6	101.4		15,000	0.950
325	D+474	70	64-22	5.20	4.50	4.24	122.5	10.0	967.5	24.86	4.24	845.6	101.4		20,000	0.946
326	D+479	70	64-22	5.20	4.50	4.17	122.5	10.0	977.0	29.22	4.56	807.9	98.1		5,000	0.964
327	D+479	70	64-22	5.20	4.50	4.17	122.5	10.0	977.0	29.22	4.56	807.9	98.1		10,000	0.956

313

328	D+479	70	64-22	5.20	4.50	4.17	122.5	10.0	977.0	29.22	4.56	807.9	98.1		15,000	0.951
329	D+479	70	64-22	5.20	4.50	4.17	122.5	10.0	977.0	29.22	4.56	807.9	98.1		20,000	0.946
330	D-9B2	40	64-22	4.20	9.50	9.32	62.5	5.0	1,790.5	13.25	7.38	1,699.1	104.7		5,000	0.994
331	D-9B2	40	64-22	4.20	9.50	9.32	62.5	5.0	1,790.5	13.25	7.38	1,699.1	104.7		10,000	0.981
332	D-9B2	40	64-22	4.20	9.50	9.32	62.5	5.0	1,790.5	13.25	7.38	1,699.1	104.7		15,000	0.977
333	D-9B2	40	64-22	4.20	9.50	9.32	62.5	5.0	1,790.5	13.25	7.38	1,699.1	104.7		20,000	0.976
334	D-9B6	40	64-22	4.20	9.50	9.08	62.5	5.0	1,896.4	11.26	7.52	1,759.4	111.8		5,000	0.974
335	D-9B6	40	64-22	4.20	9.50	9.08	62.5	5.0	1,896.4	11.26	7.52	1,759.4	111.8		10,000	0.968
336	D-9B6	40	64-22	4.20	9.50	9.08	62.5	5.0	1,896.4	11.26	7.52	1,759.4	111.8		15,000	0.964
337	D-9B6	40	64-22	4.20	9.50	9.08	62.5	5.0	1,896.4	11.26	7.52	1,759.4	111.8		20,000	0.961
338	D-9B8	40	64-22	4.20	9.50	9.30	80.0	1.0	1,520.3	13.21	6.14	1,369.7	114.6		5,000	0.779
339	D-9B8	40	64-22	4.20	9.50	9.30	80.0	1.0	1,520.3	13.21	6.14	1,369.7	114.6		10,000	0.734
340	D-9B8	40	64-22	4.20	9.50	9.30	80.0	1.0	1,520.3	13.21	6.14	1,369.7	114.6		15,000	0.708
341	D-9B8	40	64-22	4.20	9.50	9.30	80.0	1.0	1,520.3	13.21	6.14	1,369.7	114.6		20,000	0.689
342	D-9C0	40	64-22	4.20	9.50	9.13	80.0	1.0	1,610.5	12.07	6.42	1,497.5	120.0		5,000	0.809
343	D-9C0	40	64-22	4.20	9.50	9.13	80.0	1.0	1,610.5	12.07	6.42	1,497.5	120.0		10,000	0.750
344	D-9C0	40	64-22	4.20	9.50	9.13	80.0	1.0	1,610.5	12.07	6.42	1,497.5	120.0		15,000	0.715
345	D-9C0	40	64-22	4.20	9.50	9.13	80.0	1.0	1,610.5	12.07	6.42	1,497.5	120.0		20,000	0.702
346	D-9A8	70	64-22	4.20	9.50	9.69	115.0	5.0	737.4	23.00	3.46	651.3	76.0		5,000	0.950
347	D-9A8	70	64-22	4.20	9.50	9.69	115.0	5.0	737.4	23.00	3.46	651.3	76.0		10,000	0.938
348	D-9A8	70	64-22	4.20	9.50	9.69	115.0	5.0	737.4	23.00	3.46	651.3	76.0		15,000	0.929
349	D-9A8	70	64-22	4.20	9.50	9.69	115.0	5.0	737.4	23.00	3.46	651.3	76.0		20,000	0.922
350	D-9B0	70	64-22	4.20	9.50	9.76	115.0	5.0	678.1	23.90	3.29	599.3	70.1		5,000	0.957
351	D-9B0	70	64-22	4.20	9.50	9.76	115.0	5.0	678.1	23.90	3.29	599.3	70.1		10,000	0.949
352	D-9B0	70	64-22	4.20	9.50	9.76	115.0	5.0	678.1	23.90	3.29	599.3	70.1		15,000	0.944
353	D-9B0	70	64-22	4.20	9.50	9.76	115.0	5.0	678.1	23.90	3.29	599.3	70.1		20,000	0.940
354	D-9B5	100	64-22	4.20	9.50	9.46	237.5	10.0	122.0	47.36	1.37	98.3	20.8		5,000	0.951
355	D-9B5	100	64-22	4.20	9.50	9.46	237.5	10.0	122.0	47.36	1.37	98.3	20.8		10,000	0.933

356	D-9B5	100	64-22	4.20	9.50	9.46	237.5	10.0	122.0	47.36	1.37	98.3	20.8		15,000	0.920
357	D-9B5	100	64-22	4.20	9.50	9.46	237.5	10.0	122.0	47.36	1.37	98.3	20.8		20,000	0.909
358	D-9C1	100	64-22	4.20	9.50	9.13	237.5	10.0	118.8	46.88	1.34	102.7	21.1		5,000	0.903
359	D-9C1	100	64-22	4.20	9.50	9.13	237.5	10.0	118.8	46.88	1.34	102.7	21.1		10,000	0.882
360	D-9C1	100	64-22	4.20	9.50	9.13	237.5	10.0	118.8	46.88	1.34	102.7	21.1		15,000	0.869
361	D-9C1	100	64-22	4.20	9.50	9.13	237.5	10.0	118.8	46.88	1.34	102.7	21.1		20,000	0.858
362	D+9A5	70	64-22	5.20	9.50	9.35	207.5	1.0	516.2	27.11	2.55	412.2	83.4		5,000	0.852
363	D+9A5	70	64-22	5.20	9.50	9.35	207.5	1.0	516.2	27.11	2.55	412.2	83.4		10,000	0.823
364	D+9A5	70	64-22	5.20	9.50	9.35	207.5	1.0	516.2	27.11	2.55	412.2	83.4		15,000	0.807
365	D+9A5	70	64-22	5.20	9.50	9.35	207.5	1.0	516.2	27.11	2.55	412.2	83.4		20,000	0.795
366	D+997	70	64-22	5.20	9.50	9.54	207.5	1.0	548.2	27.59	2.78	440.2	86.8		5,000	0.826
367	D+997	70	64-22	5.20	9.50	9.54	207.5	1.0	548.2	27.59	2.78	440.2	86.8		10,000	0.791
368	D+997	70	64-22	5.20	9.50	9.54	207.5	1.0	548.2	27.59	2.78	440.2	86.8		15,000	0.771
369	D+997	70	64-22	5.20	9.50	9.54	207.5	1.0	548.2	27.59	2.78	440.2	86.8		20,000	0.757
370	D+9A6	100	64-22	5.20	9.50	9.42	450.0	5.0	82.1	50.96	1.13	56.3	24.0		5,000	0.809
371	D+9A6	100	64-22	5.20	9.50	9.42	450.0	5.0	82.1	50.96	1.13	56.3	24.0		10,000	0.769
372	D+9A6	100	64-22	5.20	9.50	9.42	450.0	5.0	82.1	50.96	1.13	56.3	24.0		15,000	0.745
373	D+9A6	100	64-22	5.20	9.50	9.42	450.0	5.0	82.1	50.96	1.13	56.3	24.0		20,000	0.729
374	D+9A7	100	64-22	5.20	9.50	8.91	450.0	5.0	81.0	49.30	1.21	55.8	23.1		5,000	0.770
375	D+9A7	100	64-22	5.20	9.50	8.91	450.0	5.0	81.0	49.30	1.21	55.8	23.1		10,000	0.723
376	D+9A7	100	64-22	5.20	9.50	8.91	450.0	5.0	81.0	49.30	1.21	55.8	23.1		15,000	0.696
377	D+9A7	100	64-22	5.20	9.50	8.91	450.0	5.0	81.0	49.30	1.21	55.8	23.1		20,000	0.676
378	D+9A8	100	64-22	5.20	9.50	9.06	252.5	1.0	86.4	51.22	1.15	69.3	15.3		5,000	0.858
379	D+9A8	100	64-22	5.20	9.50	9.06	252.5	1.0	86.4	51.22	1.15	69.3	15.3		10,000	0.830
380	D+9A8	100	64-22	5.20	9.50	9.06	252.5	1.0	86.4	51.22	1.15	69.3	15.3		15,000	0.814
381	D+9A8	100	64-22	5.20	9.50	9.06	252.5	1.0	86.4	51.22	1.15	69.3	15.3		20,000	0.802
382	D+9A9	100	64-22	5.20	9.50	9.11	252.5	1.0	93.2	51.05	1.47	67.4	15.4		5,000	0.827
383	D+9A9	100	64-22	5.20	9.50	9.11	252.5	1.0	93.2	51.05	1.47	67.4	15.4		10,000	0.792

315

384	D+9A9	100	64-22	5.20	9.50	9.11	252.5	1.0	93.2	51.05	1.47	67.4	15.4		15,000	0.772
385	D+9A9	100	64-22	5.20	9.50	9.11	252.5	1.0	93.2	51.05	1.47	67.4	15.4		20,000	0.758